Materials Horizons: From Nature to Nanomaterials

Narayanasamy Sabari Arul
Vellalapalayam Devaraj Nithya *Editors*

Revolution of Perovskite

Synthesis, Properties and Applications

Springer

Materials Horizons: From Nature to Nanomaterials

Series Editor

Vijay Kumar Thakur, School of Aerospace, Transport and Manufacturing, Cranfield University, Cranfield, UK

Materials are an indispensable part of human civilization since the inception of life on earth. With the passage of time, innumerable new materials have been explored as well as developed and the search for new innovative materials continues briskly. Keeping in mind the immense perspectives of various classes of materials, this series aims at providing a comprehensive collection of works across the breadth of materials research at cutting-edge interface of materials science with physics, chemistry, biology and engineering.

This series covers a galaxy of materials ranging from natural materials to nanomaterials. Some of the topics include but not limited to: biological materials, biomimetic materials, ceramics, composites, coatings, functional materials, glasses, inorganic materials, inorganic-organic hybrids, metals, membranes, magnetic materials, manufacturing of materials, nanomaterials, organic materials and pigments to name a few. The series provides most timely and comprehensive information on advanced synthesis, processing, characterization, manufacturing and applications in a broad range of interdisciplinary fields in science, engineering and technology.

This series accepts both authored and edited works, including textbooks, monographs, reference works, and professional books. The books in this series will provide a deep insight into the state-of-art of *Materials Horizons* and serve students, academic, government and industrial scientists involved in all aspects of materials research.

More information about this series at http://www.springer.com/series/16122

Narayanasamy Sabari Arul ·
Vellalapalayam Devaraj Nithya
Editors

Revolution of Perovskite

Synthesis, Properties and Applications

Springer

Editors
Narayanasamy Sabari Arul
Department of Chemical
and Biochemical Engineering
Dongguk University
Seoul, Korea (Republic of)

Vellalapalayam Devaraj Nithya
Gobichettipalayam
Tamil Nadu, India

ISSN 2524-5384 ISSN 2524-5392 (electronic)
Materials Horizons: From Nature to Nanomaterials
ISBN 978-981-15-1266-7 ISBN 978-981-15-1267-4 (eBook)
https://doi.org/10.1007/978-981-15-1267-4

This Springer imprint is published by the registered company Springer Nature Singapore Pte Ltd.
The registered company address is: 152 Beach Road, #21-01/04 Gateway East, Singapore 189721, Singapore

Preface

Perovskite oxides are ternary oxides (ABO_3) which consist of two different types of cations A (charge of 2+ or 3+) and are combined with cation B (charge of 4+ or 3+) and combined with O^{2-} anions forming a cubic or pseudo-cubic structure. In the family of perovskites, a great diversity in the combination of different A and B site cations can be found and it leads to a wide range of different physical properties. Perovskite oxide contains the freedom of combining metal, insulators, semiconductors and superconductors. Such combination of different elements in the structural framework of the perovskite unit cell can lead to a slight distortion of the ideally cubic structure. The two most common phases are rhombohedral and tetragonal with structural distortions in the percentage range which are correlated with changes in the physical properties of the material. The different phases and their transitions of perovskites are of great interest with regard to the fabrication of functional materials where researchers would like to utilize external parameters to control the material properties for specific applications.

This book solely focused on the Revolution of Perovskites and deals with the synthesis, properties, and application aspects of these materials. Moreover, the current challenges and future perspectives on the development of perovskites are expansively discussed in this book with the hope that the book will provide a deep insight into the state of the art of recent trends in perovskites. We would like to thank the editorial and production teams at Springer Nature for their help in publishing of this book.

Seoul, South Korea (Republic of) Narayanasamy Sabari Arul
Gobichettipalayam, India Vellalapalayam Devaraj Nithya

Contents

About the Editors

Narayanasamy Sabari Arul received his Ph.D. in Nanoscience and Technology from Bharathiar University, Tamil Nadu, India. His research position includes visiting PhD research fellow at Lunghwa University of Science and Technology, Taiwan and Brain-Korea (BK21) Postdoctoral Fellow at Hanyang University, Seoul, South Korea and Assistant Professor in Dongguk University-Seoul, South Korea. His research interests include synthesis of metal oxide nanocomposites and thin films, nanomaterials, quantum dots, two-dimensional dichalcogenides and perovskites for photocatalysts, photovoltaic cells, memory devices, supercapacitors, and electrochemical sensors. He has published more than 45 SCI journal articles in the field of Materials science multidisciplinary and Nanotechnology along with 20 papers in proceedings of international conferences and holds one US and Korean Patent. Dr. Arul also serves as a referee for various journals in Springer, Elsevier, Royal Society of Chemistry and Institute of Physics.

Vellalapalayam Devaraj Nithya received her Ph.D. in Physics from Bharathiar University, Tamil Nadu, India. She was awarded University gold medal in Bharathiar University for her excellence in M.Sc Physics motivated her to receive INSPIRE junior research fellowship (2010-2012) and INSPIRE senior research fellowship (2012-2014) from the Department of Science and Technology (DST), India. Her research interests mainly focus on metal oxide nanostructures and their applications for energy storage devices with special emphasis on supercapacitors and Li-ion batteries. In her academic carrier, she has published more than 20 peer-reviewed international research articles and also participated and published few national/international conferences proceedings in the field of Materials science, Physics/Chemistry Multidisciplinary.

Chapter 1
Introduction to Perovskites: A Historical Perspective

Luis Ortega-San-Martin

1 Introduction

There is no doubt that compounds with perovskite-like structure are again in the spotlight, especially for their potential applications in solar cells. The efficiency of these materials has grown so fast, and their possibility of reaching the markets seems so close since the photochemical properties of $CH_3NH_3PbI_3$ perovskite were first observed in 2006 by the research group of Tsutomu Miyasaka in Japan [1], that we are now in the middle of a new "perovskite boom" [2]. We probably have to go back to the 1990s to find the last period in which perovskites were so intensively investigated: the "boom" related with their magnetoresistance properties, see Fig. 1. This time, however, the excitement is much bigger and has even surpassed the superconductivity fever of the late 1980s: we are indeed in an explosive era of research the excitement about which has reached a much broader audience [3].

Perovskite-related materials might be new for a younger scientist that starts its Ph.D. in one of the perovskite-related fields but the study of this class of materials dates back to 1839, when the mineral *perovskite* was first described [4]. In fact, the recent perovskite solar cell "boom" is just one of the many that have occurred in the field of perovskite-related materials research (Fig. 1). Despite the incredible amount of literature regarding perovskites, it is hard to find one that has covered the events since the beginning, except for the recent scheme of key developments detailed by Patrick M. Woodward and Anton R. Chakhmouradian [5]. The aim of the present chapter is, consequently, to show the historical evolution of the perovskite research

The original version of this chapter was revised: The text in figure 1 has been amended and the patent number has been included in the references. The correction to this chapter is available at https://doi.org/10.1007/978-981-15-1267-4_12

L. Ortega-San-Martin (✉)
Dpto. Ciencias, Sección Química, Pontificia Universidad Católica del Perú,
Av. Universitaria 1801, L-32, Lima, Peru
e-mail: lortegas@pucp.edu.pe

N. S. Arul and V. D. Nithya (eds.), *Revolution of Perovskite*, Materials Horizons:
From Nature to Nanomaterials, https://doi.org/10.1007/978-981-15-1267-4_1

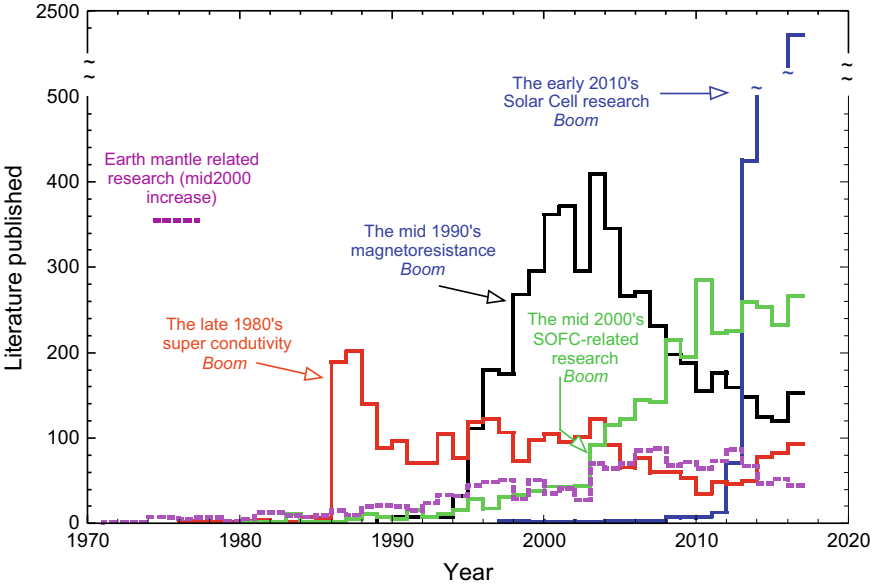

Fig. 1 Amount of literature published from 1970 to 2017 (complete years) on five different perovskite-related research fields that are still active. Data were obtained from SCOPUS database. Notes, erratum, editorials, book reviews, and news were removed from the results

from the nineteen-century mineralogical and crystallographic problem to the present date plethora of potential and real applications of these materials. The present chapter has been focused on how this field grew over time and the problems that researchers faced, especially from the structural analysis of perovskite-type materials which have always been paramount to understand their properties. It is impossible to cover here close to two hundred years of research that has resulted in more than sixty thousand papers and a number of books. In this short historical review is not at all possible to do justice to the many scientists and engineers who contributed to the development of the perovskite world that we know today. Only major highlights have been touched on and, in drawing out these highlights, personal bias has been difficult to avoid. It is expected, however, that the reader forgives the omissions which I hope they be as less as possible.

Given that this chapter will be a historical account, not many crystallographic details on the perovskite and related structures are given. If the reader needs a good compilation and crystallographic details of the perovskite structure, the reference book by Robert H. Mitchel is still the best choice [6]. A well-recommended, textbook-like, work on perovskites is the one by Richard J. D. Tilley [7]. A more specialized compilation on the different perovskite properties is the one edited by Pascal Granger and colleagues [8].

For a more up to date work, the present book would be an excellent choice. If the objective is to know how this vast field of research started, the present chapter might be a good start.

2 Working Nearly Blind: Discovery and Problems Establishing Perovskite Mineral's Crystal System (1839–1925)

The discovery of the mineral perovskite is closely related to the famous scientific journey through the Asian part of Russia carried out by Alexander von Humboldt and fully funded by Tsar Nicholas I. The journey covered around 15000 km, from May to December 1829, with the aims of increasing geological, geographical, and biological knowledge of the vast Russian region. Humboldt was a well-known expert in geography so he invited to join the trip two of the best known German scientist of the time in the other two fields he did not master: Christian Gottfried Ehrenberg for the biological part and Gustav Rose as the expert in geology and mineralogy.

Gustav Rose's responsibilities in the journey included, among others, the chemical analyses of potentially new minerals that were to be discovered either in the field or in public and private mineral collections along the country, the analysis of the Caspian Sea waters and the microscopic examinations of sands and rocks in mines and mineral deposits of the Urals in order to detect the presence of diamonds, one of the greatest commodities of the time. Rose was also in charge of writing the expedition's diary, which was published in two parts, one in 1837 and the other one in 1849 [9]. The scientific papers related to his discoveries would appear during the 20 years after the trip (1829–1849).

Among the private collections that Rose visited the one of August Kämmerer, the chief of the Mining Pharmacy of Saint Petersburg, who also was an ardent mineral collector, is of special interest [9]. In 1839, Kämmerer, who became friends with Rose after the trip, sent a piece of rock collected in the Ural Mountains to the latter's laboratory at the University of Berlin (now Humboldt University). The Russian asked Rose to examine few strange crystals of what he suspected that could be a new mineral. After the examination, Gustav Rose confirmed that the crystals belonged to a new mineral with cubic symmetry, composed of calcium and titanium oxides. As suggested by Kämmerer, Rose accepted that the new mineral be named to honor Count Lev Alekseevich von Perovskiy, a well-known aristocrat and mineral collector that would later be an active political member of the Russian government, serving as Minister of the Interior between 1841 and 1852 [4, 10].

Although Gustav Rose was the first to make public the description of the new mineral he did not determine its exact chemical composition. It would be his brother, Heinrich, in 1844, the one who fully analyzed and deduced the actual chemical composition ($CaTiO_3$) which was then given as a mixture of oxides, $CaO{\cdot}TiO_2$, as it was customary in this time. A more detailed description of the crystal morphology and crystal system (supported by the first drawings, Fig. 2) of the mineral would be given the next year, in 1845, by Alfred Des Cloizeaux, a well-known French mineralogist of the time who concluded that Rose's initial description of the crystals as being cubic was correct [11].

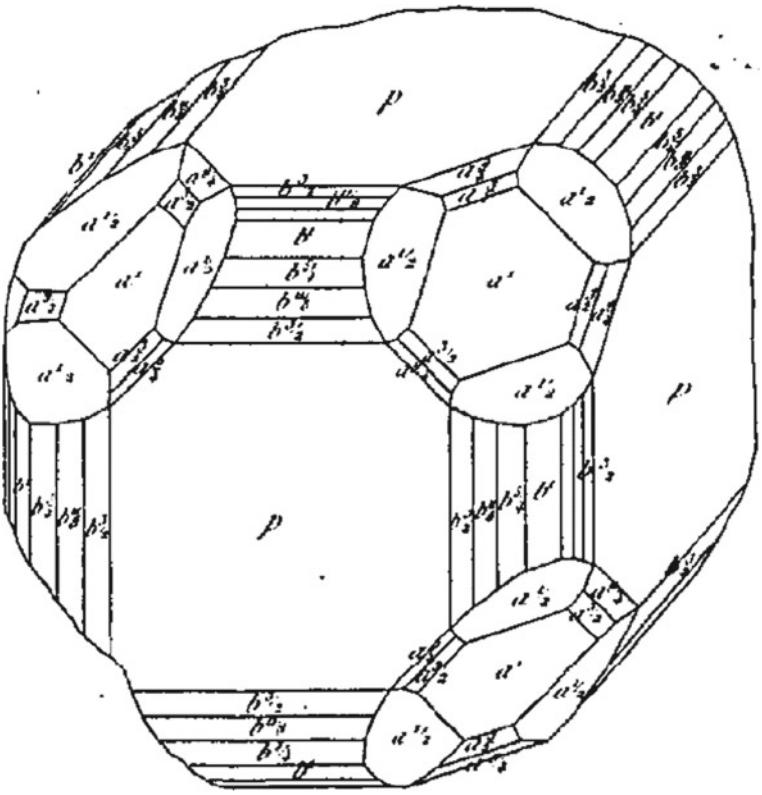

Fig. 2 Drawing of one perovskite mineral crystal collected in the Ural Mountains and studied by Des Cloizeaux in 1844. Letters refer to the different crystal forms that could be identified in perovskite, all of them belonging to the cubic crystal system according to Descloizeaux. Reproduced from Des Cloizeaux, *Ann. Chim. Phys.,* **1845**. *3(13).* 338–42. Plate II, under the terms of the Bibliothèque Nationale de France, gallica.bnf.fr/

Soon afterward, *perovskite* crystals were discovered in rocks coming from other European regions [12] and even artificial crystals were grown in different French laboratories [13, 14], attracting an increasing number of the scientist to the study of this mineral; in fact, a "perovskite" mineral entry was soon added to every mineralogy manual of the time [15–17].

Des Cloizeaux was an enthusiast mineralogist who continued studying new minerals and specialized in their optical properties. A few years after his initial analysis of the *perovskite* crystals from the Ural Mountains, he examined new samples from Switzerland and found that they showed birefringence, an optical property not compatible with cubic crystals but common in crystals of lower symmetry [18, 19]. This observation seems reasonable now that we know that perovskite mineral belongs to the orthorhombic system [20], but that proposal was not accepted by most of his colleagues [21]. The majority of the mineralogists of

the time were not acquainted with the optical properties of minerals so, in order to deduce their crystal system, the only available instruments that they trusted were optical microscopes and, by that time, even the most careful visual inspection of the crystal forms always conducted to the same result: there were no deviations in the crystal forms that deserved a symmetry reduction from the cubic system.

The matter was not a trivial one because, in the nineteenth century, two characteristics of a mineral were needed in order to be properly classified and accepted as valid. One of such properties was the chemical composition and the other was its crystal system [22]. Consequently, after Des Cloizeaux proposal, an interesting, sometimes not polite, and seemingly endless discussion started, and it was not until more than 60 years later, in 1912, when Ove Balthasar Böggild, from the University of Copenhagen, finished this first wave of discussion. In the meantime, most of the best crystallographers and mineralogist of the nineteenth century weighed in the discussion [23]. Probably, the most interesting moment being the dispute between Heinrich Adolf Baumhauer and Alfredo Bensaude. The former was a known crystallographer who became the first to use the etching method on perovskite crystals in order to analyze the symmetry of the resulting etched figures from which he found complete agreement with Des Cloizeaux conclusions: perovskite crystals were orthorhombic [24]. Bensaude, on the other hand, was a younger engineer who had just got his Ph.D. at the University of Gottingen studying perovskite crystals. In this thesis, he criticized the validity of the etching technique even when his own experiments corroborated Baumhauer's work. Although it was finally known that the dispute was a result of a misunderstanding due to printing problems in Baumhauer's work [25], this dispute delayed the solution of the *perovskite's* crystal system problem and demonstrated how difficult these mineral's crystals were to study. The conundrum was only resolved at the beginning of the new century, thanks to the works of Bowman [21] and, finally, the one by Böggild [26]. Bowman's work is remarkable because he had to improve the goniometers of the time in order to tackle the problems presented with *perovskite* crystals [27]. The relevance of Böggild's work, on the other hand, resides on his critical review of all previous data and his own work from which he concluded that $CaTiO_3$ mineral had to be orthorhombic. He also proposed a crystallographic axial ratio of 0.9881:1:1.4078, which is, in fact, extremely close to what can be found nowadays using X-ray diffraction data.

3 Let There Be Light: The X-Ray Time and the Proposition of a Structure for the Mineral *Perovskite*. (1925–1950s)

By the time that Böggild presented his results, in 1912, an enormous breakthrough in science, and particularly in crystallography, had just happened: the discovery of the X-rays and, more importantly, the discovery of the diffraction of X-rays by the

matter. Chemists, physicist, mineralogist, and material scientists in general were provided with a tool for the direct investigation of the internal structure of the crystals.

Contrary to all expectations, when this revolutionary technique was first applied to the *perovskite* crystals, the controversy with its crystal system resurrected and, again, a new, sometimes bitter, debate started among researchers. The first X-ray studies of *perovskite* crystals were independently made in 1925 by two different groups. One was based in Italy, at the Politecnico di Milano, where the experiments would be carried out by Giorgo Renato Levi and his student, the future 1963 Chemistry Nobel Prize winner, Giulio Natta [28]. The other group was from Norway, and it was based at the University of Oslo, led by Victor Moritz Goldschmidt. The first paper to be published was the report by Thomas Barth [29], one of the members of the second group, a very well organized team whose studies would later bring crystal chemistry to one of its brightest moments.

Both groups worked without knowing each other's existence but they deduced the same basic arrangement of the atoms in *perovskite's* crystals: the proposed structure was represented by a cube with calcium lying at the cube's center, titanium at the origin of the cube (cell corners), and oxygen atoms at the center of each face (Fig. 3).

Both groups felt some disappointment when they realized that the X-ray data indicated a cubic structure given that, from the previous 70 years of research, it had been concluded that *perovskite* crystals were orthorhombic. What had just happened? Doubts were initially focused on the technique, which was considered less sensitive to the true symmetry of the crystals than optical or etching experiments. Was it possible to reconcile the axis ratios determined by Böggild (*a*:*b*:*c* being 0.9881:1:1.4078).) with the cubic structure just proposed? Barth realized that those ratios were obtained if the unit cell of perovskite was constructed using the cube

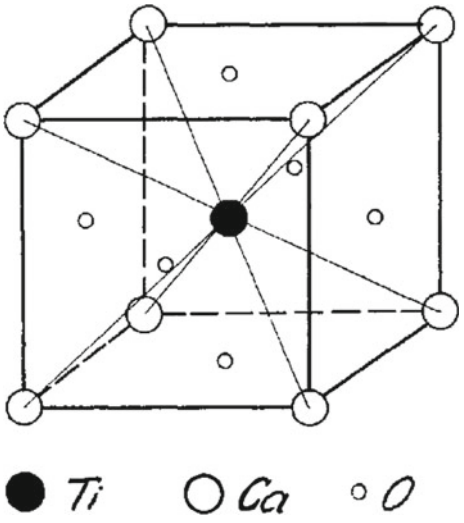

Fig. 3 The basic structural arrangement of the atoms in the mineral *perovskite* as it was shown by Thomas Barth in 1925. Atomic positions were given as Ca = 0, 0, 0; Ti = ½, ½, ½; O1 = ½, ½, 0; O2 = ½, 0, ½; O3 = 0, ½, ½. Reproduced from page 206 of Barth, T.F.W.: *Norsk Geol Tidsskr*, **1925**, *8*. 201–216 (License under CC BY 4.0. https://njg.geologi.no/vol-1-20/details/24/1002-1002). Link for the license: https://creativecommons.org/licenses/by/4.0/

diagonals as cell edges and doubling the perpendicular axis (given that the cubic cell was determined as $a = 3.795$ Å, the resulting cell parameters should be $a = 5.367$, $b = 5.367$, and $c = 7.59$ Å, in good agreement with Böggild's deductions). For this cell to be correct, however, the X-ray patterns should have shown some extra spots that Barth did not observe although Levi and Natta were unsure of their presence. *Perovskite* crystal system was again inconclusive: cubic or pseudocubic (Monoclinic?).

A few years later, it would be the German Otto Zedlitz, from the University of Tübingen, who picked up the thread of these inconclusive works [30, 31]. He was decided to finish once and for all with all the inconsistencies observed in the literature published during the last… 100 years! In his 1936 paper, however, he soon realized that the task of solving the structure and the crystal system of the mineral *perovskite* was trickier than expected [30]. Consequently, he devoted the next 3 years to study some natural specimens together with synthetic *perovskite* samples that he grew. This work was so long and contained so many figures that the author had to reduce their number in order to meet the publishers' policy. The paper is a detailed account of the morphology, chemical, and optical properties of the mineral together with X-ray diffraction data [31]. Surprisingly, Zedlitz started describing previous works as coming from just beginners, especially those of Barth and Levi and Natta in 1925, and decided to start the crystallographic study from the very beginning: measuring crystal faces and angles in order to deduce the crystal system. Nevertheless, he found himself in the same situation than his predecessors: the task of proposing a crystal system of *perovskite* only from goniometric measurements was extremely difficult because the crystals looked like cubic but some stripes and crystal sections did not obey cubic laws. Would optical measurements or etching experiments help? Not, apparently, for he did not completely trust any of them: after performing several optical measurements and various etching experiments with different solvents, he concluded that none of them were reliable enough to solve the symmetry problem of *perovskite*. He finally concentrated on the X-ray diffraction. But this task was not easy, either. Perovskite crystals were not X-ray friendly for they contained too many imperfections and stripes (Fig. 4). From all his measurements, he was only able to say that *perovskite's* crystal structure wasn't cubic. He was also unable to find any systematics in the twining laws and had to consider as valid those that Bowman had proposed 30 years before by means of optical and etching methods. He finally proposed a monoclinic unit cell which he did not manage to reconcile with Böggild axis ratios and was, essentially, the same unit cell that Levi and Natta had proposed, with a $\sim$ b $\sim$ c $\sim$ 7,6 Å.

It was clear that the structure of *perovskite* had to be a distorted version of the ideal one proposed by Barth in 1925. However, the cause of the distortion eluded researchers until 1943, when the Hungarian crystallographer István Náray-Szabó, of the University of Technical Science of Budapest, proposed a plausible explanation from his study of single crystals from the National Museum of Hungary. In order to illustrate his idea, he came up with a representation of the perovskite structure that has become the standard in the field (see Fig. 5a): according to his vision, *perovskite's* structure should be considered as composed of a three-dimensional

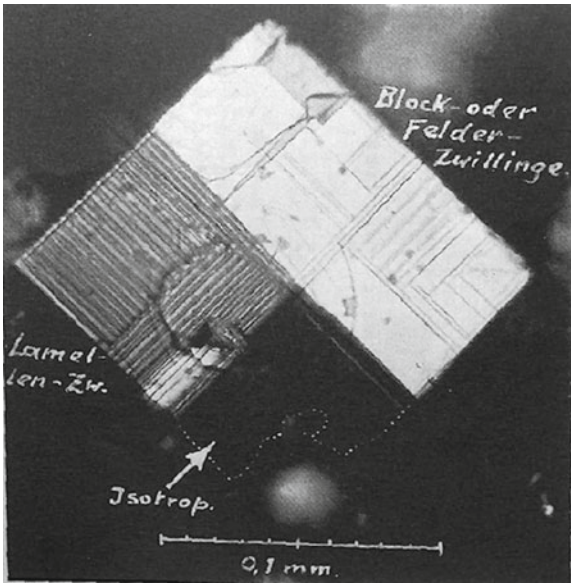

Fig. 4 Microscopic photograph of a synthetic $CaTiO_3$ *perovskite* crystal showing its characteristic striated shape that so much hampered early works. Image from *Plate XII, Fig. 2* as it appeared in Zedlitz, O.: Der Perowskit. Mineralogische und röntgenographische Untersuchungen an Perowskit, Uhligit und Dysanalyt sowie an deren synthetischen Produkten. *Neues Jahrb. Mineral., Geol., Beilage Bd. A,* **1939**. *75*. 245–96. Reproduced with permission from Schweizerbart Science Publishers

arrangement of corner-sharing TiO_6 octahedra with Ca occupying the resulting dodecahedral voids. If such a picture was made, the needed distortion from cubic symmetry would come from the tilting of those octahedra, in other words, from the deviation of the oxygen atoms from their ideal cubic positions (see Fig. 5b) [32]. This idea, missed for years, was crucial and is still correct although Náray-Szabó

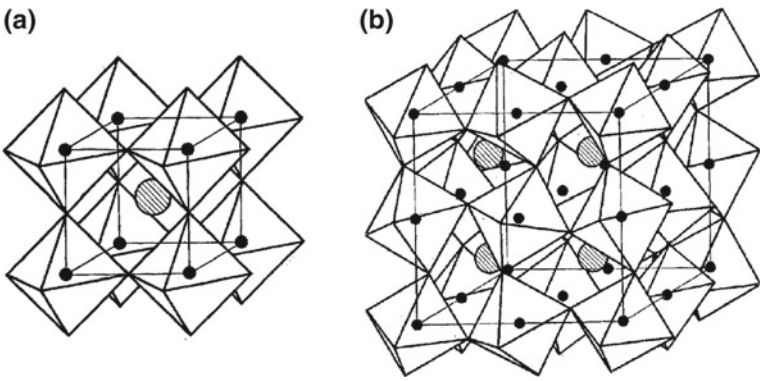

Fig. 5 Polyedron sketches of the *perovskite's* structure suggested by Náray-Szabó in 1943. **a** ideal cubic crystal structure; **b** the structural distortion as a result of the oxygen displacement. The proposed unit cell (space group $P2_1/m$, #11), was a ∼ b ∼ c ∼ 7.60 Å, β ∼ 90º, Z = 8. Sixteen independent atomic coordinates were needed to generate the structure. Reprinted by permission from Springer Nature, *Naturwissenschaften*, *31*. 202–203, Der Strukturtyp des Perowskits ($CaTiO_3$), I. Náray-Szabó. © 1943

did not correctly find the appropriate space group and stick to the monoclinic unit cell with a pseudocubic parameter of ~7.6Å, as proposed by his predecessors [31, 33]. His findings, however, were not very well received by Zedlitz who strongly criticized them for being… nonoriginal [34]! This unfair critic probably came from the fact that Náray-Szabó did not cite any of Zedlitz's works in which he had also attempted to draw the *perovskite* structure using a TiO_6 octahedron but had failed in finding the origin of the distortion. Whether the former was aware of the latter's papers or if they were intentionally not cited is not known.

A subsequent work by the outstanding English crystallographer Helen Dick Megaw, the first woman working in *perovskite* issues to that date, would prove that Náray-Szabó had slightly underestimated *Perovskite's* symmetry. Her work came in a time when other oxides which also showed a crystal structure similar to the mineral *perovskite* where being investigated by hundreds of researchers around the world for their recently discovered ferroelectric properties. The close dependence of these properties and the exact atomic structure encouraged the crystallographic studies of this type of compounds in the mid of the 1940s and later [35]. Megaw's participation was, consequently, very important and her work would later become a reference for anyone working on perovskite-type compounds. Being at that time the Assistant Director of Research in Crystallography at Birkbeck College (University of London), she prepared, among other compounds, synthetic $CaTiO_3$ samples and studied them using X-ray diffraction [36]. Megaw concluded that an orthorhombic space group could account for all the observed reflections without the need of reducing the symmetry to the monoclinic system. The orthorhombic description, first proposed in 1845, was back again. Due to the poor resolution of the powder diffraction instruments of the time, she proposed to still consider a unit cell with all parameters doubled although she knew that this would change when the X-ray detectors improved.

The scientific community would have to wait 10 more years to finally prove Megaw's findings and suggestions. The final structural model, and the end of the long saga of incorrect proposals would arrive in 1957, more than 100 years after *perovskite* discovery. This was when Kay and Bailey published their thesis results on synthetic and natural *perovskite* specimens. With some minor corrections, their structure proposal is still assumed as correct. They recognized that the task had not been easy for the preceding researchers, and neither for themselves, due to the omnipresent twining in most of the specimens [20]. As previous researchers, Kay and Bailey prepared synthetic *perovskite* samples to be compared with several natural specimens. They observed that synthetic and natural specimens were equally difficult to study but managed to find a suitable crystal for single-crystal X-ray diffraction. After careful examination of the data, they concluded that an orthorhombic unit cell was adequate for indexing the data. The proposed structure, showing the displacements of the atoms from their ideal positions, is depicted in Fig. 6 (unit cell parameters and coordinates are also included).

The crystal structure suggested by Kay and Bailey has been revised several times since their original publication but no important changes have been introduced apart from a change of the setting in the space group, the most accepted one now being

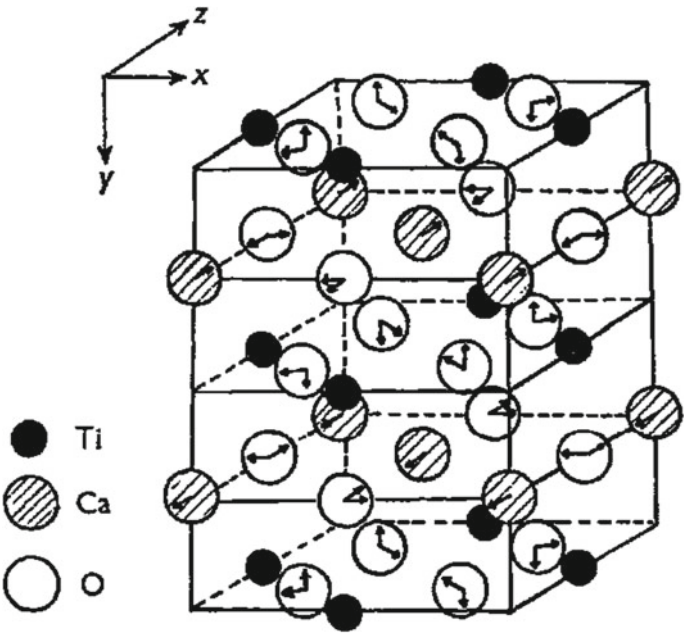

Fig. 6 Crystal structure of the mineral *perovskite* according with Kay and Bailey. Arrows inside each atom indicate their displacement from the ideal positions. The proposed unit cell in *Pcmn* space group (#62) was a = 5.3670(1)Å, b = 7.6438(1)Å, c = 5.4439(1)Å, β = 90.48º, Z = 4; with the following fractional coordinates: Ca = 0, ¼, 0.03; Ti = ½, 0, 0; O1 = 0.463, ¼, −0.018; O2 = 0.232, −0.26, 0.232. Reproduced with permission of the International Union of Crystallography from Kay and Bailey: *Acta Crystallogr*, **1957**, *10*, 219–226

Pbnm (a nonconventional setting of *Pnma*, #62) [37]. The majority of the single-crystal X-ray determinations and neutron diffraction measurements that would be carried out in the next 30 years were performed mostly on synthetic $CaTiO_3$ crystals. Detailed and definitive single-crystal studies on natural samples had to wait until the end of the 1990s [38, 39]. Most of the twinning laws were also completely determined by that decade. Modern techniques demonstrated that those laws had been correctly addressed by some of the earliest workers, such as Bowman in 1908 or even Kay and Bailey in 1957, although others were only determined after the use of modern techniques such as transmission electron microscopy (TEM).

The identification of most of the defects affecting the structure that so much had exasperated early researchers was also concluded in this period. Their complexity was finally demonstrated by a multicultural group of geologists from the University of California (USA) [40]. No wonder why nineteenth and the first half of the twentieth century's researchers had so many problems. "*Perovskites have the habit of doing the unexpected*", would someday say the British crystallographer Mike Glazer [41].

In any case, by the time Kay and Bay unambiguously determined *perovskite's* crystal structure, the number of synthetic compounds found to crystallize in the same type of structure was so high, that the word "perovskite" no longer remained associated to the mineral itself but to its crystal structure type. This change took place in the 1920s, when the group of the University of Oslo led by Victor Goldschmidt started a systematic study of the crystal structure of most of the known minerals and inorganic compounds of that time.

4 Perovskite Structure Enters in the Field of Materials Chemistry (1930–1950s)

World War I is usually remembered as the first major conflict in which chemical weapons were used at a great scale [42]. After the war, both participating and nonparticipating countries realized how important was the chemical industry in their economies and, more importantly, for their chances of victory in the event of a major conflict. When the war finished, Governments tried to gain knowledge and control of all the raw materials that could be exploited in their countries in order to be used in chemical industries. This also started a policy of taxes on chemicals and raw materials in order to favor own industries.

During WWI, Norway was a major exporter of calcium carbide (used to produce acetylene for welding metals, especially those used for the weapon industry) and the United Kingdom an important buyer. After the war, the United Kingdom established a new tax on the import of organic chemicals and included calcium carbide among them, putting at risk the Norwegian economy. This caused a lawsuit between both governments because the later did not agree that the carbide should be considered an organic chemical but rather an inorganic one.

Victor Moritz Goldschmidt, a well-known petrologist who was then the head of the Raw Materials Institute in Oslo and enjoyed great confidence from the Norwegian government [43], was chosen to support Norway's interests in the lawsuit. Goldschmidt proved to the British authorities that calcium carbide was a salt on the basis of its crystal structure so its tax was removed. In recognition, the Norwegian government equipped Goldschmidt's laboratory with an X-ray diffractometer with which he started a revolution in the field of crystal chemistry that would also lay the foundations of materials chemistry [44].

Thanks to this new instrument, he and his working group (which included who later would be well-known crystallographers and crystallochemists such as Thomas F. W. Barth, Gulbrand O. J. Lunde, Ivar W. Oftedal, and F. William Houlder Zachariasen) started studying the geochemical distribution and technical properties of economically important raw materials. By 1926, they had elucidated and rationalized the structure of at least 200 compounds of most of the known elements. Several AMO_3 oxides were among those compounds studied. To explain the different structures found in all those oxides, Goldschmidt's group adopted and

greatly expanded, the idea of the radius ratios between ions that had been proposed few years earlier by Gustav F. Hüttig for coordination compounds [45]. Using this idea, they were able to classify into different structure types most of the $A_aM_mO_x$ oxides known. This was a groundbreaking idea that is still in use nowadays. For the AMO_3 compound, this translated into the already well-known tolerance factor, t, given in Eq. 1 [46]:

$$t = \frac{r_B + r_X}{\sqrt{2}(r_B + r_X)} \tag{1}$$

Depending on the ***t*** values, they found that the crystal structures of the AMO_3 oxides could be classified into few distinct groups. On the basis of powder patterns, they found that these oxides adopted the same crystal structure that had just been found in the mineral *perovskite* if the tolerance factor was between 0.8 and 1. From now on, the name "perovskite" would be used both for the mineral itself and its structure type. It is to be noted that Goldschmidt group did not bother whether the actual symmetry was cubic of or lower symmetry.

The results of their investigation were published from 1922 to 1926 in a series of nine monographs under the common title "*Geochemische Verteilungsgesetz der elemente"* (Geochemical Laws of Distribution of the Elements), a classic work that is considered as the start of the new field of *crystal chemistry*. Soon after this important work, it would be William Zachariasen who expanded the data of all known AMO_3 oxides. Working under the supervision of Goldschmidt and later with the 1915 Physics Nobel Prize W.H.L. Bragg (during a short stay in Manchester), Zachariasen classified these oxides into four groups on the basis of their B-site coordination and on the r_B/r_O and r_A/r_O ratios (Fig. 7). He also improved the initial field of existence of perovskites narrowing their tolerance factor to $0.9 \leq \boldsymbol{t} \leq 1.1$ [47].

A similar but less thorough work, which passed almost unnoticed, was carried out by the group of the future 1963 Chemistry Nobel Prize Giulio Natta. This new study was focused on ABX_3 halides (X being F, Br, and Cl) instead of oxides [48–50]. Their work was very interesting because they demonstrated that the

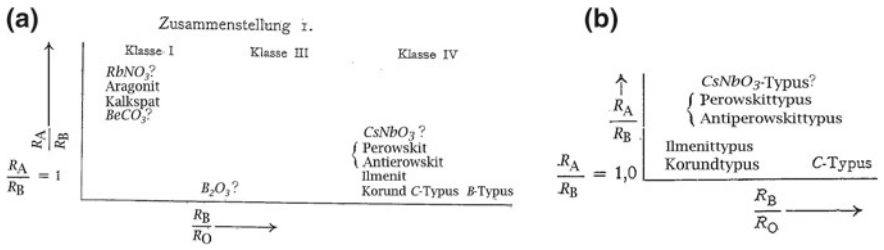

Fig. 7 First detailed classification of ABO_3 oxides according to the radius rations of their components deduced by W. H. Zachariasen in 1928. **b** is a magnification of the perovskite region shown in (**a**). Reproduced from Ref. [47] (Permission pending)

structure of the mineral *perovskite* could also be observed in ABX_3 compounds regardless of the nature of the X atom and provided that the tolerance factor described by Goldschmidt was between certain limits that they also found to be around 0.8 and 1.

These works boosted the research into ABX_3 compounds. By the end of the 1930s, more than 40 different element combinations were known to have a perovskite-type structure and it would not take long for the numbers to double [51]. Soon it became evident that this type of structure was quite versatile and capable to accommodate any type of ion regardless of its nature and oxidation state. First books on the newly created field of crystal chemistry, as the one by Robert Evans [52], drew the attention to this point: "(…) *it appears that this* [the oxidation state of an ion] *is a matter of only secondary importance and any pair of ions, provided they have radii appropriate to the co-ordination and an aggregate valency of 6 to confer electrical neutrality on the structure*" can adopt the perovskite-type structure.

The increase of compounds that were classified as having the perovskite structure came parallel to the improvements of the X-ray techniques and this posted a new problem. The structural model associated with the mineral *perovskite*, which was also taken as a reference or ideal model for similar compounds, was cubic but the mineral was orthorhombic. Moreover, crystallographers and chemists working on ABX_3 compounds increasingly realized that the X-ray diffraction patterns of most of them were, indeed, not cubic. Consequently, the appropriateness of the name "perovskite" for such compounds was put in doubt: if the mineral perovskite was not cubic, its name should not be used for cubic structures. This discussion seems superfluous now but it wasn't in the 1920 and 1930s. Several groups entered the discussion and criticized the sloppiness of Goldschmidt group for not focusing their attention on the hidden the details of the diffraction patterns but on the general tendencies. With their instruments, Goldschmidt's group recognized that, while some compounds, such as $SrTiO_3$, were strictly cubic, others showed clear indications of lower symmetry. However, they were not interested in the subtleties as their main interest was to know the laws that governed the adoption of the different types of arrangements among the hundreds of existing compounds and minerals. Perovskite as a structural group seemed to be suitable.

Symmetry played such an important role in classifying substances (similar structures having different symmetries tended to be grouped separately) that a group of well-known crystallographers of the time, including Giulio Natta, proposed that the cubic "perovskite" compounds should be renamed after a cubic compound with the ideal perovskite structure. In 1928, Natta and his group of the Politecnico di Milano [49] proposed "caesium trichrolo mercuriate, $CsHgCl_3$" as the name for the cubic arrangement because its structure, solved by his group, was cubic [48]. Luckily, this did not gain any adepts because it would had been unfair given that the first cubic perovskite described had been that of $KMgF_3$, discovered and published in 1925, at the same time that the structure of the mineral *perovskite* was published [53]. Another important crystallographer of the time, Ralph Wyckoff, joined the discussion at the beginning of the 1930s in one of his first (later indispensable) monographs on crystal structures [54]. Wyckoff not only disagreed with the fact

that perovskite structural model had been classified within the E_{21} group of cubic structures in *Strukturbericht* ("Structural Reports"), the reference work on crystal structures of the time, but with all previous crystallographers for choosing this structure model for all ABX_3 compounds irrespective of their symmetry ("*From a formal standpoint the studies upon which this choice of structure is based leave much to be desired*" he would say). In 1934, Waldbauer and McCan while studying compounds such as $NaNbO_3$, which had been classified as having a perovskite structure, came with new proposals: option one, use the name "*perovskite structure" "only for the mineral perovskite; option two discontinue the use of the name or, option three use the term 'perovskite pattern' for pseudo-cubic powder diffraction patterns"* [55].

By this time, this discussion had already crossed the field of crystal chemistry and was truly a material's chemistry problem for it is in this decade that the first "perovskite" oxides were brought to market as white and yellowish-white pigments. The first commercially available pigment would be Lead titanate, $PbTiO_3$ (commercialized as Titanox L in the USA), although the first patents of an ABO_3 compound for its use as a pigment were for $CaTiO_3$, the artificial version of the mineral. The first application was filed in Norway by Victor M. Goldschmidt and Reidar Nielsen and assigned to the Titan A/S Company of Christiania (now Oslo) [56, 57]. Their international applications, filed at the US-Patent Office the same year, would be granted at the beginning of the 1920s. Barium titanate ($BaTiO_3$) and lead titanate ($PbTiO_3$) patents came soon after the calcium titanate ones. The lead compound, initially developed by the Titanium Pigment Company in the United States, was the only one that reached the European and American markets and was classified as pigment yellow 47. It gained extensive use in Europe in the 1940s and 1950s [58–60] but was later banned for the toxicity associated with its lead content.

Going back to the previous discussion (the suitability of the "perovskite" term), the annoying fact (at least for some crystallographers and chemists) was that the term "perovskite structure" had been applied, without distinction, to cubic and non-cubic ABX_3 compounds. So now… What should be the name for distorted phases? Which one should be used for the cubic compounds? Which group would retain the name of perovskite? None? Both? Some crystallographers did not propose alternatives but noted the incongruency, such as Otto Zedlitz in 1936 and in all of his later works [34], but others went further, as Cole and Espenschied [61]. The latter were studying $PbTiO_3$ for the pigment industry and found that despite this oxide had a tolerance factor within the range of the perovskite structure its powder diffraction pattern was neither cubic nor similar to other distorted phases. What should be done in this case? Was the tolerance factor an accurate way of predicting structures? Could it be that this oxide had a new and more distorted perovskite structure than all previous compounds? Those questions crossed their minds but, after deliberation, they proposed that the last option would probably be the correct one but they weren't very convinced.

Those genuine concerns were creating a sense of discomfort among researchers until, again, the Hungarian Itsván Náray-Szabó proposed a reasonable solution to the conflicting views in 1943. He had recognized that the name perovskite was

being used for many ABX_3 compounds that did not show the ideal structure. He even realized that there were more distorted compounds than samples showing the ideal structure. Revisiting Cole and Espenschied's work on $PbTiO_3$ he confirmed that its lattice distortion was different than the usually found in other "distorted" perovskites. However, instead of disproving the perovskite name for all those compounds he decided to classify them into different subgroups and proposed the concept of "*sister structures*" (*Schwesterstrukturen* in the original German) [62, 63]. Náray-Szabó grouped all known perovskite-like compounds within this supergroup. Within these sister structures, he not only included all ABX_3 compounds (X being oxygen or a halide ion, irrespective of their distortion with respect to an idealized cubic structure) but went further and included compounds with BX_3 formula, such as ReO_3 and ScF_3, with different degrees of distortion. The reason behind this inclusion was his revolutionary way of picturing the perovskite structure: "*A common property of compounds belonging to the perovskite family is that their lattice is based on an endless three dimensional net of octahedra with the composition BX_3; the octahedra are connected by shared corners*" [63]. According to this perspective, BX_3 compounds were no other thing but perovskites with a vacant place in the A-site. With this simple conception of the perovskite structure, there was no need to debate whether a distorted phase was or wasn't a perovskite: if it was composed of corner-shared octahedra, it would be classified as a perovskite sister structure.

It is to note, however, that Náray-Szabó was not the first to notice that BX_3 compounds could be considered as ABX_3 perovskites with the A-site empty. This had already been noticed by Gunnar Hägg while studying the interesting color changes of the tungsten bronzes (Na_xWO_3 phases): as the sodium atom leaves the structure and tungsten ions reduce from W^{6+} to W^{5+}, they show a surprising variability of colors [64, 65]. The perovskite nature of the parent phase ($NaWO_3$) had been proposed few years before [66] but Hägg realized that this structure did not collapse even if a fair amount of sodium was removed from the formula meaning that the perovskite structure type could be extended to compounds without A-cations. Robert Evans mentioned this in his crystal chemistry book but, apparently, did not gain much attention and no other group realized of the importance of this observation [52]. Consequently, it is fair to credit Naray-Szabó as the one who put order in the field.

Naray-Szabó's concept of Sister Structures was readily accepted although some concerns existed around the suitability of the term "sister". Harold Pierce Rooksby, for example, favored the term "*pseudo-isomorphous*" [67], but the debate did not last long and was ended, again, by Helen Megaw [36]. Although she favored the term "homotypic" over "*pseudo-isomorphous*" and the term *ideal perovskite type* (she would later use "aristotype") for the undistorted phase: "*It seems convenient to define the term 'perovskite type' to include all structures which retain a pseudo-cell derived from that of the ideal cubic structure E_{21} by small distortions either of cell edge or of interaxial angle.*" She also considered that the cubic structure could be referred to as the "*ideal perovskite type,*" as it is customary nowadays. Although it seemed the closing of the debate, the appropriateness of the naming was resurrected

again in the 1970s by Muller and Roy [68] who preferred to use the term "[perovskite] structure" when referring to the structure and just "perovskite" when the actual mineral is mentioned. The latter did not gain much attention and Megaw's proposal is usually applied.

The rationalization of the distortions observed in "simple perovskites" would come later (at the beginning of the 1970s) as a result of the intense work carried out by Megaw and his postdoc student, Mike Glazer. A very recent, first-hand account of these events has been given by Glazer himself [69]. These studies resulted in two of the most cited papers in the perovskite world [41, 70] and were based in the detailed analysis of the idea planted by Naray-Szabó: many of the perovskite distortions are a result of oxygen displacements considering that they form part of a rigid BX_6 octahedron which adapts, by cooperative tilting, to the space left by the A-cation. Glazer produced a notation to describe these rotations which, although it has been refined over time [71–73], is still used by those studying the ABX_3 compounds of the perovskite family.

In any case, by the time when Megaw put an end to the naming dispute, the perovskite term had become a synonym of a new scientific revolution which had started just after the discovery of the ferroelectric properties of barium titanate, $BaTiO_3$, a compound known at least since 1888, the structure of which had been recently determined by Megaw itself, in 1945 [74].

5 The Ferroelectric Breakthrough: Perovskites Become "Trending Topic" (1940–1950s)

The initial discovery of the excellent dielectric properties in perovskite oxides, especially the ferroelectricity in barium titanate, is a bit blurred with several groups across the world credited as simultaneous discoverers [75–79]. The confusion seems to be related to the critical situation of the world: the start of World War II was on the horizon and any investigation that meant a military advantage or, even worse, which could fall into the enemy's hands giving him a military advantage, was subjected to a publication embargo. In the late 1930s and early 1940s, research into dielectrics was under this vigilance making it difficult to know when a research that would later be published had actually started. If instead of searching scientific papers and reports, we do a patent search the story is a bit clearer. Available data seems to indicate that the discovery of the excellent properties of titanates was carried out in the United States.

Dielectrics are insulating materials that can be temporarily polarized under the application of external electric field. The polarization attained (or charge stored) is proportional to their dielectric constant. Back then, dielectric materials were used in capacitors, which were, and still are, important components of electric devices such as radio transmitters, quite critical in war times. Before and during World War II, the capacitors employed were prepared using sheets of the mineral mica and the

state-of-the-art ones were based on titanium dioxide (TiO_2, titania). However, the reliability of the firsts was not good and the capacitance and dielectric constant of the latter was not very high. Consequently, the development of new dielectric materials was imperative for any belligerent country.

In this agitated state of the world, the discovery of the barium titanate properties fell on Eugene Wainer and his coworkers of the Titanium Alloy Manufacturing Company of New York. By 1940 Wainer was the head of the chemical and physical research laboratory [80]. Few years earlier, in the late 1930s, Wainer was working on the improvement of titanium dioxide dielectrics and found that adding alkaline earth titanates to titanium dioxide greatly improved the latter's dielectric properties. On April 27, 1939, Wainer and Norman R. Thielke filed a patent (granted in 1942) claiming that discovery: "*the dielectric characteristics* [of titania-based dielectrics] *are also considerably improved by adding to a titanium dioxide base a minor quantity of either barium, strontium or calcium titanate, or any mixture thereof. Of these, the best are barium titanate and strontium titanate*" [81]. They mentioned such advantages in a series of four consecutive patents (US 2277733 to 2,277736) filed in the same year and granted in the early 1940s [82]. From the filing to the final granting of those patents, other companies had already found the advantages of barium titanate over titanium dioxide and filed new, but very similar, patents [83]. By the time some of these patents came to light, several papers and reports were available in different parts of the world (United Kingdom, Russia, and Japan [76, 84]) highlighting the importance of Barium Titanate as a new dielectric material for capacitors.

The discovery was of great importance because $BaTiO_3$ had a hundredfold higher dielectric constant than any available dielectric material. Due to the significance of this discovery for the US Government, Wainer's paper describing the properties of several alkaline earth titanates (including strontium and barium titanate) which was submitted to the Journal of the Electrochemical Society in 1943 was banned from publication until a year after the end of World War II, in 1946 [85].

Although not all reports coincide [84, 86], the first recognition as of why barium titanate had such a high dielectric constant is usually credited to the work of Arthur von Hippel and his group of the Massachusetts Institute of Technology [87], who discovered that this was as a result of its ferroelectric properties (the compound attains permanent polarization after the application of an electric field). The first publication on the subject, however, is from a Russian group who announced it in 1945 [88]. Soon after, $BaTiO_3$ would also be found to be piezoelectric (which means that its polarization can also be attained after the application of a force) [89]. The discovery of both properties revolutionized the world of the electronics industry: the potential applications of barium titanate during the 1950s seemed endless and the number of researchers that started new investigations on its properties multiplied. Had it occurred in present days, there is no doubt that the word *barium titanate* would have been "trending topic."

As expected, practical applications started soon: it was used in capacitors and in piezoelectric transducers in a number of consumer and military applications, including phonographs, its first consumer product aside from military uses [76, 90].

Several studies were made during this decade to improve its properties and many of them included the addition of new elements in the A-site position of the perovskite structure. This is what led to the discovery of the piezoelectric properties of one of the most important perovskite-based ceramics together with barium titanate: the lead zirconate titanate family, better known by its acronym PZT (from $PbZr_{1-x}Ti_xO_3$ formula) [91], now ubiquitous in any appliance that needs a piezoelectric material (such as the ultrasonic transducers used in medical ultrasound imaging or in underwater sonars). Following the latter trend, it would not take long for the discovery of another group of ferroelectric perovskites of similar importance, the PMN family, a lead magnesium niobate ($PbMg_{1-x}Nb_xO_3$), which was discovered in the late 1950s by G. A. Smolenskii and A. Agranovskaya in Russia [92]. The importance of this discovery was related with the change in its dielectric constant around the Curie temperature (Tc) (the Tc is when these compounds change from being ferroelectric to paraelectric). In conventional ferroelectrics, there is a sharp maximum in dielectric constant around the Tc but, in the latter compounds, there is a blurred, rather spread out, maxima over a moderate temperature range. This allows a reasonable temperature range of operation for devices made from them. These new ceramic materials would find application a few decades later as electrostrictive actuators [78].

The decade of the 1950s was a period of rapid growth in the number of perovskite compounds (either simple ABX_3 or complex formulations such as $A_{1-x}A'_xB_{1-y}B'_yO_3$) that showed interesting ferroelectric properties. The field of dielectrics had changed forever. The 1960s would probably be the most prolific in this area but it involved the synthesis of many other families of compounds not always related with perovskites [93]. In any case, the legacy of that time is seen nowadays: $BaTiO_3$, PMN and PZT oxide perovskites are still the base for the composition of most of the world's ceramic capacitors, a market that moves millions of dollars every year.

6 The Family Grows: From the Concept of "Sister Structures" to the Actual Meaning of "Perovskite-Type Structure" (the 1940s—Today)

The discovery of the ferroelectric properties of $BaTiO_3$ and related compounds was such a scientific breakthrough in the field of dielectrics that it also caused a boom in the field of perovskite-type compounds: from that moment on, the structural study of perovskites became a common topic in the solid-state and materials chemistry fields. This was a logical consequence given that the explanation of the ferroelectric and piezoelectric properties of these oxides could only be made on the basis of a full understanding of the perovskite structure, the precise arrangements of the atoms in the unit cell, the distortions resulting from the presence of different elements in the structure, and how the different atoms rearranged with temperature [94, 95].

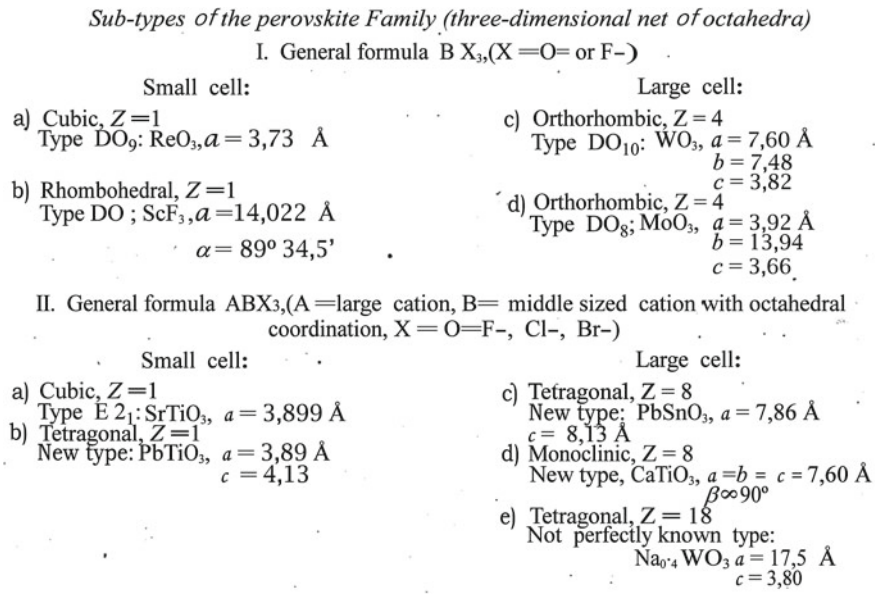

Fig. 8 Naray-Szabó's proposition for the classification of perovskites. Reproduced with permission from Naray-Szabó, I. *Muegyetemi Kozlemenyek*, **1947**, 1, 30–41

It is precisely as a result of these preceding methodical studies that today's idea of "perovskite structure family" was born. It went from covering all ABX_3 phases (whether cubic or not, old conflict overcame) to embrace a massive group of compounds that shared the basic building block identified by Naray-Szabó: a corner-shared BX_6 octahedra. The initial classification of perovskites and its sister structures is the one by Náray-Szabó shown in Fig. 8 (with minimal changes, it was the same one proposed by Megaw [36] few years later). As observed, ABX_3 phases and A-site vacant compounds were subdivided into minor groups depending on their distortion with respect to the ideal cubic structures.

In his enthusiasm to cover all possible perovskite-like compounds, he was a bit too impulsive and some non-perovskites, such as MoO_3, sneaked in his "sisterhood" list, a forgivable mistake considering the precision of the instruments of his time. In any case, he immediately recognized the implications of his propositions: *"putting together the possible A and B cations (…) well over 300 compounds with perovskite structure are possible (although not all can be prepared). Up to date about 60 of them are known, and in some cases only lack of rare elements prevented me from examining them*" [63]. The possibility of introducing several elements in the same position had not been explored yet but he anticipated "*that further investigations will reveal not only new compounds with the perovskite lattice but also new sub-types of this family.*" Náray-Szabó also revised the

Goldschmidt's concept of the tolerance factor (including Zachariasen corrections) that was used to establish the limits for the formability of perovskites, and extended its limits from 0.71 to 1.08 using recent ionic radii.

With the passage of time, the different subgroups that he considered were improved and perfected. A better organization of the ABX_3 perovskite subgroups came at the beginning of the 1950s. One of the most important works came from Elisabeth A. Wood [96]. She started the study of polymorphism in perovskites as a consequence of the different interpretations of the perovskite structure of two important ferroelectric crystals ($KNbO_3$ and $NaNbO_3$) and finished with a full rationalization of all known perovskites. Wood arranged them all according to the A and B ionic radii including the tolerance factor and the symmetry of the structures known as secondary variables. That allowed her to create field maps that showed the regions where a given structure type dominated (see Fig. 9). Those field maps resulted to be more precise than the tolerance factor to predict the existence of a perovskite structure for a given ABX_3 formula and even to predict its distortion. Such field maps or "structure fields," as they were nicknamed, became a very useful tool for the classification of the incredibly high number of new perovskite compounds that started to be made in the 1950s, one of the most fruitful decades in the field of perovskite research.

This boom was not only the result of the ability of the perovskite structure to accommodate different elements if a certain balance between the sizes of the A and B ions was maintained but it also came from the ability of the chemists, physicists, and material scientists for recognizing that every perovskite position could be filled with complex mixtures of ions if the same balance of sizes was kept. The first to observe this possibility were the early researchers on the dielectric properties of barium titanate who, as early as 1945, demonstrated that a solid solution existed between $BaTiO_3$ and $SrTiO_3$: barium could be gradually replaced by strontium in the A position, and the dielectric properties changed gradually [97, 98]. Later works, however, demonstrated that this could also have a profound effect on the B-site cations and on the properties of the resulting compounds if the oxidation states of these cations could be tuned as a result of the A-site substitution.

Worth mentioning works are those of G.H. Jonker and J.H. Van Santen, of the Philips Research Laboratories in the Netherlands, carried out on perovskite manganites of the general formula $Ln_{1-x}A_xMnO_3$ (Ln = lanthanide and A = alkaline earth cation) [99, 100]. In these studies, not only they again demonstrated that a solid solution existed for the whole x values, but that their magnetic properties, electrical conductivity, and the structural distortion could be tuned varying x. Initially expected to be antiferromagnetic and insulating, these oxides showed that, for certain x values, there was a change from a ferromagnetic and electrically conducting phase to a paramagnetic insulating one. In other cases, the changes only involved antiferromagnetic insulating states. The understanding of the those magnetic interactions (observed not only in manganites but in other transition metal-containing perovskites) was so interesting and important that new physical theories had to be introduced by outstanding physicists such as Zener [101, 102], Goodenough [103], Anderson [104], and Kanamori [105] to explain the phenomena

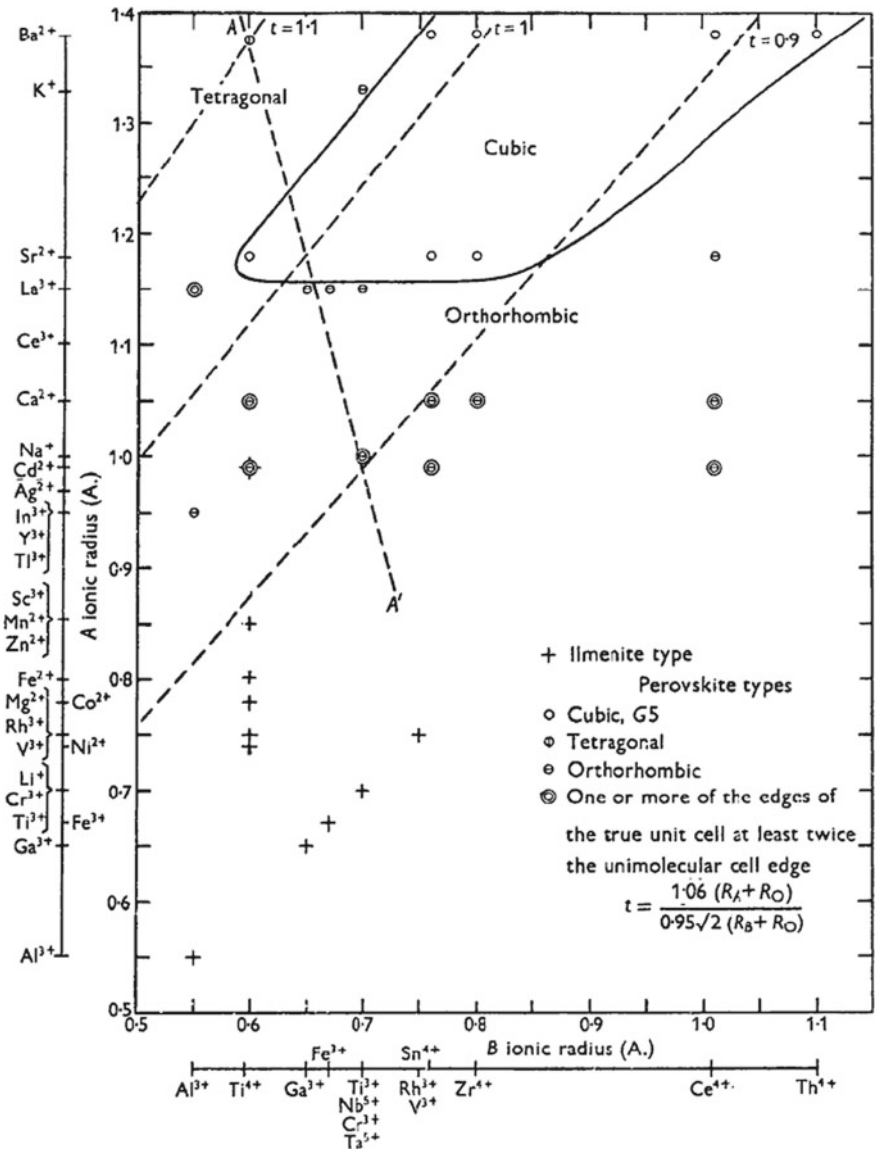

Fig. 9 An example of a structure field diagram of perovskites and ilmenites proposed by E. Wood that were common in the 1950s. Reproduced with permission of the International Union of Crystallography from page 359, E. Wood, *Acta Cryst*. **1951**, *4*, 353–62

(known since as *double exchange* and *superexchange*). Even the future 1991 Physics Nobel Prize winner Pierre Gilles de Gennes participated in the construction of the theories [106]. From then on, many physicists became fully involved in the

understanding of the magnetic properties of perovskite oxides. As it had occurred with the dielectric properties before, a deep understanding of the perovskite structure and all its distortions became very important.

The systematic studies on perovskites continued in the 50s and new field maps where constructed [107–109]. Of those, Roy and Keith's studies are the most remarkable [108, 109]. They prepared a great number of different compounds with more complex chemical compositions such as $KLaTi_2O_6$, Sr_2CrTaO_6, $Ca_3NiTa_2O_9$, and $K_2CeLaTi_4O_{12}$, among several others, with apparent formulas that did not resemble the original one, in order to create field maps of existence for the perovskite structure. They found, however, that many of them belonged to the perovskite family (their formula could be rewritten as $(A_{1-x-y}A'_xA''_y)(B_{1-x}B'_x)O_3$) which confirmed that this structure was able to tolerate almost any mixture of A- and B-cations in the A- and B-sites. Although they failed to classify many compounds as perovskites, because some of them were hexagonal variations (not considered as such by then), these works opened the doors for the preparation of innumerable oxide and halide mixtures with the perovskite structure. But more importantly, this allowed material scientists to explore all the possible properties that derived from the endless combination of ions on the A, B, or even X positions allowing for the finding of new and potential applications of perovskite materials.

It is as a result of so many studies that our concept of perovskite-type structure amplified toward our much broader concept. When did this broadening occur? A timid, but important, attempt in the right direction was made by Steward y Rooksby between 1951 and 1953. They realized that most of the compounds with the formula A_3BX_6 and $A_2BB'X_6$ prepared so far (X = O^{2-} or halide ions; A = alkaline earth or ammonia ions) were so similar "*that the term 'sister-structures' suggested by Naray-Szabó to embrace the various members of the perovskite family, appears, therefore, particularly appropriate one to apply to the present group of compounds*" [110, 111]. Note that they did not consider them as part of the perovskite family (we do now) but, at least, they were considered as a family.

It was Francis Galasso's interpretation of the above-quoted paragraph what allowed the inclusion of most of the known A_3BX_6 and $A_2BB'X_6$ compounds on the perovskite family [112]. Although Rooksby and Steward never said that they were perovskites, Galasso properly identified that A_3BX_6 phases were in fact $A(A_{0.5}B_{0.5})X_3$ perovskites and $A_2BB'X_6$ compounds could be represented as $A(B_{0.5}B'_{0.5})X_3$. A year later, Brixner insisted that compounds in which A was a bigger cation, such as ammonia (NH_4^+), shared the same basic arrangement that the one found in perovskites [113]. However, in the second edition of his massive reference work "crystal structures", Ralph Wyckoff only included the $Cs_2BB'Cl_6$ (A = Cs, B and B' = Au or Ag) halides under the perovskite group [51], but not the ammonia-based ones, which were grouped separately under the unglamorous epigraph of "*Ammonium ferric Hexafluoride, $(NH_3)_3FeF_6$, and closely related structures,*" including those structures related to the mineral elpasolite, K_2NaAlF_6 [114]. This separate, and estrange, grouping (made earlier also by Frank Wells in the first edition of his bestseller "structural inorganic chemistry" [115]) was probably influenced by the discoverers of the later compounds who never commented on this.

Lets elaborate on this further because that first group was the one of the future (1954) Chemistry Nobel Prize Laureate, Linus Pauling. In the earlier works of his group at the California Institute of Technology [116], they had already noted the similarities between the structure of the $A_2BB'X_6$ halides and the one adopted by the mineral *perovskite* but they did not propose such similarities with the structure of ammonium halides because they had elucidated them in 1924… one year before the perovskite structure was even available for comparison [117]!

Well-known monographs of the late 1960s and early 1970s that covered perovskite issues finally included them within the perovskite family [77, 115, 118]. Those compounds are now considered as a perovskite subgroup called double perovskites or "elpasolites", the latter to honor the mineral of the same name, discovered in 1883 [119, 120], the structure of which was elucidated as early as 1932 [121]. The main difference with a conventional ABX_3 perovskite is that in an $A_2BB'X_6$ (or $A_2AB'X_6$) compound the cations in the B-site show a rock-salt-type ordering in the structure. Excellent recent reviews covering their distortions and all the interesting properties that result from the ordering of the B-cations are available [122–124].

Our concept of the perovskite family of compounds still had much room to grow. The most obvious missing "sister structure" was that of the B-site deficient perovskites given by the general formula $A_2B\square O_6$, where □ indicates an empty crystallographic position. The idea had already been launched by Linus Pauling in his 1924s paper on ammonium salts and later in 1928 when he reinvestigated the structure of K_2PtCl_6 [125]: he noted that the $(NH_4)_3BF_6$ structure observed for B = Fe and Pt resembled the one found by his coworkers in the related mixed salts $(NH_4)_2SnCl_6$, K_2SnCl_6, and $(NH_4)_2SiF_6$ [126, 127]. As Pauling noted, all those salts could be described using the $(NH_4)_3BF_6$ structure in which all the octahedral sites (B-sites) that were initially occupied by the NH_4^+ ions were now empty. Again, it is probably the result of the early appearance of these papers that the B-site vacancy structures would not be included in the perovskite family until the mid-1960s when Lewis Katz and Roland Ward [128] included them… still with some reservations (even considering that this close relation had also been pointed out by Wells [129]).

With regard to the growth of the perovskite family, the above-cited work by Katz and Ward is to be remarked. In order to describe the family, they considered the approach followed by A.F. Wells for describing many inorganic crystal structures: the different forms of packing spheres. In the present case, they considered that the perovskite structure could also be described not only as a result of a corner-shared BX_6 octahedra network but also on the basis of close-packed AX_3 layers. Those layers could then be stacked in a variety of close-packed sequences giving rise to the conventional perovskite structure if the sequence was of the cubic-close-packing type (that is, ABCABC…) and a number of alternative perovskite-related structures if the sequence was alternated with hexagonal-like close packing (ABAB…). Figure 10 shows the derivation of the hexagonal structures using Katz and Ward original ideas with the corresponding, and more reader-friendly, polyhedral description that John Longo and James Kafalas constructed from their work [130].

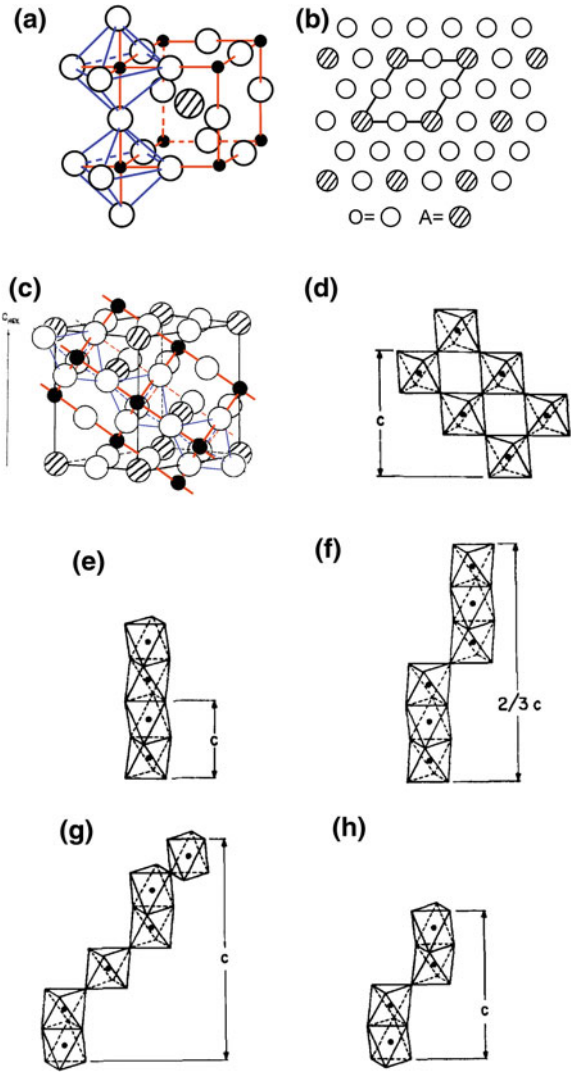

Fig. 10 The derivation of the hexagonal branch of the perovskite family from the different forms of stacking AX_3 layers. **a** the ideal perovskite structure; **b** a single AX_3 layer which is the $(22\bar{2})$ plane in the ideal perovskite structure (lines represent basis of the hexagonal cell); **c** the complete hexagonal unit cell constructed by a cubic close packing of AX_3 units (this cell contains two cubic cells shown in red); **d** the polyhedral view of corner-shared BX_6 octahedra (A-cations not shown) of the perovskite structure shown in (**c**); **e** the polyhedral view resulting from a purely hexagonal close packing of the AX_3 units; **f–h** polyhedral views of different stacking cubic and hexagonal packing sequences. Red lines indicate the cubic unit cell of the ideal perovskite and blue lines depict the BX_6 octahedra. Images **d–h**, reprinted from *J Solid State Chem*, 1, Longo J. M, Kafalas J.A., The effect of pressure and B-cation size on the crystal structure of $CsBF_3$ compounds (B = Mn, Fe, Co, Ni, Zn, Mg), 103–108, © 1969, with permission from Elsevier)

This new group of structures is now known as the hexagonal branch of the family and comprises a vast number of compounds with different stacking sequences [6]. It is to note that hexagonal perovskites were known before Katz and Ward's proposition was published: in 1948, it had already been discovered that barium titanate showed such a structural modification when it was crystallized from melts [131]. Nevertheless, given that this structural modification of $BaTiO_3$ did not show spontaneous polarization [35], the hexagonal modification of the perovskite structure did not attract much attention.

Other related structures were soon incorporated to the perovskite family. In this sense, a very interesting discovery occurred in 1953. Balz and Plietz, from the Max-Planck Society in Germany, found that besides the $KNiF_3$ perovskite, K_2NiF_4 also existed as an intermediate phase in the KF-NiF_2 system. The interesting issue there was that the new compound adopted a previously unknown structure type… but, somehow, related to the perovskite [132, 133]. Although it is difficult to relate this formula with that of an ABX_3 perovskite, the authors realized that this structure could be interpreted as a mixture of a perovskite layer of vertex sharing BX_6 octahedra alternated with a close-packed KF layer (Fig. 11a). That study was immediately followed by S.N. Ruddeslen and O. Popper, of the British Ceramic Research Association, who found that this structure was also adopted by oxides [134] but, more importantly, that this structure was also related to that of the new oxide $Sr_3Ti_2O_7$, with a more complicated formula than the previous one [135]. In the latter case, however, they realized that the structure could be described as a mixture of two perovskite layers alternated with a SrO close-packed layer (Fig. 11b). They immediately proposed that both structures could be derived from a general formula $A_{n+1}B_nX_{3n+1}$ for which n meant the number of perovskite layers alternated with a close-packed AX layer. Thus, the K_2NiF_4 was the $n = 1$ member, $Sr_3Ti_2O_7$ the $n = 2$ member, and the ABX_3, *i.e.,* the perovskite structure, was the $n = \infty$ member. It is true that they did not propose the latter generalization but they did point out that triple or quadruple perovskite layers should be possible. Consequently, compounds of the general formula $A_{n+1}B_nX_{3n+1}$ (also written as $(A_nB_nX_{3n})AX$ to emphasize the close relation with the perovskite formula) are now known as the Ruddlesden-Popper (and not the Balz-Plieth) branch of the perovskite family. The observation of ferroelectric properties on some of its members in the 1960s accelerated the research into this family and resulted in the preparation of a number of compounds of this type [136]. Moreover, the discovery of high-temperature superconductivity on the distorted $La_{1-x}Ba_xCuO_4$ oxide by Georg Bednorz and Alex Müller in 1986 [137], which granted them the 1987s Nobel Prize in Physics, made these compounds internationally famous. Superconductivity and ferroelectricity are not, however, the only interesting properties of the Ruddlesden-Popper compounds as recent reviews have demonstrated [138, 139].

A closely related layered structure had been discovered a few years earlier by Bengt Aurivillius [140, 141]. Aurivillius, an expert in bismuth related oxides from the University of Stockholm, in Sweden, discovered that $CaNb_2Bi_2O_9$ and $Bi_4Ti_3O_{12}$ oxides could be described as if they were constructed from perovskite layers separated by bismuth oxide layers. Similarly to what we do now with the Ruddlesden-Popper phases (note, however, that Aurivillius layered phases predate the former), the general formula for these new phases can be expressed as $(Bi_2O_2)(Bi_{n-x}B_nO_{3n+1})$ where n stands for the number of perovskite layers between the "bismuth oxide" layers. Figure 11(d–f) shows a comparison of this structure with other layered forms of the perovskite structure. Again, the research into this family of compounds was boosted by the observation of ferroelectric properties on some of its members [142, 143]. The main interest of the Aurivillius phases remains in the

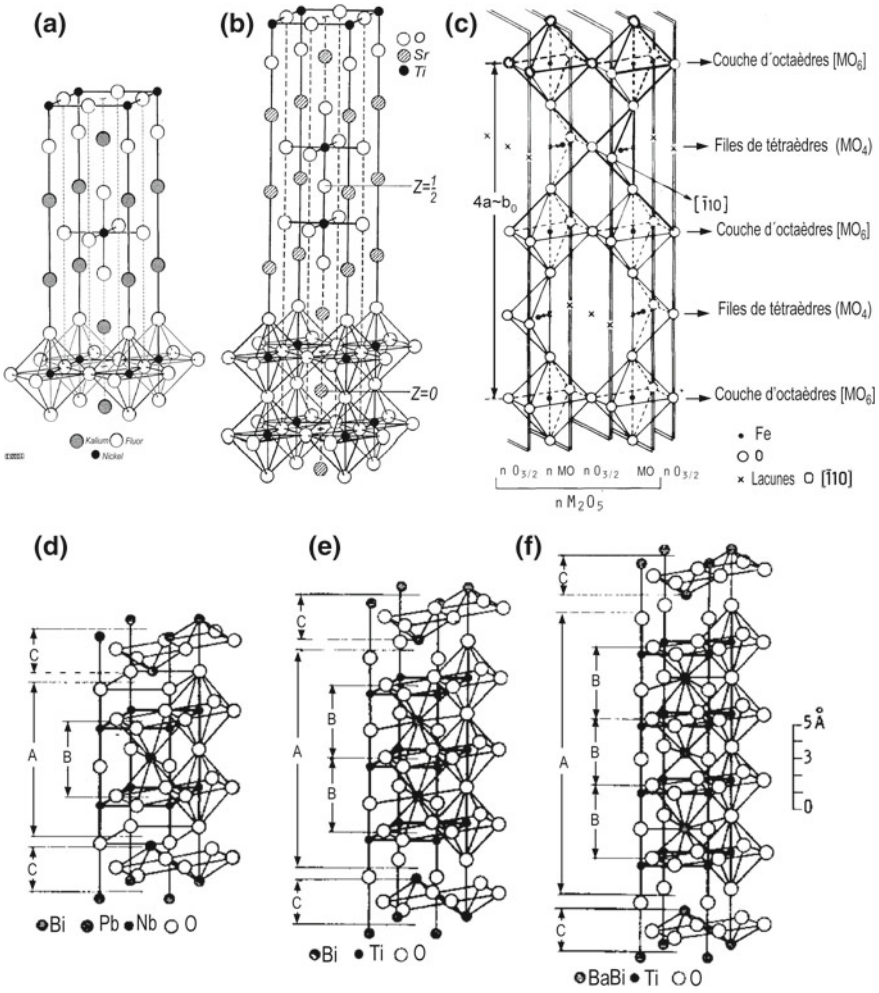

Fig. 11 Different members of the perovskite family. **a** and **b** the n = 1 and n = 2 members of the Ruddlesden-Popper layered series of the general formula $AX(A_nB_nX_{3n})$. **c** A brownmillerite structure of general formula $ABX_{2.5}$ (or $A_2B_2X_5$) with ordered oxygen vacancies (A ions not shown). **d–e** The m = 2, m = 3 and m = 4, respectively, of the layered Aurivillius phases of the general formula $(Bi_2O_2)A_{m-1}B_mX_{3m+1}$. As observed, all share different sequences of corner-shared BX_6 octahedra as in the ideal perovskite structure. **a** Reproduced with permission of the Deutsche Bunsen-Gesellschaft für physikalische Chemie and Wiley VCH from Balz D, K. Plieth (1955) *Zeitschrift für Elektrochemie, Berichte der Bunsengesellschaft für Phys Chemie* 59:545–551. **b** Reproduced with permission of the International Union of Crystallography from Ruddlesden SN, Popper P (1958) The compound $Sr_3Ti_2O_7$ and its structure. Acta Crystallogr 11:54–55. **c** Reprinted from Mater Res Bull, 8, Grenier J-C, Pouchard M, Georges R, Variation thermique de la susceptibilite magnetique et de l'aimantation du ferrite bicalcique $Ca_2Fe_2O_5$, 1413–1420, © 1973, with permission from Elsevier. **e–f** Reprinted from J Phys Chem Solids 23, Subbarao EC, A family of ferroelectric bismuth compounds, 665–676 © 1962, with permission from Elsevier

field of dielectric materials due to the necessity of replacing the current lead-containing dielectrics for environmental and health reasons [144].

The almost crazy worldwide search (the second "boom" on perovskite research) for high-temperature superconductors that started after Bednorz and Müller's discovery in 1986, led to the finding of many oxides that were superconductors above the temperature of liquid nitrogen [145–147]. It is interesting to note that another branch of the perovskite family is related to the most famous high T_c superconductor that was discovered in those years: the oxygen-deficient $YBa_2Cu_3O_{7-\delta}$ oxide [148]. This is because the latter's structure can be considered as a perovskite phase with ordered oxygen vacancies. This new branch, however, was incorporated to the family much earlier: the fact that the perovskite structure could also support anion vacancies was probably first observed by the group of Roland Ward at the Polytechnic Institute of Brooklyn, New York. At the late 1940s, his research group was trying to prepare several ABO_3 perovskites with alkaline earth cations in the A-site, and iron and cobalt in the B-site. Interest was based on finding the stability of the +4 oxidation states that were expected for the latter metals in the resulting perovskite. Nevertheless, they consistently found that the latter oxidation state was never reached but "perovskite-like" patterns were always observed so they concluded that substantial amounts of oxygen vacancies had to be tolerated by the structure without any changes to the basic perovskite arrangement [149, 150]. Those studies by Ward's group led to a very important, and completely forgotten, discovery: they found that this ability to tolerate variable amounts of oxygen vacancies resulted in a tunable mixed valence of the metal in the B-site allowing their use as effective catalysts [151]. Those studies, not yet cited, predate by almost 6 years the first usually quoted reports of perovskite catalyst, attributed to Giussepe Parravano of Princeton University in 1952 [152, 153].

The possibility of studying iron compounds by Mössbauer spectroscopy, a technique that had recently been developed, greatly helped the growth of the perovskite family. In fact, it was the works on anion defective $SrFeO_{3-x}$ ($0 < x < 0.5$) oxides carried out during that decade [154] what permitted to find that oxides classified as having the brownmillerite structure ($A_2BB'O_5$ formula) were in fact a subgroup of the perovskite family in which the oxygen vacancies were ordered in the structure (the brownmillerite structure is obtained when $x = 0.5$ in $SrFeO_{3-x}$). A model for the ordering of those vacancies would be derived later on [155, 156]. A perspective of this structure is shown in Fig. 11c together with other members of the family. This subgroup still bears the same name.

As the reader may note, by the early 1980s, the perovskite family had so greatly expanded that it was very difficult to recognize many of its members and their relation to the structure that more than 50 years ago had been proposed by Thomas Barth for the mineral *perovskite*. A new classification was desperately needed. Some classifications of the perovskite structure had been attempted before [118, 128, 157], the best one probably being that by Longo and Goodenough in 1970 when they covered the magnetic properties of perovskites and related structures (including layered compounds) [158]. This reference book, however, did not enjoy widespread knowledge and even later classifications by Wells or Megaw did not

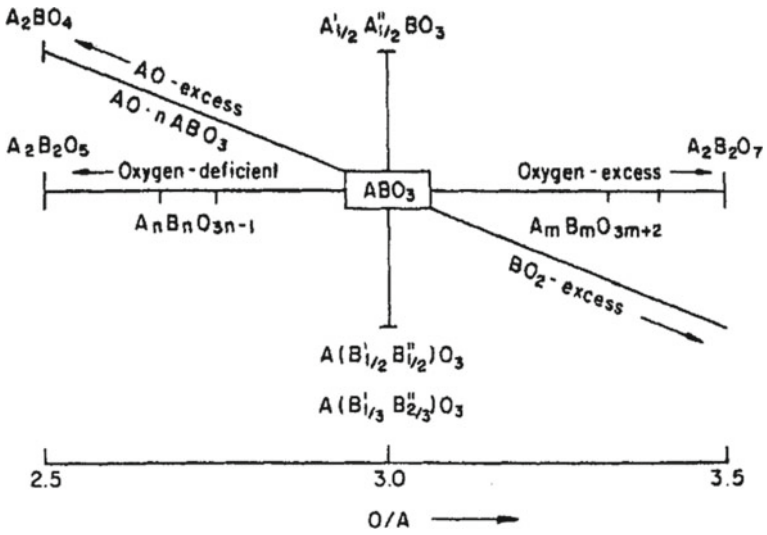

Fig. 12 The "perovskite space" as conceived by D. Smyth in order to rationalize all forms of the perovskite family. He published this updated version in his inspiring paper "travels through the perovskite space." Reproduced from Smyth D.M., Chang E.K., Liu D.H. (1996) Travels through perovskite space. *Phase Transitions*, 58:57–73. Reprinted by permission of Taylor & Francis Ltd, http://www.tandfonline.com

use their classification scheme. Another attempt to rationalize all variants, including the different possibilities resulting from the presence of cation and anion vacancies, was carried out by Donald Smyth, from Lehigh University in Pennsylvania. Initially, Smyth focused on oxides and considered the family of perovskite-related structures as if they were located along a compositional line based on the anion/cation ratio (horizontal line in Fig. 12). On the one side were the compounds with less oxygen ($A_nB_nO_{3-n}$) than the parent ABO_3 phase and, on the other side, compounds with oxygen excess ($A_nB_nO_{3n+2}$, with $n \geq 4$). He also included all forms of $AB_{1-x}B'_xO_3$ compounds, irrespective of the type of ordering between B-cations and or hexagonal/cubic variations but missed the Aurivillius or Ruddlesden-Popper phases. Consequently, he revised his classification in 1989 and later in 1996 [159], to include those branches as shown in the diagonal lines of Fig. 12.

This classification was the basis for the rationalization of the structures adopted by *perovskite*-related minerals, and not just synthetic compounds, carried out by Roger Mitchell in 1996 [160] which has been revised in recent times [6, 161] showing that not all members of the family have been observed in nature.

For synthetic oxides, however, the best (and probably better known) classification and derivation of the perovskite structural family was that of Chintamani N.R. Rao and Bernard Raveau, developed in 1995 and updated in 1998 [162]. However, the most comprehensive rationalization of the perovskite family, including present and future

members, is probably that of Kirill S. Aleksandrov and his coworkers, of the Kirenskii Institute of Physics in Russia. From 1997 to 2001, he published a series of papers rationalizing all possible members of the family (and their structural distortions) on the basis of two approaches: on the one side considering all possible derivations of the structure from a polyhedral view of the perovskite (the three-dimensional network of corner-sharing BX_6 octahedra) and, on the other side, considering that the perovskite structure derived from the close packing (cubic or hexagonal) of AX_3 units [163–165], as it had been previously done by Katz and Ward [128]. In his 2001 work, he realized that if all members of the "perovskite family tree" (as he dubbed it) were combined with the possibility of cation and anion mixtures in each of their positions, it was "*probably impossible to say, at present, how many substances belong to the perovskite family.*" Aleksandrov had been working on perovskites since the 1960s and was relatively well known for his work on the sequences of structural phase transitions on simple perovskites [166]. Although his results were very much the same than the ones proposed by Mike Glazer in the early 1970s [41, 70], his notation proposal was less "user-friendly" and did not gain many adepts.

In 1997, he coauthored a paper with B.V Beznosikov entitled "Hierarchies of perovskite crystals" where they organized all known and recently proposed perovskite family members using a system of windows as in the operative system of the same name. Each window could them be opened and a new group of windows appeared (Fig. 13 shows the "starting screen").

The paper was a summary in English of their book on the same subject published in Russian that gained almost no attention from the international community. Surprisingly,

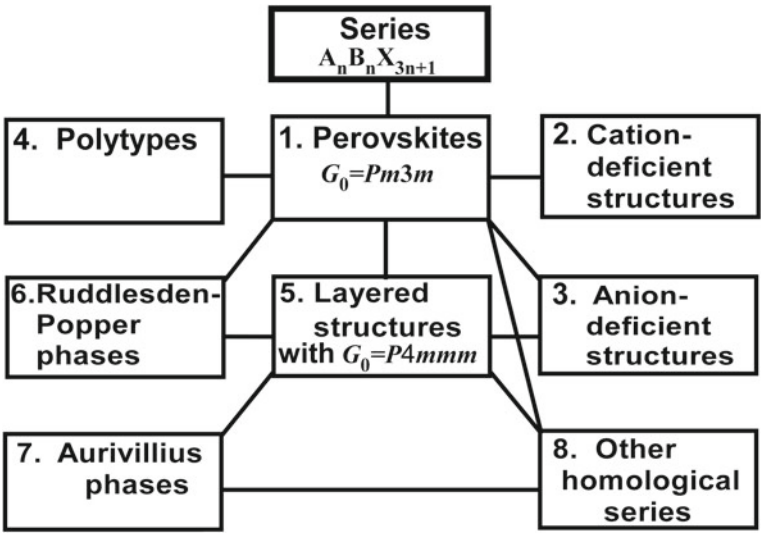

Fig. 13 The "Windows-like" tree of the perovskite family as viewed by Aleksandrov and Beznosikov in 1997 [162]. Every one of these "windows" opens a new tree of "windows". This classification system is, so far, the most comprehensive perovskite "family tree" to date. Reprinted by permission from Springer Nature, Physics of the Solid State, 39:695–715. Hierarchies of perovskite-like crystals (Review), Aleksandrov K.S., Beznosikov V.V. © 1997

their paper also passed almost unnoticed although later revisions have gained more visibility [164]. Despite the low visibility of these works, their classification is, so far, the most comprehensive perovskite "family tree" to date and is, essentially, the same one that appears in the better known book by Roger Mitchell [6] although less beautifully illustrated and with a minor amount of references than the latter. Mitchell's book is still the most important one about the perovskite family yet published. For natural perovskites, the best compilation is also a Roger Mitchell paper [161].

7 Golden Decades: Studies Diversify and New Properties and Many Potential Applications Are Discovered (the 1970s—Today)

By the end of the 1960s, the number of publications related to, and research groups around the world working with compounds having a perovskite-type structure, was so large that the need for extensive reviews was getting necessary in order to be able to organize, systematize, and understand all the data. The first general review covering most of the aspects of Perovskite-type compounds was written by Francis Galasso in 1969: "*Structure, properties, and preparation of perovskite-type compounds*" [77]. The book, although concise, basically covered all the fields in which perovskites were being studied by the time, *i.e.,* their crystal structures (including phase transitions), electrical conductivity (from insulators to superconductors), dielectric properties (ferroelectrics and piezoelectrics mainly), optical properties (from their use in lasers to filters), catalytic properties (both their application in fuel cells and as heterogeneous catalysts for CO were reviewed), thermal conductivity, and magnetic properties. Some space was also reserved in the book for the preparation procedures (powders, single crystals, and thin films) of the more than 550 compounds that were included in the review, from oxides to nitrides.

The hottest topic of the time was the dielectric properties of perovskites and Galasso's book, however comprehensive, was not encyclopedic and did not completely cover the vast amount of work that was being carried out in this particular field. In fact, by the same time that the book was published, a large reference book covering ferroelectric materials came to light. In the new book, the volume 3 (group III) of the new Landolt-Börnstein series, a comprehensive collection of many of the perovskite family ferroelectrics, from the conventional $A_{1-x}A_x'B_{1-y}B'_yO_3$ oxides to layered phases and A-site deficient oxides, was included, although not all of them were classified under the perovskite family [93]. Contrary to Galasso's book, this was a true reference work that included data of more than four hundred compounds and thousands of references, a good deal of them on oxides of the perovskite family. The field of ferroelectrics grew so fast that the number of papers published every year followed a logarithmic trend that was calculated as $N = e^{(0.14*(Y-1921))}$ where N was the number of papers published in the year Y [167]. Nearly, 40% of the papers were related to perovskites, a truly overwhelming literature for the non-initiated. This

uncontrolled growth made that the Landolt-Börnstein volume focused on ferroelectrics had to update their compilation in 1974, 1981, and, again, in 1990.

Dielectric and related properties were not, however, the only interesting properties of perovskites. Their magnetic properties, although not being so popular because they had not yet found practical applications, were also being widely studied among physicists, chemists, and material scientists. Magnetic perovskites were studied because of their promising applications in magnetic recording devices, for example, but also because of the intricate magnetic phenomena they presented, which still weren't well understood despite the intense research carried out during the 1950s and 1960s. Although they were also covered in Galasso´s textbook-like work, the complete guide to the magnetic properties of inorganic compounds of the perovskite family came almost at the same time than its ferroelectric counterpart. The data was compiled by John B. Goodenough and John M. Longo [158] in order to provide the reader with a complete picture of both the perovskite crystal structure and the different types of magnetic interactions possible in the structure, and not just as a collection of hundreds of references with scattered data. Again, however, the advances in this field were so fast that by 1975 almost two thousand papers existed on the field, so this work was updated and revised in 1978, in the 1990s and at the beginning of the twenty-first century.

More recent updates were the result of the discovery of colossal magnetoresistance in perovskite manganites of the general formula $Ln_{1-x}A_x'MnO_3$ in the early 1990s [168–170]. Given that, contrary to their ferroelectric counterparts, the past two decades had again finished with no practical devices based on the magnetic properties of perovskites, the new discoveries were enthusiastically received in the hope that they would soon result in new revolutionary devices. Magnetoresistance (the property of changing the electric resistance by the application of a magnetic field, or vice versa) was the basis of the magnetic recording media and, consequently, the potential applications for perovskite materials broadened and included anything from magnetic recording heads to sensors and actuators [171]. After the fever of the late 1980s due to the discovery of high-temperature superconductivity, a new "research boom" started and studies on this topic multiplied across the world at a pace of nearly 200 papers on average every year from 1994 onward (see Fig. 1). Keeping up with the literature became a difficult task for any researcher. It is interesting to note that this discovery occurred in oxides that had already been studied in the 1950s [99, 100, 172]. The magnetoresistance itself had even been described in the 1960s [173].

Despite such intense work, magnetoresistive perovskites did not find the applications expected but new interesting properties and promising applications are still being discovered in such compounds [174]. Although perovskites show other interesting magnetic properties (a reader-friendly summary of which is included in Tilley's book [7]) magnetoresistance, and more recently multiferroic properties, have by far concentrated the research efforts after the 1990s discovery.

If, however, a decade has to be considered as the golden era of the perovskite's research history in what concerns to their properties and potential applications, it wasn't the 1990s but the 1970s. It might not be remembered as one decade where

groundbreaking discoveries were made, but it was in this decade when the diversification of studies truly began. It is in this period that the members of the perovskite family demonstrated that the "structure–property" relation as the key to the understanding of materials science was not an elemental truth: "*the perovskite structure stands as the outstanding example proving the error of this over-simplistic cliché*" [175]. This is because it was in this decade when many new important properties were observed which would also set the basis for future research. It is in this period, for example, when the first superconducting ABX_3 perovskites were found [176]. It was also in this decade when their ability for being the host for lasing elements, which have resulted in practical perovskite-based lasers, was developed [177, 178]. New electro-optic properties were also discovered and found applications in this decade [179, 180]. Their great stability (mixed with other compounds) for the immobilization of nuclear waste materials was also proved [181] and even resulted in practical use. Despite having been discovered more than 20 years before (and then forgotten), it was also in this decade that the most promising catalytic properties were reported and extensively investigated [182, 183]. The latter example is especially interesting because it also involved another Nobel laureate, Williard Frank Libby, 1960 Chemistry Nobel Prize, who started working on perovskite catalysts aiming at using them in automobile exhausts [184]. It was also in this decade when perovskite chromites were found as viable interconnecting materials for the newly born solid oxide fuel cell (SOFC) technology opening this field to the anxious perovskite researchers [185, 186]. Table 1 shows a short summary of several perovskites that have found application and the particular properties in which these applications are based.

But this decade is not just a golden era for material scientists but also for geologists. Since the 1940s, they had almost been relegated from the overwhelming amount of literature regarding perovskite-structured compounds. However, they would be back again. This was a result of two important findings that also caught the eye of the public opinion. On the one hand, it is in this decade when the first *perovskite* crystals were found in different meteorites [187, 188] but, more importantly, it is in this decade when it was found that, under pressures similar to those existing around the 600 km discontinuity of the Earth's mantle, both the pyroxene $MgSiO_3$ and the pyrope $Mg_3Al_2Si_2O_{12}$ transformed into a $MgSiO_3$ phase with the perovskite structure [189, 190]. The latter discovery was very important because it implicated that most of the elements present below this depth (in other words, most of the Earth's lower mantle) were arranged in the perovskite structure, making perovskite the most common structure on our planet [191].

Many of the developments in perovskite-related research in the next years were based, to a great deal, on the properties found in the 70s or on the preexisting ones. It is true, however, that many new properties have been discovered in recent days the most outstanding being their photochemical properties that make them potential candidates for the next generation of solar cells. Many of these properties, however, will be reviewed on the following chapters of the present book which would be a much better way for keeping track of the updates and for knowing the state of the art in each case.

Table 1 Properties and applications of some important perovskites. Note that some compositions may vary over a wide range of x. Data from Refs. [78, 175, 192]

Compound	Reference property	Application example
$BaTiO_3$	Ferroelectricity	Multilayer capacitors in almost every electronic device
Pb(Zr, Ti)O_3	Piezoelectricity	Piezoelectric transducers
$Ba_{1-x}Sr_xTiO_3$	Positive temperature dependence of resistivity	P.T.C. Thermistor (used in temperature sensors, fuses, etc.)
$(Pb_{1-x}La_x)(Zr_{1-x}Ti_x)O_3$	Transparent under visible light and piezoelectricity	Electro-optical modulator (used in military pilot goggles)
$LiNbO_3$	Electro-optic effect (change in optical properties under an applied field)	Optical switches (used in lasers and optical fibers)
$BaZrO_3$	High dielectric constant and low dielectric loss in the microwave region	Dielectric resonator in communication devices and antennas
Nd^{3+} doped $YAlO_3$	Efficient laser Host	Lasers (common in dentistry)
$KNbO_3$	Nonlinear optical properties	Second harmonic generator (the ability to combine the energy of two photons to double the frequency) in lasers
$Pb(Mg_{1-x}Nb_x)O_3$	Relaxor ferroelectric	Electrostrictive actuator (used in devices where high precision movement is required)
$YBa_2Cu_3O_{7-x}$	Superconductivity	Thin superconducting wires
$BaRuO_3$	Electrical resistivity	Thin-film resistor (used in old printers)
$La_{1-x}Sr_xMnO_3$	Mixed ionic electronic conductivity	Solid oxide fuel cell cathode in pre-commercial devices
$LaCrO_3$	Mixed ionic electronic conductivity and stability under oxidizing and reducing conditions	Solid oxide fuel cell interconnecting material in pre-commercial devices
$PbTiO_3$	High refractive index	Paints (discontinued for health reasons)
$CH_3NH_3PbI_3$	Photochemical activity	Photoactive die for semiconductors used in solar cells (prospective)

8 Conclusions

Perovskites comprise a vast number of compounds that can be described by simple formulas such as that of the original mineral, $CaTiO_3$, or complex ones such as the ferroelectric Aurivillius compound $Ba_2Bi_4Ti_5O_{18}$. This chapter has shown how such different compounds became part of the same family at the same time that many important properties and applications were being discovered in each of them. Each discovery boosted the research into these compounds and new family members appeared making it a non-closing circle that still continues. The ability of the

perovskite lattice to adapt to complex mixtures of elements in each atomic position makes them excellent models for the study of several physical properties but also makes them very promising for finding new ones. What started as the crystallographic study of a rare mineral has completely changed to become an interesting and huge field of active research.

Acknowledgements This work would have been impossible without the help of many colleagues (and librarians) who have provided me with many of references cited here and who have helped me with the understandings of those papers that were written in German or French. As naming all of them is impossible, I will just mention the institutions from which they have helped: the University of Edinburgh (particularly from CSEC), University of British Columbia, Universidad del País Vasco/Euskal Herriko Unibertsitatea, Universidad Complutense de Madrid, Universidad de Murcia, Universidad de Zaragoza, and Pontificia Universidad Católica del Perú.

References

1. Kojima A, Teshima K, Shirai Y, Miyasaka T (2009) Organometal halide perovskites as visible-light sensitizers for photovoltaic cells. J Am Chem Soc 131:6050–6051
2. Scientific American Custom Media (2018) The Perovskite boom. Sci Am. https://www.scientificamerican.com/custom-media/pictet/the-perovskite-boom/. Accessed 20 Aug 2018
3. Sivaram V, Stranks SD, Snaith HJ (2015) Outshining silicon. Sci Am 313:54–59
4. Rose G (1839) Beschreibung einiger neuer Mineralien vom Ural. Ann der Phys und Chemie 48:551–572
5. Chakhmouradian AR, Woodward PM (2014) Celebrating 175 years of perovskite research: a tribute to Roger H. Mitchell. Phys Chem Miner 41:387–391
6. Mitchell RH (2002) Perovskites: modern and ancient, 1st edn. Almaz Press Inc., Thunder Bay, Ontario
7. Tilley RJD (2016) Perovskites. Structure-property Relationships, 1st ed. Wiley, Chichester
8. Granger P, Parvulescu VI, Kaliaguine S, Prellier W (2016) Perovskites and related mixed oxides. Concepts and applications. Wiley-VCH Verlag, Weinheim
9. Sinkankas J, Sinkankas GM (1994) Humboldt's travels in siberia 1837-1842 and the gemstones by Gustav Rose. Geoscience Press, Phoenix
10. Navrotsky A, Weidner DJ (1989) Perovskite_ a structure of great interest to geophysics and materials science. Am Geophys Union, Washington, D.C
11. Des Cloizeaux A (1845) Notes sur les formes cristallines de la Perowskite. Ann Chim Phys 3:338–342
12. Damour A (1855) Notice sur la pérowskite de Zermatt: espèce minérale. Victor Dalmont, Paris
13. Ébelmen JJ (1851) Recherches sur la cristallisation par la voie séche. Compt Rend Séan Acad Scien XXXII:710–712
14. Hautefeille P (1864) De la reproduction du sphene et de la pérowskite. Comptus Rendus des Séances L'Académie des Sci 59:698–701
15. Philips W, Miller WH, Brooke HJ (1852) An elementary introduction to mineralogy, 10th edn. Longman, London
16. Dana JD (1854) A system of mineralogy (comprising the most recent discoveries), vols 1 and 2, 4th ed. George P. Putnam and Co., New York
17. Dufrénoy A (1856) Traité de Miéralogie, 12th edn. Victor Dalmont, Paris
18. Des Cloizeaux A (1859) Nouvelles recherches sur les proprietés biréfringentes des corps cristallisés. Comptus Rendus des Séances L'Académie des Sci 48:263–267

19. Des Cloizeaux A (1858) Memoire sur l'emploi des proprietes optiques birefringentes, pour la distinction et la classification des mineraux cristallises. Ann des Mines 14:339–420
20. Kay HF, Bailey PC (1957) Structure and properties of CaTiO3. Acta Crystallogr 10:219–226
21. Bowman HL (1908) On the structure of perovskite from the Burgumer alp, Pfitschthal, Tyrol. Mineral Mag 15:156–176
22. Miers HA (1902) Mineralogy. An introduction to the scientific study of minerals. Macmillan and Co. Limited, New York
23. Holmquist PJ (1898) Synthetische Studien über die perowskit- und Pyrocholremineralien. Bull Geol Inst Univ Upsala III:181–266
24. Baumhauer H (1880) Ueber den Perowskit. Zeitschrift für Krist-Cryst Mater 4:187
25. Baumhauer H (1883) (Auszüge) A. Ben Saude: Über den Perowskit. Zeitschrift für Krist-Cryst Mater 7:612–615
26. Böggild OB (1912) Krystallform und zwillingsbildungen des Kryolits, des Perowskits und des Boracits. Zeitschrift für Krist-Cryst Mater 50:349–429
27. Bowman HL (1908) An attachment to the goniometer for use in the measurement of crystals with complex faces. Mineral Mag 15:177–179
28. Levi GR, Natta G (1925) Sulla struttura cristallina della perowskite. Rend Accad Naz Lincei 2:39–46
29. Barth TFW (1925) Die Kristallstruktur von Perowskit und verwandten Verbidungen. Nor Geol Tidsskr 8:201–216
30. Zedlitz O (1936) Untersuchungen an perowskit, Uhligit und dysanalyt. Fortschr Miner Krist Petrog 20:66–68
31. Zedlitz O (1939) Der Perowskit. Mineralogische und röntgenographische Untersuchungen an Perowskit, Uhligit und Dysanalyt sowie an deren synthetischen Produkten. Neues Jahrb Miner Geol, Beilage Bd A 75:245–296
32. Náray-Szabó I (1943) Der Strukturtyp des Perowskits (CaTiO3). Naturwissenschaften 31:202–203
33. Tanaka Y (1941) Studies on the reactions between oxides in solid state at higher temperatures II. The reaction between calcium oxide and titanium oxide and the photosensitivity of calcium titanate. Bull Chem Soc Jpn 16:455–463
34. Zedlitz O (1943) Der Strukturtyp des Perowskit (CaTiO3)-Zur Original-Mitteilung von Náray-Szabó. Naturwissenschaften 31:369
35. Megaw HD (1956) Ferroelectricity In Crystals. Methuen, London
36. Megaw HD (1946) Crystal Structure of double oxides of the perovskite type. Proc Phys Soc 58:133–152
37. Sasaki S, Prewitt CT, Bass JD, Schulze WA (1987) Orthorhombic perovskite CaTiO3 and CdTiO3: structure and space group. Acta Crystallogr Sect C 43:1668–1674
38. Beran A, Libowitzky E, Armbruster T (1996) A single-crystal infrared spectroscopic and X-ray-diffraction study of untwinned San Benito perovskite containing OH groups. Can Mineral 34:803–809
39. Arakcheeva AV, Pushcharovsky DY, Gekimyants VM et al (1997) Crystal structure and microtwinning of natural orthorhombic perovskite catio3. Crystallogr Rep 42:46–54
40. Meisheng Hu, Wenk HR, Sinitsyna D (1992) Microstructures in natural perovskites. Am Mineral 77:359–373
41. Glazer AM (1975) Simple ways of determining perovskite structures. Acta Crystallogr Sect A 31:756–762
42. Szinicz L (2005) History of chemical and biological warfare agents. Toxicology 214: 167–181
43. Mason B (1992) Victor moritz goldschmidt: father of modern geochemistry. The Geochemical Society, San Antonio
44. Bernal JD (1948) The goldschmidt memorial lecture. J Chem Soc 2108–2114
45. Jensen WB (2010) The origin of the ionic-radius ratio rules. J Chem Educ 87:587–588

46. Goldschmidt VM, Barth T, Lunde G, Zachariasen WH (1926) Geochemische Verteilungsgesetz der elemente (VII). Skr Nor Vidensk Akad Oslo I, Mat Naturv Klasse 2:1–117
47. Zachariasen WH (1928) The crystal structure of sesquioxides and compounds of the type ABO3. Skr Nor Vidensk Akad Oslo I, Mat Naturv Klasse 4:7–165
48. Natta G (1927) Struttura cristallina del tricloromercuriato di cesio. Rend Accad Naz Lincei 5:1003–1008
49. Natta G, Passerini L (1928) isomorfismo, polimorfismo e morfotropia-I. Composti del tipo ABX3. Gazz Chim It 58:472–484
50. Ferrari A, Baroni A (1927) Sulla struttura del cloruro doppio de cadmio e cesio CsCdCl3. Considerazioni sulla struttura monometrica tipo ABX3. Rend Accad Naz Lincei 6:418–422
51. Wyckoff RWG (1964) Crystal structures. Inorganic Compounds RXn, RnMX2, RnMX3, vol 2, 2nd ed. Interscience Publishers (Wiley), New York
52. Evans RC (1939) An introduction to crystal chemistry. Cambridge University Press, London
53. van Arkel AE (1925) Kristalstruktuur van magnesium fluoride en andere verbindingen van hetzelfde krystaltype. Physica 5:162–171
54. Wyckoff RWG (1931) The structure of crystals. The chemical catalog company Inc, New York
55. Waldbauer L, McCann DC (1934) Caesium nitrate and the perovskite structure. J Chem Phys 2:615–617
56. Nielsen R, Goldschmidt VM (1920) Process of producing pigments, US1343468, pp 1–3
57. Nielsen R, Goldschmidt VM (1920) Titanium products and the process of producing same from precipitated titanium hydrates, US1343469, pp 1–3
58. Robertson DW (1936) Lead titanate. Ind Eng Chem 28:216–218
59. Robertson DW, Jacobsen AE (1936) Physical study of two-coat paint systems. Ind Eng Chem 28:403–407
60. Rinse J (1958) Lead titanate paints in Holland. Paint Varn Prod 98–100
61. Cole SS, Espenschied H (1937) Lead titanate: crystal structure, temperature of formation, and specific gravity data. J Phys Chem 41:445–451
62. Náray-Szabó I (1943) Die Strukturen von Verbindungen ABO3. "Schwesterstrukturen." Naturwissenschaften 31:466
63. Náray-Szabó I (1947) The perovskite-structure family. Muegyetemi Kozlemenyek 1:30–34
64. Hägg G (1935) The spinels and the cubic sodium-tungsten bronzes as new examples of structures with vacant lattice points. Nature 135:874
65. Hägg G (1935) Zur Kenntnis der kubischen Natrium—Wolfram-Bronzen. Zeitschrift für Phys Chemie 29B:192–204
66. de Jong WF (1932) Die Kristallstruktur der regulären Na-W-Bronzen. Zeitschrift für Krist-Cryst Mater 81:314
67. Rooksby H (1945) Compounds of the structural type of Calcium Titanate. Nature 155:484
68. Muller O, Roy R (1974) The major ternary structural families. Springer, New York
69. Glazer AM (2011) A brief history of tilts. Phase Trans 84:405–420
70. Glazer AM (1972) The classification of tilted octahedra in perovskites. Acta Crystallogr Sect B 28:3384–3392
71. Woodward PM (1997) Octahedral tilting in perovskites. I. Geometrical considerations. Acta Crystallogr Sect B Struct Sci 53:32–43
72. Stokes HT, Kisi EH, Hatch DM, Howard CJ (2002) Group-theoretical analysis of octahedral tilting in ferroelectric perovskites. Acta Crystallogr Sect B 58:934–938
73. Howard CJ, Stokes HT (2005) Structures and phase transitions in perovskites-A group-theoretical approach. Acta Crystallogr Sect A Found Crystallogr 61:93–111
74. Megaw HD (1945) Crystal structure of barium titanate. Nature 155:484–485
75. Setter N, Colla EL (1993) Ferroelectric ceramics. Tutorial reviews, theory, processing, and applications, 1st ed. Birkhäuser, Basel
76. Jaffe B, Cook WR, Jaffe H (1971) Piezoelectric ceramics. Academic Press Inc., London

77. Galasso FS (1969) Structure, properties and preparation of perovskite-type compounds. Pergamon Press
78. Haertling GH (2004) Ferroelectric ceramics: history and technology. J Am Ceram Soc 82:797–818
79. Cross LE, Newnham RE (1987) History of ferroelectrics. In: Kingery WD (ed) Ceramics and civilization 3, High technology ceramics: past, present, and future. The American Ceramic Society, Westerville, pp 289–305
80. U.S. National Research Council (1940) Industrial research laboratories of the United States including consulting research laboratories, 7th ed. National Research Council, National Academy of Sciences, Washington, D.C
81. Wainer E, Thielke NR (1942) Dielectric material and method of making the same, US2277733, pp 1–4
82. Wainer E, Thielke NR (1942) Dielectric material and method of making the same, US2277736, pp 1–2
83. Thurnauer H, Deaderick J (1947) Insulating material, US2429588, pp 1–3
84. Newnham RE, Cross LE (2005) Ferroelectricity: the foundation of a field from form to function. MRS Bull 30:845–848
85. Wainer E (1946) High titania dielectrics. J Electrochem Soc 89:331–356
86. Acosta M, Novak N, Rojas V et al (2017) BaTiO3-based piezoelectrics: fundamentals, current status, and perspectives. Appl Phys Rev 4:41305
87. von Hippel A, Breckenridge RG, Chesley FG, Tisza L (1946) High dielectric constant ceramics. Ind Eng Chem 38:1097–1109
88. Wul B (1945) Dielectric constants of some titanates. Nature 156:480
89. Jaffe H (1950) Titanate ceramics for electromechanical purposes. Ind Eng Chem 42:264–268
90. Fujishima S (2000) The history of ceramic filters. IEEE Trans Ultrason Ferroelectr Freq Control 47:1–7
91. Jaffe B, Roth RS, Marzullo S (1954) Piezoelectric properties of lead zirconate-lead titanate solid-solution ceramics. J Appl Phys 25:809–810
92. Smolenskii GA, Agranovskaya AI (1958) Dielectric polarization and losses of some complex compounds. Sov Phys Tech Phys 3:1380–1382
93. Mitsui T, Abe R, Furuhata Y, et al (1969) Ferro and antiferroelectric substances. Landolt-Bornstein numerical data and functional relationships, vol 3. Springer, Berlin
94. Megaw HD (1947) Temperature changes in the crystal structure of barium titanium oxide. Proc R Soc Lond A 189:261–283
95. Kay HF, Vousden P (1949) XCV. Symmetry changes in barium titanate at low temperatures and their relation to its ferroelectric properties. Philos Mag 40:1019–1040
96. Wood EA (1951) Polymorphism in potassium niobate, sodium niobate, and other AB03 compounds. Acta Crystallogr 4:353–362
97. Jackson W, Reddish W (1945) High permittivity crystalline aggregates. Nature 156:717
98. Rushman DF, Strivens MA (1946) The permittivity of polycrystals of the perovskite type. Trans Faraday Soc 42:A231–A238
99. Van Santen JH, Jonker GH (1950) Electrical conductivity of ferromagnetic compounds of manganese with perovskite structure. Physica 16:599–600
100. Jonker GH, Van Santen JH (1950) Ferromagnetic compounds of manganese with perovskite structure. Physica 16:337–349
101. Zener C (1951) Interaction between d Shells in the transition metals. Phys Rev 81:440–444
102. Zener C (1951) Interaction between d Shells in the transition metals. II. Ferromagnetic Compounds of manganese with perovskite structure. Phys Rev 82:403–405
103. Goodenough JB (1955) Theory of the role of covalence in the perovskite-type manganites [La, M(II)]MnO3. Phys Rev 100:564–573
104. Anderson PW, Hasegawa H (1955) Considerations on double exchange. Phys Rev 100: 675–681
105. Kanamori J (1959) Superexchange interaction and symmetry properties of electron orbitals. J Phys Chem Solids 10:87–98

106. de Gennes P-G (1960) Effects of double exchange in magnetic crystals. Phys Rev 118: 141–154
107. Roth RS (1957) Classification of perovskite and other ABO3-type compounds. J Res Natl Bur Stand 58:75–88
108. Keith ML, Roy R (1954) Structural relations among double oxides of trivalent elements. Am Miner 39:1–23
109. Roy R (1954) Multiple Ion substitution in the perovskite lattice. J Am Ceram Soc 37:581–588
110. Steward EG, Rooksby HP (1953) Transitions in crystal structure of cryolite and related fluorides. Acta Crystallogr 6:49–52
111. Steward EG, Rooksby HP (1951) Pseudo-cubic alkaline-earth tungstates and molybdates of the R3MX6 type. Acta Crystallogr 4:503–507
112. Galasso F, Katz L, Ward R (1959) Substitution in the octahedrally coordinated cation positions in compounds of the perovskite type. J Am Chem Soc 81:820–823
113. Brixner LH (1960) Preparation and structure determination of some new cubic and tetragonally distorted perovskites. J Phys Chem 54:1956–1957
114. Wyckoff RWG (1965) Crystal Structures. Inorganic Compounds Rx(MX4)y, Rx(MnXp)y, Hydrates and ammoniates, vol 3, 2nd ed. Interscience Publishers (Wiley), New York
115. Wells AF (1945) Structural inorganic chemistry. Clarendon Press, Oxford
116. Elliott N, Pauling L (1938) The crystal structure of cesium aurous auric chloride, Cs2AuAuCl6, and cesium argentous auric chloride, Cs2AgAuCl6. J Am Chem Soc 60:1846–1851
117. Pauling L (1924) The crystal structures of ammonium fluoferrate, fluo-aluminate and OXYFLUOMOLYBDATE. J Am Chem Soc 46:2738–2752. https://doi.org/10.1021/ja01677a019
118. Megaw HD (1973) Crystal structures: a working approach, 1st ed. W. B. Saunders Company, London
119. Cross W, Hillebrand WF (1883) On minerals of the cryolite group recently found in Colorado. Am J Sci XXVI:271–294
120. Cross W, Hillebrand WF (1885) Contributions to the mineralogy of the Rocky Mountains
121. Menzer G (1932) Ueber die Kristallstrukturen der Kryolithgruppe. Fortschritte der Mineral 17:61
122. Vasala S, Karppinen M (2015) A2B′B″O6 perovskites: a review. Prog Solid State Chem 43:1–36
123. Flerov IN, Gorev MV, Aleksandrov KS et al (1998) Phase transitions in elpasolites (ordered perovskites). Mater Sci Eng R Rep 24:81–151
124. Anderson MT, Greenwood KB, Taylor GA, Poeppelmeier KR (1993) B-Cation arrangements in double perovskites. Prog Solid State Chem 22:197–233
125. Ewing FJ, Pauling L (1928) The crystal structure of potassium chloroplatinate. Zeitschrift für Krist-Cryst Mater 68:223
126. Dickinson RG (1922) The crystal structures of potassium and ammonium chlorostannates. J Am Chem Soc 44:276–288
127. Bozorth RM (1922) The crystal structure of ammonium fluosilicate. J Am Chem Soc 44:1066–1070
128. Katz L, Ward R (1964) Structure relations in mixed metal oxides. Inorg Chem 3:205–211
129. Wells AF (1962) Structural inorganic chemistry, 3rd edn. Oxford University Press, Oxford
130. Longo JM, Kafalas JA (1969) The effect of pressure and B-cation size on the crystal structure of CsBF3 compounds (B = Mn, Fe Co, Ni, Zn, Mg). J Solid State Chem 1:103–108
131. Evans HT, Burbank RD (1948) The crystal structure of hexagonal barium titanate. J Chem Phys 634:634
132. Balz D, Plieth K (1955) Die Struktur des Kaliumnickelfluorids, K2NiF. Zeitschrift für Elektrochemie, Berichte der Bunsengesellschaft für Phys Chemie 59:545–551
133. Balz D (1953) Über die Struktur des K2NiF4. Naturwissenschaften 40:241

134. Ruddlesden SN, Popper P (1957) New compounds of the K2NIF4 type. Acta Crystallogr 10:538–539
135. Ruddlesden SN, Popper P (1958) The compound Sr3Ti2O7 and its structure. Acta Crystallogr 11:54–55
136. Smolenskii GA, Isupov VA, Agranovskaya AI (1961) Ferroelectrics of the oxygen-octahedral type with layered structure. Sov Phys Solid State 3:651–655
137. Bednorz JG, Müller KA (1986) Possible high Tc superconductivity in the Ba-La-Cu-O system. Zeitschrift für Phys B Condens Matter 193:267–271
138. Yani C, Yong S, Jiajun P et al (2017) 2D Ruddlesden-Popper Perovskites for Optoelectronics. Adv Mater 30:1703487
139. Gu X-K, Samira S, Nikolla E (2018) Oxygen sponges for electrocatalysis: oxygen reduction/evolution on nonstoichiometric, mixed metal oxides. Chem Mater 30:2860–2872
140. Aurivillius B (1949) Mixed bismuth oxides with layer lattices: I, structure type of CaNb2Bi209. Ark för Kemi 1:463–480
141. Aurivillius B (1949) Mixed bismuth oxides with layer lattices. II. Structure of Bi4Ti3O12. Ark för Kemi 1:499–512
142. Subbarao EC (1961) Ferroelectricity in Bi4Ti3O12 and its solid solutions. Phys Rev 122:804–807
143. Subbarao EC (1962) A family of ferroelectric bismuth compounds. J Phys Chem Solids 23:665–676
144. Moure A (2018) Review and perspectives of aurivillius structures as a lead-free piezoelectric system. Appl Sci 8:62
145. Hazen RM (1988) Superconductors, the breakthrough. Unwin and Hyman Ltd, London
146. Cr J (2000) Oxide superconductors. J Am Ceram Soc 83:5–28
147. Galasso FS (1990) Perovskites and high Tc superconductors. Gordon and Breach Science Publishers, New York
148. Hazen RM (1988) Perovskites. Sci Am 258:52–61
149. Strauss SW, Fankuchen I, Ward R (1951) Barium cobalt oxide of the perowskite type. J Am Chem Soc 73:5084–5086
150. Erchak M, Fankuchen I, Ward R (1946) Reaction between ferric oxide and barium carbonate in the solid phase. Identification of phases by x-ray diffraction1. J Am Chem Soc 68:2085–2093
151. Erchak M, Ward R (1946) Catalytic properties of the products of the solid phase reaction between barium carbonate and ferric oxide. J Am Chem Soc 2085:2093–2096
152. Parravano G (1952) Ferroelectric transitions and heterogenous catalysis. J Chem Phys 20:342–343
153. Parravano G (1953) Catalytic activity of lanthanum and strontium manganite. J Am Chem Soc 75:1497–1498
154. Macchesney JB, Sherwood RC, Potter JF (1965) Electric and magnetic properties of the strontium ferrates. J Chem Phys 43:1907–1913
155. Grenier J-C, Pouchard M, Georges R (1973) Variation thermique de la susceptibilite magnetique et de l'aimantation du ferrite bicalcique Ca2Fe2O5. Mater Res Bull 8:1413–1420
156. Grenier J-C, Darriet J, Pouchard M, Hagenmuller P (1976) Mise en evidence d'une nouvelle famille de phases de type perovskite lacunaire ordonnee de formule A3M3O8 (AMO2,67). Mater Res Bull 11:1219–1225
157. Schippers ABA, Brandwijk V, Gorter EW (1973) Derivation and discussion of crystal structures of compounds ABX3 and A2BX6: Part I. Derivation of the structures. J Solid State Chem 6:479–492
158. Goodenough JB, Graper W, Holtzberg F, et al (1970) Magnetic and other properties of oxides and related compounds, vol 4. Landolt-Bornstein, Numerical Data and Functional Relationships in Science and Technology, New Series, Group III. Springer, Berlin
159. Smyth DM, Chang EK, Liu DH (1996) Travels through perovskite space. Phase Trans 58:57–73

160. Mitchell RH (1996) Perovskites: a revised classification scheme for an important rare earth element host in alkaline rocks. In: Jones AP, Wall F, Williams CT (eds) Rare earth minerals: chemistry, origin and ore deposits. Chapman & Hall, pp 41–76
161. Mitchell RH, Welch MD, Chakhmouradian AR (2017) Nomenclature of the perovskite supergroup: a hierarchical system of classification based on crystal structure and composition. Mineral Mag 81:411–461
162. Rao CNR, Bernard Raveau (1998) Transition metal oxides. Structure, properties, and synthesis of ceramic oxides, 2nd ed. Wiley-VCH, New York
163. Aleksandrov KS, Beznosikov VV (1997) Hierarchies of perovskite-like crystals (Review). Phys Solid State 39:695–715
164. Aleksandrov KS, Bartolomé J (2001) Structural distortions in families of perovskite-like crystals. Phase Trans 74:255–335
165. Beznosikov BV, Aleksandrov KS (2000) Perovskite-like crystals of the Ruddlesden-Popper series. Crystallogr Rep 45:792–798
166. Aleksandrov KS (1976) The sequences of structural phase transitions in perovskites. Ferroelectrics 14:801–805
167. Mitsui T, Nomura S, Adachi M, et al (1981) Ferroelectrics and related substances. Landolt-Bornstein numerical data and functional relationships, vol 16. Springer, Berlin
168. Jin S, Tiefel TH, Mccormack M, et al (1994) Thousandfold change in resistivity films in magnetoresistive La-Ca-Mn-O films. Science (80-) 264:413–415
169. Chahara K, Ohno T, Kasai M, Kozono Y (1993) Magnetoresistance in magnetic manganese oxide with instrincic antiferromagnetic spin structure. Appl Phys Lett 63:1990–1992
170. von Helmolt R, Wecker J, Holzapfel B et al (1993) Giant magnetoresistance in perovskitelike La2/3Ba1/3MnOx ferromagnetic films. Phys Rev Lett 71:2331–2333
171. Simonds JL, John L (1995) Magnetoelectronics today and tomorrow. Mater Today 48:26–32
172. Jonker GH (1956) Magnetic compounds with perovskite structure IV conducting and non-conducting compounds. Physica 22:707–722
173. Tokura Y (2006) Critical features of colossal magnetoresistive manganites. Rep Prog Phys 69:797–851
174. Mathur N (2006) All aboard the manganite rollercoaster. Nat Mater 5:849–850
175. Bhalla A, Guo R, Roy R (2000) The Perovskite structure-a review of its role in ceramic science and technology. Mater Res Innov 4:3–26
176. Sleight AW, Gillson JL, Bierstedt PE (1975) High-temperature superconductivity in the BaPb1-xBixO3 systems. Solid State Commun 17:27–28
177. Weber MJ, Bass M, Andringa K et al (1969) Czochralski growth and properties of YAlO3 laser crystals. Appl Phys Lett 15:342–345
178. Massey GA (1970) Criterion for selection of CW laser host materials to increase available power in the fundamental mode. Appl Phys Lett 17:213–215
179. Haertling GH, Land CE (1971) Hot-Pressed (Pb, La)(Zr, Ti)O3 ferroelectric ceramics for electrooptic applications. J Am Ceram Soc 54:1–11
180. Haertling GH (1971) Improved Hot-pressed electrooptic ceramics in the (Pb, La)(Zr, Ti)O3 system. J Am Ceram Soc 54:303–309
181. Ringwood AE, Kesson SE, Ware NG et al (1979) Immobilisation of high level nuclear reactor wastes in SYNROC. Nature 278:219
182. Voorhoeve RJH, Johnson DW, Remeika JP, Gallagher PK (1977) Perovskite oxides: materials science in catalysis. Science 195:827–833
183. Meadowcroft DB (1970) Low cost oxigen electrode material. Nature 226:847–848
184. Libby WF (1971) Promising catalyst for auto exhaust. Science (80-) 171:499 LP-500
185. Sverdrup EF, Warde CJ, Eback RL (1973) Design of high-temperature solid-electrolyte fuel-cell batteries for maximum power output per unit volume. Energy Convers 13:129–141
186. Feduska W, Isenberg AO (1983) High-temperature solid oxide fuel cell—technical status. J Power Sources 10:89–102
187. Frost MJ, Symes RF (1970) Zoned perovskite-bearing chondrule from the Lance meteorite. Mineral Mag 37:724–726

188. Grossman L (1975) Petrography and mineral chemistry of Ca-rich inclusions in the Allende meteorite. Geochim Cosmochim Acta 39:433–454
189. Lin-gun L (1974) Silicate perovskite from phase transformations of pyrope-garnet at high pressure and temperature. Geophys Res Lett 1:277–280
190. Lin-gun L (1975) Post-oxide phases of forsterite and enstatite. Geophys Res Lett 2:417–419
191. Hemley RJ, Cohen RE (1992) Silicate Perovskite. Annu Rev Earth Planet Sci 20:553–600
192. Tejuca LG, Fierro JL (1993) Properties and applications of perovskite-type oxides. Marcel Dekker Inc, New York

Chapter 2
Magnetic, Electronic, and Optical Properties of Perovskite Materials

Lin Fu, Bo Li, Shuang Li and Longwei Yin

1 Introduction

The emergence of organic-inorganic hybrid halides perovskite materials has generated enormous interest in the photovoltaic research community. The materials present numerous advantages in electronic, magnetic, and optical properties. In the last few years, because of the strong electron–electron interaction with the 3d manifold and considerable physical strength, scientists have paid a great deal of attention to magnetic properties of perovskite materials, especially B-site substituted perovskite and perovskite manganite. The B-site substituted perovskites are a great playground for magnetic properties, as various combinations of different paramagnetic cations are possible at all of the three cation sites, allowing for a wide range of magnetic behaviors. Perovskite manganites have a wide range of magnetic properties, such as colossal multiferroic property, magnetocaloric effect, and magnetoresistance. There are various applications in magnetism such as magnetic refrigeration, bioprocessing, and miniaturized magnetic sensor applications. In addition, the electronic structure of perovskite materials is predominantly determined by the BX_6 ions, while the distinctive electronic character of perovskite materials is basically induced by the lone pair of lead ions. Moreover, one of the remarkable aspects of halide perovskites is that the grain boundaries are electrically benign. Therefore, it is promising to produce high-quality semiconductor films from solution processing methods for various photoelectric devices.

L. Fu · B. Li · S. Li · L. Yin (✉)
Key Laboratory for Liquid-Solid Structural Evolution and Processing of Materials, Ministry of Education, School of Materials Science and Engineering, Shandong University, Jinan 250061, People's Republic of China
e-mail: yinlw@sdu.edu.cn

N. S. Arul and V. D. Nithya (eds.), *Revolution of Perovskite*, Materials Horizons: From Nature to Nanomaterials, https://doi.org/10.1007/978-981-15-1267-4_2

2 Magnetic Properties

Recently, because of the discovery of B-site substituted perovskite oxides $A_2B'B''X_6$ and nanoscale manganese-based perovskite oxides ($AMnO_3$) which have colossal magnetoresistance, the studies of magnetic properties of perovskite materials have attracted a great deal of attention. They are used in the areas of sensors, catalysts, magneto-optical materials, fuels cells, et al.

Because of their unusual magnetic properties, recently there has been particular interest in the case of transition metal perovskite oxides. These perovskite oxides have special magnetic properties due to the strong electron–electron interaction with the 3d manifold and a considerable physical strength [1]. For instance, Cai reported that half-metallic ferromagnetism leads to giant magneto-optical Kerr effects in the $BiNiO_3$ with the orthorhombic structure. In the Hessler compound PtMnSb, Kerr rotation reached 1.28° at 1.87 eV, which is compared to the accepted maximum polarity Kerr rotation of 1.35° at 1.75 eV. The great p-d exchange influences half-metallic ferromagnetism with the semiconducting majority-spin electrons and the metallic minority-spin electrons, leading to large Kerr rotation of $BiNiO_3$ finally [2].

The perovskite structure has the compositional flexibility and excellent structue. Recently, half of the B-site cations have attracted a lot of attention, and these cations have been replaced by another cation. In this case, B′ and B″ may keep disordered, or they can order at the B-site, forming a so-called $A_2B'B''X_6$, of which B-site ordered double perovskite. There are three ways that the B-site cations ordered, the structure increases the modifiability and complexity of the perovskite compounds, as shown in Fig. 1. In addition, the two different cations existing in B-site leads to novel and interesting combinations, ranging from 3d, 4d, or 5d transition metals from actinoides and lanthanoides to main group elements, whose oxidation states are various. Because of the fact that B-site cations determine the

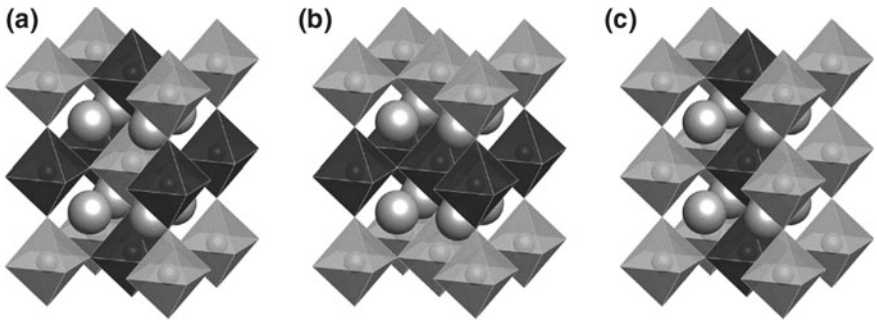

Fig. 1 The B-site cation combinations of $A_2B'B''X_6$ perovskites: **a** rock-salt, **b** layered and **c** columnar order [3] (Reprinted with permission from Ref. [3]. Copyright 2010, Published by The Royal Society of Chemistry)

magnetic order and electrical conductivity of $A_2B'B''X_6$, potential new materials with each cation combination and ordering can be ensured in a wide range.

The double perovskites are of good magnetic properties. For the reason that various combinations of paramagnetic cations are able to fit in these cation sites of $A_2B'B''X_6$, a large number of magnetic performances can be achieved. Although some compounds are antiferromagnetic (AFM), a variety of ferromagnetic (FM) or ferrimagnetic (FiM) compounds have been found in $A_2B'B''X_6$ perovskite" compared to other oxides. Some have very high magnetic ordering temperature (T_C). In addition, considering the magnetic properties, the degree of cation order is very important. The spin-glass behavior has been observed with significant long-range magnetic properties in several disordered compounds. For example, low-dimensional magnetic properties have been found in JT distorted $A_2CuB''X_6$.

In so far as a single paramagnetic B-site cation in the $A_2B'B$ "X_6 perovskite, the super-exchange interaction occurs over a relatively long distance. What is interesting is that the strength of the 90° B″–O–(B′)–O–B″nearest-neighbor (NN) interactions and the 180° B′–O–B″–O–B′ next-nearest-neighbor (NNN) interactions can often be of the same order, and can compete. The relative strength of these interactions depends on the nature of the paramagnetic ions. For example, it has been noted that the 90° B′–O–O–B′ interactions are stronger compared to 180° B′–O–B″–O–B′ in certain Ru compounds, due to the fact that the, e.g., orbitals of Ru are empty, so only π-interactions possible [4]. Similarly we would expect compounds with full t_{2g} orbitals and half-filled, e.g., orbitals to have relatively stronger 180° interactions.

In case of two magnetic B-site cations, things are a bit more complicated. There may be short-range B′–O–B″ interactions between the B-site cations, as well as long-range B′–O–(B″)–O–B′ and B″–O–(B′)–O–B″ ones. It would perhaps be expected that the short-range B′–O–B″ interactions would be the strongest interaction in the system, dominating the magnetic ordering. However, in $A_2B'B''X_6$ perovskites, the B″–O–(B′)–O–B″ superexchange interactions may sometimes be stronger than B′–O–B″ interactions, due to weaker energetic orbital overlap of the two different B-site cations. This has been shown for example in case of Sr_2CoOsO_6, where the two B-cation sublattices order independently and at different temperatures [5]. Several compounds with B′ = R and B″ = transition metal, such as various A_2RRuO_6 compounds, Sr_2TbIrO_6 and Ba_2NdOsO_6, show the same behavior of the two B-cation sublattices ordering at different temperatures. Apparently, the orbital mixing between the lantanoides and the transition metals is weak enough that the long-range superexchange interactions dominate the magnetic ordering. The energetic overlap of the two B-site cation orbitals is often poor in the $A_2B'B''O_6$ perovskites. Thus, it could be relatively common for the long-range B′–O–(B″)–O–B′ superexchange to be stronger than the short B′–O–B″ interaction in these compounds.

It is also possible to place paramagnetic cations at the A-position of the $A_2B'B''O_6$ perovskite. Compounds having Mn^{2+} or paramagnetic R in A-position are well-known. In this case, between A and B-site cations, there is possibly a magnetic coupling. For instance, Mn and Fe of Mn_2FeSbO_6 are spin-coupled to produce an elliptical spin helix with a disproportionate propagation vector [6].

The paramagnetic ions are also likely to occupy all three cation sites, such as Nd_2NiMnO_6, in which Ni and Mn order FM to each other at 200 K while Nd is ordered AFM to the B-site cations at 45 K [7]. However, the interaction between the A and B cations is usually very weak. For example, in R_2LiRuO_6, the Ru–O–(Li)–O–Ru interaction is stronger than the R–O–R or R–O–Ru interaction [8]. This may be mainly because of the weak orbital mixing of lanthanide and transition metal elements. It is interesting to point out that Pb in A-site can improve magnetic properties because of the super-exchange interactions of electrons in Pb 6s [9]. Comparing with Pb or Sr in A-site, it has been found that the magnetic temperatures of $A_2B'NbO_6$, A_2NiReO_6, A_2MnWO_6, and A_2FeTiO_6 are higher [10].

JT distortion due to d^1 configuration is rare but has been found in $A_2B'B''X_6$ perovskites occasionally. In the case of Ba_2SmMoO_6, both JT distortion coincides and T_N appears, where the relatively high value of T_N = 130 K is influenced by orbital ordering [11]. In addition, JT distortion in Ba_2NdMoO_6 influences magnetic ordering, though the relations between magnetic order and orbital are slight [12, 13]. In Ba_2NaOsO_6, the JT distortion is not obvious, where the degeneracy of the track leads to weak ferromagnetic order. A similar compound, Ba_2LiOsO_6 is AFM indicating a fairly good balance between the two compounds.

In respect of 4d/5d metal, the spin-orbit coupling and spin delocalization covalently bonded by the bond are significantly improved compared with the 3d metal. Therefore, the magnetic moment of the 4d/5d element is significantly brought down, just as some compounds with Ru [14]. It is particularly interesting that because of its powerful SOC, Ir^{5+} compounds (Ba_2HoIrO_6 or R_2NaIrO_6) shows neither magnetic ordering of the Ir sublattic nor reduced moment at Ir. The reason is explained that the great SOC lifts the t_{2g} orbital degeneracy and creates a non-magnetic ground state, even though the Ir^{5+} ions with typical low-spin d^4 are expected to be paramagnetic. In so far as R_2LiIrO_6, the nonmagnetic ground state was found for Ir, while magnetic properties are resulted from the R ions. However, an Ir set the stage for the magnetic properties was found at higher temperatures. At low temperature, a nonmagnetic ground state of Ir is observed in R_2LiIrO_6 while the magnetic properties are ascribed to R ions at A-site. Nevertheless, Ir contributes to magnetic properties when the temperature gets higher. Structural distortions can quench the effect of SOC as it does in the case of Sr_2YIrO_6.

In addition, most of the reported $A_2B'B''X_6$ perovskites with magnetic ordering are AFM, and some AFM order of more than 200 compounds has been reported. A single B′ or B″ cation forms a face-centered cubic (FCC) lattice, and when magnetic cations of this FCC array shows up, a few common types of magnetic ordering are found. These are three types of orderings shown in Fig. 2. The types of I, II, and III are relied on the relative strengths of the NN and NNN of magnetic ions. Type I is found under the condition of stronger NN interactions than the NNN ones, where eight of the twelve NN cations are ordered AFM while the other NNN cations all ordered FM. We can easily find type II when the NNN interaction is more significant than the NN interaction. Type III is an intermediate form with relatively strong NN interactions and apparent NNN interactions. Similar to type I,

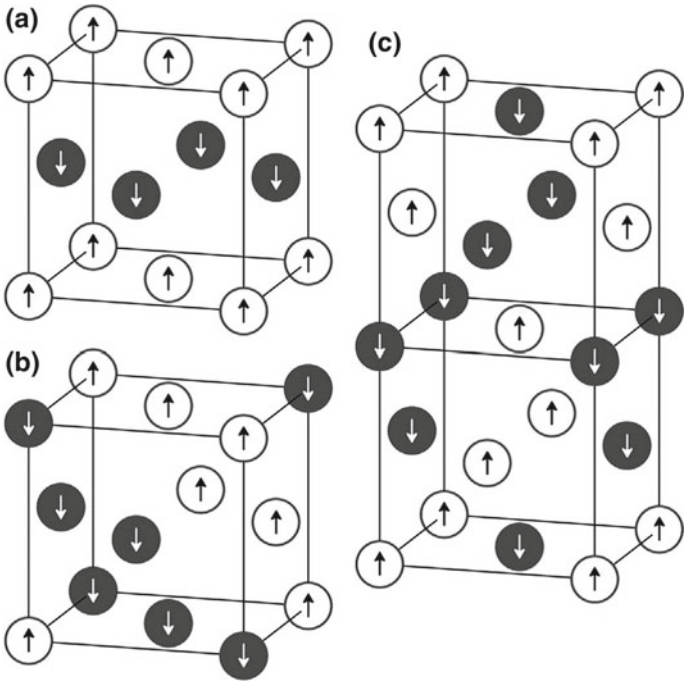

Fig. 2 Common orderings of $A_2B'B''O_6$ antiferromagnetic perovskites: **a** type I, **b** type II and **c** type III [15]. (Reprinted with permission from Ref. [15]. Copyright 1999, Published by The American Physical Society)

eight of the twelve NN cations are ordered AFM, but two of the six NNN cations are ordered AFM [15].

Magnetic properties lean on the orbital overlap of spatial ions while the overlap leans on the structure. For instance, the interaction of T_C and bandwidth which is estimated by bond length and angle has been established in the compound of $A'A''FeMoO_6$ with A′, A″ = Ca, Ba or Sr. Comparably, a linear dependence between T_N values and electronic bandwidth is found for some other Mo or W compounds.

Due to the presence of CMR, perovskite manganese oxide has a strong core electronic system, and strong interactions within the electron lead to complex electronic properties and magnetic properties [16]. The rich physics involving manganese oxides, such as phase separation [17], charge ordering (CO), and semi-metallicity, make it one of the highlights in the field of condensed matter physics along with many prototype devices designed and development of scientific research and formulation technology.

At present, nanoscale perovskite manganite has vast development potential and broad market prospects. There are various applications in magnetism such as magnetic refrigeration, bio-processing, and miniaturized magnetic sensor applications. A large number of researches make clear that as the size is reduced to the

nanometer scale strong rearranges, the magnetic properties of perovskite manganite will change dramatically, including large coercivities and surface spin-glass (SG) [18]. According to the scientists, when the particle size of perovskite manganate drops to the nanometer level, the spin core–shell structure is easily observed. In this process, the nature of the core is similar to the nature of the homologous sample, while the core has a large number of crystal defects leading to ineffective rotation of the core, leading to the appearance of magnetic dead layers. In addition, as the particle size decreases, the surface effect of the shell becomes stronger. At the same time, scientists have concluded that the surface super-exchange interaction is conducive to the development of the FM core [19].

For instance, nanosized FM manganite $La_{0.67}Ca_{0.33}MnO_3$ (LCMO) exhibits a reduced saturated magnetization with smaller grain size. On account of the magnetic properties of perovskite manganite, scientists put forward the core–shell model nanoparticles, where the core exists the original nature and the magnetic properties of the shell make a difference. The thickness of the shell is approximately 3 nm; this magnetic dead layer has been detected to exist along with the FM crystalline core [20]. Nevertheless, for the core–shell structure of $La_{0.25}Ca_{0.75}MnO_3$, the temperature of the CO transition gradually decreases and the pyramid becomes wide and weak as the grain size decreases. Pyramid, FM becomes the CG state [21]. This phenomenon involves endless rotation of the grain size while improving the FM interaction and suppressing the AFM state.

Nevertheless, for the core–shell structure of $La_{0.25}Ca_{0.75}MnO_3$, the temperature of the CO transition gradually decreases and the pyramid becomes wide and weak as the grain size decreases [21]. This phenomenon involves endless rotation of the grain size while improving the FM interaction and suppressing the AFM state. Phan and Yu [22] reviewed the RCP of various perovskite materials and summarized that compositions of $La_{0.845}Sr_{0.155}MnO_3$, $La_{0.815}Sr_{0.185}MnO_3$, $La_{0.7}Ca_{0.25}Sr_{0.05}MnO_3$, $Gd_5Si_2Ge_2$, and $Pr_{0.63}Sr_{0.37}MnO_3$ contributed the highest RCP values of 670, 533, 462, 535, and 511 J/kg in turn. In the report, some additional compositions such as $HoMnO_3$, $La_{0.6}Ca_{0.4}MnO_3$, $Pr_{0.8}Na_{0.2}MnO_3$, $Pr_{0.8}Na_{0.15}K_{0.05}MnO_3$, $Pr_{0.8}Na_{0.1}K_{0.1}MnO_3$, and $Pr_{0.8}Na_{0.05}K_{0.15}MnO_3$ have performed the RCP of 540, 508, 356, 326, 292, and 293 J/kg. In addition, facile cooling power was contributed by the rest of manganites. For $Yb_{0.9}Er_{0.1}MnO_3$ and $Yb_{0.8}Er_{0.2}MnO_3$ with higher value of ΔH, this cooling power is increased [23].

3 Electronic Properties

The electronic structures of perovskites are determined by BX_6 blocks, of which are near the band edge in particular. For example, the Pb 6s-I 5p-antibonding orbital of the $[PbI_6]^{4-}$ units settles the valence band while the Pb 6p-I 5p σ-antibonding and Pb 6p-I 5s σ-antibonding orbitals control the conduction band [24]. The unique electronic properties of perovskite materials are essentially induced by lone pairs of lead ions. Unlike the electronic properties of most cations, Pb has an electron orbit

that occupies 6 s below the top of valence band (VB) [25]. The valence band maximum (VBM) has a stable antibonding interaction between I and Pb. Due to the special ionic and covalent nature of the electronic structure in perovskite materials, conduction band minimum (CBM) is mainly caused by the Pb state. As shown in Fig. 3, the electronic properties of the perovskite are attributed to the molecular structure of the perovskite material and to each ion. Like the perovskite structure of $MAPbI_3$, the iodide ion produces VB at the A-site, while the iodide ion produces a conduction band at the B-site.

As can be seen from Fig. 3a, the density distribution of the different ions can have an effect on the electronic properties of the perovskite material. We can conclude that the cation-related state density is very low compared to VBM, which has no effect on the electronic band structure. The unique electronic structures of perovskites are displayed in Fig. 3, in contrast with the first and second generation, taking the Si and GaAs solar cell as examples. In traditional semiconductors, the CBM mainly depends on s orbital while the VBM on p orbital [27]. However, halide perovskite exhibits an inverted electronic band structure, leading to strong optical absorption compared with the first-and second-generation semiconductors.

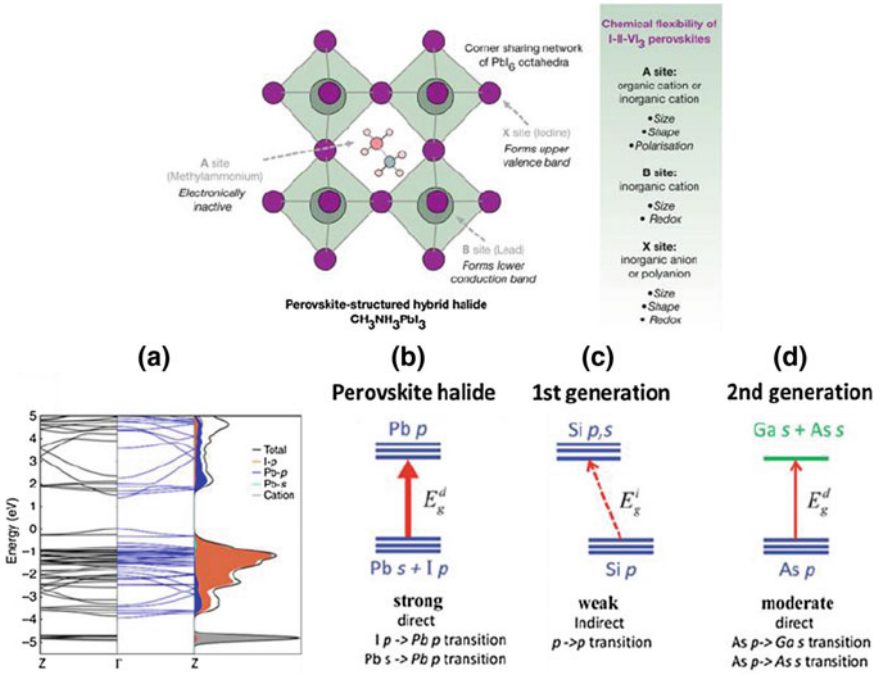

Fig. 3 **a** Contributions of MA, Pb, and I on the density of state of $MAPbI_3$ perovskite [26] (Reprinted with permission from Ref. [26]. Copyright 2014, Published by Springer Nature). Schematic optical absorption of **b** perovskite, **c** Si and **d** GaAs [27]) (Reprinted with permission from Ref. [27]. Copyright 2015, Published by Royal Society of Chemistry)

Compared with the previous absorber, perovskite materials are direct bandgap semiconductors and its transition possibility is much higher than others.

Although both $MAPbI_3$ and GaAs have direct bandgap, their electronic structures are quite different. First, the bottom end of the conduction band (CB) of the perovskite material is determined by the Pb b band. Instead, the lower end of the CB is determined by the delocalized s orbit of GaAs. Thus, the perovskite material has a higher state density (Fig. 4a) and a combined density of states (Fig. 4b). On the other hand, the band transition between CB and VB originates from the mixed halides of Pb s and I p to Pb p orbitals. The possible transition from Pb s to Pb p is higher than that of GaAs, as the ability of optical absorption for perovskites is much stronger than that of GaAs (see in Fig. 4c, d) (Fig. 5).

Another uniqueness of perovskites is the electrically benign grain boundary (GB). Different from the conventional polycrystalline GBs that are noxious for performance, the GBs of perovskite polycrystalline films are usually invisible [29], which has been reported to benefit the device performance [30]. There is a stable interaction between Pb s and I p, resulting in a higher VBM. Therefore, there

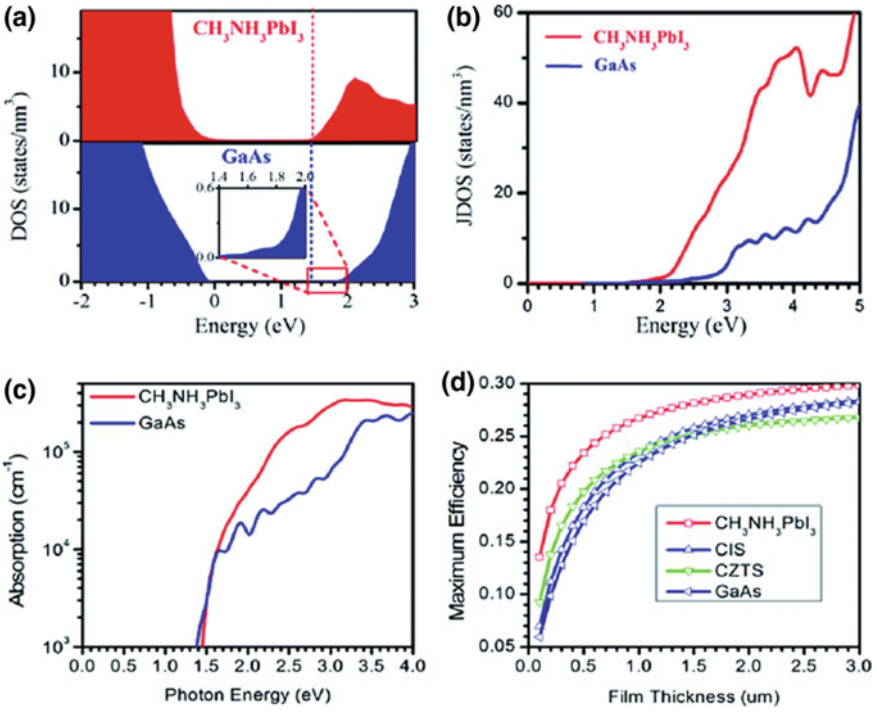

Fig. 4 **a** Density of states of $MAPbI_3$ and GaAs. The VBMs are referred to as zero energy and CBMs are marked in dashed lines, **b** Joint density of states of $MAPbI_3$ and GaAs, **c** optical absorptions of $MAPbI_3$ and GaAs, **d** maximum efficiencies calculated for $MAPbI_3$, CIS, CZTS, and GaAs as a function of film thickness [27] (Reprinted with permission from Ref. [27]. Copyright 2015, Published by Royal Society of Chemistry)

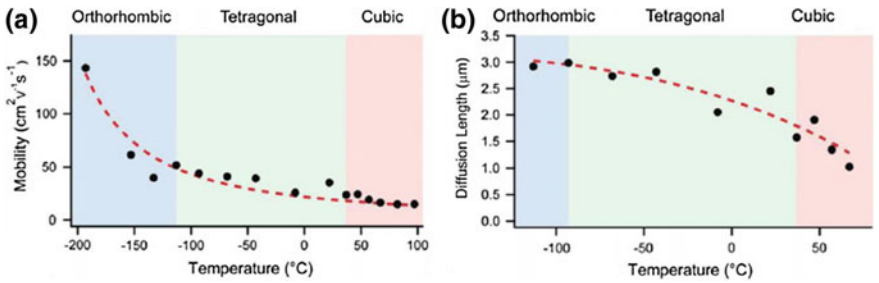

Fig. 5 Temperature dependence of (a) mobility and (b) diffusion lengths of $MAPbI_3$ [28] (Reprinted with permission from Ref. [28]. Copyright 2014, Published by Springer Nature)

are lower defect states and charge carrier recombination [27]. Due to the specific electronic structure, the perovskite material has strong carrier transport and carrier collection properties, which is advantageous for electronic performance. [27, 31, 32].

By solution method engineering, perovskite films with high quality can be produced. For example, the mobility of $MAPbI_3$ thin film can be enhanced by four magnitude (8–35 $cm^2\ V^{-1}\ s^{-1}$) through optimized deposition techniques [33]. At the same time, the diffusion length of the perovskite material varies with the preparation method. The relationship between the electronic properties of the perovskite material and the crystal structure can be seen from Fig. 2. As shown in Table 1, it can be clearly seen that various measurement methods and material compositions result in the electronic properties of the perovskite. When the phase of perovskite transforms to a cubic structure at room temperature, electronic properties are relatively reduced.

Table 1 Diffusion length and mobility of some hybrid perovskites

Compound (Perovskite Thin Films)	Measurement technique	Mobility (μ) ($cm^2\ v^{-1}\ s^{-1}$)	Diffusion length, L_D (μm)	Charge lifetime, τ (ns)	Reference
$MAPbI_3$	PLQ	0.66	0.13	9.6	[34]
	PLQ	1.4	0.13	4.5	[35]
	TRTS	8.2	1.2	67	[36]
$MAPbI_{3-x}Cl_x$	PLQ	1.6	1.07	273	[34]
	TRTS	11.6	2.4	200	[36]
$MAPbBr_3$	PLQ	8.9	1.06	51	[37]
$CH(NH_2)_2PbI_3$	PLQ	0.16	0.18	75	[38]
	TRTS	27	3.1	140	[39]
$CH(NH_2)_2PbBr_3$	TRTS	14	1.3	50	[39]
$MASnI_3$	TRTS	1.6	0.03	0.2	[40]

4 Optical Properties

Perovskites are under intense research for the use in optoelectronics, not only in solar cells but also light detectors [41–43] and light-emitting diodes (LEDs) [44, 45]. This can be attributed to their excellent optical properties which are absolutely requested for the light absorbers as well as light-emitting materials, for example, the high absorption coefficients and tunable direct bandgaps.

The large absorption coefficients on the order of 10^5 cm^{-1} make it possible to reduce the thickness of organic-inorganic hybrid perovskites, which means easy fabrication and low cost. Therefore, the thicknesses of TiO_2 in perovskite are relatively low compared to the solid-state dye sensitized solar cells. This may encourage the development and commercialization of perovskite solar cells to some extent.

According to Shockley and Queisser (SQ) calculations, the upper limit for solar energy conversion efficiency using single-junction solar cell is close to 33% at 1.4 eV absorber energy bandgap. In spite of this, the recorded efficiencies of single-junction solar cells can hardly achieve the upper limit. Different kinds of adverse factors including defects, impurities, interfacial potential barriers, put off the approaching of the theoretical maximum. Figure 6 [46] gives the detailed description of the relationship between the maximum power conversion efficiency and the bandgap of absorber materials along with the recorded efficiencies by experiments. We can see that as the bandgap of absorber materials shifts away from

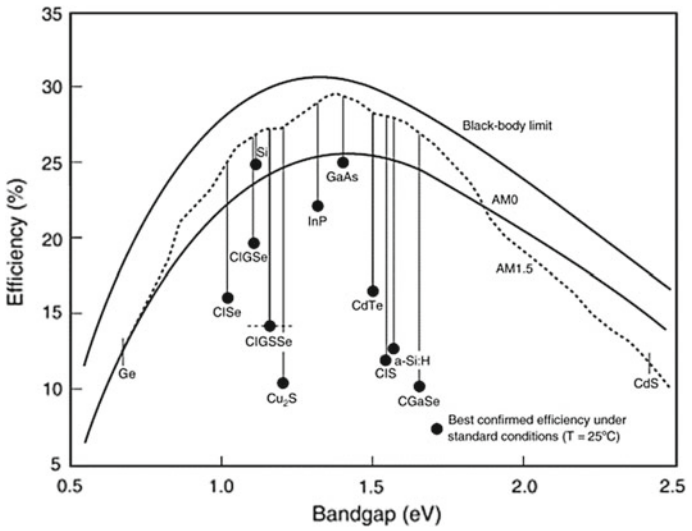

Fig. 6 Performance gaps between the best device efficiencies in the laboratory and attainable efficiencies for several solar cell technologies [46] (Reprinted with permission from Ref. [46]. Copyright 2006, Published by ELSEVIER BV)

the ideal value of 1.4 eV, the limit of maximal power conversion efficiency will decrease.

It is known that perovskite materials can be described as ABX_3, where X is an anion and A and B are cations of different sizes. For the organic-inorganic halide perovskites of present interest, the larger cation A is organic group. It is generally methylammonium $\left(CH_3NH_3^+,\ MA^+\right)$ ethylammonium $\left(CH_3CH_2NH_3^+,\ EA^+\right)$, and formamidinium $\left(NH_2CH = NH_2^+,\ FA^+\right)$. For efficient cells, cation B has universally been Pb^{2+} or Sn^{2+}. The anion X is a halogen, generally iodine (I^-), bromine (Br^-) and chlorine (Cl^-).

A remarkable versatility of perovskite is the tunability of the optical energy band through all of these compositions of A, B, and X. There are three kinds of structures of bulk perovskite that we usually observe: cubic, tetragonal, and orthorhombic, in order of decreasing symmetry. In general, once the size of the A cation is reduced, the structure would evolve from the original tetragonal symmetric structure to cubic symmetry [47]. The increased symmetry can make differences in the bandgap. On the other hand, the band structure of the perovskite is primarily dependent on the inorganic components. For example, in $MAPbI_3$, its valence band maxima originate from the σ bonding orbital composed of Pb 6s–I 5p. The conduction band minima consist of Pb 6p–I 5s σ and Pb 6p–I 5p π antibonding orbitals [48]. Therefore, the bandgap is mainly determined by the $[PbI_6]^{4-}$, which is also confirmed by the first principles modeling [49].

The cation A plays an important role in the phase structure of perovskites based on the empirical Goldschmidt tolerance factor theory, which is usually accompanied by the change in bandgap. In cubic perovskite structures, the alternation on A can still tailor the band structure to a small extent. For example, the bandgap of archetypal hybrid perovskite $MAPbI_3$ is around 1.5 eV. To narrow the bandgap of $MAPbI_3$ closer to 1.4 eV, $NH_2CH = NH_2^+$, a similar group to $CH_3NH_3^+$ has been applied, forming FAPbI3 with a bandgap of 1.4 eV and significantly extended photocurrent generation spectrum at 870 nm. As for the $CsPbI_3$, the bandgap is in the range of 1.67 eV. The tendency has been described that with the increase in the size of A, like from Cs^+ to MA^+ or FA^+, the value of the bandgap will gradually decrease (Fig. 7). However, further increasing the size of A to EA, the perovskite structure turns into orthorhombic symmetry with a larger bandgap of 2.2 eV [50]. According to the structural formation criterion, the volume threshold is $CH_3CH_2NH_2$ for the formation of cubic $APbI_3$. From this point, there are quite a limited number of molecules that can be applied in the A-position to modulate the band structures of perovskites.

However, the change of B and X in ABX_3 gives more considerable changes in bandgap. To avoid toxic lead (Pb), the development of lead-free or lead-less perovskite materials has attracted more and more interest all over the world. Tin (Sn), which is in the same family as Pb, is the first candidate as the alternative. Ogomi et al. [51] observed that the bandgap of $MASn_{1-x}Pb_xI_3$ can be tuned between 1.17 and 1.55 eV along with the absorption spectrum extended from the visible to the near-infrared region. The first demonstration of the lead-free $MASnI_3$ perovskite

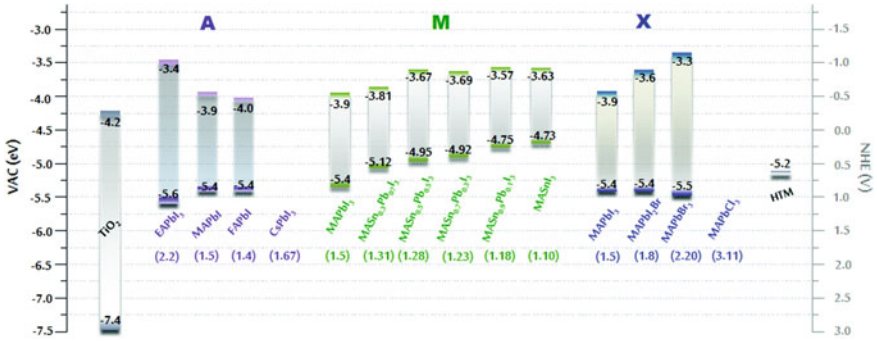

Fig. 7 Energy levels for some perovskites, TiO_2 and a conventional hole transporting material, 2, 2′, 7, 7′-tetrakis-(N, N-dimethoxyphenyl-amine-)-9, 9′-spirobifluorene (spiro-MeOTAD). The values under the chemical formula are the corresponding bandgap in eV [47] (Reprinted with permission from Ref. [47]. Copyright 2014, Published by RSC Pub)

came from Hao et al. [52]. With the narrowed bandgap of 1.3 eV, the PCE of this tin-based perovskite solar cell was over 5%. Nevertheless, the biggest problem to deal with the $MASn_{1-x}PbxI_3$ or $MASnI_3$ perovskite is yet to solve. It is difficult to prevent the oxidation of Sn to SnI_4 in the iodide perovskite. What is more, the low surface coverage and low crystal quality of Sn-based perovskite also cause low efficiency of the cell devices compared with the Pb equivalents.

In the X position of perovskites, halogen elements, Cl, Br, and I, are used mostly. The alternation of X can bring great changes in their bandgaps. For $MAPbX_3$, the bandgaps of Cl, Br, and I are 3.11, 2.20, and 1.50 eV, respectively (see in Fig. 7). Figure 8 [38, 53, 54] shows the continuous change of absorption spectra of different perovskite materials with mixed halides. The works on altering A and X simultaneously represented exhibited similar results [55]. Substitution of B and X in Fig. 7 at the same time shows a large range of bandgap modulation which is from 1.10 to 3.11 eV. This tunability could be useful for multijunction perovskite solar cells or hybrid tandem solar cells with silicon or copper indium gallium diselenide (CIGS) thin films in pursuit of higher energy conversion efficiency.

The optical properties of low-dimension semiconductors, such as two-dimension (2D) nanowires and quantum dots (QDs), are usually revealed to be different from the commonly mentioned three-dimension (3D) materials. Analogously, with quantum confinement effect, the 2D-nanostructrued perovskites and QDs perovskites show variable absorption edges and PL peak positions, in addition to better air- and photo-stability than the 3D ones. Taking advantage of defect tolerance, perovskite QDs exhibit unique optical properties in spite of the nature of intrinsic structural defects which are abundant in this system. These defects do not act as traps as the other compounds. Nearly all types of perovskite QDs, including the organic-inorganic hybrid and the all-inorganic materials, have been reported in recent years. What is more, the perovskite colloidal nanocrystals (NCs) offer highly saturated colors compared with the CIE (Fig. 9c) [56, 57]. By adjusting the

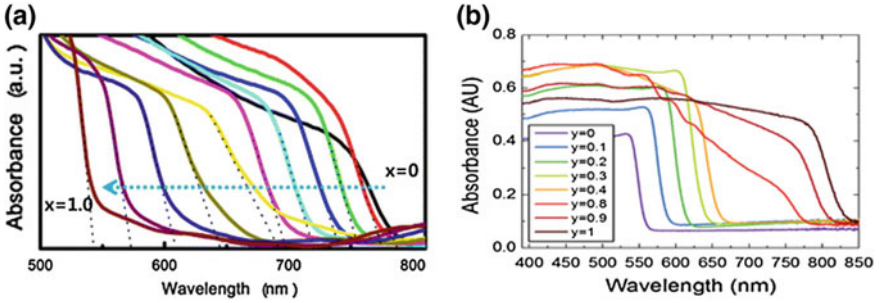

Fig. 8 Absorption spectra of **a** $MAPbBr_xI_{3-x}$, [53] (Reprinted with permission from Ref. [53]. Copyright 2013, Published by American Chemical Society). **b** $FAPbI_yBr_{3-y}$ [38] (Reprinted with permission from Ref. [38]. Copyright 2014, Published by RSC Publishing) perovskite films with different x or y increasing from 0 to 1

composition of X and A as well as the size and shape of these NCs, their photoluminescence (PL) peaks move in a continuous way. Like the $CH_3NH_3PbX_3$ NCs, the wide-color gamut and tunable color range are desirable, which can be seen in Fig. 9a, b [57]. At room temperature, the perovskite NCs are synthesized as the phases as follows: $MAPbI_3$ NCs are tetragonal; $FAPbBr_3$, $MAPbBr_3$, and $FAPbI_3$ NCs are cubic; $CsPbBr_3$ and $CsPbI_3$ NCs are orthorhombic. The narrow emission bandwidths, high photoluminescence quantum efficiency (PLQY), and tunable PL

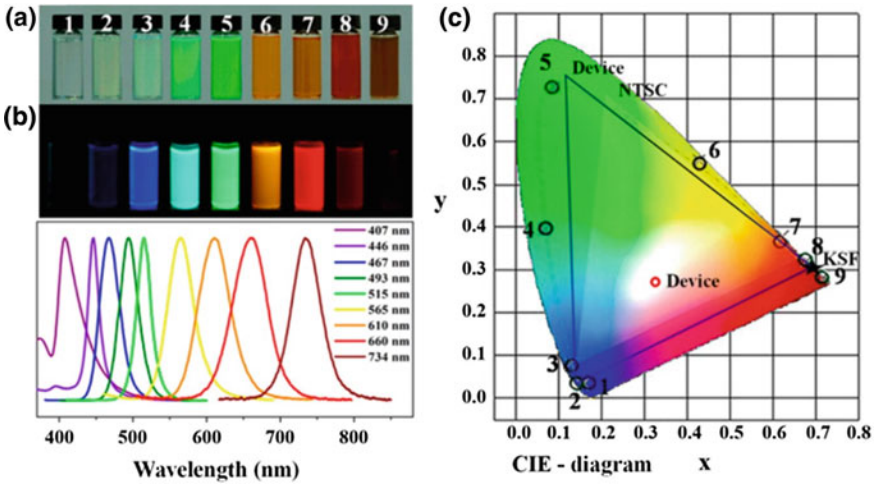

Fig. 9 Photographs (under mixed daylight and 365 nm UV excitation) (**a**) and corresponding PL spectra (**b**) of composition-tuned $CH_3NH_3PbX_3$ NCs. **c** PL spectra of $CH_3NH_3PbX_3$ NCs plotted on CIE chromaticity coordinates (no. 1–9, black circle) compared with common color standards (pc-WLED devices (blue lines), and NTSC standard (bright area)) [57] (Reprinted with permission from Ref. [57]. Copyright 2015, Published by American Chemical Society)

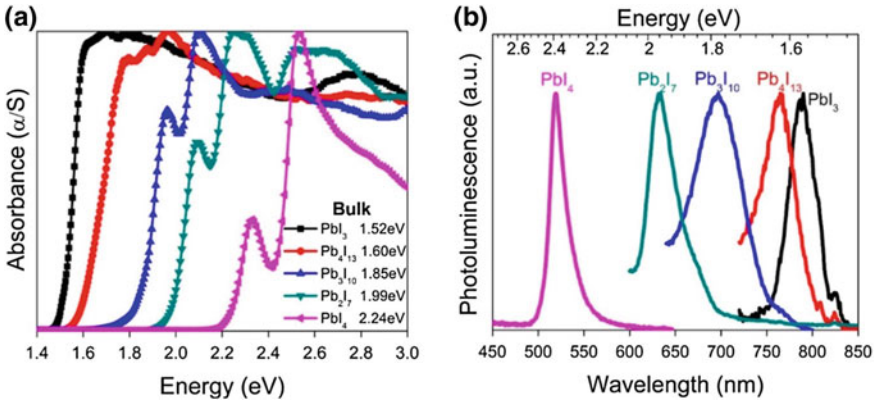

Fig. 10 Absorption (**a**) of bulk and photoluminescence (PL) spectra (**b**) of the thin films of $MAPbI_3$ and $(BA)_2(MA)_{n-1}Pb_nI_{3n+1}$ with the value of n varying from 1 to 4 [58]. (Reprinted with permission from Ref. [58]. Copyright 2015, Published by American Chemical Society)

peak positions (from ultraviolet to near-infrared) of perovskite NCs meet the requirement for wide-color-gamut liquid-crystal displays (LCDs).

Compared to 3D-perovskites, 2D-perovskites are composed of layered structures divided by organic spacers. The composing formula of 2D-perovskites is as follow, $A_nA'_{n-1}M_nX_{3n+1}$, where A, A' are cations, M is metal and X is halide. The number of n determines the quantum-well thickness and, as a result, the optical bandgap [58]. For instance, the detailed optical information of the $(BA)_2(MA)_{n-1}Pb_nI_{3n+1}$ family is displayed in Fig. 10. In addition, some researchers also found that the well designed 2D/3D hybrid perovskite can cover the virtues of both 2D- and 3D-perovskite, being an aggregate of desirable photo-electronic properties as well as the stability against moisture.

References

1. Mahadevan Shanthi (1996) Sarma, Estimates of electronic interaction parameters for LaMO3 compounds (M = Ti–Ni) from ab initio approaches. Phys Rev B: Condens Matter Mater Phys 54:11119
2. Cai MQ, Tan X, Yang GW, Wen LQ, Wang LL, Hu WY, Wang YG (2008) Giant Magneto-optical kerr effects in ferromagnetic perovskite BiNiO3 with half- metallic state. J Phys Chem C 112:16638
3. King G, Woodward PM (2010) Cation ordering in perovskites. J Mater Chem 20:5785
4. Philipp JB, Majewski P, Alff L, Erb A, Gross R, Graf T (2003) Structural and doping effects in the half-metallic double perovskite A2CrWO6 (A = Sr, Ba, and Ca). Phys Rev B 68:144431
5. Morrow R, Mishra R, Restrepo OD, Ball MR, Windl W, Wurmehl S (2013) Independent ordering of two interpenetrating magnetic sublattices in the double perovskite Sr2CoOsO6. J Am Chem Soc 135:18824

6. Dos Santos-García AJ, Ritter C, Solana-Madruga E (2013) S_aez-Puche R, Magnetic and crystal structure determination of Mn2FeSbO6 double perovskite. J Phys: Condens Matter 25:206004
7. S_anchez-Benítez J, Martínez-Lope MJ, Alonso JA, García-Mu ∼ noz JL Magnetic and structural features of the NdNi1−xMnxO3 perovskite series investigated by neutron diffraction. J Phys Condens Matter 23, 226001 (2011)
8. Makowski SJ, Rodgers JA, Henry PF, Attfield JP, Bos J-WG (2008) Coupled spin ordering in the Ln2LiRuO6 double perovskites. Chem Mater 21, 264
9. Raevski IP, Kubrin SP, Raevskaya SI, V Titov V, Sarychev DA, Malitskaya MA et al (2009) Experimental evidence of the crucial role of nonmagnetic Pb cations in the enhancement of the Néel temperature in perovskite Pb1−xBaxFe1/2Nb1/2O3. Energy Environ Phys Rev B 80:24108
10. Karppinen M, Yamauchi H (2005) In: Narlikar AV (ed) Frontiers in magnetic materials, vol 84, p 153. Springer, Berlin
11. Mclaughlin AC (2008) Simultaneous Jahn-Teller distortion and magnetic order in the double perovskite Ba2154SmMoO6. Phys Rev B 78:132404
12. Cussen EJ, Lynham DR, Rogers J (2006) Magnetic order arising from structural distortion: structure and magnetic properties of Ba2LnMoO6. Chem Mater 18:2855
13. Cussen EJ, Battle PD (2003) The influence of structural disorder on the magnetic properties of Sr2Fe1-xGaxTaO6. J Mater Chem 13:1210
14. Triana CA, Corredor LT, Landínez T_ellez DA, Roa-Rojas J (2011) High temperature-induced phase transitions in Sr2GdRuO6 complex perovskite. Phys B Condens Matter 407:3150
15. Wang R, Mahesh R, Itoh M (1999) Hydrostatic-pressure-induced magnetic structure transformation in polycrystalline La0.5Ca0.5MnO3-δ. Phys Rev B 60:14513
16. Battle PD, Goodenough JB, Price R (1983) The crystal structures and magnetic properties of Ba2LaRuO6 and Ca2LaRuO6. J Solid State Chem 46:234
17. Qian T, Li G, Zhang T, Zhou TF, Kang XW, Li XG (2007) Surface spin-glass behavior in La2/3Sr1/3MnO3 nanoparticles. Phys Rev 76:014433
18. Zhu T, Shen BG, Sun JR, Zhao HW, Zhan WS (2001) Surface spin-glass behavior in La2/3Sr1/3MnO3 nanoparticles. Appl Phys Lett 78:3863
19. Arodhiya SK, Placke A, Kocher J (2017) Core-Shell magnetic structure of La1 − xSrxMnO3 + δ nanocrystallites. Intermag 53:11
20. Curiale J, Granada M, Troiani HE, S_anchez RD, Leyva AG, Levy P, Samwer K (2009) Magnetic dead layer in ferromagnetic manganite nanoparticles. Appl Phys Lett 95:043106
21. Zhang T, Li G, Qian T, Qu JF, Li XG (2006) Effect of particle size on the structure and magnetic properties of La0.6Pb0.4MnO3 nanoparticles. J Appl Phys 100:094324 (2006)
22. Tlili R, Omri A, Bekri M, Bejar M, Dhahri E (2016) Hlil effect of Ga substitution on magnetocaloric effect in La0.7(Ba, Sr)0.3Mn1-xGaxO3 polycrystalline at room temperature. EK.: J Magn Magn Mater 399:143 (2016)
23. Oumezzine E, Hcini S, Baazaoui M, Hlil EK, Oumezzine M (2015) Structural, magnetic and magnetocaloric properties of Zn0.6 − xNixCu0.4Fe2O4 ferrite nanoparticles prepared by Pechini sol-gel method. Pow. Technol. 278:189–195
24. Koutselas IB, Ducasse L, Papavassiliou GC (1996) Electronic properties of three- and low-dimensional semiconducting materials with Pb halide and Sn halide units. J Phys: Condens Matter 8:1217
25. Walsh A, Watson GW (2005) The origin of the stereochemically active Pb (II) lone pair: DFT calculations on PbO and PbS. J Solid State Chem 178:1422
26. Filip MR, Eperon GE, Snaith HJ, Giustino FN (2014) Steric engineering of metal-halide perovskites with tunable optical band gaps. Commun 5:5757
27. Yin W-J, Yang J-H, Kang J, Yan Y, Wei S-H (2015) Halide perovskite materials for solar cells:a theoretical review. J Mater Chem A 3:8926
28. Milot RL, Eperon GE, Snaith HJ, Johnston MB, Herz LM (2015) Temperature-dependent charge-carrier dynamics in CH3NH3PbI3 perovskite thin films. Adv Funct Mater 25:6218

29. Edri E, Kirmayer S, Henning A, Mukhopadhyay S, Gartsman K, Rosenwaks Y, Hodes G, Cahen D (2014) Why Lead Methylammonium Tri-Iodide perovskite-based solar cells require a mesoporous electron transporting scaffold (but not necessarily a hole conductor). Nano Lett 14:1000
30. Yun JS, Ho-Baillie A, Huang S, Woo SH, Heo Y, Seidel J, Huang F, Cheng Y-B, Green MA (2015) Benefit of grain boundaries in organic—inorganic halide planar perovskite solar cells. J Phys Chem Lett 6:87
31. Miyasaka T (2015) Perovskite photovoltaics: rare functions of organo lead halide in solar cells and optoelectronic devices. Chem Lett 44:720
32. Wang Q, Bi C (2015) Huang, Doped hole transport layer for efficiency enhancement in planar heterojunction organolead trihalide perovskite solar cells. J Nano Energy 15:275
33. Yin W-J, Shi T, Yan Y (2014) Doped hole transport layer for efficiency enhancement in planar heterojunction organolead trihalide perovskite solar cells. Adv Mater 26:4653
34. Stranks SD, Eperon GE, Grancini G, Menelaou C, Alcocer MJP, Leijtens T, Herz LM, Petrozza A, Snaith HJ (2013) Electron-Hole diffusion lengths exceeding1 micrometer in an organometal trihalide perovskite absorber. Science 342:341
35. Xing G, Mathews N, Sun S, Lim SS, Lam YM (2013) Long-Range balanced electron and Hole-Transport lengths in Organic-Inorganic CH3NH3PbI3. Science 342:344
36. Wehrenfennig C, Eperon GE, Johnston MB, Snaith HJ, Herz LM (2014) High charge carrier mobilities and lifetimes in organolead trihalide perovskites. Adv Mater 26:1584
37. Sheng R, Ho-Baillie A, Huang S, Chen S, Wen X, Hao X, Green MA (2015) Methylammonium lead bromide perovskite-based solar cells by vapor-assisted deposition. J Phys Chem C 119:3545
38. Eperon GE, Stranks SD, Menelaou C, Johnston MB, Herz LM, Snaith HJ (2014) Formamidinium lead trihalide: a broadly tunable perovskite for efficient planar heterojunction solar cells. Energy Environ Sci 7:982
39. Rehman W, Milot RL, Eperon GE, Wehrenfennig C, Boland JL, Snaith HJ, Johnston MB, Herz LM (2015) Charge-carrier dynamics and mobilities in formamidinium lead mixed-halide perovskites. Adv Mater 27:7938
40. Noel NK, Stranks SD, Abate A, Wehrenfennig C, Guarnera S, Haghighirad A-A, Sadhanala A, Eperon GE, Pathak SK, Johnston MB (2014) Lead-free organic–inorganic tin halide perovskites for photovoltaic applications. Energy Environ Sci 7:3061
41. Dong R, Fang Y, Chae J, Dai J, Xiao Z, Dong Q, Yuan Y, Centrone A, Zeng XC, Huang J (2015) High-Gain and Low-Driving-Voltage photodetectors based on organolead triiodide perovskites. Adv Mater 27:1912
42. Saidaminov MI, Adinolfi V, Comin R, Abdelhady AL, Peng W, Dursun I, Yuan M, Hoogland S, Sargent EH, Bakr OM (2015) Planar-integrated single-crystalline perovskite Photodetectors. Nat Commun 6:8724
43. Edri E, Kirmayer S, Cahen D, Hodes G (2013) High open-circuit voltage solar cells based on organic-inorganic lead bromide perovskite. J Phys Chem Lett 4:897
44. Xing G, Mathews N, Lim SS, Yantara N, Liu X, Sabba D, Grätzel M, Mhaisalkar S, Sum TC (2014) Low-temperature solution-processed wavelength-tunable perovskites for lasing. Nat Mater 13:476
45. Sutherland BR, Hoogland S, Adachi MM, Wong CTO, Sargent EH (2014) Conformal organohalide perovskites enable lasing on spherical resonators. ACS Nano 8:10947
46. Kazmerski LL (2006) Solar photovoltaics R&D at the tipping point: a 2005 technology overview. J Electron Spectrosc Relat Phenom 150:105
47. Wang BH, Xiao XD, Chen T (2014) Perovskite photovoltaics: a high-efficiency newcomer to the solar cell family. Nanoscale 6:12287
48. Umebayashi T, Asai K, Kondo T, Nakao A (2003) Electronic structures of lead iodide based low-dimensional crystals. Phys Rev B: Condens Matter 67:155405
49. Mosconi E, Amat A, Nazeeruddin MK, Grätzel M, De Angelis F (2013) First-Principles modeling of mixed halide organometal perovskites for photovoltaic applications. J Phys Chem C 117:13902

50. Im J-H, Chung J, Kim S-J, Park N-G (2012) Synthesis, structure, and photovoltaic property of a nanocrystalline 2H perovskite-type novel sensitizer ($CH_3CH_2NH_3$)PbI_3. Nanoscale Res Lett 7:353
51. Ogomi Y, Morita A, Tsukamoto S, Saitho T, Fujikawa N, Shen Q, Toyoda T, Yoshino K, Pandey SS, Ma T, Hayase S (2014) $CH_3NH_3Sn_xPb_{(1-x)}I_3$ perovskite solar cells covering up to 1060 nm. J Phys Chem Lett 5:1004
52. Hao F, Stoumpos CC, Chang RPH, Kanatzidis MG (2014) Anomalous band gap behavior in mixed Sn and Pb perovskites enables broadening of absorption spectrum in solar cells. J Am Chem Soc 136:8094
53. Noh JH, Im SH, Heo JH, Mandal TN, Seok SI (2013) Chemical management for colorful, efficient, and stable inorganic-organic hybrid nanostructured solar cells. Nano Lett 13:1764
54. Sutton RJ, Eperon GE, Miranda L, Parrott ES, Kamino BA, Patel JB, Hörantner MT, Johnston MB, Haghighirad AA, Moore DT (2016) Bandgap-Tunable cesium lead halide perovskites with high thermal stability for efficient solar cells. Adv Energy Mater 6:1502458
55. McMeekin DP, Sadoughi G, Rehman W, Eperon GE, Saliba M, Hörantner MT, Haghighirad A, Sakai N, Korte L, Rech B (2016) A mixed-cation lead mixed-halide perovskite absorber for tandem solar cells. Science 351:151
56. Protesescu L, Yakunin S, Bodnarchuk MI, Krieg F, Caputo R, Hendon CH, Yang RX, Walsh A, Kovalenko MV (2015) Nanocrystals of cesium lead halide perovskites ($CsPbX_3$, X = Cl, Br, and I): novel optoelectronic materials showing bright emission with wide color gamut. Nano Lett 15:3692
57. Zhang F, Zhong H, Chen C, Wu X-G, Hu X, Huang H, Han J, Zou B, Dong Y (2015) Brightly luminescent and color-tunable colloidal CH3NH3PbX3 (X = Br, I, Cl) quantum dots: potential alternatives for display technology. ACS Nano 9:4533
58. Cao DH, Stoumpos CC, Farha OK, Hupp JT, Kanatzidis MG (2015) 2D homologous perovskites as light-absorbing materials for solar cell applications. J Am Chem Soc 137:7843

Chapter 3
Preparation Methods of Perovskite-Type Oxide Materials

Weiren Xia, Yao Lu and Xinhua Zhu

1 Introduction

Perovskite-type oxide materials are one of the most important class functional materials, which exhibit abundant physical properties such as ferroelectric, piezoelectric, dielectric, ferromagnetic, magnetoresistant, and multiferroic properties [1–5], which are widely investigated in the past century. The perovskite oxide structures with a chemical formula ABO_3 is coined from the prototype $CaTiO_3$ mineral called perovskite, where A and B are two different metal ions with very different ionic sizes, and O anions are bonded to them. In a cubic perovskite structure, A ions occupy at cube corner positions (0, 0, 0), B ions sit at the body center position (1/2, 1/2, 1/2), and oxygen anions are located at face-centered positions such as (1/2, 1/2, 0), (1/2, 0, 1/2), and (0, 1/2, 1/2), as illustrated in Fig. 1a. A-sited ions are coordinated by 12 oxygens, fitting into the dodecahedral site of the framework (Fig. 1b). The B-sited ions are coordinated by six oxygens in octahedral coordination, which are transition metal ions such as 3d, 4d, and/or 5d elements. Since most of the metal elements in the periodic table can be used for constructing perovskite oxides by rationally combining different metal ions at A- and B-sites [6], therefore, the perovskite structure is featured to be structural simplicity and flexibility. By appropriate chemical substitutions at the A- and/or B-sites many desirable properties of perovskite oxides can be tailored. However, in practice, most perovskite oxides display a distorted structure rather than a cubic structure to accommodate the A- and B-cations. In the past century, the perovskite-type oxides are probably the most studied family of oxides. In the 1920s Goldschmidt et al. [1] carried out the pioneering structural works on the perovskites. Up to now, numerous perovskite oxide compounds with a variety of

W. Xia · Y. Lu · X. Zhu (✉)
National Laboratory of Solid State of Microstructures, School of Physics, Nanjing University, Nanjing 210093, China
e-mail: xhzhu@nju.edu.cn

N. S. Arul and V. D. Nithya (eds.), *Revolution of Perovskite*, Materials Horizons: From Nature to Nanomaterials, https://doi.org/10.1007/978-981-15-1267-4_3

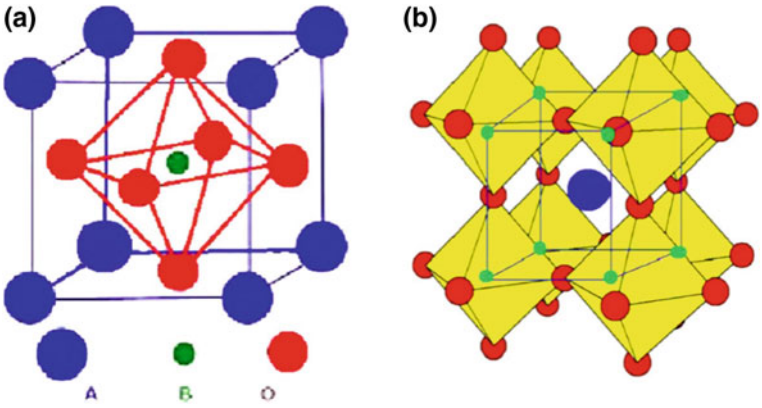

Fig. 1 **a** Unit cell of a cubic ABO_3 perovskite structure and **b** framework of an ABO_3 perovskite structure where corner-shared oxygen octahedral extending in three dimensions

properties have been synthesized. It is also demonstrated that the diversity of the synthesized perovskite oxide compounds provides the wide spectrum of ferroelectric, dielectric, piezoelectric, magnetic, optical and multiferroic properties, which have important applications in memory devices, sensors, actuators, ceramic capacitors, and multiple-state memories and spintronic devices controlled by electric and magnetic fields [7–10].

Many perovskite oxide compounds prepared by solid-state reaction exhibit polycrystalline nature. The problems of this synthesis technique arise from that some starting oxides (e.g., PbO, Bi_2O_3) may vaporize, and the resulting microstructures of perovskite oxides obtained by this method exhibit poor chemical homogeneity, significant particle agglomeration, and coarse large particle sizes. To solve the above problems and to produce homogeneous and stoichiometric perovskite oxide powders, wet chemical routes such as sol–gel process [11, 12], hydrothermal synthesis [13], microwave-hydrothermal synthesis [14], and microemulsion synthesis [15] techniques have been developed in recent years. Perovskite oxide nanopowders and thin films with controlled levels of dopants have been prepared via sol–gel process by using metal alkoxides as precursors. Perovskite oxide thin films are also successfully grown by physical vapor deposition (PVD) or pulsed laser deposition (PLD). With the progress of the miniaturization of microelectronic devices, electronic devices based on perovskite-type 3D oxide nanostructures are highly required, which have recently been developed. For example, artificial 3D perovskite (La,Pr,Ca)MnO_3 (LPCMO) nanoboxes have been fabricated by employing a combination of nanoimprint and PLD techniques for high performance correlated perovskite oxide nanoelectronics [16]. It is believed that the promising nanofabrication and nanoscale properties of the perovskite-type 3D oxide nanostructures will provide new possibilities for exploring novel size-induced perovskite oxide nanoelectronics.

Generally, perovskite oxide nanostructured materials can be classified as zero-dimensional (0D) (nanopowders), one-dimensional (1D) (such as nanowires, nanotubes, and nanorods), two-dimensional (2D) (e.g., thin films, nanodot arrays, and lamellae patterns), and three-dimensional (3D) (such as vertically aligned nanowires, rods, or tubes) nanostructures. In the past decades, much progress has been achieved in the fabrications of nanoscale perovskite oxide materials. In this chapter, we focus on the preparation methods of perovskite-type oxide materials, which cover bulk perovskite oxide ceramics, perovskite oxide nanopowders, perovskite (1D, 2D, and 3D) oxide nanostructures. First, we introduce the synthesized methods for bulk perovskite oxide ceramics and then summarize the prepared methods of perovskite oxide nanopowders, where solid, liquid, or gas phase precursors are used. Emphasizes are given to the preparation methods of perovskite (1D, 2D, and 3D) oxide nanostructures due to their superior physical and chemical properties, and the possibility for exploring intrinsic size effects of physical properties. Finally, we provide a future outlook of preparation methods of perovskite-type oxide materials.

2 Preparation of Bulk Perovskite-Type Oxides

The fabrication of perovskite-type oxide ceramics includes powder preparation, calcination, and final sintering. For the electrical property measurement, the perovskite-type oxide ceramic samples are needed to be machined, electroded, and poled. The poling process is performed by application of a DC field to orient the ferroelectric domains and induce piezoelectricity. A flowchart of a typical manufacturing process for perovskite piezoelectric ceramics with metal oxides as starting materials is shown in Fig. 2. Since the electromechanical properties of piezoelectric ceramics are highly dependent upon the processing conditions, to obtain the best piezoelectric properties, the poling voltage and temperature should be optimized in poling process. The physical properties (e.g., ferroelectric, piezoelectric, and dielectric properties) of perovskite oxide ceramics can be measured by different methods. Details can be found elsewhere [17].

3 Synthesis of Perovskite-Type Oxide Nanopowders

3.1 Solid-State Reaction Route

Solid-state reaction method is one of the most conventional routes for synthesizing perovskite oxide nanopowders (e.g., $BiFeO_3$ (BFO), $KNbO_3$, etc.) [18, 19]. This process consists of weighting the starting materials (the corresponding oxides or carbonates), mixing, milling, and then calcinating them at elevated temperatures to

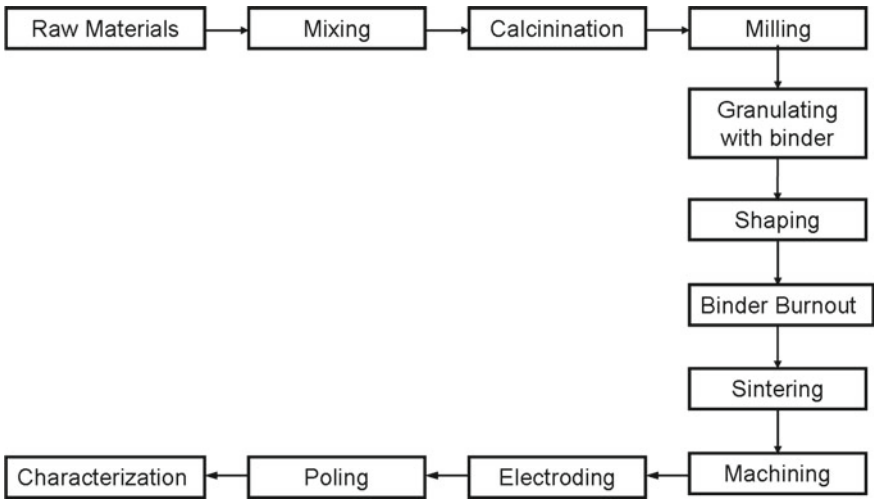

Fig. 2 Flowchart of a typical oxide manufacturing process for perovskite piezoelectric oxide ceramics

form the perovskite phase. For example, BFO multiferroic nanoparticles are obtained by solid-state reaction method with Bi_2O_3 and Fe_2O_3 as the starting oxides in the temperature range of 800–830 °C. This process includes weighting the starting materials (Bi_2O_3 and Fe_2O_3), mixing, milling, and calcinating them at high temperatures to form the perovskite phase. However, in the synthesis of perovskite stoichiometric BFO nanoparticles via solid-state reaction method, it is difficult to avoid the formation of impurity phases such as sillenite-type $Bi_{25}FeO_{39}$ and mullite-type $Bi_2Fe_4O_9$. To understand the formation process of BFO nanoparticles, the reaction pathways in the solid-state synthesis of multiferroic BFO were investigated [20]. It was found that the diffusion of Bi^{3+} ions into Fe_2O_3 controlled the whole process which involves the formation of impurity phases. A schematic diagram illustrating the reaction paths in the solid-state synthesis of BFO nanopowders is shown in Fig. 3 [20], which explains why small amounts of impurity phases are always companied with BFO nanoparticles. In addition, the particle size of Fe_2O_3 powder controls the diffusion distance, which plays an important role in controlling the formation of unreacted phases in this system. A similar condition also appears in the formation of BT nanoparticles from a mixture of $BaCO_3$ and TiO_2, where the growth of $BaTiO_3$ is governed by the diffusion of Ba^{2+} ions through a perovskite layer [21, 22]. Besides the BT nanopowders, $BaZrO_3$ (BZ) powders are also synthesized by a similar method [23]. Besides the conventional solid-state reaction method, other prepared methods such as molten salt synthesis, mechanical milling method, sol–gel process, and hydrothermal synthesis are also developed, which are described below.

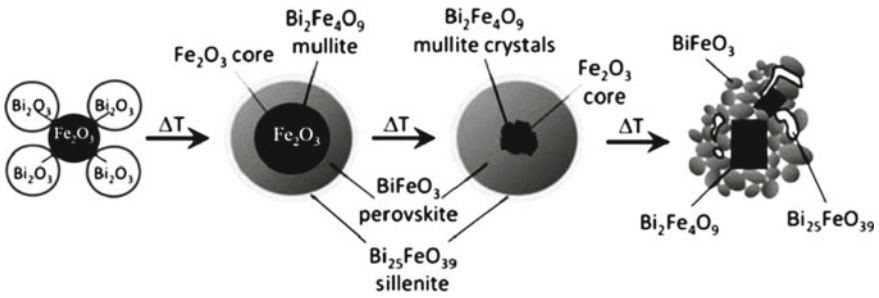

Fig. 3 A schematic diagram illustrating the reaction paths in the solid-state synthesis of $BiFeO_3$. When the solid-state reaction proceeds, the penetration profile of the Bi ions into the Fe_2O_3 particles leads to the formation of different compounds. Initially, the 25:1 (Bi:Fe) sillenite phase is formed in the outer surface and the 1:1 $BiFeO_3$ perovskite phase is developed as moving inside the structure. But the nuclei of the 1:2 $Bi_2Fe_4O_9$ phase is also formed in deeper inside, constituting the diffusion/reaction front toward the iron oxide core. As the temperature increases diffusion will be favored and more perovskite may be formed in spite of the iron-rich nucleus. Due to the competition between the complete formation of BFO and the crystallization of $Bi_2Fe_4O_9$ mullite crystals, the formation of BFO is blocked and eventually three phases coexist simultaneously. Reproduced with permission from [20], M. S. Bernardo, T. Jardiel, M. Peiteado, A. C. Caballero, M. Villegas. Reaction pathways in the solid state synthesis of multiferroic $BiFeO_3$. J. Eur. Ceram. Soc. 31(2011) 3047–3053

3.2 Molten Salt Synthesis (MSS)

As one of the simplest, most versatile, and cost-effective methods MSS method is widely used for preparing perovskite oxide powders [24]. For example, multiferroic BFO nanoparticles and La-doped BFO nanoparticles have been synthesized by MSS process in the NaCl [25, 26], NaCl–KCl [27, 28], NaCl–Na_2SO_4 [29], or KNO_3–$NaNO_3$ [30] molten salts. The formation mechanisms of BFO have also been investigated. It is found that the molten salts (e.g., NaCl, NaCl–Na_2SO_4, KNO_3–$NaNO_3$) play an important role in promoting the formation of BFO phase. Recently, Pb-based perovskite relaxors such as $Pb(Mg_{1/3}Nb_{2/3})O_3$ (PMN), $Pb(Ni_{1/3}Nb_{2/3})O_3$ (PFN) [31], Ba-based dielectric oxides such as $Ba(Sr,Ti)O_3$, $Ba(Mg_{1/3}Ta_{2/3})O_3$ [32], and perovskite $La_{1-x}Sr_xMnO_3$ (LSMO) nanoparticles [33, 34], are also synthesized by MSS process. Overall, MSS method is a simple, cost-effective, and environmental-friendly approach for obtaining perovskite oxide nanopowders with uniform compositions, ideal morphology, and high purity.

3.3 Mechanical Milling Method

Recently, perovskite oxide nanoparticles such as BT, PT, PZ, and BST have been successfully synthesized by using several mechanical milling methods [35, 36]. For example, by ball milling method perovskite manganite $Pr_{0.7}Ca_{0.3}MnO_3$

nanopowders with average crystallite size of 29 nm were also prepared [37]. X-ray powder diffraction patterns revealed that the $Pr_{0.7}Ca_{0.3}MnO_3$ nanopowders crystallized in an orthorhombic perovskite structure with a Pnma space group at room temperature. Magnetic measurements demonstrated that the $Pr_{0.7}Ca_{0.3}MnO_3$ nanopowders underwent a phase transition from ferromagnetic phase to paramagnetic phase at $\sim$120 K. However, as viewed from the point of energy efficiency, the vibro-mill (or vibratory mill or vibro-energy mill) seems to be more attractive than the ball milling [35]. The vibro-milling has several advantages over the conventional ball milling produces, such as finer particles, narrower size distribution at a faster rate, simple equipment, low-cost starting precursors, and large-scale production of nanopowders. Therefore, the vibro-milling method can be recognized as a powerful method for synthesizing perovskite nanopowders. By choosing suitable milling time and the calcination conditions, high purity perovskite oxide nanopowders such as BT, PT, PZ with the smallest particle size of 100 nm, 17 nm, and 31 nm can be mass produced, respectively [38].

Recently, complex perovskite oxides such as $(Bi,Na)TiO_3$, $(K,Na)NbO_3$, $Pb(Zr,Ti)O_3$ have also been synthesized from micron-sized reactant powders via a mechanochemical reaction using a highly energetic ball milling process [39]. During the mechanical milling process, the mechanochemical activation by the heavy milling is the key step, which alters the physicochemical properties of the starting materials and the mechanism of synthesis. Welham [40] demonstrated that single-phase perovskite nanocrystalline BT powders were obtained in a very short milling time of ca. 30–40 min. Recently, multiferroic BFO nanopowders have also been synthesized directly at room temperature by mechanochemical synthesis [41].

Although mechanochemical method has the ability to produce the products with particle sizes at nanometer scale at room temperature, its small batch sizes and very long processing times make it unsuitable in large-scale industrial applications. In addition, intensive ball milling process may result in unfavorable contaminations from the milling media.

3.4 Wet Chemical Routes

3.4.1 Sol–Gel Processing

Since the reacting species are homogenized at the atomic level in a sol–gel process, the diffusion distances are much reduced in comparison to the conventional solid-state reaction. As a consequence, the final products can be obtained at much lower temperatures by sol–gel process. Up to date multicomponent perovskite oxide nanopowders with a controlled stoichiometry have well been prepared by sol–gel process [42–44]. The processing parameters such as the starting materials, concentration, pH value, and heat treatment schedule have an important effect on the

physical properties of perovskite nanopowders. A typical example is the sol–gel derived perovskite oxide BT nanopowders [45, 46]. To control the grain size and its distribution, the process parameters of the gels (e.g., post-annealing temperature, time and atmosphere, heating rate) must be optimized [47]. It is found that the annealing temperature plays an important role in controlling the BFO nanoparticle size. For example, the particle sizes of BFO nanoparticles annealed at 350 °C were less than 15 nm, whereas they are increased up to more than 100 nm as the annealed temperature was increased up to ~650 °C [48, 49]. In order to obtain the BFO nanoparticles with controlled grain size, shape, and crystallinity without additional sintering steps, modified sol–gel techniques such as Pechini method, polymer complex solution, and glycol-gel reaction were developed to synthesize BFO nanoparticles. Now the BFO nanoparticles with sizes from a few nanometers to micrometers can be obtained by carefully controlling the processing parameters such as solid-state polymerization and the heat treatment process.

3.4.2 Alkoxide-Hydroxide Sol–Precipitation Synthesis

Alkoxide–hydroxide sol–precipitation process was first proposed by Flaschen [50], which is widely used to produce crystalline perovskite oxide nanopowders at low temperatures and no further calcination at high temperatures are required. Perovskite BT powders have been synthesized by this method [50–53]. In this process, the hydrolysis and condensation processes are found to be the key processes of crystal growth. To well control the particle size and the shape of precipitates the water content and its additional method to the reaction system must be optimized. It is reported that BT nanopowders can be synthesized at low temperature as 80–100 °C via alkoxide-hydroxide method by using aqueous alkaline solution as a starting material [52]. That is ascribed to the hydrolysis–condensation reaction taking place instantly upon mixing the aqueous and alcohol solutions. However, the final products exhibit much agglomerated and inhomogeneous morphologies, which are unsuitable for the next powder processing and sintering. By using the solid barium hydroxide octahydrate as starting material, it is possible to modify the hydrolysis–condensation reaction due to the water molecules released in situ as $Ba(OH)_2 \cdot 8H_2O$ was dissolved in the alcoholic solution. The experimental results have shown that BT nanoparticles with sizes smaller than 6 nm first nucleate at 50 °C without forming the intermediate TiO_2 anatase, and corner-sharing TiO_6 octahedra are formed at 60 °C. The average sizes of BT powders are increased up to about 7.5 nm at 80 °C, and the BT nanopowders exhibit an anomalous lattice expansion with a relatively high tetragonality [54].

3.4.3 Hydrothermal Routes

Hydrothermal Process

The hydrothermal method, also named as the autoclave method, involves heating an aqueous suspension of insoluble salts in an autoclave at a moderate temperature and pressure where a desired phase structure is formed. It is widely used for preparing perovskite nanoparticles due to synergetic effects from solvent, temperature, and pressure, which can provide stable final products and prevent the formation of impure phases. Perovskite BFO nanoparticles with controllable particle size and morphology have been synthesized by hydrothermal synthesis [55–60]. For example, Han et al. [55] reported on $Bi_{12}Fe_{0.63}O_{18.945}$ nanocrystals, nano- and submicrometer-sized BFO, and $Bi_2Fe_4O_9$ nanoparticles with different shapes synthesized under special hydrothermal conditions. Similarly, Wang et al. [56] also reported on hydrothermal synthesis of bismuth ferrite compounds, which were assisted by using various alkali metal ions such as K^+, Na^+, and Li^+ ions. Pure BFO nanoparticles were synthesized at 200 °C by using 7 mol l^{-1} KOH and 12 mol l^{-1} KOH, whereas NaOH and $LiNO_3$ solutions can stabilize $Bi_2Fe_4O_9$ and $Bi_{12}(Bi_{0.5}Fe_{0.5})O_{19.5}$ phases, respectively, in the final products regardless of their concentrations. When KNO_3 is used as the mineralizer, phase-pure BFO nanoparticles with particle size of $\sim$5 nm are synthesized. These results reveal that the alkali metal ions (K^+, Na^+, and Li^+) play an important role in the formation of rhombohedral BFO, orthorhombic $Bi_2Fe_4O_9$, and cubic $Bi_{12}(Bi_{0.5}Fe_{0.5})O_{19.5}$ nanoparticles [61]. The reaction mechanism for the synthesis of the BFO nanoparticles by the hydrothermal method can be understood from the dissolution–crystallization process. In this process, Bi^{3+} and Fe^{3+} ions are first transformed into hydroxide $Fe(OH)_3$ and $Bi(OH)_3$ in the precursors, and then they are dissolved in the precursors under the presence of alkaline mineralizers (e.g., KOH, NaOH, LiOH) in hydrothermal conditions. As the Bi^{3+} and Fe^{3+} ionic concentrations in the alkaline solution are larger than their saturated concentrations, the BFO phase starts to be nucleated and precipitated from the supersaturated hydrothermal fluid, following the crystal growth [62]. Therefore, the particle size and morphology of BFO particles are closely related to the nucleation and crystal growth rate, which in turn are affected by the degree of supersaturation. A highly supersaturated precursor with high KOH concentration and high pH value will lead to a high nucleation rate but low growth rate, and thus smaller particle size [59]. In addition, the cationic radii of mineralizers have great effect on the size and morphology of nanoparticles. Hojamberdiev et al. [63] reported that the average particle sizes of BFO powders synthesized under mineralizers of LiOH, NaOH, and KOH, were 64 nm, 120 nm, 200 nm, respectively, indicating that the average particle size was increased with the cationic radii of the added mineralizers. Hydrothermal reaction is usually performed at temperature below 250 °C and even as low as 130 °C, much lower than the sol–gel process.

While the perovskite oxide nanopowders are synthesized directly by hydrothermal process, however, their products are usually highly defective in their

crystallographic structure [64, 65]. For example, in the BT nanopowders synthesized by hydrothermal method there exists structural defects such as lattice OH^- ions and barium vacancies (V''_{Ba}). The latter one is created at the surfaces of particles to maintain the whole electroneutrality of nanoparticle [64, 65]. Due to the coexistence of point defects such as barium, titanium, and oxygen vacancies and their annihilation each other the BT lattice becomes unstable. Since the point defects with different charges may compensate each other to neutrality, some vanishing vacancies are formed upon dehydration, leading to the formation of intragranular pores (shown in Fig. 4a), which partly disappears upon grain growth above 800 °C. In the MLCCs ceramics made from the hydrothermal BT powders, a strange expansion called "bloating phenomena" (shown in Fig. 4b) appeared at the final stage of sintering ceramics, which was resulted from the inherently OH^- ions and protons formed during the hydrothermal process [66].

Solvothermal Process

Solvothermal synthesis is normally carried out in a nonaqueous solution (e.g., NH_3, methanol, ethanol, and n-propanol), which has the following advantages in comparison with the hydrothermal process [67]: (i) the reaction occurs under mild conditions and gives cubic-phase perovskite powder; and (ii) the powders with particle size on the nanometer scale, exhibiting low agglomeration and a narrow particle-size distribution, due to the differences between the solvents. Up to date, several attempts have been made to synthesize superfine BT nanopowder by solvothermal synthesis [67–69]. For example, using benzyl alcohol as solvent, BT and BZ nanoparticles were synthesized by solvothermal process at relatively low

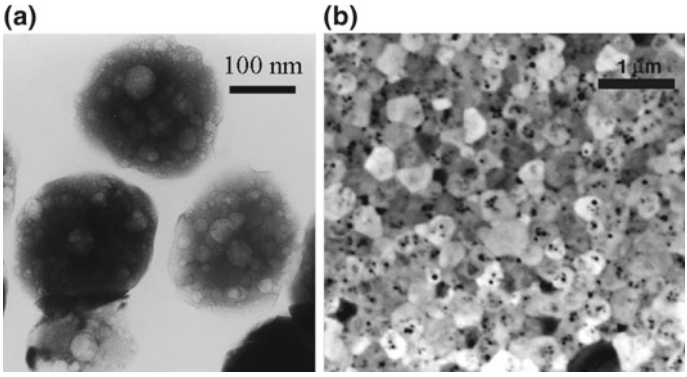

Fig. 4 **a** TEM image of the intragranular pores in the hydrothermal $BaTiO_3$ powders, and **b** dielectric X7R ceramics sintered at 1320 °C with many intragranular pores in the grains. Reproduced with permission from [66], C. Pithan, D. Hennings, R. Waser. Progress in the synthesis of nanocrystalline $BaTiO_3$ powders for MLCC. Int. J. Appl. Ceram. Technol. 2 (2005) 1–14 Copyright © 2005, American Ceramic Society

temperatures of 200–220 °C [70]. TEM image of the synthesized BT nanoparticles is shown in Fig. 5a, and an inset in which is their selected area electron diffraction (SAED) pattern, indicating the formation of cubic and tetragonal modifications of the BT perovskite structure. HRTEM images of two isolated particles with orientations in the [110] and [111] directions are shown in Fig. 5b and c, respectively. Figure 5d is a fast Fourier transform (FFT) pattern (equivalent to experimental electron diffraction pattern of the local region) obtained from the HRTEM image is shown in Fig. 5c, which confirms the well crystallization of the particles without defects. By using alcohol-based solvents such as ethanol, methanol, and n-propanol, nanosized (∼20–60 nm) cubic-phase BT powders were obtained [67]. However, the tetragonal BT nanopowders with sizes of 50–100 nm were synthesized by using EtOH as a solvent [68]. It was found that the particle size was dependent upon the feedstock concentration (e.g., the precursor concentration). With decreasing the particle size from 89 to 58 nm, the amount of the tetragonal phase in the powder was decreased from 85 to 57%, and the cell parameter ratio (*c*/*a*) also decreased from 1.0080 to 1.0071.

Microwave-Hydrothermal Process

The microwave-hydrothermal (M-H) process is a modified hydrothermal process, in which microwave is introduced to enhance the crystallization kinetics of hydrothermal process. In 1992, Komarneni et al. [69] performed the pioneering

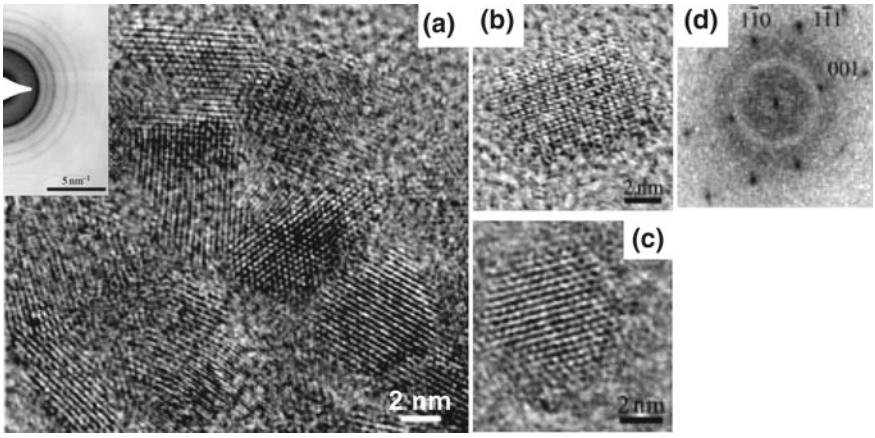

Fig. 5 **a** HRTEM image of an assembly of $BaTiO_3$ nanoparticle. The inset is the selected area electron diffraction (SAED) pattern. **c**, **d** HRTEM images of two isolated particles, and **e** the fast Fourier transform pattern obtained from the HRTEM image shown in (**c**). Reproduced with permission from [70], M. Niederberger, N. Pinna, J. Polleux, M. Antonietti. A general soft-chemistry route to perovskites and related materials: synthesis of $BaTiO_3$, $BaZrO_3$, and $LiNbO_3$ nanoparticles. Angew Chem. Int. Edt. 43(17) (2004) 2270–2273 Copyright Wiley-VCH Verlag GmbH & Co. KGaA

works on the microwave-hydrothermal synthesis of inorganic materials in liquid phase, and later they investigated the differences between the conventional hydrothermal syntheses (performed with conventional means of heating) and the M-H syntheses (performed under heating special autoclaves with microwaves). It is found that this process has some distinct advantages such as rapid internal heating, cost savings, as compared with the conventional hydrothermal synthesis. Up to date, the M-H process is widely used to rapidly synthesize numerous perovskite oxide nanopowders such as BT [71, 72], BST [73], and BFO [74, 75]. Microwave heating provides a new route for faster synthesizing novel inorganic nanomaterials, especially in the field of the perovskite oxide nanopowders, and it also allows to utilize more environmentally friendly solvents, yielding cleaner and purer products.

3.5 Chemical or Physical Vapor Deposition

Besides wet chemical solution methods, perovskite oxide nanopowders are also prepared by vapor deposition methods, in which the initial step is the preparation of gaseous precursor molecules by using suitable physical or chemical methods in aersol reactors [76, 77]. Next, the precursor molecules react to each other in the vapor phase to produce tiny nuclei of the desired phase (namely gas-to-particle conversion). Subsequently, the primary particles become coalescence via collision, forming agglomerates linked together by van der Waals force [78]. The mechanism involved in the gas phase condensation process allows one to link the properties of gaseous precursors to the nanoparticles formed. Among the different physical vapor deposition processes such as thermal evaporation, magnetic sputtering, and laser ablation the main difference is their interaction process used to generate a vapor and/or plasma by the removal of the target material. The type, density, energy, and excitation of atoms, molecules, clusters, and micro- and macro-particles within the generated vapor (plasma) lead to different microstructures of nanocrystalline particles and thin films. The important parameters involved in the processing are time, temperature, and the amount of particles produced per unit volume. The decisive characteristics of the prepared nanoparticles include the size distribution of the primary particles, the grain boundaries, the pore sizes, the defect concentrations, and crystallinity. Recently, monodisperse PZT nanoparticles (4–20 nm in diameter) are prepared by gas phase deposition [79]. This process involves several steps, including the production of amorphous and irregularly shaped PZT nanoparticles; crystallization of the particles by an online thermal treatment; screening the crystallized particles by a low-pressure differential mobility analyzer to yield monodisperse, highly pure, and single-crystalline PZT nanoparticles. Monodisperse perovskite oxide nanoparticles produced by this method not only provide good opportunity for investigating the size effects in ferroelectric oxide nanoparticles but also are useful for the fabrication of ferroelectric nanodevices.

4 Preparation Methods of 1D Perovskite-Type Oxide Nanostructures

In the past decade, many 1D perovskite oxide nanostructures have been prepared. The most used techniques are "bottom-up" routes (such as template-based synthesis, hydrothermal synthesis, molten salt synthesis, electrospinning, solution-based chemical decomposition), and "top-down" approaches (such as focus ion beam (FIB) milling, nanoimprint lithography (NIL) techniques). Basically, the prepared methods for 1D perovskite nanostructures can be divided into two categories. One is template-free synthesis, and the other one is template-assisted synthesis. In this subsequent section, the recent progress in the fabrications of 1D perovskite oxide nanostructures is summarized.

4.1 Template-Free Synthesis

Up to date, several template-free methods such as hydro/solvothermal synthesis, molten salt method, electrospinning process have been used to synthesize 1D perovskite-type oxide nanostructures (e.g., nanowires, nanotubes). For example, Joshi et al. [80] reported the synthesis of single-crystalline perovskite BT and ST nanowires by solution-based template-free method. Single-crystalline BT [81], PT [82, 83], and PZT [84] nanowires were also synthesized by template-free hydrothermal method. Since no organic templates are used in this process, there is no need to remove the templates after synthesis of perovskite oxide nanowires. Single-crystalline BT, ST, and PT nanowires are also synthesized by molten salt method [85–87]. The key factors for nanowire formation by molten salt method are well controlling the surface and interface energies of precursors and the selected molten salts. Monocrystalline BT nanowires are also synthesized by a modified hydrothermal process with alkali metal titanates as synthetic precursors [88]. Tetragonal PT single-crystalline nanowires with necklace-like morphology are also synthesized by electrospinning method [89]. Their lengths are in the range of tens to several tens of micrometers, and the diameters vary from 100 to 200 nm. Similarly, tetragonal PZT nanofibers are synthesized by a sol–gel electrophoresis, which is used for constructing nanogenerators for mechanical energy harvesting [90, 91]. Multiferroic BFO nanowires were also synthesized by template-free hydrothermal method [92]. The diameter of an individual BFO nanowire was in the range of 45–200 nm and the length varied from hundreds of nanometers to several microns. Besides the perovskite ferroelectric oxide nanowires, single-crystalline perovskite manganite nanowires such as $La_{0.5}Ca_{0.5}MnO_3$ nanowires with an orthorhombic perovskite structure were also synthesized by a hydrothermal method [93]. They grew along [100] and had uniform diameter ($\sim$80 nm), and the lengths varied from several to several tens of micrometers. Similarly, single-crystalline $La_{0.5}Sr_{0.5}MnO_3$, $La_{0.5}Ba_{0.5}MnO_3$, and $Pr_{0.5}Ca_{0.5}MnO_3$ nanowires with a cubic perovskite structure

were synthesized by hydrothermal method [94–96]. In the $Pr_{0.5}Ca_{0.5}MnO_3$ nanowires the charge ordering transition was suppressed and a ferromagnetic phase was observed, whereas the antiferromagnetic transition disappeared.

Besides the above "bottom-up" approaches based on chemical routes, the "top-down" approaches such as FIB milling process is also used to fabricate 1D perovskite ferroelectric nanostructures such BT nanocolumns cut from BT single crystal [97, 98]. This process offers the advantage of user-defined morphological control of the produced nanostructures exception time-consuming and low-throughput characters.

Perovskite oxide nanotubes (PONTs) are also synthesized by using template-free method such as hydrothermal synthesis. For example, BT [99] and BST [100] nanotube arrays were fabricated on titanium substrates by hydrothermal method. Isolated crystalline BT and ST PONTs were also prepared by hydrothermal process performed at low temperature, where TiO_2 nanotubes were used as a bona fide precursor materials [101].

4.2 Template-Assisted Methods

The template-assisted method is a high efficient method for mass production of regular nanostructured arrays. To date, the popular templates are colloidal monolayers, anodic aluminum oxide (AAO), block copolymers (BCPs), and nanoimprint molds [102–105]. Through template-assisted methods, 1D perovskite oxide nanostructures (e.g., nanowires, nanotubes, nanorings, nanobelts) have been prepared, which offer the following advantages: (a) high-density regular nanostructured arrays; (2) large surface-to-volume ratio; and (3) dimension sizes of the final products with well control by the channels of the template. Among the commonly used template-assisted methods, the sol–gel template method is a popular one, which is widely used to fabricate highly ordered perovskite oxide nanostructures such as BT [106–108] nanowires, PT [109–111] nanotubes, and PZT [112–114] nanowires. In addition, perovskite manganite nanowires such as $La_{1-x}Ca_xMnO_3$ (LCMO, $x = 0.20$) nanowires with nearly uniform diameter of about 30 nm, and ordered array of $La_{0.67}Sr_{0.33}MnO_3$ nanowires with diameter of 60–70 nm and length up to tens of microns were also prepared using a simple sol–gel process combined with AAO as template [115]. Following the success of this method, perovskite oxide $La_{0.825}Sr_{0.175}MnO_3$ nanowires were also synthesized, which exhibited polycrystalline perovskite structure [116].

Besides perovskite oxide nanowires, perovskite oxide nanotubes are also fabricated by using a sol–gel template-based method. Hernandez et al. [117] reported the pioneering works on the synthesis of perovskite BT and PT nanotubes by using AAO templates involving the so–gel technique. By the same method, PZT nanotubes [117–122] and multiferroic BFO nanotubes [123–127] have been synthesized. Although the sizes and shapes of the nanotubes are easily controlled by the used templates, the nanotubes synthesized by template-based methods in general

exhibit polycrystalline structure, which is ascribed to the heterogeneous nucleation on the pore walls; few single-crystalline perovskite oxide nanotubes are synthesized by this method. Anti-ferroelectric PZ PONTs were synthesized by pulse laser deposition within AAO templates [128], which were composed of nanoparticles with sizes of 3–7 nm and the wall thickness was about 10 nm. Sol–gel electrodeposition process was also used to fabricate PZT nanotube arrays, where the channels of the AAO template were filled by prepared PZT sol driven by DC electrophoretic voltages [129]. Thus, the filling effect was greatly increased. Besides the negative templates, positive templates such as silicon and ZnO nanowires are also used to fabricate ferroelectric PZT nanotubes and metal-ferroelectric-metal composite nanotubes (Pt/PZT/Pt) by magnetron sputtering and/or pulsed laser deposition [130].

Perovskite manganite nanotube arrays (e.g., highly ordered $La_{2/3}Ca_{1/3}MnO_3$ nanotubes) were also reported, which are prepared by combining AAO template-assisted synthesis with microwave irradiation [131]. This method provides a convenient route to fabricate nanotube arrays at relative low temperatures. By using porous polycarbonate templates rare-earth manganese oxide nanotubes with nominal composition of $La_{0.325}Pr_{0.30}Ca_{0.375}MnO_3$ are also synthesized by pore wetting with the liquid precursor and then followed by microwave irradiation and further calcination at 800 °C [132]. Perovskite $La_{0.59}Ca_{0.41}CoO_3$ nanotubes are also prepared by a sol–gel template method [133]. By using a template-inorganic precursor under relatively low-temperature calcination perovskite $LaNiO_3$ nanotubes were also synthesized [134]. It was found that the $LaNiO_3$ nanotubes exhibited a polycrystalline structure, which were composed of very small crystals with size about 3–5 nm.

Ferroelectric PZT nanorings [135] and their periodic arrays [136] are also fabricated. Their microstructures are well characterized. Figure 6 shows the morphology of the resulting perovskite oxide PZT nanorings in bright-field TEM (Fig. 6a) and dark-field STEM contrast (Fig. 6b and c). The dimensions of the PZT nanorings are dependent on the channel size of the AAO template, but the narrowest of pores made are able to produce rings of the form illustrated in Fig. 6c. The perovskite crystallography nature of the PZT nanoring was confirmed by its SAED shown in Fig. 7a, and also revealed by direct imaging of lattice fringes Fig. 7b. The morphology of periodic arrays of PZT nanorings is revealed by SEM image (Fig. 8a), and the cross-sectional TEM image (Fig. 8b) demonstrates that the height of the PZT nanorings was in the order of $\sim$10 nm [136].

Ordered $BiFeO_3$ nanorings are also successfully fabricated by combining AAO template-assisted PLD with ion beam etching techniques [137]. Their morphologies were revealed by AFM and TEM images (Fig. 9). Recently, Han et al. reported wafer-scale arrays of well-ordered $Pb(Zr_{0.2}Ti_{0.8})O_3$ (PZT) nanodiscs and nanorings fabricated by laser interference lithography (LIL) process companied with PLD method on $SrTiO_3$ single-crystal substrate with $SrRuO_3$ as bottom electrode [138]. Figure 10 shows SEM images of PZT nanodiscs and nanorings, which were obtained by post-annealing the amorphous PZT nanodiscs at a 650 °C and 700 °C, respectively. The epitixal growth of PZT nanostructures on the $SrRuO_3(001)$

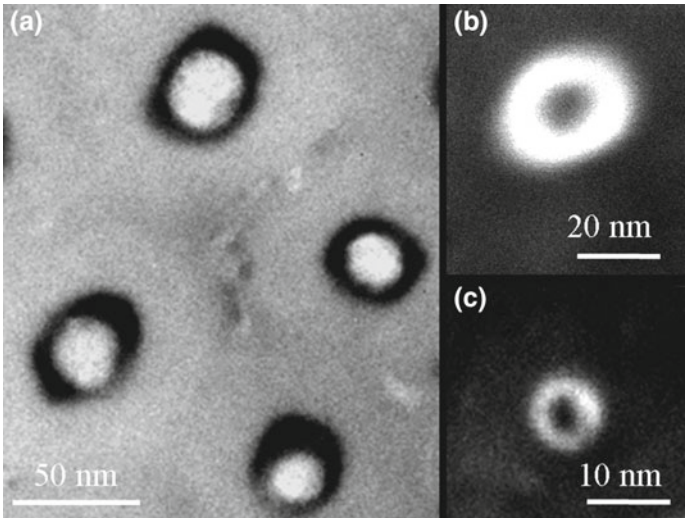

Fig. 6 **a** Bright-field cross-sectional TEM image of the PZT nanorings. **b**, **c** Dark-field STEM images of the nanorings with different outer diameters. Reproduced with permission from [135], X. H. Zhu, P. R. Evans, D. Byrne, A. Schilling, C. Douglas, R. J. Pollard, R. M. Bowman, J. M. Gregg, F. D. Morrison, J. F. Scott. Perovskite lead zirconium titanate nanorings: towards nanoscale ferroelectric "Solenoids"? Appl. Phys. Lett. 89 (2006) 122913(1–3) Copyright © 2006, American Institute of Physics

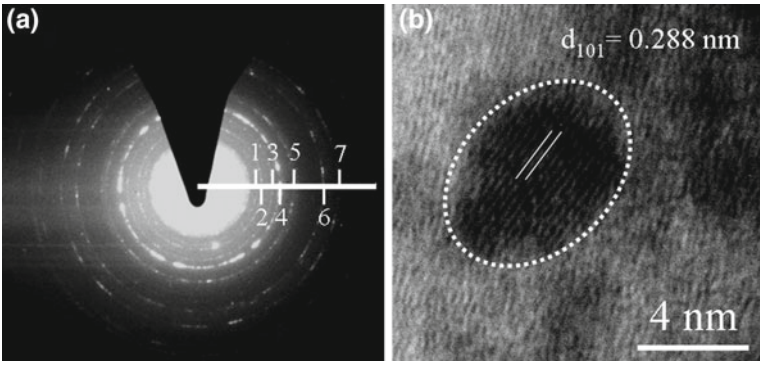

Fig. 7 **a** SAED pattern taken from the conformally coated PZT films. The first seven diffraction rings marked in the figure can be indexed as 001, 100, 101, 110, 111, 102, and 112, respectively of the perovskite form of PZT. **b** Lattice fringes of an elliptical PZT grain with size of ~5 nm in width and ~8 nm in length. The lattice spacing is characteristic of d_{101} perovskite PZT. Reproduced with permission from [135], X. H. Zhu, P. R. Evans, D. Byrne, A. Schilling, C. Douglas, R. J. Pollard, R. M. Bowman, J. M. Gregg, F. D. Morrison, J. F. Scott. Perovskite lead zirconium titanate nanorings: towards nanoscale ferroelectric "Solenoids"? Appl. Phys. Lett. 89 (2006) 122913(1–3). Copyright © 2006, American Institute of Physics

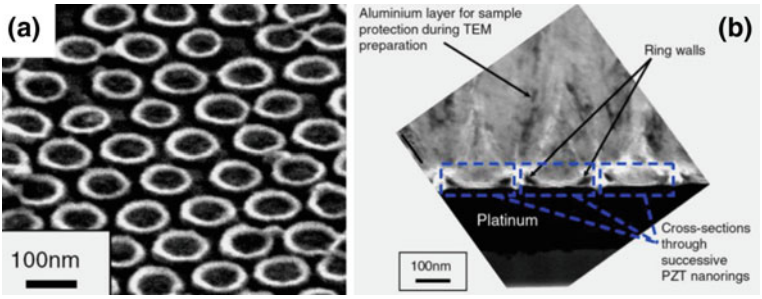

Fig. 8 **a** SEM image of the resultant PZT nanoring array (sample inclined to give some three-dimensional information) produced using nanospheres with a diameter of ~100 nm and wall thickness of ~10 nm. **b** Cross-sectional TEM image of the morphology and dimensions of the PZT nanorings. Reproduced with permission from [136], D. Byrne, A. Schilling, J. F. Scott, J. M. Gregg. Ordered arrays of lead zirconium titanate nanorings. Nanotechnology 19 (2008) 165608(1–5) Copyright © 2008, IOP Publishing Ltd.

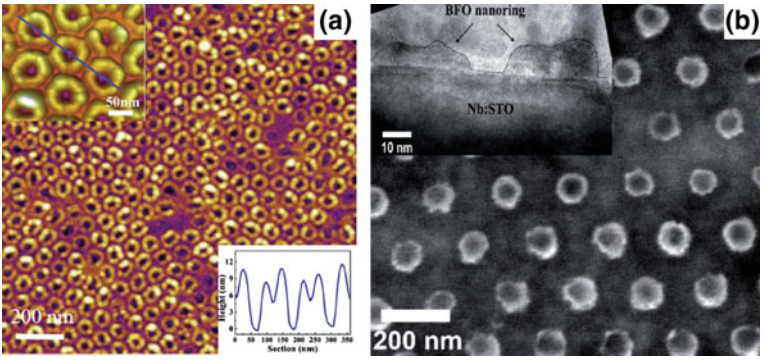

Fig. 9 **a** AFM topography and **b** planar TEM images of a large-scale BFO nanoring array. Two insets in (**a**) are the three-dimensional AFM image of the isolated BFO nanorings and the corresponding cross section line profile along the blue line. Inset in (**b**) is a cross-sectional TEM image of a single BFO nanoring. Reproduced with permission from [137], G. Tian, D. Chen, J. Yao, Q. Luo, Z. Fan, M. Zeng, Z. Zhang, J. Dai, X. Gao, J. Liu. $BiFeO_3$ nanorings synthesized via AAO template-assisted pulsed laser deposition and ion beam etching. RSC Adv. 7 (2017) 41210–41216 Copyright © 2017, The Royal Society of Chemistry

bottom electrode layer covering the (001)-oriented single-crystal substrate was revealed XRD and TEM images. PFM measurements demonstrate that the ferroelectricity is well retained in the PZT nanodiscs and nanorings.

$NaNbO_3$ nanobelt arrays with tunable aspect ratios are fabricated via a precursor-template route [139]. SEM images of $Na_7(H_3O)Nb_6O_{19}{\cdot}14H_2O$ nanobelt are shown in Fig. 11a. The precursor was post-annealed in air at 500–550 °C for 1–4 h to yield single-crystalline monoclinic $NaNbO_3$ nanobelt arrays, as shown in Fig. 11b.

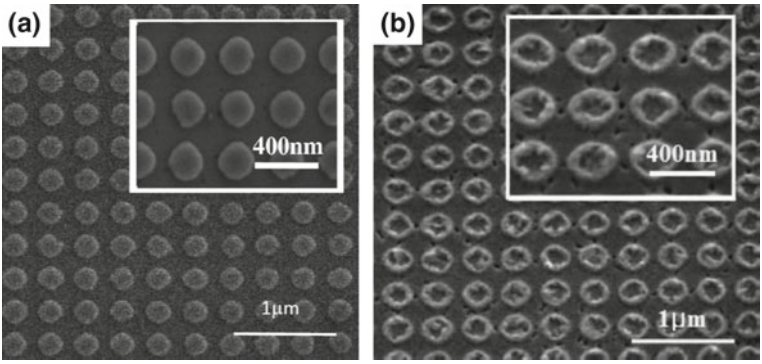

Fig. 10 SEM images of $Pb(Zr_{0.2}Ti_{0.8})O_3$ **a** nanodiscs and **b** nanorings, which were formed by post-annealing the amorphous PZT nanodiscs at 650 °C for 1 h and 700 °C for 1 h, respectively. Reproduced with permission from [138], H. Han, R. Ji, Y. J. Park, S. K. Lee, G. L. Rhun, M. Alexe, K. Nielsch, D. Hesse, U. Gösele, S. Baik. Wafer-scale arrays of epitaxial ferroelectric nanodiscs and nanorings. Nanotechnology 20 (2009) 015301 (1–6)

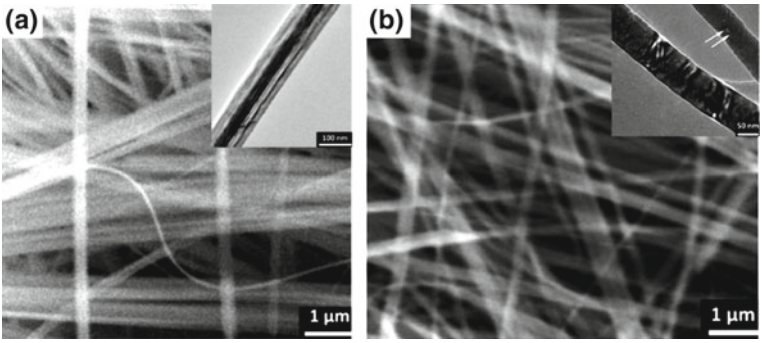

Fig. 11 SEM images of **a** $Na_7(H_3O)Nb_6O_{19}{\cdot}14H_2O$ nanobelts, and **b** $NaNbO_3$ nanobelts which are derived from the atomic rearrangements in the crystal structure of $Na_7(H_3O)Nb_6O_{19}{\cdot}14H_2O$ during post-annealing high temperature. Inset in (**a**) shows a TEM image of a single $Na_7(H_3O)Nb_6O_{19}{\cdot}14H_2O$ nanobelt with uniform width and some contrasty stripes along the nanobelt growth direction. Inset in (**b**) displays a TEM image of a single $NaNbO_3$ nanobelt, where some pits formed by thermal defects in original sublattices expanding to the surface during the high-temperature post-annealing are observed as marked by arrowheads in the inset. Reproduced with permission from [139], J. Wu, D. Xue. In situ Precursor-template route to semi-ordered $NaNbO_3$ nanobelt arrays. Nanoscale Res. Lett. 6 (2010) 14 (1–8)

5 Preparation Methods of 2D Perovskite-Type Oxide Nanostructures

Perovskite oxide 2D nanostructures include perovskite oxide thin films, nanodot arrays, lamellae patterns, nanosheets, nanoplates, nanowalls, which have important applications in the modern microelectronics. Therefore, in the past few years, several methods have been developed to synthesize perovskite oxide 2D nanostructures [140–142]. In this section, we introduce the fabrications of perovskite oxide thin films or multilayers, 2D perovskite ferroelectric oxide nanostructures based on planar structures, and perovskite oxide nanosheets.

5.1 Perovskite Oxide Thin Films or Multilayers

The growths of perovskite oxide thin films or multilayers are the process of converting the starting materials into the forms of films or multilayers on a substrate from their atoms, molecules, or ions in a gaseous state. The widely used methods for growth perovskite oxide thin films or multilayers include physical vapor deposition (PVD) methods such as PLD, RF magnetron sputtering, and chemical methods such as chemical solution deposition (CSD), chemical vapor deposition (CVD) and metalorganic chemical vapor deposition (MOCVD), and molecular beam epitaxy (MBE). Here, we shortly introduce widely used techniques such as PLD, CSD, CVD and MOCVD, and MBE.

5.2 Pulsed Laser Deposition (PLD)

In 1965 Smith and Turner first used the PLD technique to grow dielectric thin films [143], now the PLD technique becomes a popular method for thin film growth. The most important feature of the PLD process is the ability to achieve the compositions of the films almost identical with that of the target, even though the target involves a complex stoichiometry. By controlling the PLD process parameters (e.g., the laser influence, wavelength, pulse-duration and repetition rate, target to substrate distance, substrate temperature, chamber pressure) many perovskite oxide thin films or multilayers can be grown. Good reviews on the epitaxial growth of perovskite oxide thin films and superlattices can be found in the literature [140–142].

5.2.1 Chemical Solution Deposition (CSD)

CSD is an effective route for fabricating thin films with the advantages of low-cost, easy set-up, and coating of large areas. The development of which for perovskite

oxide thin films is dated to the mid-1980s [144, 145]. Up to date, many perovskite oxide thin films have been synthesized by CSD method [146–148]. In general, there are four basic steps during the growth of perovskite oxide thin films: (a) precursor solution preparation; (b) spin- or dip-coating the solution on substrate; (c) pyrolysis of the deposited solution at low temperatures; (d) crystallization of the films at high temperatures [147]. The growth rate and the degree of crystallinity of perovskite oxide thin films are dependent upon the temperature of the solution. To obtain the films with the desired thickness, the deposition/pyrolysis/crystallization steps are usually repeated several times. The processing factors such as precursor solution concentration, substrate and (eventual) bottom electrode stack, and annealing temperature play an important role in affecting the film nucleation and growth. Details can be found in good reviews contributed from Schwartz [146], Bassiri-Gharb et al. [147], and Zhang et al. [148].

5.2.2 CVD and MOCVD

CVD is one of the most popular routes to prepare perovskite oxide thin films in a large area with high quality and good performance. The key feature of the CSD process is the prepared materials that are required to have high vapor pressure using as the precursor and the substrate should be heated to a particular temperature to promote the deposition reaction as well as the motion of adatoms [149]. In the CVD process, the film composition and structure are greatly dependent upon the substrate temperature, the precursor delivery ratio, and the vaporizer temperature. In order to deposit successfully the complex multicomponent perovskite oxide thin films with uniform compositions over a large area, the used precursors should have matched thermal properties and reasonable vapor pressures. To better control the film quality some modified CVD technologies based on liquid injection [150] or the use of aerosol formation [151] have been developed. For example, perovskite PZT and lanthanum barium manganite ($La_{1-x}Ba_xMnO_3$) thin films were synthesized by liquid injection CVD method [152], and perovskite thin films of $La_{1-x}Sr_xMnO_3$ were deposited by aerosol and plasma-assisted CVD method [153].

Metal-organic chemical vapor deposition (MOCVD) is used to grow perovskite oxide thin films and superlattices [154]. This technique has some advantages over other physical deposition processes such as good control in film stoichiometry, high crystallization quality, and the ability to coat complex shapes and large areas. To meet the diversity of requirements, different MOCVD variants are developed such as low-pressure MOCVD, atmospheric pressure MOCVD, direct liquid injection MOCVD, and plasma-enhanced MOCVD [155]. In injection MOCVD process, the production of microdroplets of precursor solution is controlled by a high-speed electro-valve, which is injected into the evaporator system. The appropriate growth rates for different deposited materials are adjusted by the frequency as well as the time of the injection. Therefore, the final film stoichiometry can be well adjusted by controlling the respective concentrations of the precursors in the precursor liquid

source. Up to date, injection MOCVD is widely used to grow ferroelectric perovskite oxide thin films such as BST [156], PT [157], PZT [158], and BFO [159], and perovskite oxide superlattices such as $(BT/ST)_n$ and $(LSMO/STO)_n$ [160].

5.2.3 Molecular Beam Epitaxy (MBE)

The growth of perovskite oxide thin films by MBE method can be thought of as atomic spray painting, in which alternately shuttered elemental sources are employed to control the cation stoichiometry precisely, thus producing perovskite oxide thin films with high quality. The key steps for MBE growth of multicomponent oxides are the controlling oxide substrates terminated at well-defined ionic planes and monitoring the deposition of individual molecular/atomic layers, and so on. Reflection high-energy electron diffraction (RHEED) is widely used in MBE for the in situ monitoring the growing surface. Up to date, MBE has been used to grow perovskite oxide thin films and epitaxial heterostructures with exceptional quality [161–163].

5.3 2D Perovskite Oxide Nanostructures Based on Planar Structures

5.3.1 Top-Down Methods

Up to date different "top-down" methods such as electron beam lithography (EBL), nanoimprint lithography (NIL), have been used to fabricate 2D perovskite oxide nanostructures based on planar structures. For example, Alexe et al. performed the pioneering researches on the 2D arrangement of perovskite ferroelectric oxide nanostructures to be used for high-density ferroelectric memories [164]. By using EBL method regular arrays of $SrBi_2Ta_2O_9$ and PZT nanoisland capacitors with lateral dimensions $\sim$100 nm were successfully fabricated. The BT nanodots were also fabricated by FIB methodology cutting from the BT single crystal, and the domain structures within the BT dots were examined [165].

5.3.2 Bottom-up Methods

Besides the top-down methods, bottom-up methods such as template-assisted synthesis have been used to fabricate 2D perovskite oxide nanostructures based on lateral arrays of nanodots. For example, 2D ordered ferroelectric oxide nanodots of BT, PZT, and $SrBi_2Ta_2O_9$ with narrow size distributions are fabricated by template-assisted "bottom-up" synthetic approaches such as nanosphere lithography (NSL) [166]. In order to deposit multilayers of materials from the same template

and to increase their crystallization quality of perovskite oxide ferroelectrics, silicon nitride shadow mask, AAO membranes, and gold nanotube membranes have been used as nanostencil masks for the fabrication of 2D arrays of perovskite oxide nanodots. For example, Lee et al. [167] fabricated the PZT nanodot arrays on the Pt/MgO substrates by using ultrathin AAO membranes as a stencil mask and PLD method. The density of ordered arrays of individually addressable Pt/PZT/Pt nanocapacitors can reach 176 Gb/inch^2, which have promising applications in the ferroelectric memories with ultrahigh density.

5.4 Perovskite Oxide Nanosheets

Perovskite oxide nanosheets are also grown by wet chemical methods. Gao et al. [168] reported the synthesis of 2D single-crystal perovskite $ZnSnO_3$ nanoplates with the (111) facets as exposed plate surfaces via a one-step hydrothermal reaction. The morphology of as-synthesized perovskite $ZnSnO_3$ nanoplates is shown in Fig. 12, where the typical SEM and TEM images reveal the as-synthesized hexagonal plate-like $ZnSnO_3$ samples. The lattice fringes with spacing of 0.26 nm are clearly resolved in HRTEM image of an individual nanoplate, indicating the single-crystalline nature of the $ZnSnO_3$ nanoplate. The corresponding SAED is shown as inset in Fig. 12d, also confirms the single-crystalline nature of the ZnSnO nanoplate. Rectangular perovskite $La_2Ti_2O_7$ platelets are also grown by molten salt method [169], where the Na_2SO_4–K_2SO_4 flux was used as molten salt and analytical grade TiO_2 and La_2O_3 oxides were used as the starting materials. While the syntheses of perovskite oxide 2D nanostructures are still at the embryonic stage, the applications of perovskite oxide 2D nanostructures in oxide microelectronic devices are full of great challenges. Much work remains to be done in this direction.

6 Preparation Methods of 3D Perovskite-Type Oxide Nanostructures

Generally, 3D nanostructures can be fabricated via “bottom-up” and “top-down” approaches. The “bottom-up” approaches to the fabrication of nanostructures start at the atomic or molecular level, and solution-based routes (e.g., sol–gel-based CSD, templating, and hydro/solvothermal synthesis) are the most commonly employed in the this approaches for fabricating 3D perovskite-type oxide nanostructures (i.e., vertically aligned nanowires, rods or tubes). The “top-down” approaches (e.g., FIB milling and some lithographical methods such as NIL) to fabrication of nanostructures include carving away the bulk ferroelectric material and creating coherently and continuously ordered nanosized structures by FIB technique [170]. For example, by FIB method Rémiens et al. created PZT

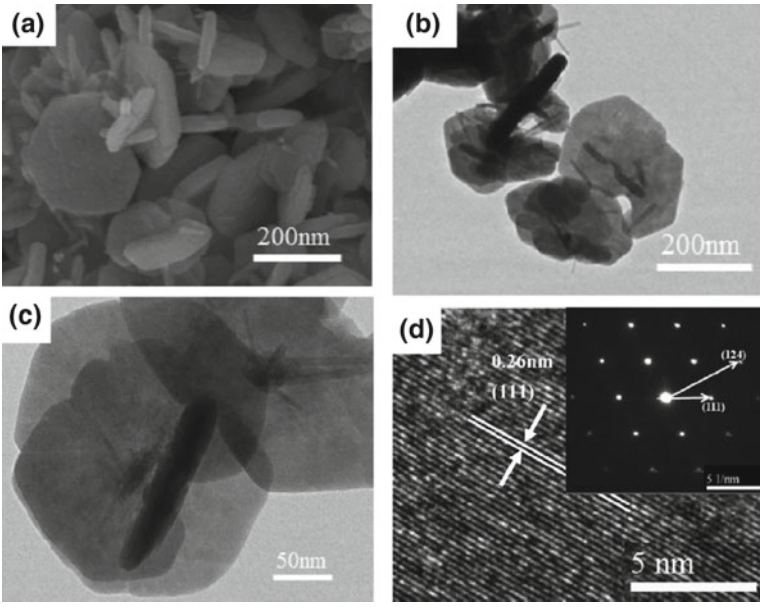

Fig. 12 Typical **a** SEM, (**b**, **c**) TEM, and **d** HRTEM images and SAED pattern (inset) of $ZnSnO_3$ nanoplates synthesized at 260 °C via a one-step hydrothermal reaction. Reproduced with permission from [168], R. Guo, Y. Guo, H. Duan, H. Li, H. Liu. Synthesis of orthorhombic perovskite-type $ZnSnO_3$ single-crystal nanoplates and their application in energy harvesting. ACS Appl. Mater. Interfaces 9(9) (2017) 8271–8279 Copyright © 2017, American Chemical Society

nanoislands (with diameter of 50 nm), which were milled from an amorphous film layer and subsequently converted into crystalline PZT thin film by high-temperature annealing [171]. The advantages of "top-down" approaches for fabricating 3D perovskite oxide nanostructures via FIB milling are the precision positioning and well controlling in the shapes and sizes of the fabricated nanostructures. However, the FIB milling technique has significant drawbacks such as slow milling and patterning speeds, especially for fabricating larger structures, and it is not suitable for volume patterning nanostructures. In addition, problems are also arisen at the nanoscale due to the induced damages by the incident ions at the surfaces of the samples. Considering that the properties of 3D perovskite oxide nanostructures are much sensitive to their structures and ordered alignments, the fabrication of a large-scale nanostructure arrays with well control in the morphology and structure becomes much important [104]. To achieve the above goal, several techniques including photolithography, electron beam lithography, and scanning probe lithography have been used [172, 173]. Recently, PLD in combination with the AAO template has also been used to prepare 3D perovskite ferroelectric nanostructures. Ferroelectric PZT nanocapacitor arrays with Pt top electrodes were fabricated with ultrahigh density of $\sim$Tb/inch^2 density [170]. Besides the AAO template-assisted fabrication, other methods such as 3D nanotemplate PLD have

also been used to prepare 3D perovskite oxide nanostructures. In this method, an inclined substrate deposition onto the side surfaces of a 3D nanopatterned substrate is used as a 3D nanotemplate, which is schematically shown in Fig. 13, and details can be found in reference [174]. As one example, crystalline $(La_{0.275}Pr_{0.35}Ca_{0.375})MnO_3$ (LPCMO) nanobox were grown on a MgO(001) substrate using 3D nanotemplate [16]. Figure 14 illustrates the fabrication procedure of the LPCMO nanobox, their typical SEM image, and the relationship between the wall-width of the LPCMO nanobox and the deposited time. It is found that the wall-width of the LPCMO nanoboxes can be controlled in the range of 30–160 nm by changing the deposition time. These LPCMO nanoboxes exhibit an insulator-metal transition at

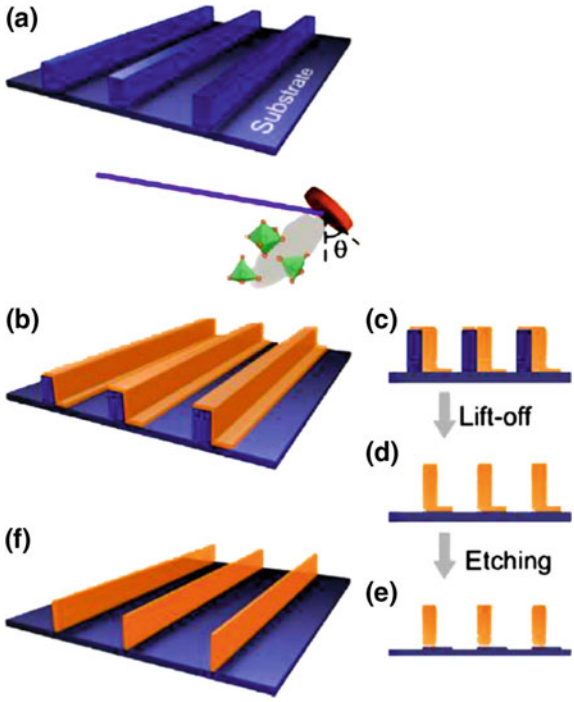

Fig. 13 Schematic flowchart of the 3D nanotemplate PLD method for perovskite oxide nanostructure fabrication. **a** First, template wall structures are patterned onto substrate by NIL using an organic resist (blue region). **b** Functional perovskite oxides (orange region) is then deposited onto the side surface of the template patterns by PLD. **c** Cross-sectional image of (**b**). Cross-sectional images for nanowall-wire structure after **d** liftoff and **e** etching. **f** Finally, self-standing perovskite oxide nanowall-wire arrays are obtained. Reproduced with permission from [174], T. Kushizaki, K. Fujiwara, A. N. Hattori, T. Kanki, H. Tanaka. Controlled fabrication of artificial ferromagnetic $(Fe,Mn)_3O_4$ nanowall-wires by a three-dimensional nanotemplate pulsed laser deposition method. Nanotechnology 23(48) (2012) 485308 (1–5)

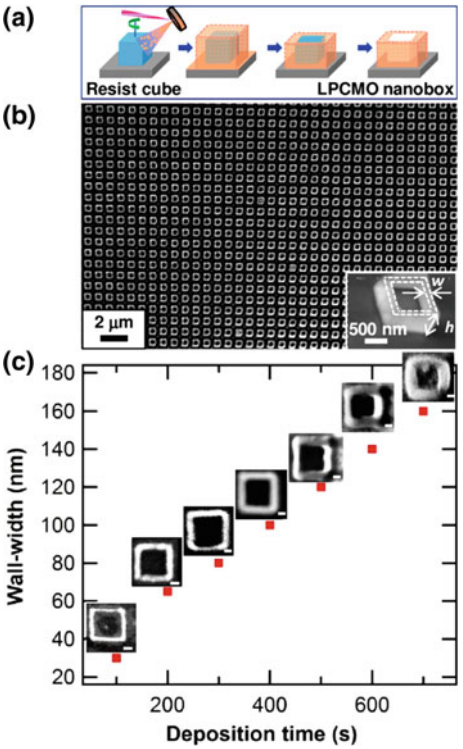

Fig. 14 **a** Schematic image for the fabrication procedure of the $(La_{0.275}Pr_{0.35}Ca_{0.375})MnO_3$ nanoboxes. **b** Typical SEM image of $(La_{0.275}Pr_{0.35}Ca_{0.375})MnO_3$ nanoboxes with 100 nm wall-width and 400 nm height. **c** The relationship between the wall-width of the $(La_{0.275}Pr_{0.35}Ca_{0.375})MnO_3$ nanoboxes and the deposition time. Reproduced with permission from [16], T. V. A. Nguyen, A. N. Hattori, Y. Fujiwara, S. Ueda, H. Tanaka. Colossal magnetoresistive (La,Pr,Ca)MnO_3 nanobox array structures constructed by the three-dimensional nanotemplate pulsed laser deposition technique. Appl. Phys. Lett. 103(22) (2013) 223105 (1–4) Copyright © 2013, American Institute of Physics

higher temperature than that in the corresponding film, which has promising appliactions in the fields of oxide spintronics. 3D nanotemplate PLD technique provides a novel route to fabricate 3D perovskite oxide nanostructures.

7 Conclusions and Outlook

This chapter reviewed the state of art in preparation methods of perovskite-type oxide materials, with a wide range scope from bulk perovskite oxide ceramics to perovskite oxide nanopowders, and to perovskite 1D, 2D, and 3D oxide nanostructures. Conventional solid-state reaction is usually used to synthesize perovskite oxide ceramics. However, their resulting microstructures exhibit poor chemical homogeneity, serious particle agglomeration, and coarse large grains. Advances toward nanoscale oxide electronics have stimulated interests in the fields of perovskite oxide nanopowders. Therefore, the synthesis methods of perovskite oxide nanopowders with controlled particle size, morphology, and stoichiometry are highly required to be developed. Over the past decades, various synthesized methods using solid, liquid, or gas phase precursors have been developed to

synthesize high purity, ultra-fine, and agglomerate-free perovskite oxide nanopowders. 1D perovskite oxide nanostructures such as perovskite oxide nanowires and nanotubes are important structural units for constructing nanoscale electronic devices, and their novel properties open up new avenues of applications in the fields of electronics, energy harvesting, data storage. Both top-down-based direct lithography techniques and chemical bottom-up-based methods based on a solution or a dispersion (i.e., deposition in AAO templates, electrospinning, hydrothermal, and molten salt method) have been developed to synthesize 1D perovskite oxide nanostructures. Similarly, these methods are also used to fabricate 2D perovskite oxide nanostructures, which are now considered to be excellent candidates for future oxide electronic applications. Recently, 3D nanotemplate PLD technique has been developed to fabricate 3D perovskite oxide nanostructures (e.g., perovskite $(La_{0.275}Pr_{0.35}Ca_{0.375})MnO_3$ nanobox arrays) with controllable size and morphology. This technique makes use of epitaxial thin film deposition technique and nanolithography together, which can be used to fabricate nanoboxes with tunable wall-widths or the diameters, and their adjacent distance is reduced down to 10 nm, realizing the formation of 3D perovskite oxide nanostructures beyond the resolution limitations of top-down methods. 3D perovskite-type oxide nanostructures such as $(La_{0.275}Pr_{0.35}Ca_{0.375})MnO_3$ nanobox array structures fabricated by 3D nanotemplate PLD technique, exhibit an insulator-metal transition at higher temperature than that in the corresponding thin film, which provide a way to tune the physical properties of CMR oxide nanostructures, and find a promising application in oxide nanoelectronics taking the advantage of the huge electronic/spintronic phase transition. At present the growth techniques of perovskite oxide thin films used for perovskite oxide nanoelectronic devices are still in their infancy, and accurate compositional and structural controls at the atomic layer level are highly required. Recently, new techniques such as laser-MBE and reactive molecular beam epitaxy are developed, which permit to grow perovskite oxide thin films with thickness down to a mololayer limit [175]. Therefore, such 2D perovskite ultrathin films are as useful as graphene in exploring unconventional 2D correlated quantum phases and find promising applications in multifunctional electronic nanodevices.

Acknowledgements The authors acknowledge the financial supports from the National Natural Science Foundation of China (grant nos. 11674161 and 11174122), Natural Science Foundation of Jiangsu Province (grant no. BK20181250), and six big talent peak project from Jiangsu Province (grant no. XCL-004).

References

1. Bhalla AS, Guo R, Roy R (2000) The perovskite structure-a review of its role in ceramic science and technology. Mater. Res. Innova. 4(1):3–26
2. Nourafkan R, Marsiglio F, Kotliar G (2012) Model of the electron-phonon interaction and optical conductivity of $Ba_{1-x}K_xBiO_3$ superconductors. Phys Rev Lett 109(1):017001(1–5)

3. Markovich V, Fita I, Wisniewski A, Jung G, Mogilyansky D, Puzniak R, Titelman L, Gorodetsky G (2010) Spin glass-like properties of $La_{0.8}Ca_{0.2}MnO_3$ nanoparticles ensembles. Phys Rev B 81(13):134440(1–11)
4. Sarkar T, Raychaudhuri AK, Bera AK, Yusuf SM (2010) Effect of size reduction on the ferromagnetism of the manganite $La_{1-x}Ca_xMnO_3$ ($x = 0.33$). New J Phys 12(12):123026 (1–21)
5. Grutter A, Wong F, Arenholz E, Liberati M, Vailionis A, Suzuki Y (2010) Enhanced magnetism in epitaxial $SrRuO_3$ thin films. Appl Phys Lett 96(8):082509(1–3).
6. Pena MA, Fierro JLG (2001) Chemical structures and performance of perovskite oxides. Chem Rev 101(7):1981–2018
7. Dawber M, Rabe KM, Scott JF (2005) Physics of thin-film ferroelectric oxides. Rev Mod Phys 77(4):1083–1103
8. Fiebig M, Lottermoser T, Fröhlich D, Goltsev AV, Pisarev RV (2002) Observation of coupled magnetic and electric domains. Nature 419(6909):818–820
9. Gruverman A, Kholkin A (2006) Nanoscale ferroelectrics: processing, characterization and future trends. Rep Prog Phys 69(8):2443–2474
10. Haertling GH (1999) Ferroelectric ceramics: history and technology. J Am Ceram Soc 82 (4):797–818
11. Brinker CJ, Hurd AJ, Schunk PR, Frye GC, Ashley CS (1992) Review of sol–gel thin film formation. J Non-crystalline Solids 147–148:424–436
12. Dimitriev Y, Ivanova Y, Iordanova R (2008) History of sol–gel science and technology. J Univ Chem Technol Metallurgy 43(2):181–192
13. Yoshimura M, Byrappa K (2008) Hydrothermal processing of materials: past, present and future. J Mater Sci 43(7):2085–2103
14. Zhu XH, Hang QM (2013) Microscopical and physical characterization of microwave and microwave-hydrothermal synthesis products. Micron 44:21–44
15. Ganguli A, Ganguly A, Vaidya S (2010) Microemulsion-based synthesis of nanocrystalline materials. Chem Soc Rev 39(2):474–85
16. Nguyen TVA, Hattori AN, Fujiwara Y, Ueda S, Tanaka H (2013) Colossal magnetoresistive (La,Pr,Ca)MnO_3 nanobox array structures constructed by the three-dimensional nanotemplate pulsed laser deposition technique. Appl Phys Lett 103(22):223105(1–4)
17. Zhu XH (2010) Piezoelectric ceramics: processing, properties, characterization, and applications. In: Nelson WG (ed) Piezoelectric materials: structure, properties and applications. Nova Science Publishers, New York, pp 1–36
18. Silva J, Reyes A, Esparza H, Camacho H, Fuentes L (2011) $BiFeO_3$: A review on synthesis, doping and crystal structure. Integr. Ferroelectrics 126:47–59
19. Chaiyo N, Ruangphanit A, Muanghlua R, Niemcharoen S, Boonchom B, Vittayakorn N (2011) Synthesis of potassium niobate ($KNbO_3$) nanopowder by a modified solid-state reaction. J Mater Sci 46:1585–1590
20. Bernardo MS, Jardiel T, Peiteado M, Caballero AC, Villegas M (2011) Reaction pathways in the solid state synthesis of multiferroic $BiFeO_3$. J Eur Ceram Soc 31:3047–3053
21. Beauger A, Mutin JC, Niepce JC (1983) Synthesis reaction of metatitanate $BaTiO_3$. J Mater Sci 18(10):3041–3046
22. Rössel M, Höche H-R, Leipner HS, Völtzke D, Abicht H-P, Hollricher O, Müller J, Gablenz S (2004) Raman microscopic investigations of $BaTiO_3$ precursors with core-shell structure. Anal Bioanal Chem 380:157–162
23. Ubaldini A, Buscaglia V, Uliana C, Costa G, Ferretti M (2003) Kinetics and mechanism of formation of barium zirconate from barium carbonate and zirconia powders. J Am Ceram Soc 86(1):19–25
24. Kimura T (2011) Molten salt synthesis of ceramic powders. In: Sikalidis C (ed) Advances in ceramics-synthesis and characterization, processing and specific applications, 1st edn. INTECH Open Access Publisher; Rijeka, Croatia, pp 75–100

25. Chen J, Yu RB, Li LH, Sun C, Zhang T, Chen HW, Xing XR (2008) Structure and shape evolution of $Bi_{1-x}La_xFeO_3$ perovskite microcrystals by molten salt synthesis. Eur J Inorg Chem 23:3655–3660
26. Zheng XH, Chen PJ, Ma N, Ma ZH, Tang DP (2012) Synthesis and dielectric properties of $BiFeO_3$ derived from molten salt method. J Mater Sci Mater Electron 23:990–994
27. Zhu X, Zhou J, Jiang M, Xie J, Liang S, Li S, Liu Z, Zhu Y, Zhu J, Liu Z (2014) Molten salt synthesis of bismuth ferrite nano- and microcrystals and their structural characterization. J Am Ceram Soc 97(7):2223–2232
28. Liu Z, Liang S, Li S, Zhu Y, Zhu X (2015) Synthesis, microstructural characterization, and dielectric properties of $BiFeO_3$ microcrystals derived from molten salt method. Ceram Int 41 (Sup 1):S19–25
29. Chen J, Xing XR, Watson A, Wang W, Yu RB, Deng JX, Lai Y, Sun C, Chen XB (2007) Rapid synthesis of multiferroic $BiFeO_3$ single crystalline nanostructures. Chem Mater 19:3598–3600
30. He X, Gao L (2009) Synthesis of pure phase $BiFeO_3$ powders in molten alkali metal nitrates. Ceram Int 35:975–978
31. Yoon KH, Cho YS, Kang DH (1998) Molten salt synthesis of lead-based relaxors. J Mater Sci 33(12):2977–2984
32. Thirumal M, Jain P, Ganguli AK (2001) Molten salt synthesis of complex perovskite-related dielectric oxides. Mater Chem Phys 70(1):7–11
33. Kačenka M, Kaman O, Jirák Z, Maryško M, Žvátora P, Vratislav S, Lukeš I (2014) Magnetic properties of $La_{1-x}Sr_xMnO_3$ nanoparticles prepared in a molten salt. J Appl Phys 115(17):17B525(1–3)
34. Xia WR, Li L, Wu H, Xue PJ, Zhu XH (2017) Molten salt route of $La_{1-x}Ca_xMnO_3$ nanoparticles: microstructural characterization, magnetic and electrical transport properties. Mater Charact 131:128–134
35. McCormick PG, Tsuzuki T, Robinson JS, Ding J (2001) Nanopowders synthesized by mechanochemical processing. Adv Mater 13(12–13):1008–1010
36. Kong LB, Zhang TS, Ma J, Boey F (2008) Progress in synthesis of ferroelectric ceramic materials via high-energy mechanochemical technique. Prog Mater Sci 53(2):207–322
37. Zouari S, Ellouze M, Nasri A, Cherif W, Hlil EK, Elhalouani F (2014) Morphology, structural, magnetic, and magnetocaloric properties of $Pr_{0.7}Ca_{0.3}MnO_3$ nanopowder prepared by mechanical ball milling method. J Supercond Novel Magnetism 27(2):555–563
38. Khamman O, Wongmaneerung R, Chaisan W, Yimnirun R, Ananta S (2008) Preparation of perovskite nanopowders by vibro-milling technique. J Alloy Compd 456(1–2):492–497
39. Lee G-J, Park EK, Yang SA, Park JJ, Bu SD, Lee MK Rapid and direct synthesis of complex perovskite oxides through a highly energetic planetary milling. Sci Rep 7:46241(1–11)
40. Welham NJ (1998) Mechanically induced reaction between alkaline earth metal oxides and TiO_2. J Mater Res 13(6):1607–1613
41. Szafraniak I, Połomska M, Hilczer B, Pietraszko A, Kepinski L. Characterization of $BiFeO_3$ nanopowder obtained by mechanochemical synthesis. J Eur Ceram Soc 27:4399–4402
42. Chandler CD, Roger C, Hampdensmith MJ (1993) Chemical aspects of solution routes to perovskite-phase mixed-metal oxides from metal-organic precursors. Chem Rev 93:1205–1241
43. Hench LL, West JK (1990) The sol–gel process. Chem Rev 90(1):33–72
44. Brutchey RL, Morse DE (2006) Template-free, low-temperature synthesis of crystalline barium titanate nanoparticles under bio-inspired conditions. Angew Chem Int Ed 45 (39):6564–6566
45. Viviani M, Lemaitre J, Buscaglia MT, Nanni P (2000) Low-temperature aqueous synthesis (LTAS) of $BaTiO_3$: a statistical design of experiment approach. J Eur Ceram Soc 20(3):315–320
46. Ciftci E, Rahaman MN, Shumsky M (2001) Hydrothermal precipitation and characterization of nanocrystalline $BaTiO_3$ particles. J Mater Sci 36(20):4875–4882

47. Liu C, Zou BS, Rondinone AJ, Zhang ZJ (2001) Sol–gel synthesis of free-standing ferroelectric lead zirconate titanate nanoparticles. J Am Chem Soc 123(18):4344–4345
48. Yang H, Xian T, Wei ZQ, Dai JF, Jiang JL, Feng WJ (2011) Size-controlled synthesis of $BiFeO_3$ nanoparticles by a soft-chemistry route. J Sol-Gel Sci Technol 58:238–243
49. Hu Y, Fei L, Zhang Y, Yuan J, Wang Y, Gu HJ (2011) Synthesis of bismuth ferrite nanoparticles via a wet chemical route at low temperature. J Nanomaterials 2011:797639(1–6)
50. Flaschen SS (1955) An aqueous synthesis of barium titanate. J Am Chem Soc 77(23):6194–6194
51. Kiss K, Magder J, Vukasovich MS, Lockhart RJ (1966) Ferroelectrics of ultrafine particle size: I, synthesis of titanate powders of ultrafine particle size. J Am Ceram Soc 49(6):291–295
52. Kamiya H, Gomi K, Iida Y, Tanaka K, Yoshiyasu T, Kakiuchi T (2003) Preparation of highly dispersed ultrafine barium titanate powder by using microbial-derived surfactant. J Am Ceram Soc 86(12):2011–2018
53. Golubko NV, Yanovskaya MI, Golubko LA, Kovsman EP, Listoshina MB, Rotenberg BA (2001) Preparation of barium titanate and related materials by the alkoxide-hydroxide route. J. Sol-Gel Sci. Tech. 20(2):135–143
54. Bruno SA, Monson WL (1993) Process for preparing crystalline mixed metal oxides. US Patent 5242674
55. Han JT, Huang YH, Wu XJ, Wu CL, Wei W, Peng B, Huang W, Goodenough JB (2006) Tunable synthesis of bismuth ferrites with various morphologies. Adv Mater 18:2145–2148
56. Wang YG, Xu G, Yang LL, Ren ZH, Wei X, Weng WJ, Du P, Shen G, Han GR (2007) Alkali metal ions-assisted controllable synthesis of bismuth ferrites by a hydrothermal method. J Am Ceram Soc 90:3673–3675
57. Gao F, Yuan Y, Wang KF, Chen XY, Chen F, Liu J-M, Ren ZF (2006) Preparation and photoabsorption characterization of $BiFeO_3$ nanowires. Appl Phys Lett 89:102506 (1–3)
58. Wang GM, Lin C, Liu ST, Deng QR, Mao YW, Wang SG (2018) Hydrothermal synthesis of bismuth ferrite with controllable phase structure, morphology and visible light photocatalytic activities. J Mater Sci Mater Electron 29(6):4926–4932
59. Han SH, Kim KS, Kim HG, Lee H-G, Kang H-W, Kim JS, Cheon CI (2010) Synthesis and characterization of multiferroic BiFeO3powders fabricated by hydrothermal method. Ceram Int 36:1365–1372
60. Liu B, Hu BB, Du ZL (2011) Hydrothermal synthesis and magnetic properties of single-crystalline $BiFeO_3$ nanowires. Chem Commun 47(28):8166–8168
61. Wang YG, Xu G, Ren ZH, Wei X, Weng WJ, Du PY, Shen G, Han GR (2007) Mineralizer-assisted hydrothermal synthesis and characterization of $BiFeO_3$ nanoparticles. J Am Ceram Soc 90:2615–2617
62. Chen C, Cheng JR, Yu SW, Che LJ, Meng ZY (2006) Hydrothermal synthesis of perovskite bismuth ferrite crystallites. J Cryst Growth 291(1):135–139
63. Hojamberdiev M, Xu Y, Wang F, Wang J, Liu J, Wang W (2009) Morphology-controlled hydrothermal synthesis of bismuth ferrite using various alkaline mineralizers. Ceramics-Silikáty 53(2):113–117
64. Hennings D, Schreinemacher S (1992) Characterization of hydrothermal barium titanate. J Eur Ceram Soc 9(1):41–46
65. Waser R (1988) Solubility of hydrogen defects in doped and undoped $BaTiO_3$. J Am Ceram Soc 71(1):58–63
66. Pithan C, Hennings D, Waser R (2005) Progress in the synthesis of nanocrystalline $BaTiO_3$ powders for MLCC. Int J Appl Ceram Technol 2(1):1–14
67. Chen DR, Jiao XL (2000) Solvothermal synthesis and characterization of barium titanate powders. J Am Ceram Soc 83(10):2637–2639
68. Kwon SG, Choi K, Kim BI (2006) Solvothermal synthesis of nano-sized tetragonal barium titanate powders. Mater Lett 60(7):979–982

69. Komarneni S, Roy R, Li QH (1992) Microwave-hydrothermal synthesis of ceramic powders. Mater Res Bull 27(12):1393–1405
70. Niederberger M, Pinna N, Polleux J, Antonietti M (2004) A general soft-chemistry route to perovskites and related materials: synthesis of $BaTiO_3$, $BaZrO_3$, and $LiNbO_3$ nanoparticles. Angew Chem 43(17):2270–2273
71. Jhung SH, Lee JH, Yoon JW, Hwang YK, Hwang JS, Park SE, Chang JS (2004) Effects of reaction conditions in microwave synthesis of nanocrystalline barium titanate. Mater Lett 58 (25):3161–3165
72. Sun WA, Li CH, Li JQ, Liu W (2006) Microwave-hydrothermal synthesis of tetragonal $BaTiO_3$ under various conditions. Mater Chem Phys 97(2–3):481–487
73. Pązik R, Hreniak D, Strek W (2007) Microwave driven hydrothermal synthesis of $Ba_{1-x}Sr_xTiO_3$ nanoparticles. Mater Res Bull 42(7):1188–1194
74. Zhu XH, Hang QM, Xing ZB, Yang Y, Zhu JM, Liu ZG, Ming NB, Zhou P, Song Y, Li ZS, Yu T, Zou ZG (2011) Microwave hydrothermal synthesis, structural characterization, and visible-light photocatalytic activities of single-crystalline bismuth ferric nanocrystals. J Am Ceram Soc 94(8):2688–2693
75. Joshi UA, Jang JS, Borse PH, Lee JS (2008) Microwave synthesis of single-crystalline perovskite $BiFeO_3$ nanocubes for photoelectrode and photocatalytic applications. Appl Phys Lett 92(24):242106(1–3)
76. Swihart M (2003) Vapor-phase synthesis of nanoparticles. Curr Opin Colloid Interface Sci 8 (1):127–133
77. Pratsinis SE, Mastrangelo SVR (1989) Material synthesis in aerosol reactors. Chem Eng Prog 85:62–66
78. Wu MK, Windeler RS, Steiner CKR, Börs T, Friedlander SK (1993) Controlled synthesis of nanosized particles by aerosol processes. Aerosol Sci Technol 19(4):527–548
79. Seol KS, Tomita S, Takeuchi K, Miyagawa T, Katagiri T, Ohki Y (2002) Gas-phase production of monodisperse lead zirconate titanate nanoparticles. Appl Phys Lett 81:1893–1895
80. Joshi UA, Yoon S, Baik S, Lee JS (2006) Surfactant-free hydrothermal synthesis of highly tetragonal barium titanate nanowires: a structural investigation. J. Phys. Chem. B. 110 (25):12249–12256
81. Urban JJ, Yun WS, Gu Q, Park H (2002) Synthesis of single-crystalline perovskite nanorods composed of barium titanate and strontium titanate. J Am Chem Soc 124(7):1186–1187
82. Gu H, Hu Y, You J, Hu Z, Yuan Y, Zhang T (2007) Characterization of single-crystalline $PbTiO_3$ nanowire growth via surfactant-free hydrothermal method. J Appl Phys 101:024319 (1–7)
83. Hu Y, Gu H, Sun X, You J, Wang J (2006) Photoluminescence and Raman scattering studies on $PbTiO_3$ nanowires fabricated by hydrothermal method at low temperature. Appl Phys Lett 88:193120(1–3)
84. Wang J, Durussel A, Sandu CS, Sahini MG, He ZB, Setter N (2012) Mechanism of hydrothermal growth of ferroelectric PZT nanowires. J Cryst Growth 347(1):1–6
85. Mao YB, Banerjee S, Wong SS (2003) Large-scale synthesis of single-crystalline perovskite nanostructures. J Am Chem Soc 125(51):15718–15719
86. Deng H, Qiu Y, Yang S (2009) General surfactant-free synthesis of $MTiO_3$ (M = Ba, Sr, Pb) perovskite nanostrips. J Mater Chem 19:976–982
87. Cai Z, Xing X, Yu R, Sun X, Liu G (2007) Morphology-controlled synthesis of lead titanate powders. Inorg Chem 46(18):7423–7427
88. Bao N, Shen L, Gupta A, Tatarenko A, Srinivasan G, Yanagisawa K (2009) Size-controlled one-dimensional monocrystalline $BaTiO_3$ nanostructures. Appl Phys Lett 94:253109(1–3)
89. Lu X, Zhang D, Zhao Q, Wang C, Zhang W, Wei Y (2006) Large-scale synthesis of necklace-like single-crystalline $PbTiO_3$ nanowires. Macromol Rapid Commun 27(1):76–80
90. Chen X, Xu S, Yao N, Shi Y (2010) 1.6 V Nanogenerator for mechanical energy harvesting using PZT nanofibers. Nano Lett 10(6):2133–2137

91. Teo WE, Ramkrishna S (2006) A review on electrospinning design and nanofibre assemblies. Nanotechnology. 17(14):R89–106
92. Liu B, Hu B, Du Z (2011) Hydrothermal synthesis and magnetic properties of single-crystalline $BiFeO_3$ nanowires. Chem Commun 47:8166–8168
93. Zhang T, Jin CG, Qian T, Lu XL, Bai JM, Li XG (2004) Hydrothermal synthesis of single-crystalline $La_{0.5}Ca_{0.5}MnO_3$ nanowires at low temperature. J Mater Chem 14:2787–2789
94. Zhu D, Zhu H, Zhang YH (2002) Hydrothermal synthesis of single-crystal $La_{0.5}Sr_{0.5}MnO_3$ nanowire under mild conditions. J Phys Condens Matter 14:L519–L524
95. Zhu D, Zhu H, Zhang Y (2002) Hydrothermal synthesis of $La_{0.5}Ba_{0.5}MnO_3$ nanowires. Appl Phys Lett 80(9):1634–1636
96. Rao SS, Anuradha KN, Sarangi S, Bhat SV (2005) Weakening of charge order and antiferromagnetic to ferromagnetic switch over in $Pr_{0.5}Ca_{0.5}MnO_3$ nanowires. Appl Phys Lett 87:182503(1–3)
97. McQuaid RGP, McMillen M, Chang LW, Gruverman A, Gregg JM (2012) Domain wall propagation in meso- and nanoscale ferroelectrics. J Phys Condens Matter 24:024204 (1–6)
98. Schilling A, Bowman RM, Catalan G, Scott JF, Gregg JM (2007) Morphological control of polar orientation in single-crystal ferroelectric nanowires. Nano Lett 7:3787–3791
99. Padture NP, Wei X (2003) Hydrothermal synthesis of thin films of barium titanate ceramic nanotubes at 200 °C. J Am Ceram Soc 86(12):2215–2217
100. Singh S, Krupanidhi SB (2007) Synthesis and structural characterization of $Ba_{0.6}Sr_{0.4}TiO_3$ nanotubes. Phys Lett A 367:356–359
101. Mao Y, Banerjee S, Wong SS (2003) Hydrothermal synthesis of perovskite nanotubes. Chem Commun 3(3):408–409
102. Tian TL, Dong JP, Xu JQ (2016) Direct electrodeposition of highly ordered gold nanotube arrays for use in non-enzymatic amperometric sensing of glucose. Microchim Acta 183:1925–1932
103. Kasera S, Biedermann F, Baumberg JJ, Scherman OA, Mahajan S (2012) Quantitative SERS using the sequestration of small molecules inside precise plasmonic nanoconstructs. Nano Lett 12:5924–5928
104. Li Y, Duan GT, Liu GQ, Cai WP (2013) Physical processes-aided periodic micro/nanostructured arrays by colloidal template technique: fabrication and applications. Chem Soc Rev 42:3614–3627
105. Ding T, Sigle DO, Hermann LO, Wolverson D, Baumberg JJ (2014) Nanoimprint lithography of Al nanovoids for seep-UV SERSACS. Appl Mater Interfaces 6:17358–17363
106. Limmer SJ, Seraji S, Wu Y, Chou TP, Nguyen C, Cao GZ (2002) Template-based growth of various oxide nanorods by sol–gel electrophoresis. Adv Funct Mater 12:59–64
107. Anuradha TV (2014) Template-assisted sol–gel synthesis of nanocrystalline $BaTiO_3$. J. Chem. 7(3):894–898
108. Boucher R, Renz P, Li C, Fuhrlich T, Bauch J, Yoon KH, Lupascu DC. Large coercivity and polarization of sol–gel derived $BaTiO_3$ nanowires. J Appl Phys 110(6):064112(1–5)
109. Zhao L, Steinhart M, Yu J, Gösele U (2006) Lead titanate nano- and microtubes. J Mater Res 21:685–690
110. Liu L, Ning T, Ren Y, Sun Z, Wang F, Zhou W, Xie S, Song L, Luo S, Liu D, Shen J, Ma W, Zhou Y (2008) Synthesis, characterization, photoluminescence and ferroelectric properties of $PbTiO_3$ nanotube arrays. Mater Sci Eng, B 149(1):41–46
111. Rørvik PM, Tadanaga K, Tatsumisago M, Grande T, Einarsrud MA (2009) Template-assisted synthesis of $PbTiO_3$ nanotubes. J Eur Ceram Soc 29(12):2575–2579
112. Zhang XY, Zhao X, Lai CW, Wang J, Tang XG, Dai JY (2004) Synthesis and piezoresponse of highly ordered $Pb(Zr_{0.53}Ti_{0.47})O_3$ nanowire arrays. Appl Phys Lett 85(18):4190–4192
113. Wen T, Zhang J, Chou TP, Limmer SJ, Cao G (2005) Template-based growth of oxide nanorod arrays by centrifugation. J Sol-Gel Sci Technol 33(2):193–200

114. Shen ZK, Chen ZH, Li H, Qu XP, Chen Y, Liu R (2011) Nanoembossing and piezoelectricity of ferroelectric $Pb(Zr_{0.3}Ti_{0.7})O_3$ nanowire arrays. Appl Surf Sci 257 (21):8820–8823
115. Shankar K, Raychaudhuri A (2004) Growth of an ordered array of oriented manganite nanowires in alumina templates. Nanotechnology 15(9):1312–1316
116. Chen F, Liu HW, Wang KF, Yu H, Dong S, Chen XY, Jiang XP, Ren ZF, Liu J-M (2005) Synthesis and characterization of $La_{0.825}Sr_{0.175}MnO_3$ nanowires. J Phys Condens Matter 17: L467–L475
117. Hernandez BA, Chang KS, Fisher ER, Dohout PK (2002) Sol–gel template synthesis and characterization of $BaTiO_3$ and $PbTiO_3$ nanotubes. Chem Mater 14:480–482
118. Jang GSH, Bernadette A, Fisher Ellen R, Dorhout PK (2002) Sol–gel template synthesis and characterization of PT, PZ and PZT nanotubes. J Korean Chem Soc 46(3):242–251
119. Luo Y, Szafraniak I, Zakharov ND, Nagarajan V, Steinhart M, Wehrspohn RB, Wendorff JH, Ramesh R, Alexe M (2003) Nanoshell tubes of ferroelectric lead zirconate titanate and barium titanate. Appl Phys Lett 83:440–442
120. Kim J, Yang SA, Choi YC, Han JK, Jeong KO, Yun YJ, Kim DJ, Yang SM, Yoon D, Cheong H, Chang KS, Noh TW, Bu SD (2008) Ferroelectricity in highly ordered arrays of ultra-thin-walled Pb(Zr, Ti)O3 nanotubes composed of nanometer-sized perovskite crystallites. Nano Lett 8(7):1813–1818
121. Xu SY, Shi Y (2009) Power generation from piezoelectric lead zirconate titanate nanotubes. J Phys D: Appl Phys 42(8):085301(1–5)
122. Nourmohammadi A, Bahrevar MA, Hietschold M (2009) Template-based electrophoretic deposition of perovskite PZT nanotubes. J. Alloys Compd. 473:467–472
123. Park TJ, Mao Y, Wong SS (2004) Synthesis and characterization of multiferroic $BiFeO_3$ nanotubes. Chem Commun 23(23):2708–2709
124. Singh S, Krupanidhi SB (2008) Fabrication, structural characterization and formation mechanism of multiferroic $BiFeO_3$ nanotubes. J Nanosci Nanotechnol 8(1):335–339
125. Zhang XY, Lai CW, Zhao X, Wang DY, Dai JY (2005) Synthesis and ferroelectric properties of multiferroic $BiFeO_3$ nanotube arrays. Appl Phys Lett 87:143102(1–3)
126. Xu X, Qian T, Zhang G, Zhang T, Li G, Wang W, Li X (2007) Fabrication and magnetic properties of multiferroic $BiFeO_3$ nanotube arrays. Chem Lett 36(1):112–113
127. Wei J, Xue D, Xu Y (2008) Photoabsorption characterization and magnetic property of multiferroic $BiFeO_3$ nanotubes synthesized by a facile sol–gel template process. Scripta Mater 58:45–48
128. Singh S, Krupanidhi SB (2007) Synthesis and structural characterization of the antiferroelectric lead zirconate nanotubes by pulsed laser deposition. Appl Phys A Mater Sci Process 87(1):27–30
129. Nourmohammadi A, Bahrevar MA, Schulze S, Hietschold M (2008) Electrodeposition of lead zirconate titanate nanotubes. J Mater Sci 43(14):4753–4759
130. Alexe M, Hesse D, Schmidt V, Senz S, Fan HJ, Zacharias M, Gösele U (2006) Ferroelectric nanotubes fabricated using nanowires as positive templates. Appl Phys Lett 89:172907 (1–3)
131. Sousa CT, Lopes AML, Proenca MP, Leitão DC, Correia JG, Araújo JP (2009) Rapid synthesis of ordered manganite nanotubes by microwave irradiation in alumina templates. J. Nanosci Nanotechol. 9(10):6084–6099
132. Levy P, Leyva AG, Troiani HE, Sánchez RD (2003) Nanotubes of rare-earth manganese oxide. Appl Phys Lett 83:5247–5249
133. G. Zhang, J. Chen. Synthesis and Application of $La_{0.59}Ca_{0.41}CoO_3$ Nanotubes. J. Electrochem. Soc. 152(10) (2005) A2069-A2073
134. Tagliazucchi M, Sanchez RD, Troiani HE, Calvo EJ (2006) Synthesis of lanthanum nickelate perovskite nanotubes by using a template-inorganic precursor. Solid State Commun 137:212–215
135. Zhu XH, Evans PR, Byrne D, Schilling A, Douglas C, Pollard RJ, Bowman RM, Gregg JM, Morrison FD, Scott JF (2006) Perovskite lead zirconium titanate nanorings: towards nanoscale ferroelectric "Solenoids"? Appl Phys Lett 89:122913(1–3)

136. Byrne D, Schilling A, Scott JF, Gregg JM (2008) Ordered arrays of lead zirconium titanate nanorings. Nanotechnology 19:165608(1–5)
137. Tian G, Chen D, Yao J, Luo Q, Fan Z, Zeng M, Zhang Z, Dai J, Gao X, Liu J (2017) $BiFeO_3$ nanorings synthesized via AAO template-assisted pulsed laser deposition and ion beam etching. RSC Adv. 7:41210–41216
138. Han H, Ji R, Park YJ, Lee SK, Rhun GL, Alexe M, Nielsch K, Hesse D, Gösele U, Baik S (2009) Wafer-scale arrays of epitaxial ferroelectric nanodiscs and nanorings. Nanotechnology 20:015301(1–6)
139. Wu J, Xue D (2010) In situ Precursor-template route to semi-ordered $NaNbO_3$ nanobelt arrays. Nanoscale Res Lett 6:14(1–8)
140. Tanaka H (2015) Epitaxial growth of oxide films and nanostructures. In: Kuech TF (ed) Handbook of crystal growth thin films & epitaxy, 2nd edn. Elsevier, pp 555–604
141. Yoshimoto M, Sasaki A, Akiba S (2004) Nanoscale epitaxial growth control of oxide thin films by laser molecular beam epitaxy—towards oxide nanoelectronics. Sci Technol Adv Mater 5(4):527–532
142. Schlom DG, Chen LQ, Pan XQ, Schmehl A, Zurbuchen MA (2008) A thin film approach to engineering functionality into oxides. J Am Ceram Soc 91(8):2429–2454
143. Smith HM, Turner AF (1965) Vacuum deposited thin films using a ruby laser. Appl Opt 4:147–148
144. Fukushima J, Kodaira K, Matsushita T (1984) Preparation of ferroelectric PZT films by thermal decomposition of organometallic compounds. J Mater Sci 19:595–598
145. Budd KD, Dey SK, Payne DA (1985) Sol–gel processing of $PbTiO_3$, $PbZrO_3$, PZT and PLZT thin films. Brit. Ceram. Soc. Proc. 36:107–121
146. Schwartz RW (1997) Chemical solution deposition of perovskite thin films. Chem Mater 9 (11):2325–2340
147. Bassiri-Gharb N, Bastanib Y, Bernal A (2014) Chemical solution growth of ferroelectric oxide thin films and nanostructure. Chem Soc Rev 43:2125–2140
148. Zhang Q, Sando D, Nagarajan V (2016) Chemical route derived bismuth ferrite thin films and nanomaterials. J Mater Chem C 4(19):4092–4124
149. Stinton DP, Besmann TM, Lowden RA (1988) Advanced ceramic by chemical vapor deposition techniques. Am Ceram Soc Bull 67:350–355
150. Senateur JP, Dubourdieu C, Weiss F, Rosina M, Abrutis A (2000) Pulsed injection MOCVD of functional electronic oxides. Adv Mater Opt Electron 10(3–5):155–161
151. Schafer P, Waser R (2000) MOCVD of perovskite thin films using an aerosol-assisted liquid delivery system. Adv Mater Opt Electron 10(3–5):169–175
152. Wright PJ, Anthony CJ, Crosbie MLJ, Donohue PP, Lane PA, Todd MA (2004) CVD of oxide materials for thermal imaging—the role of precursor chemistry. J Mater Chem 14:3251–3258
153. Wang HB, Meng GY, Peng DK (2000) Aerosol and plasma assisted chemical vapor deposition process for multicomponent oxide $La_{0.8}Sr_{0.2}MnO_3$ thin film. Thin Solid Films 368:275–278
154. Weiss F, Lindner J, Senateur JP, Dubourdieu C, Galindo V, Audier M, Abrutis A, Rosina M, Fröhlich K, Haessler W, Oswald S, Figueras A, Santiso J (2000) Injection MOCVD: ferroelectric thin films and functional oxide superlattices. Surf Coat Technol 133–134:191–197
155. Singha MK, Yang Y, Takoudisa CG (2009) Synthesis of multifunctional multiferroic materials from metalorganics. Coord Chem Rev 253:2920–2934
156. Basceri C, Streiffer SK, Kingon AI, Waser R (1997) The dielectric response as a function of temperature and film thickness of fiber-textured (Ba, Sr)TiO3 thin films grown by chemical vapor deposition. J Appl Phys 82:2497–2504
157. Kwak BS, Boyd EP, Erbil A (1988) Metalorganic chemical vapor deposition of $PbTiO_3$ thin films. Appl Phys Lett 53:1702–1704

158. Sakashita Y, Segawa H, Tominaga K, Okada M (1993) Dependence of electrical properties on film thickness in $Pb(Zr_xTi_{1-x})O_3$ thin films produced by metalorganic chemical vapor deposition. J Appl Phys 73:7857–7863
159. Yang SY, Zavaliche F, Mohaddes-Ardabili L, Vaithyanathan V, Schlom DG, Lee YJ, Chu YH, Cruz MP, Zhan Q, Zhao T, Ramesh R. Metalorganic chemical vapor deposition of lead-free ferroelectric $BiFeO_3$ films for memory applications. Appl. Phys. Lett. 87 (2005) 102903(1–3)
160. Weiss F, Audier M, Bartasyte A, Bellet D, Girardot C, Jimenez C, Kreisel J, Pignard S, Salaun M, Ternon C (2009) Multifunctional oxide nanostructures by metal-organic chemical vapor deposition (MOCVD). Pure Appl Chem 81(8):1523–1534
161. Eckstein JN, Bozovic I (1995) High-temperature superconducting multilayers and heterostructures grown by atomic layer-by-layer molecular beam epitaxy. Annu Rev Mater Sci 25:679–709
162. Brooks CM, Kourkoutis LF, Heeg T, Schubert J, Muller DA, Schlom DG (2009) Growth of homoepitaxial $SrTiO_3$ thin films by molecular-beam epitaxy. Appl Phys Lett 94:162905(1–3)
163. Lei Q, Golalikhani M, Davidson BA, Liu G, Schlom DG, Qiao Q, Zhu Y, Chandrasena RU, Yang W, Gray AX, Arenholz E, Farrar AK, Tenne DA, Hu M, Guo J, Singh RK, Xi X (2017) Constructing oxide interfaces and heterostructures by atomic layer-by-layer laser molecular beam epitaxy. NPJ Quant Mater 2:10(1–7)
164. Alexe M, Harnagea C, Hesse D, Gösele U (1999) Patterning and switching of nanosize ferroelectric memory cells. Appl Phys Lett 75(12):1793–1795
165. Ahluwalia R, Ng N, Schilling A, McQuaid RG, Evans DM, Gregg JM, Srolovitz DJ, Scott JF (2013) Manipulating ferroelectric domains in nanostructures under electron beams. Phys Rev Lett 111(16):165702(1–5)
166. Hulteen JC, Vanduyne RP (1995) Nanosphere lithography: nanoparticle arrays and surface clusters. J Vac Sci Technol A 13(3):1553–1558
167. Lee W, Han H, Lotnyk A, Schubert MA, Senz S, Alexe M, Hesse D, Baik S, Gösele U (2008) Individually addressable epitaxial ferroelectric nanocapacitor arrays with near Tb $inch^{-2}$ density. Nat Nanotechnol 3:402–407
168. Guo R, Guo Y, Duan H, Li H, Liu H (2017) Synthesis of orthorhombic perovskite-type $ZnSnO_3$ single-crystal nanoplates and their application in energy harvesting. ACS Appl Mater Interfaces 9(9):8271–8279
169. Arney D, Porter B, Greve B, Maggard PA (2008) New molten-salt synthesis and photocatalytic properties of $La_2Ti_2O_7$ particles. J Photochem Photobiol, A 199:230–235
170. Burns SR, Gregg JM, Nagarajan V (2016) Nanostructuring ferroelectrics via focused ion beam methodologies. Adv Funct Mater 26:8367–8381
171. Rémiens D, Liang RH, Soyer C, Deresmes D, Troadec D, Quignon S, Da Costa A, Desfeux R (2010) Analysis of the degradation induced by focused ion Ga^{3+} beam for the realization of piezoelectric nanostructures. J Appl Phys 108:042008
172. Liu G-Y, Xu S, Qian Y (2000) Nanofabrication of self-assembled monolayers using scanning probe lithography. Acc Chem Res 339(7):457–466
173. Piner RD, Zhu J, Xu F, Hong S, Mirkin CA (1999) Dip-pen nanolithography. Science 283:661–663
174. Kushizaki T, Fujiwara K, Hattori AN, Kanki T, Tanaka H (2012) Controlled fabrication of artificial ferromagnetic $(Fe,Mn)_3O_4$ nanowall-wires by a three-dimensional nanotemplate pulsed laser deposition method. Nanotechnology 23(48):485308(1–5)
175. Ji DX, Cai SH, Paudel TR, Sun HY, Zhang CC, Han L, Wei YF, Zang YP, Gu M, Zhang Y, Gao WP, Huyan HX, Guo W, Wu D, Gu ZB, Tsymbal EY, Wang P, Nie YF, Pan XQ (2019) Freestanding crystalline oxide perovskites down to the monolayer limit. Nature 570:87–90

Chapter 4
Perovskite Materials in Biomedical Applications

Jue Gong and Tao Xu

1 Introduction

Biomedical technology plays a vital role in modern medical science and is of notable applications in the fields of cloning [1], biosensor [2], tissue engineering [3–6], artificial organ [7, 8], and regenerative medicine [9, 10]. So far, most of these biomedical applications were realized with the aid of complex bio-functional materials (e.g., hydrogel [6], porous silicon nanoparticles [11], 3D graphene scaffolds [12]), whose synthesis typically require advanced manufacturing for tailored control over the materials' morphology, sizes, structures, chemical, and mechanical properties [13–16], thereby rendering the fabrication processes economically and technically challenging. Moreover, majority of such bio-functional materials are applied in vivo [17, 18], where their biocompatibility, biodegradability, and potential toxicological effects have to be rigorously elucidated via long-term research studies under biophysical, biochemical, and clinical settings before commercialization [5, 16], which greatly hinders their practicality. Therefore, it is imperative to explore novel materials with relatively simpler fabrications for high-performance biomedical applications in vitro, so as to synergistically achieve large-scale accessibility at low costs and small health risks.

In recent years, biomedical applications employing perovskite materials have rapidly advanced due to in-depth understanding of their remarkable thermal, optoelectronic, and magnetic properties, as mentioned in previous chapters. In this chapter, we study current research progress of perovskite-based biomedical applications. Section 2 reviews X-ray detection and imaging achieved by organic–inorganic hybrid perovskites, and Sect. 3 analyzes novel practices of adopting

J. Gong · T. Xu (✉)
Department of Chemistry and Biochemistry, Northern Illinois University, Dekalb, IL 60115, USA
e-mail: txu@niu.edu

N. S. Arul and V. D. Nithya (eds.), *Revolution of Perovskite*, Materials Horizons: From Nature to Nanomaterials, https://doi.org/10.1007/978-981-15-1267-4_4

magnetic perovskite nanoparticles for fast magneto-temperature control and adsorption of bovine serum albumin. Next, we discuss biocompatibility and cytotoxicity profile of hydroxyapatite–$CaTiO_3$ composite through introducing ongoing investigations in Sect. 4. At the end, limitations and future research directions of biomedical perovskites will be concluded in Sect. 5.

2 Organic–Inorganic Hybrid Perovskites for X-Ray Detection and Imaging

2.1 $CH_3NH_3PbI_3$ ($MAPbI_3$) Photodiode for Sensitive X-Ray Detection

X-ray has been known to possess exceptional penetrating ability in objects since its discovery [19], which greatly facilitates diagnostic and therapeutic treatments through various medical techniques, such as computed tomography (CT) [20], radiography [21], and radiotherapy [22].

Previously, X-ray photodetectors with outstanding sensitivities, responsivities, and detectivities were successfully demonstrated on lead halide perovskites due to promising material merits such as high charge carrier mobility–lifetime products ($\mu\tau$, $\sim 10^{-2}$ to $\sim 10^{-4}$ cm^2/V), long carrier diffusion lengths, large material densities, and electron-rich (high atomic number Z) Pb, I, and Br elements that contribute to phenomenal X-ray absorption cross sections [23–29]. Yakunin et al. [25] previously came up with X-ray photodetectors in the form of $MAPbI_3$-based photovoltaic cell, whose architecture is shown in Fig. 1a. Since photovoltaic cell relies on the built-in electrical potential of p–i–n junction upon photoinduced carrier generation [25], they are essentially photodiodes, in which poly(3,4-ethylenedioxythiophene)–poly (styrenesulfonate) (PEDOT:PSS) and [6]-phenyl C61 butyric acid methyl ester (PCBM), respectively, serve as p-type and n-type charge transport layers [30–35]. Such photodiode showed functional response to simulated one-sun AM1.5 illumination (Fig. 1b), corresponding to a 10.4% power conversion efficiency. Most importantly, when applied toward 50-Hz X-ray photons (with peak energy of 75 keV and average energy of $\sim$37 keV) [25], photodiode with $MAPbI_3$ active layer showed sensitive photocurrents (Fig. 1c, red), as compared with a reference silicon diode/YAG:Ce photodetector (Fig. 1c, blue) [25]. Characteristically, average photocurrent obtained from $MAPbI_3$ photodiode increased linearly with the dose rate (as measured in $mGys^{-1}$ in air) of X-ray illumination (Fig. 1d), where greater thickness of $MAPbI_3$ layer led to concomitantly higher sensitivity with a maximum of 25 $\mu C\ mGy_{air}^{-1}\ cm^{-3}$ at 480 nm (Fig. 1d inset). This is due to more absorption of X-ray photons that have much longer penetration depths than visible light in $MAPbI_3$ ($\sim$10 μm at 10^4 eV, $\sim$20 nm at 550 nm) [25, 36, 37], owing to very small

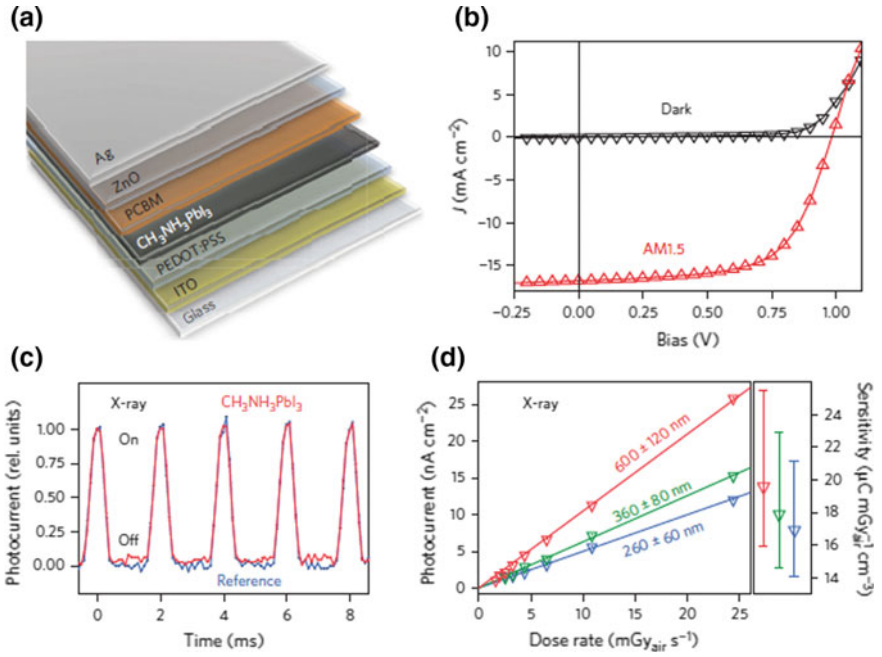

Fig. 1 **a** Device architecture of photovoltaic cell with $MAPbI_3$ as light-harvesting active layer; **b** Photocurrent–voltage curves of $MAPbI_3$ based photovoltaic cell under dark scan (black) and one-sun AM1.5 illumination (red); **c** Unbiased photocurrent response of $MAPbI_3$ photovoltaic cell (red) and silicon/YAG:Ce photodetector (blue) under pulsed X-ray illumination; **d** Photocurrent densities of photovoltaic cells with different thicknesses of $MAPbI_3$ active layers as a function of X-ray dose rate (left), specific sensitivities of photovoltaic cells with corresponding $MAPbI_3$ thicknesses (right). **a**–**d** reprinted from Ref. [25] with permission from Nature Publishing Group. Copyright 2015 Springer Nature

absorption coefficient μ in the range of X-ray energy (10^2–10^5 eV) through the following relationship:

$$\mu \propto \rho Z^4 / AE^3 \tag{1}$$

where ρ, Z, A, and E represent density, atomic number, atomic mass, and X-ray photon energy, respectively.

2.2 *$MAPbI_3$ Photoconductor for X-Ray Imaging with High Responsivity*

To achieve complete conversion of X-ray photons, it demands further increase in $MAPbI_3$ thickness to around 100 μm that corresponds to peak X-ray energy of 75 keV [25]. Such motif was realized by means of $MAPbI_3$-based lateral

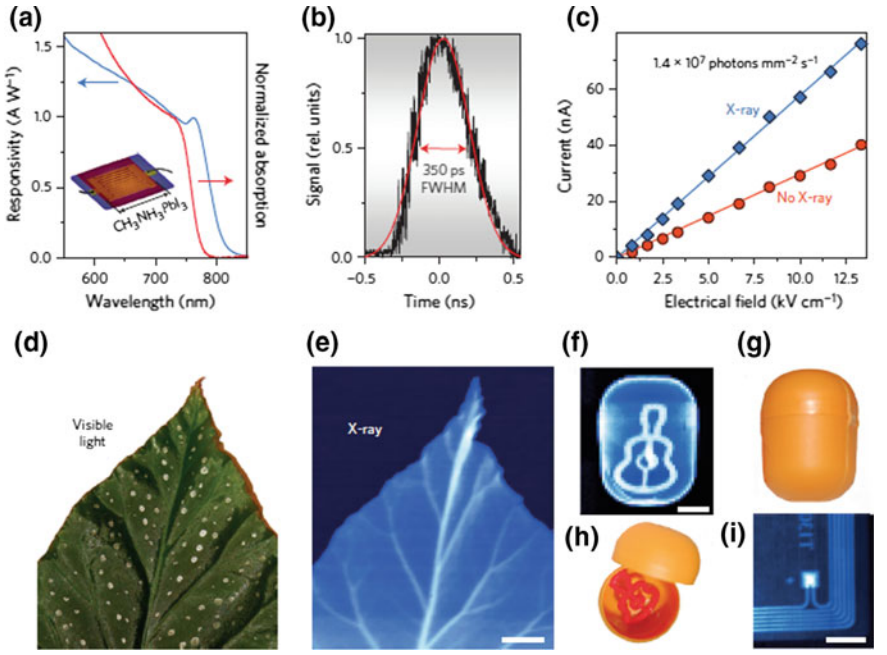

Fig. 2 **a** Responsivity (blue) and optical absorption (red) spectra of $MAPbI_3$-based lateral photoconductor; **b** Photoluminescence peak with experimental signal (black) and Gaussian fit (red), where a 350-ps full width at half maximum is achieved; **c** Current–voltage curves of photoconductor based on $MAPbI_3$ with 60-μm thickness in darkness (orange) and under X-ray illumination (blue); X-ray imaging of a plant leaf where its veins are clearly seen (**d**, **e**) as achieved by the 60-μm $MAPbI_3$ photoconductor, a Kinder Surprise egg showing contained gadget (**f**, **g**, **h**), and an electronic key card showing embedded chip and antenna (**i**). Scale bars in **e**, **f**, and **i**: 10 mm. **a**–**i** reprinted from Ref. [25] with permission from Nature Publishing Group. Copyright 2015 Springer Nature

photoconductor (Fig. 2a, inset) that showed excellent responsivity (R, >1.0 AW^{-1}) at 2-μm $MAPbI_3$ thickness under visible light ranging from 550 to 750 nm (Fig. 2a, blue), closely matching its intrinsic absorption that edged at around 780 nm (Fig. 2a, red), where R is calculated as [38, 39]

$$R = \eta q G / E \tag{2}$$

in which η, q, G, and E stands for incident photon-to-electron conversion efficiency, electron charge, photoconductive gain, and photon energy, respectively. Moreover, a time-domain photoluminescence peak with full width at half maximum (FWHM) of 350 ps was obtained after 10-ps laser excitation (Fig. 2b) [25] indicating fast optoelectronic response of $MAPbI_3$-based photoconductor. Specifically, with X-ray

intensity of 1.4×10^7 photons/mm^2, a photocurrent closed to 60 nA was achieved on a photoconductor with $MAPbI_3$ thickness of 60 μm and electrode distance of around 100 μm at active area of 0.0057 cm^2 and 10.0 kV/cm electric field (Fig. 2c), which corresponds to responsivity of 1.9×10^4 charge carriers/photon [25]. Such outstanding responsivity enabled high-resolution X-ray imaging of a plant leaf (Fig. 2d, e), a Kinder Surprise egg (Fig. 2f–h), and an electronic key card (Fig. 2i).

2.3 $CH_3NH_3PbBr_3$ (MAPbBr$_3$) Single Crystal for Low-Dose X-Ray Imaging with High Sensitivity

One desired property of X-ray imaging is low-dose exposure for patients during medical examinations [26, 40]. Wei et al. [26] previously showed that 2-mm-thick $MAPbBr_3$ single crystal was able to grow on brominated (3-aminopropyl) triethoxysilane-modified silicon substrate with interfacial $–NH_3–Br–$ atomic connection, which consequently permitted X-ray imaging with ultrahigh sensitivity and thus very low detectable dose. To assemble functional photodetector device upon $MAPbBr_3$/silane-modified silicon substrate, Wei and coworkers deposited fullerene (C_{60}) and bathocuproine (BCP) layers with respective thicknesses of 20 nm and 8 nm on top of $MAPbBr_3$ to form electron transport layers, before a 25-nm gold cathode was finally evaporated to finish constructing the device, as shown in Fig. 3a. Noteworthy, the $–NH_3–Br–$ bonded perovskite interfacial layer exhibited a long carrier lifetime of 692 ns (Fig. 3b), thereby signifying that silane molecules did not create outstanding charge quench states that negatively impacted the carrier properties of $MAPbBr_3$ [26]. When compared with 150-μm-thick $MAPbBr_3$ photodetector, a 2-mm-thick counterpart notably achieved a formidable sensitivity of 322 μC Gy_{air}^{-1} cm^{-2} at −1 V bias under 50 keV X-ray radiation, thus allowing much lower detectable dose rate of 0.036 μ$Gy_{air}s^{-1}$ [26]. Most importantly, by fabricating C_{60}/BCP/gold microstructures (200-μm dimension, 400-μm spacings) that electrically connected with external current amplifier through copper wires on such 2-mm $MAPbBr_3$ single-crystal device (see schematics and inset photograph of Fig. 3d), a linear pixel detector array was formed.

Unidirectional scan of a N-shaped object made of copper cylinders (Fig. 3d) resulted in high-quality X-ray image under an ultralow dose rate of 247 n$Gy_{air}s^{-1}$ where protruding shapes due to heavily absorbing copper cylinders are clearly viewable, as shown in Fig. 3e. Significantly, the applied small dose rate is equivalent to a dose–area product (DAP) of 2.5 Gy_{air} cm^2 h^{-1} for a 20-cm-thick human examination area, and therefore is of more than one order of magnitude lower than current operational X-ray dose [26, 41–43].

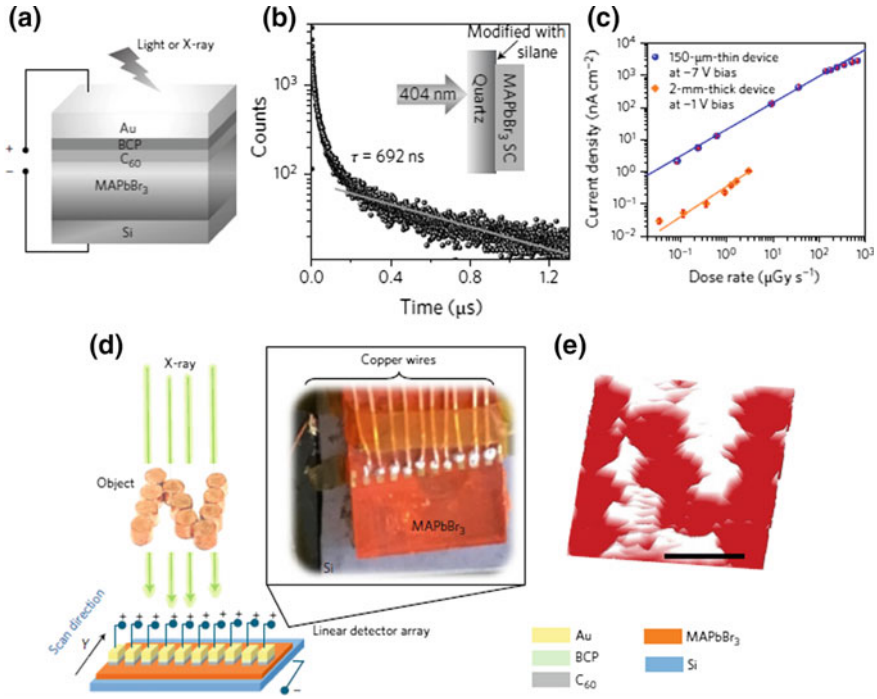

Fig. 3 **a** Device architecture of $MAPbI_3$ single-crystal-based X-ray photodetector; **b** Time-resolved photoluminescence decay of $–NH_3–Br–$ interfaced $MAPbBr_3$ layer upon 404-nm laser excitation. Inset: schematic illustration of quartz, $MAPbBr_3$ single-crystal layers as well as laser direction. **c** Photocurrent density as a function of X-ray dose rate for detectors based on 150-μm (blue) and 2-mm (orange) thickness of $MAPbBr_3$ single crystal. **d** Schematics of X-ray imaging experiment on a N-shaped object comprised of copper cylinders based on the 2-mm single-crystal detector. Inset: photograph of zoomed-in $MAPbBr_3$ single crystal with microscale pixels made of C_{60}/BCP/gold stacking. **e** X-ray image of the N-shaped object shown in **d.** Scale bar: 5 mm. **a**–**e** reproduced from Ref. [26] with permission granted by Nature Publishing Group. Copyright 2017 Springer Nature

2.4 Polycrystalline $MAPbI_3$ Photoconductor with Polymer–Perovskite Interlayers for Large-Area and Low-Dose X-Ray Imaging

Although Wei et al. successfully realized X-ray imaging based on bulk $MAPbBr_3$ single-crystal absorber and predicted a promisingly low DAP on human body, their application is still limited by the small detecting area (5.8 mm × 5.8 mm surface area of $MAPbBr_3$ crystal) [26], which subsequently hindered potential application on commercial X-ray imaging that usually relies on large-area flat panels (50 cm × 50 cm) [40]. Additionally, another vital requisite for demonstrating X-ray imaging on large flat panels is the capability of materials to be prepared on

thin-film transistor (TFT) array matrices, which are required to convey electronic signal onto pixelated detectors for image generation [25, 26, 44–47]. It was not until Kim and coworkers that large-area hybrid perovskite layers were first deposited on TFT array that was made of hydrogen doped amorphous silicon, directly forming a large active area of 25.088 cm × 28.672 cm (Fig. 4a) [40]. Kim et al. novelly constructed photodetector consisting of $MAPbI_3$ polycrystalline layer (MPC) with hundreds of micrometers thickness, as interfaced with polyimide-$MAPbI_3$ ($PIMAPbI_3$) and polyimide-$MAPbBr_3$ ($PIMAPbBr_3$) interlayers between charge collection electrodes, as shown in Fig. 4b.

Significantly, such device was featured with large-size perovskite crystallites (∼20–100 μm) with sharp edges and distinctive crystallographic planes (Fig. 4c–f), thus indicating high crystallinities of perovskite layers and good charge transport properties [48, 49] that are desired for optoelectronic applications including photodetection of X-ray. Also, $PIMAPbI_3$ and $PIMAPbBr_3$ layers were prepared by spin-coated viscous polyimide/*N*-methyl-2-pyrrolidone solution blend [40], which gave rise to good physical contact between polymer–perovskite composites and electrodes (Fig. 4c and f), as indicated by the highly covered composite film with very flat surface (Fig. 4a).

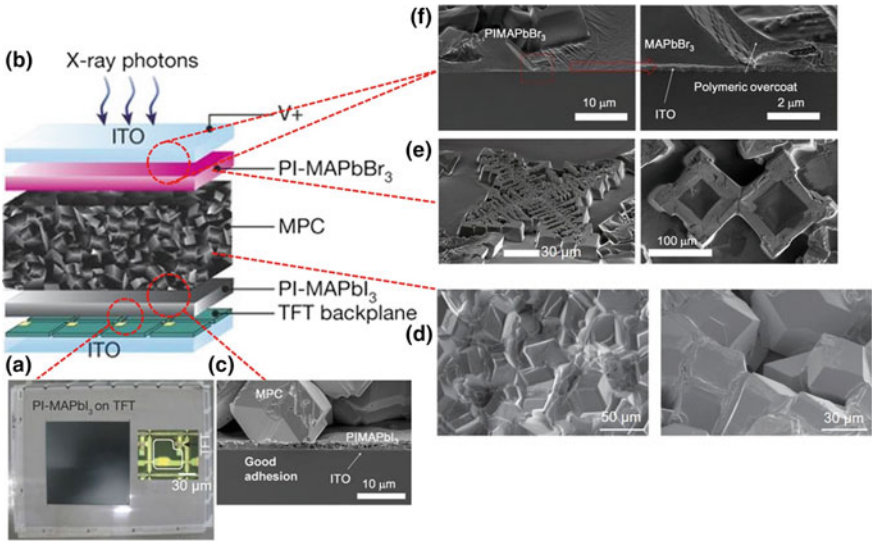

Fig. 4 **a** Photograph of $PIMAPbI_3$ film deposited on TFT array, with inset showing the pixel schematics. **b** Device structure of photodetector, showing different perovskite layers; **c** Scanning electron microscopy (SEM) image showing the crystal morphology of MPC layer and interface with $PIMAPbI_3$, TFT/ITO electrode; **d**, **e** SEM images of MPC and $PIMAPbBr_3$ layers, respectively. Large crystallites with decades of micrometers size are observed; **f** SEM image of interfacial $PIMAPbBr_3$/ITO structure, where polyimide textures are seen. **a**–**f** reproduced from Ref. [40] with permission from Nature Publishing Group. Copyright 2017 Springer Nature

The exceptional physical adhesion should facilitate transport of photocarriers through mitigating interfacial effects.

To characterize the optical and electronic properties of thick MPC layer by comparing with conventionally one-step deposited $MAPbI_3$ film, Kim and coworkers subsequently performed photoluminescence and optical absorption studies on MPC and spin-coated $MAPbI_3$ (adduct $MAPbI_3$) films, as shown in Fig. 5a. It can be clearly seen that MPC film has absorption onset and photoluminescence peak wavelength greater than adduct $MAPbI_3$ counterpart, thus indicating its smaller optical band gap and much greater crystallinity [50–54] in contrast with conventionally synthesized $MAPbI_3$ [55–58]. Time-resolved photoluminescence decay revealed a notably longer carrier lifetime on MPC film in comparison with adduct $MAPbI_3$ counterpart (Fig. 5b), thereby signifying the outstanding optoelectronic properties as suitable for subsequent device application. Furthermore, under ultraviolet laser excitation (337.1 nm), greater magnitude of applied voltage bias resulted in concomitantly shortened charge transit time of both electrons and holes (Fig. 5c and d), which therefore indicated the functional carrier response of MPC layer.

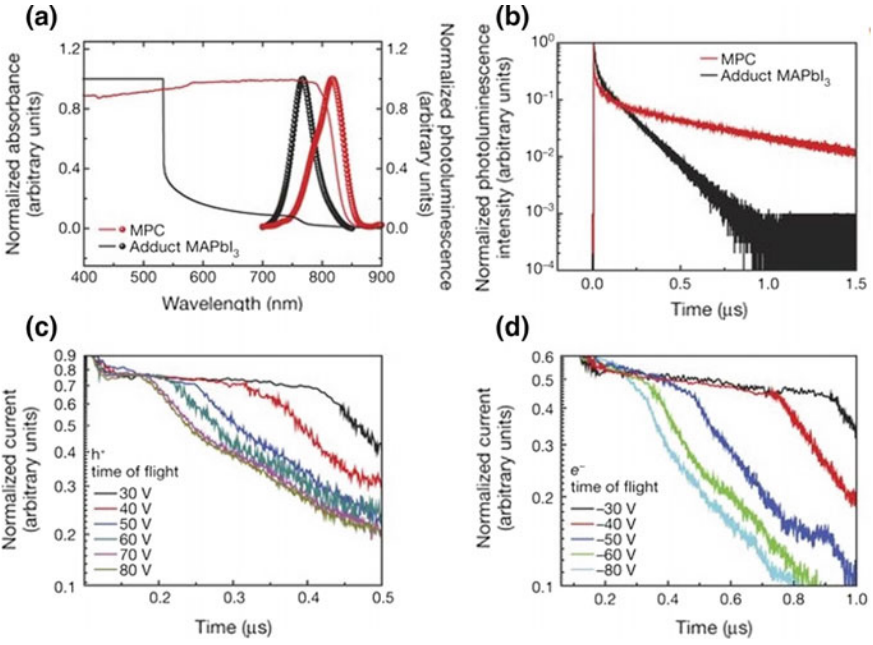

Fig. 5 **a** Static photoluminescence and absorption spectra of MPC (red) and adduct $MAPbI_3$ (black) films; **b** Time-resolved photoluminescence decays of MPC (red) and adduct $MAPbI_3$ (black) films; Time-dependent charge transients of holes **c** and electrons **d**, under externally applied positive and negative voltage biases, respectively. **a–d** reprinted from Ref. [40] with permission from Nature Publishing Group. Copyright 2017 Springer Nature

To fundamentally explore the characteristics of fabricated MPC-based X-ray detector, Kim and coworkers compared the calculated mass attenuation coefficients of $MAPbI_3$ to prototypical materials used in flat-panel X-ray detectors—amorphous selenium (α-Se) [45, 59] as well as cadmium zinc telluride ($Cd_{0.9}Zn_{0.1}Te$) [60], and found out that $MAPbI_3$ owns distinctively better X-ray attenuation ability than α-Se in the energy range of 30–200 keV (Fig. 6a), as due to *K*-edge absorption of high-*Z* I and Pb atoms, respectively, at around 33 and 88 keV [40].

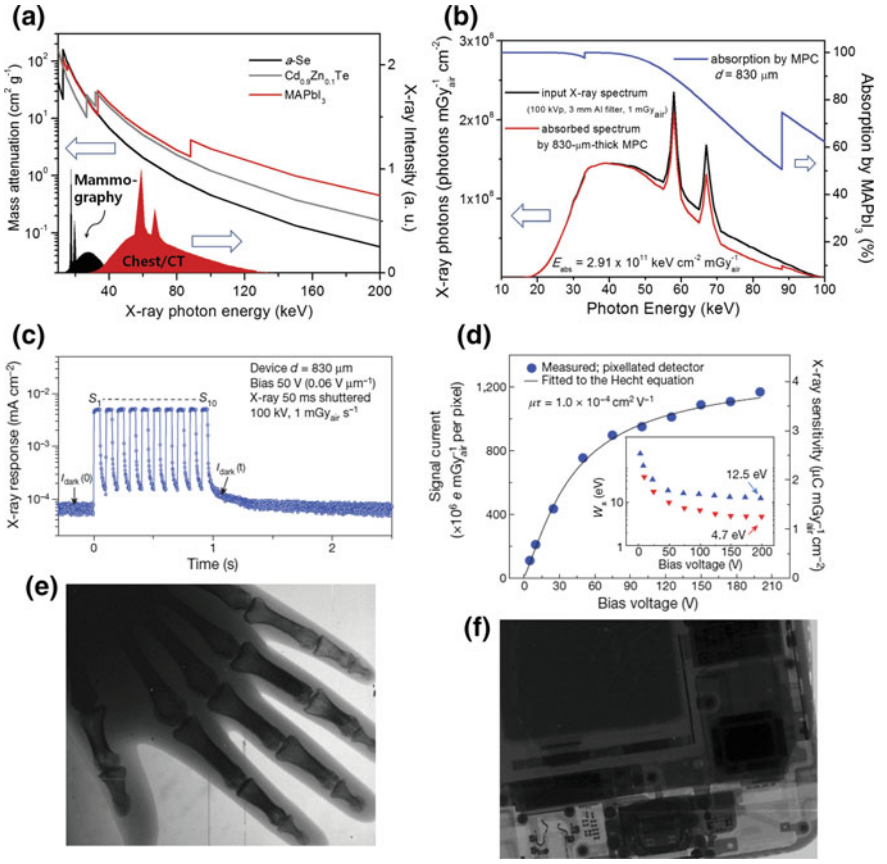

Fig. 6 **a** Mass attenuation coefficients of α-Se (black), $Cd_{0.9}Zn_{0.1}Te$ (gray), $MAPbI_3$ (red) and medical X-ray spectra; **b** X-ray absorption spectrum (red) and percentage (blue) by $MAPbI_3$, under 100-kV peak voltage tungsten-source X-ray spectrum (black); **c** Photocurrent response of MPC-based detector under X-ray irradiation with 50-ms pulse widths; **d** Characterization of currents collected at pixel detector for MPC device. Inset: Voltage bias-dependent electron–hole pair separation energy ($W_{\pm}$). X-ray images of a hand (**e**) and a smartphone (**f**) with respective dose exposure of 25 μGy_{air} and 10 μGy_{air}. **a**–**f** reproduced from Ref. [40] with permission granted by Nature Publishing Group. Copyright 2017 Springer Nature

Such large X-ray attenuation by heavily absorbing $MAPbI_3$ should accordingly facilitate medical application of X-ray in mammography and chest/CT, which have average populations of X-ray photons centered at around 30 keV and 60 keV (Fig. 6a), respectively. The stunning X-ray absorption capability by $MAPbI_3$ was further quantitatively evaluated by its X-ray absorption spectrum (Fig. 6b, red) under a tungsten radiation excited at peak voltage of 100 kV and attenuated by a 3-mm aluminum filter [40], where an 830-μm-thick $MAPbI_3$ layer achieved >80% absorption of X-ray ranging from 20 keV to around 65 keV (Fig. 6b, blue). Characteristically, the applied tungsten-source radiation was equivalent to dose rate ranging from 1 to 5 $mGy_{air}s^{-1}$ and total dose as 10–200 μGy_{air} [40]. With a dose rate of 1 $mGy_{air}s^{-1}$ and voltage bias of 50 V, this 830-μm MPC-based detector exhibited fast rise/fall of photocurrent under X-ray irradiation with 50-ms pulse width [40], as shown in Fig. 6c. Since the ultimate purpose of X-ray detector is to realize medical imaging, photocurrents were probed at pixelated detector, in which current magnitude (as measured in e mGy_{air}^{-1} $pixel^{-1}$) and device sensitivity monotonically increased with positive bias voltage (Fig. 6d) because of correspondingly enhanced charge extraction ability. While by fitting with Hecht equation [40, 61],

$$Q = Q_0 \mu\tau V d^{-2}[1 - e^{(-d^2/\mu\tau V)}] \tag{3}$$

$\mu\tau$ was obtained as 1.0×10^{-4} cm^2 V^{-1}, in which Q, Q_0, V, and d, respectively, stand for total charge, asymptotically collected charge, voltage bias, and thickness of detector. Due to extra impedance incurred with TFT pixel arrays, the energy required to separate electron–hole pairs ($W_{\pm}$) for pixelated detector is corresponding greater than TFT-free diode setting (Fig. 6d inset). Eventually, at voltage bias of 50 V (referring to $\sim$2.5 μC mGy_{air}^{-1} cm^{-2} and $\sim 8\times10^8$ e mGy_{air}^{-1} $pixel^{-1}$), a high-resolution X-ray image was acquired on a hand with clearly outlined phalanges (Fig. 6e) with total dose exposure of only 25 μGy_{air} under 5 $mGy_{air}s^{-1}$ for 5 ms. Likewise, X-ray image of a smartphone (Fig. 6f) with just 10-μGy_{air} dose exposure was acquired at dose rate of 1 $mGy_{air}s^{-1}$ for 10 ms.

3 Magnetic Perovskite Nanoparticles for In Vitro Applications

3.1 *$La_{0.7}Sr_{0.3}Mn_{0.98}Ti_{0.02}O_3$ Perovskite Nanoparticles with Magneto-Temperature Properties*

Due to the fact that most transition metals have unpair d-orbital electrons, oxide perovskites based on transition metals usually have prominent magnetic properties [62–69] and have been exploited in various applications, such as ferroelectrics [70, 71], ferromagnets [72], multiferroics [73, 74], and topological insulator [75].

Soleymani et al. [76] previously synthesized mixed-cation perovskite oxide—$La_{0.7}Sr_{0.3}Mn_{0.98}Ti_{0.02}O_3$ in the form of nanoparticles, via reaction between cetyltrimethylammonium bromide (CTAB)/*n*-butanol functionalized La/Sr/Mn/Ti nitrate salts as suspended in *n*-hexane (Mic-A), and CTAB/*n*-butanol functionalized

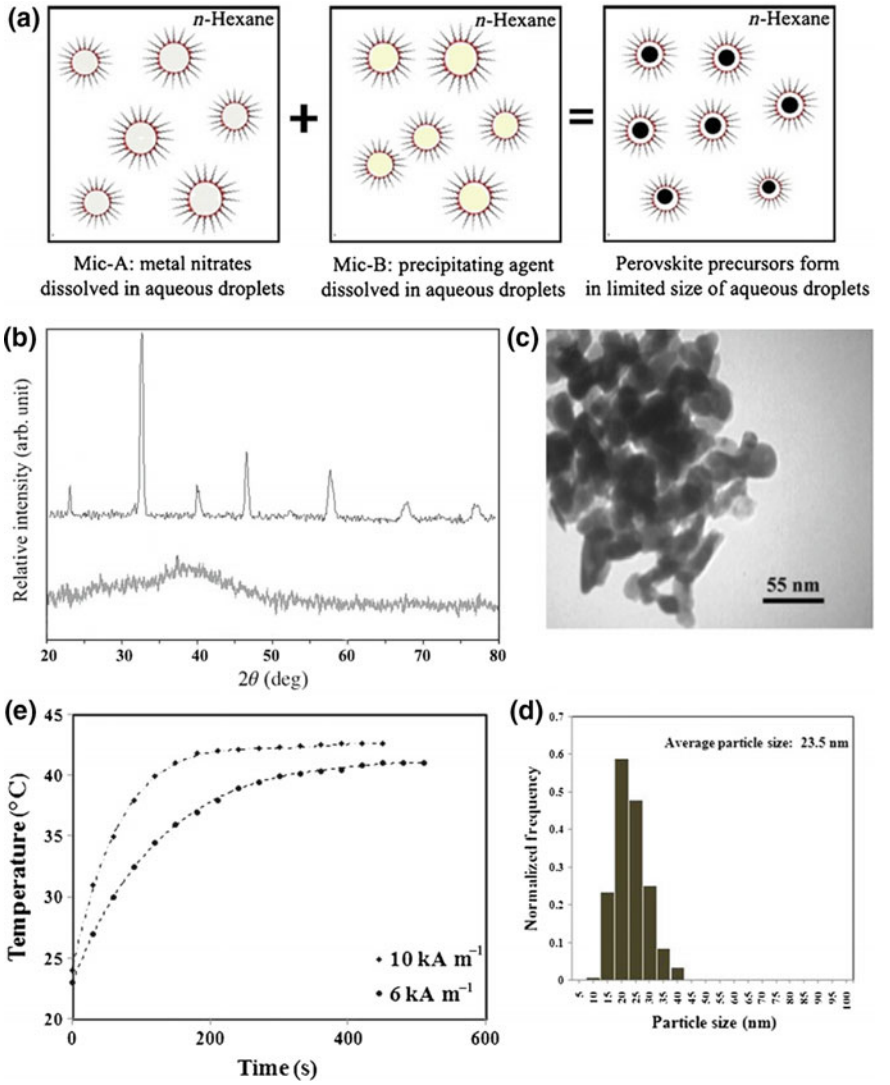

Fig. 7 **a** Schematic representation of synthesizing $La_{0.7}Sr_{0.3}Mn_{0.98}Ti_{0.02}O_3$ precursor; **b** X-ray diffraction patterns of crystalline $La_{0.7}Sr_{0.3}Mn_{0.98}Ti_{0.02}O_3$ (top) and amorphous precursor before calcination (bottom); **c** TEM image of $La_{0.7}Sr_{0.3}Mn_{0.98}Ti_{0.02}O_3$ nanoparticles; **d** Size distribution of $La_{0.7}Sr_{0.3}Mn_{0.98}Ti_{0.02}O_3$ nanoparticles; **e** Temperature rising curves under magnetic fields of 10 and 6 kA/m. **a**–**e** reprinted from Ref. [76] with permission from Springer Nature. Copyright 2016 Indian Academy of Sciences

ammonium oxalate in *n*-hexane (Mic-B), as shown in Fig. 7a. The as-formed precipitate upon mixture of Mic-A and Mic-B had amorphous nature, as confirmed by X-ray diffraction pattern (Fig. 7b bottom), was eventually calcined at 700 °C to obtain $La_{0.7}Sr_{0.3}Mn_{0.98}Ti_{0.02}O_3$ that was crystalline, as evidenced by the distinctive crystallographic orientations (Fig. 7a top). Furthermore, the nanoparticle format of $La_{0.7}Sr_{0.3}Mn_{0.98}Ti_{0.02}O_3$ was morphologically characterized by transmission electron microscopy (TEM) image, as shown in Fig. 7c, where the average size of perovskite nanoparticles was determined to be 23.5 nm (Fig. 7d) and closely corroborated with the calculated average size (20.1 nm) through Scherrer equation [76–79]:

$$D_{hkl} = k\lambda / b\cos\theta \tag{4}$$

where D_{hkl} is the average crystalline size; k is the shape factor (0.9); λ is the wavelength of X-ray (1.54 Å for $Cu_{K\alpha}$ radiation), and b, θ are, respectively, the FWHM, angle position for the most intensive diffraction peak ($\sim 33°$ for the present work). Most importantly, under magnetic fields, the as-synthesized $La_{0.7}Sr_{0.3}Mn_{0.98}Ti_{0.02}O_3$ nanoparticles exhibited kinetic rise in temperature (Fig. 7e), where the threshold temperature was reached as heat generation equilibrated with the loss. The responsive rise in temperature under externally applied magnetic field, along with stabilized threshold temperature thus indicate the valuable potential of perovskite $La_{0.7}Sr_{0.3}Mn_{0.98}Ti_{0.02}O_3$ as heating mediators for hyperthermia-based cancer treatment.

3.2 *Perovskite La_2NiMnO_6 Nanoparticles for Adsorption of Bovine Serum Albumin (BSA)*

Many manganite perovskites (e.g., Ca-doped $BiMnO_3$ and $LaMnO_3$) demonstrate remarkable magnetic properties [80, 81]. When fabricated in the form of nanoparticles, the magnetic nature of manganite perovskites potentially allows useful applications in sensors [82], environmental remediation [83], drug delivery [84], magnetic resonance imaging [85, 86], immunoassay [87], and sorbents [88], as already achieved in Fe_3O_4–metal–organic framework (MOF) core–shell structures [89] owing to their high porosity and large surface areas. Wu et al. [90] previously synthesized double-perovskite La_2NiMnO_6 (crystal structure shown in Fig. 8a) via co-precipitation of constituent metal ions, as followed by high-temperature sintering. The crystalline structures of as-prepared La_2NiMnO_6 after sintering at different temperatures were confirmed by X-ray diffraction patterns as shown in Fig. 8b, while the spherical shapes of nanoparticles sintered at 750 °C were verified by high-resolution TEM (HRTEM) image shown in Fig. 8c. On average, the size of La_2NiMnO_6 nanoparticles reached ~ 37 nm over the annealing

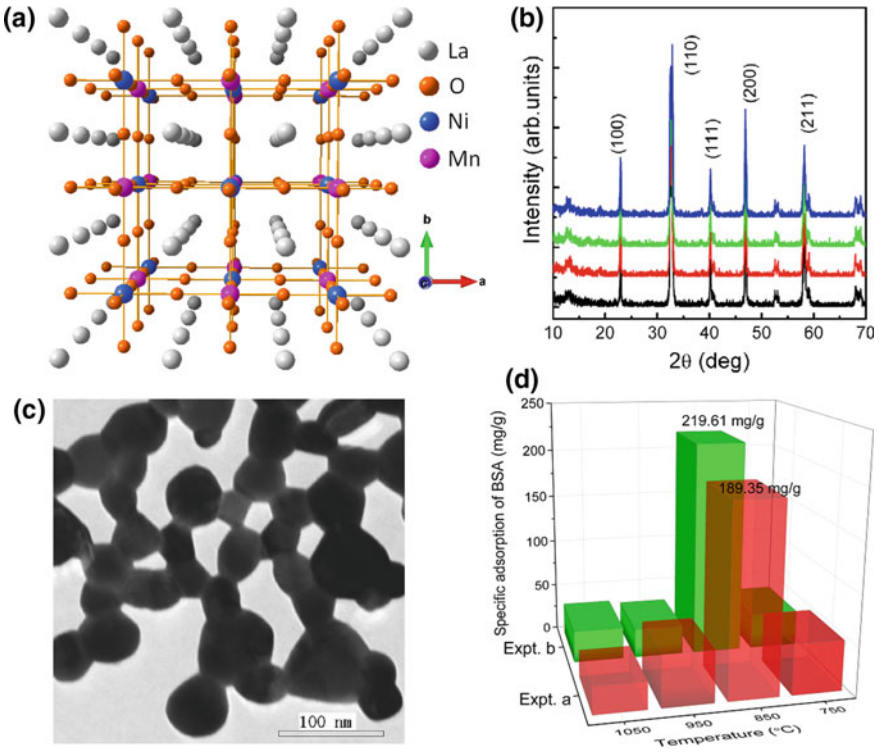

Fig. 8 **a** Crystal structure of double-perovskite La_2NiMnO_6 from (00l) direction; **b** X-ray diffraction patterns of La_2NiMnO_6 sintered at 1050 °C (blue), 950 °C (green), 850 °C (red) and 750 °C (black) for 2 h; **c** HRTEM image of La_2NiMnO_6 nanoparticles sintered at 750 °C for 2 h; **b**, **c** reprinted from Ref. [90] with permission granted by Springer. Copyright 2013 Wu et al.; licensee Springer **d** Three-dimensional bar graph showing the specific adsorption of BSA on La_2NiMnO_6 nanoparticles annealed at different temperatures over two experiments, with data taken from Ref. [90]

temperatures at 750, 850, 950, and 1050 °C [90]. Wu and coworkers subsequently performed adsorption studies of BSA (a globular protein valuable in medical research) as characterized by ultraviolet spectra at 280 nm with two groups of experiments, and found that all the nanoparticle samples had astonishing adsorptive capacities for BSA protein (Fig. 8d), where La_2NiMnO_6 nanoparticles annealed at 850 °C achieved ~200 mg/g specific adsorption of BSA across two experimental sets. This research work identifies La_2NiMnO_6 nanoparticles as promising adsorbents for extracting BSA and is of great significance in relevant medical applications (e.g., probe for cancer cell targeting, biosensors [91, 92]).

4 In Vitro Biocompatibility of ($Ca_{10}(PO_4)_6(OH)_2$–$CaTiO_3$) Composites in Cellular Cultures

Perovskite calcium titanate ($CaTiO_3$) has been known to play a major role in promoting the growth of hydroxyapatite ($Ca_{10}(PO_4)_6(OH)_2$, HA) (main constituent of bones) as supporting substrate [93–96]. Also, $CaTiO_3$ favorably facilitates osseointegration and osteoblast adhesion between human body and implanted biomaterials [97]. Most of all, $CaTiO_3$ has notable electronic and mechanical properties, such as electrical conductivity [98], corrosion resistance [99], ferroelectricity [100], high bonding strength and stability [101], thus enabling valuable biomedical applications in biosensors [102], orthopedics [95], and maxillofacial reconstruction [103]. Although $CaTiO_3$ has demonstrated such extensive uses in conjunction with bones, the detailed biocompatible and toxicological profiles of the composite materials await insightful study.

Dubey et al. [98] previously conducted in vitro cell proliferation experiments to show that $SaOS_2$ human osteoblast cells (Fig. 9) and L929 mouse fibroblast cells (Fig. 10) can robustly culture on pristine HA (denoted H_1C_0), 60 wt% HA–40 wt%

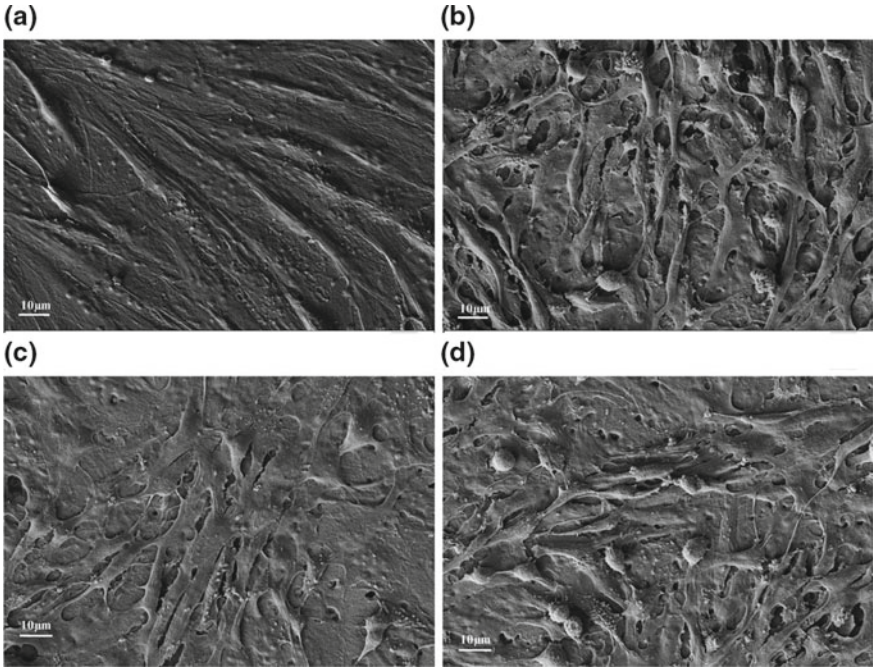

Fig. 9 SEM images of $SaOS_2$ human osteoblast cells cultured on **a** polymer disc substrate; **b** H_6C_4; **c** H_4C_6; **d** H_2C_8 composites. **a**–**d** reprinted from Ref. [98] with permission granted by John Wiley and Sons. Copyright 2010 Wiley Periodicals, Inc.

$CaTiO_3$ (H_6C_4), 40 wt% HA–60 wt% $CaTiO_3$(H_4C_6), and 20 wt% HA–80 wt% $CaTiO_3$ (H_2C_8) composites. It can be clearly seen that dense bridge-like cytoplasmic connections were formed among cells (Fig. 10), with the studied cells firmly adhered on underlying composite substrates via flattened structures and extended filopodia (Fig. 9), thereby indicating biocompatibility of the synthesized HA–$CaTiO_3$ composites [98].

Furthermore, by utilizing 3(4,5-dimethylthiazol-2-yl)-2,5-diphenyltetrazolium bromide (MTT) assay, Dubey and coworkers suggested that the population sizes of metabolically active $SaOS_2$ (Fig. 11a) and L929 (Fig. 11b) cells enlarged after incubation on HA–$CaTiO_3$ composites, as imparted by the increased mean optical density from the MTT assay plate reader over three experiments for each incubation period, as shown in Fig. 11. Such results indicated cytotoxicity of HA–$CaTiO_3$ composites did not adversely affect the cell viability, or at most, negligible on the studied cell subjects.

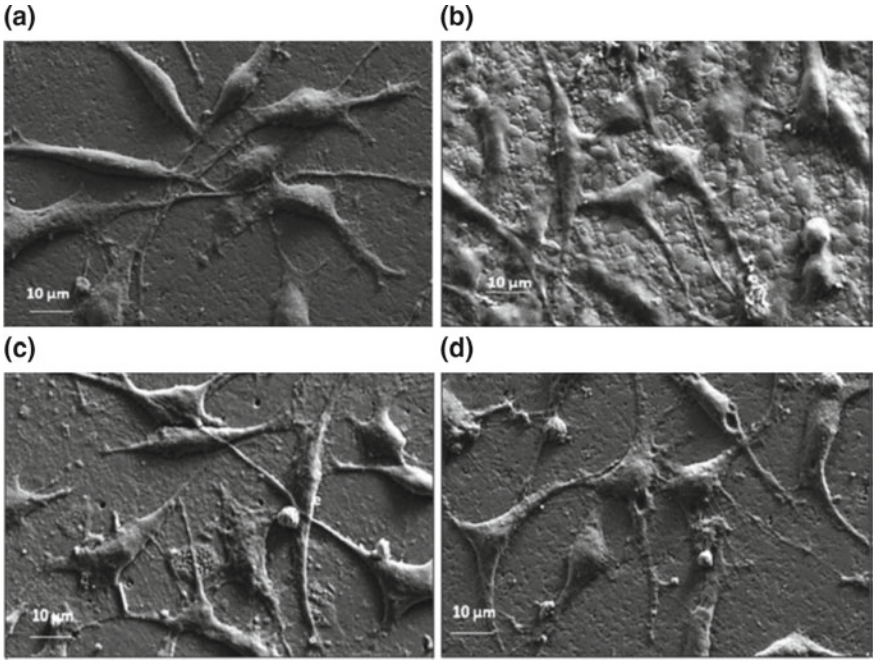

Fig. 10 SEM images of L929 mouse fibroblast cells proliferated on **a** H_1C_0; **b** H_6C_4; **c** H_4C_6; **d** H_2C_8 composite substrates. **a**–**d** reprinted from Ref. [98] with permission granted by John Wiley and Sons. Copyright 2010 Wiley Periodicals, Inc.

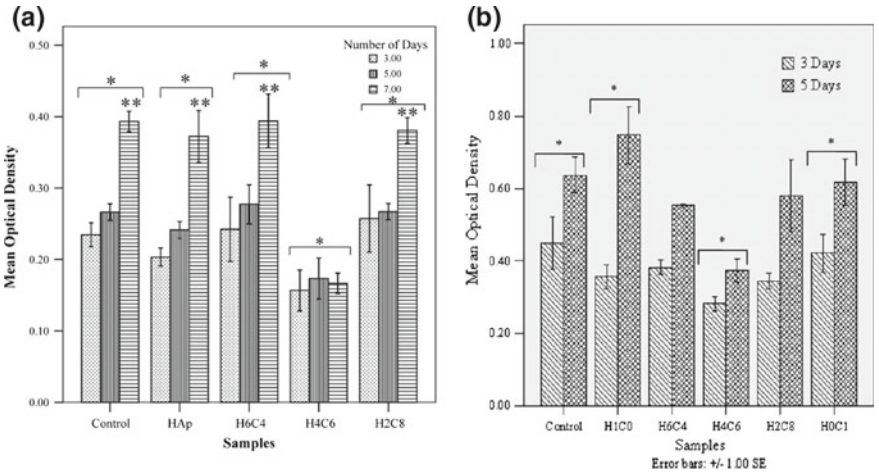

Fig. 11 Statistically summary of viable cell populations for human $SaOS_2$ (**a**) and mouse L929 (**b**) after incubation on different substrates for various periods. "*" indicates significant difference between average optical densities across incubation periods at $p < 0.05$, and "**" refers to statistically significant difference of 7 days incubation as compared to samples at 3 and 5 days at $p < 0.05$. **a**, **b** reprinted from Ref. [98] with permission from John Wiley and Sons. Copyright 2010 Wiley Periodicals, Inc.

5 Concluding Remarks

In this chapter, we systematically summarized the ongoing research progress that harnessed perovskites in biomedical applications. Because of the extraordinary solution processability, desirable crystallization kinetics, suitable optical band gaps, and high-Z Pb/I/Br heavy elements, $MAPbX_3$ perovskites ($X = I^-$, Br^-) have achieved successful demonstrations of X-ray detection and imaging. However, it demands stabilization of perovskite absorbers to further mature the relevant technologies, where we believe switching to Cs^+-cationed or MA^+/Cs^+ alloyed motifs not only widens the band gaps for suppressed dark currents, but also significantly results in enhanced structural stabilities [104, 105] of perovskite materials. In addition, previous studies showed that two-dimensional (2D) lead halide perovskites enabled out-of-plane orientations of crystals on underlying substrates [106, 107], which may consequently lead to highly directional transport of X-ray-induced photocarriers. Based on this perspective, future research direction for realizing X-ray detectors and imagers with high sensitivities and responsivities should focus on fabricating large-area and thick 2D perovskite absorbers on thin-film transistor arrays through compatible printing (polycrystalline) and self-assembled (monocrystalline) methods.

Although Soleymani and coworkers provided clear evidence of magneto-temperature response on $La_{0.7}Sr_{0.3}Mn_{0.98}Ti_{0.02}O_3$ perovskite nanoparticles, the detailed material phases still have not been unambiguously elucidated due to inaccurate relative compositions of metal cations (the oxidation state of Mn is

calculated to be 3.22/0.98 based on +3, +2, +4, and −2 oxidation states of La, Sr, Ti, and O, respectively, indicating the existence of segregated crystal phase). Therefore, insightful structural analysis of material is needed for confirmation of the magnetically thermally active phase. In case of perovskite La_2NiMnO_6 nanoparticles, their ability to desorb BSA protein molecules has not been studied, which is required to fully comprehend the binding/detachment dynamics of enzyme reactions. As $CaTiO_3$-based composites were proven to have promising biocompatibility and cytotoxicity, the future research direction of these composite materials is to further understand their structure–property relationships under more complicated chemical environments with variations in temperature, pH, and pressure.

References

1. Liu Z, Cai Y, Wang Y, Nie Y, Zhang C, Xu Y (2018) Cloning of macaque monkeys by somatic cell nuclear transfer. Cell 172:881–887
2. Rodriguez GA, Hu S, Weiss SM (2015) Porous silicon ring resonator for compact, high sensitivity biosensing applications. Opt Express 23:7111–7119
3. Gershlak JR, Hernandez S, Fontana G, Perreault LR, Hansen KJ, Larson SA (2017) Crossing kingdoms: using decellularized plants as perfusable tissue engineering scaffolds. Biomaterials 125:13–22
4. Munarin F, Guerreiro SG, Grellier MA, Tanzi MC, Barbosa MA, Petrini P, Granja PL (2011) Pectin-based injectable biomaterials for bone tissue engineering. Biomacromolecules 12:568–577
5. O'Brien FJ (2011) Biomaterials & scaffolds for tissue engineering. Mater Today 14:88–95
6. Amini AR, Laurencin CT, Nukavarapu SP (2012) Bone Tissue Engineering: Recent Advances and Challenges. Crit Rev Biomed Eng 40:363–408
7. Cohrs NH, Petrou A, Loepfe M, Yliruka M, Schumacher CM, Kohll AX (2017) A soft total artificial heart-first concept evaluation on a hybrid mock circulation. Artif Organs 41:948–958
8. Ott HC, Matthiesen TS, Goh SK, Black LD, Kren SM, Netoff TI et al (2008) Perfusion-decellularized matrix: using nature's platform to engineer a bioartificial heart. Nat Med 14:213–221
9. Brown TE, Anseth KS (2017) Spatiotemporal hydrogel biomaterials for regenerative medicine. Chem Soc Rev 46:6532–6552
10. Zhao Y, Feric NT, Thavandiran N, Nunes SS, Radisic M (2014) The role of tissue engineering and biomaterials in cardiac regenerative medicine. Can J Cardiol 30:1307–1322
11. Martinez JO, Chiappini C, Ziemys A, Faust AM, Kojic M, Liu X, Ferrari M, Tasciotti E (2013) Engineering multi-stage nanovectors for controlled degradation and tunable release kinetics. Biomaterials 34:8469–8477
12. Lalwani G, D'agati M, Gopalan A, Rao M, Schneller J, Sitharaman B (2017) Three-dimensional microporous graphene scaffolds for tissue engineering. J Biomed Mater Res A 105:73–83
13. Tasciotti E, Cabrera FJ, Evangelopoulos M, Martinez JO, Thekkedath UR, Kloc M et al (2016) The emerging role of nanotechnology in cell and organ transplantation. Transplantation 100:1629–1638
14. Martinez JO, Brown BS, Quattrocchi N, Evangelopoulos M, Ferrari M, Tasciotti E (2012) Multifunctional to multistage delivery systems: the evolution of nanoparticles for biomedical applications. Chin Sci Bull 57:3961–3971

15. Tasciotti E, Liu X, Bhavane R, Plant K, Leonard AD, Price BK (2008) Mesoporous silicon particles as a multistage delivery system for imaging and therapeutic applications. Nat. Nanotech. 3:151–157
16. Lee Kenry, Loh WC, Lim CT (2018) When stem cells meet graphene: opportunities and challenges in regenerative medicine. Biomaterials 155:236–250
17. Shahbazi MA, Hamidi M, Makila EM, Zhang H, Almeida PV, Kaasalainen M (2013) The mechanisms of surface chemistry effects of mesoporous silicon nanoparticles on immunotoxicity and biocompatibility. Biomaterials 34:7776–7789
18. Li C, Yang D, Ma P, Chen Y, Wu Y, Hou Z (2013) Multifunctional upconversion mesoporous silica nanostructures for dual modal imaging and in vivo drug delivery. Small 9:4150–4159
19. Allen HS (1931) X-Rays and their Applications. Nature 127:356–358
20. Dierolf M, Menzel A, Thibault P, Schneider P, Kewish CM, Wepf R (2010) Ptychographic X-ray computed tomography at the nanoscale. Nature 467:436–439
21. Guillard F, Marks B, Einav I (2017) Dynamic X-ray radiography reveals particle size and shape orientation fields during granular flow. Sci Rep 7:8155
22. Tamura M, Ito H, Matsui H (2017) Radiotherapy for cancer using X-ray fluorescence emitted from iodine. Sci Rep 7:43667
23. Shrestha S, Fischer R, Matt GJ, Feldner P, Michel T, Osvet A, Levchuk I, Merle B, Golkar S, Chen H, Tedde SF, Schmidt O, Hock R, Ruhrig M, Goken M, Heiss W, Anton G, Brabec CJ (2017) High-performance direct conversion X-ray detectors based on sintered hybrid lead triiodide perovskite wafers. Nat Photon 11:436–440
24. Wei H, Fang Y, Mulligan P, Chuirazzi W, Fang HH, Wang C (2016) Sensitive X-ray detectors made of methylammonium lead tribromide perovskite single crystals. Nat Photon 10:333–339
25. Yakunin S, Sytnyk M, Kriegner D, Shrestha S, Richter M, Matt GJ, Azimi H, Brabec CJ, Stangl J, Kovalenko MV, Heiss W (2015) Detection of X-ray photons by solution-processed lead halide perovskites. Nat Photon 9:444–449
26. Wei W, Zhang Y, Xu Q, Wei H, Fang Y, Wang Q (2017) Monolithic integration of hybrid perovskite single crystals with heterogeneous substrate for highly sensitive X-ray imaging. Nat Photon 11:315–321
27. Chen Y, Yi HT, Wu X, Haroldson R, Gartstein YN, Rodionov YI, Tikhonov KS, Zakhidov A, Zhu XY, Podzorov V (2016) Extended carrier lifetimes and diffusion in hybrid perovskites revealed by Hall effect and photoconductivity measurements. Nat Commun 7:12253
28. Stranks SD, Eperon GE, Grancini G, Menelaou C, Alcocer MJP, Leijtens T (2013) Electron–hole diffusion lengths exceeding 1 micrometer in an organometal trihalide perovskite absorber. Science 342:341–344
29. Xing G, Mathews N, Sun S, Lim SS, Lam YM, Gratzel M (2013) Long-range balanced electron- and hole-transport lengths in organic–inorganic $CH_3NH_3PbI_3$. Science 342: 344–347
30. You J, Meng L, Song TB, Guo TF, Yang YM, Chang WH (2016) Improved air stability of perovskite solar cells via solution-processed metal oxide transport layers. Nat Nanotech 11:75–81
31. Yang WS, Noh JH, Jeon NJ, Kim YC, Ryu S, Seo J, Seok SI (2015) High-performance photovoltaic perovskite layers fabricated through intramolecular exchange. Science 348:1234–1237
32. Gong J, Guo P, Benjamin SE, Van Patten PG, Schaller RD, Xu T (2018) Cation engineering on lead iodide perovskites for stable and high-performance photovoltaic applications. J Energy Chem 27:1017–1039
33. Huang D, Goh T, Kong J, Zheng Y, Zhao S, Xu Z, Taylor AD (2017) Perovskite solar cells with a DMSO-treated PEDOT:PSS hole transport layer exhibit higher photovoltaic performance and enhanced durability. Nanoscale 9:4236–4243

34. Hu L, Sun K, Wang M, Chen W, Yang B, Fu J (2017) Inverted planar perovskite solar cells with a high fill factor and negligible hysteresis by the dual effect of NaCl-doped PEDOT: PSS. ACS Appl Mater Interfaces 9:43902–43909
35. Yu JC, Hong JA, Jung ED, Kim DB, Baek SM, Lee S, Cho S, Park SS, Choi KJ, Song MH (2018) Highly efficient and stable inverted perovskite solar cell employing PEDOT:GO composite layer as a hole transport layer. Sci Rep 8:1070
36. Jiang Q, Rebollar D, Gong J, Piacentino EL, Zheng C, Xu T (2015) Pseudohalide-induced moisture tolerance in perovskite $CH_3NH_3Pb(SCN)_2I$ thin films. Angew Chem Int Edition 54:7617–7620
37. Kazim S, Nazeeruddin MK, Gratzel M, Ahmad S (2014) Perovskite as light harvester: a game changer in photovoltaics. Angew Chem Int Ed 53:2812–2824
38. Jin Z, Wang J (2014) Flexible high-performance ultraviolet photoconductor with zinc oxide nanorods and 8-hydroxyquinoline. J Mater Chem C 2:1966–1970
39. Sze SM, Ng KK (2006) *Physics of semiconductor devices*, 2nd edn. Wiley, New York, pp 667–671
40. Kim YC, Kim KH, Son DY, Jeong DN, Seo JY, Choi YS et al (2017) Printatble organometallic perovskite enables large-area, low-dose X-ray imaging. Nature 550:87–91
41. Nof E, Lane C, Cazalas M, Cuchet-Soubelet E, Michaud GF, John RM (2015) Reducing radiation exposure in the electrophysiology laboratory: it is more than just fluoroscopy times! Pacing Clin Electrophysiol 38:136–145
42. Davies AG, Cowen AR, Kengyelics SM, Moore J, Sivananthan MU (2007) Do flat detector cardiac X-ray systems convey advantages over image-intensifier-based systems? Study comparing X-ray dose and image quality. Eur Radiol 17:1787–1794
43. Viggiano A, De Potter TJR, Celentano E, Stefan L, Peytchev P, Geelen P (2013) Exposure reduction by optimization of the imaging toolchain in pulmonary vein isolation. Eur Heart J 34:P2344
44. Kasap S, Frey JB, Belev G, Tousignant O, Mani H, Greenspan J et al (2011) Amorphous and polycrystalline photoconductors for direct conversion flat panel X-ray image sensors. Sensors 11:5112–5157
45. Zhao W, Rowlands JA (1995) X-ray imaging using amorphous selenium: feasibility of a flat panel self-scanned detector for digital radiology. Med Phys 22:1595–1604
46. Kasap SO (2002) Rowlands JA (2002) Direct-conversion flat-panel X-ray image sensors for digital radiography. Proc IEEE 90:591–604
47. Moy JP (2000) Recent developments in X-ray imaging detectors. Nucl Instrum Methods Phys Res 442:26–37
48. Huang J, Shao Y, Dong Q (2015) Organometal trihalide perovskite single crystals: a next wave of materials for 25% efficiency photovoltaics and applications beyond? J Phys Chem Lett 6:3218–3227
49. Nie W, Tsai H, Asadpour R, Blancon JC, Neukirch AJ, Gupta G (2015) High-efficiency solution-processed perovskite solar cells with millimeter-scale grains. Science 347:522–525
50. Saidaminov MI, Abdelhady AL, Murali B, Alarousu E, Burlakov VM, Peng W (2015) High-quality bulk hybrid perovskite single crystals within minutes by inverse temperature crystallization. Nat Commun 6:7586
51. Amat A, Mosconi E, Ronca E, Quarti C, Umari P, Nazeeruddin MK, Gratzel M, De Angelis F (2014) Cation-induced band-gap tuning in organohalide perovskites: interplay of spin–orbit coupling and octahedra tilting. Nano Lett 14:3608–3616
52. Saidaminov MI, Abdelhady AL, Maculan G, Bakr OM (2015) Retrograde solubility of formamidinium and methylammonium lead halide perovskites enabling rapid single crystal growth. Chem Commun 51:17658–17661
53. Han Q, Bae SH, Sun P, Hsieh YT, Yang Y, Rim YS (2016) Single crystal formamidinium lead iodide ($FAPbI_3$): insight into the structural, optical, and electrical properties. Adv Mater 28:2253–2258
54. Weller MT, Weber OJ, Frost JM, Walsh A (2015) Cubic perovskite structure of black formamidinium lead iodide, α-$[HC(NH_2)_2]PbI_3$, at 298 K. J Phys Chem Lett 6:3209–3212

55. Pang S, Zhou Y, Wang Z, Yang M, Krause AR, Zhou Z et al (2016) Transformative evolution of organolead triiodide perovskite thin films from strong room-temperature solid–gas interaction between $HPbI_3$–CH_3NH_2 precursor pair. J Am Chem Soc 138:750–753
56. Mokhtar MZ, Chen M, Whittaker E, Hamilton B, Aristidou N, Ramadan S et al (2017) $CH_3NH_3PbI_3$ films prepared by combining 1- and 2-step deposition: how crystal growth conditions affect properties. Phys Chem Chem Phys 19:7204–7214
57. Chen P, Zhang Y, Du J, Wang Y, Zhang X, Liu Y (2018) Global control of $CH_3NH_3PbI_3$ formation with multifunctional ionic liquid for perovskite hybrid photovoltaics. J Phys Chem C 122:10699–10705
58. Zhang T, Long M, Yan K, Zeng X, Zhou F et al (2016) Facet-dependent property of sequentially deposited perovskite thin films: chemical origin and self-annihilation. ACS Appl Mater Interfaces 8:32366–32375
59. Yaffe MJ, Rowlands JA (1997) X-ray detectors for digital radiography. Phys Med Biol 42:1
60. Szeles C (2004) CdZnTe and CdTe materials for X-ray and gamma ray radiation detector applications. Phys Status Solidi B 241:783–790
61. Kasap SO (2000) X-ray sensitivity of photoconductors: application to stabilized a-Se. J Phys D 33:2853
62. Yoo YZ, Chmaissem O, Kolesnik S, Ullah A, Lurio LB, Brown DE (2006) Diverse effects of two-dimensional and step flow growth mode induced microstructures on the magnetic anisotropies of $SrRuO_3$ thin films. Appl Phys Lett 89:124104
63. Sale AG, Kazan S, Gatiiatova JI, Valeev VF, Khaibullin RI, Mikailzade FA (2013) Magnetic properties of Fe implanted $SrTiO_3$ perovskite crystal. Mater Res Bull 48:2861–2864
64. Shevchuk YA, Gagulin VV, Korchagina SK, Ivanova VV (2004) Dielectric and magnetic properties of $SrTiO_3$–$BiMnO_3$ solid solutions. Inorg Mater 40:292
65. Chen H, Kolpak AM, Ismail-Beigi S (2010) Electronic and magnetic properties of $SrTiO_3$/$LaAlO_3$ interfaces from first principles. Adv Mater 22:2881–2899
66. Zhai X, Mohapatra CS, Shah AB, Zuo JM, Eckstein JN (2013) Magnetic properties of the $(LaMnO_3)_N$/$(SrTiO_3)_N$ atomic layer superlattices. J Appl Phys 113:173913
67. Zhang H, Zhang J, Yang H, Lan Q, Hong D, Wang S et al (2016) Structural and Magnetic Properties of $LaCoO_3$/$SrTiO_3$ Multilayers. ACS Appl Mater Interfaces 8:18328–18333
68. Mota DA, Barcelay YR, Senos AMR, Fernandes CM, Tavares PB, Gomes IT et al (2014) Unravelling the effect of $SrTiO_3$ antiferrodistortive phase transition on the magnetic properties of $La_{0.7}Sr_{0.3}MnO_3$ thin films. J Phys D Appl Phys 47:43
69. Li B, Louca D, Niedziela J, Li Z, Zhang L, Zhou J, Goodenough JB (2016) Lattice and magnetic dynamics in perovskite $Y_{1-x}La_xTiO_3$. Phys Rev B 94:224301
70. Ponath P, O'Hara A, Cao HX, Posadas AB, Vasudevan R, Okatan MB (2016) Contradictory nature of Co doping in ferroelectric $BaTiO_3$. Phys Rev B 94:205121
71. Li Z, Cho Y, Li X, Aimi A, Inaguma Y, Alonso JA et al (2018) New mechanism for ferroelectricity in the perovskite $Ca_{2-x}Mn_xTi_2O_6$ synthesized by spark plasma sintering. J Am Chem Soc 140:2214–2220
72. Xia H, Dai J, Xu Y, Yin Y, Wang X, Liu Z et al (2017) Magnetism and the spin state in cubic perovskite $CaCoO_3$ synthesized under high pressure. Phys Rev Materials 1, 024406 (2017)
73. Tyson TA, Wu T, Ahn KH, Kim SB, Cheong SW (2010) Local spin-coupled distortions in multiferroic hexagonal $HoMnO_3$. Phys Rev B 81:054101
74. Gao P, Chen Z, Tyson TA, Wu T, Ahn KH, Liu Z (2011) High-pressure structural stability of multiferroic hexagonal $RMnO_3$ (R = Y, Ho, Lu). Phys Rev B 83:224113
75. Jin H, Rhim SH, Im J, Freeman AJ (2013) Topological Oxide Insulator in Cubic Perovskite Structure. Sci Rep 3:1651
76. Soleymani M, Edrissi M (2016) Preparation of manganese-based perovskite nanoparticles using a reverse microemulsion method: biomedical applications. M Bull Mater Sci 39:487
77. Zaraska L, Mika K, Hnida KE, Gajewska M, Lojewski T, Jaskula M, Sulka GD (2017) High aspect-ratio semiconducting ZnO nanowires formed by anodic oxidation of Zn foil and thermal treatment. Mater Sci Eng, B 226:94–98

78. Ciocarlan RG, Seftel EM, Mertens M, Pui A, Mazaj M, Tusar NN, Cool P (2018) Novel magnetic nanocomposites containing quaternary ferrites systems $Co_{0.5}Zn_{0.25}M_{0.25}Fe_2O_4$ (M = Ni, Cu, Mn, Mg) and TiO_2-anatase phase as photocatalysts for wastewater remediation under solar light irradiation. Mater Sci Eng, B 230:1–7
79. Patterson AL (1939) The Scherrer formula for X-ray particle size determination. Phys Rev 56:978–982
80. Woo H, Tyson TA, Croft M, Cheong SW, Woicik JC (2001) Correlations between the magnetic and structural properties of Ca-doped $BiMnO_3$. Phys Rev B 63:134412
81. Qian Q, Tyson TA, Kao CC, Croft M, Ignatov AY (2002) Local magnetic ordering in $La_{1-x}Ca_xMnO_3$ determined by spin-polarized X-ray absorption spectroscopy. Appl Phys Lett 80:3141
82. Wu Y, Ma Y, Xu G, Wei F, Ma Y, Song Q (2017) Metal-organic framework coated Fe_3O_4 magnetic nanoparticles with peroxidase-like activity for colorimetric sensing of cholesterol. Sens Actuators B Chem 249:195–202
83. Zhao X, Liu S, Tang Z, Niu H, Cai Y, Meng W et al (2015) Synthesis of magnetic metal-organic framework (MOF) for efficient removal of organic dyes from water. Sci Rep 5:11849
84. McBain SC, Yiu HHP, Dobson J (2008) Magnetic nanoparticles for gene and drug delivery. Int J Nanomedicine 3:169–180
85. Ito A, Shinkai M, Honda H, Kobayashi T (2005) Medical application of functionalized magnetic nanoparticles. J Biosci Bioeng 100:1–11
86. Peller M, Boll K, Zimpel A, Wuttke S (2018) Metal-organic framework nanoparticles for magnetic resonance imaging. Inorg Chem Front Advance Article
87. Tang D, Yuan R, Chai Y (2006) Magnetic core–shell Fe_3O_4@Ag nanoparticles coated carbon paste interface for studies of carcinoembryonic antigen in clinical immunoassay. J Phys Chem B 110:11640–11646
88. Bagheri A, Taghizadeh M, Behbahani M, Asgharinezhad AA, Salarian M, Dehghani A et al (2012) Synthesis and characterization of magnetic metal-organic framework (MOF) as a novel sorbent, and its optimization by experimental design methodology for determination of palladium in environmental samples. Talanta 99:132–139
89. Chen Y, Xiong Z, Peng L, Gan Y, Zhao Y, Shen J, Qian J, Zhang L, Zhang W (2015) Facile preparation of core–shell magnetic metal-organic framework nanoparticles for the selective capture of phosphopeptides. ACS Appl Mater Interfaces 7:16338–16347
90. Wu ZY, Ma CB, Tang XG, Li R, Liu QX, Chen BT (2013) Double-perovskite magnetic La_2NiMnO_6 nanoparticles for adsorption of bovine serum albumin applications. Nanoscale Res Lett 8:207
91. Yang Y, Jia TW, Xu F, Li W, Tao S, Chu LQ et al (2018) Fluorescent neomannosyl bovine serum albumin as efficient probe for mannose receptor imaging and MCF-7 cancer cell targeting. ACS Appl Nano Mater 1:1058–1065
92. Feng LJ, Zhang XH, Zhao DM, Wang SF (2011) Electrochemical studies of bovine serum albumin immobilization onto the poly-*o*-phenylenediamine and carbon-coated nickel composite film and its interaction with papaverine. Sens Actuators B Chem 152:88–93
93. Coreno J, Coreno O (2005) Evaluation of calcium titanate as apatite growth promoter. J Biomed Mater Res 75A:478–484
94. Song HJ, Kim MG, Moon WJ, Park YJ (2011) Formation of hydroxyapatite nanorods and anatase TiO_2 on $CaTiO_3$ powder using hydrothermal treatment. Mater Sci Eng, C 31:558–561
95. Dubey AK, Basu B, Balani K, Guo R, Bhalla AS (2011) Multifunctionality of Perovskites $BaTiO_3$ and $CaTiO_3$ in a Composite with Hydroxyapatite as Orthopedic Implant Materials. Integr Ferroelectr 131:119–126
96. Wei D, Zhou Y, Jia D, Wang Y (2008) Formation of $CaTiO_3/TiO_2$ composite coating on titanium alloy for biomedical applications. J Biomed Mater Res 84B:444–451
97. Webster TJ, Ergun C, Doremus RH, Lanford WA (2003) Increased osteoblast adhesion on titanium-coated hydroxyapatite that forms $CaTiO_3$. J Biomed Mater Res 67A:975–980

98. Dubey AK, Tripathi G, Basu B (2010) Characterization of hydroxyapatite-perovskite ($CaTiO_3$) composites: Phase evaluation and cellular response. J Biomed Mater Res 95B:320–329
99. Krupa D, Baszkiewicz J, Kozubowski JA, Barcz A, Sobczak JW, Bilinski A, Lewandowska-Szumiel M, Rajchel B (2001) Effect of calcium-ion implantation on the corrosion resistance and biocompatibility of titanium. Biomaterials 22:2139–2151
100. Biegalski MD, Qiao L, Gu Y, Mehta A, He Q, Takamura Y et al (2015) Impact of symmetry on the ferroelectric properties of $CaTiO_3$ thin films. Appl. Phys Lett 106:162904 (2015)
101. Stanishevsky AV, Holliday S (2007) Mechanical properties of sol-gel calcium titanate bioceramic coatings on titanium. Surf Coat Technol 202:1236–1241
102. Wang L, Li J, Feng M, Min L, Yang J, Yu S (2017) Perovskite-type calcium titanate nanoparticles as novel matrix for designing sensitive electrochemical biosensing. Biosens Bioelectron 96:220–226
103. Hench LL (1998) Bioceramics. J Am Ceram Soc 81:1705–1728 (1998)
104. Li B, Zhang Y, Fu L, Yu T, Zhou S, Zhang L, Yin L (2018) Surface passivation engineering strategy to fully-inorganic cubic $CsPbI_3$ perovskites for high-performance solar cells. Nat Commun 9:1076
105. Niu G, Li W, Li J, Liang X, Wang L (2017) Enhancement of thermal stability for perovskite solar cells through cesium doping. RSC Adv 7:17473–17479
106. Tsai H, Nie W, Blancon JC, Stoumpos CC, Asadpour R, Harutyunyan B et al (2016) High-efficiency two-dimensional Ruddlesden-Popper perovskite solar cells. Nature 536:312–316
107. Chen AZ, Shiu M, Ma JH, Alpert MR, Zhang D, Foley BJ et al (2018) Origin of vertical orientation in two-dimensional metal halide perovskits and its effect on photovoltaic performance. Nat Commun 9:1336

Chapter 5
Ion Transport and Stability Issues in Organic–Inorganic Perovskite Materials

Monojit Bag and Priya Srivastava

1 Introduction

Hybrid organic–inorganic perovskites (HOIPs) have emerged as an important class of material in the field of photovoltaics. One of their intriguing properties which make them more attractive is that they are mixed ionic–electronic conductors. That means they have both electrons and ions as charge conductors. The electronic transport follows the band transport mechanism, whereas ionic transport is by hopping of ions between thermodynamically favorable ion vacancies. Unique behavior is noticed when the electronic conductivity is modulated by ion transport or when ion transport is modulated by electronic transport. The interplay between this electronic and ionic transport leads to some undesirable issues such as hysteresis in current–voltage curves, thermoelectricity, switchable photovoltaic effects, instability to heat and light, and increased power conversion efficiencies. For the development of new HOIPs with reduced hysteresis, improved stability, and hence superior device performance for energy harvesting along with other electronic applications, the understanding of electronic and ionic conductivity and their relationship especially is critical.

Here, we have tried to explain the underlying mechanism of the ionic transport in perovskites under different external disturbances and its effect on the total conductivity and hence the performance of device by analyzing the relationship between electronic and ionic transport. We have first focused on vacancy-mediated ion transport in perovskites theoretically and explained it through experimental evidences in only perovskite material (metal/perovskite/metal) and device geometry (metal/ETL (HTL)/perovskite/HTL (ETL)/metal). The behavior of the device performance under different external disturbances is discussed. At the end, some stability issues related to HOIPs devices are introduced.

M. Bag (✉) · P. Srivastava
Department of Physics, Indian Institute of Technology, Roorkee, Uttarakhand, India
e-mail: mbagfph@iitr.ac.in

N. S. Arul and V. D. Nithya (eds.), *Revolution of Perovskite*, Materials Horizons: From Nature to Nanomaterials, https://doi.org/10.1007/978-981-15-1267-4_5

2 Vacancy-Mediated Ion Transport (Microscopic Transport Mechanism of Ion Migration)

Ionic conductivity is broadly classified into two types: migration of defect sites and the migration of different ionic species. Nevertheless, the defect sites are also responsible for migration of ionic species. Transport of intrinsic ionic vacancy and interstitial defects in organolead halide perovskites has significant consequences on perovskite-based devices in terms of performance and long-term stability. Migration pathways with their corresponding activation energies and the exact nature of the mobile ionic species can be well understood through vacancy-assisted migration of ions.

Microscopic transport mechanism of vacancy-mediated ion transport reflects mixed ionic–electronic conduction in these organic–inorganic hybrid perovskites. As illustrated in Fig. 1, the perovskite-type structure ABX_3, where A is organic cation, B is metal, and X is halide ion, comprised of an extended framework of PbI_6 octahedra sharing the corners with the alkyl ammonium cation at the body central A-site and surrounded by 12 edge-centered nearest neighbor iodide ions. This can be understood in more simple way as a cubic structural lattice with organic cation A at body central position, metal ion B at corners and halide ions at the edge centers or alternatively as metal ion B at body central position, organic cation A at the corners, and halide ions at face-center position.

Organolead halide perovskites are prone to the defect formation, mostly point defects including ionic vacancies (V_{MA}, V_{Pb}, and V_I) and interstitials (MA_i, Pb_i, and I_i) along with some cation substitutions (MA_{Pb} and Pb_{MA}) and antisite substitutions (MA_I, Pb_I, I_{MA} and I_{Pb}), attributed to the low thermal stability of the perovskite material. Among all these types of point defects, the vacancy and interstitial defects are most likely due to their low formation energies and primarily responsible for the diffusion of ions in the material by creating shallow donor and acceptor levels near the band edges. Further in $CH_3NH_3PbI_3$, the vacancy-mediated ion transport is supported more because of the ease of formation of these Schottky disorders with the intrinsic vacancies of concentration exceeding 0.4% at room

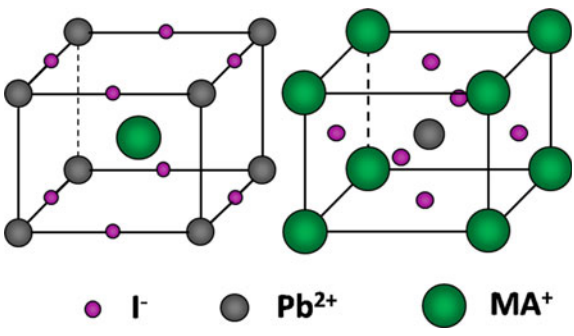

Fig. 1 Structure of perovskite crystal lattice

temperature. All these Schottky- and Frenkel-type ionic disorders associated with vacancies and interstitials prevailing over electronic disorder specifically in $CH_3NH_3PbI_3$ can be shown by the following reaction in Kröger–Vink notation,

$$nil \rightarrow V'_{MA} + V''_{PB} + 3V^{\bullet}_{I} + I_i + CH_3NH_3PbI_3 \quad (1)$$

where nil indicates the perfect $CH_3NH_3PbI_3$ lattice, *V* represents a vacancy, subscripts are the ionic species, and superscripts are the effective defect charge (a prime for each negative charge and dot for each positive charge). I_i is the interstitials iodine. Interstitial defects due to the other two ions are not included here, as they are much bigger in size to be accommodated in the interstitial sites in the crystal of $CH_3NH_3PbI_3$.

2.1 Vacancy-Mediated Ion Transport Mechanism

Defect migration across the perovskite crystal has been modeled considering these four basic defects [1]. Migration pathway by conventional hopping between neighboring favorable positions is devised as shown in Fig. 2.

(i) **V_I Migration**:
For V_I, I^- ion migration takes place from the axial site to the equatorial position along an octahedron edge leading the vacancy V_I to migrate toward that axial site from the equatorial position, i.e., in the opposite direction (Fig. 2a). The activation energy of V_I(0.01–0.60 eV) is lowest among all other ion migrating vacancies V_{MA} and V_{Pb} showing the V_I-dominated defect migration in $CH_3NH_3PbI_3$ perovskites.

(ii) **V_{MA} Migration**:
Regarding V_{MA}, MA^+ ion hops between the adjacent cavities. The MA^+ ion migrate into the neighboring vacant A-site which involves the motion of ion through the unit cell face plane comprised of four I^- and four Pb^{2+}, i.e., crossing the Pb_4I_4 framework perpendicularly (Fig. 2b). The activation energy of MA^+ (0.45–0.90 eV) is higher than that of I^- ion implying slow MA^+ migration and need of the external disturbance for the significant MA^+ ion migration in the perovskite material.

(iii) **V_{Pb} Migration**:
For V_{Pb}, an in-plane migration has been investigated. The V_{Pb} migrate along the side of the face square of cubic unit cell formed by four Pb^{2+} ions at the corners and I^- ions at the edge centers tilted slightly (Fig. 2c). The high

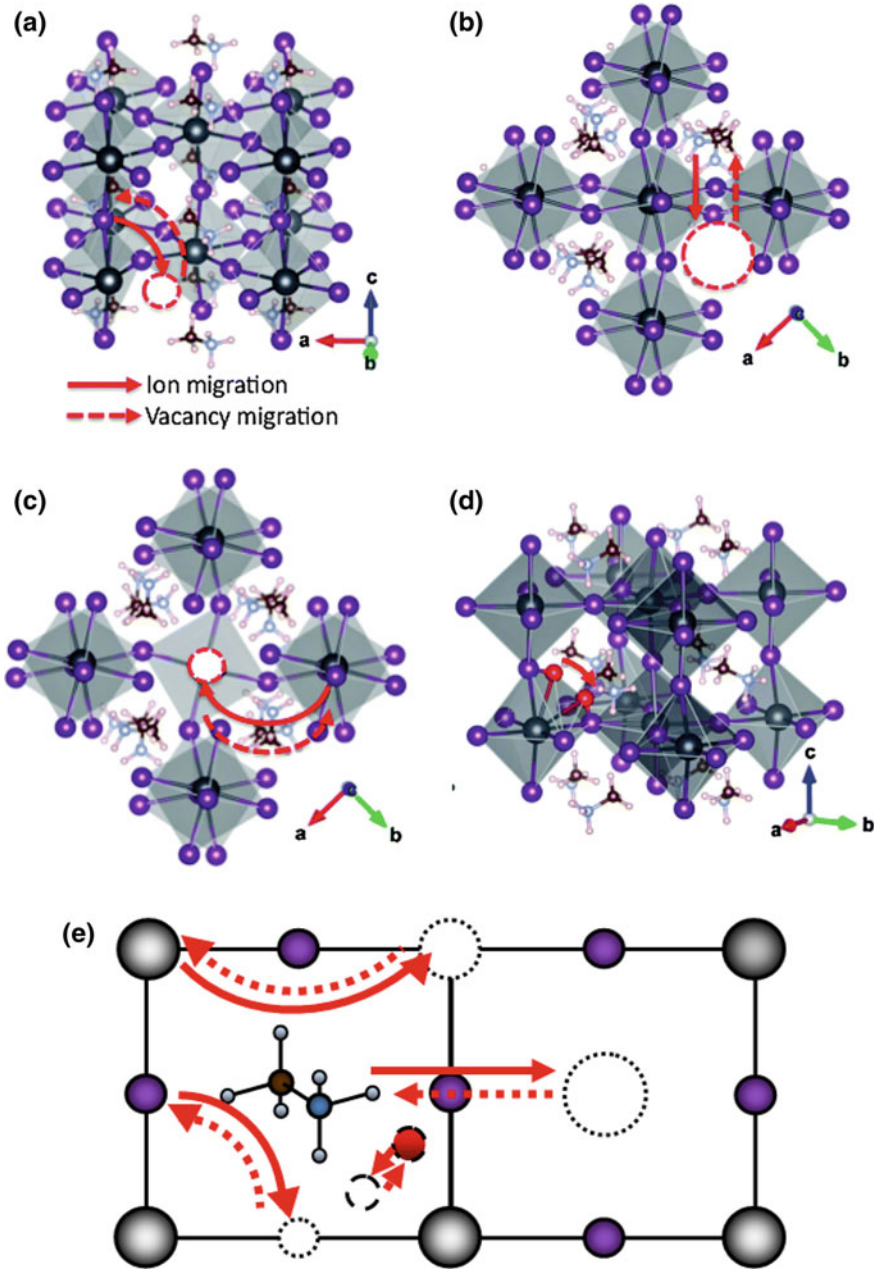

Fig. 2 Diffusion paths for the V_I (**a**), V_{MA} (**b**), V_{Pb} (**c**), and I_i (**d**). Schematic illustration of the ion migrations in 2D. White = H, brown = C, blue = N, purple = I, red = interstitial I, and black = Pb atoms. Reprinted with permission from (Defect migration in methylammonium lead iodide and its role in perovskite solar cell operation [1]. Copyright (2015). Reproduced with permission from the Royal Society of Chemistry

energy barrier for V_{Pb} migration (0.80–2.50 eV) suggests an immobile Pb sublattice.

(iv) **I_i Migration**:
The I_i migration takes place between the adjacent interstitial sites in the crystal lattice via path along the *c*-axis (Fig. 2d). The initial and final positions of the interstitial iodine ion are at almost equal distance between a couple of axial and equatorial iodine atoms. The activation energy of the I_i migration is same as that of V_I, suggesting the dominance of I_i migration along with V_I over V_{MA} and V_{Pb} migrations in case of I-rich perovskite crystals.

Diffusion coefficient or migration rate of the ions can be estimated from the calculated corresponding activation energies assuming Boltzmann-like barrier hopping transport. The estimated diffusion coefficient of I^- ions is about four orders of magnitude higher than that of MA^+ ions, suggesting the dominance of iodine ion migration over negligible diffusion of methylammonium ions in $CH_3NH_3PbI_3$ perovskite crystals. These results clearly confirm the mixed ionic–electronic conductance in the hybrid organic–inorganic perovskite materials. The key factor for majority ionic carrier iodine ions is the concentration of intrinsic iodine vacancies and interstitial iodine in the material, which is sensitive to thermal processing routes and synthesis conditions.

2.2 *Paths of Vacancy Migration*

In perovskite crystals, depending on the relative initial and final positions of the migration, there are more than one possible diffusion pathway for ion transport. However, in the cubic perovskite crystal lattice, these pathways specifically for iodine and methylammonium ions are isoenergetic and hence equivalent. But in tetragonal and trigonal crystal structure, all the migration pathways are not equivalent in energy due to the different surrounding structural configurations of a particular lattice point from another. Considering the tetragonal lattice structure of $CH_3NH_3PbI_3$ crystal, there are more than one possible diffusion pathway for iodine and methylammonium ions, which are discussed here.

(i) **I^- ion migration pathways**

In the perovskite crystal lattice, the iodine ions are placed at the six corners of the PbI_6 octahedron. In this octahedron, there are two types of position of the iodine ions which are equatorial and axial sites [2]. Depending on the final and initial sites, there could be three possible pathways for iodine migration across the octahedron (Fig. 3). These are (a) P1: from axial site to axial site, (b) P2: from axial site to equatorial site (or equatorial to axial site), and (c) P3′: from equatorial to equatorial site. The third pathway requires very high impossible energy as it needs to cross the doubly positively charged Pb ion. Therefore, the third pathway P3′ is not a feasible

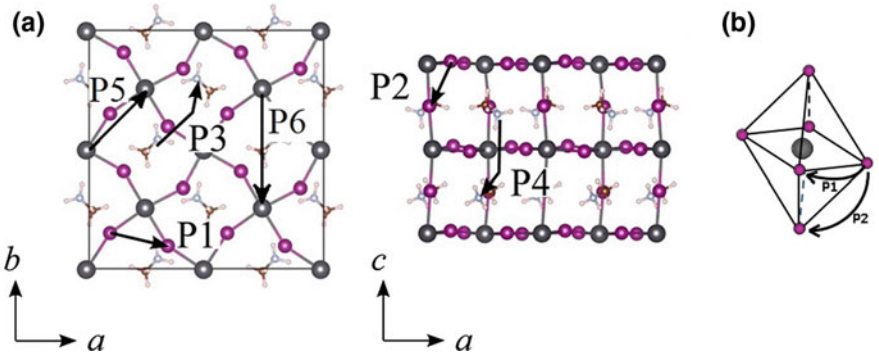

Fig. 3 **a** Vacancy migration paths of $MAPbI_3$. Arrows (P1, P2), (P3, P4), and (P5, P6) represent V_I, V_{MA}, and V_{Pb} paths, respectively. **b** Representation of paths P1 and P2 in the PbI_6 octahedral. White = H, brown = C, blue = N, purple = I, and black = Pb atoms. Adapted with permission from (First-Principles Study of Ion Diffusion in Perovskite Solar Cell [2]. Copyright (2015). Reproduced with permission from the American Chemical Society

path. Only P1 and P2 are possible feasible paths in case of tetragonal perovskite crystal.

The path P1 and P2 migration takes place along the <100> and <111> directions, respectively. The activation energy required along the path P1 is obviously less than along the path P2 since migration along the path P1 is between the equivalent positions in the same plane and to a smaller distance. However, migration along the path P2 leads to a completely different iodine position in the octahedron crossing a larger distance as compared to the path P1. Therefore, path P1 is more favorable as compared to the path P2. In case of cubic crystal lattice of $CH_3NH_3PbI_3$, both axial and equatorial positions in the octahedron are almost equivalent considering the energy aspect. Hence, both the pathways P1 and P2 are isoenergetic and equivalent.

(ii) **MA^+ ion migration pathways**

For MA^+ ion, the ion transport takes place by hopping to the corresponding position of the next adjacent crystal lattice. All the positions of MA^+ ions are equivalent in the material, but the direction of migration makes the difference in case of tetragonal lattice structure, indicating anisotropic diffusion. In tetragonal crystal structure, the lattice parameters are $a = b \neq c$ and $\alpha = \beta = \gamma = 90°$. Therefore, migration along the *a*- and *b*-axes is the equivalent and isoenergetic as the ion moves to the equal distance crossing the similar surrounding charge configuration along these two directions. However, the migration of ion along the *c*-axis requires covering more distance and a different surrounding charge configuration. Hence, there are basically two diffusion pathways for methylammonium ion migration in tetragonal crystal lattice (Fig. 3a). These are (a) P3: along the *a*- or *b*-axes covering the distance equal to a and (b) P4: along the *c*-axis covering the distance equal to *c*. These MA^+ ion migration takes place along the straight line direction along <110> for P3 and <001> for P4. Obviously, the pathway P3 has less activation

energy, and hence more favorable as compared to pathway P4 as it requires less distance to be covered.

In case of cubic crystal lattice, $a = b = c$ and hence migration along all the three axes is equivalent and isoenergetic. Hence, these two types of different pathways are not seen in the cubic crystal lattice.

(iii) **Pb^{2+} ion migration pathways**

As described earlier, the Pb^{2+} migration takes place in the aforementioned Pb_4I_4 framework which is a plane formed by four Pb^{2+} ions at the corners and I^- ions at the edge centers. In this plane, Pb^{2+} ion can move either along the side of the square plane or along the diagonal. Therefore, there are two possible paths for Pb^{2+} migration which are (a) P5: along the side of the square plane and (b) P6: along the diagonal of the square plane (Fig. 3a). However, the Pb^{2+} migration in either of these two directions is difficult practically due to their high activation energy as compared to other two ions, but path P5 is more favorable and has less activation energy when compared to the pathway P6 along the diagonal of the square plane. These two types of migration pathways of Pb^{2+} ion are seen in both tetragonal and cubic perovskite crystal lattice.

3 Experimental Evidences of Ionic Transport

The migration of ions (vacancies as well as different ionic species) can also be verified by experimental means. Ionic conductivity significantly differs from the electronic conductivity in these types of perovskite materials. Normally, the activation energy (E_a) is in order of few hundreds of meV to few eV depending on the nature of ionic species, pathways for ions and vacancies migrations, light activation and thermal expansion of the lattice. In this current chapter, two kinds of device geometry will be discussed to elucidate the nature of ion migration and the impact of the device structure.

3.1 Charge Transport Dynamics in Organolead Halide Perovskite Materials (Metal/Perovskite/Metal Geometry)

Consider the simplest geometry of the hybrid perovskite material between two conducting metal electrodes (generally Au/$CH_3NH_3PbI_3$/Au) to study the ion migration and transport through the perovskite channel in the absence of ETL or HTL as shown in Fig. 4a [3]. Due to the absence of any ETL or HTL, there is no internal driving force such as built-in electric field at the interface. There is no heterojunction formed due to depletion or accumulation of ions at the metal/perovskite/metal interface. Therefore, there is a need for external modulation such

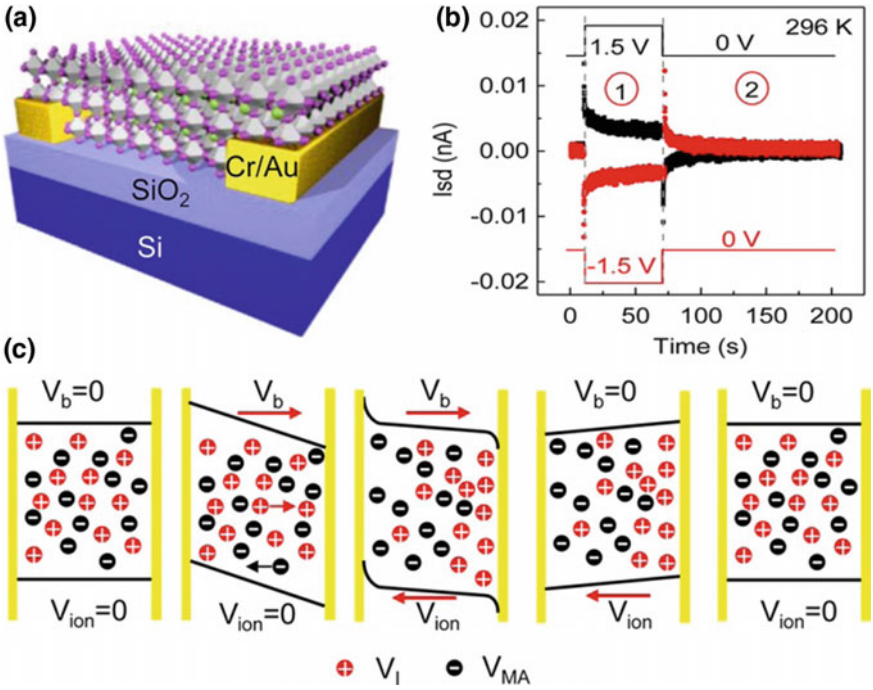

Fig. 4 Temporal response and schematics of the ion migration in organolead halide perovskite. **a** Schematic of a two-probe halide perovskite film device fabricated on a 300 nm SiO_2/Si substrate with 5 nm Cr/50 nm Au as electrodes. **b** Temporal response curves following positive and negative biasing at 296 K. **c** Schematic diagrams indicating the dynamics of ionic transport following the external bias. Reprinted with permission from (Electronic and Ionic Transport Dynamics in Organolead Halide Perovskites [3]. Copyright (2016). Reproduced with permission from the American Chemical Society

as bias, illumination, or temperature to study the charge transport dynamics through the perovskite active layer.

In the organolead halide perovskite materials such as $CH_3NH_3PbI_3$, the common defects are vacancies (V_{MA}, V_{Pb}, and V_I standing for $CH_3NH_3^+$, Pb^{2+}, and I^-, vacancies, respectively) and interstitials (MA_I, Pb_I, I_{MA}, and I_{Pb}) due to their low formation energy. These defects generally assist in vacancy-mediated ion migration and mixed electronic–ionic conduction in hybrid perovskites by creating shallow donor and acceptor levels near the band edge which migrate from one site to another under external or built-in field. But as reported in the studies till date, these three types of vacancies do not contribute in the conduction equally because of their different activation energies for the transport. Among all three types of vacancies, V_I migration has the smallest activation energy barrier and considered to be the primary migration species in the hybrid perovskites. However, few studies also show the small contribution of V_{MA} vacancy to the conduction due to comparable activation energy. But the activation energy of V_{Pb} is much higher than that of other

two vacancies, and hence they are considered to be immobile and at rest during the investigation of ion transport.

The dynamics of the ion migration is described using the schematic as shown in Fig. 4b. The schematic is generally the spin-coated polycrystalline perovskite thin film coated on the substrate between two-probe symmetric metal electrodes (preferably Au or Cr/Au). The channel length is about 20–50 μm.

3.1.1 Mechanism

In the beginning, when no external bias is applied and the perovskite material is in dark (zero illumination) at room temperature, the vacancies (V_{MA}, V_{Pb}, and V_I) are randomly distributed throughout the device channel. After applying the positive external bias at time t_1 and removing at time t_2, the interplay between electronic and ionic transport can be understood in the following stages since no other external disturbance is applied, i.e., the device is in dark at room temperature and at zero applied bias.

(i) **Stage 0 (0 to t_1 seconds)**

During this stage, no external bias is applied across the channel. The vacancies are distributed randomly in the film. There is no driving force for any kind of motion, and all the ions are at rest and hence there isn't any kind of ion migration and photoconductivity. Both the applied positive bias (V_b) and ion-induced electric field (V_{ion}) are zero, and hence the net potential across the channel (V_{net}) is also zero.

(ii) **Stage I (t_1 to t_2 seconds)**

This stage can be further divided into three more stages to have a more deeper understanding which are (a) t_1 to $t_1 + \delta$ seconds, (b) $t_1 + \delta$ to $t_1 + \delta + \alpha$, and (c) $t_1 + \delta + \alpha$ to t_2 seconds where δ is about less than $t_1/20$, and α is about $t_1/2$. Simplifying this, if the external bias is applied for about 60 s, then stage I (a) is from t_1 to t_1 + (2–3) s, stage I (b) is from t_1 + (2–3) s to t_1 + (32–33) s, and stage I (c) is from t_1 + (32–33) s to t_1 + 60 s or t_2.

Stage I (a): During this stage, an external bias is just applied to the device at t_1. All the charged species electrons/holes and ions respond to the applied bias and start moving. However, due to high mobility and much faster speed of electrons/holes than ions, an electronic current is observed instantly in very short time δ. But ions being heavy require more time to show any conductivity, and hence during this stage the current which shoots up is only the electronic current due to the applied bias, without any contribution from the ions (negligible ionic current). Let this instant electronic current due to the applied external bias be $\mathbf{I_1}$ (at $t_1 + \delta$) for stage I.

Stage I (b): In this stage, after δ s of applying external bias, the ions start to drift slowly under the effect of external bias, leading to an ionic current with the same polarity as that of the electronic current. After few seconds, with continued motion of the ions under external bias, these oppositely charged ions start to pile up at the perovskite–electrode interface. This accumulation of ions at the electrodes leads to

an ion-induced electric field which is in opposite direction to that of the applied electric field. This opposing electric field partially cancels the applied electric field and results in the reduction of net electric field across the channel which leads to the decrease in the electronic current. With time, as more and more oppositely charged ions move toward the corresponding perovskite–electrode interface and accumulate there, the ion-induced electric field increases continuously and net electric field across the channel decreases leading to the continuous and gradual reduction in the total current.

Stage I (c): After some time (α seconds), the accumulation of ions at the interface reaches the equilibrium condition and gets saturated. This saturation is attributed mainly to the lack of mobile ion vacancies for further motion. After the equilibrium condition is reached, there is no more increase in the ion-induced electric field and the net electric field across the interface becomes stable with no further changes. During this stage, the total current through the device become constant with no further reduction. This current is the resultant of the interaction between electronic current due to applied bias and ion-induced current and can be considered to be the difference of bias-induced and ion-induced current. Let this constant total current after the device reached the equilibrium is denoted as $\mathbf{I_{10}}$. However, since the magnitude of bias-induced current is more than the ion-induced current, the direction of total current is same as the direction of the bias-induced current as shown in Fig. 4c.

(iii) **Stage II (after t_2 seconds)**

As in stage I, this stage can also be further divided into three substages as (a) t_2 to $t_2 + \delta'$ seconds, (b) $t_2 + \delta'$ to $t_2 + \delta' + \alpha'$, and (c) $t_2 + \delta' + \alpha'$ seconds onward where δ' is about less than $t_1/20$, α' is about $t_1/2$ (very similar to δ and α).

Stage II (a): At time t_2, the external bias is just removed and only the ion-induced electric field exists across the channel which is in opposite direction (to the previous net electric field across the device before t_2). This results in the instant switching of the polarity of the net electric field, and hence the current across the device (during the δ' seconds). During this stage, the net current is only the electronic current due to ion-induced electric field, and hence this instant current right after the external bias is removed (at $t_2 + \delta'$) at stage II can be denoted as $\mathbf{I_2}$.

Stage II (b): After $t_2 + \delta'$ seconds, due to the absence of the external bias which were acting as the driving force for the accumulation of ions, the accumulated ions start diffusing away from the perovskite–electrode interface toward the bulk of the material with time. This leads to the gradual decrease in the ion-induced electric field and hence continuous reduction in the net current across the channel.

Stage II (c): After sufficient time, when all the ions are returned back to their initial equilibrium position in the bulk of the material, the ion-induced electric field is reduced to zero. This leads to a zero total current in the device.

This behavior of current under this kind of applied bias is studied by Li et al, and the above-explained temporal behavior of current curves of the thin-film perovskite device of this type upon the application and removal of the bias voltage is shown in Fig. 4 along with the applied bias sequence. Such switchable behavior of current

under external bias is attributed to the ion migration within the organolead halide perovskite as explained above.

3.1.2 Quantification

Dehui Li and group characterized the contributions from electronic transport and ionic conduction quantitatively and determined the magnitude of ion-induced electric potential in these devices by investigating the temporal response of current in stage I (external bias applied) and stage II (external bias removed). They fitted the transient response at both stage I and stage II using the bi-exponential function. The example of fitting results for the temporal response of the total current under the applied external bias of 3 V is shown in Fig. 5a [3].

For stage I, the fitting bi-exponential function is expressed as

$$I(t) = I_{10} + (I_e - I_1)\exp\left(\frac{-t - t_1}{t_e}\right) + (I_1 - I_{10})\exp\left(\frac{-t - t_1 - \delta''}{\tau_1}\right) \quad (2)$$

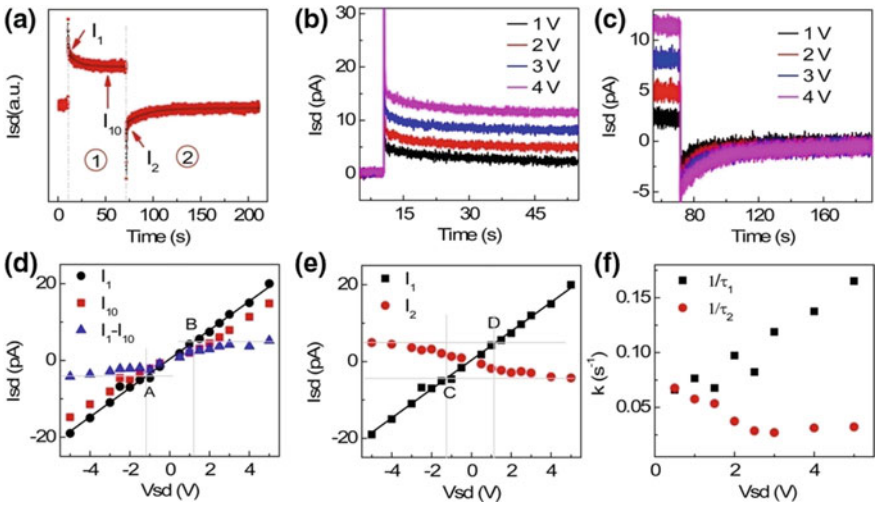

Fig. 5 External bias-dependent temporal response in organolead halide perovskite. **a** Temporal response curves following +3 V biasing at 296 K for a organolead halide device in the dark. **b**, **c** The applied external bias dependence of the temporal response curves for stage I (**b**) and stage II (**c**) for organolead halide perovskite film in the dark. **d** The applied external bias dependence of I_1, I_{10}, and I_1–I_{10}. **e** The applied external bias dependence of I_1 and I_2. **f** The applied external bias dependence of ion decay rate [3]. Copyright (2016). Reprinted with permission from the American Chemical Society

where I_e and τ_e are related to the equipment response (RC delay) which are nearly identical for both stage I and stage II; τ_1 is the time constant of ion migration under applied bias for stage I; δ'' is the relaxation time of the equipment (less than 1 s).

Similarly, the temporal response curve of stage II can be fitted using the same bi-exponential function as

$$I(t) = I_{20} + (I_e - I_2)\exp\left(\frac{-t - t_2}{\tau_e}\right) + (I_2 - I_{20})\exp\left(\frac{-t - t_2 - \delta''}{\tau_2}\right) \quad (3)$$

where I_{20} is the total constant current when the device reaches the equilibrium condition after removal of external bias at stage II (c) which is essentially zero; I_e and τ_e are related to the equipment response (RC delay) which are nearly identical for both stage I and stage II; τ_2 is the time constant for ion diffusion or restoration at stage II; and δ'' is the relaxation time of the equipment (less than 1 s).

Therefore, these parameters are measured experimentally, and the information on the electronic and ionic transport are extracted. The dynamics of ion transport can be deciphered by the decay time constants τ_1 and τ_2 since ion transport is responsible for the decay in the current. This study is also done by *D*. Li as described in the following section.

3.2 Bias Dependent

On increasing the applied external bias, the more number of mobile electrons/holes move at higher speed toward the corresponding electrode, and hence the instant current produced due to this external applied electric field right after switching on the applied bias I_1 also increases. The ion-induced electric field also increases with the increase in the applied external bias but only up to a certain extent. After reaching a particular value, the ion-induced electric field does not increase further and saturates. This may be attributed to the lack of available mobile ion vacancies for migration and accumulation. Therefore, the ion-induced electric current across the perovskite channel also first increases with applied external bias and then saturates. This behavior under applied external bias is also verified by *D*. Li group as shown in Fig. 5(b–d).

In the study done by *D*. Li and group, the bias-induced electronic current I_1 shows a linear relationship with the applied external bias (V_{sd}) as shown in Fig. 5d which indicates the formation of the Ohmic contacts between the metal electrodes and the perovskite thin films. However, I_{10} the constant total current, after the device reaches equilibrium condition, shows a nonlinear behavior. This is due to the ion-induced electric field on increasing the applied bias. Here, I_1 is the current purely by the applied external bias and I_{10} is the resultant electronic current induced by the interaction between applied external bias and ion-induced electric potential

which means $I_{10} = I_1 – I_{\text{ion-induced}}$, and hence the electronic current induced by the ion-induced electric potential ($I_{\text{ion-induced}}$) is $I_1 – I_{10}$. Therefore, the difference between I_1 and I_{10} ($I_1 – I_{10}$) is the electronic current induced by the ion-induced electric field which is opposite in direction. This current is equivalent to the instant current I_2 after the removal of the applied external bias at stage II which is also the electronic current induced by the ion-induced electric potential only but with opposite polarity. Therefore, $I_1 – I_{10}$ and I_2 follow the same trend with increasing applied bias but with opposite polarity. As expected, in the study by *D*. Li and group ($I_1 – I_{10}$) first increases with increasing external bias (V_{sd}) and then saturates and reaches a stable value around ±4.5 pA when the external applied bias V_{sd} reaches ±3 V as shown in Fig. 5c. Based on the I_1 versus V_{sd} plot from Fig. 5d, the voltage required to generate the current of ±4.5 pA is found to be ±1.2 V. Therefore, from this, the conclusion is drawn that the maximum value of ion-induced electric potential across the device of channel width 20 μm is around 1.2 V. Similarly, I_2 first increases with V_{sd} and then saturates at the same saturation current ±4.5 pA and voltage ±1.2 V as shown in Fig. 5e. The identical saturation behavior of I_2 and $I_1 – I_{10}$ with completely identical saturation current and voltage verifies that the contribution of ionic current to the total current is negligible.

The dynamics of ionic transport is also determined by studying the behavior of decay rate *k*, defined as τ^{-1} $\left(k_1 = \tau_1^{-1}, k_2 = \tau_2^{-1}\right)$ since ion transport is mainly responsible for the decay in the current. The time constant τ_1 represents the dynamics of ion transport with the applied external bias (V_{sd}) for stage I, whereas τ_2 represents the dynamics without external bias (V_{sd}) for stage II. As expected for stage I, at higher applied external bias (V_{sd}), the ions migrate faster and reach the equilibrium conditions. This means with increase in the applied bias, the time required to reach the equilibrium condition reduces, i.e., τ_1 decreases and hence the decay rate k_1 continuously increases with increase in applied external bias for stage I. However, k_2 (for stage II) first decreases and then reaches a saturation value. This is attributed to the fact that for the stage II, the accumulated ions barely depend on the diffusion to reach stable equilibrium state. Therefore, in this stage the decay rate, k_2, relies more on the distribution of the accumulated ions near the electrodes rather than diffusion. Before the ion-induced electric field reaches the saturation value, the ions in the channel become more polarized, i.e., more separated from each other toward the opposite perovskite–electrode interface. This leads to a longer average diffusion length, and hence more time (τ_2) is required to restore the separated ions back to their initial positions. Therefore, the ion restoration rate or decay rate k_2 decreases with increase in bias for stage II. However, when the ion-induced electric field reaches saturation, there is no more increase in the separation between the ions toward the opposite electrodes and the distribution of the polarized ions reaches a stable state with no further change, resulting in the constant restoration rate k_2. Here, k_1 increases linearly with the applied bias, whereas k_2 first decreases till the saturation state is reached at 3 V, after saturation, i.e., V_{sd} = 3 V the decay rate k_2 becomes constant.

3.3 Illumination Dependent

In the perovskite materials and devices, the illumination is reported to enhance the ion transport leading to degradation of device. Instead of band-like transport of high mobility electrons, the ion transport takes place by hopping mechanism to the neighboring sites with varying activation energies under different illumination intensities. Increasing the illumination intensity reduces the activation energy significantly, enhancing the ion migration, and hence reducing the stability of the device.

This ion transport and the gradual transformation of $CH_3NH_3PbI_3$ into PbI_2 under illumination can be understood considering the stage 0 and stage I explained in Sect. 1 under the subsection mechanism. Let's take the same case of applying the external bias across the perovskite material thin film in the lateral device structure: metal/perovskite thin film/metal (more specifically Au/$CH_3NH_3PbI_3$/Au) but this time under illumination. The whole process occurs in the same way as explained earlier in stage 0 and stage I, but this time the illumination plays a major role. After I^- and MA^+ ions have migrated to their corresponding electrodes at the end of stage I, I^- reduction and subsequent I_2 volatilization process takes place at cathode under high-field poling supported by the illumination. Also, the MA^+ ions migrated toward anode evaporate in form of CH_3NH_2 assisted by moisture along with illumination. This MA^+ migration from cathode to anode and evaporation leads to the gradual transformation of $CH_3NH_3PbI_3$ to PbI_2. This behavior is confirmed in the study by Y.C. Zhao and group, where they analyzed the change in the contrast of optical images of perovskite thin film under high electric field poling along with different illumination intensities.

In a study to quantize light-enhanced ionic transport in lead iodide perovskite thin films, Zhao and group analyzed high-field poling behavior of the Au/$CH_3NH_3PbI_3$/Au lateral structure device with a 50-μm gap filled with $CH_3NH_3PbI_3$ perovskite and applied bias of 100 V under three different illumination intensities (0, 5, and 20 mW cm^{-1}). The change in the contrast of the optical images as a result of mobile ions under high-field poling was recorded under the optical microscope as shown in Fig. 6(a–c) [4]. Under illumination, black lines were observed after 10 s of poling expanding from cathode toward anode, whereas no contrast change in the images of perovskite film induced by ion migration was observed under dark conditions as shown in Fig. 6c. This change in the contrast of the films as a result of exposing to the illumination serves as the evidence for light-enhanced ion migration in perovskites.

3.3.1 Quantification

The ionic conductivity (σ_{ion}) is determined by subtracting the electronic conductance from the mixed conductance, i.e., $\sigma_{ion} = \sigma_{total} - \sigma_e$. The mixed conductivity σ_{total} in the perovskite film is obtained by performing a current–voltage (I-V) scan

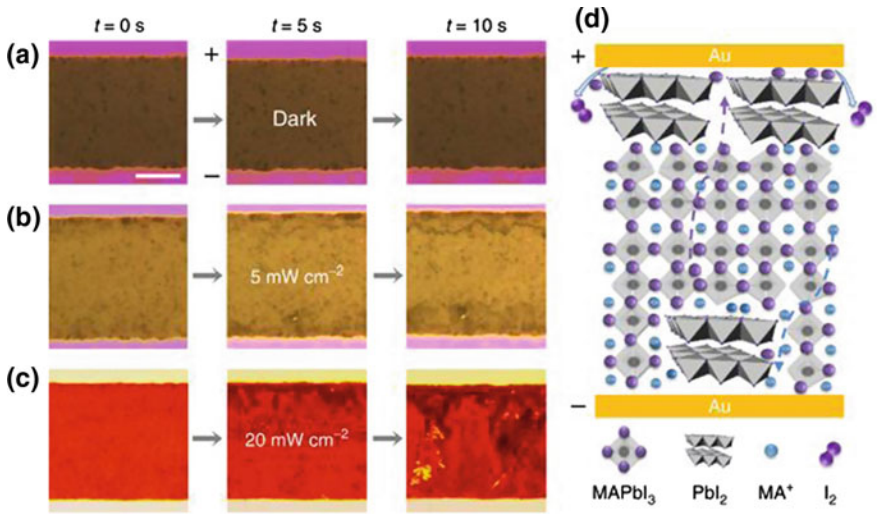

Fig. 6 **a–c** Optical dynamic images of perovskite film under electric poling and illumination of various intensities in ambient air at room temperature. **d** Schematic illustration of the ion migration of I^- anions and MA^+ cations through the film [4]. Copyright (2017) Nature. Reprinted with permission from Nature

first at the scan rate of 50 Vs^{-1} in the Au/$CH_3NH_3PbI_3$/Au device. After this, the standard technique for investigation of mixed conductors, galvanostatic characterization is performed with a sufficiently weak current to separate the pure electronic conductivity σ_e from the mixed conductivity σ_{total}. The rate-determining processes are ion migration and accumulation, whereas the electronic conductivity σ_e is used to determine the equilibrium value.

The schematic of the complete characterization of light-enhanced ionic transport is as shown in Fig. 7(a–e) [4]. In region I, initially both ions and electrons contribute to the conductance, corresponding to the fast I-V scan measurements (Fig. 7c). Subsequently, in region II only few ions contribute to the conductance of the perovskite films as these mobile ions get depleted gradually due to the accumulation at the two sides of the films (Fig. 7d). Finally, when all the mobile ions get blocked at the boundary, the conductance reaches a constant value with only electronic conductivity remaining in region III (Fig. 7e).

Zhao and group has extracted the pure electronic and ionic conductivities through the analysis described above over a wide range of illumination intensities and temperatures using the apparatus as shown in Fig. 6a. Under illumination, the screening effect produced by the photo-generated charge carriers leads to the reduction in ionization energy level. The corresponding ionization energies, under

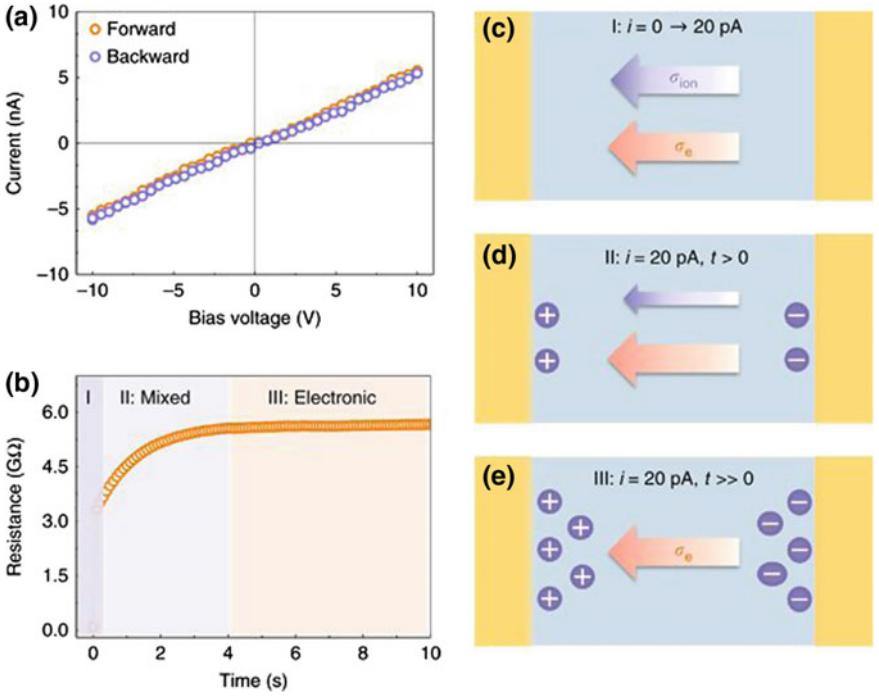

Fig. 7 Characterization method for separating the ionic conductance from the mixed conductance in the perovskite film **a** Voltage–Current (V-I) measurement of Au/perovskite/Au lateral device at 290 K under dark conditions. **b** Galvanostatic characterization of the lateral structure under dark conditions. **c–e** Schematic illustration of the conductance contribution from both ions and electrons in Regions I, II, and III, respectively [4]. Copyright (2017) Nature. Reprinted with permission from Nature

illumination intensities of 0, 0.05, 1, 5, and 20 mW cm^{-2} are 92, 84, 73, 44, and 53 meV, respectively, for the defects in the perovskite films. The semi-empirical formula is used to describe the corresponding electronic conductivity,

$$\sigma_e = ne\mu = N_d \times \exp(-\beta E_a) \times e\left(\mu_0 + aT^{-3/2}\right) + f(L_0) \times e \times \left(\mu_0 + aT^{-3/2}\right) \quad (4)$$

where N_d is the total defect concentration, β is the $1/k_BT$, k_B is the Boltzmann constant, E_a is the activation energy for the defects, a is the constant, L_0 is the light intensity, and $f(L_0)$ is the concentration of carrier generated by photo-excitation at an excitation power of L_0.

The formula describing the hopping-like mechanism of ionic transport depends on the energy barrier E_a as

$$\sigma_{\text{ion}}T = ne\mu = \frac{Z_i e^2 N_A C_{v0} D_0}{k_B V_m} \exp\left(\frac{-G_v}{5k_B T} - \frac{E_a}{k_B T}\right) = \sigma_0 \exp\left(\frac{E_a^{eff}}{k_B T}\right) \quad (5)$$

where Z_i is the ionic charge, N_A is the Avogadro's number, C_v is the concentration of intrinsic defects, V_m is the molar volume of perovskite, D is the diffusion coefficient, G_v is the formation energy of the vacancy defects, E_a is the activation energy for ionic diffusion, and E_a^{eff} is considered as excess vacancy formation energy in a vacancy-mediated mechanism.

Reflecting the reduction in activation energy for ionic transport, the corresponding slopes markedly decreases with increasing illumination intensities as seen from the linear region of the plot of $\sigma_{ion}T$ versus $1000/T$ from 140 to 295 K (Fig. 7e). There are two separate linear regions of the ionic conductance summarized in Table 1 as E_{a1} (T > 250 K) and E_{a2} (180 < T < 250 K). The E_{a1} values obtained in the range from 0.82 to 0.14 eV are assigned to MA^+ and I^-, whereas the quite small values of E_{a2} from 0.13 to 0.06 eV are assigned to H^+. For both types of ions I^-/MA^+ and H^+, as seen from the table, the activation energy shows a significant decline as the illumination intensity increases. This is consistent with the enhanced ionic conductivity observed in perovskites under high-intensity illumination. At constant external electric field, the ionic accumulation is accelerated by exposure to light because of the increased diffusion coefficient, $D = D_0 \exp\left(\frac{-E_a}{k_B T}\right)$. Therefore, ionic transport becomes facile when light intensity increases.

This behavior of enhanced ion migration upon illumination has also been verified by D. Li in his study. Continuing to his work as explained in Sect. 3, he has performed the same experiment of applying external bias for a constant time and removing across the perovskite material in dark as well as under illumination. Based on the current decay rate k_2, he calculated the ionic transport activation energy in dark and under illumination. The activation energy for ion transport under illumination (80 meV) was found to be much smaller than that in dark (260 meV), confirming that light illumination enhances the ion migration, consistent with the study done by Zhao as mentioned above. Lower activation energy for ion migration under light increases ion transport across the grain boundaries. Also, the ion-induced electric potential across the device of the perovskite thin film under

Table 1 The activation energies extracted from the ionic/electronic conductivities under different light intensities for $MAPbI_3$

Light intensity (mW cm^{-2})	E_{a1} (T > 250 K) (meV)	E_{a2} (180 < T < 250 K) (meV)	E_a (electronic) (meV)
0	Null	134	92
0.05	824	84	84
1	851	63	73
5	334	Null	44
20	144	Null	53

light illumination has been derived to be about 0.9 V, which is slightly smaller than that in dark (1.2 V). This may be attributed to the screening effect induced by photo-generated charge carriers.

3.4 Temperature Dependent

Among all the other factors responsible for the device degradation, temperature is also one of the most significant one. The temperature variations under the device operating conditions challenge the stability of the device. This may be attributed to the change in the behavior of ion migration with changes in the operating temperature as described below.

Continuing the study done by D. Li and group as in Sects. 3 and 3.1, he measured the temporal response of ionic and electronic transport at different temperatures has been explored. The external bias applied is 3 V to reach the saturation voltage. The thermally activated nature of the electronic current is verified by the exponential decay of the temperature-dependent I_1 and I_2 extracted from the temporal response curve (as explained in earlier section) with decreasing temperature. Arrhenius function is used to fit these exponential decay plots as

$$\ln(I) = C - E_a/k_B T \tag{6}$$

where I can be either the current decay (I_1 or I_2) or decay rate (k_1 or k_2), C is a constant, k_B is the Boltzmann's constant, T is the temperature, and E_a is the activation energy. The decay rate k representing the ionic transport was used to study the ionic transport dynamics. The relationship of k_1 or k_2 with T was well fitted using a single exponential function as shown in Fig. 8d. This suggests that only one type of ions (V_I) dominates the ionic transport in perovskite thin films. Otherwise, in case of contribution from more than one type of ionic species, bi- or tri-exponential function should have been used for fitting the k_1 and k_2 versus T curves.

In a more detailed study by Zhao, continuing his work as mentioned in previous section over a more wide range of temperature from 17 to 295 K is as shown in Fig. 9. There is a gradual increase in the resistance of the perovskite thin film because of slow depletion of ionic conductivity across the channel as reflected in the galvanostatic measurements at different temperatures (Fig. 9). Because of the reduced vibration frequency of ions at lower temperature, ionic relaxation time become large at low temperature and it is inversely correlated with temperature. This ionic relaxation time required to reach the steady-state resistance represents the kinetic constant k (=1/τ) for ion migration at different temperatures from 100 to 295 K.

As expected, the pure electronic resistance decreases exponentially with increasing temperature and the corresponding defect ionization appears in an obvious linear region above 150 K (Fig. 9). Also, there is a conductivity flip below

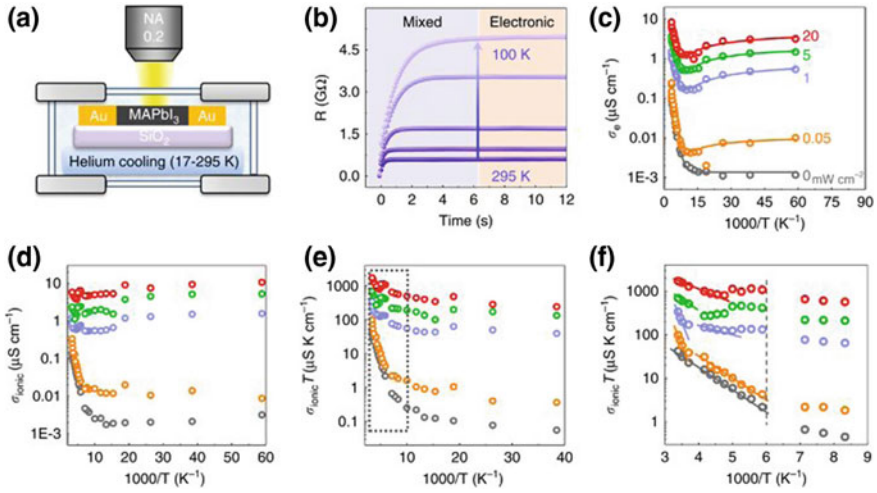

Fig. 8 Determination of electronic and ionic conductivities of perovskite film at various temperatures and various illumination intensities from 0 to 20 mW cm^{-2}. **a** The apparatus used in the experiments, with a helium cooling system. **b** Five typical galvanostatic curves (resistance vs. time) recorded at different temperatures. **c** Electronic conductivities at various temperatures from 17 to 295 K under various illumination intensities. **d** Ionic conductivities at various temperatures from 17 to 295 K under various illumination intensities. **e** Ionic conductivity multiplied by temperature, $\sigma_{ion}T$, as a function of $1000/T$ under various illumination intensities. **f** Zoomed-in view of the data in the dashed box in **e** [4]. Copyright (2017) Nature. Reprinted with permission from Nature

70 K under illumination. This behavior reflects an inverse power relationship of the mobility with the temperature as $\mu \propto T^{-3/2}$, from temperature 150 to 17 K. This is also reflected in mobility term of Eq. (5). The conductivity flip is very weak near 100 K without photo-excitation (f (L_0) = 0). This may be because of the extremely low carrier concentration near 100 K. The temperature-dependent ionic conductivity is as shown in Fig. 10 [3].

3.5 Morphology Dependent

A plethora of research is going on for the morphology optimization of perovskite thin film for the efficiency improvement of the perovskite solar cell devices. It has been reported in lot of studies that the efficiency and stability of the perovskite solar cell devices have been improved by optimizing the quality of perovskite thin-film devices. More compact, uniform, pinhole-free, and smooth films lead to more efficient and stable solar cell devices. The underlying reason behind this is the impact of large grain size, less grain boundaries, minimum vacancy concentration, and crystalline quality of the material in the device.

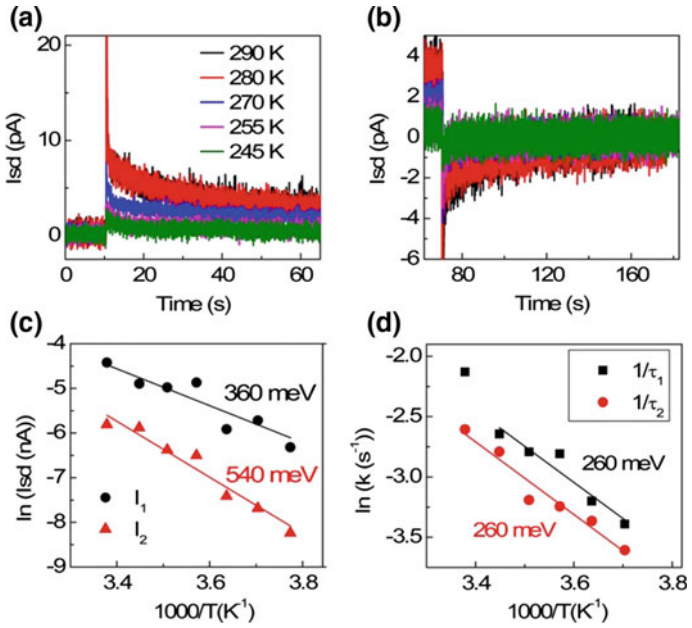

Fig. 9 Temperature-dependent temporal response in organolead halide perovskite. **a**, **b** The temperature dependance of temporal response curves for stages I (**a**) and II (**b**) under applied external bias of 3 V for the device under dark. **c** Arrhenius plots of the temperature dependence of I_1 and I_2. **d** Arrhenius plots of the temperature dependence of ion decay rate [3]. Copyright (2016). Reprinted with permission from the American Chemical Society

The perovskite grain size is expected to affect the migration of ions since the devices with larger perovskite grain size have small number of grain boundaries and lower vacancy concentration. The ion migration is mediated by the ion vacancy concentration as discussed earlier. In case of highly crystalline single crystals, the perovskite grains are bigger in size and have fewer grain boundaries. This leads to lower concentration of ion vacancy required for ion migration, and hence activation energy for ion transport is much larger in more crystalline perovskite devices. However, in less crystalline or polycrystalline perovskite thin films, reduced grain size leads to larger grain boundaries and more defects in terms of ion vacancies. Therefore, perovskite thin films have more defects and ion vacancy as compared to the single crystals and facilitate ion migration. This enhanced ion migration in polycrystalline thin films leads to device degradation. Hence, a lot of research is going on to fabricate more crystalline perovskite thin-film devices to enhance device stability and efficiency.

Li and group also performed the same temporal response study (Sect. 3) on nearly single-crystalline microplate devices along with polycrystalline perovskite thin films with grain size typically of the order of 10 nm (Fig. 11) [5]. The perovskite thin films devices are fabricated by conventional spin-coating technique,

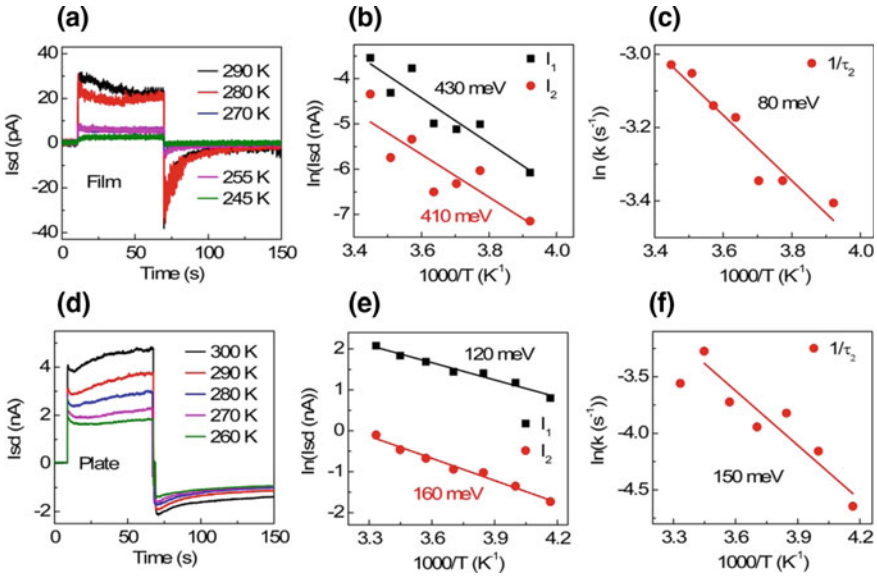

Fig. 10 Comparisons of the temperature-dependent temporal response in organolead halide perovskite film and microplate devices under illumination. The temperature dependence of the temporal response curves under the applied external bias of 3 V in the halide perovskite film device (**a**) and microplate device (**d**) under white light illumination. Arrhenius plot of the temperature dependence of I_1 and I_2 and ion decay rate k_2 in the halide perovskite film device (**b**, **c**) and microplate device (**e**, **f**) [3]. Copyright (2016). Reprinted with permission from the American Chemical Society

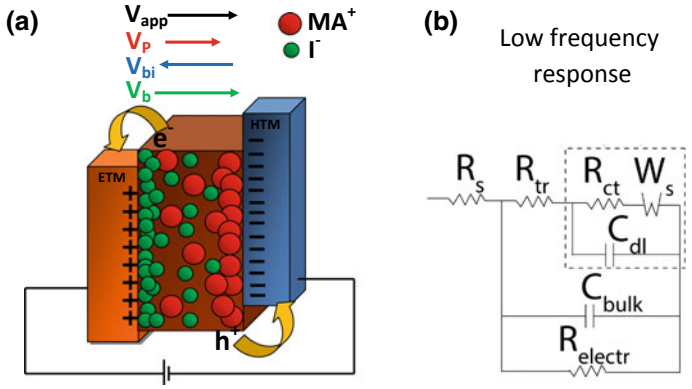

Fig. 11 **a** Schematic of the different fields V_b, V_{bi}, V_P, and V_{app} inside the perovskite material. **b** The equivalent circuit model of the device [5]. Copyright (2018). Reproduced with permission from the American Chemical Society

while the microplate devices are obtained by vapor-phase intercalation approach with larger grain sizes of micrometer-scale and fewer grain boundaries. Due to high crystalline quality of microplates with few defects leading to the lack of intrinsic charge carriers (electrons and holes), there is not any detectable dark current either under the applied bias V_{sd} or under the ion-induced potential, and hence transient measurement under illumination has been conducted to investigate the ionic and electronic charge dynamics in microplates.

3.6 Electronic and Ionic Transport Dynamics in Organolead Halide Perovskites

The ion migration activation energy is about 150 meV in microplate devices and about 80 meV in perovskite thin-film devices. The ionic transport rate in perovskite microplate devices is only about 10–25% than that in thin films.

The ion transport activation energy in microplates is considerably larger as compared to the thin-film devices. This large difference between the ionic migration energies of the microplates and films can be attributed to the better crystalline quality with larger grain size and fewer grain boundaries along with significantly reduced concentration of vacancy in microplates when compared with polycrystalline thin films. Therefore, ionic transport is highly suppressed in crystalline microplate devices; however, electronic transport is much easier than that in thin films. This is suggested by the low electronic transport activation energy in microplate devices (120–160 meV) as compared to that in thin-film devices (430 meV), which may be due to reduced scattering and charge trapping states at fewer grain boundaries in nearly single-crystalline microplates structure. More importantly, the higher ion migration activation energy and lower vacancy concentration leads to a considerably smaller ion-induced electric field of 0.3 V in the microplates (Vs 0.9–1.2 V in thin-film devices) and greatly suppressed hysteresis in current–voltage curves. Therefore, the improved crystalline quality of the material can significantly reduce the ionic transport, suppress or eliminate hysteresis, enhance electronic transport, and upgrade the efficiency and stability of the organolead halide perovskite solar cell devices.

4 Charge Transport Dynamics in Organolead Halide Perovskite Solar Cell (Device Geometry)

As discussed in the earlier section, in the absence of any ETM and HTM, there is no initial driving force for ion migration in the Au/$CH_3NH_3PbI_3$/Au device geometry. Therefore, the ions are either moving randomly or are at rest in the absence of any external disturbance. There is no net charge transport and accumulation in this case.

However, in perovskite solar cell device due to the presence of ETM and/or HTM, there is an initial driving force for the charge carriers created by the potential difference between ETM and HTM across the device.

In the device geometry of perovskite solar cells, the electron and hole transport layers are at different potentials creating a potential difference across the device (Fig. 11a). The absolute value of this potential difference between ETM and HTM across the device in the absence of any external bias is called **built-in potential** or **built-in voltage ($\mathbf{V_b}$)**. This acts as the initial driving force for the migration of ions in perovskite. As a response to this V_b, the ions MA^+ and I^- start migrating even in dark and no-bias conditions. The V_b is in the direction from ETM to HTM, and hence positively charged MA^+ ions migrate toward HTM and negatively charged I^- ions migrate toward ETM accumulating at the corresponding electrodes. The accumulation of ions at these respective transport layers results in the modification of original built-in voltage. As the positively charged MA^+ is at HTL and the negatively charged I^- is at ETL, the resultant modified built-in field is from HTM toward the ETM (opposite to the direction of original V_b). Let this field created after modification of original built-in field due to the accumulation of ions at the respective electrode be effective **built-in field ($\mathbf{V_{bi}}$)**. This field plays an important role in deciding the kinetics of ion migration in the presence of external disturbance.

In the presence of illumination, the charges (electrons and holes) induced due to light are known as photo-carriers or photo-generated charge carriers. On application of external forward bias, the electrons move toward the ETM and holes migrate toward HTM leading to **photoinduced voltage ($\mathbf{V_P}$)** due to this charge transfer. The direction of this V_P is from ETM to HTM, opposite to the effective built-in field (V_{bi}), and hence it tries to discharge the ions accumulated as a response to the original V_b under dark conditions. The interplay between these effective built-in field (V_{bi}), photoinduced voltage (V_P) and applied bias (V_{app}) decides the migration kinetics of ions in the perovskite material. Now under the combined effect of all abovementioned fields (V_{bi}, V_p, and V_{app}), the charges (ions and free electrons and holes) can follow different paths leading to the different behaviors of transport at the interface and bulk (Fig. 11a). Considering the charge transport in detail, the first and very common resistance in the path is contact resistance mostly due to connections of the device, from ETM and/or HTM and from the measurement apparatus itself ($\mathbf{R_s}$).

After the charges have entered the device, they follow different paths attributed to their thermodynamics and kinetics. Most of the free charges electrons and holes due to their high mobility either pass easily or recombine facing the resistance due the charges at the interface and bulk known as electronic resistance ($\mathbf{R_{electr}}$). Some of the charges (mostly ions) get stored in the bulk of the perovskite layer and accumulate there due to the existing fields in the bulk leading to a capacitive behavior at the bulk ($\mathbf{C_{bulk}}$). The remaining free charges (electrons and holes) do not pass through the device easily as they are coupled with ion diffusion and accumulation at the interface. These free charges along with the coupled ions face the recombination/transport resistance ($\mathbf{R_{tr}}$) at the interface. After that, these ions along with associated free charges either get accumulated at the interface due to

charge trapping and storage leading to the capacitive behavior at the interface or pass through the interface. The charge accumulation at the interface leads to the formation of a double-layer capacitance ($\mathbf{C_{dl}}$). In the transport of ions and the associated free charges across the interface, there is transfer of charge as well as mass across the interface due to the ions. The charge transfer faces the resistance due to imperfect electrode contacts arising from imperfect films and double-layer capacitance known as interfacial charge transfer resistance ($\mathbf{R_{ct}}$) and mass transfer is hindered by Warburg impedance ($\mathbf{W_S}$) in Warburg ion diffusion across the interface. Considering this model of charge transport, the kinetic across the interface is modeled in form of an electrical circuit as shown below (Fig. 11b).

Generalized Warburg diffusion W_S is defined by the equation

$$W_S = A_W \frac{\tanh(j\omega T_W)^P}{(j\omega T_W)^P} \tag{7}$$

where T_W is the Warburg time constant; A_W is the Warburg impedance; and the exponent P is ~ 0.5 for finite-length Warburg diffusion. Warburg diffusion arises due to alkyl ammonium ion migration across the interface in hybrid perovskites, and hence it is a low-frequency component as described below.

As stated earlier, the hybrid organic–inorganic perovskite materials are mixed ionic–electronic conductors. This means that there is transport of ions as well as free carrier electrons and holes simultaneously in the device. Therefore, it is difficult to study the transport of only ions by normal techniques as they don't distinguish between ionic and electronic charge transport. However, Electrochemical Impedance Spectroscopy (EIS) is a powerful and nondestructive technique to study the ion transport processes in such mixed ionic–electronic conductors. EIS is able to distinguish between ionic and electronic charge transports as it allows the separation of the processes that occur on different time scales by examining the current response over a range of AC voltage frequencies. The alkylammonium ions are heavy and low in mobility transfer across the material in longer time (tens of milliseconds) as compared to the electrons (<1 μs). Therefore, the high-frequency spectrum is attributed to the impedance arising from the electronic transport and the low-frequency component is attributed to the impedance arising either from charge or mass transfer at the interface or Warburg ion diffusion. However, the time scale associated with iodine ion migration (<1 μs) is comparable to that of electronic transport. Therefore, the impedance response of iodine ion transport too is attributed to the high-frequency component of the spectrum and overlaps with the electronic response in the high-frequency semi-circle. Therefore, the low-frequency component of the EIS spectrum is only because of the alkylammonium ions in hybrid perovskites.

In the presence of external disturbance such as applied bias, illumination, and temperature, the migration of these ions is varied. This variation in the ion migration as a result of external disturbance is discussed below.

4.1 Bias Dependent

On application of forward bias to perovskite solar cells under illumination, the direction of applied bias (V_{app}) inside the perovskite material is in the direction from ETM to HTM. Since the direction of V_{app} is same as that of V_P and hence V_{app} adds to existing V_P, this added field induces further redistribution of ions throughout the bulk of the material. Therefore, V_{app} and V_P acting in same direction add up and compete with the oppositely directed V_{bi} and induce further redistribution of ions throughout the bulk and migration across the device.

Due to the interplay between these three fields, the nature of net field acting changes depending on the magnitude of applied bias V_{app} (Fig. 12). Let the net field acting across the material be denoted by V_{net}. This V_{net} is defined as resultant of all the three acting fields described above, i.e., $V_{net} = V_{bi} - (V_P + V_{app})$. Depending on the relative magnitude of these three fields, the behavior of ion transport across

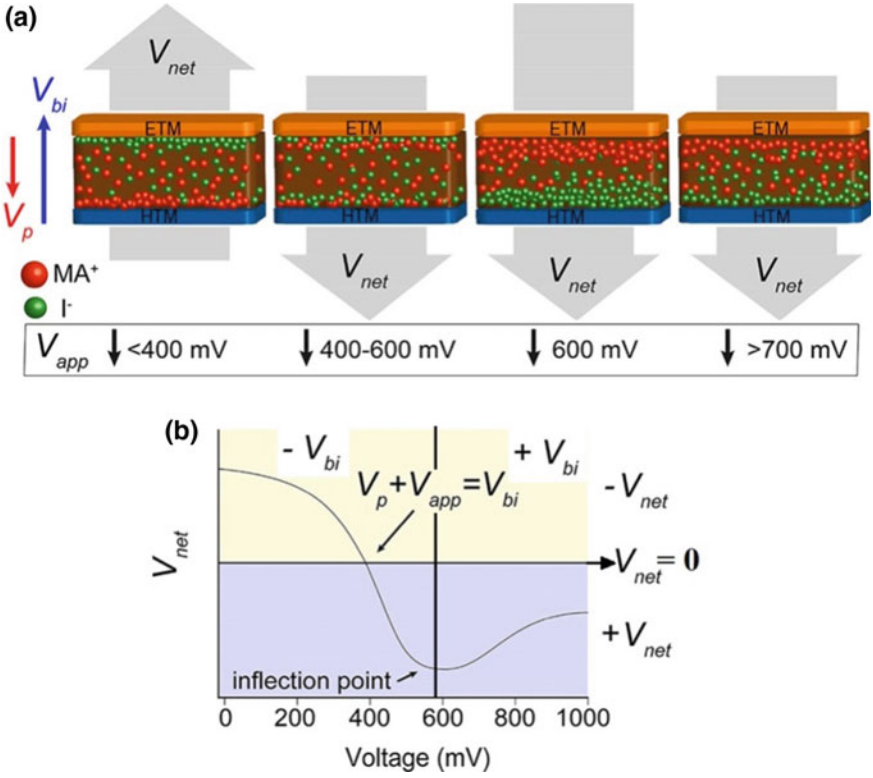

Fig. 12 **a** Schematic of the response in a perovskite device under the varying applied bias (V_{app}) as a result of interplay between V_{bi}, V_P, and V_{app}. **b** A qualitative representation of the magnitude shifts in V_{net} as a function of V_{app} [5]. Copyright (2018). Reproduced with permission from the American Chemical Society

the material can be described by considering three distinct response regions: in the low, medium, and high levels of V_{app} (Fig. 12a). In the beginning in the absence of any applied bias, the MA^+ ions are at HTM and I^- ions are at ETM as a response to the original built-in field (V_b) giving rise to effective built-in field (V_{bi}) as discussed earlier.

When the low level of V_{app} is applied, the added effect of V_P and V_{app} tries to compete and discharge the ion accumulation as a result of original built-in field (V_b). But this added field is not much higher in magnitude to affect the charge accumulation much. Therefore, the ions remain at their initial position and do not move much. However, as the V_{app} increases, the screening of the charges accumulated starts.

At a certain point, when the $V_P + V_{app}$ becomes equal to V_{bi} there will be no net directional driving force to induce ion migration. On increasing V_{app} beyond this point applying medium levels of V_{app}, the sum of V_P and V_{app} becomes more than V_{bi} and there is reversal in the direction of V_{net}. This reversal of the driving force will lead to the redistribution of ions and re-accumulation at the opposite electrodes of the device. Now, after reversal of V_{net} the MA^+ and I^- ions will start moving toward the ETM and HTM, respectively. These ions start getting accumulated there with increasing V_{app} in the medium level of V_{app}. As the ions start to accumulate at the opposite electrodes of the device, there is buildup of Coulombic potential and decay of effective V_{bi}. As the V_{app} increases, the Coulombic potential in the direction opposite to V_{bi} increases and V_{bi} decreases leading to continuous increase in V_{net} in the reverse direction.

At the end of the medium region, the ions get completely accumulated at the opposite electrodes. This means all the MA^+ ions get accumulated at ETM and all the I^- ions get accumulated at HTM. At this point, the effective built-in potential (V_{bi}) is generated again, but with opposite polarity. Since the positively charge MA^+ ions are at ETM and negatively charged I^- ions are at HTM, the direction of effective built-in field (V_{bi}) now is from ETM to HTM. Therefore, after this point, all the acting fields V_{bi}, V_P, and V_{app} are in the same direction and all will add up. This point at which V_{bi} changes polarity due to accumulation of ions at opposite electrodes is known as inflection point. On applying high level of V_{app}, V_{net} will increase further in the direction of V_P. At higher levels of V_{app}, V_{bi} gets saturated after all the ions got accumulated, and hence there is no further significant increase in V_{net}.

Therefore, these three regions can also be defined in terms of two significant points described above. The region starting from the zero volts to the point where $V_P + V_{app}$ become equal to V_{bi} is designated as low level of V_{app}. From this point ($V_P + V_{app} = V_{bi}$) to inflection point is the region of medium level of V_{app}, after the inflection point is higher level of V_{app}. For ITO/PEDOT: PSS/$MAPbI_3$/PCBM/Ca/Al device geometry, these regions come out to be as low (0–400 mV), medium (400–600 mV), and high (>600 mV) levels of V_{app} from experimental observations. In all these three regions, the parameters (C_{dl}, C_{bulk}, and A_W) described earlier changes with the change in distribution and migration of ions. The trends in circuit elements at low and high levels of applied bias are opposite in nature. The inflection

point is seen in the medium level of applied bias and the voltage at this point corresponds closely to the voltage at maximum power point of the device (V_{mpp}). These trends are attributed to the ion migration through the bulk and ion accumulation at the interfaces of the device as described below.

The double-layer capacitance (C_{dl}) and bulk capacitance (C_{bulk}) are associated with the accumulation of ion at the interface, and the resulting redistribution of electronic charges in the bulk, respectively. This type of ion buildup at the interface and in bulk may also pin electron charges and thus these can contribute to the absolute values of the capacitance. As already explained earlier, at low level of V_{app}, the distribution of ions is not much disturbed and they stay where they are until the V_{app} is increased further. Therefore, at low V_{app} there is very minimal change in both C_{dl} and C_{bulk} in the device with a certain degree of active layer degradation. At the low level of V_{app}, the ETM being positively charged under forward external bias attracts the I^- ions more toward itself with increasing voltage. Due to increase in the number of defect sites in the bulk, the ions are more mobile in the bulk leading to increase in the buildup of ions at the interface faster. This results in decreasing the depletion width at the interface leading to steady increase in the double-layer capacitance (C_{dl}) as the bias increases in this region. This kind of redistribution of ions at the interface induces changes in ion distribution within the bulk leading to a steady increase in the C_{bulk} too. The C_{dl} increases by $\sim$900%, whereas there is very modest increase in C_{bulk} of $\sim$42%, This may be attributed to the fact that effect of applied forward bias (V_{app}) is more near the interfaces as compared to in the bulk. Therefore, the redistribution of ions is more effecting at the interface than in the bulk leading to more significant change in the C_{dl} as compared to the C_{bulk}. At the point $V_P + V_{app} = V_{bi}$, the ions start moving toward the opposite interfaces leading to the discharging of interfacial ion accumulation and hence the capacitance C_{dl} at the interface during the medium region of V_{app}. Therefore, after this point there is continuous decrease in the value of C_{dl} in the medium V_{app} region. However, the value of C_{bulk} is still increasing during the discharging of C_{dl}. This may be attributed to the fact that discharging of ions accumulated at interface and their motion toward the opposite interface leads to accumulation of these ions in the bulk with decreasing depletion width for C_{bulk} for a short time interval during their motion toward the opposite electrode. This leads to steady increase in C_{bulk} during this interval at medium V_{app}. This means discharge of C_{dl} is accompanied by charge redistribution within the bulk leading to increase in the C_{bulk} during discharging of C_{dl}. This is the reason why the maximum value of C_{bulk} appears at higher V_{app} than the C_{bulk} maximum. At high V_{app}, the value of C_{bulk} starts decreasing after the inflection point is reached as the charges have already moved to the opposite electrodes and accumulated there. Also, there is continuous decrease in the value of C_{dl} since the point $V_P + V_{app} = V_{bi}$ till about the inflection point. After the inflection point, the value of C_{dl} decreases to its lowest value and saturates accompanying the continuous decrease in C_{bulk} during this time. At higher voltage, the value of C_{bulk} also starts saturating after reaching its lowest value attributed to saturation in the value of V_{bi} in this region of high V_{app}. Therefore, the maxima in C_{dl} occurs at the point $V_P + V_{app} = V_{bi}$ and the

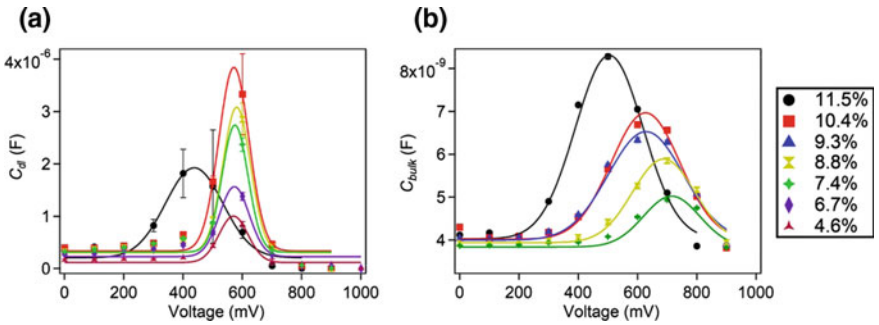

Fig. 13 Values for **a** double-layer capacitance (C_{dl}) and **b** bulk capacitance (C_{bulk}) from EIS equivalent fit circuit elements plotted as a function of DC bias at different device power conversion efficiencies [5]. Copyright (2018). Reproduced with permission from the American Chemical Society

maxima in C_{bulk} occurs at inflection point. As explained above, there is reversal in the trends of both double-layer and bulk capacitance at low and high level of V_{app} (Fig. 13). This can be attributed to the opposite nature of ion migration occurring in the two regions. At low level, the ions are accumulating more at their respective initial electrodes; however, at high level of V_{app} the ions are discharging and accumulating at opposite electrode. The direction of V_{bi} is also opposite in both the regions with respect to V_P. All these opposite trends of ion migration lead to the opposite trends in the circuit elements at low and high biases.

As discussed earlier, the ions are not much mobile at low V_{app}. On increasing the bias, they start discharging and moving in the opposite direction. Under higher biases in medium and high levels of V_{app}, they become more mobile. Therefore, Warburg impedance (A_W) and Warburg time constant (T_W) decrease on increasing V_{app} (Fig. 14). In the low V_{app} region, the ions don't significantly move. Hence, the A_W and T_W are almost constant and don't change much in this region. However, after the point $V_P + V_{app} = V_{bi}$, the ions start moving in opposite direction more significantly, and hence there is appreciable decrease in A_W and T_W after this point. Again at much higher bias, there is saturation in ion motion after they have reached the opposite interfaces and accumulated there. This leads to the constant A_W and T_W again at much higher bias.

Diffusion coefficient (D) and ionic conductivity (σ_{ion}) for the mobile ions can be estimated from T_W and A_W, respectively, using the following equations.

$$D = \frac{L_D^2}{T_W} \tag{8}$$

$$\sigma_{ion} = \frac{d}{a \times A_W} \tag{9}$$

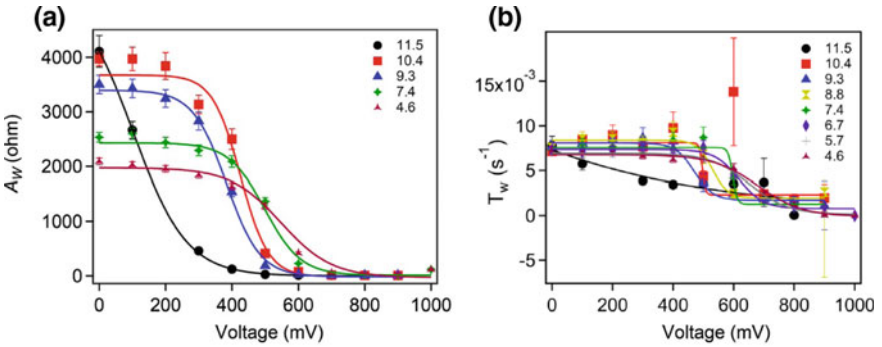

Fig. 14 **a** Warburg resistance (A_W) and **b** Warburg time constant (T_W) as a function of bias at different PCEs [5]. Copyright (2018). Reproduced with permission from the American Chemical Society

where L_D is the effective ion diffusion length, corresponding to the film thickness, a is the device active area, and d is the effective thickness of the active layer.

The effective diffusion coefficient and ionic conductivity remains constant at lower biases and steadily increase after the point $V_P + V_{app} = V_{bi}$ with increase in V_{app} as expected because of the similar reasons described above (Fig. 15).

4.2 Illumination Dependent

As discussed in the previous section, the fields responsible for the migration of ions in the hybrid perovskite materials are V_{bi}, V_P, and V_{app}. Under dark condition, the photo-generated field V_P will be absent. In this case, even after applying bias V_{app}, there will not be any ion transport. V_{app} alone will not be able to overcome V_{bi} to move ions to the opposite interfaces as described earlier. Therefore, the EIS plots under dark condition will show only a single charge transport regime at low forward

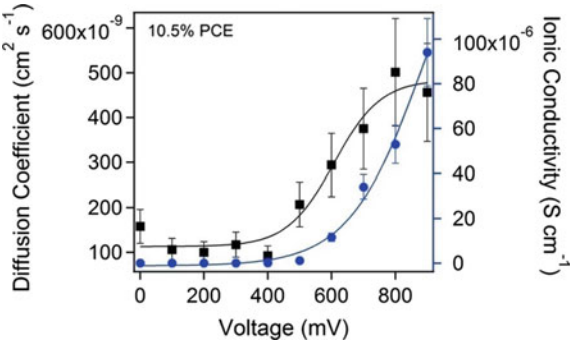

Fig. 15 Ionic diffusion coefficient (black, left) and ionic conductivity (blue, right) as a function of applied bias for device with PCE 10.5% [5]. Copyright (2018). Reproduced with permission from the American Chemical Society

bias voltage which is high-frequency spectrum attributed to impedance arising from electronic transport (Fig. 16a) [6]. However, the low-frequency spectrum attributed to the impedance arising from charge and mass transfer at the interface or Warburg diffusion will not be present. This indicates that only one type of charge transport (electronic) is predominant under dark conditions. The low-frequency component in EIS arises only in the illuminated perovskite associated predominately with the diffusion of ions (Fig. 16b).

In addition to the above effect of illumination on charge transport, the type of illumination also plays important role in ion migration dynamics. Comparing three types of light sources AM 1.5 G solar simulator, commercial white-LED light, and IR-only source (150 W commercial IR lamp), there is significant decrease in the low-frequency ion transport component under white-LED illumination [6]. The white light used does not emit IR or UV components. This indicates that ion transport is slower under white-LED as compared to solar simulator and IR-only source. Also, a lattice expansion is observed in the perovskite crystal (Fig. 17a) in case of solar simulator and IR-only source measured at operating temperature. However, no such structural lattice change occur when the device is exposed to white-LED alone at measured operating temperature of 28 °C (301 K). However, this transition reverses when the illumination is turned off. This reversible nature of device degradation is discussed in more detail in the upcoming section.

4.3 Temperature Dependent

As obvious, increasing the temperature will enhance ion migration and lead to faster degradation of the device. With increase in temperature, the activation energy for

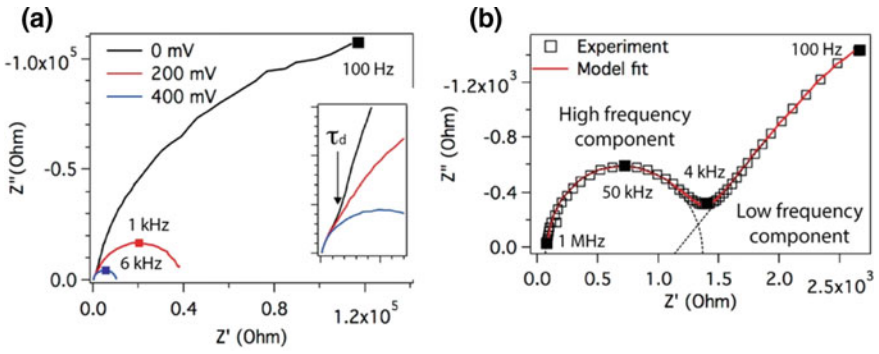

Fig. 16 **a** Nyquist plot of $MAPbI_3$ samples under dark. Inset: High-frequency component showing transport regime. **b** EIS plot of $MAPbI_3$ sample at 45 °C at 100 mW cm^{-2} light intensity and 0 V applied bias showing both high- and low-frequency components [6]. Copyright (2015). Reproduced with permission from the American Chemical Society

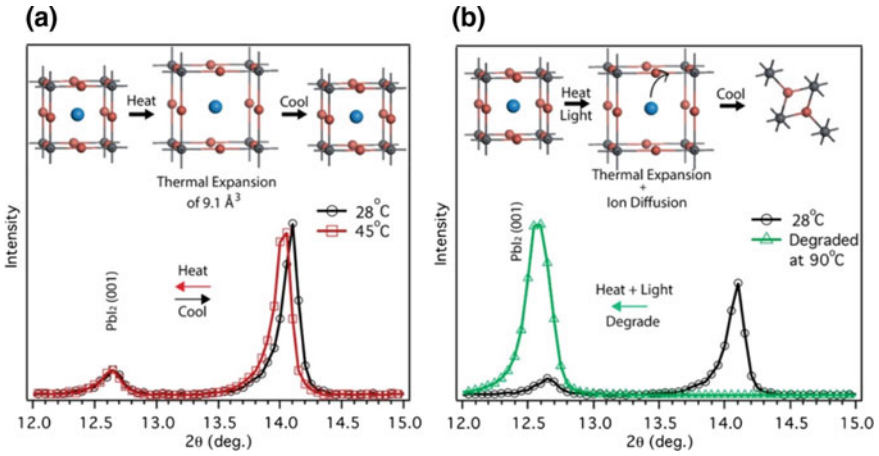

Fig. 17 **a** PXRD of $MAPbI_3$ sample at room temperature (28 °C) and after heating with infrared lamp (~45 °C) in dark. The process is reversible once the device gets cooled. **b** PXRD pattern of perovskite sample after prolonged heating in the presence of visible light, showing degradation of perovskite to PbI_2 structure [6]. Copyright (2015). Reproduced with permission from the American Chemical Society

ion migration decreases and ions became more mobile. This leads to easier ion transport inside the device and hence easier degradation.

On heating the perovskite device, lattice expansion is seen as discussed in previous section (Fig. 17b) leading to the conversion of $CH_3NH_3PbI_3$ perovskite to PbI_2 on further cooling. This transformation is not reversible as in case of illumination induced expansion. This may explained as the MA^+ ions after migration to one electrode breaks the bond with the crystal and evaporate at higher temperature leaving the lattice. Only Pb^{2+} and I^- ions are left in the sample and they combine to form PbI_2.

The activation energy (E_a) for ion diffusion can be estimated by the following relationship:

$$\frac{1}{T_W} = \frac{kT}{h}\frac{a^2\alpha}{L_D^2}\exp\left(\frac{-E_a}{kT}\right) \tag{10}$$

where a is the lattice parameter for the perovskite, α is the coordination factor, and h is the Planck's constant.

As seen in Fig. 18, there is a discontinuity in Arrhenius-like behavior of ionic transport in $CH_3NH_3PbI_3$. This discontinuity may be attributed to the discontinuous volume change induced by a phase transition during lattice expansion. Also, as measured from the Arrhenius plot, the activation energy for ion migration is high at low temperature and it reduces significantly at higher temperature enabling the ease of ion migration at higher temperature in $CH_3NH_3PbI_3$.

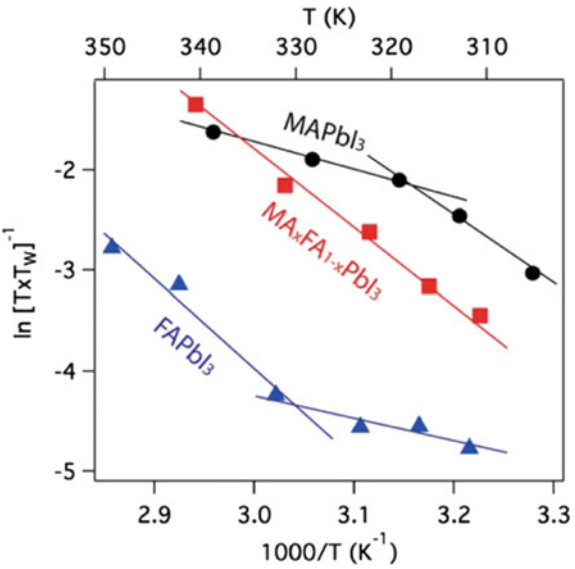

Fig. 18 Arrhenius-like plot of $1/(T \cdot T_W)$ versus T^{-1} for $MAPbI_3$, $FAPbI_3$, and $MA_xFA_{1-x}PbI_3$ [6]. Copyright (2015). Reproduced with permission from the American Chemical Society

4.4 Size of Alkyl Ammonium Ion Dependent

The movement of ions also depends on the size of ion. The larger the size of the ion, the lower will be its mobility. Comparing the $MAPbI_3$, $MA_XFA_{1-X}PbI_3$, and $FAPbI_3$ perovskites, the migration of FA^+ will be more difficult as compared to their counterparts in $MAPbI_3$ and $MA_XFA_{1-X}PbI_3$. The ionic diffusion coefficients follow the order of MA > MA_XFA_{1-X} >> FA. This means the diffusion coefficient is decreasing with increasing size of the ions. Ionic transport is slower in the perovskite with large-sized cation. Due to this reason, $FAPbI_3$ and $MA_XFA_{1-X}PbI_3$ are more stable than $MAPbI_3$ devices.

Also, $MA_XFA_{1-X}PbI_3$ does not undergo any kind of lattice expansion and structural phase transition. Their thermal expansion is quite low as compared to that of $MAPbI_3$. This can be seen in the Arrhenius plot (Fig. 18). The ionic diffusion in mixed system follows continuous Arrhenius behavior. For $MA_XFA_{1-X}PbI_3$, the same activation energy was observed for all the temperatures. Arrhenius plot for $FAPbI_3$ is also discontinuous indicating the phase transition. However, $FAPbI_3$ devices are stable attributed to their low diffusion coefficient.

5 Stability Issues

Despite tremendous progress in terms of device efficiency, perovskite-based materials lack stability especially under sunlight. The key issue of photoinduced degradation of perovskite-based solar cells prevents it from immediate

commercialization. There has been plethora of research to understand the degradation mechanism of perovskite-based solar cells under environmental condition. One of the common reasons for degradation of perovskite solar cells observed experimentally by multiple groups is the migration of mobile ions through the bulk of the film. The factors affecting the migration of ions and the overall device stability are discussed in the following sections.

5.1 Role of Organic Cation

It has been observed that the methylammonium lead triiodide degrades more rapidly than formamidinium lead triiodide-based perovskite devices or even a mixed cationic system due to the lower activation energy (shown in the table below) of methylammonium ions. The migration of ions can be even faster due to lattice expansion when the device is exposed to heat. $MAPbI_3$ transforms from tetragonal to cubic symmetry when it is heated up to 55 °C and the activation energy drops due to significant volume expansion of the lattice. A systematic study of perovskite solar cells reveals that the photodegradation under room light (no infrared component) is relatively low compared to the device exposed to sunlight or the device is exposed to room light at elevated temperature. By replacing methylammonium ion to a bigger ion like formamidinium or caesium or the combination of all three resulted in not only higher stability under dark condition but also the photostability in perovskite solar cells. The degradation is quasi-reversible as some of migrated ions diffuse back into the lead halide octahedral cadge once the illumination is off. However, due to the trapping of ions at the grain boundaries as well as at the ETL or HTL interfaces result in gradual drop in device efficiency.

5.2 Role of Halide Ion

Although lead triiodide-based perovskites have shown the highest reported efficiency in the literature, the stabilities of such devices are poor compared to that of lead tribromide-based perovskite devices. Lead bromide has a shorter and stronger bond than lead iodide due to the smaller ionic radius of Br (1.96 Å) than iodine (2.2 Å). Therefore, the free volume of the octahedral cadge is less in case of lead tribromide perovskites. Furthermore, the crystal structure of $MAPbBr_3$ at room temperature is densely packed cubic structure with $Pm\bar{3}m$ space group, whereas $MAPbI_3$ is disordered tetragonal with $I4/mcm$ space group. The activation energy required to migrate either halide ions or the organic cations can be significantly increased by shortening the lead–halide bond length with less amount of free space available for ion migration (Table 2).

Table 2 Activation energy of ions as reported by different groups

References	$MAPbI_3$			$MAPbBr_3$		$FAPbI_3$		
	Defect		E_a (eV)	Defect	E_a (eV)	Defect		E_a (eV)
[1]	V_I		0.08 (0.16)	V_{Br}	0.09			
	V_{MA}		0.46	V_{MA}	0.56			
	V_{Pb}		0.80	V_{Pb}	–			
	I_i		0.08 (0.16)					
[2]	V_I		0.58					
	V_{MA}		0.84					
	V_{Pb}		2.31					
[3] (Fig. 2.3)	V_I/V_I^+	Path P1	0.32/0.33			V_I/V_I^+	Path P1	0.55/0.50
		Path P2	0.44/0.45				Path P2	0.48/0.42
	V_{MA}/V_{MA}^+	Path P3	0.57/0.55			V_{FA}/V_{FA}^+	Path P3	0.61/0.57
		Path P4	0.89/0.89				Path P4	0.61/0.59
[4]	V_{MA}	<320 K	0.58	$\mathbf{MA_xFA_{1-x}PbI_3}$		V_{FA}	Operating Temp.	0.22
				V_{MA}/V_{FA}	0.63			
		>320 K	0.23				Higher Temp.	0.79

5.3 *Role of Crystal Size and Purity*

The photodegradation of perovskite nanocrystals is visualized by super-resolution luminescence microspectroscopy. Photoluminescence spectrum represents the crystal structure and its purity. The optical band gap of perovskite materials depends on the lead–halide–lead angle. If the angle is maximum, i.e., 180°, the band gap is minimum. As defect density of states increases, the bond angle decreases, and hence the band gap increases. Completely degraded structure will have bond angle of 120°. Therefore, by monitoring the PL spectrum, the structural changes are observed. It is also observed that the degradation rate of perovskite nanocrystals at its initial stage is slow and the photoluminescence remains unperturbed till the crystals starts to degrade rapidly. A three-dimensional perovskites then degrade into two-dimensional lead halide structure as shown in Fig. 19 [7]. Corresponding emission spectrum shows a gradual blueshift. Initial slow degradation is due to lack of defect sites present in the crystals; therefore, the migration of ions or vacancies is much slower. However, as the nanocrystal degrades, more number of defects sites, mostly vacancies get created. Increased defect density of states not only increases the ion mobility by opening up new pathways for ion migration, but also increases the probability of rapid collapse of the structure itself.

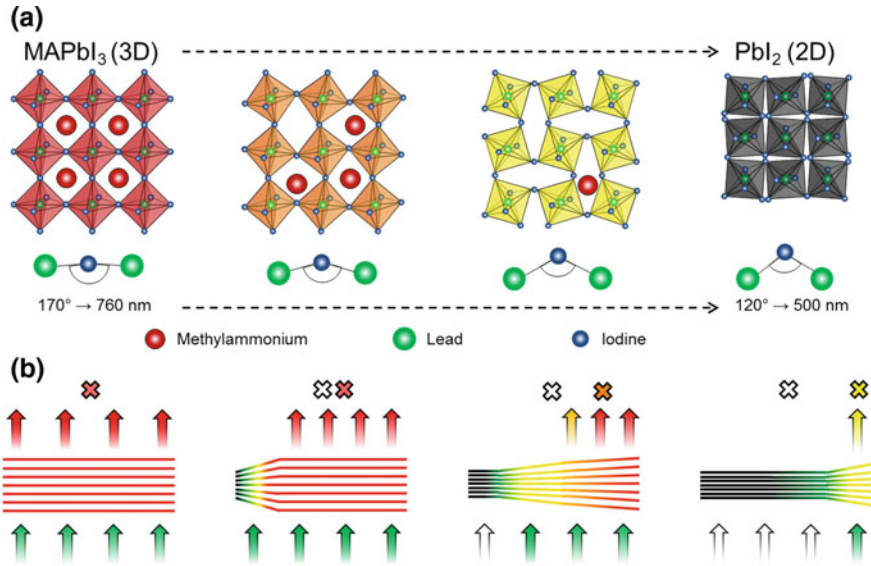

Fig. 19 Schematic representation of $MAPbI_3$ nanocrystal degradation under light exposure [7]. Copyright (2016). Reproduced with permission from the American Chemical Society

6 Conclusion

Ion transport in lead halide-based perovskite materials is unavoidable but can be minimized by many ways described in this chapter. The main cause of photodegradation in these materials is migration of ions, and hence it is important to stop the ion conductivity by reducing ion vacancies, increasing the size of cations, or by reducing space for ion migration. There have been numerous reports with strategy to improved photostability of perovskite solar cells. Clear understanding of ion migration in these mixed conductors will further help us to improve the photostability of lead halide-based perovskite solar cells for commercial utilization.

References

1. Azpiroz JM, Mosconi E, Bisquert J, De Angelis F (2015) Defect migration in methylammonium lead iodide and its role in perovskite solar cell operation. Energy Environ Sci 8:2118–2127
2. Haruyama J, Sodeyama K, Han L, Tateyama Y (2015) First-principles study of ion diffusion in perovskite solar cell sensitizers. J Am Chem Soc 137:10048–10051
3. Li D, Wu H, Cheng HC, Wang G, Huang Y, Duan X (2016) Electronic and ionic transport dynamics in organolead halide perovskites. ACS Nano 10:6933–6941

4. Zhao YC, Zhou WK, Zhou XU, Liu KH, Yu DP, Zhao Q (2017) Quantification of light-enhanced ionic transport in lead iodide perovskite thin films and its solar cell applications. Light Sci Appl 6:e16243
5. Smith Emily C, Ellis Christie L C, Javaid Hamza, Renna Lawrence A, Liu Yao et al (2018) Interplay between ion transport, applied bias and degradation under illumination in hybrid perovskite p-i-n devices. J Phys Chem C 122(13986):13994
6. Bag M, Renna LA, Adhikari RY, Karak S, Liu F, Lahti PM et al (2015) Kinetics of ion transport in perovskite active layers and its implications for active layer stability. J Am Chem Soc 137:13130–13137
7. Merdasa Aboma, Bag Monojit, Tian Yuxi, Källman Elin, Dobrovolsky Alexander, Scheblykin Ivan G (2016) Super-resolution luminescence micro-spectroscopy reveals mechanism of photo-induced degradation in $CH_3NH_3PbI_3$ perovskite nano-crystals. J Phys Chem C 120:10711–10719

Chapter 6
Perovskite Materials in Batteries

John Henao, Yilber Pacheco and Lorenzo Martinez-Gomez

1 Introduction to Perovskite Materials

Perovskite materials have been extensively studied since past decades due to their interesting capabilities such as electronic conductivity, superconductivity, magnetoresistance, dielectric, ferroelectric, and piezoelectric properties [1, 2]. Perovskite materials are known for having the structure of the $CaTiO_3$ compound and have the general formula close or derived from ABO_3. Interestingly, perovskite materials can accommodate around 90% of metallic elements of the periodic table at positions A and/or B, maintaining the characteristic perovskite structure. This fact is incredibly advantageous for creating various combinations and allows obtaining compounds with a wide range of properties due to the complete or partial substitutions of cations [3].

Perovskite materials have been widely explored in applications related to their electrical, optical, and magnetic properties. They have been also used for the control of environmental pollution due to their thermal stability and catalytic properties. Other applications include sensing and adsorption of various aqueous and gas-phase

J. Henao (✉)
CONACYT-CIATEQ A.C, National Council of Science and Technology, Querétaro, Mexico
e-mail: jhenao@conacyt.mx

Y. Pacheco · L. Martinez-Gomez
Universidad Nacional Autónoma de México(UNAM), Instituto de Ciencias Físicas, Campus Morelos, Cuernavaca, Mexico
e-mail: ypacheco@gmail.com

L. Martinez-Gomez
e-mail: lmg@icf.unam.mx

Y. Pacheco
Faculty of Engineering, Universidad Autónoma Del Estado de Morelos (UAEM), Cuernavaca, Mexico

N. S. Arul and V. D. Nithya (eds.), *Revolution of Perovskite*, Materials Horizons: From Nature to Nanomaterials, https://doi.org/10.1007/978-981-15-1267-4_6

species. In the field of electrochemistry, these materials have been employed as electrodes in rechargeable batteries and fuel cells [4].

Specific examples of perovskite materials in engineering applications are $EuTiO_3$ and $CaMnO_3$ for energy-harvesting devices [5], doped $LaFeO_3$ and $LaCoO_3$ for solid oxide fuel cells [6], doped $BaSrO_3$ and $BaFeO_3$ for oxygen membrane separation [7, 8], $SmFeO_3$ and $LaMnO_3$ for gas sensing [9, 10], and $NaTaO_3$ and $LaTiO_3$ for photocatalytic cells [11, 12]. Due to its properties, perovskite materials have also called the attention of researchers for battery applications. For instance, the $LaFeO_3$ compound has been studied as negative electrode material for nickel–metal hydride (Ni/MH) batteries [13]. Other applications include perovskites as negative electrodes in Li–ion and Li–air batteries [4, 14]. The present chapter is focused on reviewing perovskite materials for battery applications and introduce to the main concepts related to this field.

1.1 Perovskite Structure

Perovskite materials took their name from the mineral called Perovskite ($CaTiO_3$), which was discovered by Gustav Rose in Russia in 1839 [15]. Ideal perovskite oxides present a crystal cubic structure with space group Pnma (Pm3−m cubic system) described by the general formula ABO_3, where A is a rare or alkaline earth metal and B is a first-row transition metal [16]. In this structure, cations with a large ionic radius coordinate to 12 oxygen atoms and reside in A-sites, while cations with a smaller ionic radius coordinate 6 atoms and reside in B-sites, Fig. 1.

According to the Goldschmidt's tolerance factor (t), which is an indicator for the stability and distortion of crystal structures and is defined by $t = (rA + rO)/\sqrt{2}(rB + rO)$ (where rA, rB, and rO are the average ionic radiuses of A, B, and O atoms), the perovskite structure results most stable when t is close to the unit, that is, when it

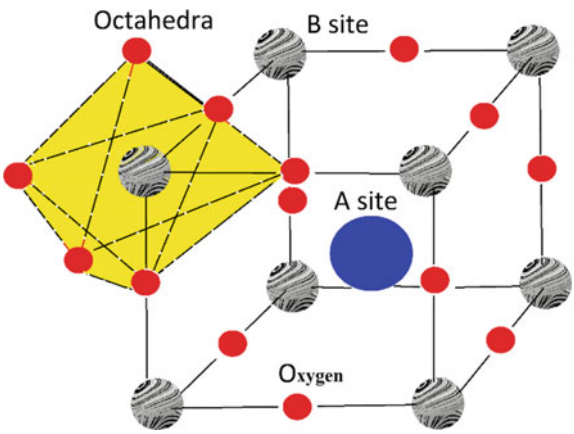

Fig. 1 Schematic representation of the ABO_3 perovskite-type structure

forms a cubic structure. When t has deviation from the unit, the crystal structure tends to change from cubic to rhombohedral, orthorhombic, hexagonal, tetragonal, and monoclinic structures, depending on the deviation the from Goldschmidt's tolerance factor. Overall, perovskites form in the interval from 0.75 to 1 [17].

Hundreds of compounds are known for presenting the perovskite structure, for instance, the $FeMgSiO_3$ called bridgmanite is one of the most abundant perovskite compounds in the earth [18]. Other types of perovskites are also found in the nature. For example, the $Sr_3Ti_2O_7$ is a layered perovskite compound, which is a common material in rocks [19]. Layered perovskites are usually a variation from ideal cubic perovskites. Especially, layered perovskites present a double-perovskite structure, that is, the unit cell is twice the unit cell of a conventional perovskites. They are formed by slabs of ABO_3 structure, which are separated by a secondary structure. The differentiating features for the layered perovskites are the type of secondary structure that separate the ABO_3 layers and the offsetting of the layers [20].

Three different basic layered perovskite structures are distinguished: (1) Dion–Jacobson-type structures, (2) Perovskite-like layered structures (PLS), and (3) hexagonal-type structures. They are formed by cutting the cubic perovskite structure across the (100), (110), (111) planes and by insertion of additional oxygen atoms. These structures have the following general formulas: $A'A_{n-1}B_nO_{3n+1}$, $A_nB_nO_{3n+2}$, and $A_nB_{n-1}O_{3n}$, respectively, where n represents the number of BO_6 octahedra that span one layer, and therefore specifies the thickness of the perovskite layer. In this structure, alkaline earth or lanthanide metals usually are located on the A positions, while the B cations are often niobium or titanium [20, 21]. Among the three different basic perovskite layered structures, the $A_nB_nO_{3n+2}$ PSL family has attracted most attention for technological applications due to their interesting ferroelectric and electrochemical properties [22]. In particular, perovskite layered oxides have been used as electrodes and materials for catalysis in metal–air, Li–ion, and Ni–MH batteries.

1.2 Preparation Methods

Several synthesis methods for the production of perovskite oxides are reported in open literature available [23]. Three main methods are distinguished among the several studies carried out in the field of batteries; these methods are the glycine–nitrate method, the solid-state reaction route, and the sol–gel technique [24]. The glycine–nitrate method involves the use of nitrates instead of oxides as precursors, nitric or stearic acid as dispersant, and glycine as fuel. Precursors, dispersant, and fuel are all mixed in distilled water and heated until the excess free water evaporates. Afterward, the resulting viscous liquid is autoignited by placing it in a preheated plate, which is then calcined at a temperature of about 1200 K for 3–5 h [25]. Several authors have used this method to obtain perovskite powders for battery applications. For example, Wang et al. [26] employed the glycine nitrate

method to prepare ABO_3 perovskite-type oxide to built-up negative electrodes for Ni/MH batteries. They used stearic acid ($C_{17}H_{35}COOH$) as both solvent and dispersant. In addition, they employed analytical grade precursors in stoichiometric amounts including the $La(NO_3)_3.6H_2O$ and $Fe(NO_3)_3.9H_2O$. The mixture was stirred by a magnetic mixer until a homogeneous solution was produced. The solution was ignited in air and the powders obtained were used as feedstock powder for the production of negative electrodes for Ni–MH batteries. It is worth mentioning that other investigations add a final step of calcination at 1123 K to favor the development of the perovskite-type structure.

Alternatively, in the solid-state reaction route, the mechanical mixing of high purity precursor oxides (99% purity) and carbonates or salts is followed by heating at temperatures of about 1500 K. The solid-state reaction route is often performed for 8–24 h, which allows the rearrangement of cations and favors the formation of the perovskite-type structure [27]. The reactions are usually presented at the interface of the mixed solids as ions diffuse from the bulk to the interface between particles. As a final step, the sintered material is often milled to obtain micrometric powders that subsequently are used to produce electrodes for batteries.

Another common synthesis method for the production of perovskite-type oxides is the sol–gel method. In particular, the sol–gel "Pechini" method is very common for the preparation of perovskite-type compounds [28]. The Pechini method involves the mixing of precursors (nitrates and/or oxides) by the addition of a chelating agent, ethylene glycol as the sol-forming product, desiccation, and calcination. Previous studies involving the usage of perovskite oxides for battery applications have reported the synthesis of ABO_3 perovskite-type powders by means of the Pechini method. For example, Song et al. [29] prepared $LaCrO_3$ starting from a mixture of $La(NO_3)_36H_2O$, $Cr(NO_3)_39H_2O$, citric acid, and ethylene glycol. These reagents were then dissolved in distilled water to form an aqueous solution and then stirred in a water bath at 353 K until a gel was formed. The gel was then desiccated in a dying oven at 353 K for 24 h. The gel obtained was ground and calcined at 1073 K for 2 h to form the final powders.

Overall, the sol–gel method is usually employed when small particle size is required. The sol–gel method allows the preparation of nanometric size powder while keeping homogeneous composition. This fact makes very attractive this method for the battery applications where diffusional and kinetic processes depend on the surface area of materials involved and its chemical composition. Alternatively, the solid-state reaction route is considered a high-temperature process that allows the preparation of micrometric powders. Comparing with the glycine–nitrate route and the sol–gel technique, the solid-state reaction route requires higher calcination temperatures and longer calcination times to yield pure crystals of oxides.

As an example, in the present book chapter, a layered perovskite-type oxide $Nd_2Ti_2O_7$ (Neodymium Titanate) with general formula $A_nB_nO_{3n+2}$ for $n = 4$ was synthesized by means of the sol–gel route. Tetrabutyl titanate (Ti(OBu)4) and Nd_2O_3 were used as the precursors of Ti and Nd. The molar ratio of Nd/Ti was fixed at 1/1 and the amount of citric acid used was determined by nCitricAcid/(nNd + nTi) = 2. Nd_2O_3 (0.005 mol) was dispersed in a spot of water, and then 5 mL concentrated

HNO_3 was added to it drop by drop to dissolve the rare earth oxide. Citric acid (0.04 mol) was dissolved in 5 mL H_2O and then poured into the solution. The mixture was thoroughly stirred by the magnetic mixer. Then, the appropriate amount of $Ti(OBu)_4$ (0.01 mol) was added with vigorous stirring. The solution was placed in a 60 °C liquid bath to vaporize water during 0.5 h. After 5 h, the mixture solution changed from colorless solution to pink solution and then to violet gel, see Fig. 2. The gel was then take out and calcined at 850 °C for 2 h in air.

In order to confirm the manufacturing temperature of the $Nd_2Ti_2O_7$ powder, DSC–TGA curves of the gel precursor were evaluated on the DSC–TGA–SDT Q600 thermal analysis instrument in ambient air and calefactive velocity of 20 °C/min as shown in Fig. 3. The DSC–TGA curve reveals the formation of four peaks. The first exothermic peak (90–125 °C) with relatively large weight loss (27%) is caused by the evaporation and burning of the organic substance. The second exothermic peak (360 °C) is attributed to the combustion of remaining organic substance and the third exothermic peak (514 °C) is related to the crystal lattice energy released during the formation of perovskite-type structure. The last exothermic peak is from the final formation of $Nd_2Ti_2O_7$. The measured overall weight loss is 77.26%, which indicates the complete removal of all the citric acid and all the organic substance. No further weight loss was above 815 °C, suggesting that the $Nd_2Ti_2O_7$ can be fabricated at about 815 °C.

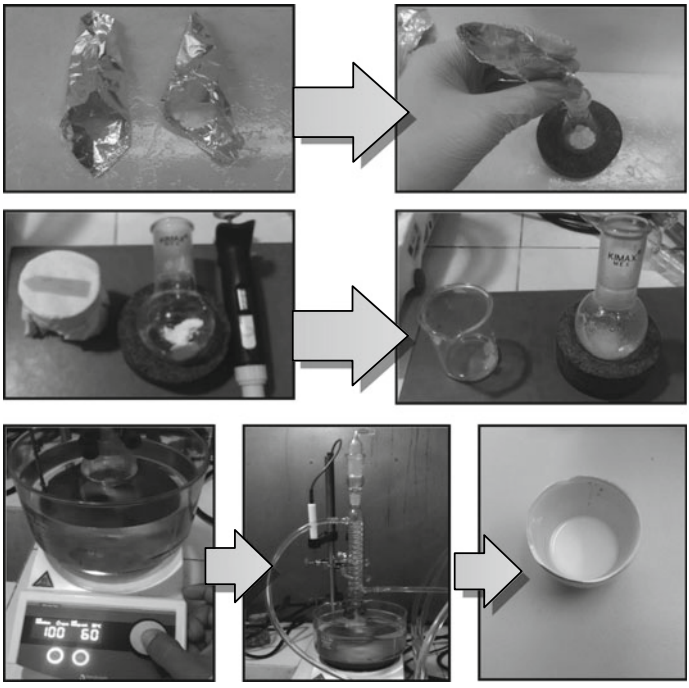

Fig. 2 Synthesis route for the gel precursor

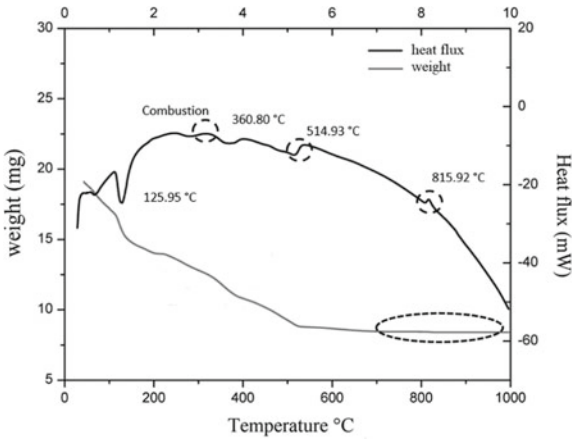

Fig. 3 DSC–TGA analysis of the gel precursor

The crystal structure of the calcined neodymium titanate powder was analyzed by X-ray diffraction (XRD) using a specular reflection mode (Bruker D8 Advanced, Cu Ka radiation, k = 0.154056 nm) over the angular range of 20°< Θ <80° with a step size of 0.008° and measuring time of 300 s per step. Figure 4 shows the XRD patterns of $Nd_2Ti_2O_7$. This pattern confirms the high crystallinity of the product. The XRD pattern is quite consistent to a single phase of layered perovskite $Nd_2Ti_2O_7$ and is indexed based on a monoclinic structure (a = 7.6951494 Å, b = 13.044494 Å, c = 5.4716635 Å y β = 98.91025) (CIF-2237725). These results suggest that the $Nd_2Ti_2O_7$-layered perovskite oxide, which usually forms at high temperature in conventional method (1100 °C) with a long reaction time (50 h), can be successfully synthesized at a relatively low temperature (815 °C) with shortened reaction time (2 h) by using sol–gel.

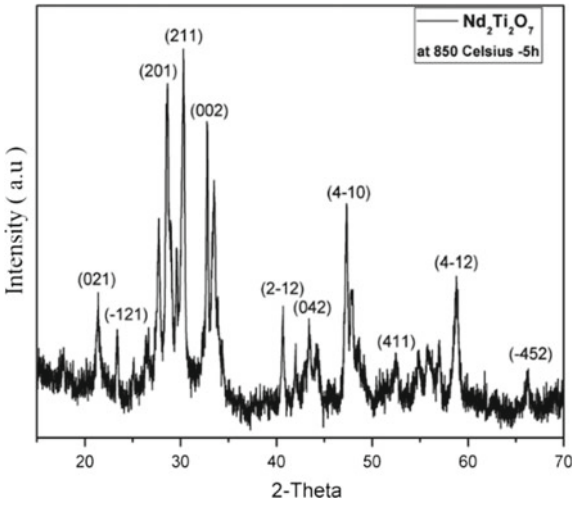

Fig. 4 XRD analysis of the $Nd_2Ti_2O_7$ powder obtained

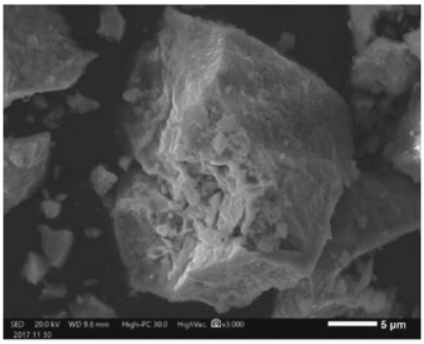

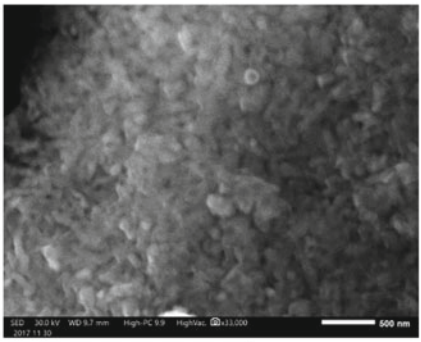

Parameter	Units (µm)
d_{50}	3.601
d_{10}	1.115
d_{90}	6.537

Fig. 5 SEM images of the calcined $Nd_2Ti_2O_7$ powder and particle size distribution analysis

The morphology and particle size distribution of the calcined powder was also studied by means of Scanning Electron Microscopy (SEM) and by using a laser diffraction equipment (LS1057083 Laser Diffraction, Malvern Instruments). The results of morphology and particle size analysis are presented in Fig. 5. These results reveal that irregular particles were obtained, which formed agglomerates of small nanometric powders. The agglomerates presented a mean particle diameter of 3.601 µm.

Usually, the perovskite-type oxide powders obtained by any of the methods described in the present section are further processed to build up electrodes or bulk parts that are intended to be used in batteries. In the next section, specific applications of perovskites in batteries will be discussed.

2 Perovskite Materials in Batteries

Open literature suggests that perovskite-type oxides have been often studied for applications in metal–air (Li–air, Al–air, Zn–air) [30, 31], Li–ion, and Ni–metal hydride (Ni–MH) batteries [32, 46]. To understand the usage of perovskites in the different battery technologies, a brief description of the operation of these technologies is presented in this section.

One of the battery technologies linked to numerous reports of the usage of perovskite-type oxides is the metal–air technology. The operation of a metal–air battery is associated with the metal oxidation at the anode, while an oxygen

reduction reaction occurs at the air-breathing cathode during discharge. Catalysis particles are often used on the surface of the air diffusion cathode, which reduces the O_2 from the surrounding air. Typically, these types of batteries use an aqueous or an aprotic electrolyte. The reactions in a metal–air battery can be described by the following equations [31]:

$$\begin{aligned} \text{Anode}: \ & \mathrm{M} \leftrightarrow \mathrm{M}^{n+} + \mathrm{ne}^- \\ \text{Cathode}: \ & \mathrm{O_2} + \mathrm{ne}^- + 2\mathrm{H_2O} \leftrightarrow 4\mathrm{OH}^- \\ & (\text{Forward}: \text{ charge; Reverse}: \text{ discharge}) \end{aligned} \tag{1}$$

where M presents the metal and n is the oxidation number of the metal ion. The metal anodes are often alkali metals (e.g., Li, K, and Na), alkaline earth metals (e.g., Mg), or first-row transition metals (e.g., Fe and Zn) with good electrochemical equivalence; the air-breathing cathode often has an open porous architecture that allows continuous oxygen supply from surrounding air.

Alternatively, the Li–ion battery technology has been another opportunity field for the usage of perovskite materials. The operating principle of a Li–ion cell is based on the reversible exchange of lithium ions between the positive and negative electrodes, throughout the cycles of charge (positive delithiation) and discharge (positive lithiation). Each of the electrodes is made of materials that can be inserted or detached by lithium ions in their crystalline structure; these are called "active materials" or "intercalation materials." During its use (cell in discharge), the negative electrode (site of an oxidation reaction) releases lithium ions which migrate through the electrolyte (ions conductor); these ions are inserted in the crystal lattice of the active material at the positive electrode (site of a reduction reaction). The passage of each lithium–ion by the internal circuit of the battery is exactly compensated by the passage of an electron in the external circuit to maintain electrical neutrality in each of the electrodes, thereby generating an electric current. During the charge, the cell operation is exactly the reverse process; in that case, external energy is necessary to reverse the reaction in electrodes. The reactions in a Li–ion battery can be described by the following equations [33]:

$$\begin{aligned} \text{Cathode}: \ & \mathrm{Li-XXO}_n \leftrightarrow \mathrm{Li}_{1-y}\mathrm{XXO}_n + \mathrm{Li}^+ + \mathrm{ye}^- \\ \text{Anode}: \ & \mathrm{C} + \mathrm{yLi}^+ + \mathrm{ye}^- \leftrightarrow \mathrm{Li}_y\mathrm{C} \\ & (\text{Forward}: \text{ charge; Reverse}: \text{ discharge}) \end{aligned} \tag{2}$$

where X represents a metal and n is the number of oxygen in the oxide compound. Some examples of materials used as cathodes are $LiCoO_2$, $LiFePO_4$, and $LiMn_2O_4$. At the anode, the most common materials are carbons (graphite, coke, or hard carbon) and lithium titanate [34].

Another battery technology involving the usage of perovskite materials is the Ni–MH or Ni–oxide. This technology consists of a positive electrode (cathode) which experiences +2/+3 oxidation state change promoted by the electrochemical reaction during charge. Protons released from the cathode recombine with

hydroxide ions in the electrolyte. In the anode, a hydrogen storage compound is in charge of storing hydrogen in a reversible way. During charge, the applied voltage splits water molecules into hydroxide ions and hydrogen protons. Consequently, the reduction of water permits hydrogen protons to be in contact with the hydrogen storage alloy. Protons enter then into the bulk of the alloy to form a hydride driven by the voltage and diffusion caused by the concentration gradient. The reactions in a Ni–MH battery can be described by the following equations [46]:

$$\begin{aligned} \text{Cathode}: \ & \mathrm{xNi(OH)_2 + OH-} \leftrightarrow \mathrm{NiOOH + xH_2O} \\ \text{Anode}: \ & \mathrm{M + xH_2O + xe^- \leftrightarrow MHx + HO^-} \\ & (\text{Forward}: \text{ charge; Reverse}: \text{ discharge}) \end{aligned} \tag{3}$$

where M represents an intermetallic or an oxide compound. The most common materials used at the cathode and anode are $Ni(OH)_2$ and $LaNi_5$, respectively.

Perovskite oxides have been widely studied as catalysis materials for Li–air batteries [36, 37]. In Li–air batteries, it is essential to catalyze the charge and discharge reactions in order to reduce kinetic losses because of breaking and forming of the O–O bond at the air-breathing cathode [35]. There is a growing interest in employing perovskite oxides in Li–air batteries due to their capacity to promote oxygen reduction (ORR) and oxygen evolution reaction (OER) and excellent catalytic performance [38, 39]. In fact, perovskite materials have been widely used as catalysts for fuel cells. Overall, perovskite oxides provide good catalytic performance when the structure in the B-site has a single electron-filled, and therefore, provides the favorable bond energy of M–O bond for the ORR and OER. One example of a perovskite oxide used as catalytic compound in Li–air batteries is the $LaNiO_3$ [40]. Some studies have suggested that both B-site and/or A-site doping on $LaNiO_3$ can be beneficial for catalytic properties. For example, Du et al. [41] prepared perovskite oxide nanoparticles by means of the sol–gel route. They synthesized $LaNiO_3$, $LaNi_{0.92}Mg_{0.08}O_3$, and $LaNi_{0.85}Mg_{0.15}O_3$. Especially, the $LaNi_{0.85}Mg_{0.15}O_3$ presented the highest catalytic activity among the compound studied. Overall, the improved OER activities of perovskites are related to the high covalency of transition metal–oxygen bonds. Doping the B position is then beneficial for the transition metal–oxygen covalency, which favors the catalytic behavior in perovskites. Other examples of perovskites in Li–air batteries are $Sr_{0.95}Ce_{0.05}CoO_{3\text{-d}}$ and the $La_{1.7}Ca_{0.3}Ni_{0.75}Cu_{0.25}O_4$ with a layered perovskite structure, which exhibit high catalytic activity toward electrochemical Li_2O_2 oxidation in aqueous and a nonaqueous aprotic electrolyte, respectively [42, 43].

Perovskite materials have been also studied as cathode material for the Li–ion battery technology [32]. In Li–ion batteries, cathode materials with both high ionic and high electronic conductivities are required for large energy density. Most of the cathode materials used in rechargeable Li–ion batteries possess hexagonal-layered structure or spinel structure and are usually poor electronic conductors [35]. Perovskite oxides have called the attention of researchers because their electronic properties can be controlled by doping A- or B-sites. In addition, due to the different

atomic sizes in the A- and B-sites and different valence states that can be obtained, the perovskite materials can act as materials for the intercalation and deintercalation of Li–ions during the charge and discharge processes. Examples of perovskite oxides studied as cathode materials for Li–ion batteries are $La_{1-x}Li_xTiO_3$ and $LiNi_{1/3}Co_{1/3}Mn_{1/3}O_2$ [44, 45].

Recently, ABO_3 perovskite systems were mainly focused on their electrochemical properties for the anode of Ni/MH batteries establishing what is normally called Ni–oxide batteries [46, 47]. Previous studies have revealed exciting results of their electrochemical capacity and cycle life especially in extreme environmental conditions [46]. Perovskite materials are known for their catalytic behavior in hydrogen-rich media, which have been the motivation to study these materials for electrochemical hydrogen storage. Overall, the usage of perovskite oxides in Ni–oxide batteries is based on the advantages presented for these materials in the catalysis and ionic conduction applications. For instance, perovskite oxides can be designed with a range of compositions and elements in A- and B-sites, which allow to tailor the electrochemical properties. In this sense, the stoichiometry and valance can be modified, so enhancing their hydrogen absorption properties. Other properties of interests for Ni-battery application are the high corrosion resistance of perovskite oxides and their thermal stability.

One of the first studies using perovskite oxides in the field of Ni–oxide batteries was carried out by Esaka et al. [48], who reported the ($SrCe_{0.95}Yb_{0.05}O_3$) composition as negative electrode material for Ni–oxide batteries. Interestingly, this composition presented aqueous hydrogen absorption and desorption at room temperature. In fact, perovskite oxides have been widely studied as negative electrodes materials for aqueous Ni–oxide batteries. For instance, Deng et al. [13] also studied ABO_3 perovskite systems as negative electrodes reporting that compositions such as $La_{1-x}Sr_xFeO_3$ (for X = 0.2 and 0.4) present electrochemical activity, which is improved with temperature and is affected by the crystalline array. One of the key findings is that a rhombohedral structure in the $La_{1-x}Sr_xFeO_3$ system (X = 0.4) can accept more hydrogen within its structure in comparison to the orthorhombic one (X = 0.2). For example, the discharge capacity value of the rhombohedral structure was 77 mAh/g at room temperature; meanwhile, the orthorhombic structure presented a discharge capacity value of 54 mAh/g at room temperature. The environmental temperature is another crucial factor in the performance of perovskite materials in Ni–oxide batteries. Different authors have reported an increase of the electrochemical capacity of perovskites two to four times the value reported at room temperature. For example, Henao et al. [46] reported capacity values of the $La_{0.4}Sr_{0.6}CO_{0.8}Fe_{0.2}O_3$ compound that increased from 51.4 mAh/g at room temperature to 462 mAh/g at 333 K. Other authors have reported similar results [26, 29].

In perovskite oxides employed as negative electrode materials in Ni–oxide batteries, hydrogen insertion is associated with the electrochemical capacity of the system. Hydrogen absorption is given by the reduction of water at the interface electrolyte/electrode, where hydrogen protons are inserted within the perovskite

structure. The following reactions describe the behavior of an electrochemical Ni–perovskite (ABO_3-type) oxide half-cell [46]:

$$ABO_3 + xH_2O + xe^- \leftrightarrow AB_{1-x}B_xO_3H_x + xHO^- \quad (\text{Forward}: \text{charge}; \text{Reverse}: \text{discharge}) \tag{4}$$

In this manner, the total electrochemical reaction of a Ni/perovskite (ABO_3-type) oxide battery is given by

$$xNi(OH)x + ABO_3 \leftrightarrow xNiOOH + AB_{1-x}B_xO_3H_x \quad (\text{Forward}: \text{charge}; \text{Reverse}: \text{discharge}) \tag{5}$$

According to the mechanisms proposed in the literature available, hydrogen protons are bonded with the lattice oxygen in perovskites. The chemical bond between oxygen and hydrogen is less strong when the bond between transition metals on the perovskite structure and oxygen is stronger. This phenomenon has been elucidated in various studies that have shown the effect of A-site and B-site substitution in ABO_3 compounds. In fact, it has been noted that doping affects strongly the electronic structure and chemical bonds, resulting in the enhancement of electrochemical properties [46, 49].

The improvement of the electrochemical properties of perovskite oxides in aqueous electrolytes in Ni–oxide batteries is another key property that motivates its application in these systems. The substantial improvement of the electrochemical capacity in perovskite oxides with temperature is often attributed to the improved atomic motion at the electrode/electrolyte interface and to their excellent corrosion resistance. It worth mentioning that mechanisms of improved electrochemical capacities of perovskite oxides have not been exposed at all; however, since hydrogen absorption is related to the bond H–O in the lattice, one can assume that when increased the environmental temperature more hydrogen protons are inserted in some extent into the perovskite structure. In fact, some authors have reported that free hydrogen atoms are usually present on perovskites because H–O bonds are broken with temperature [49]. At the same time, the increase of temperature favors their diffusion. Several experimental studies have demonstrated that hydrogen diffusion increases with the increment of temperature in perovskites [29, 46]. Table 1 summarizes the electrochemical properties of ABO_3 perovskite-type oxide used as negative electrode materials in Ni–oxide batteries so far.

Despite the numerous studies regarding the electrochemical properties of perovskites oxides, there is no evidence in the literature available on studying layered perovskite materials as negative electrode materials for Ni–oxide batteries. As mentioned above in this section, the basic lattice array is one of the key factors influencing the electrochemical properties of perovskites. For instance, in the $La_{1-x}Sr_xFeO_3$ perovskite compound, the electrochemical behavior changes remarkably when its basic lattice array is transformed from orthorhombic to rhombohedral because of the addition of the doping element from $x = 0.2$ to $x = 0.4, 0.6$, respectively [50]. Therefore,

Table 1 Compilation of properties for different ABO_3 perovskite-type oxide electrodes for Ni–oxide batteries reported in the literature

Perovskite-type oxides ABO_3	Steady discharge capacity (mAh/g) at 125 mA/g		Diffusion coefficient (D) (cm^2/s)		Exchange current density (I_o) (mA/g)		Reference
	298 K	333 K	298 K	333 K	298 K	333 K	
$La_{0.6}Sr_{0.4}Co_{0.8}Fe_{0.2}O_3$	51.4	462	1.87×10^{-14}	*	39.9	*	[46]
$LaFeO_3$	80	350	0.8×10^{-17}	4×10^{-17}	1.2	2.9	[13]
Nano-$LaFeO_3$	130	375	1.1×10^{-14}	2.9×10^{-14}	28	80	[26]
$LaCrO_3$	107	285	2.9×10^{-15}	*	38	*	[29]
$LaGaO_3$	*	12	*	2.9×10^{-10}	*	70.6	[47]
$La0.8Sr0.2FeO_3$	50	230	1.6×10^{-17}	4×10^{-17}	37.8	83.2	[50]
$La0.6Sr0.4FeO_3$	70	350	0.8×10^{-17}	2×10^{-17}	42.8	78.3	[50]

*value not reported in the literature available

it may be very interesting to compare the mechanisms acting on layered perovskites with respect to traditional ABO_3 compounds. Due to the lack of literature available related to the usage of layered perovskites, in the present book chapter, it is presented one of the first studies carried out on layered perovskites as negative electrode material for Ni–oxide batteries. Electrode preparation and electrochemical studies performed on a layered perovskite oxide will be introduced in the next section.

3 Layered Perovskites as New Electrode Materials in Ni–Oxide Batteries

Layered perovskite oxides differ from conventional ABO_3 oxides in the sense that layered ones have a more complex structure including separation of basic perovskite array forming a type of channels. This subtle variation in the geometrical configuration of layered perovskites in comparison to conventional ones can be possibly reflected on the electrochemical performance of layered perovskites. Considering that hydrogen absorption in perovskites is associated with oxygen-related positions, one can expect that layered perovskites can also be able to support the insertion of hydrogen protons in their structure. In this section, a first approach on the study of layered perovskites as electrode material in Ni–oxide batteries is introduced. To achieve this goal, the $Nd_2Ti_2O_5$-layered perovskite compound previously prepared as nanometric powder by means of the sol–gel method according to the procedure presented in Sect. 2 has been used to prepare negative electrodes for a Ni–oxide cell.

3.1 $Nd_2Ti_2O_5$ Electrode Preparation and Electrochemical Setup

The $Nd_2Ti_2O_7$ electrodes were fabricated using the "latex" method. The $Nd_2Ti_2O_7$ nanometric powder was mixed with black carbon and polytetrafluoroethylene (PTFE). This mixture was prepared to provide the compound with good electrical conductivity and good handling during the electrochemical tests. The weight ratio of the $Nd_2Ti_2O_7$, carbon black, and PTFE was 90:5:5, respectively. Before depositing the powder mixture on the Ni-mesh, ethylene glycol was added to form a viscoelastic paste. A 1 cm^2 Ni-mesh was used as current collector, and consequently, it acted as support to deposit the active material. The deposited viscoelastic paste was dried for 2 h to evaporate the solvent. Then, a cold pressing machine was employed to cold-press the deposited active material onto the Ni-mesh at a pressure of 40 MPa.

The electrochemical performance of the prepared neodymium titanate electrodes was tested in a conventional three-electrode open-air cell (Potentiostat–Galvanostat, Gamry 1000E) using the layered perovskite compound as the working electrode, Hg/HgO as the reference electrode, $Ni(OH)_2$ as the counter electrode, and KOH (6 M) solution as the electrolyte.

3.2 $Nd_2Ti_2O_5$ Electrochemical Performance

Cyclic voltammetry experiments were performed to reveal the electrochemical reactions of the $Nd_2Ti_2O_7$ electrode in 6 M KOH aqueous solution. Figure 6 shows the cyclic voltammogram of the $Nd_2Ti_2O_7$ negative electrode.

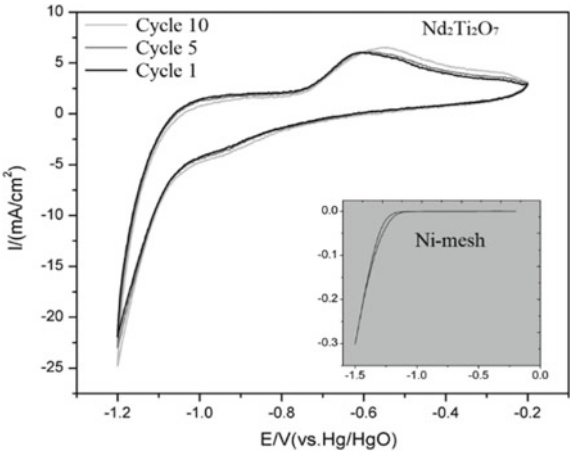

Fig. 6 Cyclic voltammogram of the $Nd_2Ti_2O_7$ electrode

Cyclic voltammetry is normally used to study qualitative information about electrochemical processes, including the occurrence of oxidation and reduction reactions and the reversibility of a reaction [51]. In the present study, an oxidation peak appears at −0.9 V with respect to the Hg/HgO reference electrode, and a reduction peak appears at −0.625 V with respect to the Hg/HgO reference electrode. This pair of redox peaks suggests that a reversible electrochemical reaction is occurring on the $Nd_2Ti_2O_7$ working electrode. Interestingly, these peaks exhibit similar potential values compared with conventional electrodes used in Ni–MH batteries [52]. The desorption peak of hydrogen appears prior to the electrochemical oxidation peak of hydrogen, suggesting the possible existence of hydrogen chemisorption. Moreover, the reduction peak becomes more visible with increasing number of cycles, indicating that the $Nd_2Ti_2O_7$ electrode must be possibly activated. The inset in Fig. 6 corresponds to the cyclic voltammogram of the Ni-mesh used as current collector. Interestingly, the results demonstrate that there are no peaks indicating oxidation and reduction reactions involving the current collector material. In addition, if compared with the curve of the layered perovskite, it is clearly observable that the area under the curve of the layered perovskite is larger than that of the Ni-mesh, which directly related to the electrochemical capacity of the material. To quantify the capacity values of the layered perovskite electrode, the charge/discharge properties of the $Nd_2Ti_2O_7$ negative electrode were investigated using the chronopotentiometry technique. The working electrodes were fully charged and discharged at constant current densities of 10, 30, 60, and 125 mA/g. Table 2 summarizes the maximum discharge capacity values obtained in the experiments:

Results in Table 2 reveal that the electrochemical capacity of the layered $Nd_2Ti_2O_7$ perovskite compound is comparable with the electrochemical capacity values obtained for conventional ABO_3 perovskite oxides. For instance, recent studies focused on the usage of $La_{0.6}Sr_{0.2}Co_{0.2}FeO_3$ as negative electrode material for Ni–oxide batteries has reported electrochemical capacity values of about 51.4 mAh/g at 298 K and discharge current density of 125 mAh/g [46]. The fact that the electrochemical capacity of the electrodes increases when the applied current decreases is associated with the kinetics of the process. This phenomenon has been widely observed in Ni–MH and Ni–oxide cells.

One can also observe in Fig. 7 that the maximum electrochemical capacity of the electrodes depends on the number of electrochemical cycles. In all applied current densities, the capacity of the electrodes increases up to a maximum and then it

Table 2 Maximum discharge capacity values of the $Nd_2Ti_2O_7$ layered perovskite compound

Applied current density (mA/g)	Electrochemical capacity (mAh/g)
10	356.13
30	291.83
60	123.59
125	59.76

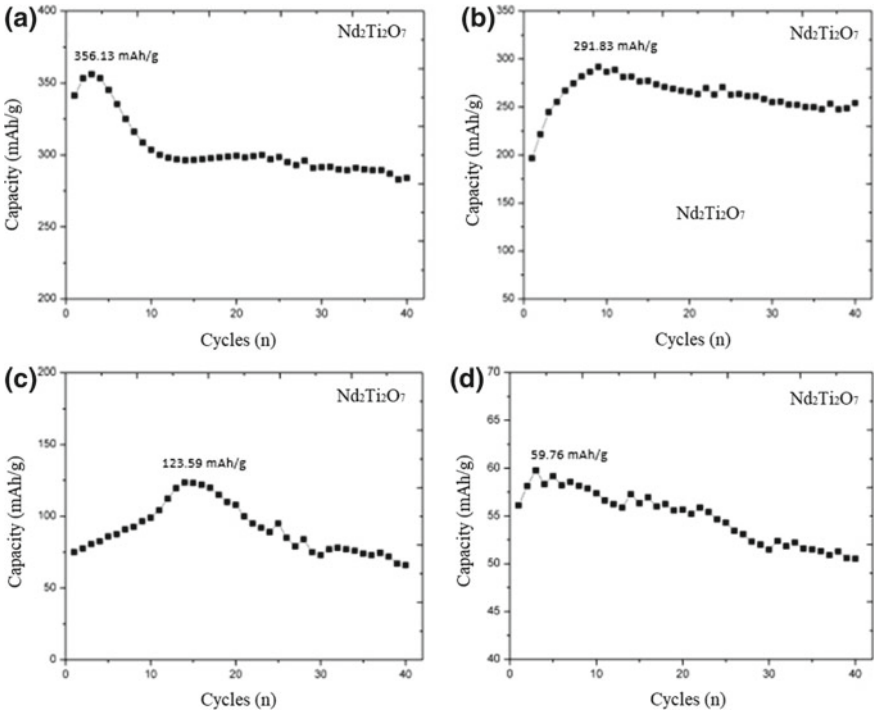

Fig. 7 Performance of the $Nd_2Ti_2O_7$ perovskite layered electrode at **a** 10 mA/g, **b** 30 mA/g, **c** 60 mA/g, **d** 125 mA/g applied current densities

stabilizes. This observation suggests that this layered perovskite composition must be activated electrochemically as normally occurs in conventional intermetallic electrodes used in Ni–MH batteries [53]. Activation is often associated with the expansion of the structure and cracking of the surface, which becomes exposed to the electrolyte. Figure 8 shows the SEM images of the electrodes before and after activation. The SEM image of the as-prepared electrodes shows a compacted powder typical of cold-pressed electrodes. Once the electrodes are activated, one can note that small particles appear on the surface of these electrodes indicating some perturbation on the initial structure of the electrode. Previous studies have obtained similar results after studying ABO_3 perovskite compounds due to the penetration of the electrolyte into the perovskite structure [54].

The hydrogen diffusion coefficient of the $Nd_2Ti_2O_7$ oxide was also calculated in the present study by the potential-step discharge technique. This method consists of applying a potential step while monitoring the anodic current–time response. The semi-logarithmic curve obtained from this experiment is often divided into two-time regions [55]. In the first one, the current undergoes a rapid decrease because of the rapid consumption of hydrogen on the surface of the electrode. The first region is governed by the charge transfer kinetics and/or by charge transfer and

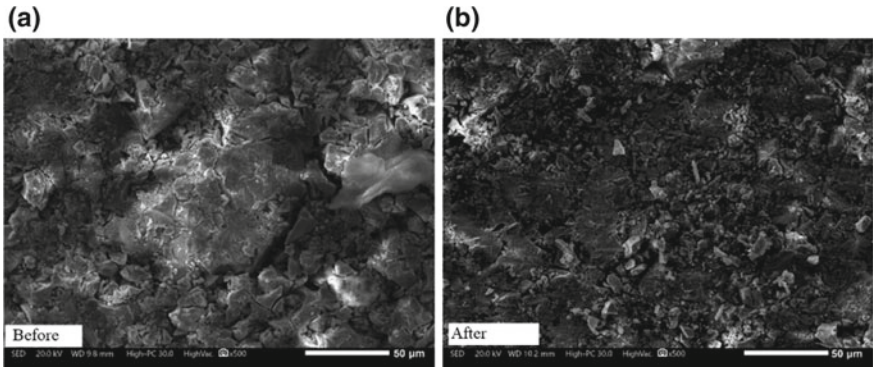

Fig. 8 SEM micrograph of the $Nd_2Ti_2O_7$ perovskite layered electrode **a** as-prepared electrode; **b** after 20 activation cycles

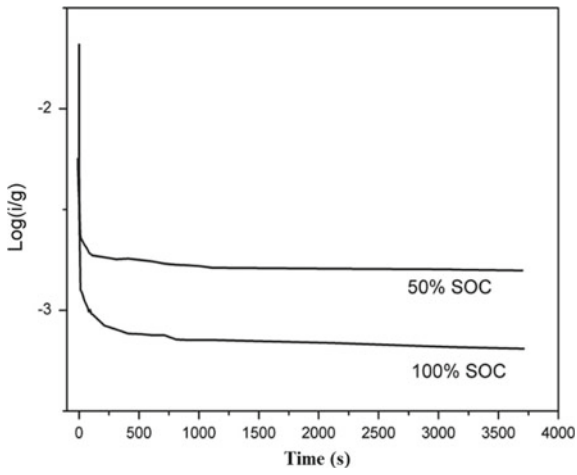

Fig. 9 Semi-logarithm curve of the $Nd_2Ti_2O_7$ electrode

diffusion (mixed kinetics). Nevertheless, in the second-time region, the current gradually decreases in a linear way with time and is controlled by the hydrogen diffusion. Figure 9 shows the semi-logarithmic curve of the anodic current–time response for the $Nd_2Ti_2O_7$ electrode at 50 and 100% state of charge (SOC). The results reveal that the current time response of the $Nd_2Ti_2O_7$ electrode presents both regions (mixed- and diffusion-controlled), which are descaled to each other due to the effect of SOC. The hydrogen diffusion coefficient D_H is often calculated from the diffusion-controlled region in the electrode bulk according to the following equation [46, 55]:

$$\log i = \log\left[\frac{6FD_H}{da^2}(C_0 - C_s)\right] - \frac{\pi^2}{2.303}\frac{D_H t}{a^2} \quad (6)$$

In Eq. (6), i is the anodic current density (A/g), D_H is the hydrogen diffusion coefficient (cm^2/s), d is the density of the compound (g/cm^3), a is the average radius of the particles, C_o is the initial hydrogen concentration in the bulk of the electrode (mol/cm^3), C_s is the surface hydrogen concentration of the electrode (mol/cm^3), and t is the discharge time (s). According to Eq. (2), D_H was estimated as 5.69×10^{-13} and 4.84×10^{-13} and for the $Nd_2Ti_2O_7$ electrode at 50 and 100% SOC, that is, D_H decreases with the state of charge. These results can be related to the fact that diffusion paths are linked to oxygen-related positions within the perovskite oxide structure. Once the electrode initiates the charge process, many of these oxygen positions become occupied forming an O–H chemical bond. However, when the number of H^+ ions inserted into the unit cell of perovskite oxides increases, the O–H bond reduces its strength and consequently the activation energy necessary to break the O–H bond. This fact makes easier the hydrogen ion transportation [49]. Interestingly, the $Nd_2Ti_2O_7$-layered electrode presents similar D_H values than conventional perovskite ABO_3 oxide electrodes [46].

The results obtained in the present chapter have shown that layered perovskite materials can be useful as electrode materials for Ni–oxide batteries since they can show reversibility and can store hydrogen electrochemically. Further studies involving techniques such as impedance and molecular dynamic simulations are encouraged for comparing the mechanisms acting on conventional perovskites and layered perovskites.

4 Perspectives and Suggestions Regarding the Selection of Perovskite Materials for Ni–Oxide and Metal–Air Batteries

It has already been noted that Ni–oxide battery performance is often better when the perovskite electrode is a doped material. The ABO_3 compound is predominantly orthorhombic or rhombohedral structures that generally are affected in the type of dopants used. There are several requirements for the electrochemical properties of Ni–oxide battery electrode, and all these properties must be balanced for practical use. It has been found that rare earth perovskite-type compounds have high electrochemical capacities with respect to conventional perovskite oxides since rare earth elements present high affinity for hydrogen absorption among the elements of the periodic table. Therefore, multiple elements including rare elements are needed in ABO_3 perovskite compounds to achieve good electrochemical capacities. In case

layered perovskite materials such as $A_2B_2O_7$-type compounds are only the beginning of the way to understand their behavior, thus, new experiment involving different compositions should be performed.

Alternatively, for metal–air battery applications, a common target is to develop electrode materials with enhanced catalytic performance (electrical and chemical). In this sense, it is recommended the selection of small particles with a large surface area. The development of a rechargeable metal–air battery technology is expected to become one of the most widely used technologies in the future because of the high energy density that these systems can develop. In this sense, one of the critical points to solve before commercializing the metal–air technology is the slow kinetics of discharging and charging reactions at the air electrode.

5 Concluding Remarks

Perovskite materials have been associated with different applications in batteries, especially, as catalysis materials and electrode materials in rechargeable Ni–oxide, Li–ion, and metal–air batteries. Numerous perovskite compositions have been studied so far on the technologies previously mentioned; this is mainly because perovskite materials usually present reversible electrochemical behavior, high natural abundance, facile synthesis, low price, and environmental benignity. Some examples of demonstrated technological usage of perovskites are full cells where perovskite materials are often employed as materials for ionic transportation. Different forms of structural perovskites can be often produced by means of different chemical methods, which provides a great field of opportunity in different types of batteries. One of the examples given in the present book chapter was the layered perovskite material that, as far as authors concern, there is no at this time literature available regarding layered $A_2B_2O_7$ perovskites as negative electrode materials for Ni–oxide batteries. As already demonstrated in this chapter, layered perovskite materials can be alternative electrode materials for Ni–oxide batteries. Overall, ABO_3 perovskite oxides present excellent discharge capacity at high temperatures, and consequently, are regarded as a prominent alternative for negative electrode materials for the next generation of high-temperature and high-performance Ni/oxide batteries. Further research work is expected to optimize the properties and performance of $A_2B_2O_7$ layered compounds and on this way be able to discriminate the type of perovskite-type structure offering the best electrochemical performance.

Acknowledgements The authors gratefully acknowledge the support to the National Science and Technology Council (CONACYT) and the Secretary of Energy of Mexico (SENER) through the founding "CONACYT-SENER-Sustentabilidad Energética" (Project No. 232611). Eng. Y. Pacheco would like to thank the support of CONACYT through the grant No. 445176. Dr. John Henao acknowledge the support to the CONACYT's "Cátedras" program, Project 848. Thanks to Dr. Maura Casales, Dr. Oscar Sotelo and MsC. Jose Juan Ramos from ICF-UNAM for the technical support during the preparation of this work.

References

1. Petrović M, Chellappan V, Ramakrishna S (2015) Perovskites: solar cells & engineering applications–materials and device developments. Sol Energy 122:678–699
2. Dogan F, Lin H, Guilloux-Viry M, Peña O (2015) Focus on properties and applications of perovskites. Sci Tech Adv Mater 16(2)
3. Bhalla AS, Guo R, Roy R (2000) The perovskite structure–a review of its role in ceramic science and technology. Mater Res Innov 4(1):3–26
4. Suntivich J, Gasteiger HA, Yabuuchi N, Nakanishi H, Goodenough JB, Shao-Horn Y (2011) Design principles for oxygen-reduction activity on perovskite oxide catalysts for fuel cells and metal–air batteries. Nat chem 3(7):546
5. Populoh S, Brunko O, Karvonen L, Sagarna L, Saucke G, Thiel P, Weidenkaff A (2015) Perovskite and related oxides for energy harvesting by thermoelectricity. Perovskites Relat Mix oxides: Concepts Appl
6. Huang K, Lee HY, Goodenough JB (1998) Sr-and Ni-doped LaCoO3 and LaFeO3 perovskites new cathode materials for solid-oxide fuel cells. J Electrochem Soc 145(9):3220–3227
7. Brinkman K, Iijima T, Takamura H (2007) Acceptor doped BiFeO3 ceramics: a new material for oxygen permeation membranes. Jpn J Appl Phys 46(2L):L93
8. Wei Y, Xue J, Fang W, Chen Y, Wang H, Caro J (2015) Enhanced stability of Zr-doped Ba (CeTb) O 3− δ-Ni cermet membrane for hydrogen separation. Chem Commun 51(58):11619–11621
9. Sorita R, Kawano T (1997) A highly selective CO sensor using LaMnO3 electrode-attached zirconia galvanic cell. Sens Actuators B: Chem 40(1):29–32
10. Giang HT, Duy HT, Ngan PQ, Thai GH, Toan NN (2011) Hydrocarbon gas sensing of nano-crystalline perovskite oxides LnFeO3 (Ln= La, Nd and Sm). Sens Actuators B Chem 158(1):246–251
11. Bradha M, Vijayaraghavan T, Suriyaraj SP, Selvakumar R, Ashok AM (2015) Synthesis of photocatalytic La (1–x) AxTiO3. 5–δ (A= Ba, Sr, Ca) nano perovskites and their application for photocatalytic oxidation of congo red dye in aqueous solution. J Rare Earths 33(2):160–167
12. Iwase A, Kato H, Kudo A (2013) The effect of Au cocatalyst loaded on La-doped NaTaO3 on photocatalytic water splitting and O2 photoreduction. Appl Catal B 136:89–93
13. Deng G, Chen Y, Tao M, Wu C, Shen X, Yang H, Liu M (2010) Electrochemical properties and hydrogen storage mechanism of perovskite-type oxide LaFeO3 as a negative electrode for Ni/MH batteries. Electrochim Acta 55(3):1120–1124
14. Ma C, Chen K, Liang C, Nan CW, Ishikawa R, More K, Chi M (2014) Atomic-scale origin of the large grain-boundary resistance in perovskite Li-ion-conducting solid electrolytes. Energy Environ Sci 7(5):1638–1642
15. Attfield JP, Lightfoot P, Morris RE (2015) Perovskites. Dalton Trans 44(23):10541–10542
16. Pena MA, Fierro JLG (2001) Chemical structures and performance of perovskite oxides. Chem Rev 101(7):1981–2018
17. Kieslich G, Sun S, Cheetham AK (2015) An extended tolerance factor approach for organic–inorganic perovskites. Chem sci 6(6):3430–3433
18. Wehinger B, Bosak A, Nazzareni S, Antonangeli D, Mirone A, Chaplot SL, Ghose S (2015) Lattice dynamics of $MgSiO_3$ perovskite (bridgmanite) studied by inelastic x-ray scattering and ab initio calculations. arXiv:1509.06164
19. Mitchell RH (1995) Perovskites: a revised classification scheme for an important rare earth element host in alkaline rocks. Mineral Soc Ser 7:41–76
20. Glasser L (2017) Systematic thermodynamics of layered perovskites: ruddlesden-popper phases. Inorg Chem 56(15):8920–8925
21. Granger P, Parvulescu VI, Kaliaguine S, Prellier W (2015) Perovskites and related mixed oxides: concepts and applications. Wiley

22. Lichtenberg F, Herrnberger A, Wiedenmann K (2008) Synthesis, structural, magnetic and transport properties of layered perovskite-related titanates, niobates and tantalates of the type AnBnO3n+ 2, A′ Ak–1BkO3 k+ 1 and AmBm–1O3m. Prog Solid State Chem 36(4):253–387
23. Nakayama S (2001) LaFeO3 perovskite-type oxide prepared by oxide-mixing, co-precipitation and complex synthesis methods. Journal of materials science 36(23):5643–5648
24. Henao J, Martinez-Gomez L (2017) On rare-earth perovskite-type negative electrodes in nickel–hydride (Ni/H) secondary batteries. Mater Renew Sustain Energy 6(2):7
25. Vidal K, Morán-Ruiz A, Larrañaga A, Porras-Vázquez JM, Slater PR, Arriortua MI (2015) Characterization of LaNi0. 6Fe0. 4O3 perovskite synthesized by glycine-nitrate combustion method. Solid State Ion 269:24–29
26. Wang Q, Deng G, Chen Z, Chen Y, Cheng N (2013) Electrochemical hydrogen property improved in nano-structured perovskite oxide LaFeO3 for Ni/MH battery. J Appl Phys 113 (5):053305
27. Kowal K, Kowalczyk M, Czekaj D, Jartych E (2015) Structure and some magnetic properties of (BiFeO3) x-(BaTiO3) 1–x solid solutions prepared by solid-state sintering. Nukleonika 60 (1):81–85
28. Rida K, Pena MA, Sastre E, Martinez-Arias A (2012) Effect of calcination temperature on structural properties and catalytic activity in oxidation reactions of LaNiO3 perovskite prepared by Pechini method. J Rare Earths 30(3):210–216
29. Song M, Chen Y, Tao M, Wu C, Zhu D, Yang H (2010) Some factors affecting the electrochemical performances of LaCrO3 as negative electrodes for Ni/MH batteries. Electrochim Acta 55(9):3103–3108
30. Weidenkaff A, Ebbinghaus SG, Lippert T (2002) Ln_{1-x} A_x CoO3 (Ln= Er, La; A= Ca, Sr)/ Carbon nanotube composite materials applied for rechargeable Zn/Air batteries. Chem Mater 14(4):1797–1805
31. Takeguchi T, Yamanaka T, Takahashi H, Watanabe H, Kuroki T, Nakanishi H, Matsuda M (2013) Layered perovskite oxide: a reversible air electrode for oxygen evolution/reduction in rechargeable metal-air batteries. J Am Chem Soc 135(30):11125–11130
32. Shan YJ, Chen L, Inaguma Y, Itoh M, Nakamura T (1995) Oxide cathode with perovskite structure for rechargeable lithium batteries. J Power Sources 54(2):397–402
33. Etacheri V, Marom R, Elazari R, Salitra G, Aurbach D (2011) Challenges in the development of advanced Li-ion batteries: a review. Energy Environ Sci 4(9):3243–3262
34. Li H, Wang Z, Chen L, Huang X (2009) Research on advanced materials for Li-ion batteries. Adv Mater 21(45):4593–4607
35. Kraytsberg A, Ein-Eli Y (2011) Review on Li–air batteries—Opportunities, limitations and perspective. J Power Sources 196(3):886–893
36. Lu F, Wang Y, Jin C, Li F, Yang R, Chen F (2015) Microporous La 0.8 Sr 0.2 MnO 3 perovskite nanorods as efficient electrocatalysts for lithium–air battery. J Power Sources 293:726–733
37. Cheng F, Chen J (2012) Metal–air batteries: from oxygen reduction electrochemistry to cathode catalysts. Chem Soc Rev 41(6):2172–2192
38. Wang Q, Xue Y, Sun S, Li S, Miao H, Liu Z (2017) La0. 8Sr0. 2Co1-xMnxO3 perovskites as efficient bi-functional cathode catalysts for rechargeable zinc-air batteries. Electrochim Acta 254:14–24
39. Li C, Yu Z, Liu H, Chen K (2018) High surface area LaMnO3 nanoparticles enhancing electrochemical catalytic activity for rechargeable lithium-air batteries. J Phys Chem Solids 113:151–156
40. Park HW, Lee DU, Park MG, Ahmed R, Seo MH, Nazar LF, Chen Z (2015) Perovskite–nitrogen-doped carbon nanotube composite as bifunctional catalysts for rechargeable lithium-air batteries. Chemsuschem 8(6):1058–1065
41. Du Z, Yang P, Wang L, Lu Y, Goodenough JB, Zhang J, Zhang D (2014) Electrocatalytic performances of LaNi1− xMgxO3 perovskite oxides as bi-functional catalysts for lithium air batteries. J Power Sources 265:91–96

42. Yang W, Salim J, Li S, Sun C, Chen L, Goodenough JB, Kim Y (2012) Perovskite Sr 0.95 Ce 0.05 CoO 3− δ loaded with copper nanoparticles as a bifunctional catalyst for lithium-air batteries. J Mater Chem 22(36):18902–18907
43. Jung KN, Lee JI, Im WB, Yoon S, Shin KH, Lee JW (2012) Promoting Li 2 O 2 oxidation by an La 1.7 Ca 0.3 Ni 0.75 Cu 0.25 O 4 Layered perovskite in lithium–oxygen batteries. Chem Commun 48(75):9406–9408
44. Li L, Wang L, Zhang X, Xie M, Wu F, Chen R (2015) Structural and electrochemical study of hierarchical LiNi1/3Co1/3Mn1/3O2 cathode material for lithium-ion batteries. ACS Appl Mater Interfaces 7(39):21939–21947
45. Nakayama M, Ikuta H, Uchimoto Y, Wakihara M (2003) Study on the AC impedance spectroscopy for the Li insertion reaction of Li x La1/3NbO3 at the Electrode—Electrolyte Interface. J Phys Chem B 107(38):10603–10607
46. Henao J, Sotelo O, Casales M, Martinez-Gomez L (2017) Electrochemical performance of the rare-earth perovskite-type oxide La0. 6Sr0. 4Co0. 2Fe0. 8O3 as negative electrode material for Ni/oxide rechargeable batteries. Mater Renew Sustain Energy 6(4):16
47. Kaabi A, Tliha M, Dhahri A, Khaldi C, Fenineche N, Elkedim O, Lamlouli J (2018) Effect of temperature on behavior of perovskite-type oxide LaGaO3 used as a novel anode material for Ni-MH secondary batteries. Int J Energy Res
48. Esaka T, Sakaguchi H, Kobayashi S (2004) Hydrogen storage in proton-conductive perovskite-type oxides and their application to nickel–hydrogen batteries. Solid State Ion 166 (3–4):351–357
49. Wang Q, Chen Z, Chen Y, Cheng N, Hui Q (2011) Hydrogen storage in perovskite-type oxides ABO3 for Ni/MH battery applications: A density functional investigation. Ind Eng Chem Res 51(37):11821–11827
50. Deng G, Chen Y, Tao M, Wu C, Shen X, Yang H (2009) Electrochemical properties of La1− xSrxFeO3 (x= 0.2, 0.4) as negative electrode of Ni–MH batteries. Electrochim Acta 54 (15):3910–3914
51. Compton RG, Laborda E, Ward, KR (2014) Understanding voltammetry: simulation of electrode processes
52. Mohamedi M, Sato T, Itoh T, Umeda M, Uchida I (2002) Cyclic voltammetry and AC Impedance of MmNi3. 55Co0. 75Mn0. 4Al0. 3 alloy single-particle electrode for rechargeable Ni/MH battery. J Electrochem Soc 149(8):A983–A987
53. Srivastava S, Srivastava ON (1998) Investigations on synthesis, characterization and hydrogenation behaviour of the spin-and thermal-melted versions of LaNi5− xSix (x= 0.1, 0.3, 0.5) hydrogen storage materials. J Alloy Compd 267(1–2):240–245
54. Kaabi A, Tliha M, Dhahri A, Khaldi C, Lamloumi J (2016) Study of electrochemical performances of perovskite-type oxide LaGaO3 for application as a novel anode material for Ni-MH secondary batteries. Ceram Int 42(10):11682–11686
55. Yuan X, Xu N (2001) Comparative study on electrochemical techniques for determination of hydrogen diffusion coefficients in metal hydride electrodes. J Appl Electrochem 31(9):1033–1039

Chapter 7
Perovskite Materials in Photovoltaics

Wei Wang and Zongping Shao

1 Introduction

Energy is fundamental to the quality of our lives. Currently, we fully rely on an abundant and continuous supply of energy for living and working. However, modern society relies too heavily on fossil fuels based on the low-efficiency combustion technology, and their excessive consumption has caused serious greenhouse effects on the Earth. Furthermore, the fossil fuel resources will run out in the near future due to their nonrenewable nature, which will cause a serious energy crisis in the future. In order to solve abovementioned problems, alternative energy conversion systems with high efficiency based on renewable energy resources such as solar energy and wind energy are pursued. Among the renewable energies, solar energy is the most abundant energy source. One-day solar irradiation on the Earth's surface can provide us with about 10,000 times more energy than the entire energy demand of our planet per day [1–4]. Photovoltaic (PV) systems, which directly convert sunlight into electricity, have attracted more and more attention recently since they are considered as the key solutions to the extreme energy demand by efficient utilization of the abundant solar energy [5–9].

Various types of solar cells have been developed and intensively exploited such as silicon-based solar cells, dye-sensitized solar cells (DSSCs), perovskite solar cells (PSCs), etc. Numerous research efforts have been conducted to develop and design new-generation solar cells with higher efficiency and lower cost since the dominated silicon-based solar cells suffer from high cost and complex fabrication

W. Wang · Z. Shao (✉)
WA School of Mines: Minerals, Energy and Chemical Engineering (WASM-MECE), Curtin University, Perth, WA 6845, Australia
e-mail: zongping.shao@curtin.edu.au

Z. Shao
State Key Laboratory of Materials-Oriented Chemical Engineering, College of Chemical Engineering, Nanjing Tech University, Nanjing 210009, China

N. S. Arul and V. D. Nithya (eds.), *Revolution of Perovskite*, Materials Horizons: From Nature to Nanomaterials, https://doi.org/10.1007/978-981-15-1267-4_7

procedures [10–15]. Among various new-generation solar cells, DSSCs exhibit a promising future due to their relatively high PCE, ease of fabrication, low cost, and flexibility [16–19]. Recently, a compound with a perovskite structure plays a critical role in the field of solar cells. The perovskites have been used as the photoelectrodes in DSSCs and the light absorbers in PSCs [20–23]. In this chapter, we will outline the recent advances in the applications of perovskites in DSSCs and PSCs and then give some useful guidance for the future design and development of perovskite compounds in various photovoltaic-based applications.

2 Organic–Inorganic Solar Cells

2.1 A Brief Introduction of PSCs

During the past few years, hybrid organic–inorganic perovskites have become one of the hottest topics in chemistry and materials science disciplines, which have developed rapidly due to the attractive features in the solar-energy-based applications [24–27]. In particular, hybrid organic–inorganic perovskite was demonstrated as a game changer in the field of photovoltaics (solar cells), with great achievements in PCEs, which are comparable to those of conventional silicon solar cells and cadmium telluride and copper indium gallium selenide/sulfide-based solar cells [28]. PSCs have been developed quickly in the past 6 years as evidenced by more than 6000 publications on this hot and dynamic field.

Miyasaka et al. reported the first use of organic–inorganic perovskite in solar cells [29]. The new solar cells were created on a DSSC configuration with a thin perovskite layer such as $CH_3NH_3PbI_3$ ($MAPbI_3$) and $CH_3NH_3PbBr_3$ ($MAPbBr_3$) on the mesoporous TiO_2 and delivered PCEs of 3.8% and 3.1%, respectively. However, the stability of these solar cells was very poor due to the corrosive properties of the liquid electrolyte used in this configuration. In 2011, Park and co-workers developed a solar cell with the same dye-sensitized configuration and an improved PCE of 6.5% was achieved [30]. A solid-state electrolyte, spiro-OMeTAD was demonstrated to act as a hole transporting material (HTM) to replace the corrosive liquid electrolyte to enhance the cell stability [31]. Park et al. demonstrated a one-step fabrication of PSC with a solid-state electrolyte by a solution-based technique, as shown in Fig. 1 [31]. A PCE of 9.7% and a reasonable durability were achieved with this PSC.

PSCs have attracted more and more attention due to their rapid increase in PCE during only several years (3.8% in 2009, 10.9% in 2012, 19.3% in 2014, and 22.1% in 2017) [29, 32–34]. The high PCE essentially benefits from the attractive opto-electrical properties of the hybrid halide perovskites, such as the high sunlight absorption coefficient, superior electron/hole mobility, long lifetime and diffusion length of the carriers, and a direct band gap [35–39]. Furthermore, the organic–inorganic halide perovskites can produce loosely bonded excitons with a small

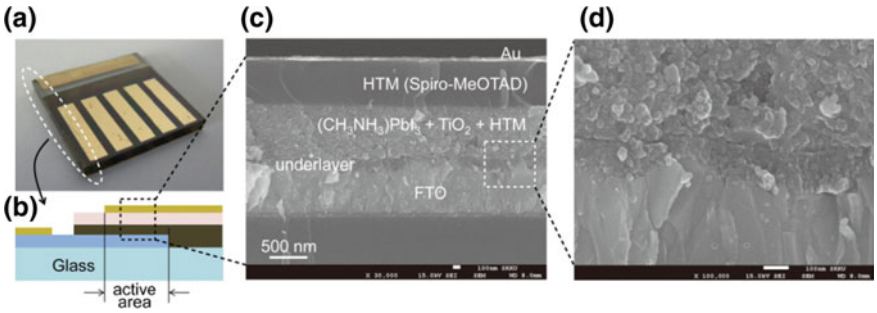

Fig. 1 **a** The real image of the PSC. **b** Cross-sectional structure of the PSC. **c** Cross-sectional SEM image of the PSC. **d** Active layer–underlayer–fluorine-doped tin oxide (FTO) interfacial junction structure. Reprinted with permission from Ref. [31]. Copyright 2012, Springer Nature

bonding energy, which promotes the production of free charge carriers in the perovskite with a small driving force [40, 41]. Thus, the rapid enhancement of the PCEs of PSCs can be very close to the theoretical efficiency level by combining the design and development of the perovskite materials with various elemental compositions, the crystalline film formation, interface construction and optimization as well as the unique architecture of the device, etc. [28, 30, 31, 33, 42–51].

TiO_2 is widely used as the electron transportation material (ETM) in PSCs and a high PCE of above 20% can be obtained with TiO_2 as the ETM [52–54]. Some other materials such as doped TiO_2, ZnO, SnO_2, Zn_2SnO_4, and $BaSnO_3$ are also reported as ETMs in PSCs although the PSCs based on some of these materials produced lower PCEs as compared with that of TiO_2 [55–59]. In this section, recent advances in perovskites for the use as light absorbers and ETMs in PSCs are outlined and discussed.

2.2 *Light Absorbers*

The recent progress of perovskite-based light absorbers in PSCs is divided into three aspects including the processing of perovskite films, the compositional engineering, and the device operational stability. This section aims to give some helpful guidelines for the future material design and better understanding of perovskite-based light absorbers in PSCs.

2.2.1 Processing of Perovskite Films

The improvement of the PCEs of PSCs requires the increase in the film quality of perovskite layers and the perovskite-based thin films should be pinhole-free, smooth and uniform, etc. A PCE as high as 15% was obtained by Liu et al. in

planar PSCs with the help of a vapor deposition method as shown in Fig. 2a [60]. Perovskite films with excellent uniformity over a range of length scales were obtained by this method. Thus, a high PCE was then delivered. This vapor deposition method can also be used in the preparation of the multi-stack thin films with larger cell areas [61].

Solution-based fabrication technique is widely used in solar cells due to the advantages of low energy consumption at a large-scale manufacture. However, the halide perovskites are demonstrated to be difficult to form compact, uniform, and flat films due to the strong tendency of the anisotropic crystallization when the used solvent was evaporated. As a result, it is necessary to develop new and efficient fabrication methods to improve the crystallization rate of the halide perovskites. In general, the kinetic control between nucleation and crystal grain growth is an effective route to produce halide perovskite layers with superior optoelectronic performance. Jeon et al. used a solvent engineering route to develop uniform perovskite films to achieve high PSC performance [62]. It was found that the use of dimethyl sulfoxide (DMSO) led to the formation of a MAI–PbI_2–DMSO intermediate to slow down the crystal growth of perovskites, which has attracted more and more attention by several research groups in the world after Jeon et al.'s work [21, 63, 64]. Park and co-workers also demonstrated a fast crystallization method based on spin coating of a $MAPbI_3$/dimethylformamide (DMF) solution with a subsequent exposure to chlorobenzene in order to promote the formation of uniform perovskite films (Fig. 2b) [65]. A gas-assisted solution-processing method was demonstrated by Huang et al., and uniform perovskite layers composed of densely packed single crystalline grains were obtained [66].

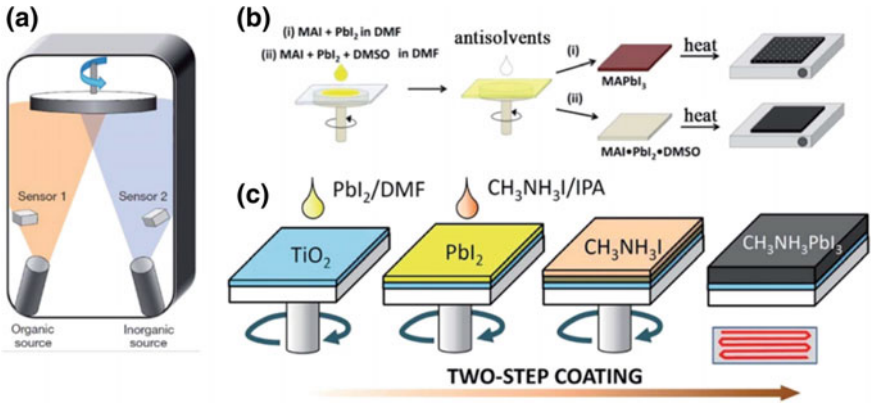

Fig. 2 Different deposition methods for high-quality perovskite films: **a** vapor deposition. Reprinted with permission from Ref. [60]. Copyright 2013, Springer Nature. **b** anti-solvents. Reprinted with permission from Ref. [65]. Copyright 2015, American Chemical Society. **c** two-step method. Reprinted with permission from Ref. [198]. Copyright 2015, Royal Society of Chemistry

Two-step method was also used to prepare uniform perovskite layer with high performance (Fig. 2c). Burschka et al. first developed a novel two-step method, in which PbI_2 was first deposited onto a porous TiO_2 film and the PbI_2 was converted into the $MAPbI_3$ perovskite by the subsequent exposure to the MAI solution. A PCE of 15% was obtained by mesoporous PSCs based on a perovskite film with an enhanced film quality [67]. Afterward, an interdiffusion method with a subsequent spin coating of PbI_2 and MA was reported by Xiao et al. and a PCE of 15.4% was obtained by PSCs with a planar configuration [68]. By further combining the interdiffusion method with a solvent annealing strategy, the quality of the perovskite films was further enhanced to reach a high PCE (15.6%) [69]. Recently, Bi et al. demonstrated that poly(methyl methacrylate) (PMMA) was used as the template for the production of perovskite films with fewer defects and bigger oriented grains by tailoring the nucleation and crystal growth rates and a certified PCE of 21.02% was obtained [70].

The fabrication of perovskite films with well-controlled morphology, superior surface coverage, and fewer pinholes can be obtained by different advanced fabrication techniques such as vapor-assisted solution process, spin coating, surface passivation, and fast deposition crystallization [60, 62, 67, 71, 72]. $MAPbI_3$ was successfully prepared by the spin coating method [67]. However, the achievement of high-quality films of pure-phase $MAPbI_3$ perovskites with excellent coverage was still very difficult. Some functional modifiers were added to the fabrication process of $MAPbI_3$ such as NH_4Cl, 1, 8-diiodooctane as well as solvent replacement of DMF by DMSO, and then higher PCEs and more uniform morphology are obtained [73–75].

Unfortunately, there are several disadvantages for the use of spin coating to prepare the $MAPbI_3$ perovskite since it is hard to obtain suitable solvents for the organic and inorganic parts of the halide perovskites. Vacuum evaporation is a promising technique to prepare $MAPbI_3$ film with a precise control of the film property [60]. The halide perovskites synthesized by co-evaporation of $PbCl_2$ and CH_3NH_3I exhibited considerable film uniformity and coverage [60]. Co-evaporation of MAI and $PbCl_2$ led to a $MAPbI_3$ phase, and the perovskite film uniformity was much superior to that of the solution-processed one, as shown in Fig. 3 [60]. However, the use of high vacuum in this technique was not practical for large-scale manufacture. A vapor-assisted solution process based on the favorable reaction between the PbI_2 film and CH_3NH_3I vapor was used to fabricate perovskite films with full coverage and small grain sizes with a 100% precursor transformation efficiency [76].

2.2.2 Compositional Engineering

One of the largest superiorities of the organic–inorganic perovskites is the structural and compositional flexibility and their optoelectronic properties can be well tuned by functional doping or replacement. The I in $MAPbI_3$ can be fully replaced with both Cl and Br to form $MAPbCl_3$ and $MAPbBr_3$ [77], and large single crystals of

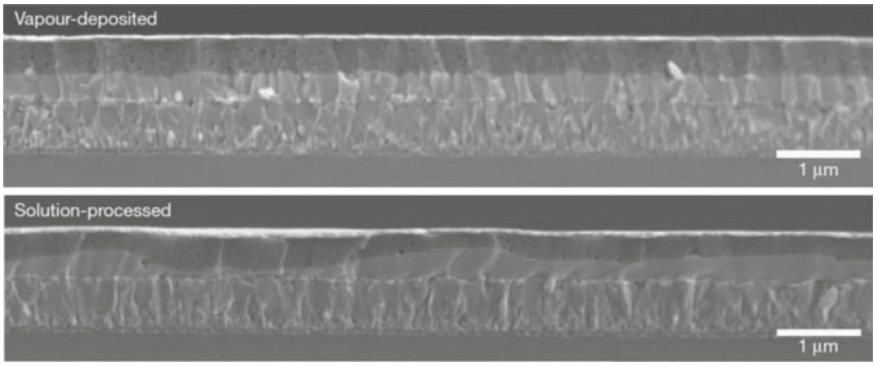

Fig. 3 Comparison of the perovskite film uniformity between vapor deposition and solution-processing methods. From top to bottom, the six layers are Ag, Spiro-OMeTAD, perovskite, compact TiO_2, FTO and glass. Reprinted with permission from Ref. [60]. Copyright 2013, Springer Nature

$MAPbCl_3$, $MAPbBr_3$, and $MAPbI_3$ have been successfully prepared (Fig. 4) [78]. The band gaps of the halide perovskites increased with the decrease in the ionic size of the halide and the band gaps of $MAPbCl_3$, $MAPbBr_3$, and $MAPbI_3$ single crystals were 2.97, 2.24, and 1.53 eV, respectively [78]. However, the measured band gaps of the polycrystalline perovskite films were larger than those of single crystals [37, 79]. For example, the measured band gaps of polycrystalline $MAPbCl_3$, $MAPbBr_3$, and $MAPbI_3$ were 3.1, 2.3, and 1.6 eV, respectively [77, 80].

The diffusion length of the photo-generated electron–hole pair of the halide perovskite played a critical role in determining the PCEs of PSCs, which generally limited the thickness of the perovskite layer to several hundred nanometers [35, 36, 38, 81, 82]. For instance, Stranks et al. found that the electron and hole diffusion lengths for $MAPbI_3$ were 130 and 100 nm, respectively. Longer electron diffusion length (1069 nm) and hole diffusion length (1213 nm) were reported for Cl-doped perovskite ($MAPbI_{3-x}Cl_x$) [36]. It was also found that the Cl doping in $CH_3NH_3PbBr_3$ increased the lifetimes of the electron–hole pairs as shown in Fig. 5 [82]. For $CH_3NH_3PbBr_{2.4}Cl_{0.6}$, the average recombination lifetime was as high as 446 ns compared with 100 and 44 ns for $CH_3NH_3PbBr_3$ and $CH_3NH_3PbI_{3-x}Cl_x$, respectively. However, the corresponding average recombination lifetime of the $CH_3NH_3PbBr_{3-x}Cl_x$ perovskite decreased with a higher Cl doping amount. The high values of diffusion length and lifetime of the mixed halide perovskites presented some potential for the possible fabrication of PSCs with thicker perovskite layers without impairing the high performance.

Hao et al. studied the performance of PSCs with $CH_3NH_3Sn_{1-x}Pb_xI_3$ as the light absorbers [83]. The band gaps of these perovskites did not follow a linear trend (Vegard's law) in between these two extremes of 1.55 and 1.35 eV but had a smaller band gap (less than 1.3 eV), which extended the sunlight harvesting region to as high as 1050 nm. The PSCs with $CH_3NH_3Sn_{0.5}Pb_{0.5}I_3$ as the light absorber

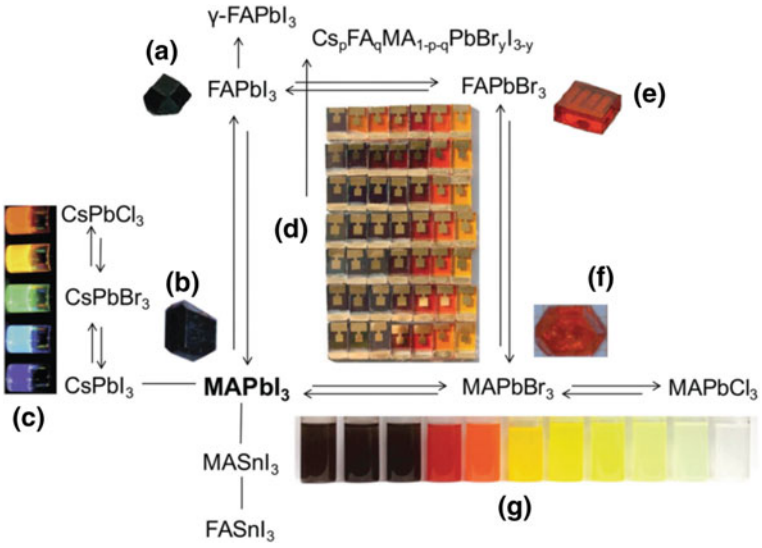

Fig. 4 The versatility of halide perovskites and their sunlight absorption capability. **a** single crystal of formamidinium ion (FA)PbI_3, **b** single crystal of $MAPbI_3$, **c** colloidal solutions of $CsPbX_3$ (X = Cl, Br, I) perovskites, **d** PSCs of 49 different compositions based on the MA/FA–Pb–Br/I systems, **e** single crystal of $FAPbBr_3$, **f** single crystal of $MAPbBr_3$ and **g** colloidal nanocrystals of $MAPbX_3$ (X = Cl, Br, I) perovskites. Reprinted with permission from Ref. [5]. Copyright 2017, Royal Society of Chemistry

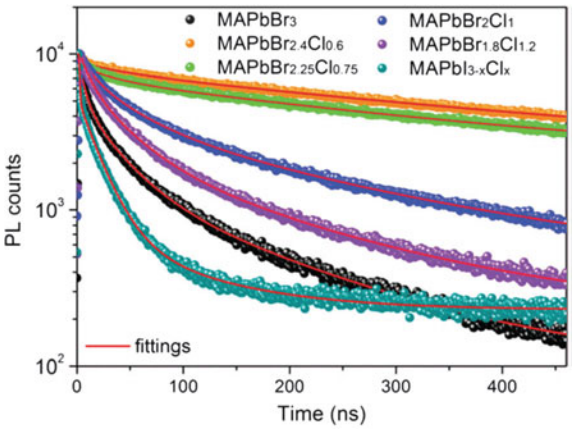

Fig. 5 Time-resolved photoluminescence (PL) decay detected at the peak wavelength of emission for various $MAPbX_3$ (X = Cl, Br, I) perovskites. Reprinted with permission from Ref. [82]. Copyright 2014, Royal Society of Chemistry

delivered a high short-circuit current density (J_{sc}) of over 20 mA cm^{-2} under simulated sunlight irradiation. Noel et al. demonstrated a totally Pb-free $CH_3NH_3SnI_3$ halide perovskite with a band gap of 1.23 eV for PSCs [84]. A PCE of higher than 6% was obtained under simulated sunlight irradiation. However, the $CH_3NH_3SnI_3$ perovskite suffered from poor stability and the main

issue was the stabilization of the valence states of Sn in this material, which needed to be solved. Importantly, this finding demonstrates that the replacement of Pb-based materials by nontoxic elements is possible to achieve high-performance PSCs. More recently, Krishnamoorthy et al. demonstrated that germanium (Ge) was also a suitable replacement for Pb in halide perovskites for PSCs by the computational screening and experimental investigation [85]. $CsGeI_3$ crystals with stable rhombohedral crystal structures were prepared experimentally, which showed no phase changes under the solar cell working conditions. $MAGeI_3$ crystals were also prepared, and their crystal structure, band gaps, and thermal stability were compared with $CsGeI_3$ crystals. The PSCs with $CsGeI_3$ and $MAGeI_3$ displayed photocurrent densities of 5.7 and 4.0 mA cm^{-2}, respectively, although the PCEs were very low (less than 0.2%). This study demonstrated the potential of Ge-based halide perovskites for the applications in PSCs.

Besides the X-site doping and B-site doping, the A-site cation in halide perovskites can also be substituted or doped. MA was doped by the FA ions with slightly larger ionic radius, which expanded the lattice and changed the tilting of the PbI_6-octahedra [21, 86]. As a result, a decrease of the band gap is from 1.59 eV for the $MAPbI_3$ to 1.45–1.52 eV for the $FAPbI_3$ [80, 86]. For example, the effect of the A-site cation size on the band gaps of the halide perovskites was studied as shown in Fig. 6 [87]. It was found that the lattice of the perovskite was enlarged when the A-site cation showed a larger ionic radius. The band gap was then reduced and a redshift in the sunlight absorption spectra was achieved. Thus, $FAPbI_3$ was more efficient than $MAPbI_3$ in PSCs. Due to the reduced band gap of $FAPbI_3$ (1.48 eV), a J_{sc} of >23 mA cm^{-2} and a PCE of 14.2% were obtained [87]. Choi et al. used Cs doping in $MAPbI_3$ perovskites to enhance the PCEs of the PSCs. The PSCs assembled by $Cs_xMA_{1-x}PbI_3$ perovskite with a 10 mol% Cs doping amount showed an obvious enhancement in PCE from 5.51 to 7.68% [88]. This improvement in the PCE was assigned to the improved film morphology. The band bap of $Cs_xMA_{1-x}PbI_3$ perovskite was gradually increased from 1.52 eV ($MAPbI_3$)

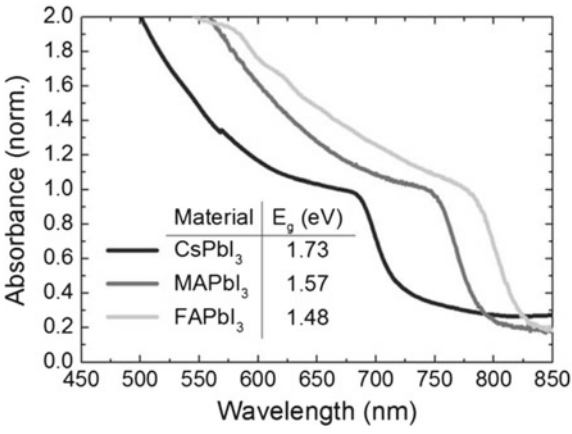

Fig. 6 UV–Vis spectra for the $APbI_3$ perovskites formed, where A is Cs, MA or FA. Reprinted with permission from Ref. [87]. Copyright 2014, Royal Society of Chemistry

to 2.05 eV ($CsPbI_3$) with the increased Cs doping amount, implying that the band gaps of the mixed halide perovskites can be easily tuned by controlling the Cs doping amount in $Cs_xMA_{1-x}PbI_3$ perovskites to achieve the best performance.

2.2.3 Device Operational Stability

In the past 5 years, PSCs have been demonstrated as highly efficient sunlight conversion devices with PCEs comparable to those of conventional solar cells such as Si solar cells. However, the durability of PSCs is not satisfied up to now. Thus, the next challenge and future research direction is to make the halide perovskite as stable as other cell components in PSCs. There are several potential degradation factors to affect the stability of the PSCs. Humidity was reported to be the most critical factor for the performance degradation of PSCs due to the strong interaction of halide perovskites with water [89]. There are several deterioration mechanisms based on perovskite and other cell components, which was caused by this so-called extrinsic factor (humidity) [89]. The encapsulation strategy was reported to be useful to enhance the PSC stability by isolating the PSCs from the potential external (extrinsic) degradation factors [90]. However, the potential intrinsic degradation factors were also active under the inert conditions, which may impact the perovskite and other cell components. For example, small-molecule HTMs suffered from the crystallization at relatively high temperature, which reduced the electronic contact with the halide perovskite and the metal current collector and as a result, a degradation in the PSC performance was observed as shown in Fig. 7a [91]. Gold (Au) was widely applied as the current collector to fabricate lab-scale PSCs, and the quick performance degradation of PSCs was assigned to the Au migration within small-molecule HTMs as shown in Fig. 7b [92]. Thus, reducing the Au migration behavior was very important to improve the stability of PSCs with small-molecule HTMs. Carbon-based HTMs should be one of the possible solutions to solve abovementioned problem although the PCEs of PSCs with carbon-based HTMs were not as high as the PSCs based on small-molecule HTMs [93, 94]. Polymeric HTM was demonstrated to be an effective barrier to prevent the Au migration while the addition of chromium interlayers and alumina nanoparticle buffer layers also improved the PSC stability by inhibiting the Au migration behavior [92, 95–97].

Several kinds of water-resisting layers were demonstrated to be effective to enhance the PSC stability under humidified conditions. For example, hydrophobic ammonium ion was used as a water-resisting layer to decorate the perovskite surface to enhance the stability of perovskites in PSCs under humidified atmospheres [98]. In another work, Bi et al. used an amphiphilic 1, 1, 1-trifluoro-ethyl ammonium iodide as a moisture-resistant layer to improve the device stability under humidified conditions due to the hydrophobic CF_3 groups [99]. A water absorption polymer (PEG) was also used to prevent the reaction between water and the halide perovskite. PEG also displayed a self-healing behavior for the perovskite whereby the retained MAI reacted with PbI_2 again [100]. Wang et al. demonstrated a

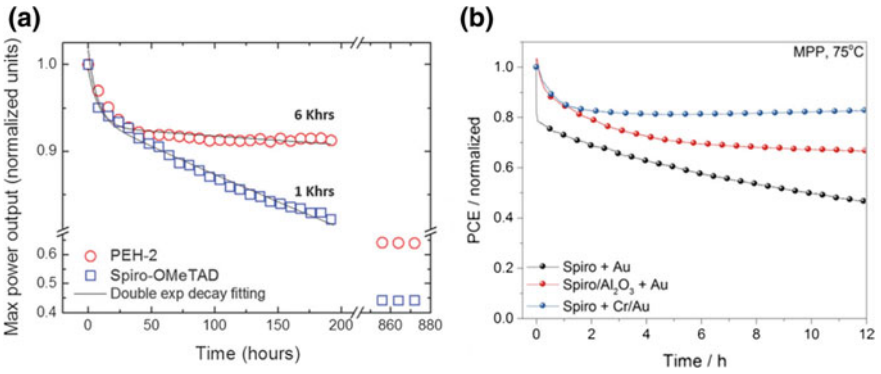

Fig. 7 **a** Maximum power point tracking (MPPT) over time with two different HTMs. Reprinted with permission from Ref. [91]. Copyright 2015, Royal Society of Chemistry. **b** MPPT of PSCs at 75 °C on a spiro-based device with different interlayers. Reprinted with permission from Ref. [92]. Copyright 2016, American Chemical Society

hydrophobic fluorosilane layer to protect the perovskite film to achieve a superior stability of the perovskite film in water [101].

The perovskite light absorber layer is the core part of the PSCs, and its durability is critical to the commercialization of PSCs in the future. The stability of perovskites may be relevant to the ionic defects. These defects did not seem to be particularly harmful within the bulk of the perovskite layer, since they can introduce donor and acceptor electronic states close or within the conduction band and valence band, respectively [102]. However, the ionic defects migrated from the bulk to the interface with the selective contact, which may have a negative effect on the PSC stability [103]. The ionic defects accumulated to form a space charge layer, which reduced the charge separation efficiency. Although the effect of this potential intrinsic factor (ionic defects) on the PSC stability is still under investigation, it is confirmed that the interface between the perovskite and the selective contact plays an essential role in the durability of PSCs. Suppressing the amount of defects by functional doping/substitution and surface passivation should be useful strategies to improve the PSC stability [104, 105].

2.3 Electron Transportation Materials

As mentioned above, the durability of PSCs can be governed by many factors such as the instability of the halide perovskites, the interfaces, and also the charge transport materials, such as ETMs and HTMs. More specifically, when TiO_2 was utilized as the ETM, it showed poor stability under ultraviolet (UV) light irradiation [12, 99, 106]. Different methods have been developed to enhance the durability of PSCs, such as the modification of TiO_2, the development of new ETMs, and the

introduction of interfacial layers between the cell components [55–59]. However, one approach without any additional processes is to develop new ETMs to replace or modify TiO_2 to obtain durable PSCs without impairing their high performance.

$BaSnO_3$ (BSO) perovskite oxide with a band gap of 3.2 eV has been applied in different fields such as transparent conducting oxide, gas sensor, and transistor [107–109]. Recently, BSO perovskite oxide is also used as an ETM to replace TiO_2 in PSCs due to its higher electron mobility and the same perovskite structure as the halide perovskites [59]. It was found that PSCs with BSO as ETM showed a higher PCE than that of TiO_2 (12.3 vs. 11.1%), which was assigned to the better contact between BSO and $MAPbI_3$. The high electron mobility of BSO allowed an efficient charge collection and the wide band gap of BSO also avoided the sunlight absorption competition against $MAPbI_3$. However, there are also some issues needed to be solved in this new BSO-based PSC. For example, BSO showed a higher electron–hole recombination rate under a high voltage, which should be solved in the future in order to make BSO a competitive ETM candidate for the applications in PSCs with high stability.

More recently, well-dispersed BSO nanoparticles were prepared by a simple peroxide-precipitation method [110]. A better coverage of BSO film greatly decreased the leakage problem of the current, and an optimized thickness of ETM layer was beneficial to the decrease in the cell resistance, which contributed to the improved PCEs of the PSCs. By comparing with the PSCs with pristine TiO_2 as an ETM, a PCE enhancement of 12% was achieved by PSCs with BSO as ETM due to the enhanced charge transfer capability and the reduced electron–hole pair recombination. Although this work may provide a new way to use perovskite oxides as ETMs in PCEs, the performance of this new BSO-based PSC can be further improved by tailoring the preparation methods of perovskite material as well as by rationally constructing the interfaces of the solar cells, which can be the future research directions and topics.

La-doped BSO (LBSO) perovskite oxide was reported to have a superior electron mobility of 320 $cm^2\ V^{-1}\ s^{-1}$ and a conductivity of 4000 $S\ cm^{-1}$ at room temperature [111]. However, LBSO films cannot be used on the flexible substrates and glass substrates due to the high formation temperature of the LBSO perovskite phase (>1000 °C) [108]. The development of advanced methods to fabricate the phase-pure LBSO thin film below 500 °C is then critical. The use of amorphous precursors with peroxo groups reduced the perovskite phase formation temperature to 900 °C, which was still too high for the PSC application [112].

A mesoporous ETM based on LBSO has been investigated by Dai and co-workers [113]. The LBSO nanoparticles were synthesized and applied as mesoporous ETMs by spin coating with a low fabrication temperature of 510 °C. It was found that LBSO film showed a suitable transmittance and no strong sunlight absorption competition against the halide perovskite. After optimization, the mesoporous LBSO-based PSC delivered a high PCE of 15.1%. As compared with the PSCs with BSO and TiO_2 as ETMs, the PSC with LBSO as ETM displayed the highest J_{sc} (Fig. 8a) which was assigned to the superior electron mobility of LBSO (the best quenching effect as shown in Fig. 8b). However, the fabrication

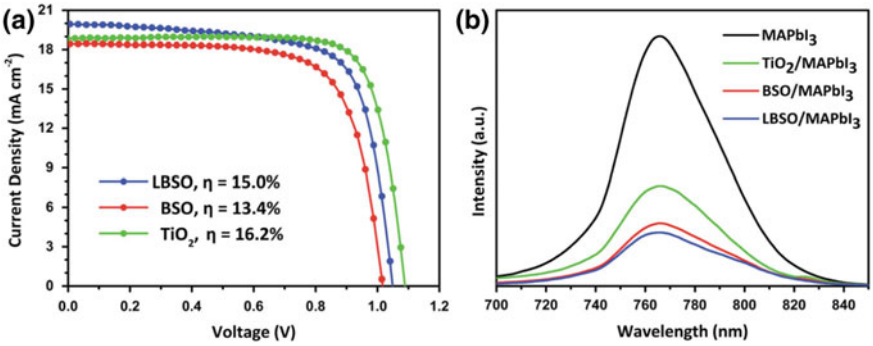

Fig. 8 **a** *J-V* curves of typical PSCs with LBSO, BSO, and TiO_2 obtained under AM 1.5 illumination. **b** Steady-state PL spectra of glass/X/$MAPbI_3$ (X = LBSO, BSO, TiO_2 or none) films with an excitation wavelength of 473 nm. Reprinted with permission from Ref. [113]. Copyright 2017, Royal Society of Chemistry

temperature (510 °C) of BSO perovskite was still too high to prepare solar cells on a glass substrate with high performance. Furthermore, the stability of LBSO-based PSCs was not addressed.

Huang et al. demonstrated a peroxo-precursor-based route for the preparation of BSO perovskite oxide at a temperature as low as 300 °C [114]. However, it is difficult to use this method to produce a colloidal solution to prepare the BSO film. Therefore, the development of a totally dispersed precursor colloidal solution for the preparation of BSO thin films at a large scale remains a challenge to achieve highly efficient and stable PSCs. For the first time, Shin et al. reported a crystalline superoxide–molecular cluster (CSMC) colloidal solution method to obtain LBSO perovskite phase at 300 °C [115]. The compact LBSO layer was then prepared from the CSMC colloidal solution by spin coating onto a FTO glass substrate and the PSC displayed a PCE of 21.2% by using LBSO as the ETM and $MAPbI_3$ as the light harvester.

The UV light-induced degradation in PCEs for PSCs with TiO_2 as ETM is considered as a serious issue for the practical use of PSCs under natural sunlight [12, 99, 106]. Up to now, the stability of PSCs was always tested with white light-emitting diode or UV light-filtered solar simulators [116, 117]. Shin et al. reported a light-soaking experiment under AM 1.5G irradiation with a xenon or metal-halide lamp (including UV light) to investigate the stability of PSCs with LBSO and TiO_2 as the ETMs [115]. The PSC with LBSO ETM displayed a much better stability than that of TiO_2. However, this cell architecture that included organic spiro-OMeTAD HTM was not suitable for studying the long-term stability of PSCs with LBSO as ETM because organic HTMs degraded the PSC performance as mentioned before. The PSCs with a two-sided glass-encapsulated architecture and NiO HTM were prepared and the stability tests of PSCs with LBSO and TiO_2 as ETMs were conducted under AM 1.5G irradiation. The PCE of the PSC with LBSO ETM kept 93.3% of its initial PCE after 1000 h' operation, while the

PSC with TiO_2 ETM showed no PCE within 500 h. The development of LBSO perovskite as ETM in PSCs may accelerate the commercialization of PSCs without requiring a UV filter for the conventional TiO_2-based PSCs.

Besides the BSO-based perovskite oxides as the ETMs, some Ti-based perovskite oxides such as $SrTiO_3$ have also been used as the ETMs for PSCs [118]. Bera et al. used $SrTiO_3$ as a new ETM in PSCs [119]. PSCs with $SrTiO_3$ as ETM and $CH_3NH_3PbI_{3-x}Cl_x$ as light absorber exhibited an open-circuit voltage (OCV) of 1.01 V, which was 25% higher than that of TiO_2 (0.81 V). An enhancement of 17% in the fill factor (FF) was also obtained by controlling the thickness of the $SrTiO_3$ ETM layer. The use of $SrTiO_3$ led to a halide perovskite layer with large grain sizes and an excellent surface coverage, and as a result, an enhanced performance was achieved. The above results strongly recommended $SrTiO_3$ as a useful ETM for further development of the high-performance PSCs. However, the stability of PSCs with $SrTiO_3$ as ETM was not studied, which should be a future research direction.

The construction of double-layer or composite ETM is demonstrated to be a useful way to enhance the performance of PSCs with single-phase or single-layer perovskite oxide ETM [120, 121]. For example, Okamoto and Suzuki found that the construction of $BaTiO_3/TiO_2$ mesoporous double layer (MDL) as ETM enhanced the photovoltaic performance of PSCs [121]. The PCE of PSCs was increased from 9.89% of the cell with TiO_2 mesoporous single layer (MSL) as ETM to 12.4% of the cell with $BaTiO_3/TiO_2$ MDL as ETM. The larger $MAPbI_3$ crystals accompanied with the $BaTiO_3/TiO_2$ MDL resulted in the better sunlight absorption and improved J_{sc}. Moreover, the OCV of the PSC with $BaTiO_3/TiO_2$ MDL as ETM was also enhanced by reducing the electron–hole recombination, which was assigned to the reduced amount of $MAPbI_3$ crystal boundaries and unique band structure of $BaTiO_3/TiO_2$ MDL. Further optimization of the thickness of each layer in the MDL ETM is critical for the further enhancement of the cell performance of PSCs.

Although the PSC with $SrTiO_3$ as ETM showed a high OCV, its average J_{sc} was still much lower than that of PSCs with TiO_2 as ETM. Okamoto et al. utilized a $SrTiO_3/TiO_2$ composite ETM to overcome the drawback of lower J_{sc} of PSCs when pure $SrTiO_3$ was used as the ETM [120]. By optimizing the ratio of $SrTiO_3$ to TiO_2, PSCs assembled by a $SrTiO_3/TiO_2$ composite with 5 vol.% anatase TiO_2 as ETM showed the highest PCE of 10.6%, which was even higher than that of TiO_2 ETM (9.98%). Wang et al. developed a graphene/$SrTiO_3$ composite as a new ETM for PSCs [122]. Due to the superior charge mobility and conductivity of graphene, an improved J_{sc} was demonstrated. The graphene amount in the composite played an important role on the PCEs of PSCs. Excessive graphene reduced the sunlight harvesting capability of perovskite layer by introducing new recombination centers. By optimization the graphene amount, a remarkable PCE of 10.0% and a J_{sc} of 18.08 mA cm^{-2} were obtained, which were 46.0 and 45.6% higher than those of the $SrTiO_3$-based PSCs, indicating the use of graphene was a useful way to enhance the J_{sc} of PSCs with $SrTiO_3$ as ETM. However, the FF of these PSCs was still too low, which strongly hindered the achievement of high PCE. This should be further studied in the future research.

3 Dye-Sensitized Solar Cells

3.1 A Brief Introduction of DSSCs

The development of DSSCs in 1991 opened up a new horizon in the PV technology due to the relatively lower recombination rate in DSSCs than those of traditional solar cells [16]. DSSCs have attracted more and more attention as one of the most promising solar cells. In addition, DSSCs can be fabricated into a large variety of shapes, colors, and transparencies with a superior PCE under low sunlight irradiation intensity [6], which extends the indoor applications of DSSCs. The main challenges for commercialization of DSSCs are relatively low PCE, poor stability, and high price. A DSSC is typically composed of a dye-sensitized mesoporous semiconductor photoanode, a photocathode (also called counter electrode, CE) and an electrolyte with redox couples. To improve the PCEs of DSSCs, tremendous efforts are devoted to several aspects such as using nanostructured oxides and using additional compact and dense layers to improve the injection and collection efficiencies of the photoinduced electron–hole pairs and using panchromatic dyes or multi-dye systems to enhance the sunlight harvesting performance. In the past two decades, significant progress has been achieved in enhancing the PCEs of DSSCs. Figure 9 shows that superior DSSC performance can be obtained by using optimized and matched cell components. The PCE of DSSCs increased from 7.12% in 1991 to 13% in 2014 [10, 11, 16], suggesting that the DSSC technology is now practical if the cost of solar cell components can be reduced with further increased PCE.

Research for optimizing and enhancing the PV performance of DSSCs mainly focuses on modulating the physicochemical properties of main cell components of DSSCs: the sensitized dye, the metal oxide semiconductor (photoanode), the redox couple-based electrolyte, and the photocathode. To enable efficient DSSCs, the

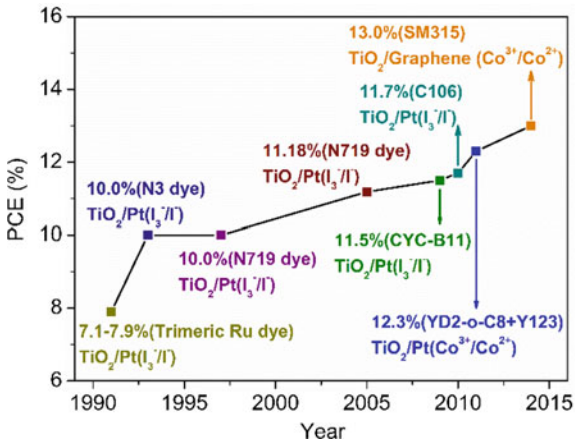

Fig. 9 Selected PCE landmarks in DSSCs

rational design for all the components is required. In this section, the application of perovskite oxides as the photoelectrodes (photoanode and photocathode) will be summarized and discussed.

3.2 Photoanodes

Among the various strategies to improve the PCEs of DSSCs, the development of the photoanode is very important since the photoanode can allow the practical utilization of the photoinduced electron–hole pairs to determine the DSSC performance. The photoanode of DSSC is a mesoporous oxide-based layer composed of nanoparticles sintered on a conducting substrate such as the FTO glass. This mesoporous photoanode film functions as an effective support for the dye sensitizer, a pathway for the electron transfer and a porous membrane for electrolyte diffusion. The most widely used photoanode is TiO_2 with a band gap of 3.2 eV, and most of the research efforts have focused on the modification/decoration of the TiO_2 photoanodes [123–125]. However, the sole use of TiO_2 greatly limits the selection of other cell components in DSSCs such as the dye or the sensitizer. For instance, semiconducting quantum dot cannot be applied as a sensitizer for a TiO_2 photoanode since the conduction band of the quantum dot is lower than that of TiO_2, which prevents the injection of excited photoelectron from the quantum dot sensitizer to TiO_2. Although some other simple or complex oxides such as SnO_2, ZnO, Nb_2O_5, and Zn_2SnO_4 have also been demonstrated as photoanodes in DSSCs, they all showed much inferior PCE to that of TiO_2 [126–128]. Thus, it is critical to develop and design efficient photoanodes to replace TiO_2. Some perovskites with ABO_3 structure had superior photovoltaic activity than TiO_2, and their activity could be easily tuned by the functional doping or substitution in the A-site, B-site, and O-site.

As mentioned above, BSO and LBSO exhibited high electron mobility and electrical conductivity at room temperature. Recently, BSO and doped BSO have been widely used as photoanodes in DSSCs due to their superior light harvesting capability and electron conductivity/mobility to those of TiO_2 [129–131]. Due to the flexible structure of perovskite oxides, their sunlight harvesting capability, electron conductivity/mobility, and band structure can be tailored by rational selection and doping of the compositional elements and the tailoring of the synthesis methods. For example, different preparation methods were used to prepare BSO to enhance the PCE of BSO-based DSSCs [129]. The DSSC with co-precipitation-derived BSO photoanode showed a PCE of 1.1%. On the other hand, Li et al. also demonstrated the preparation of one-dimensional (1D) BSO hollow architectures by using $BaCO_3$@SnO_2 core–shell nanorods as precursor for the application as photoanodes of DSSCs [130]. However, the PCE of this BSO-based DSSC was very low (<1.1%).

BSO nanoparticles have been synthesized through a facile liquid-phase reaction with a subsequent sintering procedure [131]. An attractive PCE of 5.2% was

obtained for a DSSC with the BSO nanoparticles as the photoanodes. First, amorphous BSO particles were precipitated before they gradually crystallized to form peroxo-precursor particles. Afterward, highly crystalline BSO nanoparticles were formed from these precursor particles by a calcination procedure. It was found that the thickness of the BSO film had strong influence on the PCEs of DSSCs. An increase in PCE of DSSC was found when the thickness of BSO film was increased. The highest PCE obtained from the DSSC with the 43-μm-thick BSO photoanode was assigned to its excellent electron collection capability, suggesting BSO was a potential photoanode for DSSCs. In another work, BSO nanoparticles were prepared by a simple water bath route for the application as photoanodes for DSSCs [132]. A chemical bath deposition (CBD) method was demonstrated to enhance the PCE of DSSC with BSO photoanode. An improvement of 21.7% in the PCE of DSSCs after the CBD treatment was achieved due to the enhanced physical connectivity, improved electron transfer capability, and enlarged electron lifetime. Fe doping was demonstrated to enhance the performance of BSO photoanode in DSSCs [133]. By optimizing the Fe doping amount, the highest PCE (7.78%) of DSSCs was achieved by a 0.03 mol% Fe-doped BSO photoanode due to the trade-off of the created ferromagnetism and the nanostructure change.

Besides the development of the new perovskite photoanodes such as BSO and doped BSO, a substitution of cations such as Ca^{2+}, Sr^{2+}, and Ba^{2+} was used to modify the electronic structure of TiO_2 to form a perovskite oxide for the application as the photoanodes for DSSCs [134]. Undoped and Mn-doped $BaTiO_3$ nanostructures were prepared by a co-precipitation route for the application as photoanodes in DSSCs [135]. Decreased particle sizes and band gaps were obtained by the increasing Mn doping amount. The PCE of DSSC reduced (0.007%) with a lower Mn doping amount (1 at.%) as compared to undoped one (0.012%). The PCEs of DSSCs enhanced to 0.025% and 0.045% with further increment of Mn doping concentration. Furthermore, the addition of TiO_2 scattering layer promoted the electron transfer and the DSSC efficiency enhanced for 7–17 times as compared to the pristine solar cells without the modification of the scattering layers.

In addition to the pure-phase perovskite oxide as the photoanode in DSSCs, the coupling of perovskite with other functional materials is also reported to enhance the PCEs of DSSCs. $SrTiO_3:Sm^{3+}@SiO_2$ (STS@SiO_2) core–shell nanoparticles were prepared by a Stöber method in combination with a hydrothermal route [136]. This core–shell-structured composite was then used to modify TiO_2 photoanode in DSSCs. A down-conversion from UV light to visible light which well matched the light absorption region of N719 dye was achieved by STS@SiO_2 core–shell nanoparticles. By comparing with the pristine TiO_2 and STS-doped TiO_2 photoanode, the DSSC with a STS@SiO_2-doped TiO_2 photoanode showed a superior PCE. A PCE of 5.07% was obtained by 10 wt% STS@SiO_2-doped TiO_2-based DSSC, which was superior to that of pure TiO_2 (3.72%) and 10 wt% STS-doped TiO_2 (4.29%). The enhanced performance of STS@SiO_2-doped TiO_2 photoanode was assigned to the suppressed electron–hole recombination, enhanced light scattering, and down-conversion capabilities. In another study,

DSSC with a nanoporous $SrTiO_3/SnO_2$ composite photoanode showed a superior PCE of 3.4% as compared with the bare SnO_2 photoanode (2.2%) [137].

BSO is demonstrated as an important ETM in PSCs due to its superior electron mobility to TiO_2 and comparable electrical conductivity with TiO_2. BSO was also treated by $TiCl_4$ and/or the formation of BSO/scattering layer in the photoanodes in DSSCs to enhance the cell performance due to the improved collection efficiency of the photoinduced charge carriers. Rajamanickam et al. unitized BSO nanocuboids/nanoparticles as a photoanode for DSSC with a PCE of 0.71% [138]. Two scattering layer materials (TiO_2 and ZnO) at various $TiCl_4$ treatment times (1, 3, and 5 min) were conducted on the pristine BSO nanocuboids/nanoparticles for the application of photoanode in DSSCs. DSSCs with the BSO/TiO_2 scattering layer, the BSO/ZnO scattering layer, and the $TiCl_4$-treated BSO (1 min) photoanodes delivered PCEs of 1.14, 1.25, and 3.88%, respectively. Based on the combination of the $TiCl_4$ treatment and the scattering layer formation, a new composite photoanode was designed and developed [138]. DSSCs with BSO/TiO_2 scattering layer as photoanode after the treatment in $TiCl_4$ for 1 min showed a PCE of 5.68%, while a PCE of 4.28% was achieved by the BSO anode with ZnO scattering layer after treating in $TiCl_4$ for 1 min. Figure 10 shows the schematic diagram of DSSCs with pristine BSO, BSO/$TiCl_4$-treated, and BSO/$TiCl_4$-treated/scattering layer as photoanodes to obtain high PCE. It was found that, under the same $TiCl_4$ treatment, the ZnO scattering layer-based BSO photoanode showed an inferior performance to that of TiO_2 scattering layer, which was assigned to the lower dye adsorption amount of the ZnO scattering layer-based BSO photoanode caused by the smaller surface area and larger particle size of ZnO.

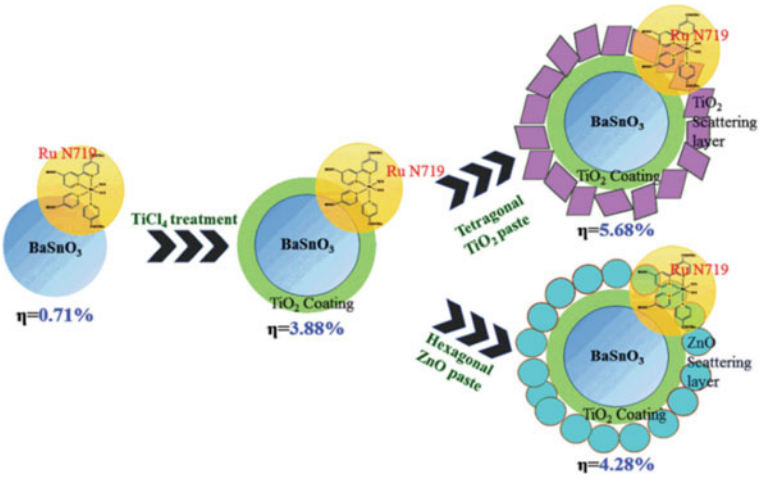

Fig. 10 Schematic diagram for the various photoanodes with achieved maximum PCE in DSSCs. Reprinted from Ref. [138] with permission from the PCCP Owner Societies

Kim et al. reported a $SrTiO_3$–TiO_2 composite as a photoanode in DSSCs, which showed an enhanced electron transfer capability and an electron–hole separation efficiency [139]. $SrTiO_3$–TiO_2 composite photoanode with rich heterojunctions and increased pore diameter was prepared by the anodization of a Ti foil and a subsequent hydrothermal procedure. As compared with the DSSC with pristine TiO_2 nanotube arrays (TNTAs) as photoanodes, DSSCs with a $SrTiO_3$–TiO_2 heterojunction photoanode showed a much higher PCE, which was assigned to the enhanced charge separation efficiency and the suppression of the recombination rate of electron–hole from $SrTiO_3$ on TiO_2 nanotube arrays through the interface with heterojuction. This successful synthetic approach in Kim et al.'s study can be easily transferred to other perovskite-based nanostructures for the applications in photoelectrochemical reactions and devices with improved efficiency. More recently, Tang and Yin presented a new Sr-doped TiO_2/$SrTiO_3$ nanorod array heterostructure as a photoanode in DSSCs [140]. This composite photoanode was prepared by a simple hydrothermal method, which showed a tunable microstructure and high photoelectrical conversion capability. The self-doping of Sr into the TiO_2 and the formation of $SrTiO_3$/Sr-doped TiO_2 heterostructure by the treatment of TiO_2 nanorod arrays in a $Sr(NO_3)_2$ solution resulted in a change in the sunlight response from UV light to visible light. By using this heterostructured photoanode, the dye loading amount was improved, which was assigned to the bonding of the hydroxide group on the photoanode surface and the carboxyl group of the dye molecule. The photoinduced electron–hole pair was also separated efficiently because of the formation of heterostructures and an improved PCE was achieved. DSSCs with the heterostructured photoanode delivered a PCE of 4.70% under the simulated sunlight irradiation (1 sun), which was almost 1.5 times higher than that of pristine TiO_2 photoanode (3.10%).

Apart from the coating of perovskite oxide on TiO_2 surface, TiO_2 nanoparticles were also used to decorate perovskite oxides to enhance the PCE of DSSCs when they are used as the photoanodes. TiO_2 nanoparticles with particle sizes of $\sim$5 nm were decorated on $BaTiO_3$ by a $TiCl_4$ treatment, which were applied as photoanodes for DSSCs [141]. The optimized photoanode, designated as $BaTiO_3$/TiO_2(4), was prepared by 4 times of $TiCl_4$ treatments as shown in Fig. 11. The PCE of DSSC with this photoanode was 15% higher than that of TiO_2 photoanode, which was assigned to the dramatically enhanced electron lifetime and then the electron–hole recombination rate was reduced. Furthermore, the compositions of the TiO_2–$BaTiO_3$ nanocomposites also played a critical role in the PCEs of the DSSCs [142]. TiO_2 and $BaTiO_3$ nanoparticles were synthesized by sol–gel and solvothermal methods, respectively, and their composites with various weight ratios were used as photoanodes for DSSCs [142]. DSSC with pure $BaTiO_3$ photoanode showed a PCE of 6.83%, whereas that made of pure TiO_2 displayed a PCE of 7.24%. Further improvement in the PCEs of DSSCs was achieved by composting $BaTiO_3$ and TiO_2. The highest PCE of 9.40% was obtained in a DSSC with the nanocomposite with TiO_2 to $BaTiO_3$ weight ratio of 85 to 15. This enhancement in PCE was assigned to less recombination of photo-generated electrons, faster charge collection, and higher dye sensitization capability.

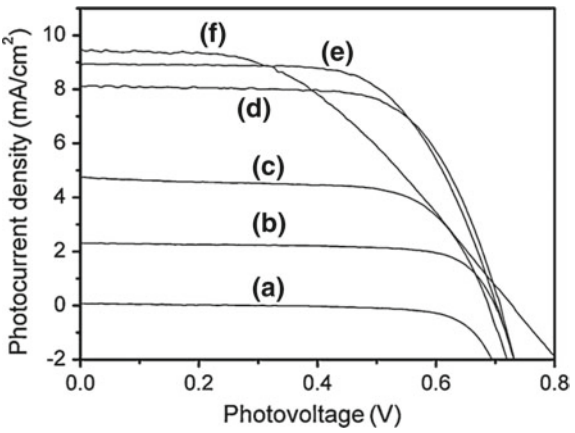

Fig. 11 *I-V* characteristics of the DSSCs with (a) $BaTiO_3$, (b) $BaTiO_3/TiO_2(1)$, (c) $BaTiO_3/TiO_2(2)$, (d) $BaTiO_3/TiO_2(3)$, (e) $BaTiO_3/TiO_2(4)$, and (f) $BaTiO_3/TiO_2(5)$ electrode, respectively. Reprinted with permission from Ref. [141]. Copyright 2011, Elsevier Inc.

3.3 Photocathodes

Besides the development of photoanode materials for DSSCs [143, 144], many dyes with high sunlight absorption capability have been studied in DSSCs [145–147]. The most frequently investigated sensitizers in DSSCs are Ru(II)-containing complexes including N719, C101, etc. [146, 148]. In addition, the temperature and treating time for dye sensitizer adsorption played essential roles on the PCE of DSSC [148]. The electrolyte is another essential component in DSSCs. A quick and uninterrupted electron transfer is a fundamental requirement for the dye reproduction by the electrolyte. On the other hand, the redox couple in the electrolyte must have complete reversibility, chemical stability, and no sunlight absorption in the visible light region. The solvent must have low viscosity to ensure the rapid diffusion of the charge carriers and to offer excellent dispersion of the redox couple without any dye desorption capability. Up to now, the triiodide/iodide (I_3^-/I^-) redox couple in the acetonitrile is the most widely used electrolyte in DSSCs due to its superior solubility and ionic mobility [149–151]. The fast dye reproduction process by I^- and the low recombination rate of I_3^- and electrons resulted in a higher PCE of DSSC than those of other redox couples such as disulfide/thiolate (T_2/T^-), Co-complex (Co^{3+}/Co^{2+}), etc. [152–154]. After I^- regenerates the dye sensitizer and converts into I_3^-, it is essential to reduce I_3^- to I^- at a very fast rate. The interface between the electrolyte and the photocathode provides the region where the I_3^- reduction reaction (IRR) happens. The photocathode should present a fast electron transfer from the outer circuit and then promote the IRR process. Thus, high conductivity and superior electrocatalytic activity are the basic requirements for photocathodes [155–157].

Pt is the most investigated photocathode in DSSCs because of its high electrocatalytic activity and excellent electron transfer capability. However, Pt suffers from several disadvantages such as prohibitive cost and scarcity, which strongly limit its large-scale application as photocathodes in DSSCs. Currently, the key

issues are to seek cost-effective and highly active electrocatalysts to replace Pt. Several low-cost candidates, such as carbons, conductive polymers, and metal oxides/sulfides/selenides, have been widely investigated as novel photocathode alternatives [158–168]. Until now, some carbons, such as carbon nanotubes (CNTs), graphene, and carbon black (CB), have been investigated as photocathodes because of the high surface area and conductivity [169, 170]. Nonetheless, their performance remains unsatisfactory [171]. Functionalization, doping, and morphology control are useful strategies to enhance the electrocatalytic performance of carbon-based photocathodes [153, 172, 173]. Nonetheless, the complex preparation routes and inferior stability of the functional groups limited the large-scale applications. In addition, several metal sulfides and metal selenides also showed excellent IRR activity [174–177]. However, the inferior chemical stability and conductivity hindered the widespread applications. Metal oxides have attracted more and more interests as photocathodes because of their abundance, superior activity, and stability as well as low cost [178–180]. As compared with simple metal oxides, complex oxides are more appealing as photocathodes in DSSCs due to the superior flexibility in chemical and physical properties. Some complex oxides including spinel and delafossite have been used as photocathodes [181–183]. Nonetheless, their electrocatalytic activities were not very satisfactory because of the limited amount of active sites. Perovskite oxides have received particular attention as catalysts in various electrocatalysis-based applications over the past decades due to the excellent compositional and structural flexibility. After rationally selecting the compositional elements in perovskite oxides, high activity for electrocatalysis-based reactions can be obtained by various perovskite oxides [184–186], suggesting a potential in the application of perovskite oxides as photocathodes in DSSCs.

Pure-phase perovskite oxides such as $La_{0.67}Sr_{0.33}MnO_3$ (LSM) were used as low-cost Pt-free photocathodes for DSSCs [187]. However, its IRR activity was not satisfied as compared with Pt. Although the performance of LSM was not very good, this work makes an attempt to develop perovskite oxide-based electrocatalysts as potential photocathodes, which can reduce the cost of DSSCs and accelerate its commercialization processes. The low IRR activity of the perovskite oxides mainly come from their low electrical conductivity, which can be solved by the incorporation of carbon materials. Some metal oxide/carbon composites were also used as photocathodes in DSSCs, such as NiO@reduced graphene oxide (RGO) composites and SnO_2@RGO composites [188, 189]. Xiong et al. proposed a solution combustion method to prepare LSM@RGO composite photocathode for DSSCs [190]. The positive synergetic effect between LSM and RGO greatly improved the IRR activity. DSSC with the LSM@RGO composite photocathode displayed a high PCE of 6.57%, which reached 92% of Pt photocathode (7.13%).

Due to the inferior electron mobility and low electrocatalytic activity of bismuth titanate ($Bi_4Ti_3O_{12}$, BTO) perovskite photocathode, Yu et al. designed BTO/graphene composites as photocathode for DSSCs to improve the PCE [191]. The BTO/graphene photocathode displayed a much higher photovoltaic performance than that of the pristine BTO photocathode due to the superior IRR activity, larger

specific surface area, and lower charge transfer resistance. After optimizing the conditions, the DSSC with BTO/graphene photocathode exhibited a superior PCE (9.70%) to pristine BTO photocathode (0.81%). The work offers a new and effective strategy to enhance the electrocatalytic activity of perovskite oxides with low conductivity. $La_{0.5}Sr_{0.5}CoO_{2.91}$ (LSC) perovskite oxides were prepared by a sol–gel route and applied as the photocathodes for DSSCs [192]. DSSC with LSC photocathode showed a PCE of 3.24%. To further improve the performance of LSC, the LSC/RGO nanocomposites were synthesized by a facile physical mixing route for the application as efficient photocathodes for DSSCs. The LSC/RGO exhibited a good IRR activity due to the synergetic effect between LSC and RGO. Therefore, the DSSC with the LSC/RGO photocathode delivered a PCE of 6.32%, which was much superior to that of pristine LSC photocathode (3.24%) or RGO photocathode (4.54%). More importantly, this PCE reached 88% of the Pt photocathode (7.18%) at the same conditions.

Strontium ruthenate ($SrRuO_3$, SRO) perovskite oxides are widely used as catalysts for oxygen evolution reaction and electro-oxidation in fuel cells to replace costly Pt catalysts [193, 194]. Recently, in 2016, Cao and co-workers reported sputtered SRO perovskite film as a Pt-free photocathode in DSSCs, demonstrating promising electrocatalytic activity for IRR and resulting in PCE close to that of traditional Pt photocathode [195]. Furthermore, the authors used epitaxial strain via lattice mismatch as a way to tailor the electrocatalytic activity for IRR. Compared with the SRO/$SrTiO_3$ photocathode, the in-plane tensile stress in SRO/$MgAl_2O_4$ films increased the adsorption strength of the adsorbed I_3^- and then accelerated the IRR at the photocathode/electrolyte interface and I_3^- diffusion in the electrolyte, which resulted in an enhancement in the PCEs of DSSCs. This work provides new insight into the enhancement of IRR activity through rational design and engineering of the crystal and microstructure of perovskite films. More recently, graphene quantum dots (GQDs) were applied to decorate SRO as a composite photocathode (SRO-GQD) [196]. The highly porous SRO photocathode prepared from hydrothermal route showed a large surface area, superior electrolyte diffusion capability, and IRR activity. As a result, a higher PCE of 7.16% than the sputtered SRO photocathode (6.48%) was achieved. The improved IRR activity of

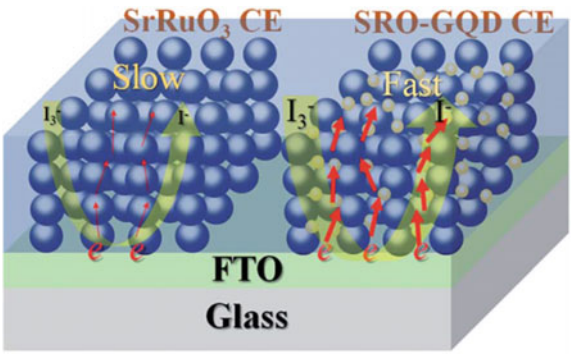

Fig. 12 The electron transfer processes of SRO and SRO-GQD composite for IRR in DSSCs. Reprinted with permission from Ref. [196]. Copyright 2017, Royal Society of Chemistry

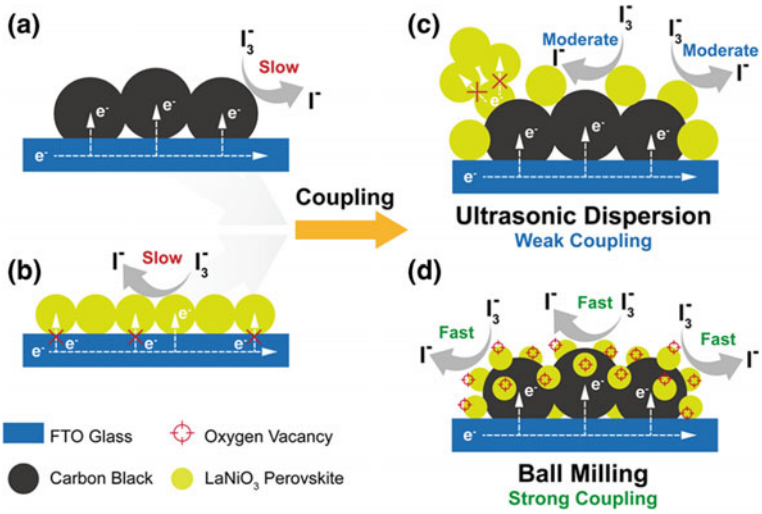

Fig. 13 Schematic illustrations of the reaction mechanisms with $LaNiO_3$, CB, and $LaNiO_3$/CB electrocatalysts for IRR. Reprinted with the permission from Ref. [197]. Copyright 2017, Wiley-VCH Verlag GmbH & Co. KGaA, Weinheim

SRO-GQD composite was attributed to the increased amount of active sites and improved electron transfer capability compared with the pristine SRO photocathode. The electron transfer pathways of SRO and SRO-GQD photocathodes for IRR were depicted in Fig. 12. Thus, DSSC with SRO-GQD photocathode delivered a high PCE of 8.05%, which was much superior to those of SRO (7.16%) and Pt (7.44%) photocathodes, further suggesting the critical role of the conductivity of photocathodes in achieving high PCEs in DSSCs.

In another work, Wang et al. reported a facile mechano-chemical route to prepare perovskite/carbon hybrids as photocathodes [197]. Large amounts of oxygen vacancies (active sites) were created in this route, which can be well tuned by the treating time of the ball milling (BM) process. DSSC assembled by the $LaNiO_3$/CB photocathode with the optimized ball milling time showed a similar PCE (7.94%) to Pt (8.11%), which was much superior to $LaNiO_3$ or CB used alone as photocathodes. As shown in Fig. 13, a strong coupling effect between $LaNiO_3$ and carbon was created in the BM process compared with the ultrasonic dispersion route, which improved the charge transfer capability and IRR activity of the $LaNiO_3$/carbon hybrid. Compared with $LaNiO_3$ and CB, the construction of strongly coupled $LaNiO_3$/CB hybrid greatly improved the charge transfer capability, which contributed to the excellent IRR activity of $LaNiO_3$/CB.

Acknowledgements The authors would like to thank the Australian Research Council for supporting the project under contract DP150104365 and DP160104835.

References

1. Wang W, Tadé MO, Shao Z (2018) Nitrogen-doped simple and complex oxides for photocatalysis: a review. Prog Mater Sci 92:33–63
2. Ong WJ, Tan LL, Ng YH, Yong ST, Chai SP (2016) Graphitic carbon nitride ($g–C_3N_4$)-based photocatalysts for artificial photosynthesis and environmental remediation: are we a step closer to achieving sustainability? Chem Rev 116:7159–7329
3. Wang W, Xu X, Zhou W, Shao Z (2017) Recent progress in metal-organic frameworks for applications in electrocatalytic and photocatalytic water splitting. Adv Sci 4:1600371
4. Zhang G, Liu G, Wang L, Irvine JT (2016) Inorganic perovskite photocatalysts for solar energy utilization. Chem Soc Rev 45:5951–5984
5. Correa-Baena JP, Abate A, Saliba M, Tress W, Jacobsson TJ, Grätzel M, Hagfeldt A (2017) The rapid evolution of highly efficient perovskite solar cells. Energy Environ Sci 10:710–727
6. Freitag M, Teuscher J, Saygili Y, Zhang X, Giordano F, Liska P, Hua J, Zakeeruddin S, Moser JE, Grätzel M, Hagfeldt A (2017) Dye-sensitized solar cells for efficient power generation under ambient lighting. Nat Photonics 11:372–378
7. Hagfeldt A, Boschloo G, Sun L, Kloo L, Pettersson H (2010) Dye-sensitized solar cells. Chem Rev 110:6595–6663
8. Carey GH, Abdelhady AL, Ning Z, Thon SM, Bakr OM, Sargent EH (2015) Colloidal quantum dot solar cells. Chem Rev 115:12732–12763
9. Wang W, Tade MO, Shao Z (2015) Research progress of perovskite materials in photocatalysis- and photovoltaics-related energy conversion and environmental treatment. Chem Soc Rev 44:5371–5408
10. Yella A, Lee HW, Tsao HN, Yi C, Chandiran AK, Nazeeruddin MK, Diau EW-G, Yeh CY, Zakeeruddin SM, Grätzel M (2011) Porphyrin-sensitized solar cells with cobalt (II/III)-based redox electrolyte exceed 12 percent efficiency. Science 334:629–634
11. Mathew S, Yella A, Gao P, Humphry-Baker R, Curchod BFE, Ashari-Astani N, Tavernelli I, Rothlisberger U, Nazeeruddin MK, Grätzel M (2014) Dye-sensitized solar cells with 13% efficiency achieved through the molecular engineering of porphyrin sensitizers. Nat Chem 6:242–247
12. Leijtens T, Eperon GE, Pathak S, Abate A, Lee MM, Snaith HJ (2013) Overcoming ultraviolet light instability of sensitized TiO_2 with meso-superstructured organometal tri-halide perovskite solar cells. Nat Commun 4:2885
13. Petrus ML, Schlipf J, Li C, Gujar TP, Giesbrecht N, Müller-Buschbaum P, Bein T, Huttner S, Docampo P (2017) Capturing the sun: a review of the challenges and perspectives of perovskite solar cells. Adv Energy Mater 7:1700264
14. Ramanujam J, Singh UP (2017) Copper indium gallium selenide based solar cells-a review. Energy Environ Sci 10:1306–1319
15. Krasikov D, Sankin I (2017) Defect interactions and the role of complexes in the CdTe solar cell absorber. J Mater Chem A 5:3503–3513
16. O'regan B, Grätzel M (1991) A low-cost, high-efficiency solar cell based on dye-sensitized colloidal TiO_2 films. Nature 353: 737–740
17. Hao Y, Yang W, Zhang L, Jiang R, Mijangos E, Saygili Y, Hammarstrom L, Hagfeldt A, Boschloo G (2016) A small electron donor in cobalt complex electrolyte significantly improves efficiency in dye-sensitized solar cells. Nat Commun 7:13934
18. Cao Y, Saygili Y, Ummadisingu A, Teuscher J, Luo J, Pellet N, Giordano F, Zakeeruddin SM, Moser JE, Freitag M, Hagfeldt A, Grätzel M (2017) 11% efficiency solid-state dye-sensitized solar cells with copper(II/I) hole transport materials. Nat Commun 8:15390
19. Zhang W, Wu Y, Bahng H W, Cao Y, Yi C, Saygili Y, Luo J, Liu Y, Kavan L, Moser J-E, Hagfeldt A, Tian H, Zakeeruddin SM, Zhu W-H, Grätzel M (2018) Comprehensive control

of voltage loss enables 11.7% efficient solid-state dye-sensitized solar cells. Energy Environ Sci 11:1779–1787
20. Im JH, Jang IH, Pellet N, Grätzel M, Park NG (2014) Growth of $CH_3NH_3PbI_3$ cuboids with controlled size for high-efficiency perovskite solar cells. Nat Nanotechnol 9:927–932
21. Yang WS, Noh JH, Jeon NJ, Kim YC, RyuS Seo J, Seok SI (2015) High-performance photovoltaic perovskite layers fabricated through intramolecular exchange. Science 348:1234–1237
22. Eames C, Frost JM, Barnes PR, O'Regan BC, Walsh A, Islam MS (2015) Ionic transport in hybrid lead iodide perovskite solar cells. Nat Commun 6:7497
23. Kim HD, Ohkita H, Benten H, Ito S (2016) Photovoltaic performance of perovskite solar cells with different grain sizes. Adv Mater 28:917–922
24. Park N-G, Grätzel M, Miyasaka T, Zhu K, Emery K (2016) Towards stable and commercially available perovskite solar cells. Nat Energy 1:16152
25. Giustino F, Snaith HJ (2016) Toward lead-free perovskite solar cells. ACS Energy Lett 1:1233–1240
26. Liang L, Gao P (2018) Lead-free hybrid perovskite absorbers for viable application: can we eat the cake and have it too? Adv Sci 5:1700331
27. Wang Z, Lin Q, Chmiel FP, Sakai N, Herz LM, Snaith HJ (2017) Efficient ambient-air-stable solar cells with 2D-3D heterostructured butylammonium-caesium-formamidinium lead halide perovskites. Nat Energy 2:17135
28. Kazim S, Nazeeruddin MK, Grätzel M, Ahmad S (2014) Perovskite as light harvester: a game changer in photovoltaics. Angew Chem Int Ed 53:2812–2824
29. Kojima A, Teshima K, Shirai Y, Miyasaka T (2009) Organometal halide perovskites as visible-light sensitizers for photovoltaic cells. J Am Chem Soc 131:6050–6051
30. Im JH, Lee CR, Lee JW, Park SW, Park NG (2011) 6.5% efficient perovskite quantum-dot-sensitized solar cell. Nanoscale 3:4088–4093
31. Kim HS, Lee CR, Im JH, Lee KB, Moehl T, Marchioro A, Moon SJ, Humphy-Baker R, Yum JH, Moser JE, Grätzel M, Park NG (2012) Lead iodide perovskite sensitized all-solid-state submicron thin film mesoscopic solar cell with efficiency exceeding 9%. Sci Rep 2:591
32. Lee MM, Teuscher J, Miyasaka T, Murakami TN, Snaith HJ (2012) Efficient hybrid solar cells based on meso-superstructured organometal halide perovskites. Science 338:643–647
33. Zhou H, Chen Q, Li G, Luo S, Song TB, Duan HS, Hong Z, You JB, Liu Y, Yang Y (2014) Interface engineering of highly efficient perovskite solar cells. Science 345:542–546
34. Yang WS, Park BW, Jung EH, Jeon NJ, Kim YC, Lee DU, Shin SS, Seo J, Kim EK, Noh JH, Seok SI (2017) Iodide management in formamidinium-lead-halide–based perovskite layers for efficient solar cells. Science 356:1376–1379
35. Xing G, Mathews N, Sun S, Lim SS, Lam YM, Grätzel M, Mhaisalkar S, Sum TC (2013) Long-range balanced electron- and hole-transport lengths in organic-inorganic $CH_3NH_3PbI_3$. Science 342:344–347
36. Stranks SD, Eperon GE, Grancini G, Menelaou C, Alcocer MJ, Leijten T, Herz LM, Petrozza M, Snaith HJ (2013) Electron-hole diffusion lengths exceeding 1 μm in an organometal trihalide perovskite absorber. Science 342:341–344
37. Dong Q, Fang Y, Shao Y, Mulligan P, Qiu J, Cao L, Huang J (2015) Electron-hole diffusion lengths >175 μm in solution-grown $CH_3NH_3PbI_3$ single crystals. Science 347:967–970
38. Vorpahl SM, Stranks SD, Nagaoka H, Eperon GE, Ziffer ME, Snaith HJ, Ginger DS (2015) Impact of microstructure on local carrier lifetime in perovskite solar cells. Science 348:683–686
39. Wehrenfennig C, Eperon GE, Johnston MB, Snaith HJ, Herz LM (2014) High charge carrier mobilities and lifetimes in organolead trihalide perovskites. Adv Mater 26:1584–1589
40. Lin Q, Armin A, Nagiri RCR, Burn PL, Meredith P (2014) Electro-optics of perovskite solar cells. Nat Photonics 9:106–112

41. D'Innocenzo V, Grancini G, Alcocer MJ, Kandada ARS, Stranks SD, Lee MM, Lanzani G, Snaith HJ, Petrozza A (2014) Excitons versus free charges in organo-lead tri-halide perovskites. Nat Commun 5:3586
42. Zuo C, Bolink HJ, Han H, Huang J, Cahen D, Ding L (2016) Advances in perovskite solar cells. Adv Sci 3:1500324
43. Saba M, Quochi F, Mura A, Bongiovanni G (2016) Excited state properties of hybrid perovskites. Acc Chem Res 49:166–173
44. Meng L, You J, Guo TF, Yang Y (2016) Recent advances in the inverted planar structure of perovskite solar cells. Acc Chem Res 49:155–165
45. Manser JS, Saidaminov MI, Christians JA, Bakr OM, Kamat PV (2016) Making and breaking of lead halide perovskites. Acc Chem Res 49:330–338
46. Johnston MB, Herz LM (2016) Hybrid perovskites for photovoltaics: charge-carrier recombination, diffusion, and radiative efficiencies. Acc Chem Res 49:146–154
47. Gao P, Grätzel M, Nazeeruddin MK (2014) Organohalide lead perovskites for photovoltaic applications. Energy Environ Sci 7:2448–2463
48. Sum TC, Mathews N (2014) Advancements in perovskite solar cells: photophysics behind the photovoltaics. Energy Environ Sci 7:2518–2534
49. Stranks SD, Nayak PK, Zhang W, Stergiopoulos T, Snaith HJ (2015) Formation of thin films of organic-inorganic perovskites for high-efficiency solar cells. Angew Chem Int Ed 54:3240–3248
50. Stoumpos CC, Kanatzidis MG (2015) The renaissance of halide perovskites and their evolution as emerging semiconductors. Acc Chem Res 48:2791–2802
51. Lotsch BV (2014) New light on an old story: perovskites go solar. Angew Chem Int Ed 53:635–637
52. Kim HS, Park NG (2014) Parameters affecting I–V hysteresis of $CH_3NH_3PbI_3$ perovskite solar cells: effects of perovskite crystal size and mesoporous TiO_2 layer. J Phys Chem Lett 5:2927–2934
53. Tan H, Jain A, Voznyy O, Lan X, de Arquer FPG, Fan JZ, Quintero-Bermudez R, Yuan M, Zhang B, Zhao Y, Fan F, Li P, Quan LN, Zhao Y, Lu Z-H, Yang Z, Hoogland S, Sargent EH (2017) Efficient and stable solution-processed planar perovskite solar cells via contact passivation. Science 355: 722–726
54. Ko HS, Lee JW, Park NG (2015) 15.76% efficiency perovskite solar cells prepared under high relative humidity: importance of PbI_2 morphology in two-step deposition of $CH_3NH_3PbI_3$. J Mater Chem A 3:8808–8815
55. Liang C, Li P, Zhang Y, Gu H, Cai Q, Liu X, Wang J, Wen H, Shao G (2017) Mild solution-processed metal-doped TiO_2 compact layers for hysteresis-less and performance-enhanced perovskite solar cells. J Power Sources 372:235–244
56. Dong X, Hu H, Lin B, Ding J, Yuan N (2014) The effect of ALD-Zno layers on the formation of $CH_3NH_3PbI_3$ with different perovskite precursors and sintering temperatures. Chem Commun 50:14405–14408
57. Liu X, Bu T, Li J, He J, Li T, Zhang J, Li T, Zhang J, Li W, Ku Z, Peng Y, Huang F, Cheng Y-B, Zhong J (2018) Stacking n-type layers: effective route towards stable, efficient and hysteresis-free planar perovskite solar cells. Nano Energy 44:34–42
58. Shin SS, Yang WS, Noh JH, Suk JH, Jeon NJ, Park JH, Kim JS, Seong WM, Seok S (2015) High-performance flexible perovskite solar cells exploiting Zn_2SnO_4 prepared in solution below 100 °C. Nat Commun 6: 7410
59. Zhu L, Shao Z, Ye J, Zhang X, Pan X, Dai S (2016) Mesoporous $BaSnO_3$ layer based perovskite solar cells. Chem Commun 52:970–973
60. Liu M, Johnston MB, Snaith HJ (2013) Efficient planar heterojunction perovskite solar cells by vapour deposition. Nature 501:395–398
61. Momblona C, Gil-Escrig L, Bandiello E, Hutter EM, Sessolo M, Lederer K, Blochwitz-Nimoth J, Bolink HJ (2016) Efficient vacuum deposited p-i-n and n-i-p perovskite solar cells employing doped charge transport layers. Energy Environ Sci 9:3456–3463

62. Jeon NJ, Noh JH, Kim YC, Yang WS, Ryu S, Seok SI (2014) Solvent engineering for high-performance inorganic-organic hybrid perovskite solar cells. Nat Mater 13:897–903
63. Li W, Fan J, Li J, Mai Y, Wang L (2015) Controllable grain morphology of perovskite absorber film by molecular self-assembly toward efficient solar cell exceeding 17%. J Am Chem Soc 137:10399–10405
64. Fu W, Yan J, Zhang Z, Ye T, Liu Y, Wu J, Yao J, Li C-Z, Li H, Chen H (2016) Controlled crystallization of $CH_3NH_3PbI_3$ films for perovskite solar cells by various PbI_2 (X) complexes. Sol Energy Mater Sol Cells 155:331–340
65. Ahn N, Son DY, Jang IH, Kang SM, Choi M, Park NG (2015) Highly reproducible perovskite solar cells with average efficiency of 18.3% and best efficiency of 19.7% fabricated via lewis base adduct of lead(II) iodide. J Am Chem Soc 137:8696–8699
66. Huang F, Dkhissi Y, Huang W, Huang W, Xiao M, Benesperi L, Rubanov S, Zhu Y, Lin X, Jiang L, Zhou Y, Gray-Weale A, Etheridge J, McNeill CR, Caruso RA, Bach U, Spiccia L, Cheng Y-B (2014) Gas-assisted preparation of lead iodide perovskite films consisting of a monolayer of single crystalline grains for high efficiency planar solar cells. Nano Energy 10:10–18
67. Burschka J, Pellet N, Moon SJ, Humphry-Baker R, Gao P, Nazeeruddin MK, Michael Grätzel (2013) Sequential deposition as a route to high-performance perovskite-sensitized solar cells. Nature 499:316–319
68. Xiao Z, Bi C, Shao Y, Dong Q, Wang Q, Yuan Y, Wang C, Gao Y, Huang J (2014) Efficient, high yield perovskite photovoltaic devices grown by interdiffusion of solution-processed precursor stacking layers. Energy Environ Sci 7:2619–2623
69. Xiao Z, Dong Q, Bi C, Shao Y, Yuan Y, Huang J (2014) Solvent annealing of perovskite-induced crystal growth for photovoltaic-device efficiency enhancement. Adv Mater 26:6503–6509
70. Bi D, Yi C, Luo J, Decoppet J-D, Zhang F, Zakeeruddin SM, Li X, Hagfeldt A, Grätzel M (2016) Polymer-templated nucleation and crystal growth of perovskite films for solar cells with efficiency greater than 21%. Nat Energy 1:16142
71. Xiao M, Huang F, Huang W, Dkhissi Y, Zhu Y, Etheridge J, Gray-Weale A, Bach U, Cheng YB, Spiccia L (2014) A fast deposition-crystallization procedure for highly efficient lead iodide perovskite thin-film solar cells. Angew Chem Int Ed 53:9898–9903
72. Chen Q, Zhou H, Song T-B, Luo S, Hong Z, Duan H-S, Dou L, Liu Y, Yang Y (2014) Controllable self-induced passivation of hybrid lead iodide perovskites toward high performance solar cells. Nano Lett 14:4158–4163
73. Zuo C, Ding L (2014) An 80.11% FF record achieved for perovskite solar cells by using the NH_4Cl additive. Nanoscale 6:9935–9938
74. Liang PW, Liao CY, Chueh CC, Zuo F, Williams ST, Xin XK, Lin J, Jen AK (2014) Additive enhanced crystallization of solution-processed perovskite for highly efficient planar-heterojunction solar cells. Adv Mater 26:3748–3754
75. Wu Y, Islam A, Yang X, Qin C, Liu J, Zhang K, Peng W, Han L (2014) Retarding the crystallization of PbI_2 for highly reproducible planar-structured perovskite solar cells via sequential deposition. Energy Environ Sci 7:2934–2938
76. Chen Q, Zhou H, Hong Z, Luo S, Duan HS, Wang HH, Liu Y, Li G, Yang Y (2014) Planar heterojunction perovskite solar cells via vapor-assisted solution process. J Am Chem Soc 136:622–625
77. Sadhanala A, Ahmad S, Zhao B, Giesbrecht N, Pearce PM, Deschler F, Hoye RL, Godel KC, Bein T, Docampo P, Dutton SE, De Volder MF, Friend RH (2015) Blue-green color tunable solution processable organolead chloride-bromide mixed halide perovskites for optoelectronic applications. Nano Lett 15:6095–6101
78. Liu Y, Yang Z, Cui D, Ren X, Sun J, Liu X, Zhang J, Wei Q, Fan H, Yu F, Zhang X, Zhao C, Liu S (2015) Two-inch-sized perovskite $CH_3NH_3PbX_3$ (X = Cl, Br, I) crystals: growth and characterization. Adv Mater 27:5176–5183
79. Shi D, Adinolfi V, Comin R, Yuan M, Alarousu E, Buin A, Chen Y, Sjoerd Hoogland, Rothenberger A, Katsiev K, Losovyj Y, Zhang Y, Dowben PA, Mohammed OF,

Sargent EH, Bakr OM (2015) Low trap-state density and long carrier diffusion in organolead trihalide perovskite single crystals. Science 347:519–522
80. Jacobsson JT, Correa-Baena JP, Pazoki M, Saliba M, Schenk K, Grätzel M, Hagfeldt A (2016) Exploration of the compositional space for mixed lead halogen perovskites for high efficiency solar cells. Energy Environ Sci 9:1706–1724
81. Edri E, Kirmayer S, Mukhopadhyay S, Gartsman K, Hodes G, Cahen D (2014) Elucidating the charge carrier separation and working mechanism of $CH_3NH_3PbI_{3-x}Cl_x$ perovskite solar cells. Nat Commun 5:3461
82. Zhang M, Yu H, Lyu M, Wang Q, Yun JH, Wang L (2014) Composition-dependent photoluminescence intensity and prolonged recombination lifetime of perovskite $CH_3NH_3PbBr_{3-x}Cl_x$ films. Chem Commun 50:11727–11730
83. Hao F, Stoumpos CC, Chang RP, Kanatzidis MG (2014) Anomalous band gap behavior in mixed Sn and Pb perovskites enables broadening of absorption spectrum in solar cells. J Am Chem Soc 136:8094–8099
84. Noel NK, Stranks SD, Abate A, Christian W, Guarnera S, Haghighirad A-A, Sadhanala A, Eperon GE, Pathak SK, Johnston MB, Petrozza A, Herz LM, Snaith HJ (2014) Lead-free organic–inorganic tin halide perovskites for photovoltaic applications. Energy Environ Sci 7:3061–3068
85. Krishnamoorthy T, Ding H, Yan C, Leong WL, Baikie T, Zhang Z, Sherburne M, Li S, Asta M, Mathews N, Mhaisalkar SG (2015) Lead-free germanium iodide perovskite materials for photovoltaic applications. J Mater Chem A 3:23829–23832
86. Lee JW, Seol DJ, Cho AN, Park NG (2014) High-efficiency perovskite solar cells based on the black polymorph of $HC(NH_2)_2PbI_3$. Adv Mater 26:4991–4998
87. Eperon GE, Stranks SD, Menelaou C, Johnston MB, Herz LM, Snaith HJ (2014) Formamidinium lead trihalide: a broadly tunable perovskite for efficient planar heterojunction solar cells. Energy Environ Sci 7:982
88. Choi H, Jeong J, Kim H-B, Kim S, Walker B, Kim G-H, Kim JY (2014) Cesium-doped methylammonium lead iodide perovskite light absorber for hybrid solar cells. Nano Energy 7:80–85
89. Song Z, Abate A, Watthage SC, Liyanage GK, Phillips AB, Steiner U, Graetzel M, Heben MJ (2016) Perovskite solar cell stability in humid air: partially reversible phase transitions in the PbI_2–CH_3NH_3I–H_2O System. Adv Energy Mater 6:1600846
90. Bella F, Griffini G, Correa-Baena JP, Saracco G, Grätzel M, Hagfeldt A, Turri S, Gerbaldi C (2016) Improving efficiency and stability of perovskite solar cells with photocurable fluoropolymers. Science 354:203–206
91. Abate A, Paek S, Giordano F, Correa-Baena JP, Saliba M, Gao P, Matsui T, Ko J, Zakeeruddin SM, Dahmen KH, Hagfeldt A, Grätzel M, Nazeeruddin MK (2015) Silolothiophene-linked triphenylamines as stable hole transporting materials for high efficiency perovskite solar cells. Energy Environ Sci 8:2946–2953
92. Domanski K, Correa-Baena JP, Mine N, Nazeeruddin MK, Abate A, Saliba M, Tress W, Hagfeldt A, Grätzel M (2016) Not all that glitters is gold: metal-migration-induced degradation in perovskite solar cells. ACS Nano 10:6306–6314
93. Gholipour S, Correa-Baena JP, Domanski K, Matsui T, Steier L, GiordanoF Tajabadi F, Tress W, Saliba M, Abate A, Ali AM, Taghavinia N, Grätzel M, Hagfeldt A (2016) Highly efficient and stable perovskite solar cells based on a low-cost carbon cloth. Adv Energy Mater 6:1601116
94. Li X, Tschumi M, Han H, Babkair SS, Alzubaydi RA, Ansari AA, Habib SS, Nazeeruddin MK, Zakeeruddin SM, Grätzel M (2015) Outdoor performance and stability under elevated temperatures and long-term light soaking of triple-layer mesoporous perovskite photovoltaics. Energy Technol 3:551–555
95. Saliba M, Matsui T, Domanski K, Seo JY, Ummadisingu A, Zakeeruddin SM, Correa-Baena JP, Tress WR, Abate A, Hagfeldt A, Grätzel M (2016) Incorporation of rubidium cations into perovskite solar cells improves photovoltaic performance. Science 354:206–209

96. Kaltenbrunner M, Adam G, Głowacki ED, Drack M, Schwödiauer R, Leonat L, Apaydin DH, Groiss H, Scharber MC, White MS, Sariciftci NS, Bauer S (2015) Flexible high power-per-weight perovskite solar cells with chromium oxide–metal contacts for improved stability in air. Nat Mater 14: 1032
97. Guarnera S, Abate A, Zhang W, Foster JM, Richardson G, Petrozza A, Snaith HJ (2015) Improving the long-term stability of perovskite solar cells with a porous Al_2O_3 buffer layer. J Phys Chem Lett 6:432–437
98. Yang S, Wang Y, Liu P, Cheng YB, Zhao HJ, Yang HG (2016) Functionalization of perovskite thin films with moisture-tolerant molecules. Nat Energy 1:15016
99. Bi D, Gao P, Scopelliti R, Oveisi E, Luo J, Grätzel M, Hagfeldt A, Nazeeruddin MK (2016) High-performance perovskite solar cells with enhanced environmental stability based on amphiphile-modified $CH_3NH_3PbI_3$. Adv Mater 28:2910–2915
100. Zhao Y, Wei J, Li H, Yan Y, Zhou W, Yu D, Zhao Q (2016) A polymer scaffold for self-healing perovskite solar cells. Nat Commun 7:10228
101. Wang Q, Dong Q, Li T, Gruverman A, Huang J (2016) Thin insulating tunneling contacts for efficient and water-resistant perovskite solar cells. Adv Mater 28:6734–6739
102. Yin W-J, Shi T, Yan Y (2014) Unusual defect physics in $CH_3NH_3PbI_3$ perovskite solar cell absorber. Appl Phys Lett 104:063903
103. Xiao Z, Yuan Y, Shao Y, Wang Q, Dong Q, Bi C, Sharma P, Gruverman A, Huang J (2015) Giant switchable photovoltaic effect in organometal trihalide perovskite devices. Nat Mater 14:193–198
104. Hadadian M, Correa-Baena JP, Goharshadi EK, Ummadisingu A, Seo J-Y, Luo J, Gholipour S, Zakeeruddin SM, Saliba M, Abate A, Grätzel M, Hagfeldt A (2016) Enhancing efficiency of perovskite solar cells via N-doped graphene: crystal modification and surface passivation. Adv Mater 28:8681–8686
105. Li X, Dar MI, Yi C, Luo J, Tschumi M, Zakeeruddin SM, Nazeeruddin NK, Han H, Grätzel M (2015) Improved performance and stability of perovskite solar cells by crystal crosslinking with alkylphosphonic acid omega-ammonium chlorides. Nat Chem 7:703–711
106. Li W, Zhang W, Van Reenen S, Sutton RJ, Fan J, Haghighirad AA, Johnston MB, Wang L, Snaith HJ (2016) Enhanced UV-light stability of planar heterojunction perovskite solar cells with caesium bromide interface modification. Energy Environ Sci 9:490–498
107. Scanlon DO (2013) Defect engineering of $BaSnO_3$ for high-performance transparent conducting oxide applications. Phys Rev B 87:161201
108. Raghavan S, Schumann T, Kim H, Zhang JY, Cain TA, Stemmer S (2016) High-mobility $BaSnO_3$ grown by oxide molecular beam epitaxy. APL Mater 4:016106
109. Cerda J, Arbiol J, Dezanneau G, Dıaz R, Morante JR (2002) Perovskite-type $BaSnO_3$ powders for high temperature gas sensor applications. Sens Actuators B Chem 84:21–25
110. Sun C, Guan L, Guo Y, Fang B, Yang J, Duan H, Chen Y, Li H, Liu H (2017) Ternary oxide $BaSnO_3$ nanoparticles as an efficient electron-transporting layer for planar perovskite solar cells. J Alloys Compd 722:196–206
111. Kim HJ, Kim U, Kim HM, Kim TH, Mun HS, Jeon BG, Hong KT, Lee WJ, Ju C, Kim KH, Char K (2012) High mobility in a stable transparent perovskite oxide. Appl Phys Express 5:061102
112. Shin SS, Kim JS, Suk JH, Lee KD, Kim DW, Park JH, Cho IS, Hong KS, Kim JY (2013) Improved quantum efficiency of highly efficient perovskite $BaSnO_3$-based dye-sensitized solar cells. ACS Nano 7:1027–1035
113. Zhu L, Ye J, Zhang X, Zheng H, Liu G, Pan X, Dai S (2017) Performance enhancement of perovskite solar cells using a La-doped $BaSnO_3$ electron transport layer. J Mater Chem A 5:3675–3682
114. Huang C, Wang X, Shi Q, Liu X, Zhang Y, Huang F, Zhang T (2015) A facile peroxo-precursor synthesis method and structure evolution of large specific surface area mesoporous $BaSnO_3$. Inorg Chem 54:4002–4010

115. Shin SS, Yeom EJ, Yang WS, Hur S, Kim MG, Im J, Seo J, Noh JH, Seok SI (2017) Colloidally prepared La-doped $BaSnO_3$ electrodes for efficient, photostable perovskite solar cells. Science 356:167–171
116. Saliba M, Matsui T, Seo J-Y, Domanski K, Correa-Baena J-P, Nazeeruddin MK, Zakeeruddin SM, Tress W, Abate A, Hagfeldt A, Grätzel M (2016) Cesium-containing triple cation perovskite solar cells: improved stability, reproducibility and high efficiency. Energy Environ Sci 9:1989–1997
117. Chen W, Wu Y, Yue Y, Liu J, Zhang W, Yang X, Chen H, Bi E, Ashraful I, Grätzel M, Han L (2015) Efficient and stable large-area perovskite solar cells with inorganic charge extraction layers. Science 350:944–948
118. Chen J, Morrow DJ, Fu Y, Zheng W, Zhao Y, Dang L, Stolt MJ, Kohler DD, Wang X, Czech KJ, Hautzinger MP, Shen S, Guo L, Pan A, Wright JC, Jin S (2017) Single-crystal thin films of cesium lead bromide perovskite epitaxially grown on metal oxide perovskite ($SrTiO_3$). J Am Chem Soc 139:13525–13532
119. Bera A, Wu K, Sheikh A, Alarousu E, Mohammed OF, Wu T (2014) Perovskite oxide $SrTiO_3$ as an efficient electron transporter for hybrid perovskite solar cells. J Phys Chem C 118:28494–28501
120. Okamoto Y, Fukui R, Fukazawa M, Suzuki Y (2017) $SrTiO_3/TiO_2$ composite electron transport layer for perovskite solar cells. Mater Lett 187:111–113
121. Okamoto Y, Suzuki Y (2016) Mesoporous $BaTiO_3/TiO_2$ double layer for electron transport in perovskite solar cells. J Phys Chem C 120:13995–14000
122. Wang C, Tang Y, Hu Y, Huang L, Fu J, Jin J, Shi W, Wang L, Yang W (2015) Graphene/$SrTiO_3$ nanocomposites used as an effective electron-transporting layer for high-performance perovskite solar cells. RSC Adv 5:52041–52047
123. Wang W, Liu Y, Qu J, Chen Y, Tadé MO, Shao Z (2017) Synthesis of hierarchical TiO_2–C_3N_4 hybrid microspheres with enhanced photocatalytic and photovoltaic activities by maximizing the synergistic effect. ChemPhotoChem 1:35–45
124. Xu C, Wu J, Desai UV, Gao D (2012) High-efficiency solid-state dye-sensitized solar cells based on TiO_2-coated ZnO nanowire arrays. Nano Lett 12:2420–2424
125. Kunzmann A, Valero S, Sepúlveda ÁE, Rico-Santacruz M, Lalinde E, Berenguer JR, García-Martínez J, Guldi DM, Serrano E, Costa RD (2018) Hybrid dye-titania nanoparticles for superior low-temperature dye-sensitized solar cells. Adv Energy Mater 8:1702583
126. Wu WQ, Xu YF, Rao HS, Feng HL, Su CY, Kuang DB (2014) Constructing 3D branched nanowire coated macroporous metal oxide electrodes with homogeneous or heterogeneous compositions for efficient solar cells. Angew Chem Int Ed 53:4816–4821
127. Wang YF, Li KN, Xu YF, Su CY, Kuang DB (2013) Hierarchical Zn_2SnO_4 nanosheets consisting of nanoparticles for efficient dye-sensitized solar cells. Nano Energy 2:1287–1293
128. He D, Sheng X, Yang J, Chen L, Zhu K, Feng X (2014) [1010] oriented multichannel ZnO nanowire arrays with enhanced optoelectronic device performance. J Am Chem Soc 136:16772–16775
129. Guo F, Li G, Zhang W (2010) Barium staminate as semiconductor working electrodes for dye-sensitized solar cells. Int J Photoenergy 2010:1–7
130. Li B, Tang Y, Luo L, Xiao T, Li D, Yuan M (2010) Fabrication of porous $BaSnO_3$ hollow architectures using $BaCO_3@SnO_2$ core-shell nanorods as precursors. Appl Surf Sci 257:197–202
131. Kim DW, Shin SS, Lee S, Cho IS, Kim DH, Lee CW, Jung HS, Hong KS (2013) $BaSnO_3$ perovskite nanoparticles for high efficiency dye-sensitized solar cells. Chemsuschem 6:449–454
132. Xie F, Li Y, Xiao T, Shen D, Wei M (2018) Efficiency improvement of dye-sensitized $BaSnO_3$ solar cell based surface treatments. Electrochim Acta 261:23–28
133. Rajamanickam N, Soundarrajan P, Jayakumar K, Ramachandran K (2017) Improve the power conversion efficiency of perovskite $BaSnO_3$ nanostructures based dye-sensitized solar cells by Fe doping. Sol Energy Mater Sol Cells 166:69–77

134. Jin KX, Li YF, Wang ZL, Peng HY, Lin WN, Kyaw AKK, Jin YL, Jin KJ, Sun XW, Soci C, Wu T (2012) Tunable photovoltaic effect and solar cell performance of self-doped perovskite $SrTiO_3$. AIP Adv 2:042131
135. Rajamanickam N, Jayakumar K, Ramachandran K (2017) Influence of Mn ion on flower shaped perovskite $BaTiO_3$ nanostructures based dye-sensitized solar cell. Nano-Struct Nano-Objects 9:19–25
136. Li Y, Guo W, Hao H, Wang L, Su Q, Jin S, Qin L, Gao W, Liu G, Hu Z (2015) Enhancing photoelectrical performance of dye–sensitized solar cell by doping $SrTiO_3:Sm^{3+}@SiO_2$ core-shell nanoparticles in the photoanode. Electrochim Acta 173:656–664
137. Aponsu GM, Wijayarathna TR, Perera IK, Perera VP, Siriwardhana AC (2013) The enhancement of photovoltaic parameters in dye-sensitized solar cells of nano-crystalline SnO_2 by incorporating with large $SrTiO_3$ particles. Spectrochim Acta Part A Mol Biomol Spectrosc 109:37–41
138. Rajamanickam N, Soundarrajan P, Vendra VK, Jasinski JB, Sunkara MK, Ramachandran K (2016) Efficiency enhancement of cubic perovskite $BaSnO_3$ nanostructures based dye sensitized solar cells. Phys Chem Chem Phys 18:8468–8478
139. Kim CW, Suh SP, Choi MJ, Kang YS, Kang YS (2013) Fabrication of $SrTiO_3$–TiO_2 heterojunction photoanode with enlarged pore diameter for dye-sensitized solar cells. J Mater Chem A 1:11820
140. Tang R, Yin L (2015) Enhanced photovoltaic performance of dye-sensitized solar cells based on Sr-doped TiO_2/$SrTiO_3$ nanorod array heterostructures. J Mater Chem A 3:17417–17425
141. Zhong M, Shi J, Zhang W, Han H, Li C (2011) Charge recombination reduction in dye-sensitized solar cells by depositing ultrapure TiO_2 nanoparticles on "inert" $BaTiO_3$ films. Mater Sci Eng, B 176:1115–1122
142. Asgari Moghaddam H, Mohammadi MR (2017) TiO_2–$BaTiO_3$ nanocomposite for electron capture in dye-sensitized solar cells. J Am Ceram Soc 100:2144–2153
143. Xu L, Aumaitre C, Kervella Y, Lapertot G, Rodríguez-Seco C, Palomares E, Demadrille R, Reiss P (2018) Increasing the efficiency of organic dye-sensitized solar cells over 10.3% using locally ordered inverse opal nanostructures in the photoelectrode. Adv Funct Mater 28:1706291
144. Liu Y, Che R, Chen G, Fan J, Sun Z, Wu Z, Wang M, Li B, Wei J, Wei Y, Wang G, Guan G, Elzatahry AA, Bagabas AA, Al-Enizi AM, Deng Y, Peng H, Zhao D (2015) Radially oriented mesoporous TiO_2 microspheres with single-crystal–like anatase walls for high-efficiency optoelectronic devices. Sci Adv 1:e1500166
145. Kakiage K, Aoyama Y, Yano T, Oya K, Fujisawa J, Hanaya M (2015) Highly-efficient dye-sensitized solar cells with collaborative sensitization by silyl-anchor and carboxy-anchor dyes. Chem Commun 51:15894–15897
146. Gao F, Wang Y, Shi D, Zhang J, Wang M, Jing X, Humphry-Baker R, Wang P, Zakeeruddin SM, Grätzel M (2008) Enhance the optical absorptivity of nanocrystalline TiO_2 film with high molar extinction coefficient ruthenium sensitizers for high performance dye-sensitized solar cells. J Am Chem Soc 130:10720–10728
147. Ren Y, Sun D, Cao Y, Tsao HN, Yuan Y, Zakeeruddin SM, Wang P, Grätzel M (2018) A stable blue photosensitizer for color palette of dye-sensitized solar cells reaching 12.6% efficiency. J Am Chem Soc 140:2405–2408
148. Sauvage F, Decoppet JD, Zhang M, Zakeeruddin SM, Comte P, Nazeeruddin M, Wang P, Grätzel M (2011) Effect of sensitizer adsorption temperature on the performance of dye-sensitized solar cells. J Am Chem Soc 133:9304–9310
149. Chiu J-M, Chen EM, Lee C-P, Shown I, Tunuguntla V, Chou J-S, Chen L-C, Chen K-H, Tai Y (2017) Geogrid-inspired nanostructure to reinforce a $Cu_xZn_ySn_zS$ nanowall electrode for high-stability electrochemical energy conversion devices. Adv Energy Mater 7:1602210
150. Hou W, Xiao Y, Han G (2017) An interconnected ternary MIn2S4 (M = Fe Co, Ni) thiospinel nanosheet array: a type of efficient platinum-free counter electrode for dye-sensitized solar cells. Angew Chem Int Ed 56:9146–9150

151. Chiang CC, Hung CY, Chou SW, Shyue JJ, Cheng KY, Chang PJ, Yang YY, Lin CY, Chang TK, Chi Y, Chou HL, Chou PT (2018) PtCoFe nanowire cathodes boost short-circuit currents of Ru(II)-based dye-sensitized solar cells to a power conversion efficiency of 12.29%. Adv Funct Mater 28: 1703282
152. Li L, Lu Q, Li W, Li X, Hagfeldt A, Zhang W, Wu M (2016) Highly efficient dye-sensitized solar cells achieved through using Pt-free Nb_2O_5/C composite counter electrode and iodide-free redox couples. J Power Sources 308:37–43
153. Ju MJ, Jeon IY, Kim HM, Choi JI, Jung SM, Seo JM, Choi IK, Kang SH, Kim HS, Noh MJ, Lee JJ, Jeong YH, Kim HK, Kim YH, Baek JB (2016) Edge-selenated graphene nanoplatelets as durable metal-free catalysts for iodine reduction reaction in dye-sensitized solar cells. Sci Adv 2:e1501459
154. Sagaidak I, Huertas G, Nguyen Van Nhien A, Sauvage F (2018) New iodide-based amino acid molecules for more sustainable electrolytes in dye-sensitized solar cells. Green Chem 20:1059–1064
155. Briscoe J, Dunn S (2016) The future of using earth-abundant elements in counter electrodes for dye-sensitized solar cells. Adv Mater 28:3802–3813
156. Wu J, Lan Z, Lin J, Huang M, Huang Y, Fan L, Luo G, Lin Y, Xie Y, Wei Y (2017) Counter electrodes in dye-sensitized solar cells. Chem Soc Rev 46:5975–6023
157. Yun S, Lund PD, Hinsch A (2015) Stability assessment of alternative platinum free counter electrodes for dye-sensitized solar cells. Energy Environ Sci 8:3495–3514
158. Chen X, Tang Q, He B, Lin L, Yu L (2014) Platinum-free binary Co–Ni alloy counter electrodes for efficient dye-sensitized solar cells. Angew Chem Int Ed 53:10799–10803
159. Jeong I, Lee J, Vincent Joseph KL, Lee HI, Kim JK, Yoon S, Lee J (2014) Low-cost electrospun WC/C composite nanofiber as a powerful platinum-free counter electrode for dye sensitized solar cell. Nano Energy 9:392–400
160. Hashmi SG, Ozkan M, Halme J, Paltakari J, Lund PD (2014) Highly conductive, non-permeable, fiber based substrate for counter electrode application in dye-sensitized solar cells. Nano Energy 9:212–220
161. Chen PY, Li CT, Lee CP, Vittal R, Ho KC (2015) PEDOT-decorated nitrogen-doped graphene as the transparent composite film for the counter electrode of a dye-sensitized solar cell. Nano Energy 12:374–385
162. Zheng X, Deng J, Wang N, Deng D, Zhang WH, Bao X, Li C (2014) Podlike N-doped carbon nanotubes encapsulating FeNi alloy nanoparticles: high-performance counter electrode materials for dye-sensitized solar cells. Angew Chem Int Ed 53:7023–7027
163. Jin Z, Zhang M, Wang M, Feng C, Wang ZS (2017) Metal selenides as efficient counter electrodes for dye-sensitized solar cells. Acc Chem Res 50:895–904
164. Wang W, Xu X, Liu Y, Zhong Y, Shao Z (2018) Rational design of metal oxide-based cathodes for efficient dye-sensitized solar cells. Adv Energy Mater 8:1800172
165. Ahn SH, Klein MJ, Manthiram A (2017) 1D Co- and N-doped hierarchically porous carbon nanotubes derived from bimetallic metal organic framework for efficient oxygen and tri-iodide reduction reactions. Adv Energy Mater 7:1601979
166. Shukla S, Loc NH, Boix PP, Koh TM, Prabhakar RR, Mulmudi HK, Zhang J, Chen S, Ng CF, Huan CHA, Mathews N, Sritharan T, Xiong Q (2014) Iron pyrite thin film counter electrodes for dye-sensitized solar cells: high efficiency for iodine and cobalt redox electrolyte cells. ACS Nano 8:10597–10605
167. Ahn SH, Manthiram A (2016) Edge-oriented tungsten disulfide catalyst produced from mesoporous WO_3 for highly efficient dye-sensitized solar cells. Adv Energy Mater 6:1501814
168. Hou Y, Wang D, Yang XH, Fang WQ, Zhang B, Wang HF, Lu GZ, Hu P, Zhao HJ, Yang HG (2013) Rational screening low-cost counter electrodes for dye-sensitized solar cells. Nat Commun 4:1583
169. Cui X, Xiao J, Wu Y, Du P, Si R, Yang H, Tian H, Li J, Zhang W-H, Deng D, Bao X (2016) A graphene composite material with single cobalt active sites: a highly efficient counter electrode for dye-sensitized solar cells. Angew Chem Int Ed 55:6708–6712

170. Shrestha A, Batmunkh M, Shearer CJ, Yin Y, Andersson GG, Shapter JG, Qiao S, Dai S (2017) Nitrogen-doped CN_x/CNTs heteroelectrocatalysts for highly efficient dye-sensitized solar cells. Adv Energy Mater 7:1602276
171. Wang H, Sun K, Tao F, Stacchiola DJ, Hu YH (2013) 3D honeycomb-like structured graphene and its high efficiency as a counter-electrode catalyst for dye-sensitized solar cells. Angew Chem Int Ed 52:9210–9214
172. Jeon I-Y, Kim HM, Choi IT, Lim K, Ko J, Kim JC, Choi H-J, Ju MJ, Lee J-J, Kim HK, Baek J-B (2015) High-performance dye-sensitized solar cells using edge-halogenated graphene nanoplatelets as counter electrodes. Nano Energy 13:336–345
173. Meng X, Yu C, Song X, Liu Y, Liang S, Liu Z, Hao C, Qiu J (2015) Nitrogen-doped graphene nanoribbons with surface enriched active sites and enhanced performance for dye-sensitized solar cells. Adv Energy Mater 5:1500180
174. Huang S, He Q, Chen W, Zai J, Qiao Q, Qian X (2015) 3D hierarchical $FeSe_2$ microspheres: controlled synthesis and applications in dye-sensitized solar cells. Nano Energy 15:205–215
175. Chiu IT, Li CT, Lee CP, Chen PY, Tseng YH, Vittal R, Ho KC (2016) Nanoclimbing-wall-like $CoSe_2$/carbon composite film for the counter electrode of a highly efficient dye-sensitized solar cell: a study on the morphology control. Nano Energy 22:594–606
176. Chen L, Zhou Y, Dai H, Yu T, Liu J, Zou Z (2015) One-step growth of $CoNi_2S_4$nanoribbons on carbon fibers as platinum-free counter electrodes for fiber-shaped dye-sensitized solar cells with high performance: polymorph-dependent conversion efficiency. Nano Energy 11:697–703
177. Meng X, Yu C, Lu B, Yang J, Qiu J (2016) Dual integration system endowing two-dimensional titanium disulfide with enhanced triiodide reduction performance in dye-sensitized solar cells. Nano Energy 22:59–69
178. Pan J, Wang L, Yu JC, Liu G, Cheng HM (2014) A nonstoichiometric $SnO_{2-\delta}$ nanocrystal-based counter electrode for remarkably improving the performance of dye-sensitized solar cells. Chem Commun 50:7020–7023
179. Hou Y, Chen ZP, Wang D, Zhang B, Yang S, Wang HF, Hu P, Zhao HJ, Yang HG (2014) Highly electrocatalytic activity of RuO_2 nanocrystals for triiodide reduction in dye-sensitized solar cells. Small 10:484–492
180. Zhou H, Shi Y, Dong Q, Wang Y, Zhu C, Wang L, Wang N, Wei Y, Tao S, Ma T (2014) Interlaced $W_{18}O_{49}$ nanofibers as a superior catalyst for the counter electrode of highly efficient dye-sensitized solar cells. J Mater Chem A 2:4347–4354
181. Du F, Yang Q, Qin T, Li G (2017) Morphology-controlled growth of $NiCo_2O_4$ ternary oxides and their application in dye-sensitized solar cells as counter electrodes. Sol Energy 146:125–130
182. Zhang C, Deng L, Zhang P, Ren X, Li Y, He T (2017) Mesoporous $NiCo_2O_4$ networks with enhanced performance as counter electrodes for dye-sensitized solar cells. Dalton Trans 46:4403–4411
183. Xiong D, Zhang Q, Verma SK, Li H, Chen W, Zhao X (2016) Use of delafossite oxides $CuCr_{1-x}Ga_xO_2$ nanocrystals in p-type dye-sensitized solar cell. J Alloys Compd 662:374–380
184. Suntivich J, May KJ, Gasteiger HA, Goodenough JB, Shao-Horn Y (2011) A perovskite oxide optimized for oxygen evolution catalysis from molecular orbital principles. Science 334:1383–1385
185. Suntivich J, Gasteiger HA, Yabuuchi N, Nakanishi H, Goodenough JB, Shao-Horn Y (2011) Design principles for oxygen-reduction activity on perovskite oxide catalysts for fuel cells and metal-air batteries. Nat Chem 3:546–550
186. Zhao B, Zhang L, Zhen D, Yoo S, Ding Y, Chen D, Chen Y, Zhang Q, Doyle B, Xiong X, Liu M (2017) A tailored double perovskite nanofiber catalyst enables ultrafast oxygen evolution. Nat Commun 8:14586

187. Zhong Y, Chen P, Yang B, Zuo X, Zhou L, Yang X, Li G (2015) Low-cost platinum-free counter electrode of $La_{0.67}Sr_{0.33}MnO_3$ perovskite for efficient dye-sensitized solar cells. Appl Phys Lett 106: 263903
188. Dao VD, Larina LL, Jung KD, Lee JK, Choi HS (2014) Graphene-NiO nanohybrid prepared by dry plasma reduction as a low-cost counter electrode material for dye-sensitized solar cells. Nanoscale 6:477–482
189. Du F, Yang B, Zuo X, Li G (2015) Dye-sensitized solar cells based on low-cost nanoscale SnO_2@RGO composite counter electrode. Mater Lett 158:424–427
190. Xiong K, Li G, Jin C, Jin S (2016) $La_{0.65}Sr_{0.35}MnO_3$@RGO nanocomposites as an effective counter electrode for dye-sensitized solar cells. Mater Lett 164:609–612
191. Yu Y, Zheng H, Zhang X, Liang X, Yue G, Li F, Zhu M, Li T, Tian J, Yin G (2016) An efficient dye-sensitized solar cell with a promising material of $Bi_4Ti_3O_{12}$ nanofibers/graphene. Electrochim Acta 215:543–549
192. Xiong K, Liu Z, Yuan J, Li K, Li G, Jin S, Luo G, Zhu L, Shi H, Xiao X (2016) $La_{0.5}Sr_{0.5}CoO_{2.91}$@RGO nanocomposites as an effective counter electrode for dye-sensitized solar cells. J Mater Sci Mater Electron 28:1679–1683
193. Chang SH, Danilovic N, Chang KC, Subbaraman R, Paulikas AP, Fong DD, Highland MJ, Baldo PM, Stamenkovic VR, Freeland JW, Eastman JA, Markovic NM (2014) Functional links between stability and reactivity of strontium ruthenate single crystals during oxygen evolution. Nat Commun 5:4191
194. Lan A, Mukasyan AS (2008) Complex $SrRuO_3$–Pt and $LaRuO_3$–Pt catalysts for direct alcohol fuel cells. Ind Eng Chem Res 47:8989–8994
195. Liu T, Hou J, Wang B, Bai F, Chen H, Gao L, Cao Y, He H, Wang J, Wang N, Cao G, Guo Z (2016) Correlation between the in-plain substrate strain and electrocatalytic activity of strontium ruthenate thin films in dye-sensitized solar cells. J Mater Chem A 4:10794–10800
196. Liu T, Yu K, Gao L, Chen H, Wang N, Hao L, Li T, He H, Guo Z (2017) A graphene quantum dot decorated $SrRuO_3$ mesoporous film as an efficient counter electrode for high-performance dye-sensitized solar cells. J Mater Chem A 5:17848–17855
197. Wang W, Liu Y, Zhong YJ, Wang L, Zhou W, Wang S, Shao Z (2017) Rational design of $LaNiO_3$/carbon composites as outstanding platinum-free photocathodes in dye-sensitized solar cells with enhanced catalysis for the triiodide reduction reaction. Sol RRL 1:1700074
198. Song T, Chen Q, Zhou H, Jiang C, Wang H, Yang Y, Liu Y, You J, Yang Y (2015) Perovskite solar cells: film formation and properties. J Mater Chem A 3:9032–9050

Chapter 8
Perovskite Materials in Electrocatalysis

Xiaomin Xu, Yangli Pan, Lei Ge and Zongping Shao

1 Introduction

Driven by pressing concerns over the growing energy demands, depleting fossil fuels, and impending climate change, one grand challenge facing humanity today is how to power the planet with renewable energy sources (e.g., wind and solar). Renewable energy is plentiful but tends to be intermittent in nature as the wind is not always blowing and the sun is not always shining. One prospective option to address the issue of energy supply intermittency is to develop electrochemical devices that can utilize electricity produced from renewable energy to enable the transformations between electrical energy and chemical energy. For example, in water electrolyzers, water molecules are split into hydrogen, which is a clean energy carrier that can be used in fuel cells to generate electricity. In fuel cells or metal–air batteries, the oxidation of hydrogen or metals is coupled with the reduction of oxygen to convert chemical energy into electrical energy. Unfortunately, these energy conversion technologies have low efficiency because of the sluggish kinetics of several key reactions involved. For instance, the overall efficiency of water electrolysis is dominated by the hydrogen evolution reaction (HER) at the cathode and the oxygen evolution reaction (OER) at the anode [1]. Likewise, the efficiency of rechargeable metal–air batteries is strongly dependent on the oxygen reduction reaction (ORR) during discharge and the OER during charge [2]. Increasing the efficiency of

X. Xu · Z. Shao (✉)
WA School of Mines: Minerals, Energy and Chemical Engineering (WASM-MECE), Curtin University, Perth, WA 6845, Australia
e-mail: zongping.shao@curtin.edu.au

Y. Pan · L. Ge
Centre for Future Materials, University of Southern Queensland, Springfield Central, QLD 4300, Australia

N. S. Arul and V. D. Nithya (eds.), *Revolution of Perovskite*, Materials Horizons: From Nature to Nanomaterials, https://doi.org/10.1007/978-981-15-1267-4_8

these devices would therefore necessitate the role of electrocatalysis to modify the rate of the relevant chemical reactions via the assistance of electrocatalysts that are active and stable.

The term "electrocatalysis" is generally referred to as a type of catalysis that leads to the change of the rate of an electrochemical reaction taking place at the interface between an electrode and an electrolyte. Despite its high relevance to renewable energy technologies, our current knowledge about the fundamental mechanisms underlying electrocatalysis is still inadequate. For instance, mechanistic insights into the OER are limited to theoretical understanding only, due to the complexity in this multistep four-electron reaction which lacks experimental observation on the details of electrode interfaces under realistic operating conditions. Nonetheless, years of intense academic research have seen significant breakthroughs in the development of electrocatalysts that can substantially lower the overpotential associated with the electrochemical reactions. While noble metal-based materials (e.g., Pt-, Ir-, and Ru-based materials) normally show optimum catalytic activity [3, 4], their widespread penetration into clean energy devices is hindered by their low abundance and high cost, which does not conform to the vision of a sustainable energy future. Hence, tremendous efforts have been devoted to the search for a wide range of inexpensive alternatives that consist of Earth-abundant elements. These include metals [5], oxides [6–8], (oxy)hydroxides [9, 10], chalcogenides [11], nonmetal carbon materials [12], and metal–organic frameworks [13], to name just a few.

Of all the candidates, perovskite materials have recently emerged as a new family of low-cost, high-efficient nonprecious metal catalysts for catalyzing relevant reactions including the ORR, OER, and HER [14]. Perovskites are known for their versatility in chemical, crystal, and electronic structures [15]. With a nominal formula generally expressed as ABO_3, the perovskite chemical structure can accommodate nearly 90% of the elements within the "Periodic Table of Elements" by partial substitution of elements at A- or/and B-sites, while also allowing a changeable stoichiometry at the O-site [16]. In addition, a range of perovskite derivatives with varied crystal structures, including double perovskite, layered perovskite, and quadruple perovskite, further add to the diversity of the perovskite family. This flexibility gives rise to the tunability in the electronic structure of perovskites, making them ideally suited for the study of the structure–performance relationship in electrocatalysis. In oxygen electrocatalysis, a veritable explosion of research activity targeting the development of perovskite catalysts has been observed. On the other hand, the role of perovskites in the field of hydrogen electrocatalysis is less explored, and has been gaining growing attention until recently. In this chapter, we mainly focus on perovskite materials for the electrocatalysis toward the ORR, OER, and HER reactions. Considering that perovskite oxides are typically stable in alkaline media and can dissolve in acids, this chapter will primarily deal with those that work in alkaline environments unless otherwise stated. The electrocatalytic mechanisms are first introduced to offer a clear picture of the reactions taking place on perovskite catalysts. This is followed by a detailed discussion on the rational design of perovskite materials toward efficient electrocatalysis, which focuses on both catalytic activity and stability. In the context of the

pursuit of a sustainable future of energy, we also present applications of perovskite materials in electrocatalysis-related energy devices which can enable efficient use of renewable energy.

2 Mechanisms in Electrocatalysis on Perovskite Materials

Fundamental insight into the reaction mechanisms is a vital step toward understanding electrocatalysis on catalyst surfaces. Due to the complex interaction at the electrode interface, there is no single governing mechanism that unifies all electrocatalytic reactions. Even for the same reaction of interest, the mechanisms can differ with catalyst chemistries. Taking the OER in alkaline media as an example, one-metal-site mechanisms have been proposed for noble metals [17], dimeric molecules [18], and perovskite oxides [19], whereas distinct two-metal-site mechanisms have been introduced for the oxygen-evolving complex of photosystem II [20] and electrodeposited oxides [21]. In this section, only the conventional mechanisms (which are considered the most favorable) underlying the oxygen and hydrogen electrocatalysis on perovskite surfaces are highlighted.

2.1 Oxygen Electrocatalysis

Conventionally, the ORR reaction in alkaline solutions can be written as $O_2 + 2H_2O + 4e^- \rightarrow 4OH^-$. Previous experimental and computational studies show that the ORR on perovskite oxides is a consecutive, four-step, proton-coupled electron transfer process taking place on single surface metal sites [22, 23]. These four sequential steps are 1, hydroxide displacement; 2, peroxide formation; 3, oxide formation; and 4, hydroxide regeneration as shown in Fig. 1a [22]. In these reaction pathways, molecular O_2 or H_2O from the electrolyte and electron interact with surface metal sites to generate four different oxygenated adsorbates including OO*, OOH*, O*, and OH* (* denotes a reactive site on the catalyst surface), which is accompanied by the oxidation and reduction (redox) of surface metal sites whose oxidation state changes between n + and n + 1. Energetically, the ORR reaction kinetics are largely determined by the binding energy of oxygen and the surface metal sites; too weak of an oxygen-binding energy leads to the first OH*-to-OO* displacement step being the rate-determining step (RDS), whereas too strong of an oxygen-binding energy renders the last O*-to-OH* transition step being rate-limiting [23]. An optimal perovskite catalyst binds to oxygen neither too weakly nor too strongly, which is commonly referred to as the Sabatier principle. For perovskite oxide surfaces that follow the same one-metal-site mechanism, the binding energies of the different reactive oxygen adsorbates involved in the ORR are highly correlated due to scaling relations [24, 25], which is the origin of the nonzero theoretical overpotential observed among many catalysts.

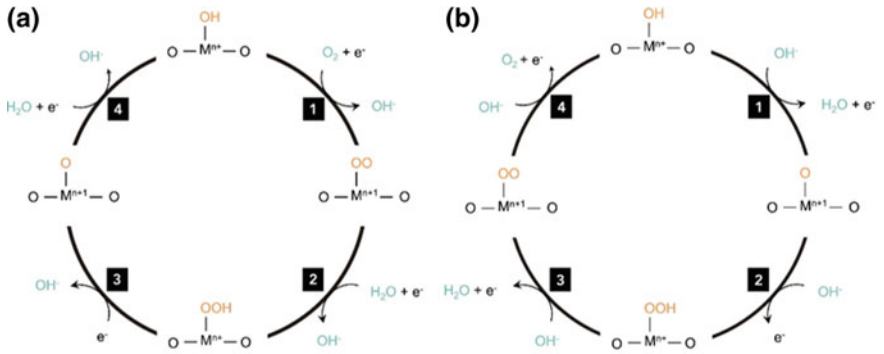

Fig. 1 **a** Four-step ORR mechanism on the surface of perovskite oxide catalysts in alkaline solutions. **b** Four-step OER mechanism on the surface of perovskite oxide catalysts in alkaline solutions (Reprinted with permission from Ref. [22]. Copyright 2017 Elsevier Inc.)

In a similar vein, the OER reaction on perovskite oxides in alkaline media, which can be written as $4OH^- \rightarrow O_2 + 2H_2O + 4e^-$, proceeds via four proton-coupled electron transfer steps including 1, hydroxide deprotonation; 2, peroxide formation; 3, peroxide deprotonation; and 4, hydroxide regeneration (Fig. 1b) [22]. In this mechanism, hydroxyl ions (OH^-) from the electrolyte interact with surface metal sites, resulting in the redox of the metal (with the oxidation state switching between n + and n + 1). The reactive intermediates generated for the OER in base are the same as those for the ORR, which are, however, in a different sequence of O*, OOH*, OO*, and OH*. Similar to the ORR, the OER reaction kinetics are primarily controlled by the oxygen-binding strength on surface metal sites. For metal sites that bind oxygen too weakly, the second O*-to-OOH* peroxide formation step is rate-limiting. On the other hand, for metal sites that bind oxygen too strongly, the RDS may be the third OOH*-to-OO* peroxide deprotonation step [26]. The binding strength of the surface oxygen adsorbates is found to obey a scaling relation [27], analogous to the case of perovskites for the ORR, again hampering the development of a perovskite OER catalyst with zero overpotential. While the conventional OER mechanism considers surface metal as the sole reactive site, novel mechanisms that involve the participation of lattice oxygen have recently been proposed [28–32].

Note that the intermediate adsorbates on perovskite oxide surfaces in the above-mentioned ORR/OER mechanisms are not identical to those on metal surfaces in relevant mechanisms proposed based on density functional theory (DFT) calculations. Despite having similar elementary reaction steps, the ORR on metal surfaces involves a series of intermediates in the order of O_2*, OOH*, O*, and OH* [24], whereas the OER on metal surfaces involves a sequence of intermediates of OH*, O*, OOH*, and O_2* [17]. This difference can be rationalized from the different surface properties of metal surfaces and perovskite oxide surfaces, the latter being able to adsorb negatively charged species (such as OH^-) in alkaline conditions at the initial stage of

electrocatalysis [33]. Such difference also points to the diversity in reaction mechanisms that have been proposed for oxygen electrocatalysis, which again highlights the complexity of the oxygen chemistries on catalyst surfaces. To date, due to the underdeveloped time-resolved techniques, experimentally accessing the reaction intermediates on perovskite oxide surfaces remains a formidable challenge. Theoretically, to gain a better mechanistic understanding of the oxygen electrocatalysis, interested readers can resort to the pioneering DFT works by Rossmeisl et al. [17, 27, 34] and Nørskov et al. [24, 35, 36].

2.2 Hydrogen Electrocatalysis

The overall reaction of the HER in basic solutions can be written as $2H_2O + 2e^- \rightarrow H_2 + 2OH^-$. Generally, the alkaline HER is a two-step electron transfer process, and may occur via either the Volmer–Heyrovsky mechanism or the Volmer–Tafel mechanism [37, 38]:

$$\text{Volmer reaction:} \quad * + H_2O + e^- \rightarrow H* + OH^- \tag{1}$$

$$\text{Heyrovsky reaction:} \quad H* + H_2O + e^- \rightarrow H_2 + OH^- + * \tag{2}$$

$$\text{Tafel reaction:} \quad 2H* \rightarrow H_2 + 2* \tag{3}$$

Both reaction pathways include the same Volmer reaction, which involves adsorption of molecular H_2O on the empty reactive sites, electrochemical reduction of adsorbed H_2O into adsorbed hydrogen atoms (H*) and OH^-, desorption of OH^- to refresh the catalyst surface, and formation of H* for H_2 evolution.

While the conventional HER mechanism has been well established based on experimental and theoretical results on metal catalysts [39], little is known about the HER process on oxide surfaces, especially in alkaline environments [40, 41]. Back in the 1990s, Goodenough et al. first experimentally observed the evolution of hydrogen on $Sr_{1-x}NbO_{3-\delta}$ ($0.05 \leq x \leq 0.3$) perovskite oxides in strong acids [19]. Based on electrochemical measurements, they proposed a possible HER reaction pathway and pointed out that the reactive site for the HER on perovskite oxides appears to be not the surface metal, but rather the surface oxygen anion. This is not unexpected considering that binding with positively charged metal cations would be kinetically unfavorable for H atoms. Very recently, Xu et al. showcased the efficacy of a $Pr_{0.5}(Ba_{0.5}Sr_{0.5})_{0.5}Co_{0.8}Fe_{0.2}O_{3-\delta}$ perovskite oxide in catalyzing the HER in bases, and proposed a reaction mechanism for the alkaline HER as shown in Fig. 2 [42], similar to that for the HER in acids [19]. Note that the O-site at the initial reaction state is not protonated here for the sake of simplicity. In this pathway, molecular H_2O from the electrolyte and electron interact with a bridging oxygen site to form an adsorbed H* intermediate, where one adjacent surface metal can be reduced or oxidized (with the oxidation state switching between n + 1 and n).

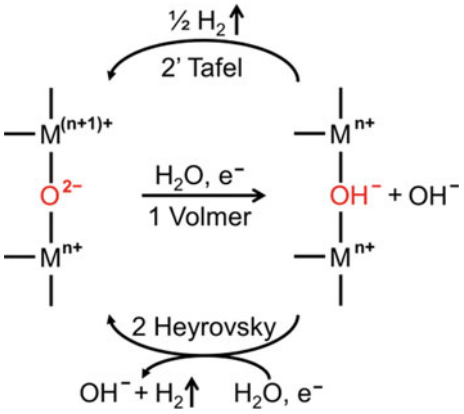

Fig. 2 Two-step HER mechanism on the surface of perovskite oxide catalysts in alkaline solutions (Reprinted with permission from Ref. [42]. Copyright 2016 John Wiley and Sons)

However, it remains difficult to determine whether the second step proceeds via the Heyrovsky reaction or the Tafel reaction.

Unlike in the case of the ORR/OER with multiple reaction intermediates, the two-electron HER involves only one intermediate (H*). Thus, no scaling relation is observed and an ideal zero overpotential can be achieved on advanced catalysts (e.g., Pt) [11], which represents a goal for optimizing the perovskite electrocatalysts. The rate of the overall HER reaction is mainly dependent on the binding strength of the H* intermediate, which is more commonly referred to as the hydrogen adsorption free energy (ΔG_H) [43]. An optimal HER catalyst should bind to hydrogen neither too weakly nor too strongly, having a ΔG_H value close to zero.

3 Rational Design of Perovskite Materials Toward Efficient Electrocatalysis

While the proposed reaction mechanisms can offer a fundamental understanding of the electrochemical processes occurring on perovskite materials, they do not have the power to screen perovskites with remarkable catalytic effects ("activity"). Given the large number of perovskite candidates and their many physical properties influencing the catalytic activity, it is necessary to realize the rational design of perovskite materials toward efficient electrocatalysis. Generally, the activity of an electrocatalyst can be improved by either increasing the intrinsic activity of each reactive site or increasing the number of reactive sites (extrinsic activity) [44]. A combination of these two strategies can lead to further enhancement in activity. To rationalize the design of improved perovskite catalysts, property–activity relationships that govern the intrinsic activity, which are often referred to as "activity descriptors", have been developed [45]. This section describes several important activity descriptors that have shown predictive power in discovering advanced perovskite catalysts, with a special emphasis on descriptors for the OER.

Nonetheless, these descriptors have their limitations and do no hold universally for all perovskite materials across all catalytic reactions. Thus, specific design strategies that aim to increase the intrinsic or extrinsic activity (or both) are discussed, focusing on a range of parameters that can be tuned in perovskite oxides to promote the catalytic performance of the ORR, OER, and HER. In addition to high activity, robust stability represents another important issue for efficient electrocatalysts. To facilitate improved catalyst design, major concerns over the stability of perovskite materials during electrocatalytic processes are included in this section.

3.1 Activity Descriptors

As mentioned earlier, the reaction rate of the OER is primarily determined by the strongly correlated binding energy of oxygen intermediates. Based on this understanding, Rossmeisl et al. utilized DFT calculations to establish the difference between the adsorption free energy of the O* and OH* intermediates ($\Delta G_{O^*} - \Delta G_{OH^*}$) as a universal activity descriptor for the OER on perovskite oxide surfaces [27], with the highest activity expected at a moderate binding of the oxygen intermediates. However, because of the experimental challenge in unambiguously distinguishing reaction intermediates, it is not straightforward to identify active perovskite catalysts using this descriptor. Directly related to the term $\Delta G_{O^*} - \Delta G_{OH^*}$ is the redox potential of transition metal cations prior to the catalytic OER, which has recently been proposed as a simpler activity descriptor [22]. Unfortunately, this approach is limited by the difficulty in the assignment of the redox transition in perovskite oxides preceding the OER. Alternatively, activity descriptors from both molecular orbital theory and band theory have proved fruitful in guiding the design of perovskite materials as efficient electrocatalysts [23, 26, 46].

3.1.1 Activity Descriptors from Molecular Orbital Theory

In the perovskite oxide structure, the B-site transition metal is sixfold coordinated to the oxygen to form an octahedron. In this octahedral environment, the transition metal d orbitals hybridize with the O 2p orbitals, forming π-bonding and π*-antibonding (called t_{2g} orbital) where d_{xy}, d_{yz}, and d_{xz} orbitals have a weak spatial overlap with adjacent O 2p orbitals, and σ-bonding and σ*-antibonding (called e_g orbital) where $d_{x^2-y^2}$ and d_{z^2} orbitals have a strong spatial overlap with nearby O 2p orbitals. Molecular orbitals depicting the metal–oxygen electronic states can be used to explain the electrocatalytic phenomena in perovskite materials. Bockris and Otagawa were the first to use the d-electron number (both t_{2g} and e_g electrons) of transition metal cations as an activity descriptor to clarify the OER activity observed on ABO_3 (B = Ni, Co, Fe, Mn, Cr, V) perovskites [47, 48]. They found an inverse trend between the OER overpotential and the number of transition metal

d electrons, which was concluded to play a major role in determining the binding strength of the OH* adsorbate via the filling of the metal–OH antibonding orbitals. Similar to this finding, recent DFT calculations showed that the binding energy of possible OER adsorbates has a scaling relationship with the transition metal d-electron number and oxidation state of perovskite oxides [49].

In contrast to the d-electron descriptor from Bockris and Otagawa, a more appropriate activity descriptor from molecular orbital principles is the filling of e_g orbital of surface transition metal cations reported by Shao-Horn and co-workers [26]. Based on the consideration that the e_g orbital has a higher overlap with a surface-anion adsorbate than does the t_{2g} orbital, the occupancy of e_g orbital can more directly influence the binding of adsorbed oxygen intermediates on surface transition metals and thus the OER activity. Through a systematic evaluation of more than 10 perovskite oxides with varying B-site elements in basic solutions, they demonstrated a volcano relationship between the OER activity (in terms of the overpotential needed to afford a 50 μA cm_{ox}^{-2} specific current density) and the e_g filling of B-site ions (Fig. 3a) [26, 45]. For the left/right branch of the volcano, perovskites having too little/much e_g orbital occupancy can result in too strong/weak interaction with oxygen intermediates, both leading to unfavorable OER activity. Sitting at the top of the volcano plot are perovskites with e_g filling close to unity, offering optimum binding of reaction intermediates and high OER performance. This observation is consistent with the Sabatier principle. The volcano trend is observed on a number of perovskite oxides, over a voltage span of 0.3 V, and across four orders of magnitude, rendering e_g filling as a universally applicable descriptor of OER activity. This descriptor has allowed the identification of a range of active perovskite OER catalysts, including $Ba_{0.5}Sr_{0.5}Co_{0.8}Fe_{0.2}O_{3-\delta}$ (BSCF) [26], $SrNb_{0.1}Co_{0.7}Fe_{0.2}O_{3-\delta}$ [50], $Ca_2Mn_2O_5$ [51], $Ca_{0.9}Yb_{0.1}MnO_{3-\delta}$ [52], and

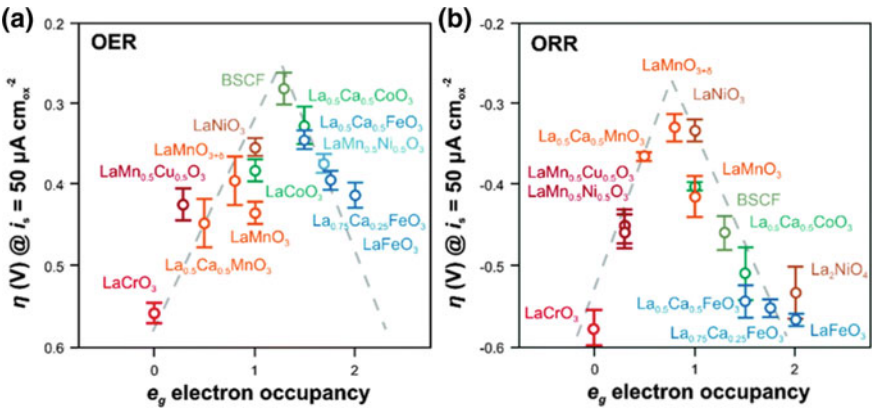

Fig. 3 The volcano relationship between **a** the OER activity or **b** the ORR activity in alkaline solutions, defined by the overpotential at a 50 μA cm_{ox}^{-2} specific current density, and the transition metal e_g electron occupancy on perovskites (Reprinted with permission from Ref. [45]. Copyright 2015 Royal Society of Chemistry)

$CaCu_3Fe_4O_{12}$ [53]. More recently, the application of the e_g-filling descriptor has been successfully extended to the screening of oxides with structures other than perovskite, for example, spinel [54] and rock salt [55] structures, for efficient OER electrocatalysts.

In a similar fashion, plotting the ORR activity (in terms of the overpotential required to give a 50 μA cm_{ox}^{-2} specific current density) of more than 10 perovskite oxides in alkaline media versus the e_g occupancy of surface transition metal cations can also obtain a volcano relationship as shown in Fig. 3b [23, 45]. Again, the perovskite ORR activity peaks at a near-unity filling of the e_g orbital for $LaNiO_3$, $LaCoO_3$, and $LaMnO_3$, outperforming $LaCrO_3$ (e_g^0) with too low an e_g occupancy at the left branch of the volcano and $LaFeO_3$ (e_g^2) with too high an e_g filling at the right branch. The e_g-filling descriptor has seen success in discovering many efficient perovskite ORR catalysts, such as $LaNi_{0.25}Co_{0.75}O_{3-\delta}$ [56], $LaNi_{1-x}Mg_xO_3$ [57], $LaNi_{1-x}Fe_xO_3$ [58], and $La_{0.8}Sr_{0.2}Mn_{0.6}Ni_{0.4}O_3$ [59]. In the case where an identical e_g occupancy of B-site cations is observed in different perovskite materials, the transition metal–oxygen covalency is found to serve as a secondary activity descriptor [23, 26]. For example, the ORR/OER activity of $LaMnO_3$, $LaCoO_3$, and $LaNiO_3$ (all having an electronic state of e_g^1) increases with the extent of the covalent mixing between transition metal ions and oxygen atoms in the order of $LaMnO_3 < LaCoO_3 < LaNiO_3$.

Despite the usefulness of the molecular orbital-based e_g filling as a universal descriptor for picking perovskite ORR/OER catalysts, this descriptor has its own limitations. On the one hand, molecular orbital theory only considers the transition metal as the reactive site, and thus cannot efficiently capture the metal–oxygen covalency of highly covalent perovskite systems where both metal and oxygen can function as reactive sites [29, 30]. On the other hand, the estimation of the e_g electron number, which is based on the transition metal oxidation state and spin state extracted from ex situ measurements, remains ambiguous. For instance, there has been an ongoing debate over the spin state of cobalt-based perovskites [60–64].

3.1.2 Activity Descriptors from Band Theory

The success of the e_g-filling descriptor highlights the importance of catalyst electronic structure on the ORR/OER. In addition to molecular orbital theory, band theory can also offer insightful understanding of the electronic structure of catalyst materials. For example, previous theoretical works have correlated the catalytic activity of metal or alloy surfaces with the metal d-band center [65]. As for perovskite oxides, band descriptions (such as bandwidth) have also been developed to describe the trend in oxygen electrocatalysis [66, 67]. Very recently, Grimaud et al. reported a correlation between the computed O p-band center relative to the Fermi level and the OER activity of cobalt-based perovskites [46]. As depicted in Fig. 4a, the electronic structure characteristics of perovskite oxides are more accurately captured by the more delocalized O p-band, while the transition metal d-character is

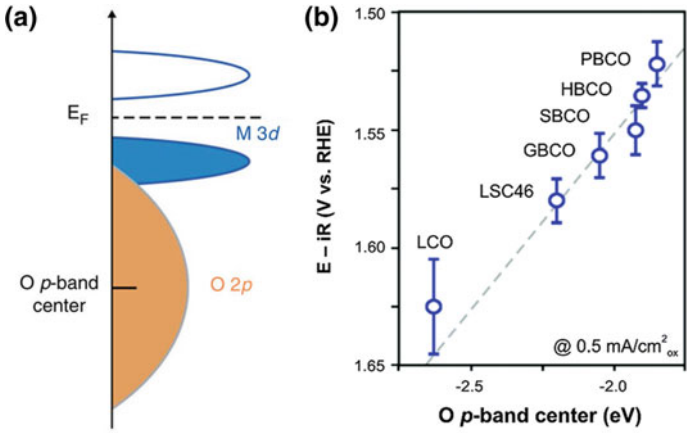

Fig. 4 **a** A schematic representation of the density of states for perovskite oxides, illustrating the O 2p and transition metal 3d bands (Reprinted with permission from Ref. [46]. Copyright 2013 Springer Nature). **b** The relationship between the OER activity in alkaline solutions, defined by the potential at a 0.5 mA cm_{ox}^{-2} specific current density, and the O p-band center relative to the Fermi level for cobalt-based perovskite oxides including $PrBaCo_2O_{5+\delta}$ (PBCO), $HoBaCo_2O_{5+\delta}$ (HBCO), $SmBaCo_2O_{5+\delta}$ (SBCO), $GdBaCo_2O_{5+\delta}$ (GBCO), $La_{0.4}Sr_{0.6}CoO_{3-\delta}$ (LSC46), and $LaCoO_3$ (LCO) (Reprinted with permission from Ref. [45]. Copyright 2015 Royal Society of Chemistry)

still reflected through hybridized density of states. The O p-band center of several double perovskite and single perovskite oxides, which was obtained from DFT calculations, was found to scale linearly with the OER performance (Fig. 4b) [45, 46]; the closer the O p-band center to the Fermi level, the greater the OER activity. Despite acting as an alternative activity descriptor, the computed O p-band center remains to be verified by experimental investigations into the metal and oxygen states. Moreover, the universality of this activity descriptor needs to be testified on perovskite systems beyond cobalt-containing ones.

3.2 Design Strategies

In spite of the success in the establishment of activity descriptors, they appear to be not explicit enough in guiding catalyst design and could present a challenge in transforming into more practical design strategies toward active perovskite electrocatalysts. In practice, the activity of a perovskite catalyst can be increased by two means. One is to take into account the electronic effects, aiming to intrinsically increase the activity of each reactive site. This can be achieved by regulating the physical/chemical properties related to the perovskite electronic structures, such as composition, oxygen vacancy, and crystal structure. The other is to consider the geometric effects that can extrinsically increase the number of reactive sites. This involves the search for novel methods to synthesize perovskite nanostructures or

composites. This section covers catalyst design strategies based on these parameters, with special attempts to illustrate how each parameter can be separately tuned in perovskites for improved electrocatalysis. Note that these parameters are actually correlated to one another. For instance, changing the composition could affect the oxygen vacancy or crystal structure [29]. Moreover, there are cases when the intrinsic and extrinsic activities can be increased simultaneously. One example is that downsizing the perovskite oxides could also bring about changes in their electronic structure [68]. Considering the huge quantity of perovskites that have been studied thus far, it appears to be impractical to mention them all and thus only typical examples are given here. Other catalyst design parameters, such as strain [69–71] and conductivity [52, 71–74], can also influence the electrocatalytic performance of perovskites. However, they are not included here given that they are currently less explored.

3.2.1 Composition

Perovskite materials are known for their flexibility in chemical compositions. Elemental substitution on the A- or/and B-site can alter the electronic structure of the B-site transition metal, thereby modifying the electrocatalytic activity. Generally, a doped perovskite oxide can be described using the formula of $A_{1-x}A'_xB_{1-y}B'_yO_3$, where A′ and B′ represent the A- and B-site dopants at a doping level of x and y, respectively. For the A-site substitution, A′ is typically a rare-earth or an alkaline-earth metal. Hyodo et al. investigated the effect of rare-earth elements on the ORR activity of $LnMnO_3$ (Ln = lanthanides and Y) in alkaline solutions, and found an activity order of La > Pr > Nd > Sm > Gd > Y > Dy > Yb, consistent with the decreasing order of the Ln^{3+} ionic radius [75]. Partial replacement of lanthanides by alkaline-earth metals can further change the catalytic performance. For example, the ORR activity of $Pr_{0.8}A'_{0.2}MnO_3$ (A′ = Ca, Sr, Ba) perovskites was reported to increase in the order of $Pr_{0.8}Ba_{0.2}MnO_3 < Pr_{0.8}Sr_{0.2}MnO_3 < Pr_{0.8}Ca_{0.2}MnO_3$ [76]. The effects of A-site doping on the ORR activity were also observed in other perovskite systems, such as $La_{1-x}Ca_xMnO_3$ [77], $La_{1-x}Sr_xMnO_3$ [78, 79], and $La_{1-x}Ca_xCoO_3$ [80]. Similar studies have also been conducted in the OER (e.g., $La_{1-x}Sr_xCoO_3$ [29, 73, 81] and $La_{1-x}Sr_xFeO_3$ [82]) and HER (e.g., $Pr_x(Ba_{0.5}Sr_{0.5})_{1-x}Co_{0.8}Fe_{0.2}O_{3-\delta}$ [42]).

Compared to the A-site doping, the B-site doping can more directly affect the catalytic activity of perovskite oxides because the B-site transition metal is considered the reactive site in conventional ORR/OER mechanisms. Sunarso et al. studied the influence of transition metals on the ORR activity of $LaBO_3$ (B = Cr, Mn, Fe, Co, and Ni) in alkaline media and found that the diffusion-limited current density of the ORR decreases in the order of $LaCoO_3 > LaMnO_3 > LaNiO_3 > LaFeO_3 > LaCrO_3$ [83], analogous to that reported by Suntivich et al. [26]. For the B-site substitution, B′ can be a redox-active transition metal or a redox-inert element or both. For instance, partial substitution of Ni in $LaNiO_3$ with Fe [58] or Mg [57] could give rise to $LaNi_{0.8}Fe_{0.2}O_3$ or $LaNi_{0.85}Mg_{0.15}O_3$ with improved ORR activity. In particular, incorporating

catalytically inactive components into the B-site can help to tune the electronic structure of the original redox-active metal and thus contribute to enhanced catalytic performance. Notably, this aspect has been extensively studied on a multitude of perovskite systems involving a range of elements as dopants, such as Sc [84, 85], Ti [86], Nb [50, 84, 87], Mo [87], W [88], Sn [89], Bi [85], Si [90], P [91–93], and S [91]. Moreover, the accommodation of multiple dopants in the B-site can also alter the catalytic behavior [84, 85, 89]. For example, Xu et al. evaluated the OER activity of a series of iron and tin co-doped $BaCo_{0.9-x}Fe_xSn_{0.1}O_{3-\delta}$ (x = 0.2, 0.3, 0.4, denoted as BCFSn-721, BCFSn-631, and BCFSn-541, respectively) [89]. Having negligible variance in physicochemical properties like surface area, morphology, crystal structure, oxygen nonstoichiometry, and surface Co oxidation state, the $BaCo_{0.9-x}Fe_xSn_{0.1}O_{3-\delta}$ series offer a good activity comparison in terms of the concentration of different dopants. As shown in Fig. 5, the OER activity increases with a higher amount of Co occupying the B-site. This indicates the intrinsically better OER performance of transition metal Co ions relative to Fe ions in a perovskite structure, similar to the finding observed on $SrB_{0.9}Ti_{0.1}O_{3-\delta}$ (B = Co, Fe) perovskites [86]. A much improved OER activity was also found on the most active $BaCo_{0.7}Fe_{0.2}Sn_{0.1}O_{3-\delta}$ compared to the non-doped and the Fe or Sn single-doped counterparts, suggesting that a synergistic effect of the two dopants may be at work.

The effect of composition can be more complicated where both the A- and B-sites are doped with foreign elements [94–96]. In this scenario, a systematic investigation, more often case-by-case, is needed to study the relationship between composition and activity before locating an optimal composition. Apart from cation

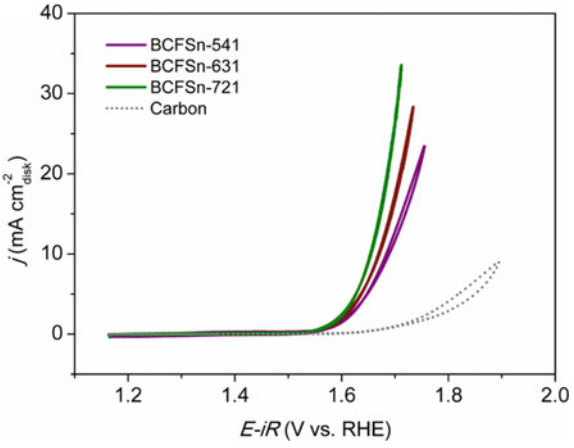

Fig. 5 The OER activity of a series of $BaCo_{0.9-x}Fe_xSn_{0.1}O_{3-\delta}$ perovskites (x = 0.2, 0.3, 0.4, denoted as BCFSn-721, BCFSn-631, and BCFSn-541, respectively) evaluated by cyclic voltammograms in 0.1 M KOH solution. The negligible OER activity of a carbon background is shown for reference (Reprinted with permission from Ref. [89]. Copyright 2015 John Wiley and Sons)

doping, the composition of perovskites can be further altered by introducing A-site cation deficiency [97–99]. For example, Zhu et al. synthesized several A-site-deficient $La_{1-x}FeO_{3-\delta}$ perovskites and obtained the optimal OER activity at a deficiency of $x = 0.05$ [97].

3.2.2 Oxygen Vacancy

A stricter way of describing the formula of perovskite oxides would actually be $ABO_{3\pm\delta}$ because many perovskite oxides have an oxygen stoichiometry that deviates from the nominal value of 3. While the effect of oxygen excess (i.e., oxygen stoichiometry of $3 + \delta$) in perovskites is merely studied in electrocatalysis, that of oxygen vacancy (i.e., oxygen stoichiometry of $3 - \delta$) has attracted plenty of research interest. Mefford et al. found that the OER activity of the $La_{1-x}Sr_xCoO_{3-\delta}$ series correlated strongly with the oxygen vacancy concentration (δ), with the highest activity obtained on $SrCoO_{2.7}$ with the largest vacancy content (Fig. 6a) [29]. Based on this, they proposed a lattice oxygen-mediated (LOM) OER mechanism that takes into consideration the involvement of lattice oxygen species and the role of surface oxygen vacancies (Fig. 6b). The validity of this LOM mechanism was further supported by DFT modeling. Later, the participation of lattice oxygen in the OER was experimentally verified by in situ ^{18}O isotope labeling mass spectrometry [30]. Different from the classically studied mechanism which only concerns surface metal sites, the LOM mechanism considers the importance of transition metal–oxygen covalency in triggering the reaction [29, 30]. These studies thus point to the critical role of oxygen vacancy, which cannot be ignored in the fundamental understanding of reaction mechanisms as well as the rational design of advanced perovskite electrocatalysts.

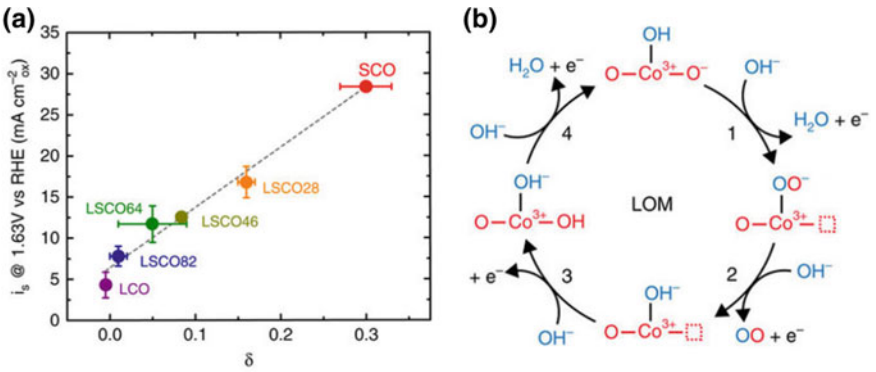

Fig. 6 **a** Correlation of the OER activity of $La_{1-x}Sr_xCoO_{3-\delta}$ with the oxygen vacancy concentration (δ), where $La_{1-x}Sr_xCoO_{3-\delta}$ is denoted as LSCO($1 - x$)x, that is, LSCO82 for $La_{0.8}Sr_{0.2}CoO_{3-\delta}$. **b** A proposed lattice oxygen-mediated (LOM) OER mechanism for perovskites in alkaline solutions (Reprinted with permission from Ref. [29]. Copyright 2016 Springer Nature)

Normally, oxygen vacancy is inherent in most of the perovskite oxides and often varies accordingly with any compositional change in order to maintain charge neutrality within the perovskite structure. For perovskites with a specific composition, there are generally two approaches to creating oxygen vacancy. One is to control the synthetic procedures, in which thermal reduction during the formation of perovskite crystallinity may be crucial to the generation of oxygen vacancy. For example, flame spray method was reported to synthesize BSCF perovskite with an oxygen deficiency up to $\sim$0.75 [100], much higher than that synthesized from other methods such as sol−gel process ($\delta \approx 0.44$) [42] and solution combustion method ($\delta \approx 0.4$) [26]. The highly oxygen-deficient BSCF was found to show a 55-fold enhancement in the OER current density relative to the sol−gel produced BSCF. The other route to increase the amount of oxygen vacancy is to conduct post-treatment on an existing perovskite, typically via reduction in H_2 or vacuum. For instance, oxygen-stoichiometric $CaMnO_3$ was converted into oxygen-deficient $CaMnO_{2.5}$ ($\delta = 0.5$) after a low-temperature reductive annealing process in 5% H_2/Ar, while the orthorhombic crystal structure was preserved [51]. With the introduction of oxygen defects, $CaMnO_{2.5}$ displayed a significantly improved OER activity compared to $CaMnO_3$. Under a much harsher reductive treatment in vacuum, Chen et al. prepared $BaTiO_{3-\delta}$ perovskite with abundant oxygen vacancies, showing enhanced performance in both the OER and ORR [101].

It should be noted, however, that increasing the number of oxygen defect sites does not necessarily lead to increased catalytic activity. This is because oxygen vacancy is not the sole factor that influences electrocatalysis. When oxygen vacancy changes, the metal electronic states (e.g., oxidation state and coordination) and metal−oxygen covalency change concomitantly. Wang et al. studied the HER activity of a series of H_2-reduction-treated $NdBaMn_2O_{6-\delta}$ double perovskites with various oxygen vacancy contents ($\delta = 0.35$, 0.54, and 0.80) [102]. The best activity was obtained for the sample with a moderate oxygen vacancy of $\delta = 0.54$, which they attributed to a combination of several factors including a distorted structure, a near-unity e_g occupancy, and an optimized O p-band center. This suggests that optimized catalytic activity may be achieved on perovskites with a moderate number of oxygen vacancy. A similar trending was also found in the $CaMnO_{3-\delta}$ perovskites ($0 < \delta \leq 0.5$) in the electrocatalysis of ORR/OER [103]. Therefore, caution needs to be exercised in the development of oxygen-deficient perovskite catalysts.

3.2.3 Crystal Structure

The crystal structure of perovskite oxides, both bulk and surface, is closely related to the electrocatalytic activity. For a perovskite with a specific nominal composition, its bulk crystal structure can vary with the synthesis conditions. For example, heat treating a $La_{0.7}Sr_{0.3}MnO_3$ precursor at 650, 750, and 850 °C led to the formation of tetragonal, cubic, and orthorhombic phase structure, respectively [104]. Electrochemical measurements indicated that the tetragonal $La_{0.7}Sr_{0.3}MnO_3$

exhibited the highest ORR activity. Another way to alter the bulk crystal structure is via post-treatment. For instance, crystalline $LaNiO_{3-\delta}$ perovskite, which has a rhombohedral phase at room temperature, transformed into a cubic-phase $LaNiO_{3-\delta}$ after being quenched from 800 °C to room temperature [105]. Such a phase transition contributed to a significant improvement in the ORR/OER catalytic activity. Apart from the quenching process, reductive annealing in H_2 can also change the perovskite bulk structure. In this respect, a cubic-phase $Pr_{0.5}Ba_{0.5}MnO_{3-\delta}$ perovskite was reported to convert into a tetragonal-phase $PrBaMn_2O_{5+\delta}$ layered perovskite after H_2 treatment, showing greatly enhanced activity toward both the ORR and OER [106].

While conventional research has mostly focused on crystalline perovskites for electrocatalysis, it has recently been shown that amorphous perovskites also exhibit considerable catalytic performance. For example, Trudel and co-workers developed a photochemical thin-film deposition technique to synthesize a series of amorphous perovskite oxides such as $LaCoO_{3-\delta}$ [107], $La_{0.7}Ca_{0.3}CoO_{3-\delta}$ [108], and BSCF [109], all showing favorable OER activity. In addition, magnetron sputtering deposition was used by Chen et al. to obtain amorphous BSCF nanofilms with exceptional OER performance [110]. The good catalytic activity may originate from the coordinately unsaturated surface metal sites of amorphous perovskites [111]. More research efforts are required to gain a better understanding of the origin of the catalytic activity of perovskite materials with an amorphous structure.

The surface crystal structure of perovskite materials can also influence the electrocatalytic performance. BSCF perovskite, which was crystallized from a conventional sol–gel process by calcination at 950 °C for 5 h, was found to have a surface amorphous oxide layer with a thickness of around 20 nm [112]. After heat treatment in argon (Ar) atmosphere, this amorphous layer gigantically grew to a thickness of 180–200 nm, deactivating the catalytic performance of BSCF toward the ORR. However, a same Ar treatment to pristine $Ba_{0.5}Sr_{0.5}Co_{0.2}Fe_{0.8}O_{3-\delta}$ with also a ≈20-nm-thick amorphous layer did not lead to further amorphization while offering an increased amount of oxygen vacancy, which resulted in a notable improvement in ORR activity. This suggests a composition-dependent behavior upon treatment in Ar between the changes in perovskite surface structure and catalytic activity.

The surface crystal structure of perovskites with an identical composition can differ with the calcination conditions. For example, the BSCF perovskite calcined at 1050 °C for 5 h exhibited a nanoscale-thick spinel-phase layer between the bulk particle and the amorphous layer on the outermost surface [113]. This spinel layer could be removed by an oxygenation process via heat treatment in oxygen atmosphere (Fig. 7), giving rise to enhanced ORR/OER performance of the BSCF catalyst.

These studies highlight the tunability of perovskite structures in both the bulk and surface, which is achieved using experimental procedures that are performed ex situ. It should also be noted that perovskite structures can undergo in situ changes under realistic electrochemical conditions. For example, the structure transformation from $BaNiO_3$ to $BaNi_{0.83}O_{2.5}$ over the OER testing in alkaline media led to an

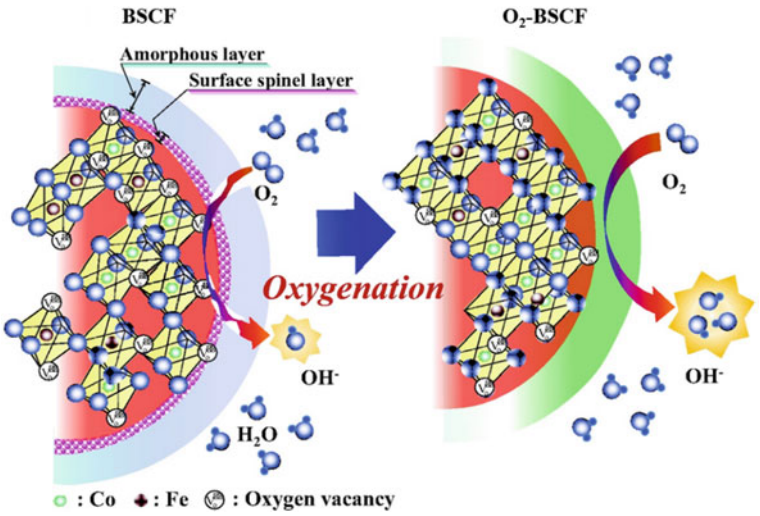

Fig. 7 A schematic representation of the effect of heat treatment in oxygen on the BSCF perovskite (Reprinted with permission from Ref. [113]. Copyright 2014 John Wiley and Sons)

improved catalytic performance [114]. To some extent, this is more of a stability issue, and thus will be discussed later in more detail in the section of stability concerns.

3.2.4 Nanostructure

Previous understanding of the electrocatalytic role of perovskites is mainly gained from bulk-sized materials, which are prepared from conventional sol–gel process [115], solid-state reaction [116], and high-pressure synthesis [117]. These bulk perovskites normally have a large particle size, a small surface area, and a featureless morphology, which can only offer limited catalytic capability. This is because a substantial proportion of inactive atoms in the bulk of perovskites are often not catalytically active toward reactions occurring at the surface. To address this issue, nanostructuring has been proposed as a technically viable approach [14]. Once a perovskite material is downsized to the nanoscale, an increase in surface area and also the number of reactive sites can be expected. Although a linearly increased number of reactive sites may not be necessarily achievable considering the accessibility issue of reactive sites, the increase in surface area does provide a greater number of reactive sites, thus contributing to an improved catalytic activity, more often on a catalyst mass basis. This has already been proved by the increased OER activity observed on the ball-milled BSCF catalyst [26], which has a particle size much reduced compared to the bulk BSCF.

Perovskite nanostructures can be attained by tailoring the synthetic parameters of conventional preparation methods. For example, Cho and co-workers developed an intriguing pattern of perovskite phase existence and particle growth by altering the calcination temperatures and lanthanum-dopant concentrations during the sol–gel synthesis of $La_x(Ba_{0.5}Sr_{0.5})_{1-x}Co_{0.8}Fe_{0.2}O_{3-\delta}$ perovskites [118]. At a reduced temperature calcination of 700 °C and a La doping content of $x = 0.7$, $La_{0.7}(Ba_{0.5}Sr_{0.5})_{0.3}Co_{0.8}Fe_{0.2}O_{3-\delta}$ perovskite with a particle size as small as 50 nm was obtained, showing a substantial improvement in the alkaline ORR/OER activity. This approach, however, requires the perovskite A-site to contain a lanthanide component, and thus may not be broadly extended to other perovskite oxides. Alternatively, a range of synthetic methods have been used to synthesize nanostructured perovskites, including precipitation method, hydrothermal synthesis, templating approach, and electrospinning [14]. In addition, several deposition-based techniques, such as physical vapor deposition (PVD), chemical vapor deposition (CVD), and electrodeposition, have also been developed to fabricate nanosized perovskite materials. The as-obtained perovskites possess plenty of morphological features, including nanowire [119], nanofiber [120], nanorod [121], nanotube [122], nanosphere [123], and nanocube [124], among others. These morphologies can lead to the different catalytic behaviors of nanostructured perovskites. For instance, compared to $LaCoO_3$ dense particles synthesized by a sol–gel route, $LaCoO_3$ porous particles and hollow nanospheres synthesized by a hydrothermal method showed an increased OER activity in an alkaline electrolyte (Fig. 8) [123].

Note that the improved catalytic performance of nanostructured perovskites may not be just a surface area effect. While $LaCoO_3$ porous particles and hollow nanospheres had a higher surface area than the dense particles, their increased OER activity was also attributed to the presence of amorphous surface structures formed during the hydrothermal synthesis [123]. Moreover, nanostructuring can further bring about a nanosize effect, that is, reducing the nanostructure size can tune the electronic state of perovskites. For example, Zhou et al. obtained $LaCoO_3$ nanoparticles with sizes of 60, 80, and 200 nm, and bulk $LaCoO_3$ particles by annealing a sol–gel precursor at 600, 700, 800, and 1000 °C, respectively [68]. Surprisingly, the best OER activity was observed on the 80 nm $LaCoO_3$, which was ascribed to its optimal e_g filling of Co ions (~ 1.2) based on Shao-Horn's activity descriptor [26]. The nanosize effect can still be at play when the perovskite size is further reduced. For instance, Zhao et al. found that the OER activity of an electrospun double perovskite nanofiber with a diameter as low as 20 nm is intrinsically higher than those with larger diameters, which was presumably due to the favorable surface electronic structure and the possible presence of heterostructures [125]. It is therefore important to understand the electrocatalytic processes on nanostructured perovskites, both experimentally and theoretically. Such understanding, combined with that gained from bulk perovskite materials, can better guide the development of improved perovskite electrocatalysts.

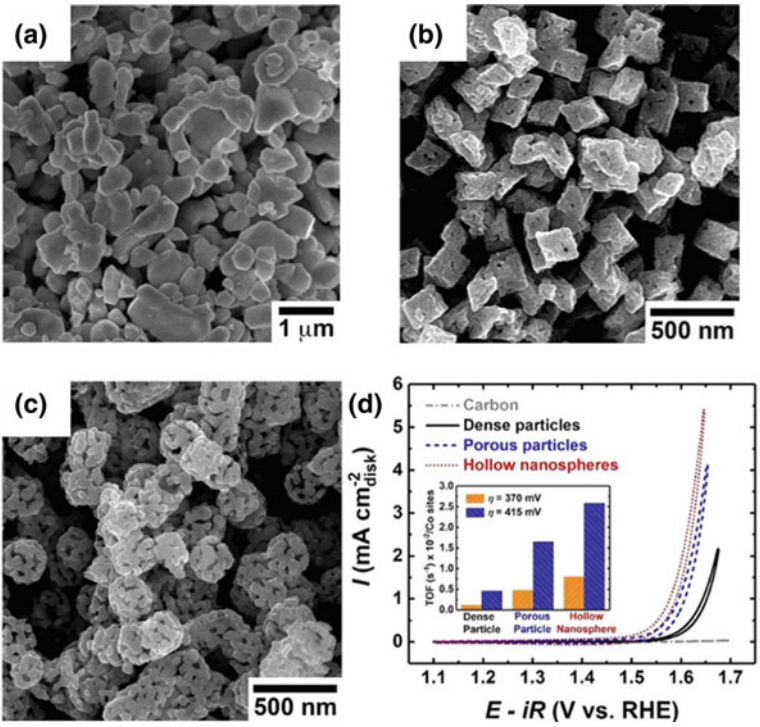

Fig. 8 Scanning electron micrographs of $LaCoO_3$ **a** dense particles, **b** porous particles, and **c** hollow nanospheres. **d** The OER activity of $LaCoO_3$ dense particles, porous particles, and hollow nanospheres evaluated by cyclic voltammograms in 0.1 M KOH solution (Reprinted with permission from Ref. [123]. Copyright 2017 American Chemical Society)

3.2.5 Composite

Forming composites with other materials, including carbons, metals, and metal oxides, among others, can also extrinsically increase the catalytic activity of perovskite materials. In particular, perovskite/carbon composites have attracted the most research interest [126]. The inclusion of carbon into a perovskite oxide was first used to remove any possible electrical conductivity limitations within some intrinsically insulating or semiconducting perovskites [127]. However, recent investigations have suggested that carbon could serve more than just the role of a conductive support [128–134]. For example, in the electrocatalytic ORR, carbon in perovskite/carbon composites was found to participate in the ORR mechanistic pathway by catalyzing the reduction of O_2 to HO_2^- [128–133]. In addition, carbon could act as a reducing agent to modify the electronic structure of perovskites. For example, acetylene black (a type of conductive carbon), when composited with BSCF, was found to reduce the cobalt cations to a lower oxidation state, which contributed to a greatly improved ORR/OER activity [134]. These observations

highlight the important roles of carbon in perovskite/carbon composites, which can be utilized to design improved perovskite-based hybrid catalysts.

Perovskite/carbon composites can be simply obtained using physical mixing, showing enhanced bifunctional activity toward the ORR and OER [135–138]. A more intimate combination between perovskites and carbons is expected to further improve the ORR/OER bifunctionality. This can be realized by means of advanced chemical synthesis, such as the CVD process [139–143], hydrothermal method [144, 145], and electrospinning [146]. However, due to the inherent incompatibility between the reductive carbon materials and the oxidative perovskite oxides, it remains challenging to obtain perovskite/carbon composites with a pure-phase perovskite component. For instance, the perovskite structure may not be preserved during the high-temperature CVD process [143]. To address this, modification to the current synthetic conditions is required. In addition, novel fabrication techniques should be developed to synthesize intact perovskite/carbon composites to achieve improved electrocatalysts.

Understanding the origin of enhanced catalytic activity on perovskite/carbon composites is important to the rational design of efficient perovskite catalysts. While conventional research has pointed to a "synergistic effect" between the perovskite and carbon, that is, two is better than one, it does not clarify the true reason behind the improved activity. Recently, Zhu et al. proposed three possible origins to explain the increased activity observed on perovskite/carbon composites (Fig. 9) [126]. First, the ligand effect at the interface can modify the electronic structure and thus lead to increased activity as mentioned earlier [134]. Second, the formation of interfacial heterostructures, in the form of covalent bonds or a new phase, can contribute to enhanced catalytic activity. This can be understood from the fact that strongly coupled perovskite/carbon composites made from chemical synthesis outperformed not only each individual component but also their physical mixtures. Third, the spillover effect can be at work for the improved bifunctionality of perovskite/carbon composites. In the composite, perovskites are considered to be more active toward the OER, whereas carbons are more active toward the ORR. During the ORR process, the OH^- generated on the carbon surface spills over to the perovskite surface, which promotes the ORR by releasing more reactive sites on the carbon surface, leading to increased ORR activity. In a similar way, during the OER process, O_2 produced on the perovskite surface spills over to the carbon surface, which facilitates the OER by releasing more reactive sites on the perovskite surface, giving rise to enhanced OER activity.

Despite the contribution to improved electrocatalysis, perovskite/carbon composites might suffer from carbon corrosion, a common issue for carbon-based materials especially in the case of the OER. This issue, although less severe in alkaline media as compared to acidic media [147], can still lead to the reduction of reactive sites and even degradation of catalysts under elevated potentials during the OER testing. One way to mitigate the carbon corrosion is by using graphitized carbon or nitrogen-doped carbon with improved corrosion resistance [148, 149].

Very recently, perovskites have also been hybridized with other conducting substrates, for example, Ni foam, via advanced synthetic methods such as

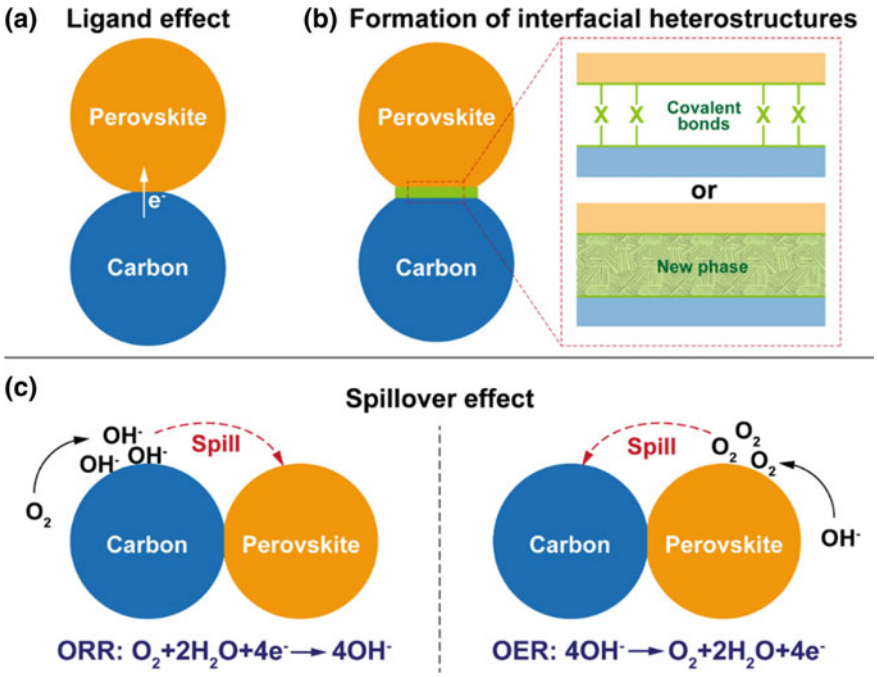

Fig. 9 A schematic illustration of three possible origins that may clarify the improved activity on perovskite/carbon composites. **a** Ligand effect. **b** Formation of interfacial heterostructures. **c** Spillover effect (Reprinted with permission from Ref. [126]. Copyright 2017 John Wiley and Sons)

hydrothermal method [150] and electrodeposition [151]. Similarly, due to the reductive nature of Ni foam, the difficulty in fabricating perovskite/Ni foam composites lies in the acquisition of pure oxidative perovskites in a high-temperature annealing process. Annealing under nonoxidative atmosphere can stabilize the Ni foam while also facilitating the formation of a perovskite phase if the precursor of perovskites is finely tuned. For example, Li et al. used electrodeposition to deposit a perovskite hydroxide precursor on Ni foam, which could convert into crystallized perovskite oxide upon a moderate annealing treatment in Ar [151]. Taking advantage from both the catalytically active perovskites and the 3D porous, highly conductive Ni foam, perovskite/Ni foam composites possess great potential in practical applications.

In addition to forming composites with conductive materials, perovskites can also be coupled with metal nanoparticles. Such hybrid materials are often synthesized by exsolution, a chemical process that is almost exclusive to perovskite oxides. Under heat treatment in a reductive atmosphere (e.g., H_2), an active metal initially incorporated in the perovskite lattice can go through a reduction process and then exsolve in the form of metal nanoparticles on the surface of the perovskite [152]. These metal nanoparticles can act as additional catalytic sites while also changing the original

perovskite electronic structure, thus leading to a different behavior in electrocatalysis. For example, Ni nanoparticle-decorated $La_{0.4}Sr_{0.4}Ti_{0.9}O_{3-\delta}$ composite, which was constructed from the $La_{0.4}Sr_{0.4}Ti_{0.9}Ni_{0.1}O_{3-\delta}$ parent perovskite using a facile exsolution process, can synergistically catalyze the alkaline HER at a significantly improved efficiency [153]. In the hybrid catalyst, $La_{0.4}Sr_{0.4}Ti_{0.9}O_{3-\delta}$ facilitates water dissociation, whereas Ni nanoparticles favor hydrogen adsorption for the recombination into H_2. In a similar fashion, a Ag nanoparticle-modified $(PrBa)_{0.95}Mn_2O_{5+\delta}$ double perovskite obtained from exsolution exhibited favorable ORR activity in alkaline electrolytes, which is due likely to the strong coupling between the perovskite and Ag nanoparticles [154]. Apart from metal nanoparticles, other nanomaterials, such as metal alloys [155–158], metal/metal oxide hybrids [159, 160], can also exsolve from the perovskite lattice by carefully tuning the perovskite composition and H_2-reduction condition. These advantages of the exsolution process can bring about ample opportunities for making perovskite-derived composites with increased electrocatalytic performance.

Other catalytically active materials, such as hydroxides [161] and metal oxides [162–165], can also composite with perovskite oxides using either an infiltration process or chemical synthesis. These composite materials showed enhanced catalytic performance with respect to the sole perovskite component. To obtain optimized activity, both the perovskite oxide and the additive functional material should be cautiously selected. For example, BSCF, which is considered the benchmark perovskite OER catalyst, was composited with the benchmark ORR catalyst, commercial Pt/C, and obtained a substantially improved catalytic activity in both the ORR and OER [166]. However, these two components were physically mixed, which may not be able to unleash the full potential of their high activity. Future efforts should be devoted to the design of strongly coupled perovskite-based materials, either through experimentally developed synthetic methods or through theoretically established modeling approaches.

3.3 Stability Concerns

Compared to the significant advances in the establishment of design principles for improvement in catalytic activity, much less attention is placed on the stability of an electrocatalyst, which is actually of more relevance to realistic device-based applications. This is especially the case when it comes to perovskite OER catalysts. Even under ambient conditions, most of perovskite oxides will become amorphous during the OER, which is often accompanied by the leaching of A- or B-site cations into the electrolyte. For instance, amorphization was observed in the bulk and surface of highly active perovskite catalysts (e.g., BSCF), leading to the structural evolution from corner-sharing octahedra to edge-sharing octahedra [167, 168]. This phenomenon is more pronounced near the catalyst surface region than in the bulk, as evidenced from ex situ X-ray absorption spectroscopic measurements (XAS) [168].

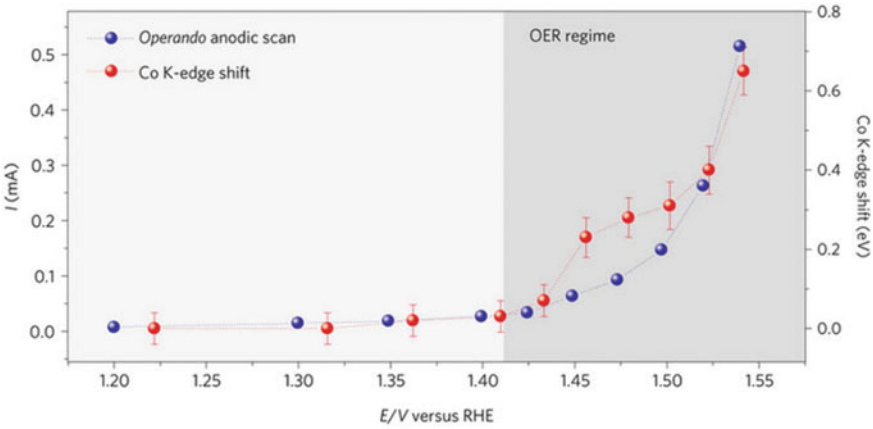

Fig. 10 OER current and shift of the Co K-edge position (taken from Operando XANES spectra) collected in situ during an anodic polarization of the BSCF-FS perovskite catalyst in 0.1 M KOH alkaline solution (Reprinted with permission from Ref. [100]. Copyright 2017 Springer Nature)

Understanding the changes occurring at the catalyst surface is therefore critical for the design of enduring perovskite electrocatalysts. This can be partially achieved through an improved understanding of the interaction between perovskite oxides and water electrolytes under a modeling system similar to the OER. For example, using in situ environmental transmission electron microscopy, Shao-Horn et al. observed structural oscillations on BSCF upon its interaction with water vapor under electron irradiation [169]. A more direct and viable way to access the changes on perovskite oxides is to use operando XAS measurements during realistic OER conditions, which was first reported by Fabbri and co-workers. Figure 10 shows an anodic polarization of a flame spray-synthesized BSCF nanocatalyst (BSCF-FS), where shift of the Co K-edge position, which was extracted from operando X-ray absorption near-edge structure (XANES) spectra, is recorded in line with the OER current [100]. It is noticeable that upon the onset of the oxygen evolution at 1.425 V versus the reversible hydrogen electrode (RHE), the Co K-edge shifts toward higher energy, corresponding to an increase in the Co oxidation state. Such change was not observed in a reverse cathodic polarization scan, indicating that the oxidation of Co is mostly an irreversible process. Further operando extended X-ray absorption fine structure (EXAFS) tests revealed the formation of a self-assembled surface layer consisting of OER-active metal (oxy)hydroxides, which is considered to be the origin of the significantly enhanced OER performance (in both activity and stability) based on an OER mechanism coupled with lattice oxygen participation.

These operando observations point to an important conclusion with respect to both catalyst activity and stability. Active perovskite OER catalysts can experience drastic changes in local chemical/electronic structures. This is substantially different from the previously mentioned activity descriptors which rely on ex situ physical properties (e.g., e_g-filling number) to guide catalyst design. On the other hand, a

perovskite oxide initially considered to be "instable" could actually evolve into a "stable" catalyst through operando changes, in which case the original perovskite can be seen as a "precursor" (or "pre-catalyst") of a real active catalyst [100]. A similar phenomenon was also found in acidic electrolytes on a $SrIrO_3$ perovskite, which transformed in situ during electrochemical testing into a highly active and stable $IrO_x/SrIrO_3$ catalyst [170].

It is noteworthy that the extent of changes on perovskite surfaces varies with different material compositions and chemistries, which may relate to the different concentrations of oxygen vacancy in perovskites [100]. Shao-Horn et al. has earlier correlated the computed O p-band center with the perovskite stability under alkaline OER conditions, and arrived at the conclusion that an optimum position of the O p-band center leads to high catalyst stability [46]. It is also important to note that not all perovskites are capable of evolving into active and durable catalysts. For example, several nickel-based and iron-based perovskite materials were found to lose activity upon prolonged OER tests under alkaline media [82, 171]. Based on these considerations, a case-by-case investigation into the stability (and activity) of a specific perovskite material can be necessary in the evaluation of its electrocatalytic performance.

Sometimes, the stability issue is of more interest to the industry than to the academia. The research community currently tends to report "stable" perovskite catalysts, more often simply from the viewpoint of electrochemical stability, without looking further into the catalyst structure either ex situ or in situ. Also, the catalyst degradation phenomena under OER testing and their origins are less explored [172–174]. In industrial settings, more rigid requirements are placed on the catalyst stability. For instance, the alkaline water electrolysis would require a catalyst to stably operate at temperatures of around 80 °C, under which condition perovskite OER catalysts may undergo changes even harsher than those at room temperature. To bridge this gap between the fundamental and applied research, more efforts should be devoted to understanding the changes in perovskites (e.g., degradation mechanisms) during the OER, which will also aid the establishment of an improved catalyst design principle that combines both catalytic activity and stability. The same holds true for perovskites in the ORR and HER electrocatalysis, although attention to these fields is still lacking.

4 Perovskite Materials for Electrocatalysis-Related Applications

The ORR/OER reactions are technologically relevant to metal–air batteries, whereas the OER/HER reactions hold key to the overall efficiency of a water electrolyzer. Over the years, a plethora of perovskite materials have been used in these devices [14, 175]. While conventional mechanistic understanding of electrocatalysis is gained mostly from bulk perovskite materials, they may not favor

practical applications because of their rather low catalytic activity, which is due to their huge particle sizes, low surface areas, and few morphological features. Comparatively speaking, nanosized and nanostructured perovskites are more suited for practical use because they offer increased reactive sites, improved accessibility of reactive sites, and better diffusion of gas reactants/products. In addition, the cost of an electrocatalyst can be more of concern for real-world devices. Also of importance is the catalyst stability, and very often a compromise has to be made between stability and activity. This section discusses the use of perovskite nanocatalysts made of Earth-abundant elements in metal–air batteries and water electrolyzers.

4.1 Metal–Air Batteries

Metal–air batteries are efficient energy conversion devices that can offer a theoretical specific energy even higher than that of the commercially available Li–ion batteries [176]. In general, a metal–air battery is composed of a metal anode, an electrolyte, and an air cathode. Among various anode candidates, Li and Zn are two of the most widely studied anode materials. The corresponding metal–air batteries are typically referred to as Li–air batteries and Zn–air batteries, respectively. Despite a major difference in electrolyte (i.e., normally nonaqueous electrolyte for Li–air batteries and aqueous electrolyte for Zn–air batteries), these two types of metal–air batteries suffer from one common scientific issue, that is, the slow kinetics of the ORR/OER reactions that determine the overall energy efficiency. At the cathode of a metal–air battery, oxygen is reduced upon discharge (ORR) and is evolved upon charge (OER). Therefore, an efficient, rechargeable metal–air battery would necessitate a bifunctional electrocatalyst that promotes both the ORR and OER.

Porosity is an important factor for achieving the practical use of perovskite catalysts in metal–air batteries. Zhang and co-workers reported the application of a three-dimensionally ordered macroporous $LaFeO_3$ perovskite (3DOM-LFO) as a cathode catalyst in a nonaqueous Li–air battery (Fig. 11a) [177]. The 3DOM-LFO catalyst had an interconnected, well-ordered, honeycomb-like pore structure (Fig. 11b), which was inherited from the polystyrene sphere template during a templating synthesis. Such a porous nanostructure could facilitate the diffusion of O_2/electrolyte during discharge/charge processes while offering significantly enhanced surface area for catalytic ORR/OER reactions, both contributing to improved performance and cycle stability of the rechargeable Li–air battery compared to the nanoparticulate $LaFeO_3$ catalyst. Porous one-dimensional (1D) nanostructures possess high surface-to-volume ratios and abundant porosity, which can favor the availability of catalytic sites as well as the diffusion of O_2 gas when used as cathode catalysts for Li–air batteries. For example, a porous nanotubular $La_{0.75}Sr_{0.25}MnO_3$ perovskite fabricated by electrospinning was found to show a significant increase in both ORR/OER electrocatalysis and battery performance in a

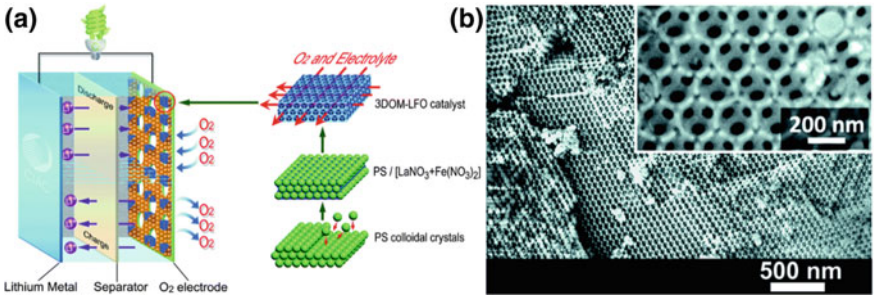

Fig. 11 **a** A schematic representation of the synthesis of a 3DOM-LFO perovskite and its application as a cathode catalyst in a rechargeable Li–air battery. **b** Scanning electron micrographs of the 3DOM-LFO catalyst, showing an interconnected, well-ordered, honeycomb-like pore structure (Reprinted with permission from Ref. [177]. Copyright 2013 Royal Society of Chemistry)

nonaqueous electrolyte [178]. Another useful way to obtain a porous cathode catalyst is via the growth of perovskites on 3D porous substrates (e.g., Ni foam). Pham et al. used hydrothermal synthesis to grow perovskite $LaNi_{0.9}Cu_{0.1}O_3$ nanosheet arrays on the surface of a 3D microporous Ni foam [150]. This composite was directly applied as a binder-free cathode, and exhibited notable ORR/OER activity and cycling performance in a nonaqueous Li–air battery.

It should be noted that the oxygen electrocatalysis in nonaqueous Li–air batteries, which follows the reaction of $O_2 + 2Li^+ + 2e^- \leftrightarrow Li_2O_2$, is quite different from that in aqueous solutions. Therefore, the design principles for advanced perovskite catalysts working in alkaline water may not be able to extend to the system of nonaqueous Li–air batteries. Despite the success of several perovskite nanocatalysts, little understanding is gained about the reaction mechanisms in nonaqueous electrolytes. While some attempts were made to evaluate the ORR/OER in nonaqueous solutions [119, 124, 150, 177, 178], more systematic investigations, rather than trial-and-error approaches, are needed in order to design better perovskite catalysts for nonaqueous Li–air batteries. By contrast, Zn–air batteries commonly adopt an aqueous alkaline electrolyte considering the stability of zinc anode and the manufacturing cost of the battery configuration. Although a higher concentration of potassium hydroxide solution (e.g., 6 M KOH) is used in Zn–air batteries, the oxygen electrocatalysis at the cathode follows the same reaction of $O_2 + 2H_2O + 4e^- \leftrightarrow 4OH^-$ as that in fundamental research. Therefore, the conventionally studied ORR/OER on perovskite materials in alkaline media is considered more relevant to the application in Zn–air batteries.

Recent years have witnessed the development of a myriad of perovskite nanomaterials for use in Zn–air batteries. Among the many candidates, perovskite/carbon composites have received more research attention, due primarily to their significantly increased electrical conductivity compared to the sole perovskites. For instance, a $LaNiO_3$ nanorod/reduced graphene oxide hybrid synthesized using a

hydrothermal method showed much enhanced conductivity relative to the $LaNiO_3$ nanorod, thereby leading to higher ORR/OER activity in alkaline solutions and also better cycle performance in rechargeable Zn–air batteries [144]. Prabu et al. reported perovskite $LaTi_{0.65}Fe_{0.35}O_{3-\delta}$ nanoparticles embedded both at the surface of and within nitrogen-doped carbon nanorods, which were prepared via electrospinning followed by calcination under Ar atmosphere [146]. Compared to $LaTi_{0.65}Fe_{0.35}O_{3-\delta}$ nanotubes without carbon, which were obtained after calcination under air, the $LaTi_{0.65}Fe_{0.35}O_{3-\delta}$/carbon nanocomposite afforded increased catalytic sites, improved electrical conductivity, and highly promoted kinetics toward both the ORR and OER, resulting in an exceptionally higher Zn–air battery performance.

Although the abovementioned perovskite/carbon composites can give rise to an improvement in Zn–air battery performance, they are produced at a small scale using bench-based hydrothermal method or electrospinning technique, which may present a hurdle toward their widespread application. Recently, CVD has emerged as a versatile process to achieve scaled-up production of nanohybrids of perovskites and carbons (especially carbon nanotubes (CNTs)), in which transition-metal-containing perovskites are applied as substrates for the catalytic growth of CNTs. Chen and co-workers reported the CVD synthesis of a core−corona structured bifunctional catalyst (CCBC) and its application as a cathode catalyst in a rechargeable Zn–air battery (Fig. 12a) [139]. This CCBC composite is comprised of a highly OER-active $LaNiO_3$ derived core component and a highly ORR-active nitrogen-doped CNTs (NCNTs) corona with a bamboo-like structure (Fig. 12b). Owing to the strong coupling effect between these two active components, an optimized CCBC-2 catalyst, which was obtained by tuning the CVD synthetic parameters, exhibited outstanding discharge and charge performance, comparable to that of the benchmark catalysts in the ORR (i.e., Pt/C) and OER (i.e., $LaNiO_3$) (Fig. 12c). In addition, the CCBC-2 catalyst showed excellent cycling stability for 75 charge−discharge cycles (Fig. 12d). Using a similar CVD method, the same researchers also obtained an intertwined core−corona structured bifunctional catalyst composed of $LaNiO_3$ nanoparticles encapsulated by NCNTs, showing bifunctionality toward the ORR/OER in rechargeable Zn–air batteries [140]. The CVD process was further extended to the synthesis of perovskite/CNTs composites involving other perovskite oxides, such as $LaMn_{0.9}Co_{0.1}O_3$ [141] and $La_{0.5}Sr_{0.5}Co_{0.8}Fe_{0.2}O_3$ [142], and good Zn–air battery performance was achieved. However, the physical origin of the catalysts' high activity and stability is less understood. Moreover, the crystalline structure of the perovskite oxides might be destroyed after the CVD synthesis because of the presence of carbon serving as a reducing agent [143], which calls for more research inputs into the preparation of intact perovskites hybridized with conductive carbons.

While much progress has been made experimentally in fabricating perovskite catalysts for metal–air batteries, theoretically less is known about the relationship between structure, morphology, and performance under operational conditions.

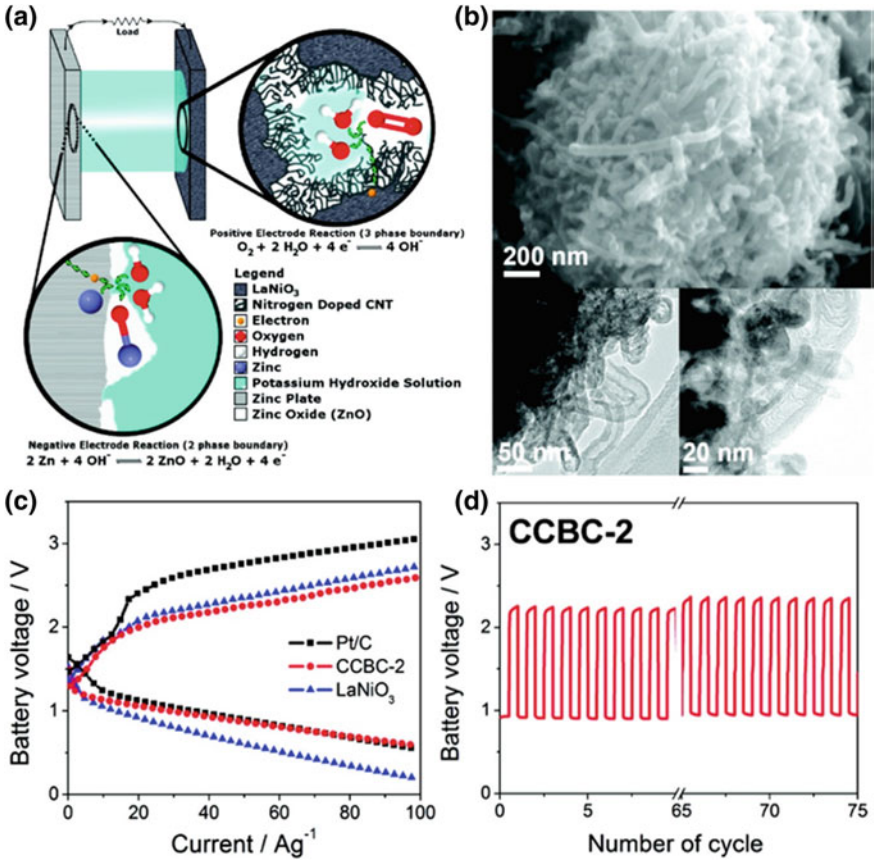

Fig. 12 **a** A schematic representation of a Zn–air battery and the reactions taking place on the electrodes. **b** Scanning electron microscopy and transmission electron microscopy images of the CCBC catalyst. **c** Discharge and charge polarization curves of the CCBC-2 catalyst in comparison to Pt/C and $LaNiO_3$. **d** Charge−discharge cycling performance of the CCBC-2 catalyst (Reprinted with permission from Ref. [139]. Copyright 2012 American Chemical Society)

This gap has to be bridged if perovskites are to be developed as practical electrocatalysts in real-world batteries. Stability remains to be another concern. Currently, lab-based metal–air batteries that adopt perovskite cathode catalysts can only sustain around 100 cycles of charge–discharge tests, which is far from the requirement of battery technologies. Another long-term goal would be to develop metal–air batteries that can work in ambient air [179], as the present catalyst performance is recorded in laboratory pure oxygen environment. This, however, could take more efforts from scientists, engineers, and the industry.

4.2 Water Electrolyzers

A water electrolyzer is one of the simplest systems for generating high-purity hydrogen. It is also a key component for the "indirect" solar to hydrogen production, converting the electricity generated from renewable solar energy (via solar panels) into chemical energy in hydrogen [180]. In water electrolysis, water is split into hydrogen and oxygen following the equation of $H_2O \rightarrow H_2 + 1/2O_2$. This reaction is a thermodynamically uphill process that necessitates an energy input of 286 kJ mol^{-1} at room temperature and pressure, corresponding to a theoretical minimum cell voltage of 1.23 V. However, the two half-reactions of water splitting, namely, the OER at the anode and the HER at the cathode, have sluggish kinetics and can cause large energy losses. For example, commercial water electrolyzers generally operate at a much higher cell voltage of 1.8–2.0 V [181]. The implementation of the water electrolysis technology would thus require highly active and stable OER/HER electrocatalysts to lower the large water-splitting overpotentials and to make the whole process more energy-efficient. While the state-of-the-art Ir-/Ru-based compounds [4] and Pt-group metals [3] offer the highest OER and HER activity, respectively, they suffer from low Earth abundance and high capital cost, hampering their commercial viability. It is thus appealing to develop perovskite materials as alternatives that contain Earth-abundant, low-cost transition metals, while still offering high catalytic activity. In addition, industrial electrolyzers work in strong alkaline electrolytes in order to avoid the corrosion from acids and reduce the total cost [182], where perovskites appear to be readily suited given the fundamental understanding of their electrocatalytic roles in alkaline media.

Ever since the first report by Xu et al. [42], showing that perovskite oxides can catalyze the HER in basic solutions, several works have focused on using perovskites as bifunctional catalysts toward both the HER and OER and the overall water splitting. A typical example was given by Zhu et al. [183], who reported the electrospinning synthesis of perovskite $SrNb_{0.1}Co_{0.7}Fe_{0.2}O_{3-\delta}$ nanorods (SNCF-NR) and their application as HER/OER catalysts in an alkaline water-splitting cell (Fig. 13a). Owing to the porous 1D nanostructure, SNCF-NR showed significantly enhanced HER and OER activity compared to the bulk-sized SNCF. When loaded on a Ni foam substrate (mass loading: 3 mg cm^{-2}) and used as the cathode and anode in a water electrolyzer containing 1 M KOH electrolyte, the SNCF-NR//SNCF-NR couple delivered a voltage of $\sim$1.68 V to reach a geometric current density of 10 mA cm^{-2} (η_{10}) (Fig. 13b), a figure of merit associated with solar-to-hydrogen production [184]. Although inferior to the state-of-the-art Pt/C cathode and IrO_2 anode couple at this voltage, the SNCF-NR//SNCF-NR couple began to overtake at elevated voltages (>1.78 V). The alkaline water electrolysis performance can be increased by coupling perovskite materials with nanocarbons. For instance, Hua et al. ultrasonically attached electrospun $La_{0.5}(Ba_{0.4}Sr_{0.4}Ca_{0.2})_{0.5}Co_{0.8}Fe_{0.2}O_{3-\delta}$ perovskite nanorods to reduced graphene oxide nanosheets and obtained a comparable η_{10} value of $\sim$1.66 V in an overall water-splitting test [185]. Further improvement in performance can be attained by introducing additional reactive sites other than perovskites. For example, Hua et al.

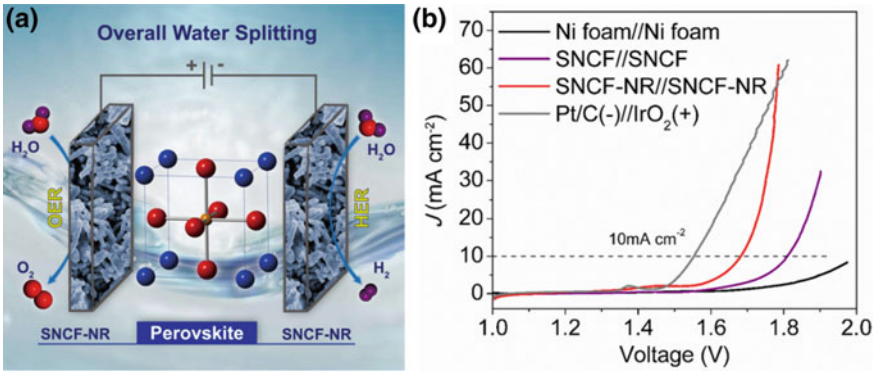

Fig. 13 **a** A schematic representation of a water electrolyzer using $SrNb_{0.1}Co_{0.7}Fe_{0.2}O_{3-\delta}$ nanorods (SNCF-NR) as both the cathode and anode. **b** Polarization curves of SNCF-NR// SNCF-NR, SNCF//SNCF, Ni foam//Ni foam, and Pt/C(−)//IrO_2(+) for overall water splitting in 1 M KOH (Reprinted with permission from Ref. [183]. Copyright 2016 John Wiley and Sons)

conducted H_2 treatment on A-site-deficient double perovskite nanowires, $(PrBa_{0.8}Ca_{0.2})_{0.95}(Co_{1.5}Fe_{0.5})_{0.95}Co_{0.05}O_{5+\delta}$, and obtained Co/$CoO_x$ nanoparticles exsolved on the surface [159]. Since metal/metal oxide components are expected to show catalytic activity [38, 186], their synergistic coupling to perovskite oxides gave rise to a significantly enhanced performance for the HER/OER electrocatalysis and the overall water electrolysis (η_{10} = 1.62 V).

Despite the attempts at developing bifunctional perovskite materials for catalyzing both the OER and HER, the currently available perovskites only show moderate catalytic activity toward the HER [42, 102, 159, 183, 185], posing an inevitable overpotential of around 0.2 V for the alkaline water electrolysis. One straightforward way to circumvent this issue is to replace the perovskite-based cathode with the state-of-the-art Pt metal. For example, Chen et al. used magnetron sputtering, which is one popular type of PVD synthesis, to deposit amorphous BSCF nanofilms onto Ni foam substrates (mass loading: 38.7 μg cm^{-2}) as highly active OER catalysts [110]. When combined with a Pt–Ni foam cathode, which was also obtained by magnetron sputtering deposition at a Pt mass loading of 38.7 μg cm^{-2}, the BSCF//Pt couple showed significantly reduced voltage for overall water splitting compared to the BSCF//BSCF couple (Fig. 14a). This is mainly attributed to the intrinsically higher HER activity of Pt relative to BSCF [42]. The cell voltage was further reduced to a η_{10} value of 1.57 V for the BSCF//Pt couple when the mass loading of BSCF on Ni foam was increased to 154.8 μg cm^{-2}. It is noteworthy that this high performance was achieved on electrodes with an ultralow catalyst mass loading, almost 20 times lower than that of SNCF-NR (3 mg cm^{-2}), which may have strong implications for practical use.

The aforementioned perovskite catalysts are evaluated in a simple, lab-based, room-temperature electrolysis cell, without taking into consideration the configuration of water electrolyzers. A more rational practice was recently reported by

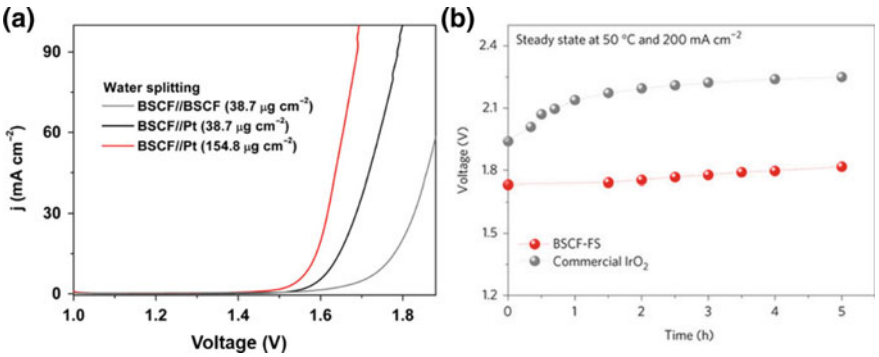

Fig. 14 **a** Polarization curves of BSCF//BSCF (both at 38.7 μg cm^{-2}), BSCF//Pt (both at 38.7 μg cm^{-2}), and BSCF//Pt (BSCF at 154.8 μg cm^{-2} and Pt at 38.7 μg cm^{-2}) for overall water splitting in 1 M KOH (Reprinted with permission from Ref. [110]. Copyright 2017 American Association for the Advancement of Science). **b** Voltage versus time at 50 °C and a steady-state current density of 200 mA cm^{-2} obtained for membrane electrode assemblies (MEAs) having BSCF-FS and IrO_2 as the anode electrocatalyst (Reprinted with permission from Ref. [100]. Copyright 2017 Springer Nature)

Fabbri et al. [100], who employed an alkaline membrane water electrolysis cell to assess the performance of BSCF-FS as an anode OER catalyst in comparison to the state-of-the-art IrO_2. Membrane electrode assemblies (MEAs) containing Pt as the cathode and BSCF-FS or commercial IrO_2 as the anode were assembled with a 3 mg cm^{-2} catalyst loading. Compared to the IrO_2-based MEA, the BSCF-FS-based MEA presented a lower and more stable cell voltage at steady-state conditions of more relevance to industrial settings, that is, a higher temperature of 50 °C and a larger current density of 200 mA cm^{-2} (Fig. 14b). Such measurement offers more solid evidence to the viability of perovskite BSCF-FS nanocatalyst as a low-cost alternative to IrO_2 for efficient water electrolysis.

While much progress has been made in the application of perovskite materials as electrocatalysts for water electrolyzers, there is still room for activity increase, especially in the case of the HER. However, bifunctionality of perovskites for both the HER and OER may appear to be a formidable challenge considering the substantially different reaction processes on perovskite oxide surfaces. Nonetheless, it should be noted that the development of perovskite HER catalysts is still in its infancy. An improved understanding of the reaction mechanism on perovskite surfaces, together with optimized catalyst design strategies, may help facilitate the location of highly active perovskite HER catalysts. At present, a water electrolyzer based on a perovskite OER catalyst coupled with a Pt HER catalyst seems to be a more practical option. Once again, the major concern remains to be the operational stability. The current understanding of catalyst stability is based on short-term electrochemical testing for no more than tens of hours, which is far from satisfactory. In addition, the testing conditions in research laboratories are found to deviate from those in industry. In this sense, application-oriented research should be more

extensively carried out for longer lifetimes at conditions more of industrial interest, for example, a temperature of 80 °C and a current density of $\sim 0.5 - 2$ A cm^{-2} [187]. Provided a combination of inputs into both fundamental and applied research, an operative water electrolyzer based on perovskite electrocatalysts can be expected.

References

1. Wang J, Cui W, Liu Q, Xing Z, Asiri AM, Sun X (2016) Recent progress in cobalt-based heterogeneous catalysts for electrochemical water splitting. Adv Mater 28(2):215–230. https://doi.org/10.1002/adma.201502696
2. Cheng FY, Chen J (2012) Metal-air batteries: from oxygen reduction electrochemistry to cathode catalysts. Chem Soc Rev 41(6):2172–2192. https://doi.org/10.1039/c1cs15228a
3. Mohammad T, Kallio T, Reynaud O, Nasibulin AG, Johans C, Sainio J, Jiang H, Kauppinen EI, Laasonen K (2015) Single-shell carbon-encapsulated iron nanoparticles: synthesis and high electrocatalytic activity for hydrogen evolution reaction. Angew Chem Int Ed 54(15):4535–4538. https://doi.org/10.1002/anie.201411450
4. Lee Y, Suntivich J, May KJ, Perry EE, Shao-Horn Y (2012) Synthesis and activities of rutile IrO_2 and RuO_2 nanoparticles for oxygen evolution in acid and alkaline solutions. J Phys Chem Lett 3(3):399–404. https://doi.org/10.1021/jz2016507
5. Tian N, Zhou Z-Y, Sun S-G (2008) Platinum metal catalysts of high-index surfaces: from single-crystal planes to electrochemically shape-controlled nanoparticles. J Phys Chem C 112(50):19801–19817. https://doi.org/10.1021/jp804051e
6. Fabbri E, Habereder A, Waltar K, Kotz R, Schmidt TJ (2014) Developments and perspectives of oxide-based catalysts for the oxygen evolution reaction. Catal Sci Technol 4 (11):3800–3821. https://doi.org/10.1039/C4CY00669K
7. Gupta S, Kellogg W, Xu H, Liu X, Cho J, Wu G (2016) Bifunctional perovskite oxide catalysts for oxygen reduction and evolution in alkaline media. Chem Asian J 11(1):10–21. https://doi.org/10.1002/asia.201500640
8. Chen DJ, Chen C, Baiyee ZM, Shao ZP, Ciucci F (2015) Nonstoichiometric oxides as low-cost and highly-efficient oxygen reduction/evolution catalysts for low-temperature electrochemical devices. Chem Rev 115(18):9869–9921. https://doi.org/10.1021/acs.chemrev.5b00073
9. Burke MS, Enman LJ, Batchellor AS, Zou S, Boettcher SW (2015) Oxygen evolution reaction electrocatalysis on transition metal oxides and (oxy)hydroxides: activity trends and design principles. Chem Mater 27(22):7549–7558. https://doi.org/10.1021/acs.chemmater.5b03148
10. Yin H, Tang Z (2016) Ultrathin two-dimensional layered metal hydroxides: an emerging platform for advanced catalysis, energy conversion and storage. Chem Soc Rev 45 (18):4873–4891. https://doi.org/10.1039/C6CS00343E
11. Benck JD, Hellstern TR, Kibsgaard J, Chakthranont P, Jaramillo TF (2014) Catalyzing the hydrogen evolution reaction (HER) with molybdenum sulfide nanomaterials. ACS Catal 4 (11):3957–3971. https://doi.org/10.1021/cs500923c
12. Hu C, Dai L (2016) Carbon-based metal-free catalysts for electrocatalysis beyond the ORR. Angew Chem Int Ed 55(39):11736–11758. https://doi.org/10.1002/anie.201509982
13. Wang W, Xu X, Zhou W, Shao Z (2017) Recent progress in metal-organic frameworks for applications in electrocatalytic and photocatalytic water splitting. Adv Sci 4(4):1600371. https://doi.org/10.1002/advs.201600371
14. Xu X, Wang W, Zhou W, Shao Z (2018) Recent advances in novel nanostructuring methods of perovskite electrocatalysts for energy-related applications. Small Methods 2(7):1800071. https://doi.org/10.1002/smtd.201800071

15. Hwang J, Rao RR, Giordano L, Katayama Y, Yu Y, Shao-Horn Y (2017) Perovskites in catalysis and electrocatalysis. Science 358(6364):751–756. https://doi.org/10.1126/science.aam7092
16. Zhu L, Ran R, Tadé M, Wang W, Shao Z (2016) Perovskite materials in energy storage and conversion. Asia Pac J Chem Eng 11(3):338–369. https://doi.org/10.1002/apj.2000
17. Rossmeisl J, Logadottir A, Nørskov JK (2005) Electrolysis of water on (oxidized) metal surfaces. Chem Phys 319(1):178–184. https://doi.org/10.1016/j.chemphys.2005.05.038
18. Mavros MG, Tsuchimochi T, Kowalczyk T, McIsaac A, Wang L-P, Voorhis TV (2014) What can density functional theory tell us about artificial catalytic water splitting? Inorg Chem 53(13):6386–6397. https://doi.org/10.1021/ic5002557
19. Goodenough JB, Manoharan R, Paranthaman M (1990) Surface protonation and electrochemical activity of oxides in aqueous solution. J Am Chem Soc 112(6):2076–2082. https://doi.org/10.1021/ja00162a006
20. Haumann M, Liebisch P, Müller C, Barra M, Grabolle M, Dau H (2005) Photosynthetic O_2 formation tracked by time-resolved X-ray experiments. Science 310(5750):1019–1021. https://doi.org/10.1126/science.1117551
21. Gerken JB, McAlpin JG, Chen JYC, Rigsby ML, Casey WH, Britt RD, Stahl SS (2011) Electrochemical water oxidation with cobalt-based electrocatalysts from pH 0–14: the thermodynamic basis for catalyst structure, stability, and activity. J Am Chem Soc 133(36):14431–14442. https://doi.org/10.1021/ja205647m
22. Kuznetsov DA, Han B, Yu Y, Rao RR, Hwang J, Román-Leshkov Y, Shao-Horn Y (2018) Tuning redox transitions via inductive effect in metal oxides and complexes, and implications in oxygen electrocatalysis. Joule 2(2):225–244. https://doi.org/10.1016/j.joule.2017.11.014
23. Suntivich J, Gasteiger HA, Yabuuchi N, Nakanishi H, Goodenough JB, Shao-Horn Y (2011) Design principles for oxygen-reduction activity on perovskite oxide catalysts for fuel cells and metal–air batteries. Nature Chem 3:546–550. https://doi.org/10.1038/nchem.1069
24. Nørskov JK, Rossmeisl J, Logadottir A, Lindqvist L, Kitchin JR, Bligaard T, Jónsson H (2004) Origin of the overpotential for oxygen reduction at a fuel-cell cathode. J Phys Chem B 108(46):17886–17892. https://doi.org/10.1021/jp047349j
25. Fernández EM, Moses PG, Toftelund A, Hansen HA, Martínez JI, Abild-Pedersen F, Kleis J, Hinnemann B, Rossmeisl J, Bligaard T, Nørskov JK (2008) Scaling relationships for adsorption energies on transition metal oxide, sulfide, and nitride surfaces. Angew Chem Int Ed 47(25):4683–4686. https://doi.org/10.1002/anie.200705739
26. Suntivich J, May KJ, Gasteiger HA, Goodenough JB, Shao-Horn Y (2011) A perovskite oxide optimized for oxygen evolution catalysis from molecular orbital principles. Science 334(6061):1383–1385. https://doi.org/10.1126/science.1212858
27. Man IC, Su H-Y, Calle-Vallejo F, Hansen HA, Martínez JI, Inoglu NG, Kitchin J, Jaramillo TF, Nørskov JK, Rossmeisl J (2011) Universality in oxygen evolution electrocatalysis on oxide surfaces. ChemCatChem 3(7):1159–1165. https://doi.org/10.1002/cctc.201000397
28. Rong X, Parolin J, Kolpak AM (2016) A fundamental relationship between reaction mechanism and stability in metal oxide catalysts for oxygen evolution. ACS Catal 6(2):1153–1158. https://doi.org/10.1021/acscatal.5b02432
29. Mefford JT, Rong X, Abakumov AM, Hardin WG, Dai S, Kolpak AM, Johnston KP, Stevenson KJ (2016) Water electrolysis on $La_{1-x}Sr_xCoO_{3-\delta}$ perovskite electrocatalysts. Nat Commun 7:11053. https://doi.org/10.1038/ncomms11053
30. Grimaud A, Diaz-Morales O, Han B, Hong WT, Lee Y-L, Giordano L, Stoerzinger KA, Koper MTM, Shao-Horn Y (2017) Activating lattice oxygen redox reactions in metal oxides to catalyse oxygen evolution. Nature Chem 9:457–465. https://doi.org/10.1038/nchem.2695
31. Yoo JS, Liu Y, Rong X, Kolpak AM (2018) Electronic origin and kinetic feasibility of the lattice oxygen participation during the oxygen evolution reaction on perovskites. J Phys Chem Lett 9(7):1473–1479. https://doi.org/10.1021/acs.jpclett.8b00154

32. Yoo JS, Rong X, Liu Y, Kolpak AM (2018) Role of lattice oxygen participation in understanding trends in the oxygen evolution reaction on perovskites. ACS Catal 8(5):4628–4636. https://doi.org/10.1021/acscatal.8b00612
33. Noh JS, Schwarz JA (1989) Estimation of the point of zero charge of simple oxides by mass titration. J Colloid Interface Sci 130(1):157–164. https://doi.org/10.1016/0021-9797(89)90086-6
34. Rossmeisl J, Qu ZW, Zhu H, Kroes GJ, Nørskov JK (2007) Electrolysis of water on oxide surfaces. J Electroanal Chem 607(1):83–89. https://doi.org/10.1016/j.jelechem.2006.11.008
35. Nørskov JK, Bligaard T, Rossmeisl J, Christensen CH (2009) Towards the computational design of solid catalysts. Nature Chem 1:37–46. https://doi.org/10.1038/nchem.121
36. García-Mota M, Vojvodic A, Metiu H, Man IC, Su H-Y, Rossmeisl J, Nørskov JK (2011) Tailoring the activity for oxygen evolution electrocatalysis on rutile TiO_2(110) by transition-metal substitution. ChemCatChem 3(10):1607–1611. https://doi.org/10.1002/cctc.201100160
37. Vilekar SA, Fishtik I, Datta R (2010) Kinetics of the hydrogen electrode reaction. J Electrochem Soc 157(7):B1040–B1050. https://doi.org/10.1149/1.3385391
38. Gong M, Zhou W, Tsai M-C, Zhou J, Guan M, Lin M-C, Zhang B, Hu Y, Wang D-Y, Yang J, Pennycook SJ, Hwang B-J, Dai H (2014) Nanoscale nickel oxide/nickel heterostructures for active hydrogen evolution electrocatalysis. Nat Commun 5:4695. https://doi.org/10.1038/ncomms5695
39. Nørskov JK, Bligaard T, Logadottir A, Kitchin JR, Chen JG, Pandelov S, Stimming U (2005) Trends in the exchange current for hydrogen evolution. J Electrochem Soc 152(3):J23–J26. https://doi.org/10.1149/1.1856988
40. Mahmood N, Yao Y, Zhang J-W, Pan L, Zhang X, Zou J-J (2018) Electrocatalysts for hydrogen evolution in alkaline electrolytes: mechanisms, challenges, and prospective solutions. Adv Sci 5(2):1700464. https://doi.org/10.1002/advs.201700464
41. Zheng Y, Jiao Y, Vasileff A, Qiao SZ (2018) The hydrogen evolution reaction in alkaline solution: from theory, single crystal models, to practical electrocatalysts. Angew Chem Int Ed 57(26):7568–7579. https://doi.org/10.1002/anie.201710556
42. Xu X, Chen Y, Zhou W, Zhu Z, Su C, Liu M, Shao Z (2016) A perovskite electrocatalyst for efficient hydrogen evolution reaction. Adv Mater 28(30):6442–6448. https://doi.org/10.1002/adma.201600005
43. Parsons R (1958) The rate of electrolytic hydrogen evolution and the heat of adsorption of hydrogen. Trans Faraday Soc 54:1053–1063. https://doi.org/10.1039/TF9585401053
44. Seh ZW, Kibsgaard J, Dickens CF, Chorkendorff I, Nørskov JK, Jaramillo TF (2017) Combining theory and experiment in electrocatalysis: insights into materials design. Science 355 (6321):eaad4998. https://doi.org/10.1126/science.aad4998
45. Hong WT, Risch M, Stoerzinger KA, Grimaud A, Suntivich J, Shao-Horn Y (2015) Toward the rational design of non-precious transition metal oxides for oxygen electrocatalysis. Energy Environ Sci 8(5):1404–1427. https://doi.org/10.1039/C4EE03869J
46. Grimaud A, May KJ, Carlton CE, Lee Y-L, Risch M, Hong WT, Zhou J, Shao-Horn Y (2013) Double perovskites as a family of highly active catalysts for oxygen evolution in alkaline solution. Nat Commun 4:2439. https://doi.org/10.1038/ncomms3439
47. Bockris JO, Otagawa T (1983) Mechanism of oxygen evolution on perovskites. J Phys Chem 87(15):2960–2971. https://doi.org/10.1021/j100238a048
48. Bockris JOM, Otagawa T (1984) The electrocatalysis of oxygen evolution on perovskites. J Electrochem Soc 131(2):290–302. https://doi.org/10.1149/1.2115565
49. Calle-Vallejo F, Inoglu NG, Su H-Y, Martinez JI, Man IC, Koper MTM, Kitchin JR, Rossmeisl J (2013) Number of outer electrons as descriptor for adsorption processes on transition metals and their oxides. Chem Sci 4(3):1245–1249. https://doi.org/10.1039/C2SC21601A
50. Zhu Y, Zhou W, Chen Z-G, Chen Y, Su C, Tadé MO, Shao Z (2015) $SrNb_{0.1}Co_{0.7}Fe_{0.2}O_{3-\delta}$ perovskite as a next-generation electrocatalyst for oxygen evolution in alkaline solution. Angew Chem Int Ed 54(13):3897–3901. https://doi.org/10.1002/anie.201408998

51. Kim J, Yin X, Tsao K-C, Fang S, Yang H (2014) $Ca_2Mn_2O_5$ as oxygen-deficient perovskite electrocatalyst for oxygen evolution reaction. J Am Chem Soc 136(42):14646–14649. https://doi.org/10.1021/ja506254g
52. Guo YQ, Tong Y, Chen PZ, Xu K, Zhao JY, Lin Y, Chu WS, Peng ZM, Wu CZ, Xie Y (2015) Engineering the electronic state of a perovskite electrocatalyst for synergistically enhanced oxygen evolution reaction. Adv Mater 27(39):5989–5994. https://doi.org/10.1002/adma.201502024
53. Yagi S, Yamada I, Tsukasaki H, Seno A, Murakami M, Fujii H, Chen H, Umezawa N, Abe H, Nishiyama N, Mori S (2015) Covalency-reinforced oxygen evolution reaction catalyst. Nat Commun 6:8249. https://doi.org/10.1038/ncomms9249
54. Wei C, Feng Z, Scherer GG, Barber J, Shao-Horn Y, Xu ZJ (2017) Cations in octahedral sites: a descriptor for oxygen electrocatalysis on transition-metal spinels. Adv Mater 29(23):1606800. https://doi.org/10.1002/adma.201606800
55. Jin YZ, Li Z, Wang JQ, Li R, Li ZQ, Liu H, Mao J, Dong CK, Yang J, Qiao SZ, Du XW (2018) Tuning spin state of rock-salt-based oxides by manipulation of crystallinity for efficient oxygen electrocatalysis. Adv Energy Mater 8(22):1703469. https://doi.org/10.1002/aenm.201703469
56. Kalubarme RS, Park GE, Jung KN, Shin KH, Ryu WH, Park CJ (2014) $LaNi_xCo_{1-x}O_{3-\delta}$ perovskites as catalyst material for non-aqueous lithium-oxygen batteries. J Electrochem Soc 161(6):A880–A889. https://doi.org/10.1149/2.012406jes
57. Du Z, Yang P, Wang L, Lu Y, Goodenough JB, Zhang J, Zhang D (2014) Electrocatalytic performances of $LaNi_{1-x}Mg_xO_3$ perovskite oxides as bi-functional catalysts for lithium air batteries. J Power Sources 265:91–96. https://doi.org/10.1016/j.jpowsour.2014.04.096
58. Zhang D, Song Y, Du Z, Wang L, Li Y, Goodenough JB (2015) Active $LaNi_{1-x}Fe_xO_3$ bifunctional catalysts for air cathodes in alkaline media. J Mater Chem A 3(18):9421–9426. https://doi.org/10.1039/c5ta01005e
59. Wang Z, You Y, Yuan J, Yin YX, Li YT, Xin S, Zhang D (2016) Nickel-doped $La_{0.8}Sr_{0.2}Mn_{1-x}Ni_xO_3$ nanoparticles containing abundant oxygen vacancies as an optimized bifunctional catalyst for oxygen cathode in rechargeable lithium-air batteries. ACS Appl Mater Interfaces 8(10):6520–6528. https://doi.org/10.1021/acsami.6b00296
60. Goodenough JB (1958) An interpretation of the magnetic properties of the perovskite-type mixed crystals $La_{1-x}Sr_xCoO_{3-\lambda}$. J Phys Chem Solids 6(2):287–297. https://doi.org/10.1016/0022-3697(58)90107-0
61. Korotin MA, Ezhov SY, Solovyev IV, Anisimov VI, Khomskii DI, Sawatzky GA (1996) Intermediate-spin state and properties of $LaCoO_3$. Phys Rev B 54(8):5309–5316. https://doi.org/10.1103/PhysRevB.54.5309
62. Maris G, Ren Y, Volotchaev V, Zobel C, Lorenz T, Palstra TTM (2003) Evidence for orbital ordering in $LaCoO_3$. Phys Rev B 67(22):224423. https://doi.org/10.1103/PhysRevB.67.224423
63. Haverkort MW, Hu Z, Cezar JC, Burnus T, Hartmann H, Reuther M, Zobel C, Lorenz T, Tanaka A, Brookes NB, Hsieh HH, Lin HJ, Chen CT, Tjeng LH (2006) Spin state transition in $LaCoO_3$ studied using soft X-ray absorption spectroscopy and magnetic circular dichroism. Phys Rev Lett 97(17):176405. https://doi.org/10.1103/PhysRevLett.97.176405
64. Křápek V, Novák P, Kuneš J, Novoselov D, Korotin DM, Anisimov VI (2012) Spin state transition and covalent bonding in $LaCoO_3$. Phys Rev B 86(19):195104. https://doi.org/10.1103/PhysRevB.86.195104
65. Hammer B, Nørskov JK (1995) Electronic factors determining the reactivity of metal surfaces. Surf Sci 343(3):211–220. https://doi.org/10.1016/0039-6028(96)80007-0
66. Egdell RG, Goodenough JB, Hamnett A, Naish CC (1983) Electrochemistry of ruthenates. Part 1.-Oxygen reduction on pyrochlore ruthenates. J Chem Soc, Faraday Trans 1 79(4):893–912. https://doi.org/10.1039/f19837900893
67. Matsumoto Y, Sato E (1986) Electrocatalytic properties of transition metal oxides for oxygen evolution reaction. Mater Chem Phys 14(5):397–426. https://doi.org/10.1016/0254-0584(86)90045-3

68. Zhou SM, Miao XB, Zhao X, Ma C, Qiu YH, Hu ZP, Zhao JY, Shi L, Zeng J (2016) Engineering electrocatalytic activity in nanosized perovskite cobaltite through surface spin-state transition. Nat Commun 7:11510. https://doi.org/10.1038/ncomms11510
69. Petrie JR, Cooper VR, Freeland JW, Meyer TL, Zhang Z, Lutterman DA, Lee HN (2016) Enhanced bifunctional oxygen catalysis in strained $LaNiO_3$ perovskites. J Am Chem Soc 138(8):2488–2491. https://doi.org/10.1021/jacs.5b11713
70. Petrie JR, Jeen H, Barron SC, Meyer TL, Lee HN (2016) Enhancing perovskite electrocatalysis through strain tuning of the oxygen deficiency. J Am Chem Soc 138 (23):7252–7255. https://doi.org/10.1021/jacs.6b03520
71. Stoerzinger KA, Choi WS, Jeen H, Lee HN, Shao-Horn Y (2015) Role of strain and conductivity in oxygen electrocatalysis on $LaCoO_3$ thin films. J Phys Chem Lett 6(3):487–492. https://doi.org/10.1021/jz502692a
72. Lee D-G, Gwon O, Park H-S, Kim SH, Yang J, Kwak SK, Kim G, Song H-K (2015) Conductivity-dependent completion of oxygen reduction on oxide catalysts. Angew Chem Int Ed 54(52):15730–15733. https://doi.org/10.1002/anie.201508129
73. Cheng X, Fabbri E, Nachtegaal M, Castelli IE, El Kazzi M, Haumont R, Marzari N, Schmidt TJ (2015) Oxygen evolution reaction on $La_{1-x}Sr_xCoO_3$ perovskites: a combined experimental and theoretical study of their structural, electronic, and electrochemical properties. Chem Mater 27(22):7662–7672. https://doi.org/10.1021/acs.chemmater.5b03138
74. Pramana SS, Cavallaro A, Li C, Handoko AD, Chan KW, Walker RJ, Regoutz A, Herrin JS, Yeo BS, Payne DJ, Kilner JA, Ryan MP, Skinner SJ (2018) Crystal structure and surface characteristics of Sr-doped $GdBaCo_2O_{6-\delta}$ double perovskites: oxygen evolution reaction and conductivity. J Mater Chem A 6(13):5335–5345. https://doi.org/10.1039/C7TA06817D
75. Hyodo T, Hayashi M, Miura N, Yamazoe N (1996) Catalytic activities of rare-earth manganites for cathodic reduction of oxygen in alkaline solution. J Electrochem Soc 143 (11):L266–L267. https://doi.org/10.1149/1.1837229
76. Hyodo T, Hayashi M, Mitsutake S, Miura N, Yamazoe N (1997) Praseodymium–calcium manganites ($Pr_{1-x}Ca_xMnO_3$) as electrode catalyst for oxygen reduction in alkaline solution. J Appl Electrochem 27(6):745–745. https://doi.org/10.1023/a:1018404308209
77. Hu J, Wang L, Shi L, Huang H (2014) Preparation of $La_{1-x}Ca_xMnO_3$ perovskite–graphene composites as oxygen reduction reaction electrocatalyst in alkaline medium. J Power Sources 269:144–151. https://doi.org/10.1016/j.jpowsour.2014.07.004
78. Tulloch J, Donne SW (2009) Activity of perovskite $La_{1-x}Sr_xMnO_3$ catalysts towards oxygen reduction in alkaline electrolytes. J Power Sources 188(2):359–366. https://doi.org/10.1016/j.jpowsour.2008.12.024
79. Stoerzinger KA, Lü W, Li C, Ariando Venkatesan T, Shao-Horn Y (2015) Highly active epitaxial $La_{(1-x)}Sr_xMnO_3$ surfaces for the oxygen reduction reaction: role of charge transfer. J Phys Chem Lett 6(8):1435–1440. https://doi.org/10.1021/acs.jpclett.5b00439
80. Hammouche A, Kahoul A, Sauer DU, De Doncker RW (2006) Influential factors on oxygen reduction at $La_{1-x}Ca_xCoO_3$ electrodes in alkaline electrolyte. J Power Sources 153(2):239–244. https://doi.org/10.1016/j.jpowsour.2005.05.028
81. Lal B, Raghunandan MK, Gupta M, Singh RN (2005) Electrocatalytic properties of perovskite-type $La_{1-x}Sr_xCoO_3$ ($0 \leq x \leq 0.4$) obtained by a novel stearic acid sol–gel method for electrocatalysis of O_2 evolution in KOH solutions. Int J Hydrog Energy 30 (7):723–729. https://doi.org/10.1016/j.ijhydene.2004.07.002
82. She S, Yu J, Tang W, Zhu Y, Chen Y, Sunarso J, Zhou W, Shao Z (2018) Systematic study of oxygen evolution activity and stability on $La_{1-x}Sr_xFeO_{3-\delta}$ perovskite electrocatalysts in alkaline media. ACS Appl Mater Interfaces 10(14):11715–11721. https://doi.org/10.1021/acsami.8b00682
83. Sunarso J, Torriero AAJ, Zhou W, Howlett PC, Forsyth M (2012) Oxygen reduction reaction activity of La-based perovskite oxides in alkaline medium: A thin-film rotating ring-disk electrode study. J Phys Chem C 116(9):5827–5834. https://doi.org/10.1021/jp211946n

84. Zhou W, Zhao M, Liang F, Smith SC, Zhu Z (2015) High activity and durability of novel perovskite electrocatalysts for water oxidation. Mater Horiz 2(5):495–501. https://doi.org/10.1039/C5MH00096C
85. Sun H, Chen G, Zhu Y, Liu B, Zhou W, Shao Z (2017) B-site cation ordered double perovskites as efficient and stable electrocatalysts for oxygen evolution reaction. Chem Eur J 23(24):5722–5728. https://doi.org/10.1002/chem.201700507
86. Su C, Wang W, Chen Y, Yang G, Xu X, Tadé MO, Shao Z (2015) $SrCo_{0.9}Ti_{0.1}O_{3-\delta}$ as a new electrocatalyst for the oxygen evolution reaction in alkaline electrolyte with stable performance. ACS Appl Mater Interfaces 7(32):17663–17670. https://doi.org/10.1021/acsami.5b02810
87. Sun H, Chen G, Sunarso J, Dai J, Zhou W, Shao Z (2018) Molybdenum and niobium codoped B-site-ordered double perovskite catalyst for efficient oxygen evolution reaction. ACS Appl Mater Interfaces 10(20):16939–16942. https://doi.org/10.1021/acsami.8b03702
88. Chen G, Hu Z, Zhu Y, Chen Z-G, Zhong Y, Lin H-J, Chen C-T, Tjeng LH, Zhou W, Shao Z (2018) Ultrahigh-performance tungsten-doped perovskites for the oxygen evolution reaction. J Mater Chem A 6(21):9854–9859. https://doi.org/10.1039/C8TA02864H
89. Xu X, Su C, Zhou W, Zhu Y, Chen Y, Shao Z (2016) Co-doping strategy for developing perovskite oxides as highly efficient electrocatalysts for oxygen evolution reaction. Adv Sci 3(2):1500187. https://doi.org/10.1002/advs.201500187
90. Xu X, Chen Y, Zhou W, Zhong Y, Guan D, Shao Z (2018) Earth-abundant silicon for facilitating water oxidation over iron-based perovskite electrocatalyst. Adv Mater Interfaces 5(11):1701693. https://doi.org/10.1002/admi.201701693
91. Zhu Y, Zhou W, Sunarso J, Zhong Y, Shao Z (2016) Phosphorus-doped perovskite oxide as highly efficient water oxidation electrocatalyst in alkaline solution. Adv Funct Mater 26(32):5862–5872. https://doi.org/10.1002/adfm.201601902
92. Shen Y, Zhu Y, Sunarso J, Guan D, Liu B, Liu H, Zhou W, Shao Z (2018) New phosphorus-doped perovskite oxide as an oxygen reduction reaction electrocatalyst in an alkaline solution. Chem Eur J 24(27):6950–6957. https://doi.org/10.1002/chem.201705675
93. Li Z, Lv L, Wang J, Ao X, Ruan Y, Zha D, Hong G, Wu Q, Lan Y, Wang C, Jiang J, Liu M (2018) Engineering phosphorus-doped $LaFeO_{3-\delta}$ perovskite oxide as robust bifunctional oxygen electrocatalysts in alkaline solutions. Nano Energy 47:199–209. https://doi.org/10.1016/j.nanoen.2018.02.051
94. Yuasa M, Tachibana N, Shimanoe K (2013) Oxygen reduction activity of carbon-supported $La_{1-x}Ca_xMn_{1-y}Fe_yO_3$ nanoparticles. Chem Mater 25(15):3072–3079. https://doi.org/10.1021/cm401276y
95. Malkhandi S, Trinh P, Manohar AK, Manivannan A, Balasubramanian M, Prakash GKS, Narayanan SR (2015) Design insights for tuning the electrocatalytic activity of perovskite oxides for the oxygen evolution reaction. J Phys Chem C 119(15):8004–8013. https://doi.org/10.1021/jp512722x
96. Zhen DX, Zhao BT, Shin HC, Bu YF, Ding Y, He GH, Liu ML (2017) Electrospun porous perovskite $La_{0.6}Sr_{0.4}Co_{1-x}Fe_xO_{3-\delta}$ nanofibers for efficient oxygen evolution reaction. Adv Mater Interfaces 4(13):1700146. https://doi.org/10.1002/admi.201700146
97. Zhu Y, Zhou W, Yu J, Chen Y, Liu M, Shao Z (2016) Enhancing electrocatalytic activity of perovskite oxides by tuning cation deficiency for oxygen reduction and evolution reactions. Chem Mater 28(6):1691–1697. https://doi.org/10.1021/acs.chemmater.5b04457
98. Liu H, Ding X, Wang L, Ding D, Zhang S, Yuan G (2018) Cation deficiency design: a simple and efficient strategy for promoting oxygen evolution reaction activity of perovskite electrocatalyst. Electrochim Acta 259:1004–1010. https://doi.org/10.1016/j.electacta.2017.10.172
99. Xue Y, Miao H, Sun S, Wang Q, Li S, Liu Z (2017) $(La_{1-x}Sr_x)_{0.98}MnO_3$ perovskite with A-site deficiencies toward oxygen reduction reaction in aluminum-air batteries. J Power Sources 342:192–201. https://doi.org/10.1016/j.jpowsour.2016.12.065

100. Fabbri E, Nachtegaal M, Binninger T, Cheng X, Kim BJ, Durst J, Bozza F, Graule T, Schaublin R, Wiles L, Pertoso M, Danilovic N, Ayers KE, Schmidt TJ (2017) Dynamic surface self-reconstruction is the key of highly active perovskite nano-electrocatalysts for water splitting. Nat Mater 16(9):925–931. https://doi.org/10.1038/nmat4938
101. Chen CF, King G, Dickerson RM, Papin PA, Gupta S, Kellogg WR, Wu G (2015) Oxygen-deficient $BaTiO_{3-x}$ perovskite as an efficient bifunctional oxygen electrocatalyst. Nano Energy 13:423–432. https://doi.org/10.1016/j.nanoen.2015.03.005
102. Wang J, Gao Y, Chen D, Liu J, Zhang Z, Shao Z, Ciucci F (2018) Water splitting with an enhanced bifunctional double perovskite. ACS Catal 8(1):364–371. https://doi.org/10.1021/acscatal.7b02650
103. Du J, Zhang TR, Cheng FY, Chu WS, Wu ZY, Chen J (2014) Nonstoichiometric perovskite $CaMnO_{3-\delta}$ for oxygen electrocatalysis with high activity. Inorg Chem 53(17):9106–9114. https://doi.org/10.1021/ic501631h
104. Wang G, Xu T, Wen S, Pan M (2015) Structure-dependent electrocatalytic activity of $La_{1-x}Sr_xMnO_3$ for oxygen reduction reaction. Sci China Chem 58(5):871–878. https://doi.org/10.1007/s11426-015-5326-9
105. Zhou W, Sunarso J (2013) Enhancing bi-functional electrocatalytic activity of perovskite by temperature shock: a case study of $LaNiO_{3-\delta}$. J Phys Chem Lett 4(17):2982–2988. https://doi.org/10.1021/jz401169n
106. Zhu Y, Zhou W, Chen Y, Yu J, Xu X, Su C, Tadé MO, Shao Z (2015) Boosting oxygen reduction reaction activity of palladium by stabilizing its unusual oxidation states in perovskite. Chem Mater 27(8):3048–3054. https://doi.org/10.1021/acs.chemmater.5b00450
107. Zhang C, Trudel S (2014) Berlinguette CP (2014) Water oxidation catalysis: Survey of amorphous binary metal oxide films containing lanthanum and late 3d transition metals. Eur J Inorg Chem 4:660–664. https://doi.org/10.1002/ejic.201300765
108. Zhang C, Zhang X, Daly K, Berlinguette CP, Trudel S (2017) Water oxidation catalysis: tuning the electrocatalytic properties of amorphous lanthanum cobaltite through calcium doping. ACS Catal 7(9):6385–6391. https://doi.org/10.1021/acscatal.7b02145
109. Zhang C, Berlinguette CP, Trudel S (2016) Water oxidation catalysis: an amorphous quaternary Ba-Sr-Co-Fe oxide as a promising electrocatalyst for the oxygen-evolution reaction. Chem Commun 52(7):1513–1516. https://doi.org/10.1039/C5CC09361A
110. Chen G, Zhou W, Guan DQ, Sunarso J, Zhu YP, Hu XF, Zhang W, Shao ZP (2017) Two orders of magnitude enhancement in oxygen evolution reactivity on amorphous $Ba_{0.5}Sr_{0.5}Co_{0.8}Fe_{0.2}O_{3-\delta}$ nanofilms with tunable oxidation state. Sci Adv 3(6):e1603206. https://doi.org/10.1126/sciadv.1603206
111. Yoon C, Cocke DL (1986) Potential of amorphous materials as catalysts. J Non Cryst Solids 79(3):217–245. https://doi.org/10.1016/0022-3093(86)90224-3
112. Jung JI, Park S, Kim MG, Cho J (2015) Tunable internal and surface structures of the bifunctional oxygen perovskite catalysts. Adv Energy Mater 5(24):1501560. https://doi.org/10.1002/aenm.201501560
113. Jung JI, Jeong HY, Kim MG, Nam G, Park J, Cho J (2015) Fabrication of $Ba_{0.5}Sr_{0.5}Co_{0.8}Fe_{0.2}O_{3-\delta}$ catalysts with enhanced electrochemical performance by removing an inherent heterogeneous surface film layer. Adv Mater 27(2):266–271. https://doi.org/10.1002/adma.201403897
114. Lee JG, Hwang J, Hwang HJ, Jeon OS, Jang J, Kwon O, Lee Y, Han B, Shul Y-G (2016) A new family of perovskite catalysts for oxygen-evolution reaction in alkaline media: $BaNiO_3$ and $BaNi_{0.83}O_{2.5}$. J Am Chem Soc 138(10):3541–3547. https://doi.org/10.1021/jacs.6b00036
115. Jung JI, Jeong HY, Lee JS, Kim MG, Cho J (2014) A bifunctional perovskite catalyst for oxygen reduction and evolution. Angew Chem Int Ed 53(18):4582–4586. https://doi.org/10.1002/anie.201311223

116. Xu X, Pan Y, Zhou W, Chen Y, Zhang Z, Shao Z (2016) Toward enhanced oxygen evolution on perovskite oxides synthesized from different approaches: a case study of $Ba_{0.5}Sr_{0.5}Co_{0.8}Fe_{0.2}O_{3-\delta}$. Electrochim Acta 219:553–559. https://doi.org/10.1016/j.electacta.2016.10.031
117. Yamada I, Fujii H, Takamatsu A, Ikeno H, Wada K, Tsukasaki H, Kawaguchi S, Mori S, Yagi S (2017) Bifunctional oxygen reaction catalysis of quadruple manganese perovskites. Adv Mater 29(4):1603004. https://doi.org/10.1002/adma.201603004
118. Jung JI, Risch M, Park S, Kim MG, Nam G, Jeong HY, Shao-Horn Y, Cho J (2016) Optimizing nanoparticle perovskite for bifunctional oxygen electrocatalysis. Energy Environ Sci 9(1):176–183. https://doi.org/10.1039/c5ee03124a
119. Zhao Y, Xu L, Mai L, Han C, An Q, Xu X, Liu X, Zhang Q (2012) Hierarchical mesoporous perovskite $La_{0.5}Sr_{0.5}CoO_{2.91}$ nanowires with ultrahigh capacity for Li-air batteries. Proc Natl Acad Sci USA 109(48):19569–19574. https://doi.org/10.1073/pnas.1210315109
120. Bu Y, Gwon O, Nam G, Jang H, Kim S, Zhong Q, Cho J, Kim G (2017) A highly efficient and robust cation ordered perovskite oxide as a bifunctional catalyst for rechargeable Zinc-air batteries. ACS Nano 11(11):11594–11601. https://doi.org/10.1021/acsnano.7b06595
121. Lu F, Wang Y, Jin C, Li F, Yang R, Chen F (2015) Microporous $La_{0.8}Sr_{0.2}MnO_3$ perovskite nanorods as efficient electrocatalysts for lithium air battery. J Power Sources 293:726–733. https://doi.org/10.1016/j.jpowsour.2015.06.022
122. Vignesh A, Prabu M, Shanmugam S (2016) Porous $LaCo_{1-x}Ni_xO_{3-\delta}$ nanostructures as an efficient electrocatalyst for water oxidation and for a Zinc-air battery. ACS Appl Mater Interfaces 8(9):6019–6031. https://doi.org/10.1021/acsami.5b11840
123. Kim J, Chen X, Shih P-C, Yang H (2017) Porous perovskite-type lanthanum cobaltite as electrocatalysts toward oxygen evolution reaction. ACS Sustain Chem Eng 5(11):10910–10917. https://doi.org/10.1021/acssuschemeng.7b02815
124. Zhang J, Zhao YB, Zhao X, Liu ZL, Chen W (2014) Porous perovskite $LaNiO_3$ nanocubes as cathode catalysts for Li-O_2 batteries with low charge potential. Sci Rep 4:6005. https://doi.org/10.1038/srep06005
125. Zhao B, Zhang L, Zhen D, Yoo S, Ding Y, Chen D, Chen Y, Zhang Q, Doyle B, Xiong X, Liu M (2017) A tailored double perovskite nanofiber catalyst enables ultrafast oxygen evolution. Nat Commun 8:14586. https://doi.org/10.1038/ncomms14586
126. Zhu Y, Zhou W, Shao Z (2017) Perovskite/carbon composites: applications in oxygen electrocatalysis. Small 13(12):1603793. https://doi.org/10.1002/smll.201603793
127. Suntivich J, Gasteiger HA, Yabuuchi N, Shao-Horn Y (2010) Electrocatalytic measurement methodology of oxide catalysts using a thin-film rotating disk electrode. J Electrochem Soc 157(8):B1263–B1268. https://doi.org/10.1149/1.3456630
128. Poux T, Napolskiy FS, Dintzer T, Kéranguéven G, Istomin SY, Tsirlina GA, Antipov EV, Savinova ER (2012) Dual role of carbon in the catalytic layers of perovskite/carbon composites for the electrocatalytic oxygen reduction reaction. Catal Today 189(1):83–92. https://doi.org/10.1016/j.cattod.2012.04.046
129. Poux T, Bonnefont A, Kéranguéven G, Tsirlina GA, Savinova ER (2014) Electrocatalytic oxygen reduction reaction on perovskite oxides: series versus direct pathway. ChemPhysChem 15(10):2108–2120. https://doi.org/10.1002/cphc.201402022
130. Malkhandi S, Trinh P, Manohar AK, Jayachandrababu KC, Kindler A, Prakash GKS, Narayanan SR (2013) Electrocatalytic activity of transition metal oxide-carbon composites for oxygen reduction in alkaline batteries and fuel cells. J Electrochem Soc 160(9):F943–F952. https://doi.org/10.1149/2.109308jes
131. Li X, Qu W, Zhang J, Wang H (2011) Electrocatalytic activities of $La_{0.6}Ca_{0.4}CoO_3$ and $La_{0.6}Ca_{0.4}CoO_3$-carbon composites toward the oxygen reduction reaction in concentrated alkaline electrolytes. J Electrochem Soc 158(5):A597–A604. https://doi.org/10.1149/1.3560170

132. Nishio K, Molla S, Okugaki T, Nakanishi S, Nitta I, Kotani Y (2015) Oxygen reduction and evolution reactions of air electrodes using a perovskite oxide as an electrocatalyst. J Power Sources 278:645–651. https://doi.org/10.1016/j.jpowsour.2014.12.100
133. Nishio K, Molla S, Okugaki T, Nakanishi S, Nitta I, Kotani Y (2015) Effects of carbon on oxygen reduction and evolution reactions of gas-diffusion air electrodes based on perovskite-type oxides. J Power Sources 298:236–240. https://doi.org/10.1016/j.jpowsour.2015.08.070
134. Fabbri E, Nachtegaal M, Cheng X, Schmidt TJ. (2015) Superior bifunctional electrocatalytic activity of $Ba_{0.5}Sr_{0.5}Co_{0.8}Fe_{0.2}O_{3-\delta}$/carbon composite electrodes: insight into the local electronic structure. Adv Energy Mater 5(17):1402033. https://doi.org/10.1002/aenm.201402033
135. Jin C, Cao X, Zhang L, Zhang C, Yang R (2013) Preparation and electrochemical properties of urchin-like $La_{0.8}Sr_{0.2}MnO_3$ perovskite oxide as a bifunctional catalyst for oxygen reduction and oxygen evolution reaction. J Power Sources 241:225–230. https://doi.org/10.1016/j.jpowsour.2013.04.116
136. Park HW, Lee DU, Zamani P, Seo MH, Zazar LF, Chen ZW (2014) Electrospun porous nanorod perovskite oxide/nitrogen-doped graphene composite as a bi-functional catalyst for metal air batteries. Nano Energy 10:192–200. https://doi.org/10.1016/j.nanoen.2014.09.009
137. Oh MY, Jeon JS, Lee JJ, Kim P, Nahm KS (2015) The bifunctional electrocatalytic activity of perovskite $La_{0.6}Sr_{0.4}CoO_{3-\delta}$ for oxygen reduction and evolution reactions. RSC Adv 5(25):19190–19198. https://doi.org/10.1039/c4ra16097e
138. Liu G, Chen H, Xia L, Wang S, Ding LX, Li D, Xiao K, Dai S, Wang H (2015) Hierarchical mesoporous/macroporous perovskite $La_{0.5}Sr_{0.5}CoO_{3-x}$ nanotubes: A bifunctional catalyst with enhanced activity and cycle stability for rechargeable lithium oxygen batteries. ACS Appl Mater Interfaces 7(40):22478–22486. https://doi.org/10.1021/acsami.5b06587
139. Chen Z, Yu A, Higgins D, Li H, Wang H, Chen Z (2012) Highly active and durable core–corona structured bifunctional catalyst for rechargeable metal–air battery application. Nano Lett 12(4):1946–1952. https://doi.org/10.1021/nl2044327
140. Lee DU, Park HW, Park MG, Ismayilov V, Chen ZW (2015) Synergistic bifunctional catalyst design based on perovskite oxide nanoparticles and intertwined carbon nanotubes for rechargeable Zinc-air battery applications. ACS Appl Mater Interfaces 7(1):902–910. https://doi.org/10.1021/am507470f
141. Lee DU, Park MG, Park HW, Seo MH, Ismayilov V, Ahmed R, Chen ZW (2015) Highly active Co-doped $LaMnO_3$ perovskite oxide and N-doped carbon nanotube hybrid bi-functional catalyst for rechargeable Zinc-air batteries. Electrochem Commun 60:38–41. https://doi.org/10.1016/j.elecom.2015.08.001
142. Park HW, Lee DU, Park MG, Ahmed R, Seo MH, Nazar LF, Chen ZW (2015) Perovskite-nitrogen-doped carbon nanotube composite as bifunctional catalysts for rechargeable lithium-air batteries. Chemsuschem 8(6):1058–1065. https://doi.org/10.1002/cssc.201402986
143. Elumeeva K, Masa J, Sierau J, Tietz F, Muhler M, Schuhmann W (2016) Perovskite-based bifunctional electrocatalysts for oxygen evolution and oxygen reduction in alkaline electrolytes. Electrochim Acta 208:25–32. https://doi.org/10.1016/j.electacta.2016.05.010
144. Hu J, Liu Q, Shi Z, Zhang L, Huang H (2016) $LaNiO_3$-nanorod/graphene composite as an efficient bi-functional catalyst for Zinc-air batteries. RSC Adv 6(89):86386–86394. https://doi.org/10.1039/c6ra16610e
145. Ge X, Goh FWT, Li B, Hor TSA, Zhang J, Xiao P, Wang X, Zong Y, Liu Z (2015) Efficient and durable oxygen reduction and evolution of a hydrothermally synthesized La$(Co_{0.55}Mn_{0.45})_{0.99}O_{3-\delta}$ nanorod/graphene hybrid in alkaline media. Nanoscale 7(19):9046–9054. https://doi.org/10.1039/c5nr01272d
146. Prabu M, Ramakrishnan P, Ganesan P, Manthiram A, Shanmugam S (2015) $LaTi_{0.65}Fe_{0.35}O_{3-\delta}$ nanoparticle-decorated nitrogen-doped carbon nanorods as an advanced hierarchical air electrode for rechargeable metal-air batteries. Nano Energy 15:92–103. https://doi.org/10.1016/j.nanoen.2015.04.005

147. Katsounaros I, Cherevko S, Zeradjanin AR, Mayrhofer KJJ (2014) Oxygen electrochemistry as a cornerstone for sustainable energy conversion. Angew Chem Int Ed 53(1):102–121. https://doi.org/10.1002/anie.201306588
148. Hardin WG, Slanac DA, Wang X, Dai S, Johnston KP, Stevenson KJ (2013) Highly active, nonprecious metal perovskite electrocatalysts for bifunctional metal-air battery electrodes. J Phys Chem Lett 4(8):1254–1259. https://doi.org/10.1021/jz400595z
149. Hardin WG, Mefford JT, Slanac DA, Patel BB, Wang X, Dai S, Zhao X, Ruoff RS, Johnston KP, Stevenson KJ (2014) Tuning the electrocatalytic activity of perovskites through active site variation and support interactions. Chem Mater 26(11):3368–3376. https://doi.org/10.1021/cm403785q
150. Pham TV, Guo HP, Luo WB, Chou SL, Wang JZ, Liu HK (2017) Carbon- and binder-free 3D porous perovskite oxide air electrode for rechargeable lithium-oxygen batteries. J Mater Chem A 5(11):5283–5289. https://doi.org/10.1039/c6ta10751f
151. Li B-Q, Tang C, Wang H-F, Zhu X-L, Zhang Q (2016) An aqueous preoxidation method for monolithic perovskite electrocatalysts with enhanced water oxidation performance. Sci Adv 2(10):e1600495. https://doi.org/10.1126/sciadv.1600495
152. Neagu D, Tsekouras G, Miller DN, Ménard H, Irvine JTS (2013) In situ growth of nanoparticles through control of non-stoichiometry. Nat. Chem 5:916–923. https://doi.org/10.1038/nchem.1773
153. Zhu Y, Dai J, Zhou W, Zhong Y, Wang H, Shao Z (2018) Synergistically enhanced hydrogen evolution electrocatalysis by in situ exsolution of metallic nanoparticles on perovskites. J Mater Chem A 6:13582–13587. https://doi.org/10.1039/C8TA02347F
154. Zhang Y-Q, Tao H-B, Liu J, Sun Y-F, Chen J, Hua B, Thundat T, Luo J-L (2017) A rational design for enhanced oxygen reduction: Strongly coupled silver nanoparticles and engineered perovskite nanofibers. Nano Energy 38:392–400. https://doi.org/10.1016/j.nanoen.2017.06.006
155. Sun Y-F, Li J-H, Cui L, Hua B, Cui S-H, Li J, Luo J-L (2015) A-site-deficiency facilitated in situ growth of bimetallic Ni-Fe nano-alloys: a novel coking-tolerant fuel cell anode catalyst. Nanoscale 7(25):11173–11181. https://doi.org/10.1039/C5NR02518D
156. Du Z, Zhao H, Yi S, Xia Q, Gong Y, Zhang Y, Cheng X, Li Y, Gu L, Świerczek K (2016) High-performance anode material $Sr_2FeMo_{0.65}Ni_{0.35}O_{6-\delta}$ with in situ exsolved nanoparticle catalyst. ACS Nano 10(9):8660–8669. https://doi.org/10.1021/acsnano.6b03979
157. Gao Y, Wang J, Lyu YQ, Lam KY, Ciucci F (2017) In situ growth of Pt_3Ni nanoparticles on an A-site deficient perovskite with enhanced activity for the oxygen reduction reaction. J Mater Chem A 5(14):6399–6404. https://doi.org/10.1039/C7TA00349H
158. Wu N, Wang W, Zhong Y, Yang G, Qu J, Shao Z (2017) Nickel-iron alloy nanoparticle-decorated K_2NiF_4-type oxide as an efficient and sulfur-tolerant anode for solid oxide fuel cells. ChemElectroChem 4(9):2378–2384. https://doi.org/10.1002/celc.201700211
159. Hua B, Li M, Sun Y-F, Zhang Y-Q, Yan N, Chen J, Thundat T, Li J, Luo J-L (2017) A coupling for success: Controlled growth of Co/CoO_x nanoshoots on perovskite mesoporous nanofibres as high-performance trifunctional electrocatalysts in alkaline condition. Nano Energy 32:247–254. https://doi.org/10.1016/j.nanoen.2016.12.044
160. Song Y, Wang W, Ge L, Xu X, Zhang Z, Julião PSB, Zhou W, Shao Z (2017) Rational design of a water-storable hierarchical architecture decorated with amorphous barium oxide and nickel nanoparticles as a solid oxide fuel cell anode with excellent sulfur tolerance. Adv Sci 4(11):1700337. https://doi.org/10.1002/advs.201700337
161. Liang F, Sunarso J, Mao J, Yang Z, Zhou W (2017) Amorphous $Ni_{0.75}Fe_{0.25}(OH)_2$-decorated layered double perovskite $Pr_{0.5}Ba_{0.5}CoO_{3-\delta}$ for highly efficient and stable water oxidation. ChemElectroChem 4(3):550–556. https://doi.org/10.1002/celc.201600718
162. Gong Y, Zhang X, Li Z, Wang Z, Sun C, Chen L (2017) Perovskite $La_{0.6}Sr_{0.4}Co_{0.2}Fe_{0.8}O_3$ nanofibers decorated with RuO_2 nanoparticles as an efficient bifunctional cathode for rechargeable Li-O_2 batteries. ChemNanoMat 3(7):485–490. https://doi.org/10.1002/cnma.201700071

163. Zhang X, Gong Y, Li S, Sun C (2017) Porous perovskite $La_{0.6}Sr_{0.4}Co_{0.8}Mn_{0.2}O_3$ nanofibers loaded with RuO_2 nanosheets as an efficient and durable bifunctional catalyst for rechargeable Li-O_2 batteries. ACS Catal 7 (11):7737–7747. https://doi.org/10.1021/acscatal.7b02153
164. Kim S, Kwon O, Kim C, Gwon O, Jeong HY, Kim KH, Shin J, Kim G (2018) Strategy for enhancing interfacial effect of bifunctional electrocatalyst: Infiltration of cobalt nanooxide on perovskite. Adv Mater Interfaces 5(12):1800123. https://doi.org/10.1002/admi.201800123
165. Liu R, Liang F, Zhou W, Yang Y, Zhu Z (2015) Calcium-doped lanthanum nickelate layered perovskite and nickel oxide nano-hybrid for highly efficient water oxidation. Nano Energy 12:115–122. https://doi.org/10.1016/j.nanoen.2014.12.025
166. Zhu Y, Su C, Xu X, Zhou W, Ran R, Shao Z (2014) A universal and facile way for the development of superior bifunctional electrocatalysts for oxygen reduction and evolution reactions utilizing the synergistic effect. Chem Eur J 20(47):15533–15542. https://doi.org/10.1002/chem.201403192
167. May KJ, Carlton CE, Stoerzinger KA, Risch M, Suntivich J, Lee Y-L, Grimaud A, Shao-Horn Y (2012) Influence of oxygen evolution during water oxidation on the surface of perovskite oxide catalysts. J Phys Chem Lett 3(22):3264–3270. https://doi.org/10.1021/jz301414z
168. Risch M, Grimaud A, May KJ, Stoerzinger KA, Chen TJ, Mansour AN, Shao-Horn Y (2013) Structural changes of cobalt-based perovskites upon water oxidation investigated by EXAFS. J Phys Chem C 117(17):8628–8635. https://doi.org/10.1021/jp3126768
169. Han B, Stoerzinger Kelsey A, Tileli V, Gamalski Andrew D, Stach Eric A, Shao-Horn Y (2017) Nanoscale structural oscillations in perovskite oxides induced by oxygen evolution. Nature Mater 16:121–126. https://doi.org/10.1038/nmat4764
170. Seitz LC, Dickens CF, Nishio K, Hikita Y, Montoya J, Doyle A, Kirk C, Vojvodic A, Hwang HY, Norskov JK, Jaramillo TF (2016) A highly active and stable $IrO_x/SrIrO_3$ catalyst for the oxygen evolution reaction. Science 353(6303):1011–1014. https://doi.org/10.1126/science.aaf5050
171. Yu J, Sunarso J, Zhu Y, Xu X, Ran R, Zhou W, Shao Z (2016) Activity and stability of Ruddlesden–Popper-type $La_{n+1}Ni_nO_{3n+1}$ (n = 1, 2, 3, and ∞) electrocatalysts for oxygen reduction and evolution reactions in alkaline media. Chem Eur J 22(8):2719–2727. https://doi.org/10.1002/chem.201504279
172. Bick DS, Kindsmüller A, Staikov G, Gunkel F, Müller D, Schneller T, Waser R, Valov I (2016) Stability and degradation of perovskite electrocatalysts for oxygen evolution reaction. Electrochim Acta 218:156–162. https://doi.org/10.1016/j.electacta.2016.09.116
173. Bick DS, Kindsmueller A, Cho D-Y, Mohamed AY, Bredow T, Laufen H, Gunkel F, Mueller DN, Schneller T, Waser R (2017) Self-assembling oxide catalyst for electrochemical water splitting. arXiv:1707.03346
174. Bick DS, Krebs TB, Kleimaier D, Zurhelle AF, Staikov G, Waser R, Valov I (2018) Degradation kinetics during oxygen electrocatalysis on perovskite-based surfaces in alkaline media. Langmuir 34(4):1347–1352. https://doi.org/10.1021/acs.langmuir.7b03733
175. Tan P, Liu M, Shao Z, Ni M (2017) Recent advances in perovskite oxides as electrode materials for nonaqueous lithium-oxygen batteries. Adv Energy Mater 7(13):1602674. https://doi.org/10.1002/aenm.201602674
176. Bruce PG, Freunberger SA, Hardwick LJ, Tarascon J-M (2012) Li–O_2 and Li–S batteries with high energy storage. Nat Mater 11:19–29. https://doi.org/10.1038/nmat3191
177. Xu J-J, Wang Z-L, Xu D, Meng F-Z, Zhang X-B (2014) 3D ordered macroporous $LaFeO_3$ as efficient electrocatalyst for Li-O_2 batteries with enhanced rate capability and cyclic performance. Energy Environ Sci 7(7):2213–2219. https://doi.org/10.1039/C3EE42934B
178. Xu J-J, Xu D, Wang Z-L, Wang H-G, Zhang L-L, Zhang X-B (2013) Synthesis of perovskite-based porous $La_{0.75}Sr_{0.25}MnO_3$ nanotubes as a highly efficient electrocatalyst for rechargeable lithium–oxygen batteries. Angew Chem Int Ed 52(14):3887–3890. https://doi.org/10.1002/anie.201210057

179. Zhang T, Zhou H (2013) A reversible long-life lithium–air battery in ambient air. Nat Commun 4:1817. https://doi.org/10.1038/ncomms2855
180. Roger I, Shipman MA, Symes MD (2017) Earth-abundant catalysts for electrochemical and photoelectrochemical water splitting. Nat Rev Chem 1:0003. https://doi.org/10.1038/s41570-016-0003
181. Zeng K, Zhang D (2010) Recent progress in alkaline water electrolysis for hydrogen production and applications. Progr Energy Combust Sci 36(3):307–326. https://doi.org/10.1016/j.pecs.2009.11.002
182. LeRoy RL (1983) Industrial water electrolysis: present and future. Int J Hydrog Energy 8 (6):401–417. https://doi.org/10.1016/0360-3199(83)90162-3
183. Zhu Y, Zhou W, Zhong Y, Bu Y, Chen X, Zhong Q, Liu M, Shao Z (2017) A perovskite nanorod as bifunctional electrocatalyst for overall water splitting. Adv Energy Mater 7 (8):1602122. https://doi.org/10.1002/aenm.201602122
184. Gorlin Y, Jaramillo TF (2010) A bifunctional nonprecious metal catalyst for oxygen reduction and water oxidation. J Am Chem Soc 132(39):13612–13614. https://doi.org/10.1021/ja104587v
185. Hua B, Li M, Zhang Y-Q, Sun Y-F, Luo J-L (2017) All-in-one perovskite catalyst: smart controls of architecture and composition toward enhanced oxygen/hydrogen evolution reactions. Adv Energy Mater 7(20):1700666. https://doi.org/10.1002/aenm.201700666
186. Jin H, Wang J, Su D, Wei Z, Pang Z, Wang Y (2015) In situ cobalt–cobalt oxide/N-doped carbon hybrids as superior bifunctional electrocatalysts for hydrogen and oxygen evolution. J Am Chem Soc 137(7):2688–2694. https://doi.org/10.1021/ja5127165
187. Li X, Walsh FC, Pletcher D (2011) Nickel based electrocatalysts for oxygen evolution in high current density, alkaline water electrolysers. Phys Chem Chem Phys 13(3):1162–1167. https://doi.org/10.1039/C0CP00993H

Chapter 9
Perovskite Material-Based Photocatalysts

Ravi Gundeboina, Venkataswamy Perala and Vithal Muga

1 Introduction

The rapid industrialization, the progression of human civilization, and escalating the use of traditional fossil fuels ensued in the extreme limits of pollution of air, water, and soil. It is observed that over the past few decades, the abusive use of pesticides, industrial chemicals, pharmaceutical and personal care products (PPCPs), organic dyes, and combustion byproducts have resulted in their undesirable accumulation in the environment. Of these, organic dyes have been extensively used in industries such as fabric, furniture, food, and paint. It is estimated that about 30–40% of these coloring agents in the form of "dye wastewater" are released (accidentally or without pretreatment) into water streams causing environmental and health problems. A few of these water-soluble dyes prevent sunlight causing damage to aquatic life. Some other dyes on exposure to sunlight decompose and generate carcinogenic byproducts. The mounting level of pollution together with the depletion of fossil fuel has forced scientists to look for new alternative energy sources and more effective mechanisms to curb pollution. Thus, the utilization of solar energy through a sustainable and cost-effective approach offers the solution to (a) reduce environmental pollution and (b) satisfy the demand for renewable energy.

Traditional methods of wastewater treatment such as coagulation, microbial degradation, adsorption of activated carbon, incineration, filtration, and sedimentation have become ineffective from an economic point of view or leave secondary pollutants. Advanced oxidation processes (AOPs), a group of established treatment methods including (i) photocatalytic oxidation using a semiconducting material as catalyst, (ii) ultrasonic cavitation, (iii) electron beam irradiation, (iv) Fenton's

R. Gundeboina · V. Perala · V. Muga (✉)
Department of Chemistry, Osmania University, Hyderabad 500 007, Telangana, India
e-mail: mugavithal@rediffmail.com

N. S. Arul and V. D. Nithya (eds.), *Revolution of Perovskite*, Materials Horizons: From Nature to Nanomaterials, https://doi.org/10.1007/978-981-15-1267-4_9

reaction, and (v) reactions using O_3/H_2O_2, UV/O_3, and UV/H_2O_2 are found to be effective. The principle of AOP is to generate robust oxidizing species such as OH radicals in situ, which initiates a series of reactions that break down the dye molecule into smaller and less harmful substances, the so-called mineralization process [1–3]. Despite the good oxidation of organic pollutants (except method (i)), the complexity of these methods (AOPs), the high chemical consumption, and the relatively high treatment costs constitute the significant barriers for large-scale applications [2]. Hence, semiconducting material as a photocatalyst is anticipated to be both supplementary and complementary to a more conventional approach for the devastation of dangerous chemical wastes and energy production.

1.1 Heterogeneous Photocatalysis—Semiconductor Oxides as Photocatalysts

The execution of a chemical or biochemical reaction on the surface of the inorganic semiconductor is referred to as heterogeneous photocatalysis. For the fundamentals of photocatalysis, the readers can go through the excellent reviews reported [4–9]. The catalyst together with reactants/pollutants, upon irradiation of light, produce an electron (in conduction band) and hole (in valence band) leading to a series of reactions in which useful products are formed, or undesirable pollutants are decomposed to less harmful byproducts. The phase pure, well-crystallized, monodisperse, nano-sized semiconductor oxide with homogeneous morphology is ideal to be an efficient and chemically stable photocatalyst. As the abovementioned properties strongly depend on the preparative conditions of material, the selection of preparation method is essential. It is well known that the efficiency of a photocatalytic reaction or photocatalyst depends on several factors such as its crystallite size, surface area, band gap energy (E_g), recombination rate of photogenerated electron–hole pair during the photoreaction, nature of the reactant/pollutant, and nature of active sites on the catalyst, to mention a few (Fig. 1) [10]. The photocatalyst used must satisfy several functional requirements with respect to semiconducting properties: (i) suitable solar visible light absorption capacity with a band gap energy about 2.0–2.2 eV (visible light region) and band edge potentials suitable for splitting of water, (ii) capability for separating photoexcited electrons from reactive holes, (iii) minimization of energy losses related to charge transport and recombination of photoexcited electron–hole pair, (iv) chemical stability against corrosion and photo-corrosion in aqueous environment, (v) kinetically sui electron transfer properties from photocatalytic surface of water, and (vi) easy and cost-effective method of preparation.

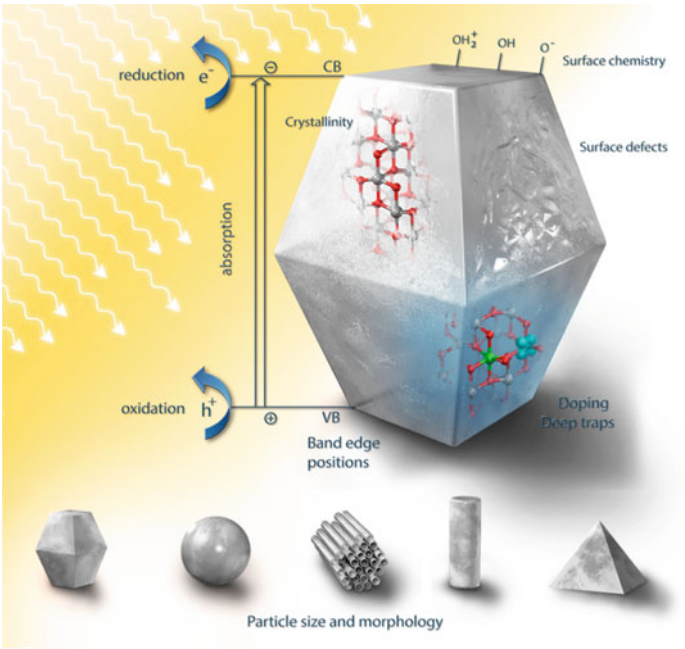

Fig. 1 Factors impacting photocatalytic activity of a single (idealized) inorganic semiconductor particle [10] Copyright 2018. Reprinted with permission from ACS publications

1.2 Mechanism of Semiconductor Photocatalysis

When a semiconductor absorbs light energy more than its band gap energy, it results in the promotion of the valence band electron into its conduction band. The formation of the electron (in the conduction band) and hole (in the valence band), known as "exciton" is the first step in the mechanism of semiconductor photocatalysis.

$$\text{Photocatalyst(PC)} + h\upsilon \rightarrow \text{PC}\left(h_{\text{VB}}^{+} + e_{\text{CB}}^{-}\right)$$

After photoexcitation, the excited electron–hole pairs either recombine or can migrate to the surface of the semiconductor. They (electron and hole) participate in various oxidation and reduction reactions with adsorbed species such as H_2O and O_2. These oxidation and reductions are the primary reactions of photocatalytic degradation of pollutants and photocatalytic hydrogen production, respectively. In the photocatalytic water splitting reactions, the photoexcited electrons in the conduction band (CB) are responsible for generation of H_2 and OH^- by reacting with water. However, in order to initiate hydrogen and oxygen production, the conduction band level of the semiconductor should be more negative than the reduction potential of H_2 (H^+/H_2) and valence band level should be more positive than the

oxidation potential of O_2 (H_2O/O_2). However, the photocatalytic dye degradation mechanism is strongly affected by different model pollutants and photocatalysts. In addition, the different dominant radical species would determine the photoactivity and the decomposition path. Hence, the dye degradation mechanism is still not fully understood, even uncertain. A basic mechanism for the photocatalytic process of a semiconductor dye degradation and water splitting is presented in Figs. 2 and 3, respectively.

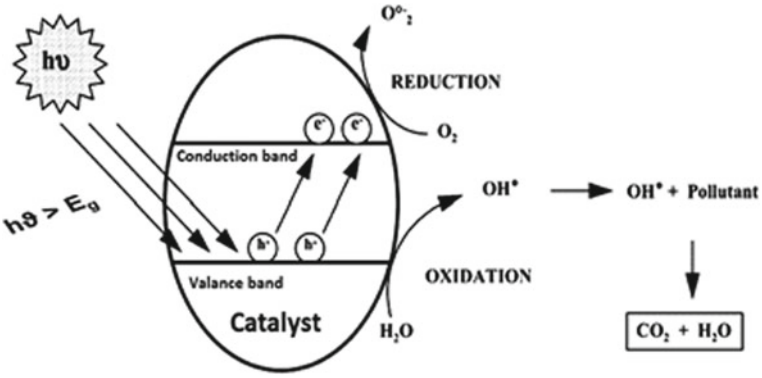

Fig. 2 Degradation process of pollutants using semiconductor oxides illuminated by UV light/ solar light

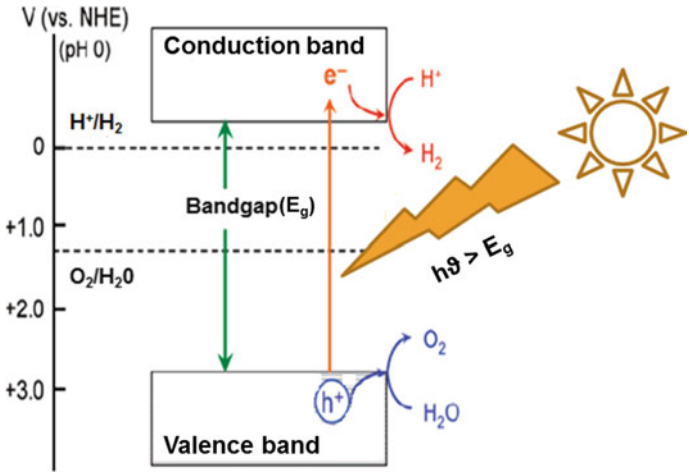

Fig. 3 Fundamental principle of semiconductor-based photocatalytic water splitting for hydrogen and oxygen production

2 Methods to Tailor the Photocatalytic Properties of Semiconductor Photocatalysts

Since the discovery of Fujishima and Honda [11] that water can be photo-electrochemically decomposed into H_2 and O_2 using a semiconductor (TiO_2) electrode under UV irradiation, extensive works have been carried out to produce hydrogen from water splitting using a variety of semiconductor photocatalysts. Since the major part (about 45%) of sunlight belongs to visible region, it is essential that the efforts to design the semiconducting photocatalysts should be toward the utilization of this part of solar light to ignite photocatalytic reactions. Hence, control of electronic band structure of material by adjusting its elemental compositions was recognized as the effective method to extend light response range.

The methods including metal and nonmetal substitution into semiconductor materials are considered to tailor its wide band gap to narrow band gap. Metal ion substitution creates impurity levels in the forbidden band as either a donor level above the valence band or an acceptor level below the conduction band as shown in Fig. 4.

These impurity energy levels decrease the band gap energy of the photocatalyst, thus shifting the photo-response of catalyst toward the visible region. There have been numerous reports on the modification of wide band gap photocatalysts using metal ion doping to make them visible light active [12–17].

It is also perceived in some cases that metal ion dopant can also act as a recombination center, resulting in decreased photocatalytic activities [12]. Doping of nonmetal ions such as N^{3-}, S^{2-}, and F^{-} is another method employed to narrow the band gap and improve the photocatalytic activity. Unlike metal ion dopants, nonmetal ion dopants are less likely to form donor levels in the forbidden band and

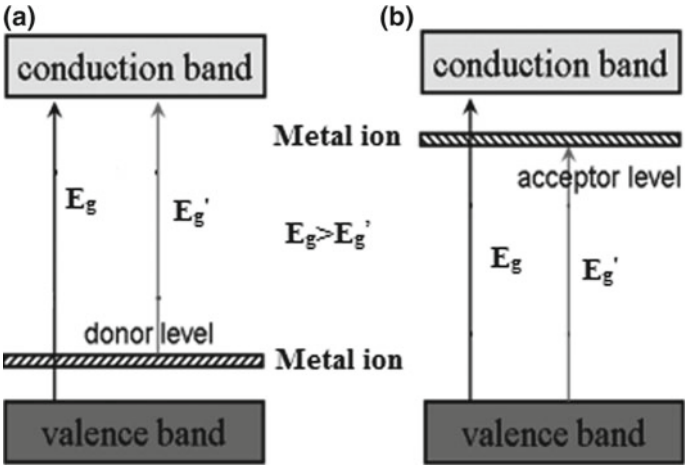

Fig. 4 **a** Donor level and **b** acceptor level formed by metal ion doping

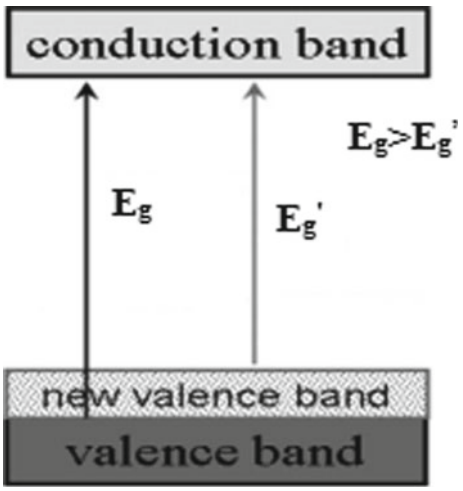

Fig. 5 New valence band formation by doping of nonmetal ions

recombination centers. Hence, anion doping is more effective to enhance the photocatalytic activity. Since the study of N-doped TiO_2 by Asahi et al., the photocatalytic studies of anion-doped semiconductors have been attracted much attention. It was found that N substitution into the metal oxide can shift its photo-response into the visible region because of the contribution of N *2p* orbitals to the valence band comprised of O *2p* orbitals, thereby narrowing the band gap by moving the valence band upward (Fig. 5) [18]. The method of nonmetal ion doping has been widely used to modify some UV-light-active oxide photocatalysts [19–24].

However, there are also two momentous drawbacks observed in visible light-responsive photocatalytic reactions. First is the rapid recombination of electron/hole (e^-/h^+) pair. The second is low utilization of visible-light-excited high-level energy electrons (HLEEs) and limited visible light absorption of semiconductor photocatalyst. Moreover, there is an additional problem of rapid backward reaction during water splitting. These drawbacks can be overcome by the development of novel photocatalysts such as metal/nonmetal doped photocatalyst, noble metal surface-modified photocatalyst [25–27], dye/semiconductor-sensitized photocatalyst, and p–n heterojunction structure composite photocatalyst [28, 29].

The dopant in lattice brings defects and tunes the amount of oxygen vacancy. It is known that the photocatalyst, having lattice defects and oxygen vacancies, shows good photocatalytic properties by narrowing the band gap and suppressing recombination rate of photogenerated electron–hole [30–32]. When the noble metal is loaded onto the surface of the photocatalyst, the photogenerated electrons migrate to the surface of the host photocatalyst and are entrapped by the noble metal cocatalyst. Meanwhile, the photogenerated holes stay at the host photocatalyst and migrate to its surface. This results in the efficient separation of the photogenerated electrons and holes. Subsequently, the separately localized electrons and holes become involved in their roles as the reducer and oxidizer, respectively, in the photocatalytic reaction. The noble metals, such as Pt, Au, Ru, Pd, Ag, and Rh, are

usually used as effective cocatalysts for photocatalytic water splitting. To date, Pt-loaded photocatalysts have the highest photocatalytic activity for hydrogen evolution from water splitting reaction under the visible light irradiation [33, 34].

The methods including sensitization with organic dyes, the coupling of either p-type and n-type semiconductor or small and large band gap semiconductors, are another ways to improve the photocatalytic properties [35–37]. In the dye-sensitized semiconductor photocatalysis, the dye molecule electrons excited by visible light can be injected into the conduction band of the semiconductor to initiate the catalytic reactions. In the composite photocatalyst (coupling of large band gap semiconductor with a small band gap semiconductor with a more negative conduction level), the excited electrons from conduction band of a small band gap semiconductor by the absorption of visible light can be injected into the conduction band of a large band gap semiconductor, while the photogenerated holes are trapped in a small band gap semiconductor. Thus, an effective electron–hole separation can be achieved by these methods and results in higher photocatalytic activity. However, in p–n heterojunction photocatalysis, because of the difference of band gap and position between the two different semiconductors, the strong internal electric field at the interface can initiate the transfer of photoinduced electrons to the conduction band (CB) of the n-type semiconductor and of holes to the valence band (VB) of the p-type semiconductor for the reduction and oxidation reactions, respectively [38, 39]. It has been observed that the visible-light-excited high-level energy electrons (HLEEs) of narrow band gap semiconductors such as Fe_2O_3, $BiVO_4$, and $BiFeO_3$ could transfer thermodynamically to the conduction band of TiO_2 with a high-energy level platform, leading to the extended lifetime of photogenerated charge carriers and hence to the improved visible light activities [40–42]. Recently, graphitic carbon nitride (g–C_3N_4) has been used as a kind of metal-free n-type semiconductor for enhancing the photocatalytic performance of materials with poor photocatalytic activity due to its unique advantages of hydrophilicity and large specific surface area [43].

3 A Short Overview of Perovskite Oxides as Photocatalysts

Among the various types of photocatalysts reported so far, the lion's share comes from oxide semiconductors. The ease of preparation, less expensive, less toxicity, possessing tunable properties, and their utility in cyclic experiments are some of the useful features that have made to investigate oxide semiconductors extensively compared to other types of materials. Oxides such as TiO_2, ZnO, WO_3, vanadates (VO_4), and molybdates have been considerably studied as photocatalysts. Oxides belonging to perovskite family with the general formula ABO_3 have attracted the scientific community due to their remarkable properties and the wide range of applications, interesting structure, and flexible compositions. The properties include

high chemical stability, catalytic properties [44], multiferroicity behavior [45], order/disorder transformations, and range of electrical and ionic conductivities that include metallic, half-metallic with spin-polarized electrical conductivity [46, 47], and superconductivity [48]. These oxides are used in SOFC technology, radioactive waste encapsulation, magnetic memory components, and dielectric resonator materials [47, 49–51]. These perovskite materials have a distinctive structural feature that is beneficial to photocatalytic activity. The relationship between crystal structure and energy delocalization shows that the closer to 180° the B–O–B bond angle is, the easier the excitation energy is delocalized leading to higher photoactivity [52, 53]. Thus, materials belonging to ABO_3 family with ideal perovskite structure are expected to exhibit higher photoactivity.

Perovskite oxides (ABO_3) with the structural flexibility to tolerate replacement of A- and B-sites with different ionic species have led to many novel compositions. This chapter exclusively deals with the research work published on the photocatalytic activity of ABO_3-based perovskite-type materials. Double, triple, and layered perovskites are not considered. Recently, there are fascinating review papers on perovskite materials related to their structure, synthesis, and applications in various fields. Ewelina Grabowska, reviewed the synthesis, characterization of selected perovskite oxides such as $SrTiO_3$, $KTaO_3$, $NaTaO_3$, $KNbO_3$, and $NaNbO_3$ and their applications in photocatalysis. Besides, the methods for enhancing the photocatalytic activity of those mentioned oxides along with the influence of different morphologies and surface properties are also discussed [54]. Guan et al. summarized the contemporary progress of perovskite materials and their photocatalytic applications in water splitting and environmental remediation, and presented the key challenges and viewpoints on the research of perovskite photocatalysts [55]. A review on photocatalytic CO_2 reduction using nano-sized perovskite oxides is reported by Sheng et al. This review correlated the physicochemical properties such as crystal structures, defect distribution, morphologies, and electronic properties to CO_2 photoreduction performance [56]. Pushkar Kanhere and Zhong Chen reviewed the perovskite materials that are classified by the B-site cations and their crystal structure, optical properties, and electronic structure accompanied by photocatalytic performance [57]. Saumyaprava et al. discussed the recent development of perovskite, layered perovskite, and their composites especially with π-conjugated carbon materials toward photocatalytic applications [58]. ABO_3-based photocatalysts for water splitting and the application of the modification scheme of ABO_3 photocatalysts in designing $A_xB_yO_z$ photocatalysts are systematically reviewed by Jinwen Shi and Liejin Guo [59]. Wei et al. described the basic principles of water splitting reaction, photodegradation of organic dyes and solar cells as well as the requirements for efficient photocatalysts [60]. Zhu et al. reviewed the catalytic performance of perovskite oxides with different morphologies for gas-, solid-, and liquid-phase reactions [61]. Shi et al. published a review on recent progress in photocatalytic CO_2 reduction over perovskite oxides. In this review, they have discussed recent advances in the design of perovskite oxides and their derivatives for photocatalytic CO_2 reduction, placing particular emphasis on structure

modulation, defect engineering, and interface construction as rational approaches for enhancing solar-driven CO_2 conversion to CH_4, CO, and other valuable oxygenates ($C_xH_yO_z$) [62].

4 Recent Developments in Enhancing the Photocatalytic Activity of Perovskite Materials

Although there are some review papers on the photocatalytic applications with simple ABO_3-based perovskite materials, a planned update is highly desirable to inform the latest progress, growing trends and updated summary of the current status concerning photocatalysis. Further, the rapid utilization of ABO_3 materials in photocatalytic applications requires a fresh assessment to provide a broad overview and possible future directions. Here, we have presented a review on the photocatalytic activity of lanthanum-based perovskites $LaMO_3$ (M = Fe, Co and Mn) and $BaMO_3$ (M = Zr and Sn) along with the recent developments in enhancing the photocatalytic behavior of alkali and alkaline earth metal-based perovskite materials ($ATiO_3$ (A = Ca, Ba, and Sr), $ATaO_3$ (A = Na and K), and $ANbO_3$ (A = Na and K)).

A succession of stable lanthanum-based perovskites, $LaMO_3$ (M = 3d transition metal) has been experimentally and theoretically expounded to be competent photocatalysts due to the unique crystal structure, electric conductivity, etc. Among these, $LaFeO_3$ has attracted a great deal of interest due to its narrow band gap, inimitable optoelectronic properties structural flexibility, and applications in removing the potential environmental pollutants. The photocatalytic performance of $LaFeO_3$ is low in spite of its narrow band gap energy ((2.1 eV (for dense polycrystalline samples) and 2.6 eV for powdered samples)) [63, 64] due to limited visible light absorption and the low utilization of visible-light-excited high-level energy electrons [65]. Hence, the research has been aimed to improve its photocatalytic properties by altering its surface properties (like morphology, size of the particle, and surface area) and metal/nonmetal ions doping into its lattice. $LaFeO_3$ nanoparticles with different morphologies have been synthesized by sol–gel method [66], sonochemical method [67], electrospinning method [68], polymeric precursor route [69], and hydrothermal method [70, 71] to improve its catalytic, magnetic, and photocatalytic properties. Shudan Li and Xianlei Wang have prepared one-dimensional $LaFeO_3$ fibers with different morphologies by electrospinning method. They have reported the concentration effect of acetic acid and ferric nitrate solutions on the morphology of $LaFeO_3$. The effects of morphology on photocatalytic activity have also been investigated [69]. The introduction of metal ion substitution in place of La/Fe in $LaFeO_3$ on its photocatalytic activity has also been explained [72–76]. Parrino et al. synthesized Cu-substituted $LaFeO_3$ perovskites ($LaFe_{1-x}Cu_xO_{3-\delta}$, where x = 0.05, 0.10, 0.20, and 0.40) by citrate auto-combustion method and discussed their photocatalytic activity by employing 2-propanol oxidation in the gas–solid regime as a probe reaction. They concluded that the

photocatalytic activity of the Cu(II)-substituted $LaFeO_3$ is improved by increasing the Cu amount up to 10 mol% and slightly decreased for higher copper contents. The higher activity of Cu(II)-substituted $LaFeO_3$ compared to that of pristine $LaFeO_3$ has been related with the presence of oxygen vacancies and with the reduced electron–hole recombination [77]. It was reported that the catalytic activities of the manganese-substituted $LaFeO_3$ were much higher than pure $LaFeO_3$ because of its higher oxygen vacancies, the variable valency of Mn ions, and the strong absorption in visible light [75]. Jauher et al. reported the synthesis of $LaMn_xFe_{1-x}O_3$ (x = 0.0–0.5) and examined their H_2O_2-assisted catalytic cationic and anionic dye degradation in the presence and absence of visible light irradiation. They observed that all the Mn-substituted ferrite compositions catalyzed the degradation of dyes both in the absence and presence of visible light irradiation and stated that the catalytic activity is not influenced significantly with increasing manganese content. $LaMn_{0.2}Fe_{0.8}O_3$ exhibited excellent photocatalytic activity for the degradation of both cationic and anionic dyes [78]. Based on these results, Dhiman et al. studied photocatalytic properties of the transition metals doped with $LaMn_{0.2}Fe_{0.8}O_3$ ($LaMn_{0.2}M_{0.2}Fe_{0.6}O_3$ (M = Cr^{3+}, Co^{2+}, Ni^{2+}, Cu^{2+}, and Zn^{2+})). All $LaMn_{0.2}M_{0.2}Fe_{0.6}O_3$ compositions (except M = Cr) have shown higher photocatalytic dye degradation which is attributed to the generation of vacancy defects and smaller band gap energy values [79].

Xicai Hao and Yongcai Zhang have synthesized porous nano-$LaFeO_3$ through a gel combustion method at the calcination temperatures of 200–400 °C and studied the photocatalytic reduction of aqueous Cr(VI) under visible light irradiation. The $LaFeO_3$ prepared at lower temperature exhibited enhanced photocatalytic activity in the reduction of Cr(VI) in aqueous solution under visible light irradiation [80]. Giuseppina et al. prepared $LaFeO_3$ nanoparticles via solution combustion method and investigated their photocatalytic efficiency for hydrogen production from glucose aqueous solution under UV and visible light emitted by light-emitting diodes (LEDs) [81]. Stable $LaFeO_3$ nanoparticles with a size of 15 nm and the band gap of 1.86 eV have been prepared by a sol–gel method using reduced graphene oxide (rGO) as a template by Ren et al. [82]. They have demonstrated that $LaFeO_3$–rGO can function as an efficient catalyst for degradation of methylene blue (MB) or rhodamine B (RhB) under visible light irradiation. From the controlled photocatalytic experiments, it was concluded that electron transfer from the dye molecule to hole dominated the oxidation process.

To overcome the low utilization of visible-light-excited high-level energy electrons (HLEEs) and limited visible light absorption of $LaFeO_3$, Muhammad et al. prepared ZnO-coupled Bi-doped porous $LaFeO_3$ and evaluated its visible light photocatalytic performance for 2,4-dichlorophenol (2,4-DCP) degradation and CO_2 conversion. The improved visible light activity is endorsed to the improved utilization of visible-light-excited HLEEs by protracting visible light absorption via the Bi-introduced surface states and coupling ZnO to introduce a suitable high-level-energy platform for accepting electrons. The mechanism of photocatalytic degradation of 2,4-DCP over ZnO/Bi-doped porous $LaFeO_3$ has also been discussed [83]. Yan et al. prepared a p–n heterojunction composed of p-type

$LaFeO_3$ and n-type g–C_3N_4 and studied its photocatalytic activity against Brilliant Blue (BB) degradation under the visible light irradiation. The improved photoactivity of g–C_3N_4 and $LaFeO_3$ is attributed to efficient separation of electron–hole pairs, a higher concentration of superoxide and hydroxyl radicals. Electron spin resonance (ESR) analysis and the active species trapping experimental results confirmed the Z-scheme photogenerated electron transfer mechanism integrated with the dye-sensitization effect of the photocatalytic reaction process [43]. Ibrahim et al. prepared n-type $LaFeO_3$ and evaluated its photoelectrochemical water splitting under simulated AM 1.5G solar illumination in view of factors influencing photocatalytic performance including the calcination temperature, the species, concentration, and the pH of the electrolyte that are evaluated [84].

A perovskite, lanthanum cobaltite ($LaCoO_3$), is considered as a promising catalytic material because of its appealing physicochemical properties such as electrical, ionic conductivities, and excellent electrochemical properties [85, 86]. But less visible light-harvesting, higher electron–hole recombination rates and a short lifetime of photogenerated charge carriers hindered its pragmatic applications. Feng et al. adopted sol–gel and deposition–precipitation method to get a PdO/$LaCoO_3$ heterojunction photocatalyst to enhance the H_2 production from formaldehyde aqueous solution without any additives at low temperature. The heterojunction structure can significantly improve the charge generation, enhance the visible light absorption, and efficiently confine the recombination of photogenerated electron–hole pairs to exhibit higher photocatalytic activity. The obtained results are demonstrated that PdO doping on the $LaCoO_3$ surface can effectively adjust band gap and Fermi energy levels to apply in hydrogen production from formaldehyde solution under visible light. It is found that the hydrogen production rate of 2 wt% PdO/$LaCoO_3$ is multiple of ten higher than pristine $LaCoO_3$ [87].

Minghui Wu et al. tried to prepare $LaCoO_3$ with propitious performance through creating oxygen vacancies in it. $LaCoO_3$ is prepared using natural sugarcane bagasse with tunable oxygen vacancy and enlightened the interaction between metal ions and sugarcane bagasse [88]. It has been stated that natural biomass like sugarcane bagasse and extract of Pichia pastoris GS115 may not only replace the usual chemical reagents because of the benefits of being green, environmental, and low cost but also provide ample functional groups to interact with the metal ions leading to varying in the surface properties, and even form a unique structure of the synthesized photocatalysts, which could tune the amount of oxygen vacancy and bring the lattice defects [89]. The characterization of bagasse is carried out to explicate its interaction with metal ions and role in the synthesis process. Moreover, the correlation between the amount of oxygen vacancy on the perovskite induced by biomass and the performance of photocatalytic hydrogen production is examined and reported that as-synthesized sugarcane bagasse-mediated $LaCoO_3$ perovskite had worthy photocatalytic performance in hydrogen production from formaldehyde solution under visible light irradiation than that prepared by conventional citric acid method [88]. Liqing et al. reported novel microbial synthesis of high efficient Cu-doped $LaCoO_3$ photocatalyst from Pichia pastoris GS115 for hydrogen production from formaldehyde solution under visible light irradiation. Copper doping

favors the formation of impurity level and appropriate oxygen vacancy. The biomass intervention in synthesis assists the adjustment of the crystal structure and surface structure of catalyst, which makes the diffraction angle and unit cell change and simultaneously regulates surface oxygen defects. Besides, the abundant organic functional groups from biomass residue on the surface act as a photosensitizer, so that the higher photocatalytic performance is obtained for the catalyst prepared by microbial synthesis than the catalyst prepared by traditional chemical methods [90]. Jayapandi et al. prepared pristine and silver (Ag)-modified $LaCoO_3$ via a hydrothermal process. Silver is considered as better metal dopant because Ag can induce transport of charge carriers and acts as an effective carbon removal, better photo absorber and provide active species for oxygen activation. Ag-modified $LaCoO_3$ degraded methylene blue (MB) in higher rate (99% in 10 min) compared to pure $LaCoO_3$ (75% in 10 min) [91].

The photodegradation of methyl orange within 90 min of visible light irradiation is observed using pure $LaMnO_3$ nanoparticles [92]. It is well known that the porous perovskite oxides with the improved specific surface area are vital to increasing the photocatalytic activity [93, 94]. Rajesh Kumar et al. examined the significance of different morphologies of $LaMnO_3$ particles for the degradation of RB dye under visible light irradiation. As-prepared porous $LaMnO_3$ nanoparticles degraded 95% of RB dye in 60 min of irradiation time. These results imply that the porous morphology and specific surface area plays a key role in the photocatalytic performance [95]. Peisong et al. studied the photodegradation of methyl orange dye under the visible light irradiation using $YbFeO_3$ [96] and $EuFeO_3$ [97].

The structural features of $BaZrO_3$ like ideal cubic crystalline phase with a bond angle of 180° of the ZrO_6 octahedral sites and largely dispersed conduction band have provoked to study its photocatalytic activity. Yupeng et al. studied for the first time the photocatalytic water splitting of $BaZrO_3$ under the UV light irradiation [98]. Later, the same group has tried to modify the electronic structure of $BaZrO_3$ to enhance the evolution rate of H_2 by doping Sn^{4+} in Zr^{4+} site. They observed that $BaZr_{0.7}Sn_{0.3}O_3$ exhibits the highest H_2 evolution rate [99]. They have also investigated the impact of Sr^{2+} substitution on photocatalytic water splitting activity of $BaSnO_3$ [100]. Borse et al. switched the UV active $BaSnO_3$ photocatalyst into a visible-light-active photocatalyst for O_2 production through the electronic structure modification by doping Pb^{2+} for Sn^{2+} [101]. Subsequently, attempts have been made to improve the photocatalytic activity of $BaZrO_3$ not only by metal ion doping [102, 103] but also preparing $BaZrO_3$ solid solutions [ex: $BaZrO_3$–$BaTaO_2N$ Solid-Solution Photocatalyst] [104] or heterojunction formation with other metal oxides [Ex: $BaZrO_3/Cu_2O/Bi_2O_3$] [105].

Titanium-based perovskite materials with the composition of $ATiO_3$ (A = Sr, Ca, and Ba) have been studied for photocatalytic applications for a long time even though having wide band gap energies due to their excellent resistance to photo-corrosion and high thermal stability [106]. Among the large number titanate perovskites, strontium titanate oxide ($SrTiO_3$) with an indirect band gap of 3.25 eV has been one of the most studied photocatalysts, exhibiting an unusual photocatalytic activity in various photocatalytic applications [107, 108]. Many researchers

have attempted to tune the electronic structure of titanium-based perovskite oxides to obtain the improved photocatalytic activity. Here, the recent developments in enhancing the photocatalytic applications of $ATiO_3$ (A = Sr, Ca, and Ba) have been presented.

A series of Au/$SrTiO_3$ nanocomposites with different Au contents have been synthesized by Xian et al., using a photocatalytic reduction method. The photocatalytic activity of the obtained composites was investigated for the photocatalytic degradation of acid orange 7 and methyl orange dyes under simulated sunlight and visible light irradiation, and a higher photoactivity observed for Au/$SrTiO_3$ nanocomposite than that of pure $SrTiO_3$ [109]. Liu et al. successfully synthesized WO_3, nanosheets with different SrTiO3 (La, Cr) contents. The photocatalytic activity of the as-prepared samples was measured in the decomposition of methylene blue under visible light irradiation [110]. Kissa et al. synthesized $SrTi_{1-x}Rh_xO_3$ photocatalyst considering different Ti/Rh ratios using a one-step hydrothermal synthesis and studied for the decomposition of methyl orange under visible light irradiation. 5% Rh-doped $SrTiO_3$ is shown to completely oxidize methyl orange within 30 min under visible light illumination [111]. Pure TiO_2, $SrTiO_3$, and $SrTiO_3$/TiO_2 nanocomposite were prepared by Devi et al. through a sol–gel method. The photoactivity of the as-prepared samples was evaluated by the degradation of 4-Nitrophenol (4-NP) under UV light irradiation, which revealed that the composite had improved photoactivity as compared to pure TiO_2 and $SrTiO_3$ [112]. Swapna et al. examined photocatalytic degradation of methylene blue under UV light with $SrTiO_3$ catalysts. The $SrTiO_3$ catalysts were prepared by a novel polymerizable sol–gel (PSG) approach for the first time [113]. $SrTiO_3$ powders were prepared by applying a polymeric precursor method by Silva et al. for the photocatalytic decomposition of methylene blue (MB), rhodamine B (RhB), and methyl orange (MO) dyes under UV illumination [108].

Goto et al. studied the photocatalytic decomposition of water over Al-doped $SrTiO_3$ ($SrTiO_3$:Al) catalyst under solar light irradiation [114]. The heterojunction semiconducting Au–Al/$SrTiO_3$ oxide was prepared by Saadetnejad et al. for hydrogen production by photocatalytic water splitting under visible light in the presence of methanol, ethanol, and isopropyl alcohol as sacrificial agents. They synthesized the Al/$SrTiO_3$ via solid-state reaction, while Au loading was done with the homogenous deposition–precipitation method. The results showed that the 0.25% Au–1.0% Al/$SrTiO_3$ composite oxide exhibited higher photocatalytic hydrogen evolution of 347 mmol/h with isopropyl alcohol as sacrificial agent [115]. Han et al. prepared Mg-modified $SrTiO_x$ photocatalysts by solid-state method. The samples were shown excellent performance for the photocatalytic water splitting under solar light illumination and the maximum H_2 evolution activity was obtained with the $Sr_{1.25}Mg_{0.3}TiO_x$ material [116].

Pure $SrTiO_3$ is not considered as a good photocatalyst because it is only active under UV irradiation, and therefore cationic/anionic dopants are often doped into $SrTiO_3$ to make it visible light-responsive. Kou et al. used the transition metal ions such as Co, Fe, and Ni as dopants to improve the photocatalytic CO_2 reduction to CH_4. Among the dopants, Co ions doped $SrTiO_3$ displays the most outstanding

photocatalytic performance for CO_2 photoreduction. Photo-deposition of Pt metal ions on co-doped $SrTiO_3$ surface further improves the CO_2 reduction to CH_4, and the yield of CH_4 under visible light irradiation is 63.6 ppm/h [117]. Luo and co-workers reported three kinds of $SrTiO_3$-containing ($SrTiO_3$, surface-Ti-rich $SrTiO_3$, and $Sr(OH)_2$-decorated $SrTiO_3$) photocatalysts for CO_2 reduction with H_2O vapor under visible light irradiation. They found that the molecular oxygen and CO were only the photoreduction products and the surface-Ti-rich $SrTiO_3$ exhibits the highest photocatalytic activity for CO_2 reduction [118]. By taking advantage of the loading/deposition of other metal or metal oxides on $SrTiO_3$ semiconductors, Li et al. prepared Rh and Au co-loaded $SrTiO_3$ through a photo-deposition process and studied the as-prepared catalysts for synthesis of syngas (CO and H_2) from photocatalytic reduction of CO_2 with water vapor under visible light irradiation [119]. Shoji et al. prepared the strontium titanate ($SrTiO_3$: STO) nanorod thin films loaded with amorphous copper oxide (CuO_x) nanoclusters. They found that compared to bare STO nanorods, the loading of the CuO_x-cocatalysts onto STO nanorods improved the photocatalytic carbon dioxide (CO_2) reduction using H_2O as an electron donor into carbon monoxide (CO) [120].

It is realized that the photocatalysts with a three-dimensional (3D) porous microsphere structure exhibited a high photocatalytic performance because they possess a high specific surface area and plenty of active sites for the target reaction, absorb more light through the reflection of pore walls, and are easy to be recycled by facile mechanical filtration [121]. Yang et al. prepared porous $SrTiO_3$ microsphere through a sol–gel method and observed its high photocatalytic performance for the Cr(VI) reduction under UV light irradiation [122]. Later, they tried to extend the photo-response of three-dimensional (3D) porous $SrTiO_3$ microspheres to the visible light region, thus enhancing their visible light photocatalytic activity [123]. They prepared three-dimensional porous La-doped $SrTiO_3$ (LST) microspheres via a modified sol–gel method. The agarose gel/$SrCO_3$ microsphere and La_2O_3 were used as the template and the La resource, respectively. The morphology of as-prepared LST-0.5 (agarose gel/$SrCO_3$/0.5 wt% of La_2O_3) sample is shown in Fig. 6. It is observed that these microspheres exhibit a higher photocatalytic activity than the undoped $SrTiO_3$ sample for the reduction of Cr(VI) under visible light irradiation. They have concluded that the observed redshift of absorption edge of $SrTiO_3$ inhibits the recombination of photogenerated electrons and holes, leading to the higher photocatalytic activity under visible light. Among all the as-prepared LST samples, LST-0.5 reduced 84% Cr(VI) within 100 min, exhibiting the highest photocatalytic activity. It is evident from Fig. 7 that the LST-0.5 sample has an excellent reusability, which may lay a good foundation for their practical application. They have also suggested photocatalytic mechanism for the reduction of Cr (VI) by porous LST microspheres under visible light as shown in Fig. 8.

Oxide mineral calcium titanate ($CaTiO_3$) was discovered in 1839 in the Ural Mountains and named for Russian mineralogist L. A. Perovski [124]. $CaTiO_3$ has also attracted a great deal of interest in the world of oxide electronics, not only as a functional material in electronic and piezoelectric devices but also as a

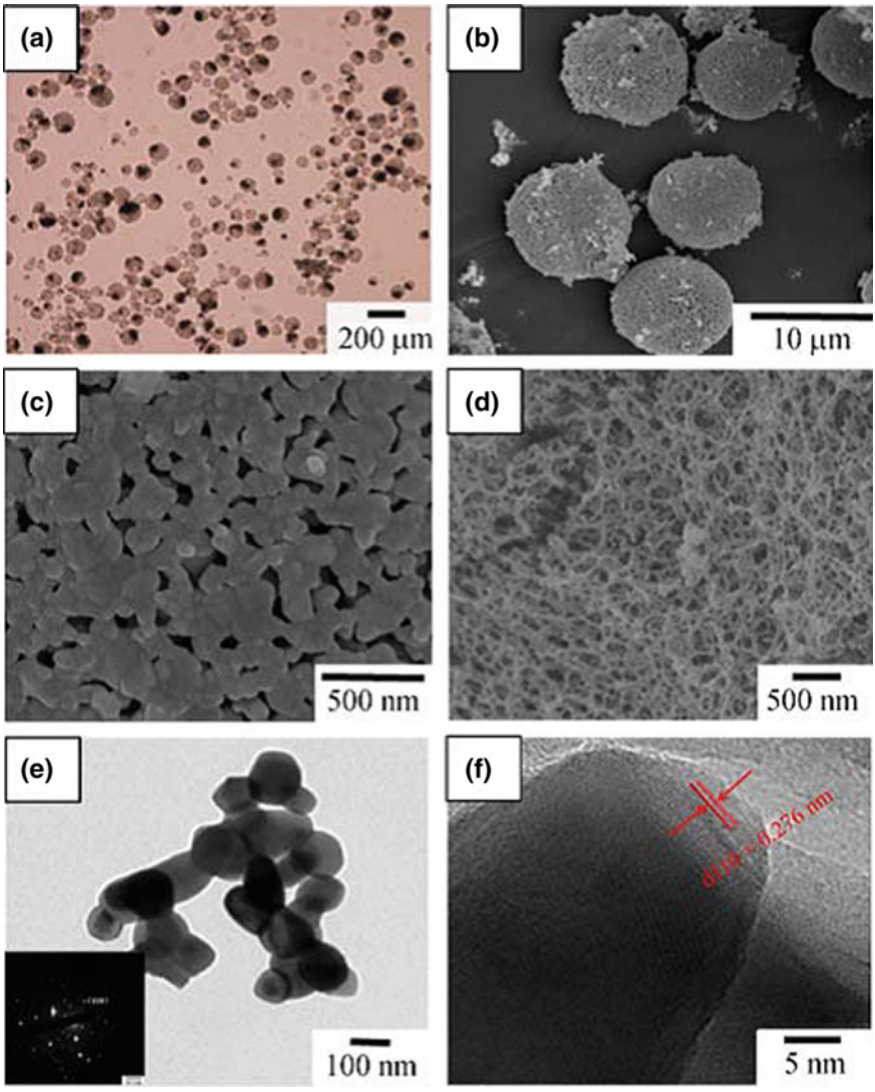

Fig. 6 **a** OM photo of agarose gel/$SrCO_3$/TiO_2/La_2O_3 composite beads; **b** low- and **c**, **d** high-magnification SEM photos of LST (**c**), outside surface; **d**, inner structure; **e** TEM photo with corresponding SAED pattern (inset); **f** HRTEM photo of LST [123] Copyright 2018. Reprinted with permission from Springer Nature

semiconducting material with a band gap of ~3.5 eV. However, due to its wide band gap (3.5 eV), $CaTiO_3$ was rarely used for the photocatalytic applications and its photoactivity is limited to UV excitation only. In the study by Yan et al., surface disorder-engineered $CaTiO_3$ were applied as the semiconducting materials for photocatalytic degradation of rhodamine B (RhB) under irradiation of simulated sunlight

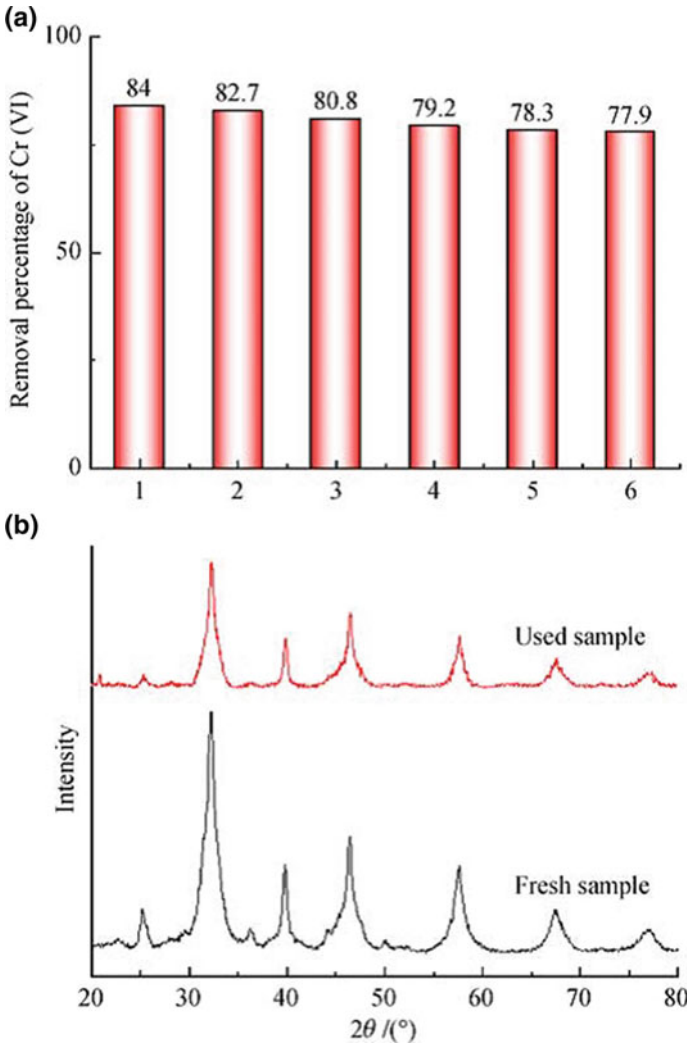

Fig. 7 **a** Recycling test of LST-0.5 for photocatalytic reduction of Cr(VI) under visible light and **b** XRD patterns of LST before and after six recycling tests [123] Copyright 2018. Reprinted with permission from Springer Nature

and UV light [125]. Graphitic carbon nitride (g–C_3N_4)–$CaTiO_3$ heterojunction photocatalysts were synthesized by Kumar et al. for the photocatalytic decomposition of rhodamine B (RhB) under UV, visible, and natural sunlight irradiation. The $CaTiO_3$ (CT) nanoflakes were homogeneously deposited onto the surface of g–C_3N_4 nanosheets by using a facile mixing method [126]. Yan et al. reported a facile hydrothermal approach to synthesize $CaTiO_3$ nanocuboids of controlled sizes that were used for degradation of rhodamine B under simulated sunlight irradiation.

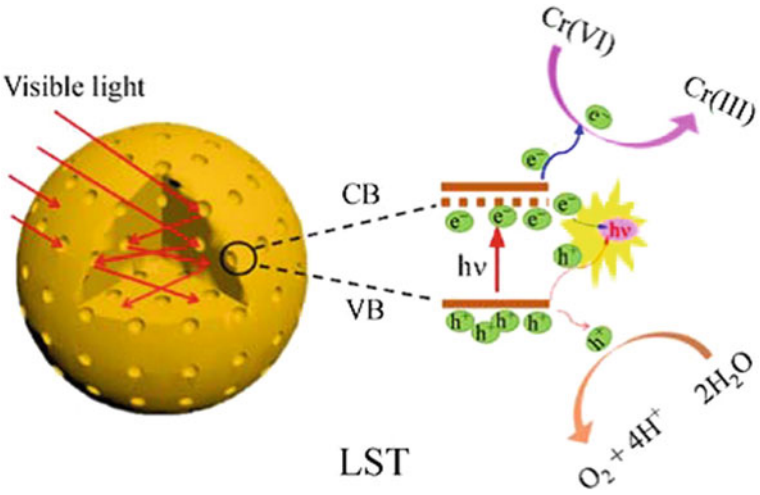

Fig. 8 Proposed photocatalytic mechanism for the reduction of Cr(VI) by porous LST microspheres under visible light [123] Copyright 2018. Reprinted with permission from Springer Nature

The photoactivity results demonstrated that $CaTiO_3$ nanocuboids exhibit superior photocatalytic activity when compared with $CaTiO_3$ nanoparticles [127]. Han et al. prepared an orthorhombic $CaTiO_3$ by solid-state, sol–gel, and hydrothermal methods and studied their photocatalytic performance for the degradation of methylene blue (MB) in an aqueous solution under the irradiation of visible light [128]. The photocatalytic activity of Ag–La co-doped $CaTiO_3$ powder for hydrogen evolution under UV and visible light was studied by Zhang et al. The photocatalyst, Ag–La co-doped $CaTiO_3$, showed higher H_2 production activity than that of pure $CaTiO_3$ powder [129]. Im et al. synthesized $CaTiO_3$@basalt fiber (BF) materials through a facile dipping method. This catalyst achieved high photocatalytic activity in CO_2 reduction (CH_4 = 17.8 μmol/g, CO = 73.1 μmol/g) [130]. Similarly, Yoshida et al. studied the composite catalysts of $CaTiO_3$@basalt fiber (BF) materials, consisting of $CaTiO_3$ with various Ca/Ti ratios, for CO_2 photochemical reduction. $CaTiO_3$ (1.5:1)@BF, had superior CO_2 adsorption and also the best CO_2 reduction performance (CH_4 = 17.8 μmol/g and CO = 73.1 μmol/g) [131].

The photocatalytic applications of Barium titanate, $BaTiO_3$, are limited due to its wide band gap energy in the range of 3.7–3.8 eV. Selvarajan et al. synthesized the novel $BaTiO_3$–SnO_2 nanocomposites by hydrothermal and precipitation deposition method. O-Chloroaniline and methylene blue were used as the model pollutants to evaluate the photocatalytic activity of the as-synthesized samples under UV–Vis light irradiation [132]. Nageri et al. reported the successful synthesis of Mn-doped barium titanate nanotube arrays by hydrothermal method, and the photocatalytic activity of these catalysts was evaluated by studying the degradation of methylene blue (MB) dye under visible light source [133]. Thamima et al. observed the

photocatalytic performance of the $BaTiO_3$ catalysts using various dyes such as Methylene Blue (MB), Malachite Green, and Alizarin Red S under UV light irradiation [134]. Maeda et al. synthesized rhodium-doped $BaTiO_3$ catalysts with five different Rh concentrations (1–5 mol%) by using a polymerized complex (PC) method to sensitize $BaTiO_3$ into visible light. The synthesized catalysts studied for hydrogen production by photocatalytic water splitting under visible light in the presence of methanol as an electron donor [135].

Tantalate-based semiconductor materials, such as alkali tantalates, which have unique crystal and energy band structures, are widely used in photocatalysis. Further, they possess both valence band and conduction band (CB consisting with Ta 5d orbitals at a high potential) potentials suitable for photocatalytic applications. Due to their high photosensitivity, nontoxicity, stability, and commercial availability, these catalysts scores highest among the large band gap semiconductors as a photocatalyst.

$NaTaO_3$ (band gap energy $\sim$4.07 eV) has attracted extensive attention in photocatalytic applications due to its good stability and high photocatalytic activity. Moreover, $NaTaO_3$ is considered as a good host material for developing visible light photocatalysts, especially when doped with rare earth elements like La [136]. Wang et al. reported that W and N co-doped $NaTaO_3$ showed higher photocatalytic activity toward degradation of rhodamine B (RhB) under visible light irradiation than single-element-doped $NaTaO_3$ [137]. Lan et al. reported the photocatalytic activity of the La/Bi co-doped $NaTaO_3$ and pure $NaTaO_3$ materials for the degradation of methylene blue under visible light irradiation. The La and Bi co-doping reduces the particle size, thereby extends the absorption edge toward longer wavelength [138]. A novel sulfur-doped $NaTaO_3$ photocatalyst was successfully synthesized by Li et al. through a simple hydrothermal process, and its photocatalytic activity was evaluated by methyl orange (MO) and phenol degradation processes [139]. The interest in $NaTaO_3$ in water splitting reaction recently increased after the discovery of its photocatalytic properties as water splitting [140]. $NaTaO_3$-based photocatalysts doped with different rare earth metal ions such as Y, La, Ce, and Yb with a constant ratio of rare earth metal ions have been synthesized by Jana and co-workers from the solid-state method and tested their photoactivity toward H_2 production by water/methanol mixture (methanol as an electron donor) under solar light. The higher H_2 production has been obtained with the Y-doped $NaTaO_3$ catalyst. Further, the deposition of Pt nanoparticles as cocatalyst, over these catalysts, improves even further the water splitting activity [141]. The photocatalytic activity of La-doped and pure $NaTaO_3$ in the H_2 evolution under UV light was studied by Lopez-Juarez et al. The higher photocatalytic activity was observed in the 2 mol% La-doped $NaTaO_3$ catalysts [142].

As a functional material, potassium tantalate ($KTaO_3$) has good photocatalytic activity and suitable band gap energy (3.2–3.8 eV). Liu et al. found that the substitution of La for K in $KTaO_3$ ($K_{1-x}La_xO_3$) can significantly improve the activity for methyl orange (MO). They demonstrated that the incorporation of La^{3+} ions in $KTaO_3$ host lattice led to a monotonous lattice contraction and increased the BET surface area [143]. Krukowska et al. investigated the photocatalytic activity of

mono- and bimetallic noble metal nanoparticles (MNPs/BNPs) decorated on the surface of $KTaO_3$ using by hydrothermal reaction of $KTaO_3$ followed by photo-deposition of MNPs/BNPs. The photocatalytic activity was estimated considering three model reactions by measuring the decomposition efficiency of phenol solution, the removal efficiency of gaseous toluene, and amount of evolved H_2 production in the presence of formic acid solution under the presence of Vis or UV–Vis light source [144]. Reduced graphene oxide-$KTaO_3$ (rGO–$KTaO_3$) hybrid composites with various graphene contents have been prepared by Bajorowicz et al. via the hydrothermal method. The photocatalytic activity of the composite was studied by the degradation of phenol under visible light irradiation. The improved photocatalytic activity can be attributed to the photosensitizer role of graphene in the rGO–$KTaO_3$ composites as well as the formation of p–n heterojunctions between p-type rGO and n-type $KTaO_3$ [145].

For the first time, Chen et al. prepared carbon-doped $KTaO_3$ via a simple combination of hydrothermal and calcination processes with glucose as the carbon source and tested the obtained powders in a photocatalytic H_2 generation under simulated sunlight illumination. The excellent photocatalytic hydrogen production should be mostly ascribed to the enhanced separation efficiency of charge carriers. The H_2 production rate was higher for C-doped $KTaO_3$ (592 μmol/h) than pure $KTaO_3$ (228 μmol/h) due to the enhanced separation efficiency of charge carriers [146]. It is generally accepted that methanol is an important industrial feedstock and is derived from the photocatalytic reduction of CO_2 using tantalum-based perovskites. Xiang et al. prepared CuO-patched cubic $NaTaO_3$ (CNTO) photocatalysts with different Cu contents and carried out the photocatalytic reduction of CO_2 to methanol in isopropanol in a self-made batch reactor. The morphologies of pure $NaTaO_3$ nanocubes and nano-CuO-patched $NaTaO_3$ (CNTOs) were observed by SEM and TEM as shown in Figs. 9 and 10. 5 wt% CNTO was found to have the best activity (CH_3OH yield of 1302.22 μmol g/1 h) and product selectivity in converting CO_2 to CH_3OH [147]. Also, authors have proposed the mechanism for photocatalytic reduction of CO2 to methanol on CuO–NaTaO3 photocatalyst (Fig. 11).

Nakanishi et al. studied the photoactivity of a set of Mg-, Ca-, Sr-, Ba-, and La-doped $NaTaO_3$ powders samples prepared by a solid-state method, while Ni, Pd, Rh, Cu, Au, and Ru cocatalysts were loaded in situ on doped photocatalysts by photo-deposition method, in photocatalytic CO_2 reduction to form CO using water as an electron donor. The best photocatalytic CO evolution obtained with Ag-loaded doped-$NaTaO_3$ photocatalysts [148].

Shao et al. synthesized highly efficient potassium tantalate ($KTaO_3$) materials, from a single-step hydrothermal method and investigated their activities in the reduction of carbon dioxide to methanol in isopropanol under UV light irradiation. Further, they found that the photoactivity of $KTaO_3$ increased with the loading of different NiOx contents and 2 wt% of NiO/$KTaO_3$ sample exhibited highest methanol formation [149]. Li et al. synthesized $KTaO_3$ (KTO)-based samples by

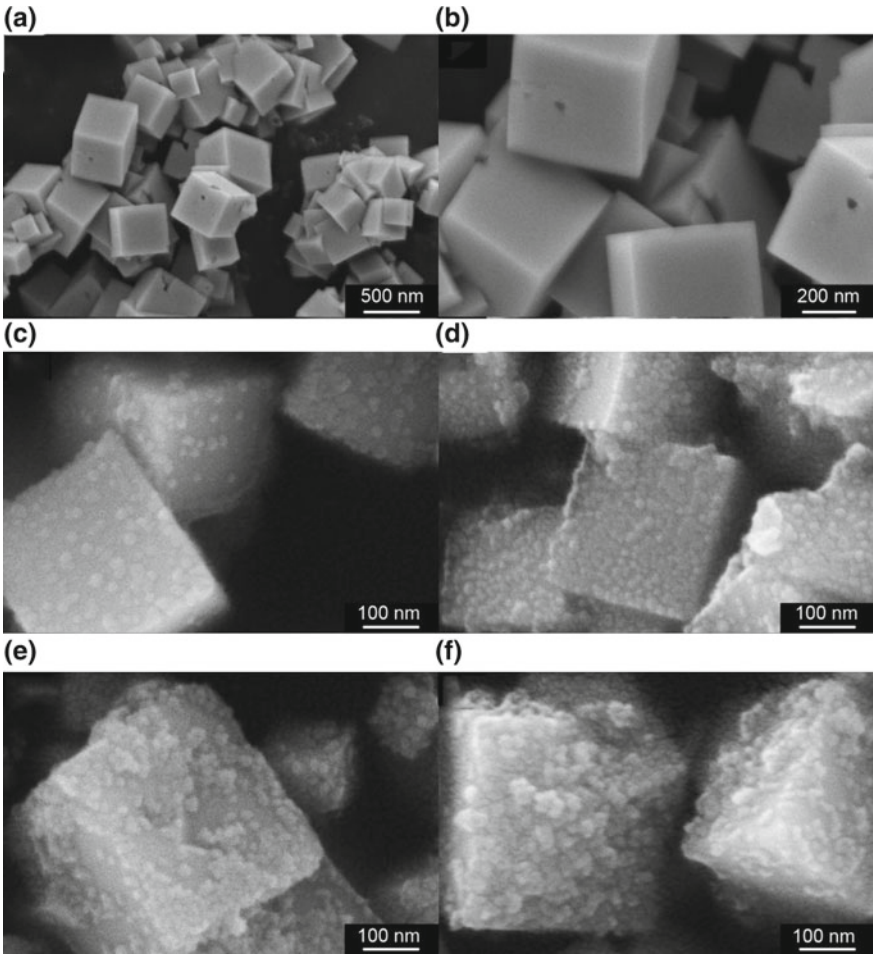

Fig. 9 SEM images: **a**, **b** pure $NaTaO_3$, **c** 2 wt% CNTO, **d** 5 wt% CNTO, **e** 7 wt% CNTO, **f** 10 wt% CNTO [147] Copyright 2018. Reprinted with permission from Elsevier

solid-state reaction (SSR-KTO) and solvothermal methods in hexane–water mixture (Hex-KTO) and ethanol (Eth-KTO) to reduce CO_2 with water under UV light irradiation. KTO prepared in hexane–water mixture sample with a nanoflake-like structure was found to have the best activity (20 times (H_2) and 7 times (CO)) and product selectivity in converting CO_2 to H_2/CO in comparison to other samples [150]. Fresno et al. compared the photocatalytic activity of $NaNbO_3$ and $NaTaO_3$ catalysts in the reduction of CO_2 under UV irradiation and found that the $NaTaO_3$ exhibits better photocatalytic properties regarding $CO/H_2/CH_3OH/CH_4$ (CO was the major product) product selectivity [151].

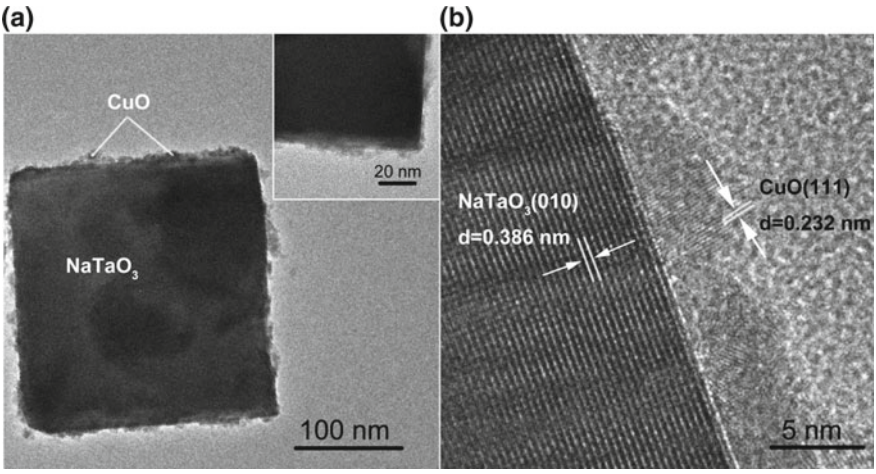

Fig. 10 **a** TEM image and **b** HRTEM image of 5 wt% CNTO [147] Copyright 2018. Reprinted with permission from Elsevier

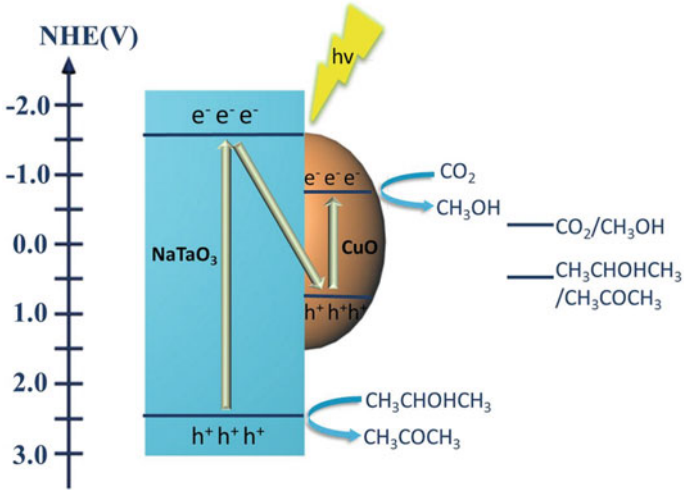

Fig. 11 The proposed mechanism for photocatalytic reduction of CO_2 to methanol on CuO–$NaTaO_3$ photocatalyst [147] Copyright 2018. Reprinted with permission from Elsevier

The niobium-based perovskite materials have been regarded as a potential candidates for a variety of photocatalytic applications compared to that of TiO_2 because the conduction band in niobates perovskite materials consists of Nb 4d which are situated at more negative potential (compared to TiO_2), thereby ensuring the separation and transfer of photoinduced charge carriers very precisely in their

photocatalytic applications. $NaNbO_3$, possibly the most studied of the alkali niobates, is a well-known transparent semiconductor (with a band gap of 3.7 eV) with extremely technological importance. The photocatalytic activity of alkali niobates under UV radiation strongly depends on the nature of the "A" cation. If the A-site in alkali niobates is replaced by Ag ion, it extends the light absorption to visible region and improves the photocatalytic efficiency of alkali niobates. $AgNbO_3$ has a band gap of 2.7 eV, and thus it absorbs visible light. Wu et al. synthesized microcrystalline $AgNbO_3$ photocatalysts as a visible light photocatalyst for the photocatalytic decomposition of cationic dyes such as rhodamine B and methyl blue [152].

Sun et al. synthesized BiOI/$NaNbO_3$ p–n junction photocatalyst at low temperature by using a facile chemical bath method. The photocatalytic activity of the BiOI/$NaNbO_3$ composites was investigated for the degradation of MB under visible light irradiation [153]. $NaNbO_3$ with cubic crystal structure photocatalyst was synthesized by Chen et al. via a convenient solvothermal method and then Ru nanoparticles were added to it by photo-deposition technique. The photocatalytic activity of Ru/$NaNbO_3$ composite was exhibited outstanding performance for the degradation of RhB under visible light irradiation than that of naked and Ru-doped $NaNbO_3$ [154]. For the photodegradation of methylene blue (MB), Wang et al. fabricated cubic $NaNbO_3$ (c-$NaNbO_3$) photocatalyst at 350 °C by a surface ligand-assisted localized crystallization (SLALC) method. They found that the as-synthesized c-$NaNbO_3$ nanoparticles could adsorb 95% of methylene blue in 3 min and photodegrades 99.3% of methylene blue (MB) in 180 min [155]. Liu et al. investigated and compared wire- and cube-like $NaNbO_3$ perovskite catalysts with Pt loading for photocatalytic H_2 production and organic-pollutant degradation. It was found that after the incorporation of Pt NPs, the Pt/$NaNbO_3$ systems exhibited noticeably higher performance due to the better light absorption and the improved separation capability of photogenerated electron–hole pairs [156]. Liu et al. synthesized single-crystalline $NaNbO_3$ with wire- and cube-like morphology by a facile and eco-friendly route including a hydrothermal as well as in-site self-assembled process via optimizing thermal treatment temperature. Photocatalytic activity of as-synthesized samples was measured in the photocatalytic water splitting of H_2 under solar light irradiation. They have found that the photocatalytic activity of $NaNbO_3$ with wire morphology showed the highest H_2 evolution rate (330.3 μmol/g) among all the studied samples. The enhanced photoactivity of $NaNbO_3$ was mainly due to the good crystallinity, fewer defects, and perfect 1D nanowire morphology [157]. The research group led by Li et al. used a polymerized complex method to prepare three $NaNbO_3$ samples that structurally differed from each other: cubic and orthorhombic and mixed cubic–orthorhombic. The sample that consisted of mixed-phase $NaNbO_3$ showed the highest activity in CO_2 reduction to CH_4. The authors explained the enhanced catalytic activity was attributed to the cubic–orthorhombic surface junctions which improved the charge separation [158]. The design of composite photocatalysts, in particular with

graphitic carbon (g–C_3N_4), has recently become most popular in research into the photocatalytic properties of niobate-based semiconductors. Shi et al. used this route to modify the photocatalytic properties of $NaNbO_3$/$KNbO_3$ semiconductors. They prepared g–C_3N_4/$NaNbO_3$ nanowire heterojunction photocatalyst via introducing polymeric g–C_3N_4 on $NaNbO_3$ nanowires (prepared by hydrothermal method) tested their photoactivity in reduction of CO_2 to CH_4 under visible light irradiation. They found that the g–C_3N_4/$NaNbO_3$ heterojunction exhibits the best photocatalytic performance than that of individual g–C_3N_4 and $NaNbO_3$ [159]. Similarly, Shi and his co-workers reported the photocatalytic reduction of CO_2 to CH_4 under visible light illumination, using g–C_3N_4/$KNbO_3$ composites as catalysts. The g–C_3N_4/$KNbO_3$ composite had more photocatalytic activity for CO_2 reduction to CH_4 as compared to pure g–C_3N_4 and $KNbO_3$ under similar reaction conditions [160].

Potassium niobate, $KNbO_3$, has also been reported as a UV light sensitive photocatalyst because of its wide band gap energy (3.14 eV). Raja et al. prepared Bi-doped $KNbO_3$ powders by the solid-state reaction by varying the ratio of K/Bi in starting materials and tested their photocatalytic activity in the degradation of methyl orange (MO) aqueous solution under UV light. They found that the photocatalytic degradation of Bi-doped $KNbO_3$ was 2.25-fold higher than that of pure $KNbO_3$ and this can due to increased BET surface area, crystallite size, and band gap alteration of the $K_{1-x}Bi_xNbO_3$ [161].

Zhang et al. reported the photocatalytic H_2 evolution from aqueous methanol with a micro-cubic structured potassium niobate ($KNbO_3$) semiconductor system under the illumination of visible light [162]. Nitrogen doping is an effective method for modifying light absorption behavior of wide band gap semiconductors. In view of this, N-doped $NaNbO_3$ nanocube structured powders were obtained by Wang et al. by applying a simple hydrothermal method. The photocatalytic activity of the N-doped $KNbO_3$ and pure $KNbO_3$ has been evaluated by photocatalytic water splitting as well as degradation of four organic contaminants (rhodamine B, orange G, bisphenol A, and pentachlorophenol) under visible light irradiation [163]. Hong et al. established a visible-light-driven photocatalytic system comprised of potassium niobate microspheres and reduced graphene oxide ($KNbO_3$/RGO) for hydrogen evolution. The hybrid nanocomposite ($KNbO_3$/RGO) exhibited the highest H_2 evolution rate compared to pure potassium niobate microspheres. This enhanced photocatalytic efficiency was attributed mainly to the proficient separation of photogenerated carriers at the heterojunction of two dissimilar semiconductors [164]. We have provided a Table 1 containing the photocatalytic activity results of recently published literatures (Years: 2015–2018) on ABO_3-type photocatalysts.

Table 1 Photocatalytic activity results of recently published (Years: 2015–2018) ABO_3 type photocatalysts

Sample	Preparative conditions	Photocatalytic reaction	Light source	References
Hetero-structured $LaFeO_3$/g–C_3N_4	Quasi-polymeric calcination method with the aid of electrostatic self-assembly interaction	Degradation of brilliant blue (BB)	300 W Xenon lamp with an UV cutoff filter ($\lambda > 420$ nm)	[43]
Cu-substituted $LaFeO_3$	Citrate auto-combustion	Degradation of 2-propanol	1500 W high-pressure Xenon lamp	[78]
Mn-substituted $LaFeO_3$	Sol–gel auto-combustion method	H_2O_2-assisted degradation of cationic and anionic dyes	Visible light	[79]
Transition metals (M = Cr^{3+}, Co^{2+}, Ni^{2+}, Cu^{2+} and Zn^{2+}) doped $LaMn_{0.2}Fe_{0.8}O_3$	Sol–gel auto-combustion route	H_2O_2-assisted degradation of cationic and anionic dyes	Visible light	[80]
$LaFeO_3$	Gel combustion method	Reduction of Cr(VI) in aqueous solution	Visible light (wavelength longer than 420 nm)	[81]
$LaFeO_3$	Solution combustion synthesis	Photocatalytic conversion of glucose to H_2	UV–LEDs (nominal power: 10 W) with wavelength emission in the range 375–380 nm	[82]
$LaFeO_3$–reduced graphene oxide nanoparticles (rGO NPs)	Reduced graphene oxide (rGO) as a template and high-temperature sol–gel method	Degradation of methylene blue (MB) or rhodamine B (RhB)	300 W xenon arc lamp with a UV-cutoff filter ($\lambda > 400$ nm)	[83]
ZnO/Bi-doped porous $LaFeO_3$ nanocomposites	Wet chemical method	2,4-dichlorophenol (2,4-DCP) degradation and CO_2 conversion	150 W GYZ220 high-pressure Xenon lamp $\lambda = 420$ nm	[84]
PdO/$LaCoO_3$ heterojunction	Sol–gel and deposition precipitation method	Hydrogen production from formaldehyde aqueous solution	125 W Xe lamp	[88]
$LaCoO_3$	Sugarcane bagasse hydrolysis by metal ions mediated process	Hydrogen production from formaldehyde solution	125 W Xe lamp	[90]
Cu-doped $LaCoO_3$	Microbial synthesis using the extract of Pichiapastoris GS115	Hydrogen production from formaldehyde solution	125 W Xe lamp	[91]

(continued)

Table 1 (continued)

Sample	Preparative conditions	Photocatalytic reaction	Light source	References
Ag-modified $LaCoO_3$	Hydrothermal method	Degradation of methylene blue (MB)	Sunlight	[92]
Porous $LaMnO_3$ sub-micron particles	Hydrothermal process	Degradation of rose bengal dye	150 W mercury lamp ($\lambda > 400$ nm)	[96]
$YbFeO_3$	Sol–gel process	Decomposition of methyl orange (MO)	150 W Xe lamp	[97]
$EuFeO_3$	One-step microwave route	Decomposition of methyl orange (MO)	Metal halogen lamp (150 W) equipped with a JB400 filter	[98]
$BaZrO_3$ modified with Cu_2O/Bi_2O_3 quantum dots	Hydrothermal process followed by chemical reduction	Phenol photodegradation process in the liquid phase under UV–Vis and toluene degradation in the gas phase under visible irradiation	High-pressure mercury lamp (Heraeus, 150 W) for liquid-phase reaction and An array of 5 Vis LEDs ($\lambda_{max} = 415$ nm) for gas-phase reaction	[105]
$SrZrO_3$ modified with Cu_2O/Bi_2O_3 quantum dots	Hydrothermal process followed by chemical reduction	Phenol photodegradation process in the liquid phase under UV–Vis and toluene degradation in the gas phase under Vis irradiation	High-pressure mercury lamp (Heraeus, 150 W) for liquid-phase reaction and An array of 5 Vis LEDs ($\lambda_{max} = 415$ nm) for gas-phase reaction	[105]
Au/$SrTiO_3$ nanocomposites with different Au contents	Photocatalytic reduction method	Degradation of acid orange 7 and methyl orange (MO)	Sunlight (200 W xenon lamp) and visible light ($\lambda = 420$ nm)	[110]
$SrTiO_3$ (La,Cr)-decorated WO_3 nanosheets	Sol–gel hydrothermal method	Degradation of methylene blue (MB)	Visible light (300 W Xe lamp; $\lambda = 420$ nm)	[111]
$SrTi_{1-x}Rh_xO_3$	Hydrothermal synthesis	Degradation of methyl orange (MO)	Visible light (300 W Xe lamp (Oriel); $\lambda > 420$ nm)	[112]
$TiO_2/SrTiO_3$ nanocomposite	Sol–gel method	Degradation of 4-Nitrophenol (4-NP)	UV light (medium pressure Hg vapor lamp of 125 W)	[113]
$SrTiO_3$	Polymerizable sol–gel (PSG) approach	Degradation of methylene blue (MB)	UV light (medium pressure Hg vapor lamp of 125 W)	[109]

(continued)

Table 1 (continued)

Sample	Preparative conditions	Photocatalytic reaction	Light source	References
$SrTiO_3$	Polymeric precursor method	Degradation of methylene blue (MB), rhodamine B (RhB) and methyl orange (MO)	UV illumination (UV lamps (TUV Philips, 15-W; λ = 254 nm)	[114]
Al-doped $SrTiO_3$	Molten-salt synthesis	Decomposition of water to H_2 production	Sunlight	[115]
Au/Al–$SrTiO_3$ heterojunction	Solid-state reaction	Hydrogen production using sacrificial agents	Visible light (150 W xenon lamp)	[116]
Mg-modified $SrTiO_x$	Solid-state method	Hydrogen production	Solar light (AM 1.5 G solar simulator; λ = 300–900 nm)	[117]
Co, Fe, and Ni-doped $SrTiO_3$	Combined hydrothermal and solid-state reaction	CO_2 reduction to CH_4	Visible light (300 W Xe lamp; λ > 420 nm)	[118]
Different $SrTiO_3$	Hydrothermal method	CO_2 reduction with H_2O vapor	Visible light (300 W Xe lamp)	[119]
Rh and Au co-loaded $SrTiO_3$	Photo-deposition process	CO_2 reduction with H_2O vapor to syngas	Visible light (300 W Xe lamp; λ > 400 nm)	[120]
$Cu_xO/SrTiO_3$ nanorod thin films	Hydrothermal method	CO_2 reduction using H_2O to CO	UV light (Hg–Xe lamp, LA-410 UV)	[121]
$CaTiO_3$	Hydrothermal route	Degradation of rhodamine B (RhB)	Simulated sunlight, and Visible light	[126]
g–C_3N_4–$CaTiO_3$	Facile mixing method	Degradation of rhodamine B (RhB)	UV (Luzchem LZC 4 V UV irradiation chamber equipped with 12 UV lamps (λ = 365 nm), visible (two 14 W white light LED bulbs), and natural sunlight irradiation	[127]
$CaTiO_3$ nanocuboids	Hydrothermal approach	Degradation of rhodamine B (RhB)	Simulated sunlight (200 W Xe lamp)	[128]
Orthorhombic $CaTiO_3$	Solid-state, sol–gel, and hydrothermal methods	Degradation of methylene blue (MB)	Visible light (500 W Hg lamp)	[129]
Core–shell structured CaTiO3@basalt fiber	Modified hydrothermal method	CO_2 reduction with H_2O into CH_4 and CO	UV light (6.0 W/cm^2 mercury lamps (365 nm)	[131]

(continued)

Table 1 (continued)

Sample	Preparative conditions	Photocatalytic reaction	Light source	References
$CaTiO_3$@basalt fiber (BF)	Flux method	CO_2 reduction with H_2O into CH_4 and CO	UV to visible light (300 W xenon lamp)	[132]
$BaTiO_3$–SnO_2	Hydrothermal and precipitation deposition method	O-Chloroaniline and methylene blue (MB)	Visible light (300 W Xe arc lamp; $\lambda > 420$ nm)	[133]
Mn-doped $BaTiO_3$ nanotube arrays	Hydrothermal method	Degradation of Methylene blue (MB) dye	Visible light (300 W Tungsten lamp)	[134]
$BaTiO_3$	Microwave-assisted peroxo route	Degradation of methylene blue, malachite green, and alizarin red S	UV light (6 W Hg lamp)	[135]
W and N co-doped $NaTaO_3$	NaOH flux method	Degradation of rhodamine B (RhB)	Visible light (300 W xenon lamp; $\lambda > 400$ nm)	[138]
La/Bi co-doped NaTaO3	Hydrothermal synthesis	Degradation of methylene blue (MB)	Visible light (250 W high-pressure Hg lamp)	[139]
Sulfur-doped $NaTaO_3$	Hydrothermal process	Degradation of methyl orange (MO) and phenol	UV (8-W Hg lamp and Visible light (250 W Hg lamp)	[140]
La-doped $NaTaO_3$	Solid-state method	H_2 evolution	UV light (high-pressure Hg lamp (I_0 = 2 $mW{\cdot}cm^{-2}$)	[143]
La-doped $KTaO_3$	Hydrothermal technology	Degradation of methyl orange (MO)	UV light (300 W lamp)	[144]
Mono- and bimetallic noble metals decorated $KTaO_3$	Hydrothermal reaction	Decomposition of phenol solution, removal of gaseous toluene, and H_2 production in the presence of formic acid solution	Visible (1000 W Xe lamp) or UV–Vis light irradiation (250 W Xe lamp)	[145]
rGO–$KTaO_3$ hybrid composite	Hydrothermal method	Degradation of phenol solution	Visible–light (1000 W Xe lamp)	[146]
Carbon-doped $KTaO_3$	Combination of hydrothermal and calcination process	H_2 generation	Simulated sunlight (300 W Xe lamp)	[147]
CuO-patched cubic $NaTaO_3$	Hydrothermal synthesis followed by phase-transfer protocol and solvothermal method	CO_2 reduction to CH_3OH in isopropanol	250 W high-pressure mercury lamp	[148]

(continued)

Table 1 (continued)

Sample	Preparative conditions	Photocatalytic reaction	Light source	References
Mg-, Ca-, Sr-, Ba-, and La-doped $NaTaO_3$	Solid-state method	CO_2 reduction to CO using water as an electron donor	400 W high-pressure Hg lamp	[149]
$KTaO_3$ and NiOx/$KTaO_3$	Hydrothermal method followed by impregnation method	Reduction of CO_2 to methanol in isopropanol	UV light (250 W high-pressure mercury lamp; λ = 365 nm)	[150]
$NaNbO_3$ and $NaTaO_3$	Solid-state reaction	Reduction of CO_2 to $CO/H_2/CH_3OH/CH_4$ (CO was the major product)	UV light (four UV fluorescent lamps of 6 W; λ = 365 nm)	[152]
BiOI/$NaNbO_3$ p–n junction	Chemical bath method	Methylene blue (MB)	Visible light (500 W Xe lamp)	[154]
Ru/$NaNbO_3$ nanocomposite	Solvothermal method followed by photo-deposition technique	rhodamine (RhB)	Visible light (500 W Xe arc lamp (420 nm < λ < 800 nm)	[155]
Cubic phase $NaNbO_3$	Surface ligand-assisted localized crystallization (SLALC) method	Methylene blue (MB)	UV to Visible (100 W Hg arc lamp; λ = 365–600 nm)	[156]
Pt/$NaNbO_3$	Hydrothermal method combined with the photo-deposition	H_2 production by water/methanol mixture and degradation of rhodamine B (RhB) and 4-chlorophenol (CP)	Mimic sunlight irradiation and visible light (300 W Xe arc lamp)	[157]
Single-crystalline $NaNbO_3$	Hydrothermal treatment	Water splitting of H_2	300 W Xe arc lamp	[158]
g–C_3N_4/$NaNbO_3$	Ultrasonic dispersion followed by heat treatment method	Reduction of CO_2 to CH_4	300 W Xe arc lamp	[161]
Bi-doped $KNbO_3$	Solid-state reaction	Methyl orange (MO)	UV light (λ = 254 nm)	[162]

5 Conclusions and Insights

Perovskite oxides with the composition ABO_3 offer ample scope in designing novel compounds by the partial substitution of metal cations in A- and B-sites, which allows the preparation of isostructural series with different physical/chemical properties. The arrangement and position of the metal ions should be taken into consideration to understand the physical properties of perovskites. From the photocatalytic point of view, these perovskite materials have a special structural feature that is beneficial to photocatalytic activity. The relationship between crystal structure and energy delocalization shows that the closer to 180° the B–O–B bond angle is, the easier the excitation energy is delocalized leading to higher photoactivity. Thus, the bond angle between metal–oxygen–metal (B–O–B) in perovskite oxide is a significant structural parameter and must be taken into account. The modification of the electronic structure of a perovskite by dopants into its lattice is an effective way to affect its photocatalytic properties. However, more efforts needed to clarify the relationship between electronic structure and photocatalytic activity to develop novel perovskites with efficient photocatalytic activity. Other than band gap energy, crystallite size, and surface area, the vacancy of a metal cation and O^{2-} anions play important roles in the photocatalytic performance of perovskites oxides. The selection of preparative method also plays a significant role in the photocatalytic performance. A traditional method like high-temperature solid-state reaction results in the destruction of pore structures, and hence too low surface areas. Hence, controlled preparation of porous perovskite materials with a high surface area is highly desirable. The strategies as discussed are widely used to enhance the photocatalytic performance of perovskites. But the literature available on the adverse effect of such methods is limited. This should be considered appropriately in future.

Acknowledgements Authors would like to acknowledge CSIR, New Delhi under the CSIR-scheme (No. 01(2857)/16/EMR-II) for their financial support. PV thanks University Grants Commission (UGC)-Dr. D. S. Kothari Postdoctoral Fellowship (DSKPDF) Scheme, New Delhi for his postdoctoral research fellowship. MV thanks UGC New Delhi for the award of BSR fellowship.

References

1. Rao AN, Sivasankar B, Sadasivam V (2009) Kinetic studies on the photocatalytic degradation of Direct Yellow 12 in the presence of ZnO catalyst. J Mol Catal A Chem 306:77–81
2. Rauf MA, Ashraf SS (2009) Radiation induced degradation of dyes—an overview. J Hazard Mater 166:6–16
3. Akyol A, Bayramoglu M (2008) The degradation of an azo dye in a batch slurry photocatalytic reactor. Chem Eng Process 47:2150–2156

4. Ohtani B (2010) Photocatalysis A to Z—what we know and what we do not know in a scientific sense. J Photochem Photobiol C 11:157–178
5. Bahnemann D (2004) Photocatalytic water treatment: solar energy applications. Sol Energy 77:445–459
6. Zhang D, Li G, Li H et al (2013) The development of better photocatalysts through composition- and structure-engineering. Chem Asian J 8:26–40
7. Ch Samuel H S, Ta YW, Ch Juan J (2011) Recent developments of metal oxide semiconductors as photocatalysts in advanced oxidation processes (AOPs) for treatment of dye waste-water. J Chem Technol Biotechnol 86:1130–1158
8. Marye AF, Maria TD (1995) Heterogeneous photocatalysis. Chem Rev 83:341–357
9. Rauf MA, Ashraf SS (2009) Fundamental principles and application of heterogeneous photocatalytic degradation of dyes in solution. Chem Eng J 151:10–18
10. Krishnan R, Abegayl T, Csaba J (2015) Photocatalytic activity of inorganic semiconductor surfaces: myths, hype, and reality. J Phys Chem Lett 6:139–147
11. Fujishima A, Honda K (1972) Electrochemical photolysis of water at a semiconductor electrode. Nature 238:37–38
12. Chen X, Shen S, Guo L et al (2010) Semiconductor-based photocatalytic hydrogen generation. Chem Rev 110:6503–6570
13. Chen X, Mao SS (2007) Titanium dioxide nanomaterials: synthesis, properties, modifications, and applications. Chem Rev 107:2891–2959
14. Ji PF, Takeuchi M, Cuong TM et al (2010) Recent advances in visible light-responsive titanium oxide-based photocatalysts. Res Chem Intermed 36:327–347
15. Kato H, Kudo A (2002) Visible-light-response and photocatalytic activities of TiO_2 and $SrTiO_3$ photocatalysts co-doped with Antimony and Chromium. J Phys Chem B 106:5029–5034
16. Liu JW, Chen G, Li ZH et al (2006) Electronic structure and visible light photocatalysis water splitting property of chromium-doped $SrTiO_3$. J Solid State Chem 179:3704–3708
17. Hwang DW, Kim HG, Lee JS et al (2005) Photocatalytic hydrogen production from water over M-Doped $La_2Ti_2O_7$ (M = Cr, Fe) under visible light irradiation ($\lambda > 420$ nm). J Phys Chem B 109:2093–2102
18. Asahi R, Morikawa T, Ohwaki T et al (2001) Visible-light photocatalysis in nitrogen-doped titanium oxides. Science 293:269–271
19. Zaleska A, Grabowska E, Sobczak JW et al (2009) Photocatalytic activity of boron-modified TiO_2 under visible light: The effect of boron content, calcination temperature and TiO_2 matrix. Appl Catal B 89:469475
20. Paven-Thivet CL, Ishikawa A, Ziani A et al (2009) Photoelectrochemical properties of crystalline perovskite lanthanum titanium oxynitride films under lisible light. J Phys Chem C 113:6156–6162
21. Lu D, Hitoki G, Katou E et al (2004) Porous single-crystalline TaON and Ta_3N_5 particles. Chem Mater 16:1603–1605
22. Yashima M, Lee Y, Domen K (2007) crystal structure and electron density of tantalum oxynitride, a visible light responsive photocatalyst. Chem Mater 19:588–593
23. Li X, Kikugawa N, Ye J (2008) Nitrogen-doped lamellar niobic acid with visible light-responsive photocatalytic activity. Adv Mater 20:3816–3819
24. Matsumoto Y, Koinuma M, Iwanaga Y et al (2009) N-doping of oxide nanosheets. J Am Chem Soc 131:6644–6645
25. Luo M, Lu P, Yao W et al (2016) Shape and composition effects on photocatalytic hydrogen production for Pt–Pd Alloy co-catalysts. ACS Appl Mater Interfaces 8:20667–20674
26. Qin J, Zeng H (2017) Photocatalysts fabricated by depositing plasmonic Ag nanoparticles on carbon quantum dots/graphitic carbon nitride for broad spectrum photocatalytic hydrogen generation. Appl Catal B 209:161–173
27. Rather RA, Singh S, Pal B (2017) A C_3N_4 surface passivated highly photoactive Au–TiO_2 tubular nanostructure for the efficient H_2 production from water under sunlight irradiation. Appl Catal B 213:9–17

28. Jiang Y, Guo S, Hao R et al (2016) A hybridized heterojunction structure between TiO_2 nanorods and exfoliated graphitic carbon-nitride sheets for hydrogen evolution under visible light. Cryst Eng Commun 18:6875–6880
29. Tay Q, Wang X, Zhao X et al (2016) Enhanced visible light hydrogen production via a multiple heterojunction structure with defect-engineered g–C_3N_4 and twophase anatase/brookite TiO_2. J Catal 342:55–62
30. Yu X, Li W, Li Z et al (2017) Defect engineered Ta_2O_5 nanorod: One-pot synthesis, visible-light driven hydrogen generation and mechanism. Appl Catal B 217:48–56
31. Hirakawa H, Hashimoto M, Shiraishi Y et al (2017) Selective nitrate-to-ammonia transformation on surface defects of titanium dioxide photocatalysts. ACS Catal 7:3713–3720
32. Chen P, Qin M, Chen Z et al (2016) Solution combustion synthesis of nanosized WOx: characterization, mechanism and excellent photocatalytic properties. RSC Adv 6:83101–83109
33. Bao N, Shen L, Takata T et al (2008) Self-templated synthesis of nanoporous CdS nanostructures for highly efficient photocatalytic hydrogen production under visible light. Chem Mater 20:110–117
34. Yan H, Yang J, Ma G et al (2009) Visible-light-driven hydrogen production with extremely high quantum efficiency on Pt–PdS/CdS photocatalyst. J Catal 266:165–168
35. Borgarello E, Kiwi J, Pelizzetti E et al (1981) Sustained water cleavage by visible light. J Am Chem Soc 103:6324–6329
36. Chen F, Deng Z, Li X et al (2005) Visible light detoxification by 2,9,16,23-tetracarboxyl phthalocyanine copper modified amorphous titania. Chem Phys Lett 415:85–88
37. Nguyen TV, Wu JCS, Chiou CH (2008) Photoreduction of CO_2 over Ruthenium dye-sensitized TiO_2-based catalysts under concentrated natural sunlight. Catal Commun 9:2073–2076
38. Tyagi M, Tomar M, Gupta V (2014) Fabrication of an efficient GLAD-assisted p–NiO nanorod/n–ZnO thin film heterojunction UV photodiode. J Mater Chem C 2:2387–2393
39. Schuster F, Laumer B, Zamani RR et al (2014) p–GaN/n–ZnO heterojunction nanowires: optoelectronic properties and the role of interface polarity. ACS Nano 8:4376–4384
40. Luan P, Xie MZ, Fu XD et al (2015) Improved photoactivity of TiO_2–Fe_2O_3 nanocomposites for visible-light water splitting after phosphate bridging and its mechanism. Phys Chem Chem Phys 17:5043–5050
41. Xie MZ, Fu XD, Jing LQ et al (2014) Long-lived, visible-light-excited charge carriers of TiO_2/$BiVO_4$ nanocomposites and their unexpected photoactivity for water splitting. Adv Energy Mater 4:1300995
42. Humayun M, Zada A, Li ZJ et al Enhanced visible-light activities of porous $BiFeO_3$ by coupling with nanocrystalline TiO_2 and mechanism. Appl Catal B 180:219–226
43. Yan W, Hou W, Wenguang T et al (2018) Quasi-polymeric construction of stable perovskite-type $LaFeO_3$/g–C_3N_4 heterostructured photocatalyst for improved Z-scheme photocatalytic activity via solid p-n heterojunction interfacial effect. J Hazard Mater 347:412–422
44. Tanaka H, Misono M (2001) Advances in designing perovskite catalysts. Curr Opin Solid State Mater Sci 5:381–387
45. Cheong SW, Mostovoy M (2007) Multiferroics: a magnetic twist for ferroelectricity. Nat Mater 6:13–20
46. Pickett WE, Singh DJ (1996) Electronic structure and half-metallic transport in the $La_{1-x}Ca_xMnO_3$ system. Phys Rev B 53:1146
47. Kobayashi KI, Kimura T, Sawada H et al (1998) Room-temperature magnetoresistance in an oxide material with an ordered double-perovskite structure. Nature 395:677–680
48. Cava RJ, Batlogg B, Krajewski JJ et al (1988) Superconductivity near 30 K without copper: the $Ba_{0.6}K_{0.4}BiO_3$ perovskite. Nature 332:814–816
49. Bhalla AS, Guo R, Roy R (2000) The perovskite structure–a review of its role in ceramic science and technology. Mater Res Innov 4:3–26

50. Huang YH, Dass RI, Xing ZL et al (2005) Double perovskites as anode materials for solid-oxide fuel cells. Science 312:254–257
51. Green MA, Ho-Baillie A, Snaith HJ (2014) The emergence of perovskite solar cells. Nat Photonics 8:506–514
52. Wiegel M, Emond MHJ, Stobbe ER et al (1994) Luminescence of alkali tantalates and niobates. J Phys Chem Solids 55:773–778
53. Kudo A, Kato H, Nakagawa S (2000) Water splitting into H_2 and O_2 on new $Sr_2M_2O_7$ (M = Nb and Ta) photocatalysts with layered perovskite structure: factors affecting the photocatalytic activity. J Phys Chem B 104:571–575
54. Ewelina G (2016) Selected perovskite oxides: characterization, preparation and photocatalytic properties—a review. Appl Catal B 186:97–126
55. Guan Z, Gang L, Lianzhou W et al (2016) Inorganic perovskite photocatalysts for solar energy utilization. Chem Soc Rev 45:5951–5984
56. Sheng Z, Piyush K, Ujwal Kumar T et al (2018) A Review on photocatalytic CO_2 reduction using perovskite oxide nanomaterials. Nanotechnology 29:052001
57. Pushkar K, Zhong Ch (2014) Review on visible light active perovskite-based photocatalysts. Molecules 19:19995–20022
58. Saumyaprava A, Satyabadi M, Prakash ChS et al (2015) Glimpses of the modification of perovskite with graphene-analogous materials in photocatalytic applications. Inorg Chem Front 2:807–823
59. Jinwen S, Liejin G (2012) ABO_3-based photocatalysts for water splitting. Prog Nat Sci Mater Int 22:592–615
60. Wei W, Moses OT, Zongping S (2015) Research progress of perovskite materials in photocatalysis- and photovoltaics-related energy conversion and environmental treatment. Chem Soc Rev 44:5371–5408
61. Zhu J, Li H, Zhong L et al (2014) Perovskite oxides: preparation, characterizations, and applications in heterogeneous catalysis. ACS Catal 4:2917–2940
62. Shi R, Waterhouse GIN, Tierui Z (2017) Recent progress in photocatalytic CO_2 reduction over perovskite oxides. Sol. RRL 1:1700126–1700143
63. Koferstein R, Jager L, Ebbinghaus SG (2013) Magnetic and optical investigations on $LaFeO_3$ powders with different particle sizes and corresponding ceramics. Solid State Ionics 249–250:1–5
64. Arima T, Tokura Y, Torrence JB (1993) Variation of optical gaps in perovskite-type 3d transition-metal oxides. Phys Rev B 48:17006–17009
65. Xu JJ, Wang ZL, Xu D et al (2014) 3D ordered macroporous $LaFeO_3$ as efficient electrocatalyst for Li–O_2 batteries with enhanced rate capability and cyclic performance. Energy Environ Sci 7:2213–2219
66. Jauhar S, Singhal S (2014) Chromium and copper substituted lanthanum nanoferrites: their synthesis, characterization and application studies. J Mol Struct 1075:534–541
67. Sivakumar M, Gedanken A, Zhong W et al (2004) Sonochemical synthesis of nanocrystalline $LaFeO_3$. J Mater Chem 14:764–769
68. Popa M, Moreno JMC (2011) Lanthanum ferrite ferromagnetic nanocrystallites by a polymeric precursor route. J Alloy Compd 509:4108–4116
69. Li S, Wang X (2015) Synthesis of different morphologies lanthanum ferrite ($LaFeO_3$) fibers via electrospinning. Optik 126:408–410
70. Thirumalairajan S, Girija K, Hebalkar NY et al (2013) Shape evolution of perovskite $LaFeO_3$ nanostructures: a systematic investigation of growth mechanism, properties and morphology dependent photocatalytic activities. RSC Adv 3:7549–7561
71. Thirumalairajan S, Girija K, Ganesh I et al (2012) Controlled synthesis of perovskite $LaFeO_3$ microsphere composed of nanoparticles via self-assembly process and their associated photocatalytic activity. Chem Eng J 209:420–428
72. Li FT, Liu Y, Liu RH et al (2010) Preparation of Ca-doped $LaFeO_3$ nanopowders in a reverse microemulsion and their visible light photocatalytic activity. Mater Lett 64:223–225

73. Dong S, Xu K, Tian G (2009) Photocatalytic activities of $LaFe_{1-x}Zn_xO_3$ nanocrystals prepared by sol–gel auto-combustion method. J Mater Sci 44:2548–2552
74. Hou L, Sun GF, Liu K et al (2006) Preparation, characterization and investigation of catalytic activity of Li-doped $LaFeO_3$ nanoparticles. J Sol–Gel Sci Technol 40:9–14
75. Wei ZX, Wang Y, Liu JP et al (2012) Synthesis, magnetization and photocatalytic activity of $LaFeO_3$ and $LaFe_{0.5}Mn_{0.5-x}O_{3-\delta}$. Mater Chem Phys 136:755–761
76. Natali Sora I, Caronna T, Fontana F et al (2012) Crystal structures and magnetic properties of strontium and copper doped lanthanum ferrites. J Solid State Chem 191:33–39
77. Parrino F, García-Lopez E, Marcìa G et al (2016) Cu-substituted lanthanum ferrite perovskites: preparation, characterization and photocatalytic activity in gas-solid regime under simulated solar light irradiation. J Alloy Compd 682:686–694
78. Jauhar S, Dhiman M, Bansal S et al (2015) Mn^{3+} ion in perovskite lattice: a potential Fenton's reagent exhibiting remarkably enhanced degradation of cationic and anionic dyes. J Sol Gel Sci Technol 75:124–133
79. Dhiman M, Tripathi M, Singhal S et al (2017), Structural, optical and photocatalytic properties of different metal ions (Cr^{3+}, Co^{2+}, Ni^{2+}, Cu^{2+} and Zn^{2+}) substituted quaternary perovskites. Mater Chem Phys 202:40–49
80. Xicai H, Yongcai Z (2017) Low temperature gel-combustion synthesis of porous nanostructure $LaFeO_3$ with enhanced visible-light photocatalytic activity in reduction of Cr(VI). Mater Lett 197:120–122
81. Giuseppina I, Vincenzo V, Diana S et al (2016) Photocatalytic conversion of glucose to H_2 over $LaFeO_3$ perovskite nanoparticles. Chem Eng Trans 47:283–288
82. Ren X, Yang HT, Gen S et al (2016) Controlled growth of $LaFeO_3$ nanoparticles on reduced graphene oxide for highly efficient photocatalysis. Nanoscale 8:752–756
83. Muhammad H, Ning S, Fazal R et al (2018) Synthesis of ZnO/Bi-doped porous $LaFeO_3$ nanocomposites as highly efficient nano-photocatalysts dependent on the enhanced utilization of visible-light-excited electrons. Appl Catal B 231:23–33
84. Ibrahim MN, Shaolong W, Liang L et al (2018) Facile preparation of n-Type $LaFeO_3$ perovskite film for efficient photoelectrochemical water splitting. ChemistrySelect 3:968–972
85. Hsish TH, Jhong FH, Roy DT et al (2012) Electrical properties of $(La_{0.9}Ca_{0.1})(Co_{1-x}Ni_x)O_{3-\delta}$ cathode materials for SOFCs. Ceram Int 38:1785–1791
86. Wang Y, Ren J, Wang Y et al (2008) Nanocasted synthesis of mesoporous $LaCoO_3$ perovskite with extremely high surface area and excellent activity in methane combustion. J Phys Chem C 112:15293–15298
87. Feng L, Okonkwo CA, Qiong X et al (2016) PdO/$LaCoO_3$ heterojunction photocatalysts for highly hydrogen production from formaldehyde aqueous solution under visible light. Int J Hydrogen Energy 41:6115–6122
88. Minghui W, Mingping L, Minxue G et al (2017) Sugarcane bagasse hydrolysis by metal ions mediated synthesis of perovskite $LaCoO_3$ and the photocatalytic performance for hydrogen from formaldehyde solution under visible light. ACS Sustainable Chem Eng 5:11558–11565
89. Malleshappa J, Nagabhushana H, Sharma SC et al (2015) Leucas aspera mediated multifunctional CeO_2 nanoparticles: structural, photoluminescent, photocatalytic and antibacterial properties. Spectrochim Acta Part A 149:452–462
90. Liqing W, Qi P, Qianqian S et al (2015) Novel microbial synthesis of Cu doped $LaCoO_3$ photocatalyst and its high efficient hydrogen production from formaldehyde solution under visible light irradiation. Fuel 140:267–274
91. Jayapandi S, Lakshmi D, Premkumar S et al (2018) Augmented photocatalytic and electrochemical activities of Ag tailored $LaCoO_3$ perovskite semiconductor. Mater Lett 218:205–208
92. Shaterian M, Enhessari M, Rabbani D et al (2014) Synthesis, characterization and photocatalytic activity of $LaMnO_3$ nanoparticles. Appl Surf Sci 318:213–217
93. Jie H, Jiahua M, Lina W et al (2014) Preparation, characterization and photocatalytic activity of co-doped $LaMnO_3$/graphene composites. Powder Technol 54:556–562

94. Mi Y, Zeng S, Li L et al (2012) Solvent directed fabrication of Bi_2WO_6 nanostructures with different morphologies: Synthesis and their shape-dependent photocatalytic properties. Mater Res Bull 47:2623–2630
95. Rajesh Kumar S, Abinaya CV, Amirthapandian S et al (2017) Enhanced visible light photocatalytic activity of porous $LaMnO_3$ sub-micron particles in the degradation of rose bengal. Mater Res Bull 93:270–281
96. Peisong T, Longlong Y, Jiayuan M et al (2017) Preparation of nanocrystalline $YbFeO_3$ by sol–gel method and its visible-light photocatalytic activities. Ferroelectrics 521:71–76
97. Peisong T, Chen H, Lv Chunyan et al (2017) Microwave synthesis of nanoparticulate $EuFeO_3$ and its visible light photocatalytic activity. Integr Ferroelectr 181:49–54
98. Yupeng Y, Xueliang Z, Lifei L et al (2008) Synthesis and photocatalytic characterization of a new photocatalyst $BaZrO_3$. Int J Hydrogen Energy 33:5941–5946
99. Yupeng Y, Zongyan Z, Jing Z et al (2010) Polymerizable complex synthesis of $BaZr_{1-x}Sn_xO_3$ photocatalysts: Role of Sn^{4+} in the band structure and their photocatalytic water splitting activities. J Mater Chem 20:6772–6779
100. Yupeng Y, Lv J, Jiang XJ et al (2007) Large impact of strontium substitution on photocatalytic water splitting activity of $BaSnO_3$. Appl Phys Lett 91:094107
101. Borse PH, Joshi UA, Ji SM et al (2007) Band gap tuning of lead-substituted $BaSnO_3$ for visible light photocatalysis. Appl Phys Lett 90:034103
102. Borja-Urby R, Díaz-Torres LA, Salas P et al (2011) Structural study, photoluminescence, and photocatalytic activity of semiconducting BaZrO3: Bi nanocrystals. J Mater Sci Eng B 176:1382–1387
103. Ziyauddin K, Mohammad Q (2012) Tantalum doped $BaZrO_3$ for efficient photocatalytic hydrogen generation by water splitting. Catal Commun 28:82–85
104. Kazuhiko M, Kazunari D (2012) Water oxidation using a particulate $BaZrO_3$–$BaTaO_2N$ solid-solution photocatalyst that operates under a wide range of visible light. Angew Chem Int Ed 51:9865–9869
105. Magdalena M, Beata B, Paweł M et al (2017) Preparation and photocatalytic properties of $BaZrO_3$ and $SrZrO_3$ modified with Cu_2O/Bi_2O_3 quantum dots. Solid State Sci 74:13–23
106. Alammar T, Hamm I, Wark M, Mudring A-V et al (2015) Low-temperature route to metal titanate perovskite nanoparticles for photocatalytic applications. Appl Catal B 178:20–28
107. Zhu S, Salvador PA, Rohrer GS et al (2017) Controlling the termination and photochemical reactivity of the $SrTiO_3$ (110) surface. Phys Chem Chem Phys 19:7910–7918
108. da Silva LF, Lopes OF, de Mendonca VR, Carvalho KTG, Longo E, Ribeiro C, Mastelaro VR et al (2016) An understanding of the photocatalytic properties and pollutant degradation mechanism of $SrTiO_3$ nanoparticles. Photochem Photobiol 9:371–378
109. Xian T, Di L, Sun X, Ma J, Zhou Y, Wei X et al (2018) Photocatalytic degradation of dyes over Au decorated $SrTiO_3$ nanoparticles under simulated sunlight and visible light irradiation. J Ceram Soc Jpn 126:354–359
110. Liu X, Jiang J, Jia Y, Qiu J, Xia T, Zhang Y, Li Y, Chen X et al (2017) Insight into synergistically enhanced adsorption and visible light photocatalytic performance of Z-scheme heterojunction of SrTiO3(La, Cr)-decorated WO_3 nanosheets. Appl Surf Sci 412:279–289
111. Kiss B, Manning TD, Hesp D et al (2017) Nano-structured rhodium doped $SrTiO_3$-Visible light activated photocatalyst for water decontamination. Appl Catal B 206:547–555
112. Devi LG, Anitha BG (2018) Exploration of vectorial charge transfer mechanism in TiO_2/$SrTiO_3$ composite under UV light illumination for the degradation of 4-Nitrophenol: a comparative study with TiO_2 and $SrTiO_3$. Surf Interfaces 11:48–56
113. Challagulla S, Nagarjuna R, Roy S et al (2017) Scalable free-radical polymerization based sol–gel synthesis of $SrTiO_3$ and its photocatalytic activity. ChemistrySelect 2:4836–4842
114. Goto Y, Hisatomi T, Wang Q et al (2018) A particulate photocatalyst water-splitting panel for large-scale solar hydrogen generation. Joule 2:509–520
115. Saadetnejad D, Yıldırım R (2018) Photocatalytic hydrogen production by water splitting over Au/Al–$SrTiO_3$. Int J Hydrogen Energy 43:1116–1122

116. Han K, Lin YC, Yang CM et al (2017) Promoting photocatalytic overall water splitting by controlled magnesium incorporation in $SrTiO_3$ photocatalysts. Chem Sus Chem 10:4510–4516
117. Kou J, Gao J, Li Z et al (2015) Construction of visible-light-responsive $SrTiO_3$ with enhanced CO_2 adsorption ability: highly efficient photocatalysts for artifical photosynthesis. Catal Lett 145:640–646
118. Luo C, Zhao J, Li Y et al (2018) Photocatalytic CO_2 reduction over $SrTiO_3$: correlation between surface structure and activity. Appl Surf Sci 447:627–635
119. Li D, Ouyang S, Xu H et al (2016) Synergistic effect of Au and Rh on $SrTiO_3$ in significantly promoting visible-light-driven syngas production from CO_2 and H_2O. Chem Commun 52:5989–5992
120. Shoji S, Yin G, Nishikawa M et al (2016) Photocatalytic reduction of CO_2 by Cu_xO nanocluster loaded $SrTiO_3$ nanorod thin film. Chem Phys Lett 658:309–314
121. Pan JH, Cai ZC, Yu Y, Zhao XS (2011) Controllable synthesis of mesoporous F–TiO_2 spheres for effective photocatalysis. J Mater Chem 21:11430–11438
122. Yang D, Sun YY, Tong ZW, Nan YH, Jiang ZY (2016) Fabrication of bimodal-pore $SrTiO_3$ microspheres with excellent photocatalytic performance for Cr(VI) reduction under simulated sunlight. J Hazard Mater 312:45–54
123. Dong Y, Xiaoyan Z, Yuanyuan S, Zhenwei T, Zhongyi J (2018) Fabrication of three-dimensional porous La-doped $SrTiO_3$ microspheres with enhanced visible light catalytic activity for Cr(VI) reduction. Front Chem Sci Eng 12:440–449
124. Cheng Z, Lin J (2010) Layered organic–inorganic hybrid perovskites: structure, optical properties, film preparation, patterning and templating engineering. Cryst Eng Commun 12:2646–2662
125. Yan Y, Yang H, Zhao X et al (2018) Enhanced photocatalytic activity of surface disorder-engineered $CaTiO_3$. Mater Res Bull 105:286–290
126. Kumar A, Schuerings C, Kumar S et al (2018) Perovskite-structured $CaTiO_3$ coupled with g–C_3N_4 as a heterojunction photocatalyst for organic pollutant degradation. Beilstein J Nanotechnol 9:671–685
127. Yan Y, Yang H, Zhao X et al (2018) A Hydrothermal route to the synthesis of $CaTiO_3$ nanocuboids using P25 as the titanium source. J Electron Mater 47:3045–3050
128. Han C, Liu J, Yang W et al (2017) Photocatalytic activity of $CaTiO_3$ synthesized by solid state, sol–gel and hydrothermal methods. J Sol–Gel Sci Technol 81:806–813
129. Zhang H, Chen G, He X et al (2012) Electronic structure and photocatalytic properties of Ag–La codoped $CaTiO_3$. J Alloys Compd 516:91–95
130. Im Y, Park S-M, Kang M (2017) Effect of Ca/Ti Ratio on the core-shell structured $CaTiO_3$@basalt fiber for effective photoreduction of carbon dioxide. Bull Korean Chem Soc 38:397–400
131. Yoshida H, Zhang L, Sato M et al (2015) Calcium titanate photocatalyst prepared by a flux method for reduction of carbon dioxide with water. Catal Today 251:132–139
132. Selvarajan S, Malathy P, Suganthi A et al (2017) Fabrication of mesoporous $BaTiO_3/SnO_2$ nanorods with highly enhanced photocatalytic degradation of organic pollutants. J Ind Eng Chem 53:201–212
133. Nageri M, Kumar V (2018) Manganese-doped $BaTiO_3$ nanotube arrays for enhanced visible light photocatalytic applications. Mater Chem Phys 213:400–405
134. Thamima M, Andou Y, Karuppuchamy S (2017) Microwave assisted synthesis of perovskite structured $BaTiO_3$ nanospheres via peroxo route for photocatalytic applications. Ceram Int 43:556–563
135. Maeda K (2014) Rhodium-doped barium titanate perovskite as a stable p-type semiconductor photocatalyst for hydrogen evolution under visible light. ACS Appl Mater Interfaces 6:2167–2173
136. Yan SC, Wang JQ, Li ZS et al (2009) Photocatalytic activities for water splitting of La-doped $NaTaO_3$ fabricated by microwave synthesis. Solid State Ionics 180:1539–1542

137. Wang S, Xu X, Luo H et al (2016) Enhanced organic dye removal of the W and N co-doped $NaTaO_3$ under visible light irradiation. J Alloys Compd 681:225–232
138. Lan NT, Phan LG, Hoang LH et al (2016) Hydrothermal synthesis, structure and photocatalytic properties of La/Bi co-doped $NaTaO_3$. Mater Trans 57:1–4
139. Li FF, Liu DR, Gao GM et al (2015) Improved visible-light photocatalytic activity of $NaTaO_3$ with perovskite-like structure via sulfur anion doping. Appl Catal B 166–167:104–111
140. Kato H, Kudo A (1999) Highly efficient decomposition of pure water into H_2 and O_2 over $NaTaO_3$ photocatalysts. Catal Lett 58:153–155
141. Jana P, Montero CM, Pizarro P et al (2014) Photocatalytic hydrogen production in the water/methanol system using Pt/RE: $NaTaO_3$ (RE = Y, La, Ce, Yb) catalysts. Int J Hydrogen Energy 39:5283–5290
142. Lopez-Juarez R, Gonzalez F, Cipagauta S et al (2016) Solid state synthesis of La-doped $NaTaO_3$ under time-reduced conditions and its photocatalytic properties. Ceram Silikáty 60:278–284
143. Liu X, Lv J, Wang S et al (2015) A novel contractive effect of $KTaO_3$ nanocrystals via La^{3+} doping and an enhanced photocatalytic performance. J Alloys Compd 622:894–901
144. Krukowska A, Trykowski G, Winiarski MJ et al (2018) Mono- and bimetallic nanoparticles decorated $KTaO_3$ photocatalysts with improved Vis and UV–Vis light activity. Appl Surf Sci 441:993–1011
145. Bajorowicz B, Reszczyńska J, Lisowski W et al (2015) Perovskite-type $KTaO_3$-reduced graphene oxide hybrid with improved visible light photocatalytic activity. RSC Adv 5:91315–91325
146. Chen Z, Xing P, Chen P et al (2018) Synthesis of carbon doped $KTaO_3$ and its enhanced performance in photocatalytic H_2 generation. Catal Commun 109:6–9
147. Xiang T, Xin F, Zhao C et al (2018) Fabrication of nano copper oxide evenly patched on cubic sodium tantalate for oriented photocatalytic reduction of carbon dioxide. J Colloid Interface Sci 518:34–40
148. Nakanishi H, Iizuka K, Takayama T et al (2017) Highly active $NaTaO_3$-based photocatalysts for CO_2 reduction to form CO using water as the electron donor. Chem Sus Chem 10:112–118
149. Shao X, Yin X, Wang J (2018) Nanoheterostructures of potassium tantalate and nickel oxide for photocatalytic reduction of carbon dioxide to methanol in isopropanol. J Colloid Interface Sci 512:466–473
150. Li K, Handoko AD, Khraisheh M et al (2014) Photocatalytic reduction of CO_2 and protons using water as an electron donor over potassium tantalate nanoflakes. Nanoscale 6:9767–9773
151. Fresno F, Jana P, Renones P et al (2017) CO_2 reduction over $NaNbO_3$ and $NaTaO_3$ perovskite photocatalysts. Photochem Photobiol Sci 16:17–23
152. Wu W, Liang S, Chen Y et al (2013) Mechanism and improvement of the visible light photocatalysis of organic pollutants over microcrystalline $AgNbO_3$ prepared by a sol–gel method. Mater Res Bull 48:1618–1626
153. Sun M, Yan Q, Shao Y et al (2017) Facile fabrication of BiOI decorated $NaNbO_3$ cubes: A p-n junction photocatalyst with improved visible-light activity. Appl Surf Sci 416:288–295
154. Chen W, Hu Y, Ba M (2018) Surface interaction between cubic phase $NaNbO_3$ nanoflowers and Ru nanoparticles for enhancing visible-light driven photosensitized photocatalysis. Appl Surf Sci 435:483–493
155. Wang L, Gu H, He J et al (2017) Scale synthesized cubic $NaNbO_3$ nanoparticles with recoverable adsorption and photodegradation for prompt removal of methylene blue. J Alloys Compd 695:599–606
156. Liu Q, Chai Y, Zhang L et al (2017) Highly efficient Pt/$NaNbO_3$ nanowire photocatalyst: its morphology effect and application in water purification and H_2 production. Appl Catal B 205:505–513

157. Liu Q, Zhang L, Chai Y et al (2017) Facile fabrication and mechanism of single-crystal sodium niobate photocatalyst: insight into the structure features influence on photocatalytic performance for H_2 evolution. J Phys Chem C 121:25898–25907
158. Li P, Xu H, Liu L et al (2014) Constructing cubic–orthorhombic surface-phase junctions of $NaNbO_3$ towards significant enhancement of CO_2 photoreduction. J Mater Chem A 2:5606–5609
159. Shi H, Chen G, Zhang C et al (2014) Polymeric g–C_3N_4 coupled with $NaNbO_3$ nanowires toward enhanced photocatalytic reduction of CO_2 into renewable fuel. ACS Catal 4:3637–3643
160. Shi H, Zhang C, Zhou C et al (2015) Conversion of CO_2 into renewable fuel over Pt–g–C_3N_4/$KNbO_3$ composite photocatalyst. RSC Adv 5:93615–93622
161. Raja S, Babu RR, Ramamurthi K et al (2018) Magnetic and photocatalytic properties of bismuth doped $KNbO_3$ microrods. Mater Res Bull 105:349–359
162. Zhang T, Zhao K, Yu J et al (2013) Photocatalytic water splitting for hydrogen generation on cubic, orthorhombic, and tetragonal $KNbO_3$ microcubes. Nanoscale 5:8375–8383
163. Wang R, Zhu Y, Qiu Y et al (2013) Synthesis of nitrogen-doped $KNbO_3$ nanocubes with high photocatalytic activity for water splitting and degradation of organic pollutants under visible light. Chem Eng J 226:123–130
164. Hong Z, Li X, Kang SZ et al (2014) Enhanced photocatalytic activity and stability of the reduced graphene oxide loaded potassium niobate microspheres for hydrogen production from water reduction. Int J Hydrogen Energy 39:12515–12523

Chapter 10
LEDs and Other Electronic Devices Based on Perovskite Materials

Anastasia Vassilakopoulou and Ioannis Koutselas

1 Introduction

During the last 20 years, new materials have been synthesized that allows the fabrication of novel electronic, optical, and optoelectronic devices, including light-emitting diodes (LEDs), solid-state lasers, sensors, and transistors. Some of the novel devices are based on low-dimensional (LD) semiconductors, the latter usually fabricated with artificial methods. However, lately new additions in these methods have included the inclusion of the natural occurring three-dimensional materials (3D) which are synthesized as two- (2D), one- (1D), or zero-dimensional (0D) forms. Low-dimensional (LD) semiconductors in general exhibit the phenomenon where the semiconductor's energy band gap (E_g) increases as the dimensionality of the material is reduced as it was experimentally verified in 1981 by Papavassiliou [1, 2] and independently by Ekimov [3]. Simultaneously as the dimensionality of the materials is reduced, the geometrical confinement of the electron and holes forces the native excitonic oscillator strength to increase. Examples of classical artificial 3D direct energy band gap semiconductors are the GaN, GaAlAs, and GaAs [4, 5] which can be formed to LD structures by virtue of methods such as molecular beam epitaxy or lithography [6]. However, a long well known, yet forgotten [7–9], class of materials has lately been revived, which is usually referred to as natural hybrid semiconductors or alternatively hybrid organic–inorganic semiconductors (HOIS). These natural materials are described as such due to their self-assembly-based synthesis and are composed out of organic and inorganic parts simultaneously; thus, these are also commonly referred to as HOIS. The most useful and robust HOIS to date are those based on single- or mixed-valency metal–halides complexes with

A. Vassilakopoulou (✉) · I. Koutselas
Materials Science Department, University of Patras, Patras 26504, Greece
e-mail: anastasia.vassil@gmail.com

I. Koutselas
e-mail: ikouts@upatras.gr

N. S. Arul and V. D. Nithya (eds.), *Revolution of Perovskite*, Materials Horizons: From Nature to Nanomaterials, https://doi.org/10.1007/978-981-15-1267-4_10

organic molecules [9], metal–oxides [10–12], and metal–chalcogenides [1, 13, 14]. Some single-valence metal halide complexes can be described by a chemical formulae of $Z_xA_yM_zH_{x+y+z}$ [where M a monovalent metal = Ga, In, Tl, Cu, Au, etc.; Z = K, Cs, Rb, $MeNH_3$, etc.; A = (amine-H) or $(diamine\text{-}2H)_{0.5}$; X = F, Cl, Br, I]. Similarly, double valence metal halide complexes can be described by the general formula $Z_xA_yM_zX_{2z+y+x}$ or $Z_xM_{z+w}X_{2z+x}H_{2w}$ or $Z_xM_zM'_wX_{2z+2w+x}$ [where M, M' divalent metals = Ge, Sn, Pb, Zn, Cd, Hg, Cu, Ni, Co, Fe, Mn, etc.] [15, 16]. Other variants based on trivalent metals can be described as $Z_xA_yM_zX_{3z+y+x}$ [M trivalent metal = As, Sb, Bi, Ga, In, etc.] [17]. HOIS can also be synthesized by mixing metal cations of a different valence. In the case where only two types of cations are used, the resultant HOIS have lately acquired the short name of double perovskites. Details can be found in the literature [1, 18–20]. Some of the most interesting such single-valence metal cation HOIS are chosen below to portray their structure, which is also related to their properties that are essential to any type of electronic device. As examples of such HOIS, Fig. 1 presents crystal structures that are composed of a lead iodide network of three or lower dimensionality, where the 3D and LD inorganic networks serve as the active semiconductor, while the organic material is structurally alternating to the inorganic component, acting as barrier for both the electrons and holes of the semiconducting material. In particular, in Fig. 1, the following crystal structures of $CH_3NH_3PbI_3$ [21], $(4F\text{–}C_6H_4CH_2CH_2NH_3)_2PbI_4$ [22], $((NH_2)C = I(NH_2))_3PbI_5$ [23], and $(CH_3NH_3)_4PbI_6.2H_2O$ [24] are depicted from left to right as 3D, 2D, 1D, and 0D HOIS. In fact, in the last years, the term perovskite is usually related to the 3D phase, while in fact all of the "perovskites" are hybrid semiconductors. Bottom row of Fig. 1 presents the absorption coefficient of these example structures as obtained from optical absorption or reflection measurements via the Kramers–Kronig causality relations. It is evident that the value of E_g shifts from low energy, c.a. 750 nm, to high energies, c.a. 350 nm, while the excitonic peaks also follow the band gap trend, as evidenced by the progressive movement of the distinguishable peak towards the left, i.e. higher energies, of the spectra in Fig. 1.

It can be easily observed that the lead–iodide network, which is 3D in Fig. 1a, transforms to a c.a. 6-Å-thick 2D lead iodide network (quantum wells) in Fig. 1b; in fact, the 2D HOIS is considered to be a superlattice of alternating organic and inorganic parts. In Fig. 1c, the right choice of organic component turns the proper stoichiometric inorganic network into 1D (quantum wires), while in Fig. 1d, excess of the same organic component that forms the 3D structure splits the inorganic network in individual PbI_6^{4-} octahedra (quantum dots).

As the dimensionality of the network decreases from 3D to 0D, the direct band gap increases while simultaneously the exciton binding energy increases to values larger than normally anticipated from classical solid-state theory for an absolutely thin 2D material, due to the dielectric enhancement; for example, the 2D HOIS excitonic binding energy can be at least ten times that of the 3D comparable material, usually in the order of 260 meV. Such large values allow for excitons to be stable at room temperature, so that novel and low-cost excitonic devices can be realized with HOIS usage, despite the soft character of HOIS that in time degrades.

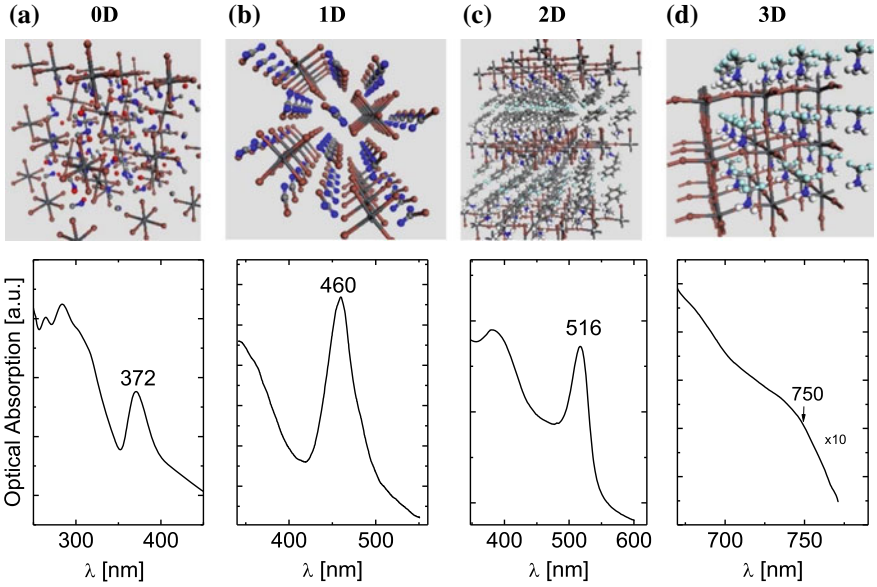

Fig. 1 Crystal structures from right to left of $CH_3NH_3PbI_3$ (**a**), $(4F\text{-}C_6H_4CH_2CH_2NH_3)_2PbI_4$ (**b**), $(NH_2C = (I)NH_2)_3PbI_5$ (**c**), and $(CH_3NH_3)_4PbI_6.2H_2O$ (**d**); where gray, red atoms stand for Pb and I, respectively; other colors represent the atoms of the organic component. Bottom row represents the corresponding optical absorption as function of λ, obtained from reflection measurements or thin-film measurements. Reproduced with permission [9] Copyright © 1997 Published by Elsevier Ltd

Finally, replacement of I to Br or Cl shift the band gap toward high energies while mixing different halide contents with Pb also allows for synthesizing materials with precise tunable band gaps in the c.a. 300–800 nm range, while the excitonic level is usually a few hundreds of meV lower than the band gap energy [25–28]. In fact, in Fig. 1 (bottom row), it can be observed that the excitonic state is almost indistinguishable from the E_g, while in the 2D and 1D cases, the excitonic peak becomes pronounced and separated from *the absorption onset of* E_g.

In general, it can be summarized that depending on the metal cation, the halide type as well as the organic component, it is possible to synthesize HOIS of various dimensionalities that have tunable band gap from 800 nm to almost 300 nm, while the choice of organic part with comparable energy band gap to the inorganic component allows for interaction among the two parts, and thus allows for energy transfer phenomena. Figure 2 presents some of the different possibilities for tuning HOIS excitonic peak, and the accompanying energy band gap, to suit any specific needs.

HOIS (perovskite) materials exhibit novel optical and excitonic properties not only because of the enhanced quantum confinement but also due to the dielectric confinement of their inherent LD excitons. In particular, the amine that usually covers the inorganic component of HOIS has much smaller dielectric constant (3 times less) and,

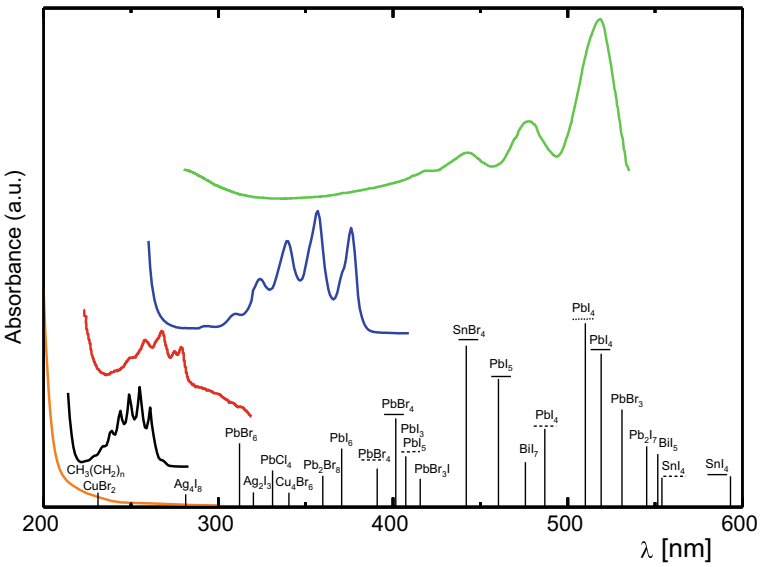

Fig. 2 Schematic presentation of the optical absorbance spectra of inorganic excitonic peaks (lower part) and organic networks (upper part) in several hybrid semiconducting systems. Adapted with permission from Ref. [29]. Copyright © 2001, Springer-Verlag/Wien

thus, allows the excitons to interact through the organic layer, increasing the excitonic binding energy as it is presented in Fig. 3, by the formation of image charges [30, 31] in the organic layer, which are used to model the inducement of boundary charges at the interfaces. In fact, the enhancing term of the excitonic binding energy is analogous to the $\frac{\varepsilon_w - \varepsilon_b}{\varepsilon_w + \varepsilon_b}$, where ε_w and ε_b are the well and barrier high-frequency dielectric constants, respectively. On the other hand, amine encapsulation is useful in terms of the excitonic binding energy, but the organic component is not conductive; thus, any electronic device based on HOIS would preferably need to allow for the passage of electrons and holes through the organic barrier, which itself would short circuit the device operation occuring through the semiconducting inorganic part. Should the barrier attain a much larger dielectric constant value than that of the quantum well, then the excitonic energy is decreased significantly.

HOIS and especially their inorganic part can attain not only the forms of 3D to 0D LD networks but also those of intermediate dimensionalities, such as the so-called quasi-0D, quasi-1D, and quasi-2D HOIS [16, 32]. Example of quasi-2D semiconductors is shown in Fig. 4, along with a schematic representation of the related 2D and 3D semiconductors. In the left of Fig. 4, the 2D semiconducting network composed of corner-sharing PbX_6 octahedra is alternated with 2D layers of the organic component. Furthermore, from left to right, the semiconducting layer is depicted as its thickness increases, while the general chemical formula of the crystalline quasi-2D HOIS is $(CH_3NH_3)_{n-1}(Z)_2Pb_nX_{3n+1}$, where $Z = a$ long amine, $X = a$ halogen atom (here bromide for the spectra in Fig. 4). For crystalline

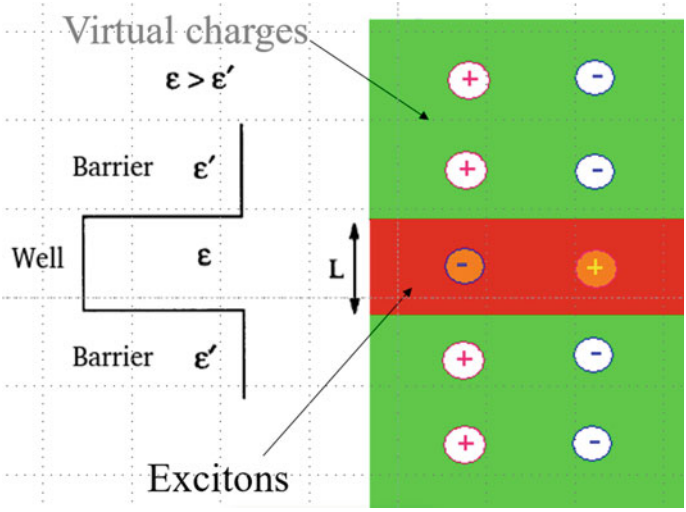

Fig. 3 Simple schematic representation of the image charges formed in the organic barrier due to the exciton electron-hole pair existing in the inorganic part of the HOIS

quasi-2D systems, the thickness of the layer increases for increasing n, n being an integer. When $n = \infty$, the material is a 3D semiconductor, commonly known as perovskite. In the case of $n = 1$, the system is the thinnest possible 2D HOIS for the lead halide materials. In fact, the $n = 1$ form is not absolutely 2D due to the finite layer thickness. Intermediate n values form the quasi-2D HOIS. Each HOIS of specific dimensionality exhibits strong excitonic optical phenomena, since excitons in HOIS have high binding energy, partly due to the dielectric confinement of the inorganic layer formed by the amines. In particular, HOIS and especially the quasi-2D class have distinct excitonic peaks and energy band gaps for every individual n value for given inorganic layer type and specific amine. This is not generally the case for all amine types. For example, when the amine is a long tail phenylalkylammonium [33], much different structures than those mentioned above, as the chemical formula, can be exhibited.

Quasi-2D semiconductors seem to be more interesting than the 0D, 1D, 2D, and 3D HOIS, although these are quite hard so synthesize in pure crystalline form. The reason is that the self-assembly nature of HOIS may allow the semiconductor to form in a mixture of various n, see Fig. 2, rather than in a unique n value system. On the other hand, mixtures of quasi-2D and 3D exhibit energy transfer phenomena. A set of quasi-2D and/or 3D nanoparticles in close proximity, such as a multi-phase powder, absorbs energy at all energy characteristic peaks relevant to the various n values, but the emission appears to originate mainly from the higher n value moiety, which has the smallest band gap [29, 35]. Such effects have been suggested to not only allow for efficient PL materials, where all optical excitation energy could be funneled to one n-phase emission only, but also for LEDs. In

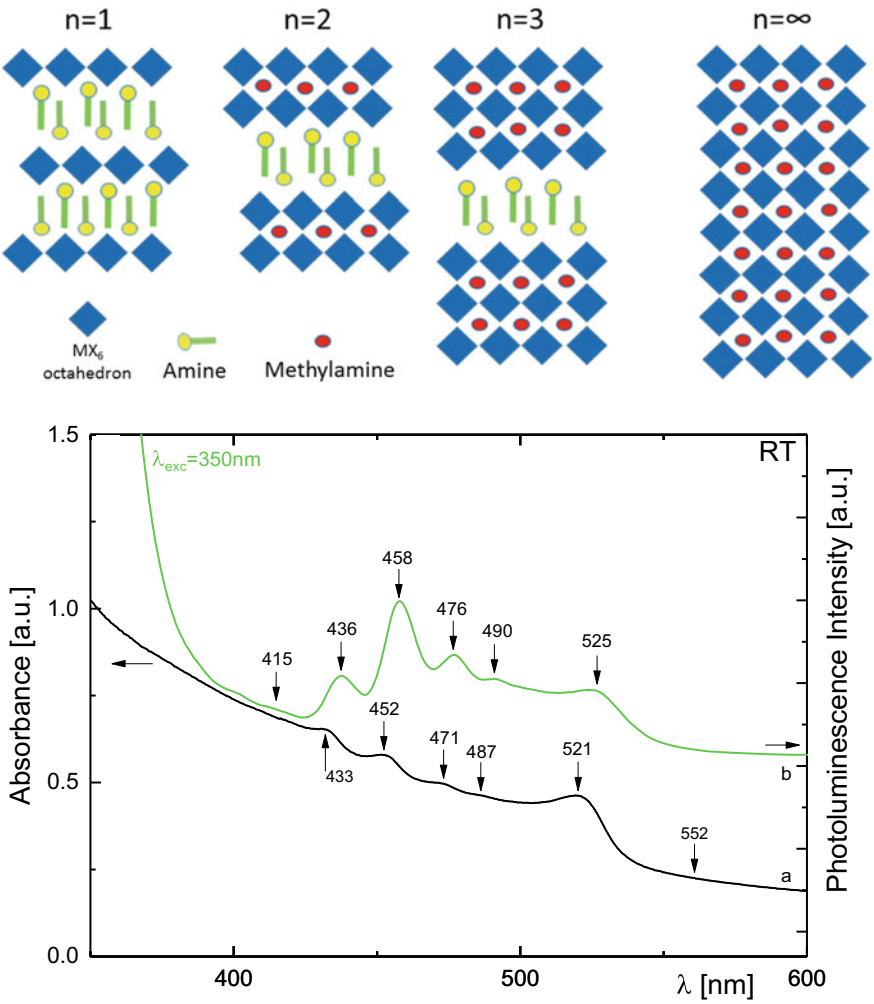

Fig. 4 Top: Layered structure for the crystalline $(CH_3NH_3)_{n-1}(Z)_2Pb_nX_{3n+1}$ LD HOIS and Z is a large amine. Left is 2D (n = 1), while right is 3D (n = ∞) as n = 1, 2, 3…, ∞. Adapted with permission from Applied Surface Science 400 (2017) 434–439. Copyright © 2017 Elsevier B.V. All rights reserved. Bottom: Optical absorption and luminescence spectra for a mixture of quasi-2D HOIS. Adapted with permission from Ref. [34]. Copyright © 2016 Elsevier B.V. All rights reserved

particular, diodes could be formed where the electrical energy is being funneled to an assortment of nanoparticles, yet the electroluminescence could appear to originate only from the smallest E_g component. Thus, all electron/hole pairs could participate to the LED emission at almost 100% efficiency. Such examples are provided below.

Due to the above phenomena, many interesting applications of halide perovskites have come to light recently. Although halide perovskites have been mainly used for photovoltaics over the past 5 years, these materials have unique features that are remarkably advantageous for various other applications. Here, we introduce a broad range of halide perovskite-related applications, such as light-emitting diodes (LEDs), lasers, electromagnetic radiation sensors (photodetectors, radiation detectors), transistors, pressure, and chemical sensors as well as lithium–ion batteries. In all cases, the active entity is the exciton; thus, the natural categorization of at least the LED devices is unraveling along with the material dimensionality as different excitonic and confinement effects arise in each type of LD structure.

Finally, it must be noted that there are other types of perovskites, inorganic perovskites, where the small organic molecules in their structure, such as $CH_3NH_3^+$, are replaced by large cations such as Cs. Despite the fact that some such HOIS may be completely inorganic, their properties are much similar to the organic–inorganic hybrids.

2 Low-Dimensional Hybrid Organic–Inorganic Semiconductors in Light–Emitting Diodes—LEDs

The most extensively studied application of halide HOIS (perovskites), after extensive work in photovoltaics over the past 5 years, is their application in LEDs. The primary advantage of halide perovskite is their controllable photoluminescence (PL) property, especially the tunable optical band gap, which makes the halide perovskite a promising material for use in LEDs [36]. Although HOIS are being studied for over 30 years, it is only recently (last 8 years) that their potential in PVs and LEDs has been valued and an increasing number of research groups have focused with powerful experimental techniques on the HOIS properties in a range of external factors, as well as in a multitude of LED devices. In fact, their use in LEDs was first reported by Japanese groups, in the 1990s, even before the advent of photovoltaic systems [37–39] but these reports provided data for low temperature experiments and high turn-on voltages.

One of the first perovskite LED (PeLED) geometries published is presented in Fig. 5, along with the energy alignment of the Fermi levels of the metal contacts used in the device, such as the indium tin oxide (ITO) and Mg–Ag alloy, as well as the energies of the conduction and valence band of the active HOIS (Phenethylammonium$_2$PbI$_4$) and the HOMO/LUMO energy levels of the electron injection and hole-blocking layer, 1,3-Bis[2-(4-tert-butylphenyl)-1,3,4-oxadiazo-5-yl]benzene (OXD7). Also, in the right image of Fig. 5, the electroluminescence (EL) and PL spectra of this first reported device can be observed where there is a coincidence of the two peaks, both of them Stokes shifted with respect to the optical absorption at room temperature peak by 10 nm. In general, a small Stokes shift of the PL peak with respect to the optical absorption peak denotes a pristine semiconductor with small number of defects.

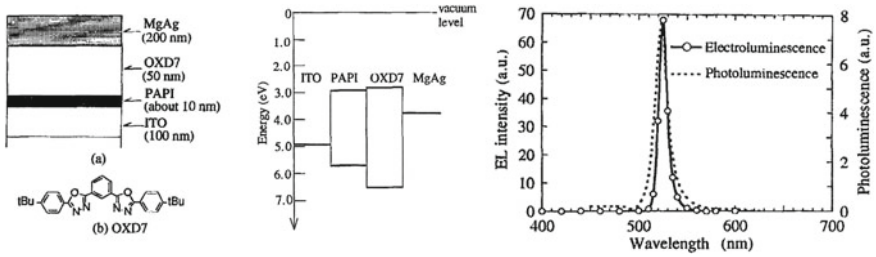

Fig. 5 Left: **a** Schematic of the first PeLED (spin-coated) along with **b** the structure of OXD7. Middle: Energy level alignment of the various device elements/layers. EL and PL spectra of the device at 77 K. Adapted with permission from Ref. [40]. Copyright © 1994 American Institute of Physics

The initial reports on PeLED did not possibly attract the attention of the scientific community because of the poor performance of these devices and their marked low stability, as these only functioned at cryogenic temperatures and high driving voltages. Also at cryogenic temperatures, Era et al. succeeded in fabricating green electroluminescent (EL) devices based on 2D-layered perovskite quantum-well structures with the use of phenylethylammonium lead iodide $(C_6H_5C_2H_4NH_3)_2PbI_4$. After years of the appearance of the previous reports, the first room-temperature operation of a PeLED was demonstrated in 2011 by Koutselas et al. for 4-fluorophenethylamine (4FPA) and oleylamine-based HOIS, followed by numerous reports [41]. The oleylamine-based 2D HOIS was also reported for the first time, where the nature of the oleylamine molecule provided the composite HOIS with strong chemical stability to acetone and water, although in general 2D HOIS are more resistant to humidity than the 3D HOIS.

Halide perovskites can be used as active materials for electrically driven photonic sources, but also HOIS can function as phosphors for optically pumped photonic sources [42]. Moreover, halide perovskites had been found to be useful as hole transport layers in LEDs based on polymeric materials [43]. In PeLEDs, there are a number of main concepts under consideration: external and internal quantum efficiencies which are not the same due to the interface coupling as light exits the perovskites, electrical charge injection from the front and back electrodes, charge transport, carrier lifetime and radiative recombination, and finally photon recycling; the light that is being generated is being absorbed and re-emitted. All these concepts need to addressed in order to fabricate useful devices, yet their experimental analysis requires a multitude of techniques; thus, many materials research groups also synthesize devices to assess all such aspects. A modern PeLED schematic can be found in Fig. 6, where a PeLED is usually fabricated with a transparent front electrode, an electron-transporting layer (ETL), emitter, a hole-transporting layer (HTL), and a back electrode. Ideally, electron and hole-blocking layers would be needed, but the application of each layer complicates the geometry and the characterization. The presented device layer structure is as follows: ETL/halide perovskite/HTL or HTL/halide perovskite/ETL, where all these layers allow for

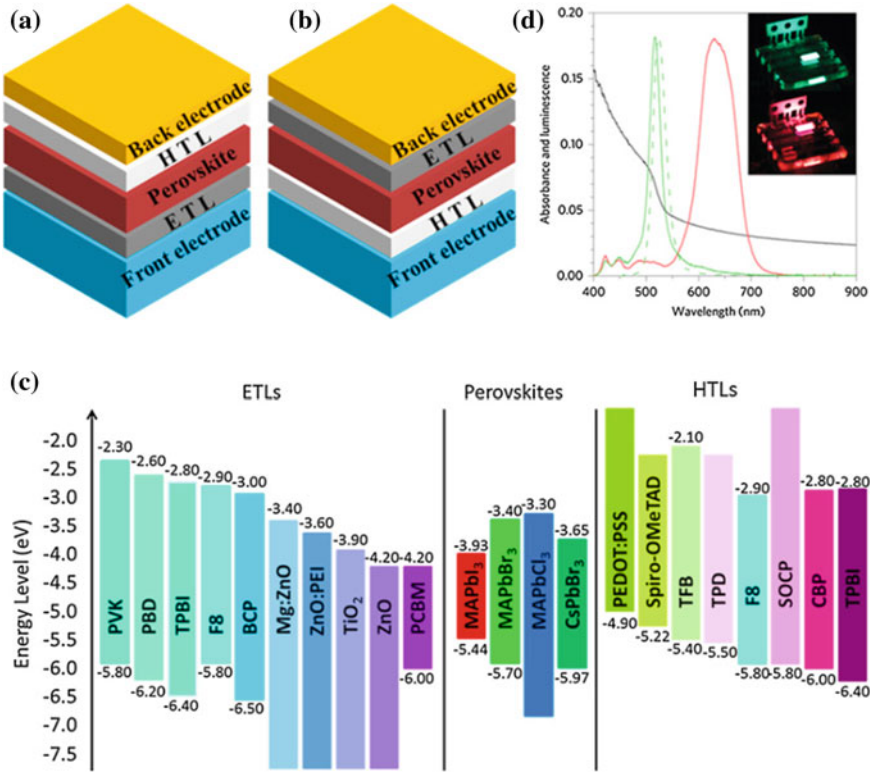

Fig. 6 **a**, **b** PeLED architectures in the conventional and inverted configuration, respectively. **c** Energy levels of materials used as perovskites, ETLs, and HTLs for PeLEDs, aligned to the vacuum level, as adapted with permission [45]. Copyright © 2017 Elsevier Ltd. **d** Optical absorption is shown with the black line. EL and PL spectra of $CH_3NH_3PbBr_3$ are shown as solid and dashed green lines, respectively. EL as red line $CH_3NH_3PbBr_2$. Inset image: green and red electroluminescence from the latter two HOIS, respectively. Adapted with permission from Ref. [46]. Copyright © 2014, Springer Nature

light emission which exits through the transparent electrode. As it was stated before, PeLEDs can be fabricated without the need of ETL/HTL layers reducing device complexity, cost, and degradability [41]. This can be performed even with plastic films where perovskites have been embedded in them. Moreover, it is usually observed that the excited electrons can also emit radiation by relaxing to empty states in the neighboring ETL/HTL layers, thus complicating the emission spectrum [44]. The first room-temperature oleylamine-based LEDs did not have high quantum efficiency and were fabricated using samples that had dried for period of months, while the first reported 2D PeLED that was fabricated based on 4FPA was only briefly discussed due to its smaller resistance to humidity [41]. Nowadays, PeLEDs can be encapsulated as well as covered with sacrificial device layers, such as MoO_3, that allow for some passivation toward oxidizing parameters.

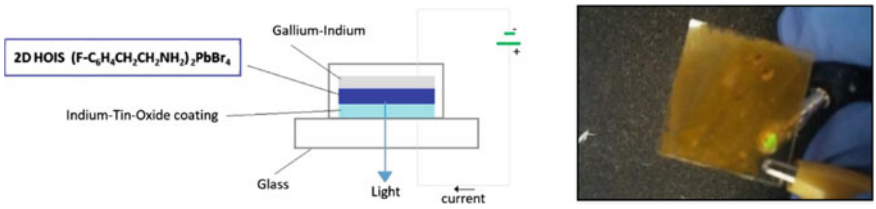

Fig. 7 Left: Schematic of a single-layer light-emitting diode based on HOIS. Right. PeLED based on $(4FPA)_2PbI_4$ coated on ITO glass and operated with a clip dipped in Ga–In eutectic as adapted with permission from Ref. [40] Copyright © 2016 Elsevier Ltd. All rights reserved

Vassilakopoulou et al. were the first to re-analyze the simple fabrication of a 2D hybrid organic–inorganic green color PeLED based on 4FPA, functioning at room temperature, within ambient conditions for a few weeks. The resistance was afforded due to the synthetic procedure and drying method followed, as in the early days many device fabrication parameters were unknown [47]. In this reference, it was found that doctor blade technique functioned much better than spin coating for the preparation of a film that would on its own act as single-layer LED, as presented in Fig. 7. In contrast, to the modern PeLED designs, the 4FPA variant can be fabricated by simply painting a layer of $(4\text{-fluorophenethylamine-H})_2PbI_4$ on an ITO substrate, without the need for spin coating the film, nor presenting any interfacial ETL/HTL layers. On the other hand, the onset voltage was high, functioning at 5–10 V, probably due to the film thickness and the appearance of some needle-like phases, also detected in Ref. [48]. Such small details in the material structure, as well as other details focusing on the solvent [49], or on the ambient humidity, emphasize the structure–property–device functionality relation. Also, since then, several reports have shown the recombination kinetic relation to excitons and defect states [50, 51], while others have managed to stabilize the LEDs by in part proper manipulation of the active material. For example, 35 W/Sr/cm^2 EL can be obtained at 744 nm with 1 V turn-on voltage, while pure 2D HOIS can sustain for 14 h of continuous operation in contrast to the 3D analogs [52].

It is interesting that using 4FPA for 2D lead bromide-based HOIS, which emits at 410 nm, does not allow the analog Br-based 2D HOIS to function as single-layer LED and in this case impurities are needed to be introduced in the synthesis of $(4\text{-fluorophenethylamine-H})_2PbBr_4$ to allow it functioning as a single-layer LED [53]. It has been suggested that impurities or conducting inclusions allow the current passing from one 2D platelet to the next. Other authors have also used 2D Pb–Br-based HOIS in more complex device structures with about the same efficiency as the single-layer devices [44, 54]. Oddly enough, pristine $(\text{phenethylamine})_2PbBr_4$ can indeed serve as a single-layer LED material but with very small diminished efficiency. Although, in the previous example, fluorine modified phenethylamine appears to enhance the HOIS LED functionality, another important publication states the production of fluorine-free perovskite LEDs, by removing fluorine from layers of spiro-OMETAD [55]. In the 4FPA LED, previously, it is crucial to

understand that the fluorine atoms in the organic molecule induce only a small separation among the organic molecules, which, however, alters the coupling of the material's phonons to the electrons that in turn can affect the EL intensity as well as linewidth [56].

Green LEDs from bromine-based 3D organic–inorganic halide perovskites have been reported [50], achieving light emissions of 1500 cd m^{-2}, as well LEDs based on organometal halide HOIS amorphous nanoparticles with 3.8% efficiency [57]. In addition, high-performance amphiphilic HOIS have been synthesized that could be also employed for LED applications [58], while high-pressure studies have shown the intricate play of excitons with photoluminescence and structure [59], which can also can be used for laser cooling, PVs and LEDs [60].

The poor performance of methylammonium lead iodide $CH_3NH_3PbI_3$-based perovskite in LED applications can be attributed to low exciton binding energies in the range of 9–60 meV, [61] where for this lead–iodide HOIS, Li and co-workers successfully demonstrated the fabrication of 2D perovskite green LED based on phenylmethanamine lead iodide $(C_6H_5CH_2)_2PbI_4$, working at room temperature [62]. The authors investigated the stability of the device under 50% relative humidity conditions and found no degradation in the XRD pattern for 5 days. The intricate interplay of the halogen atom in the final device properties has led authors to mix various halogen atoms. Thus, as it was discussed before, Liang et al. utilized quantum-confined 2D perovskite based on 2-phenethylammonium lead bromide (PEA_2PbBr_4) to realize color-pure violet LEDs. This material was found to assemble in well-confined quantum-well structures with a repeating dielectric spacer layer, sandwiching 3D $PbBr_6$ octahedra in between, which is the typical 2D HOIS structure [44]. The same group, however, has reported that the emission color of a PeLED can be controlled by changing the halide anion, which is important because in general the EL especially in the region close to UV is not easily attainable by robust PeLEDs. Tan et al. demonstrated that the electroluminescence of halide perovskites can be varied in the visible and near-infrared regions, in a similar fashion. They fabricated PeLED using a 15 nm thick layer of $CH_3NH_3PbI_{3-x}Cl_x$ perovskite as the emitter and via compositional substitution between Br and I, the emission band can be shifted leading to red and green colors [46]. In addition, the emission color of a PeLED can be controlled by changing the n values of $(RNH_3)_2A_{n-1}B_nX_{3n+1}$ formula in quasi-2D perovskites. Ma and co-workers reported color tuning approach with a quasi-2D layered structure to get highly luminescent lead bromide perovskites. The color tuning of emission was obtained through the synthetic control of the chemical formula of $(RNH_3)_2(CH_3NH_3)_{n-1}Pb_nBr_{3n+1}$. By manipulating the quasi-2D layered structure, the quantum size confinement effect enabled the color tuning of emission. As n value increased from 1 to various integer numbers, which corresponds to the increase in inorganic layer thickness, the emissive redshifted, moved from deep blue to bright green [63]. Recently, Hu et al. reported on tunable PeLEDs with fine emission and different color regions by using the 2D perovskite structure (the n values were in the range of $n = 1$ to $n = 6$) achieved through butylammonium iodide ($C_4H_9NH_3I$) as a spacer.

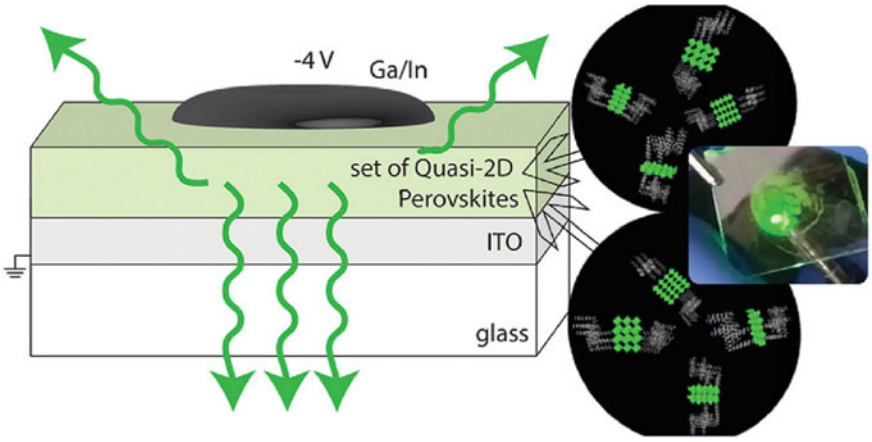

Fig. 8 Right: Schematic representation of a single-layer perovskite LED which is based on a thin film of a mixture of various quasi-2D and 3D HOIS nanoparticles in close proximity. Right a representation of the various quasi-2D nanocrystals along with an image of the LED in operation. Light is emitted only from the lowest band gap nanoparticles. Adapted with permission from Ref. [34]. Copyright © 2017, Elsevier Ltd.

As demonstrated, from Vassilakopoulou et al., mixtures of quasi-2D/3D HOIS are more stable than the single 3D or 2D HOIS and can serve as the active and single layer in PeLEDs. Also in this publication, they suggested that energy transfer effects manifest in the light emission process; thus, it is possible to fabricate an energy transfer LED. Such a concept along with a true operational device is presented in Fig. 8, presented in Ref. [34]. Later, the same concept has been proved by other more sophisticated techniques for quasi-2D HOIS embedded in polymers [64].

For completeness, it should be noted that the energy transfer effects have also been observed in other similar semiconductors, such as in Si-based systems as well as in inorganic perovskites such as $CsPbBr_3$ [65]. Energy transfer capable HOIS can be tuned so that the excitonic emission can over any position in the visible spectrum, as long as it is based on Pb halides [66].

Using the inorganic variant of the 3D HOIS, $CsPbX_3$, the group of Do investigated pure-6 colored $CsPbX_3$ perovskite quantum-dot-based monochromatic down-converted LEDs and they incorporated perovskite quantum dots with long-wavelength-pass dichroic filters and UV-curable binders [67]. Although the phenomena and PeLED devices based on HOIS for all dimensionalities have been well studied, there is always a range of conditions or treatments, such as heating or humidity, which impairs their functionality [68]. Efforts to include lead halide semiconducting units within inert matrices have already been made [69], as well as HOIS in the prospect of creating robust composites presenting properties attributed to the HOIS, alongside with the capability of sustaining these properties in time under various conditions, by virtue of the host matrix protection.

Such a protecting matrix could be served by a material with pores, as for example the MCM-41 family, which it can be either synthesized as white porous powder or in the form of thin transparent flexible films [see refs in 70], all exhibiting nm-sized mesopores achieving surface areas of the order of 1000 m^2/g. An also interesting subject for research is the quantum confinement induced on the perovskites by the limited growth within the pores, assuming that the pores are completely filled; partial growth along the pore diameter or along the axis of the pore would induce further quantum effects. Lately, research on the same subject has appeared, claiming that the entrapment of 3D perovskite nanoparticles within the pores of mesoporous matrices allows the encapsulation without the use of ligands for electronic state passivation [71].

Simultaneously with this work, authors have reported the observation of quantum confinement effects of 3D lead halide perovskites within mesoporous matrices. Koutselas group was the first to demonstrate a single-layer PeLED based on these composites of MCM-41/perovskite, where the EL signal is attributed to energy funneling from higher band gap nanoparticles toward the lowest band gap nanoparticles, which are the 3D perovskites. The MCM-41 was loaded with a set of nanoparticles all being a mixture of quasi-2D entities, i.e., in the above discussion multiple values of n. These photoluminescent composites present strong resistance to degradation due to chemicals, oxidation, or humidity due to the protecting silica matrix, providing viable routes for the stabilization of HOIS-based LEDs against degradation [70]. Such examples of novel PeLED materials are provided in Fig. 9,

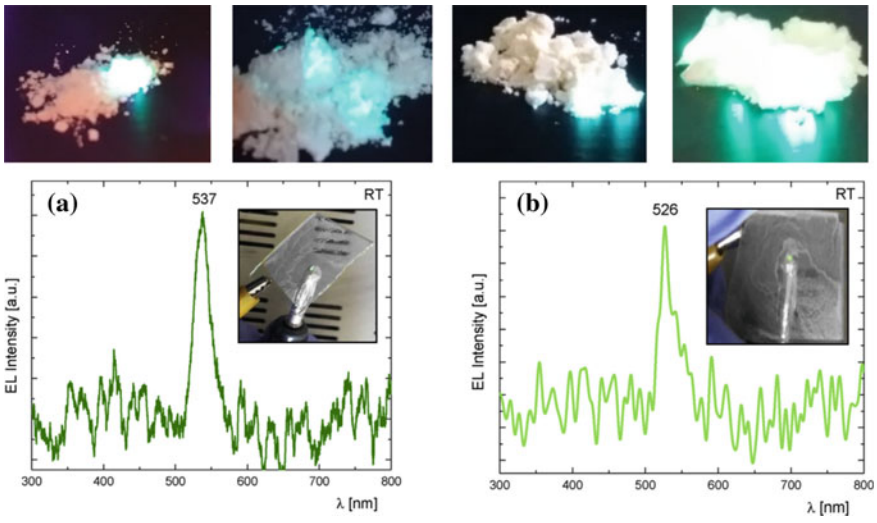

Fig. 9 Top: Images show mesoporous MCM-41 powder, spherical/nonspherical also calcined/non with entrapped mixtures of quasi-2D perovskites as these luminesce with 404 nm UV exciting radiation. Below the EL spectra and images of the single-layer LEDs. The mesoporous powders have been washed from any remaining external perovskite residues. Adapted with permission from Ref. [70].

where the PL of these perovskite-loaded white scattering MCM-41 is observed, along with the EL spectra.

PeLEDs based on entrapped perovskites within other matrices and polymer films have slowly emerged, due to the simplicity of the perovskite synthesis and the novel room temperature phenomena.

It has been possible to eliminate the non-radiative charge recombination and unbalanced charge injection to modify the interface between the HTL and the active HOIS with amphiphilic polymer in order to suppress the non-radiative recombination, yielding devices with 14.4% efficiency [72]. Other groups have shown that polymers with entrapped quasi-2D perovskites can lead up to 20% external quantum efficiency, which is interpreted as 100% internal quantum efficiency [73, 74]. Similarly, octylphosphonic and or oleylamine can be used to cap inorganic 3D perovskite nanoparticles in order to stabilize them and create 6.5% external quantum efficiency diodes [75].

Another effort published was the fabrication of a PeLED device, from a composite film containing a blend of 1D (Meth-H)$CdBr_3$ and 2D $(PhE–H)_2PbBr_4$ HOIS in a 1D:2D 1:1 weight ratio, entrapped within polystyrene matrix. Cd as well as other impurities appears to enhance the PL of 2D HOIS and possibly the EL signal [76]. The final transformed encapsulated perovskite was a mixture of 3D, 2D-like, and 0D perovskites. The intense green light emitted by the LED device was visible with naked eye, in accordance with the EL signal which presented a strong peak at 536 nm. The composite film obtained a protective behavior, since the HOIS blend remained intact after DMF and tap water rinsing procedure [77].

3 Low-Dimensional Hybrid Organic–Inorganic Semiconductors in Lasers

Lasers have undoubtedly attracted the focus of the modern research as these are utilized in a series of end commercial devices. Lately, HOIS have been used for lasing materials due to their stable excitons as well as due to their polaritonic states. Solution-processed 3D and LD HOIS allow for the synthesis of low-cost materials, whose form is in many cases equivalent to that of crystalline HOIS. The films retain the room temperature excitonic states that exhibit high binding energy as well as associated oscillator strength, both which are needed for commercial novel devices. These concepts were realized in a quite long period of time, since the first low threshold perovskite lasing device was reported in 2014 [78], after almost 20 years from the first low-temperature perovskite-based laser that was published by Kondo et al. [79]. The HOIS emission tunability by mere simple chemical substitution, their low cost and synthetic simplicity, their evidenced small defect density, even for the solution-processed films, as well as their increased photoluminescence quantum yield contribute for their usage as lasing materials, where their efficiency may allow for the fabrication of energy-saving devices. Despite their inherent

instability, their low-temperature growth has allowed the realization of low threshold laser devices that work even in steady state at room temperature. In many cases, it would be ideal to the lasing mechanism should the materials involved are formed as wire-like [80]. The active perovskite materials can be either based on 3D, 2D or quasi-2D or mixtures of quasi-2D and 3D HOIS. The lasing mechanism is itself a complex phenomenon, and it can be induced either with optical or electronic means, while lately constant lasing has also been attained. The device geometry can vary, for example, the 3D materials have been reported to attain lasing using whispering gallery mode [81], Fabry–Perot cavities [82], or vertical cavity surface-emitting laser (VCSEL) [83]. Also, the triple cation mixed-halide perovskites have been found to exhibit lasing under nanosecond excitation and it has been found that the material properties allow for emission in the visible or NIR spectrum [84]. Distributed feedback lasers can also be fabricated [84–86], while losses in the 3D materials are of the order of 100 cm^{-1}; in particular, the latter authors have shown that the DFB can be nanoimprinted, while DFB can also implement solution-processed perovskites. Amplified Spontaneous Emission (ASE) can also occur in quasi-2D perovskites at a threshold of $\sim$ 13 $\mu J/cm^2$ at 785 nm [87], while many more groups have put similar complex analysis of quasi-2D lasing [88]. 3D perovskites can also form random lasing devices [89]. Besides the exciton resonance, the 2D HOIS have long known to exhibit lasing characteristics and in fact due to the biexciton resonances [79]. It was unfortunate that the first efforts for the 2D lasers were observed at only low temperatures, up to 40 K, with excitation intensity of 600 kW/cm^2, while the intensity was increased by 30 times at 16 K.

A schematic representation of perovskite-based laser concepts is provided in Fig. 10.

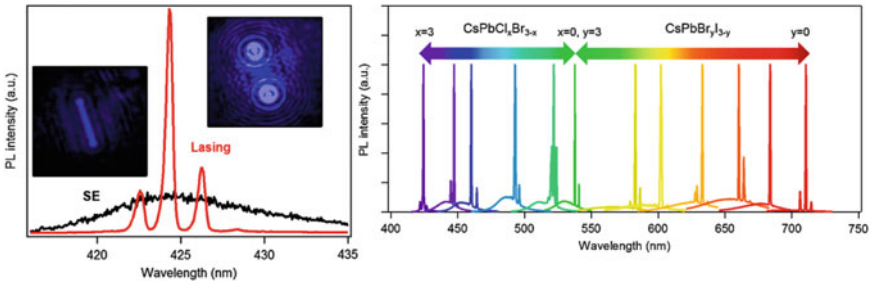

Fig. 10 Left: Emission spectra of a $CsPbCl_3$ NW below and above lasing threshold. The insets are fluorescence images of the NW below and above lasing threshold. The length of the NW is 7.2 μm. Reprinted with permission from ACS Nano 10, 8, 7963–7972. Copyright (2016) American Chemical Society. Right: Broad wavelength-tunable lasing from single-crystal NWs of $CsPbX_3$ (X = Cl, Br, and I). Reprinted by permission from: Ref. [78]. Copyright © 2014, Springer Nature

4 Low-Dimensional Hybrid Organic–Inorganic Semiconductors in Sensors

In the following section, sensors to be reviewed are grouped into the following main categories: photo-, X-ray, gamma-ray, pressure, and chemical detectors. The first three rely on the same essential underlying phenomenon where the electromagnetic radiation alters or induces phenomena in the HOIS; thus, its electrical resistance changes reflecting the radiation intensity and/or energy under detection. The induced phenomena, beyond degradation of the HOIS, can be in most cases an electron/hole pair raised to an excitonic state or created in their conduction and valence bands, respectively. Also, a high exciton density will also create free carriers due to the exciton–exciton collisions; thus, even plasma of bound quasiparticles (excitons) is capable of creating free carriers, which are in turn detectable as resistance change. It is also possible that the system will relax by emission of a secondary photon; thus, perovskites have been used as scintillators. Chemical detectors are such that the molecule under detection will induce changes to the structure of the perovskite or will follow an electrochemical redox reaction on its surface, allowing the detection of either the HOIS redox or the sensing redox current. Pressure sensors function due to the optical properties change that accompany the HOIS unit cell axes decrease. For example, using computationally fast tight-binding parameters from Ref. [90], it is possible to compute the pressure effect on any given HOIS, provided that it is composed out of corner-sharing octahedral.

The aspect of using HOIS as photodetectors also originated 20 years ago, when the active HOIS-related scientific groups were measuring photoconductivity spectra from either grown crystals or from melted HOIS [91, 92]. In fact, photoconductivity spectra had been measured for 2D HOIS [32, 35, 37, 93, 94], as well as for some of the 1D HOIS, with remarkable agreement between the optical absorption and photoconductivity peaks, which is usually the case unless the materials shows the so-called “antibaric” behavior [95]. Similarly, absorption and photoluminescence studies for the 3D and 2D HOIS [96–98] studies have shown that under hydrostatic pressure the energy band gap decreases for the 2D, while it increases for some of the 3D analogs. A useful value for the redshift that allows the 2D perovskites to be used as sensors is the redshift of 90 meV/GPa.

X-ray detectors based on 3D HOIS have lately been shown [99] to be four times more sensitive than the α-Se detectors, while operating with smaller operating fields, while gamma-ray HOIS-based detectors for energies from 50 keV to 10 MeV are sensitive, cheap, and robust due to the combination of the highly mobile and with large lifetime carriers in the HOIS [100].

In the last years, a number of new reports have appeared on pressure mechanisms on perovskites. For example, the compressibility $CH_3NH_3PbX_3$ (X = Br, I) exhibits piezochromism by first becoming lighter in color and then black, while in parallel pressure increase lowers the material’s resistivity, which complicates the calibration of the material as pressure sensor [59]. Some examples of pressure and light sensor results are presented in Fig. 11.

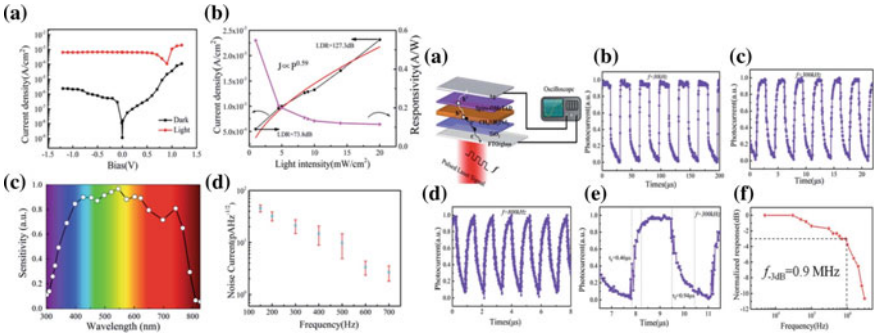

Fig. 11 Left: **a** J–V curves of the perovskite photovoltaic device in the dark and under 650 nm irradiation. **b** Linear dynamic range of the perovskite device and the responsivity. **c** Spectral response of the perovskite photodetector. **d** The noise current of the perovskite device measured under dark condition by using a lock-in amplifier (SR830) from 150 to 700 Hz frequencies at zero bias. Right: Schematic illustration of the perovskite device to measure photo-response speed. Time response characteristics of the device under different pulsed light illuminations, **a** perovskite device under pulsed light illumination (650 nm), **b** 30 kHz, **c** 300 kHz, **d** 800 kHz. **e** The magnified and normalized plots of one response cycle 300 kHz. **f** 3 dB bandwidth of perovskite device Adapted with permission: RSC Adv., 2017, **7**, 18224–18230. Published by The Royal Society of Chemistry

It is important to note that any type of photodetector can be used to detect not only maximum current at the position of the excitonic peak of each particular HOIS, but instead any HOIS can absorb, which alters its electrical resistance, of all photons above its band gap emery, making HOIS ideal for broadband detectors. Thus, besides the strong responsivity that can be attained, better than the Si photodetectors in some cases reaching 3.49 A/W, external quantum efficiency is 1190% at 365 nm, while at 780 nm the respective values are 0.0367 A/W and EQE of 5.84% at 3 V bias [101]. Schottky contacts can easily form upon such measurements; thus, in the early perovskite era, ohmic contacts were fabricated by sacrificing part of the HOIS crystal which would create ohmic contacts; yet, it is interesting that the Schottky diodes are also photoresponsive but no such publication exists to our knowledge.

Lately, a new type of perovskite sensor has also emerged based on its electrochemistry. In particular, Topoglidis and Koutselas group have for the first time used 3D and quasi-2D perovskites adsorbed on mesoporous TiO_2 electrodes that have been used as sensors [102]. In particular, it has been shown that HOIS can be indeed immobilized in a dichloromethane solution with diluted tetrabutylammonium hexafluorophosphate and can serve as the active medium for the detection of the CBr_4 pollutant in the same solution with a detection limit of 20 ppb/mol, where the addition of CBr_4 shifts the cathodic peaks to lower voltages. An example of this technique is provided in Fig. 12 where the blank material CV (black curve) exhibits cathodic peaks that are shifting left from c.a. 0.6–0.2 V upon addition of various concentrations of CBr_4. This work, along with those new research results, where

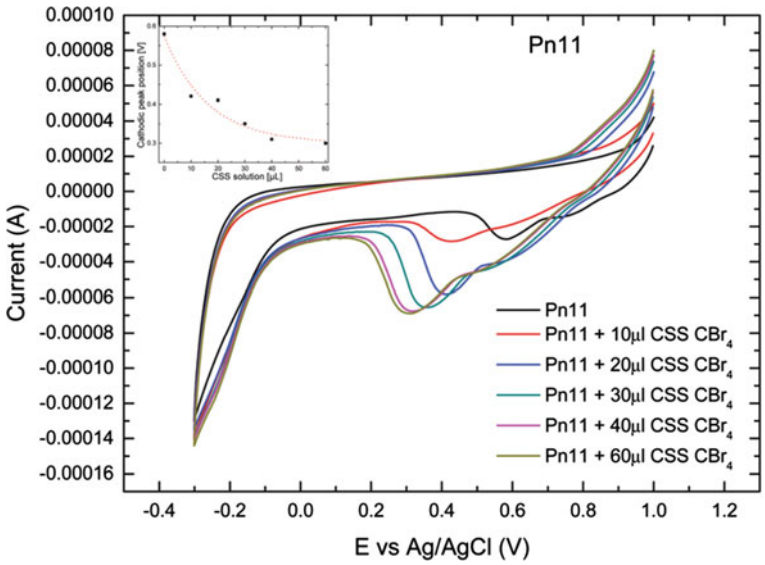

Fig. 12 Cyclic voltammetry scans for Pn11 (phenethylamine$_y$.$CH_3NH_3PbBr_{3-x}Cl_x$) in the presence of increasing amounts of CBr_4 in the solution, at a scan rate of 0.1 V/sec, where 10 μl of CSS is 10 mol of contaminant per 10^9 mol of dichloromethane. The inset shows the dependence of the cathodic peak on the added concentration. Adapted with permission: Mater. Chem. Front., 2018, 2, 730–740. Reproduced by permission of The Royal Society of Chemistry

lead halide perovskites are used in lithium rechargeable batteries, portrays the ability of the perovskites to be used as cheap, application-specific, simple alternative solutions as active materials in a variety of applications. Similarly, to this work, other researchers have also worked on the electrochemistry of perovskites.

5 Low-Dimensional Hybrid Organic–Inorganic Semiconductors in Transistors

Field-effect transistors (FETs) have been traditionally fabricated with amorphous silicon and polysilicon, although different types of materials such as organic molecules, oxides, polymer, MoS_2, and carbon nanotubes have been applied to FETs and investigated to identify their intrinsic properties [103, 104]. Recently, organic–inorganic semiconductors continue to raise considerable excitement as potential alternative channel materials for traditional inorganic materials in FETs. In transistors, current flow occurs due to the majority carriers, which enter through the source (S) and leave through the drain (D), while the gate electrode modulates the conductivity at the gate region. This is a typical architecture for FETs as it illustrated in Fig. 13.

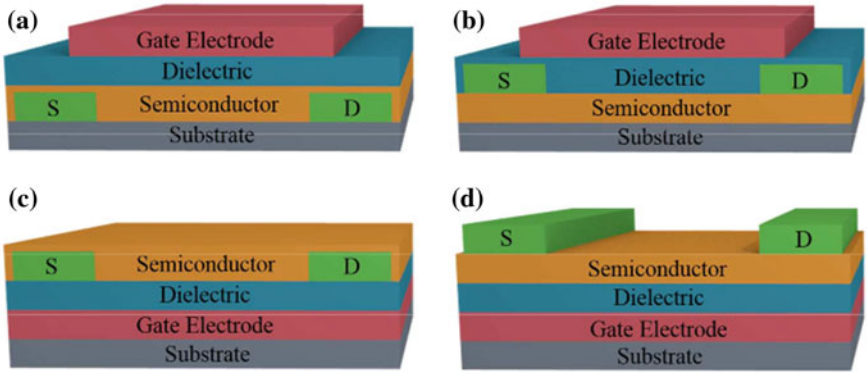

Fig. 13 Schematics of different kinds of FET architectures, where S and D refer to the source and drain electrodes, respectively: **a** top-gate bottom-contact, **b** top-gate top-contact, **c** bottom-gate bottom-contact, and **d** bottom-gate top-contact. Adapted with permission from [105]. Copyright © 2017, American Chemical Society

Mitzi and co-workers, in 1999, developed for the first time an organic–inorganic perovskite thin-film field-effect transistor. In this publication, thin-film FETs are fabricated with spin-coated 2D organic–inorganic hybrid perovskite $(C_6H_5C_2H_4NH_3)_2SnI_4$ as the semiconducting channel by making use of their fast charge-carrier transport properties, promising to be a channel material [106]. Later, efforts from the same group addressed tin(II) iodide-based organic–inorganic hybrid perovskites, in which they substituted the cation site with various phenethylammonium (PEA) series to test the impact of organic cation substitution on FET device performance, yielding an enhanced field-effect mobility of 1.4 $cm^2\ V^{-1}\ s^{-1}$ in the saturation regime [107]. However, the major challenge in halide perovskite FETs is ion migration. Many years later, in 2015, Chin et al. investigated light-emitting FETs using the 3D lead iodide perovskite ($CH_3NH_3PbI_3$) in order to show the relationship between screening effects and ionic transport by lowering the operating temperature of the FETs [108]. In the same year, Li et al. investigated halide perovskite phototransistors but found that the transistor performance with reference to field-effect mobility was relatively poor [109]. Despite the intense effort in the fabrication of perovskite FETs, instability and degradation upon repeated cycling need to be resolved to ensure the successful operation of halide perovskite FETs. To overcome these major problems, Senanayak et al. tried to developed a perovskite FET by changing the PbI_2 precursor mixture to a $Pb(Ac)_2$ precursor. As a result, the electron field-effect mobility and device stability improved, and the electron field-effect mobility of charge transport was 0.5 and 2 $cm^2\ V^{-1}\ s^{-1}$ at 300 and 100 K, respectively. Due to these modifications, the transistors exhibited current increase at the source and drain as well as reduced hysteresis behavior [110]. In addition, Duan and co-workers investigated FET performance using a thermally annealed $MAPbI_3$ microplate, which was entirely encapsulated with a boron nitride (BN) layer for greater stability [111]. This work based on a previous

report studied that the thermal annealing can change the n-type behavior of $CH_3NH_3PbI_3$ to p-type behavior, inducing a substantial decrease in the field-effect mobility [112].

In order to achieve an improved FET device, the main challenges including the charge transport, temperature-dependent transport as well stability should be overcome. However, it is considered that the results in the field of halide perovskite FET devices will reveal further developments in this area.

6 Low-Dimensional Hybrid Organic–Inorganic Semiconductors in Lithium–Ion Batteries

Besides the interesting electronic and photonic properties exhibited by hybrid perovskites, ionic migration allows for a variety of application in electrochemical devices. It is known that hybrid perovskites behave as charge storage materials for lithium–ion battery anodes [113]. The exact mechanism on how lithium–ions interact with the hybrid perovskite structure during the charging process is still an open question [114]. The architecture of a lithium–ion battery is shown in Fig. 14a. When a bias is applied, lithium ions move into the anode and intercalate with the anode material, which means that the battery is charging. When the electrons flow through an external circuit, the lithium ions go back to the cathode through the electrolyte, indicating battery discharge [115]. In 2015, the research group of Peng first reported lithium storage using $CH_3NH_3PbBr_3$ and $CH_3NH_3PbI_3$ with carbon black as the anode material via a hydrothermal method to demonstrate reversible charge–discharge capacities [113]. The first discharge capacity of $CH_3NH_3PbBr_3$

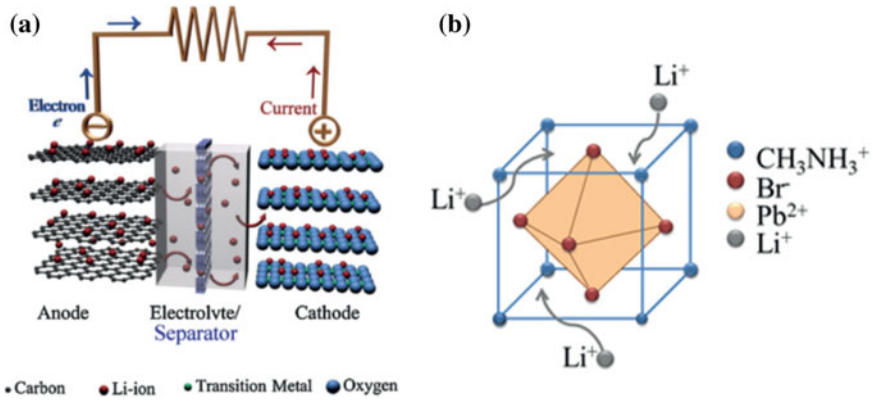

Fig. 14 **a** Schematic of a lithium–ion battery structure, as adapted with permission [115]. Copyright © 2011 Elsevier B.V. All rights reserved **b** 3D framework of a $CH_3NH_3PbI_3$ perovskite intercalated with multiple Li–ions, as adapted with permission [116]. Copyright © 2017, American Chemical Society

was 331.8 mA h g^{-1}, while that of $CH_3NH_3PbI_3$ was 43.6 mA h g^{-1}. It is noted that the discharge capacity was similar to that of a commercial $Li_4Ti_5O_{12}$ anode. Recently, Vicente and Garcia-Belmonte revealed that perovskite-based electrodes exhibit high stability upon electrochemical cycling without severe distortion of the crystal structure, as they demonstrated the intercalation mechanism between $CH_3NH_3PbBr_3$ and Li^+ ions as it shown in Fig. 14b. This fact indicates a topotactic intercalation for Li^+ storage into the perovskite host, without effective structural alternation or rearrangement [116]. This aforementioned performance proves that halide perovskite-based materials are promising candidates for high-power battery applications.

7 Conclusions

Organic–inorganic hybrid perovskites, especially those whose inorganic part is based on metal halides, have obtained a tremendous attention in both industry and academic community, due to their unique optoelectronic properties as their exceptional performance in solar cells, LEDs, lasers, sensors, transistors and lithium–ion batteries has led to their consideration as novel active materials in recent years. As it has been described before, the realm that lies beyond the excellent features of these materials is still facing big challenges due to their toxicity and stability which prevent industrial scale up as well as due to their soft character. Lead halides appear to be the most promising and stable candidates; yet, lead content, however, as small as it may be, must finalize to zero environmental footprint. Multiple research groups have partially addressed these challenges, offering promising alternatives to organic–inorganic metal halide perovskites for developing high-performance and low-cost optoelectronic devices. Given the great progresses made in such a short duration, metal halide perovskite optoelectronics is expected to have a bright future. In all cases, a subjective view is that more work needs to be addressed in energy transfer capable perovskites, to the quasi-2D materials as well as to defect variants of the perovskites as these are much more compatible with non-laboratory conditions, such as an industry, where defects can be used to strengthen the final complex perovskites properties, that lie among complex interactions of electrons, phonons, excitons, polaritons, and light.

References

1. Papavassiliou GC (1981) Luminescence spectra and raman excitation profiles in small CdS particles. J Solid St Chem 40:330–335
2. Papavassiliou GC (1982) Luminescence spectra and raman excitation profiles in small CdS particles. J Mol Struct 79:395–398
3. Ekimov AI, Onushchenko AA (1982) Quantum size effect in the optical-spectra of semiconductor semi-crystal. Sov Phys Semicond-Ussr 16:775–778

4. Weisbuch C, Vinter B (1991) Quantum semiconductor structures. Acad. Press, London
5. Chemla DS (1993) Nonlinear Optics in Quantum-Confined Structures. Phys Today 36:46
6. Feldman M (ed) (2014) Nanolithography: the art of fabricating nanoelectronic and nanophotonic devices and systems. Woodhead Publishing
7. Jongh LJ, Botterman AC, Boer FR et al (1969) Transition temperature of the two-dimensional heisenberg ferromagnet with $S = ½$. J App Phys 40:1363–1365
8. Ishihara T, Takahashi J, Goto T (1989) Exciton state in two-dimensional perovskite semiconductor $(C_{10}H_{21}NH_3)_2PbI_4$. Solid State Comm 69:933–936
9. Papavassiliou GC (1997) Three- and low- dimensional semiconductors inorganic semiconductors. Prog Solid State Chem 25:125–270
10. Li J, Guo H-Y, Zhang X (1994) $CsAg_5Te_3$: a new metal-rich telluride with a unique tunnel structure. J Alloys Comp 116:1–4
11. Zhang Z, Greenbakt M, Goodenough JB (1994) Synthesis, structure, and properties of the layered perovskite $La_3Ni_2O_7-\delta$. J Sol St Chem 108:402–409
12. Arima T, Tokura Y (1995) Optical study of electronic structure in perovskite-type RMO_3 (R = La, Y; M = Sc, Ti, V, Cr, Mn, Fe Co, Ni, Cu). J Phys Soc Jpn 64:2488–2501
13. Murray CB, Nonis DJ, Bawendi MG (1993) Synthesis and characterization of nearly monodisperse CdE (E = sulfur, selenium, tellurium) semiconductor nanocrystallites. J Am Chem Soc 115:8706–8715
14. Rossetti R, Nakahara S, Brus LE (1983) Quantum size effects in the redox potentials, resonance Raman spectra, and electronic spectra of CdS crystallites in aqueous solution. J Chem Phvs 79:1086
15. Papavassiliou GC (1996) Synthetic three-and lower-dimensional semiconductors based on inorganic units. Mol Cryst Liq Cryst 286:231–238
16. Papavassiliou GC, Mousdis GA, Koutselas IB (1999) Some new organic-inorganic hybrid semiconductors based on metal-halide units: structural, optical, and related properties. Adv Mater Opt Electron 9:265–271
17. Papavassiliou GC, Koutselas IB, Terzis A et al (1995) Preparation and characterization of $(C_6H_5CH_2CH_2NH_3)_4BiI_7.H_2O$, $(C_6H_5CH_2CH_2NH_3)_3BiBr_6$ and $(C_6H_5CH_2CH_2NH_3)_3BiCl_6$. Zeitschr fur Naturforschung Sect B 50:1566–1569
18. Papavassiliou GC (1991) Optical and related properties of metal- halide chain compounds: bulk and small particles. In: Prassides K (ed) Mixed valencv systems: application in chemistry, physics and biology, vol 343. Springer, Netherlands, pp 395–400
19. Kojima N, Hasegawa M, Kitagawa H et al (1994) P-T phase diagram and gold valence state of the perovskite-type mixed-valence compounds $Cs_2Au_2X_6$ (X = Cl, Br, and I) under high pressures. J Am Chem Soc 116:11368–11374
20. Shirai M (1993) Electronic band structures of mixed valence compounds $Cs_2Au_2X_6$ (X = Cl, Br, and I). Svnth Metals 55–57:3389–3394
21. Sharada G, Mahale P, Koore BP et al (2016) Is $CH_3NH_3PbI_3$ polar? J Phys Chem Lett 7:2412–2419
22. Kikuchi K, Takeoka Y, Rikukawa M et al (2044) Structure and optical properties of lead iodide based two-dimensional perovskite compounds containing fluorophenethylamines. Curr Appl Phys 4:599–602
23. Wang SM, Mitzi DB, Field CA et al (1995) Synthesis and characterization of $[NH_2C(I):NH_2]_3MI_5$ (M = Sn, Pb): stereochemical activity in divalent tin and lead halides containing single <110> perovskite sheets. J Am Chem Soc 117:5297–5302
24. Vincent BR, Robertson KN, Cameron TS et al (1987) Alkylammonium lead halides. Part 1. Isolated $(PbI_6)^{4-}$ ions in $(CH_3NH_3)_4PbI_6$ $2(H_2O)$. Can J Chem 65:1042–1046
25. Papavassiliou GC, Patsis AP, Lagouvardos DJ et al (1993) Spectroscopic studies of $(C_{10}H_{21}NH_3)_2PbI_4$, $(CH_3NH_3)(C_{10}H_{21}NH_3)_2Pb_2I_7$, $(CH_3NH_3)PbI_3$, and similar compounds. Synth Metals 57:3889–3894
26. Yoon SJ, Draguta S, Manser JS et al (2016) Tracking iodide and bromide ion segregation in mixed halide lead perovskites during photoirradiation. ACS Energy Lett 1:290–296

27. Hoke ET, Slotcavage DJ, Dohner ER et al (2015) Reversible photo-induced trap formation in mixed-halide hybrid perovskites for photovoltaics. Chem Sci 6:613–617
28. Escrig LG, Sempere AM, Sessolo M et al (2015) Mixed iodide-bromide methylammonium lead perovskite-based diodes for light emission and photovoltaics. J Phys Chem Lett 6:3743–3748
29. Papavassiliou GC, Mousdis GA, Koutselas IB (2001) Excitonic bands in the spectra of some organic-inorganic hybrid compounds based on metal halide units. Monatshefte fuer Chemie 132:113–119
30. Hanamura E, Nagaosa N, Kumagai M et al (1988) Quantum wells with enhanced exciton effects and optical non-linearity. Mat Sci Eng B 1:255–258
31. Ishihara T, Takahashi J, Goto T (1190) Optical properties due to electronic transitions in two-dimensional semiconductors $(C_nH_{2n+1}\ NH_3)_2PbI_4$. Phys Rev B 42:11099
32. Papavassiliou GC, Koutselas IB (1995) Structural, optical and related properties of some natural three-and lower-dimensional semiconductor systems. Synth Met 71:1713–1714
33. Kamminga ME, Fang H-H, Filip MR et al (2016) Confinement effects in low-dimensional lead iodide perovskite hybrids. Chem Mater 28:4554–4562
34. Vassilakopoulou A, Papadatos D, Zakouras I et al (2017) Mixtures of quasi-two and three dimensional hybrid organic-inorganic semiconducting perovskites for single layer LED. J All Compds 692:589–598
35. Papavassiliou GC, Mousdis GA, Koutselas IB et al (2001) Excitonic bands in the photoconductivity spectra of some organic-inorganic hybrid compounds based on metal halides units. Int J Mod Phys B 15:3727
36. Kojima A, Ikegami M, Teshima K et al (2012) Highly luminescent lead bromide perovskite nanoparticles synthesized with porous alumina media. Chem Lett 41:397–399
37. Hong X, Ishihara T, Nurmikko AV (1992) Photoconductivity and electroluminescence in lead iodide based natural quantum well structures. Sol State Commun 84:657–661
38. Hattori T, Taira T, Era M et al (1996) Highly efficient electroluminescence from a heterostructure device combined with emissive layered-perovskite and an electron-transporting organic compound. Chem Phys Lett 254:103–108
39. Matsushima T, Fujita K, Tsutsui (2005) Electroluminescence enhancement in dry-processed organic-inorganic layered perovskite films. Jpn J Appl. Phys 44:1457–1461
40. Era M, Morimoto S, Tsutsui T et al (1994) Organic-inorganic heterostructure electroluminescent device using a layered perovskite semiconductor $(C_6H_5C_2H_4NH_3)_2PbI_4$. Appl Phys Lett 65:676–678
41. Koutselas I, Bampoulis P, Maratou E et al (2011) Some unconventional organic-inorganic hybrid low-dimensional semiconductors and related light-emitting devices. J Phys Chem C 115:8475–8483
42. Sutherland BR, Sargent EH (2016) Perovskite photonic sources. Nat Photonics 10:295–302
43. Gebauer T, Schmid G (1999) Inorganic-organic hybrid structured LED's. Z Anorg Allg Chem 625:1124–1128
44. Liang D, Peng Y, Fu Y et al (2016) Color-pure violet-light-emitting diodes based on layered lead halide perovskite nanoplates. ACS Nano 10:6897–6904
45. Adjokatse S, Fang H-H, Loi MA (2017) Broadly tunable metal halide perovskites for solid-state light-emission applications. Mater Today 20:413–424
46. Tan ZK, Moghaddam RS, Lai ML et al (2014) Bright light-emitting diodes based on organometal halide perovskite. Nat Nanotechnol 9:687–692
47. Vassilakopoulou A, Papadatos D, Koutselas I (2016) Room temperature light emitting diode based on 2D hybrid organic-inorganic low dimensional perovskite semiconductor. Appl Mater Today 5:128–133
48. Ma D, He Y (2017) Syntheses of needle-shaped layered perovskite $(C_6H_5CH_2NH_3)_2PbI_4$ bundles via a two-step processing technique. J Alloy Compd 696:1213–1219
49. Seo Y-H, Kim E-C, Cho S-P, Kim S-S, Na S-I (2017) High-performance planar perovskite solar cells: influence of solvent upon performance. Appl Mater Today 9:598–604

50. Qin X, Dong H, Hu W (2015) Green light-emitting diode from bromine based organic-inorganic halide perovskite. Sci China Mater 58:186–191
51. Stranks SD, Burlakov VM, Leijtens T et al (2014) Recombination kinetics in organic–inorganic perovskites: excitons, free charge, and subgap states. Phys Rev Appl 2:034007
52. Tsai H, Nie W, Blancon J-C et al (2018) Stable light-emitting diodes using phase-pure ruddlesden-popper layered perovskites. Adv Mater 30:1704217
53. Vareli I, Vassilakopoulou A, Koutselas I (2018) Defect variants based on the 2D hybrid organic-inorganic low-dimensional semiconductor (4-Fluoro-Phenethylamine-H)$_2$PbBr$_4$ for fabrication of single-layer deep blue LEDs. ACS Appl Nano Mater 1:2129–2142
54. Wang Q, Ren J, Peng X et al (2017) Efficient sky-blue perovskite light emitting devices based on ethylammonium bromide induced layered perovskites. ACS Appl Mater Interfaces 9:29901–29906
55. Hoye RLZ, Chua MR, Musselman KP et al (2015) Enhanced performance in fluorene-free organometal halide perovskite light-emitting diodes using tunable, low electron affinity oxide electron injectors. Adv Mater 27:1414–1419
56. Gong X, Voznyy O, Ankit Jain A et al (2018) Electron–phonon interaction in efficient perovskite blue emitters. Nat Mater 17:550–556
57. Xing J, Yan F, Zhao Y et al (2016) High-efficiency light-emitting diodes of organometal halide perovskite amorphous nanoparticles. ACS Nano 10:6623–6630
58. Bi D, Gao P, Scopelliti R et al (2016) High-performance perovskite solar cells with enhanced environmental stability based on amphiphile-modified $CH_3NH_3PbI_3$. Adv Mater 28:2910–2915
59. Jaffe A, Lin Y, Beavers CM et al (2016) High-pressure single-crystal structures of 3D lead-halide hybrid perovskites and pressure effects on their electronic and optical properties. ACS Cent. Sci. 2:201–209
60. Ha S-T, Shen C et al (2016) Laser cooling of organic–inorganic lead halide perovskites. Nat Photonics 10:115–121
61. Yang Y, Ostrowski DP, France RM et al (2016) Observation of a hot-phonon bottleneck in lead-iodide perovskites. Nat Photonics 10:53–59
62. Li R, Yi C, Ge R et al (2016) Room-temperature electroluminescence from two-dimensional lead halide perovskites. Appl Phys Lett 109:151101
63. Yuanb Z, Shu Y, Xin Y et al (2016) Highly luminescent nanoscale quasi-2D layered lead bromide perovskites with tunable emissions. Chem Commun 52:3887–3890
64. Zhao B, Bai S, Kim V et al (2018) High-efficiency perovskite-polymer bulk heterostructure light-emitting diodes. arxiv:1804.09785
65. Kondo S, Kakuchi M, Masaki AM et al (2003) Strongly enhanced free-exciton luminescence in microcrystalline $CsPbBr_3$ films. J Phys Soc Jpn 72:1789–1791
66. Papavassiliou GC, Mousdis GA, Anyfantis GA (2010) Organic-inorganic hybrid compounds based on lead halide units: preparation from melts and through grinding effects. Luminescence 25:218–219
67. Yoon H-C, Kang H, Lee S et al (2016) Study of perovskite QD down-converted LEDs and six-color white LEDs for future displays with excellent color performance. ACS Appl Mater Interfaces 8:18189–18200
68. Cho H, Jeong S-H, Park M-H et al (2015) Overcoming the electroluminescence efficiency limitations of perovskite light-emitting diodes. Science 350:1222–1225
69. Koutselas I, Dimos K, Bourlinos A et al (2008) Synthesis and characterization of PbI_2 semiconductor quantum wires within layered solids. J Optoectron Adv Mater 10:58–65
70. Vassilakopoulou A, Papadatos D, Koutselas IB (2017) Light emitting diodes based on blends of quasi-2D lead halide perovskites stabilized within mesoporous silica matrix. Micr Mesopor Mat 249:165–175
71. Dirin DN, Protesescu L, Trummer D et al (2016) Harnessing defect-tolerance at the nanoscale: highly luminescent lead halide perovskite nanocrystals in mesoporous silica matrices. Nano Lett 16:5866–5874

72. Zou Y, Ban M, Yang Y et al (2018) Boosting perovskite light-emitting-diodes performance via tailoring interfacial contact. ACS Appl Mater Interfaces 10(28):24320–24326
73. Zhao B, Bai S, Kim V et al (2018) High-efficiency perovskite-polymer bulk heterostructure light-emitting diodes. Nat Photon 12:783–789
74. Tian Y, Zhou C, Worku M et al (2018) Highly efficient spectrally stable red perovskite light emitting diodes. Adv Mater 30:1707093
75. Tan Y, Zou Y, Wu L et al (2018) Highly luminescent and stable perovskite nanocrystals with octylphosphonic acid as a ligand for efficient light-emitting diodes. ACS Appl Mater Interfaces 10:3784–3792
76. Era M, Komatsu Y, Sakamoto N (2016) Enhancement of exciton emission in lead halide-based layered perovskites by cation mixing. J Nanosci Nanotechnol 16:3338–3342
77. Vassilakopoulou A, Papadatos D, Koutselas IB (2018) Polystyrene based perovskite light emitting diode. App Mat Today 12:15–20
78. Xing G, Mathews N, Lim SS et al (2014) Low-temperature solution-processed wavelength-tunable perovskites for lasing. Nat Mater 13:476–480
79. Kondo T, Azuma T, Yuasa et al (1998) Biexciton lasing in the layered perovskite-type material $(C_6H_{13}NH_3)_2Pb1_4$. Solid State Commun 105:253–255
80. Zhu H, Fu Y, Meng F et al (2015) Lead halide perovskite nanowire lasers with low lasing thresholds and high quality factors. Nat Mater 14:636–642
81. Sasaki F, Mochizuki H, Zhou Y et al Optical pumped lasing in solution processed perovskite semiconducting materials: Self-assembled microdisk lasing. Jpn J Appl Phys 55:04ES02
82. Nguyen V-C, Katsuki H, Sasaki F et al (2016) Optically pumped lasing in single crystals of organometal halide perovskites prepared by cast-capping method. Appl Phys Lett 108:261105
83. Sasaki F, Zhou Y, Sonoda Y et al (2017) Optically pumped lasing in solution-processed perovskite semiconducting materials: Self-assembled Fabry–Pérot microcavity. Jpn J Appl Phys 56:04CL07
84. Brenner P, Glöckler T, Rueda-Delgado D et al (2017) Triple cation mixed-halide perovskites for tunable lasers. Opt Mater Express 7:4082–4094
85. Saliba M, Wood SM, Patel JB et al (2016) Structured organic-inorganic perovskite toward a distributed feedback laser. Adv Mater 28:923–929
86. Gong J, Wang Y, Liu S et al (2017) All-inorganic perovskite- based distributed feedback resonator. Opt Express 25:A1154–A1161
87. Leyden MR, Matsushima T, Qin C et al (2018) Amplified spontaneous emission in phenylethylammonium methylammonium lead iodide quasi-2D perovskites. Phys Chem Chem Phys 2018:15030–15036
88. Li M, Gao Q, Liu P et al (2018) Amplified spontaneous emission based on 2D ruddlesden-popper perovskites. Adv Funct Mater 2018:1707006
89. Yakunin S, Protesescu L, Krieg F et al (2015) Low-threshold amplified spontaneous emission and lasing from colloidal nanocrystals of caesium lead halide perovskites. Nat Commun 6:8056
90. Koutselas IB, Ducasse L, Papavassiliou GC (1995) Electronic properties of three- and low-dimensional semiconducting materials with Pb halide and Sn halide units. J Phys Condens Matter 8:1217–1227
91. Papavassiliou GC, Koutselas IB, Mousdis GA, Papaioannou GJ (2002) Some organic-inorganic hybrid semiconductors obtained from melts. In: Graja A, Bulka B R, Kajzar F (eds) Molecular low dimensional and nano-structured materials for advanced applications, vol 59. Springer, Dordrecht, pp 319–322
92. Papavassiliou GC, Mousdis GA, Anyfantis GC (2010) Organic-inorganic hybrid compounds based on lead halide units: preparation from melts and through grinding effects. Z. Naturforsch. 65b:516–520
93. Ogawa T, Kanemitsu Y (eds) (1998) Optical properties of low-dimensional materials. World Scientific

94. Ishihara T, Hirasawa M, Goto T (1995) Optical properties and electronic structures of self-organized quantum well $(C_nH_{2n+1}NH_3)_2PbX_4$ (X = I, Br, Cl). Jpn J Appl Phys 34:71
95. Koutselas IB, Mitzi DB, Papavassiliou GC et al (1997) Optical and related properties of natural one-dimensional semiconductors based on PbI and SnI units. Synth Metals 86:2171–2172
96. Matsuishi K, Suzuki T et al (2001) Excitonic states of layered perovskite semiconductors. Phys Status Solidi 223:177–182
97. Fukumoto T, Hirasawa M, Ishihara T (2000) Two-photon absorption and hydrostatic pressure effects on exciton states in one-dimensional crystal $C_5H_{10}NH_2PbI_3$. J Lumin 87–89:497–499
98. Matsuishi K, Ishihara T, Onari S et al (2004) Optical properties and structural phase transitions of lead-halide based inorganic–organic 3D and 2D perovskite semiconductors under high pressure. Phys Status Solidi 241:3328–3333
99. Wei H, Fang Y, Mulligan P et al (2016) Sensitive X-ray detectors made of methylammonium lead tribromide perovskite single crystals. Nat Photonics 10:333–339
100. Yakunin S, Sytnyk M, Kriegner D et al (2015) Detection of X-ray photons by solution-processed lead halide perovskites. Nat Photonics 9:444–449
101. Hu X, Zhang X, Liang L et al (2014) High-performance flexible broadband photodetector based on organolead halide perovskite. Adv Funct Mater 24:7373–7380
102. Nikolaou P, Vassilakopoulou A, Papadatos D et al (2018) A chemical sensor for CBr_4 based on quasi-2D and 3D hybrid organic-inorganic perovskites immobilized on TiO_2 films. Mater Chem Front 2:730–740
103. Laquindanum JG, Katz HE, Dodabalapur A et al (1996) n-Channel organic transistor materials based on naphthalene frameworks. J Am Chem Soc 118:11331–11332
104. Hamedi M, Forchheimer R, Inganäs O (2007) Towards woven logic from organic electronic fibres. Nat Mater 6:357–362
105. Ward JW, Smith HL, Zeidell A et al (2017) Solution-processed organic and halide perovskite transistors on hydrophobic surfaces. ACS Appl Mater Interfaces 9:18120
106. Kagan C, Mitzi D, Dimitrakopoulos C (1999) Organic-inorganic hybrid materials as semiconducting channels in thin-film field-effect transistors. Science 286:945–947
107. Mitzi DB, Dimitrakopoulos CD, Kosbar LL (2001) Structurally tailored organic-inorganic perovskites: optical properties and solution-processed channel materials for thin-film transistors. Chem Mater 13:3728–3740
108. Chin XY, Cortecchia D, Yin J et al (2015) Lead iodide perovskite light-emitting field-effect transistor. Nat Commun 6:7383
109. Li F, Ma C, Wang H et al (2015) Ambipolar solution-processed hybrid perovskite phototransistors. Nat Commun 6:8238
110. Senanayak SP, Yang B, Thomas TH et al (2017) Understanding charge transport in lead iodide perovskite thin-film field-effect transistors. Sci Adv 3:e1601935
111. Li D, Cheng H-C, Wang Y et al (2017) The effect of thermal annealing on charge transport in organolead halide perovskite microplate field-effect transistors. Adv Mater 29:1601959
112. Conings B, Drijkoningen J, Gauquelin N et al (2015) Intrinsic thermal instability of methylammonium lead trihalide perovskite. Adv Energy Mater 5:1500477
113. Xia H-R, Sun W-T, Peng L-M (2015) Hydrothermal synthesis of organometal halide perovskites for Li-ion batteries. Chem Comm 51:13787–13790
114. Zhang W, Eperon GE, Snaith HJ (2016) Metal halide perovskites for energy applications. Nat Energy 1:16048
115. Song M-K, Park S, Alamgir FM, Cho J et al (2011) Nanostructured electrodes for lithium-ion and lithium-air batteries: the latest developments, challenges, and perspectives. Mater Sci Eng 72:203–252
116. Vicente N, Belmonte GG (2017) Methylammonium lead bromide perovskite battery anodes reversibly host high Li-ion concentrations. J Phys Chem Lett 8:1371–1374
117. Mathies F, Brenner P, Hernandez-Sosa G et al (2018) Inkjet-printed perovskite distributed feedback lasers. Opt Express 26:A144–A152

Chapter 11
Future Challenges of the Perovskite Materials

Lin Fu, Bo Li, Shuang Li and Longwei Yin

1 Lifetime and Stability

Although, both the power conversion efficiencies and working areas of solar cells are steadily improving, the lifetime and stability of perovskite solar cells are still inadequate for practical applications. It is still a challenge to achieving long-term stability of perovskite solar cells. In addition to the considerable research focused on maximizing efficiency, recent researches have also aimed at solar cell stability. Stability problems of perovskite solar cells mainly result from three aspects.

One of the stability issues reported early in the development of perovskite solar cells is originated from the influence of UV light, especially when titanium oxide is employed as the electron transport layer, whether in mesoscopic or planar structures [1, 2]. Numerous researches have shown that oxygen vacancies emerge in titanium oxide when the devices are exposed and operated under UV light. These oxygen vacancies activated the deep trap states, leading to a rapid loss of device performance with a decrease of open-circuit voltage (V_{oc}) and fill factor (FF) [3]. Recent studies have demonstrated that the oxygen vacancies can be inhibited by introducing trivalent cations such as Al^{3+}, Nd^{3+} and, In^{3+}, drastically increasing the UV stability [4, 5]. In addition, the chlorine-passivated titanium oxide compact layer exhibits much enhanced stability in air atmosphere, with <5% decay after continuous maximum power point output tracking. Even though these strategies can decrease the efficiency loss under exposure to UV light, oxygen vacancies are difficult to prevent completely, and thus the UV-induced instability issue will always be present in titanium oxide-based PSCs. Because UV-induced instability comes from the titanium oxide layer, for achieving stability another option is

L. Fu · B. Li · S. Li · L. Yin (✉)
Key Laboratory for Liquid–Solid Structural Evolution and Processing of Materials, School of Materials Science and Engineering, Ministry of Education, Shandong University, Jinan 250061, People's Republic of China
e-mail: yinlw@sdu.edu.cn

N. S. Arul and V. D. Nithya (eds.), *Revolution of Perovskite*, Materials Horizons: From Nature to Nanomaterials, https://doi.org/10.1007/978-981-15-1267-4_11

utilizing materials that either are intrinsically low in oxygen vacancies, or where the oxygen vacancy does not instigate deep trap states. Recently, an electron transport layer material using $BaSnO_3$ has been studied and developed for perovskite solar cells [6]. Unlike titanium oxide-based solar cells, devices with $BaSnO_3$ show much enhanced lifetimes under full light illumination, including both visible and UV lights.

The second obstacle for long-term stability is high temperature and moisture. Most studies of long-term stability are carried out at room temperature or inert atmospheres. In real practical application, solar devices can reach 80 °C under light exposure. Thus, it is essential to consider high temperature for studying long-term stability. The moisture is also a key role in the decomposition of perovskite materials. The degradation of perovskites is attributed to hydrolysis reactions in which the organic species of perovskite reacts with water molecules to release HI and CH_3NH_2. Recently, with the development of rubidium mixed cation perovskite, polymer-coated perovskite cells maintained 95% initial efficiency at 85 °C after 500 h under full solar illumination and maximum power point tracking [7]. In addition, all-metal-oxide p-i-n perovskite solar cells with p-type NiO_x as HTL and n-type ZnO as ETLs, respectively, show improved stability against water and oxygen degradation as compared with the devices with organic transport layers.

The third issue to be considered is continuous light/dark cycle-induced perovskite device fatigue, which causes the performance loss. According to the report, the solar device performance reduces to less than 50% compared with its initial efficiency after dark aging in an open circuit, although performance increases with subsequent continuous illumination [8]. In addition, lower temperature significantly exacerbates the fatigue behavior in dark. The recent research reveals that the cyclic movement of charge carriers gives rise to defects within the perovskite layer, causing both lattice interstitials and ionic vacancies. In some other researches, perovskite solar devices recover their initial efficiency or even increase after dark aging [9]. Thus, how this light/dark cycle influences the stability and performance of perovskite materials is not yet clear, whereas, this issue is essential and must be resolved.

2 Lead Toxicity

Despite impressive performance and extraordinary potentials, perovskite solar cells are still far from real-life availability due to serious issues of toxicity. The toxicity of hybrid lead halide perovskites has been originated to the presence of lead in its chemical composition. Lead easily dissolves in water to form a toxic solution, causing serious environmental pollution, harmful to human beings and the ecosystem. The photovoltaic community is recently well aware of the toxicity issues that came from lead, the anxiety that poses for the public and the factors which argue against the acceptance of this technology [10]. Lead salts are quickly and efficiently absorbed by the human bodies. Lead's toxicity partly results from its

ability to mimic other beneficial metals (calcium, ferrum, and zinc) that participate in biological processes. Children are more vulnerable because the rate of lead ingestion is higher owing to their developing digestive system. To address the toxicity issue, many researches employ the group IV elements, tin (Sn) and germanium (Ge), to replace lead (Pb) [11–13]. Replacing lead by tin and germanium in perovskites can maintain both 3D structure and electronic dimensionality. Indeed, tin-based perovskite devices have shown the best performance among all lead-free perovskite solar cells. It should be noted that tin-based perovskite is less stable than lead-based ones due to the fact that 5 s orbital of tin is higher in energy than 6 s orbital of lead. For instance, the tin-based perovskite solar cells reported usually exhibit less than 10% of photovoltaic conversion efficiency [14]. In addition, the easy oxidation of tin and germanium from the +2 state to the +4 state owing to their high energy states of 4–5 s orbital obstacles them for further application in stable and long-term perovskite photovoltaic devices [15]. To further improve the photovoltaic conversion efficiency of tin-based perovskite solar cells, efforts must be paid to address the instability issue. It thus stimulates the interest to develop new classes of materials which can solve the issues of toxicity and stability while still maintaining the fascinating properties of lead-based perovskite materials.

3 Hysteresis and Measurement Standards

Hysteresis behaviors in perovskite solar cells have been commonly investigated, with more obvious hysteresis behavior in planar devices than that in mesoporous devices, and the devices with metal oxide transport materials typically showing higher hysteresis than the devices with organic transport materials [16]. Hysteresis is less common in inverted perovskite solar cells with organic charge transport materials [17], and it can also be decreased by mixed halide (bromide/iodide) perovskite active materials [18]. One proposed reason for the hysteresis behaviors in the perovskite solar cells can be attributed to the material stoichiometric ratios, which can affect ion diffusion, self-healing ability, and defect concentrations. The perovskite material morphology is also an unnegligible factor, affecting grain boundaries and interfaces of perovskite films [19]. In addition, ferroelectric polarization of the capacitive effects, ionic motion within the perovskite materials, and bias-dependent traps at the interfaces are also considered as the proposed reasons causing the hysteresis behaviors [20]. Phenomena related to hysteresis, such as ion migration [21], ferroelectricity [22], and charge buildup [23] has been extensively investigated. While it is obvious that the perovskite materials are ferroelectrics which can be poled, relative results cast doubt on the ferroelectricity as the possible reason of hysteresis [24]. Ionic mitigation is expected to occur in the perovskite materials, which likely contributes to hysteresis. While the question of the hysteresis has not been fully revealed in detail, it is clear that some practical

guidelines on the test of perovskite solar devices need to be established to handle this phenomenon. It is clearly necessary to report the data with both forward and reverse scanning direction measurement. In addition, scan rate could also affect the experimental results, as well as for keeping the device at a fixed bias before measurement [24].

4 Large-Area and Flexible Devices

Perovskite materials with low formation energies for deposition are compatible with roll-to-roll and other high-volume manufacturing techniques. These features make perovskite solar cells suitable for large-area and flexible devices with low production costs and low capital expenditure [25]. In addition, flexible devices are of interest for various applications where light weight properties and flexibility are desirable, such as unmanned aerial vehicles and wearable electronics. However, the scaling of the perovskite solar devices faces extensive challenges, such as the continuous fabrication of pinhole-free perovskite films and the selective charge carrier transport layers. In the large-area perovskite photovoltaic device, surface defects, bulk defects and interfacial defects can introduce recombination centers, leading to nonradiactive recombination losses at the interface and the interior, thus causing the reduction of open-circuit voltage, short-circuit current and fill factor. In the case of flexible substrates which are suitable for roll-to-roll printing, the additional challenge is to ensure that all the device layers can be fabricated by low temperature and printable processes. To address these challenges, different fabrication procedures and architectures have been developed for large-area and flexible devices prepared such as doctor-blading and printing (inkjet printing, screen printing), direct contact intercalation method, electrode-position and spray-coating [26, 27]. However, considerable efforts are needed to optimize this process for fabricating high-efficient perovskite solar cells due to the fact that films and devices have tremendous sensitivity to some small details in fabrication procedure that affects the formation of perovskite film.

References

1. Pathak SK, Abate A, Ruckdeschel P, Roose B, G€odel KC, Vaynzof Y, Santhala A, Watanabe S-I, Hollman DJ, Noel N, Sepe A, Wiesner U, Friend R, Snaith HJ, Steiner U (2014) Performance and stability enhancement of dye-sensitized and perovskite solar cells by Al doping of TiO_2. Adv Func Mater 24:6046–6055
2. Pathak SK, Abate A, Leijtens T, Hollman DJ, Teuscher J, Pazos L, Docampo P, Steiner U, Snaith HJ (2014) Towards long-term photostability of solid-state dye sensitized solar cells. Adv Energy Mater 4:1301667
3. Leijtens T, Eperon GE, Pathak S, Abate A, Lee MM, Snaith HJ (2013) Nat Commun 4:2885

4. Pathak SK, Abate A, Ruckdeschel P, Roose B, Gödel KC, Vaynzof Y, Santhala A, Watanabe SI, Hollman DJ, Noel N, Sepe A, Wiesner U, Friend R, Snaith HJ, Steiner U (2014) Adv Funct Mater 24:6046
5. Roose B, Gödel KC, Pathak S, Sadhanala A, Baena JPC, Wilts BD, Snaith HJ, Wiesner U, Grätzel M, Steiner U, Abate A (2016) Adv Energy Mater 6:1501868
6. Shin SS, Yeom EJ, Yang WS, Hur S, Kim MG, Im J, Seo J, Noh JH, Seok SI (2017) Colloidally prepared La-doped $BaSnO_3$ electrodes for efficient, photostable perovskite solar cells. Science 356:167–171
7. Saliba M, Matsui T, Domanski K, Seo JY, Ummadisingu A, Zakeeruddin SM, Correa-Baena JP, Tress WR, Abate A, Hagfeldt A, Gratzel M (2016) Incorporation of rubidium cations into perovskite solar cells improves photovoltaic performance. Science 354:206–209
8. Huang F, Jiang L, Pascoe AR, Yan Y, Bach U, Spiccia L, Cheng Y-B (2016) Fatigue behavior of planar $CH_3NH_3PbI_3$ perovskite solar cells revealed by light on/off diurnal cycling. Nano Energy 27:509–514
9. Anaraki EH, Kermanpur A, Steier L, Domanski K, Matsui T, Tress W, Saliba M, Abate A, Gratzel M, Hagfeldt A, Correa-Baena J-P (2016) Highly efficient and stable planar perovskite solar cells by solution-processed tin oxide. Energy Environ Sci 9:3128–3134
10. Hailegnaw B, Kirmayer S, Edri E, Hodes G, Cahen D (2015) Rain on methylammonium lead iodide based perovskites: possible environmental effects of perovskite solar cells. J Phys Chem Lett 6:1543–1547
11. Shao S, Liu J, Portale G, Fang H-H, Blake GR, ten Brink GH, Koster LJA, Loi MA (2018) Adv Energy Mater 8:1702019
12. Yang D, Lv J, Zhao X, Xu Q, Fu Y, Zhan Y, Zunger A, Zhang L (2017) Chem Mater 29:524
13. Liao W, Zhao D, Yu Y, Grice CR, Wang C, Cimaroli AJ, Schulz P, Meng W, Zhu K, Xiong R-G, Yan Y (2016) Adv Mater 28:9333
14. Noel NK, Stranks SD, Abate A, Wehrenfennig C, Guarnera S, Haghighirad A-A, Sadhanala A, Eperon GE, Pathak SK, Johnston MB, Petrozza A, Hertz LM, Snaith HJ (2014) Energy Environ Sci 7:3061
15. Sun P-P, Li QS, Yang L-N, Li Z-S (2016) Nanoscale 8:1503
16. Stranks SD, Snaith HJ (2015) Metal-halide perovskites for photovoltaic and light-emitting devices. Nat Nanotechnol 10:391–402
17. Heo JH, Han HJ, Kim DS, Ahn TK, Im SH (2015) Hysteresis-less inverted $CH_3NH_3PbI_3$ planar perovskite hybrid solar cells with 18.1% power conversion efficiency. Energy Environ Sci 8:1602–1608
18. Zhang T, Chen HN, Bai Y, Xiao S, Zhu L, Hu C, Xue QZ, Yang SH (2016) Understanding the relationship between ion migration and the anomalous hysteresis in high-efficiency perovskite solar cells: A fresh perspective from halide substitution. Nano Energy 26:620–630
19. Frost JM, Walsh A (2016) What is moving in hybrid halide perovskite solar cells? Acc Chem Res 49:528–535
20. Ono LK, Qi YB (2016) Surface and interface aspects of organometal halide perovskite materials and solar cells. J Phys Chem Lett 7:4764–4794
21. Fan Z, Xiao JX, Sun K, Chen L, Hu YT, Ouyang JY, Ong KP, Zeng KY, Wang J (2015) Ferroelectricity of $CH_3NH_3PbI_3$ perovskite. J Phys Chem Lett 6:1155–1161
22. Miyano K, Yanagida M, Tripathi N, Shirai Y (2016) Hysteresis, stability, and ion migration in lead halide perovskite photovoltaics. J Phys Chem Lett 7:2240–2245
23. Tress W, Marinova N, Moehl T, Zakeeruddin SM, Nazeeruddin MK, Grzatzel M (2015) Understanding the rate-dependent J-V hysteresis, slow time component, and aging in CH3NH3PbI3 perovskite solar cells: the role of a compensated electric field. Energy Environ Sci 8:995–1004
24. Leijtens T, Eperon GE, Noel NK, Habisreutinger SN, Petrozza A, Snaith HJ (2015) Stability of metal halide perovskite solar cells. Adv Energy Mater 5:1500963

25. Ye M, Hong X, Zhang F, Liu X (2016) Recent advancements in perovskite solar cells: flexibility, stability and large scale. J Mater Chem A 4:6755
26. Zhou Y, Cai B, Zhou B, Yao TT, Yu W, Liu SZF, Zhang W-H, Li C (2015) An up-scalable approach to $CH_3NH_3PbI_3$ compact films for high-performance perovskite solar cells. Nano Energy 15:670–678
27. Williams ST, Rajagopal A, Chueh C-C, Jen AK-Y (2016) Current challenges and prospective research for upscaling hybrid perovskite photovoltaics. J Phys Chem Lett 7:811–819

Correction to: Introduction to Perovskites: A Historical Perspective

Luis Ortega-San-Martin

Correction to:
Chapter 1 in: N. S. Arul and V. D. Nithya (eds.),
***Revolution of Perovskite*, Materials Horizons:**
From Nature to Nanomaterials,
https://doi.org/10.1007/978-981-15-1267-4_1

The original version of the book was inadvertently published with an incorrect spelling of the text in figure 1 in chapter 1 and the patent numbers has been added to the references of the chapter 1. The chapter and book have been updated with the changes.

The updated version of this chapter can be found at
https://doi.org/10.1007/978-981-15-1267-4_1

N. S. Arul and V. D. Nithya (eds.), *Revolution of Perovskite*, Materials Horizons:
From Nature to Nanomaterials, https://doi.org/10.1007/978-981-15-1267-4_12